LOCAL HYDRODYNAMIC FORCE COEFFICIENTS FROM FIELD DATA AND PROBABILISTIC ANALYSIS OF OFFSHORE STRUCTURES EXPOSED TO RANDOM WAVE LOADING

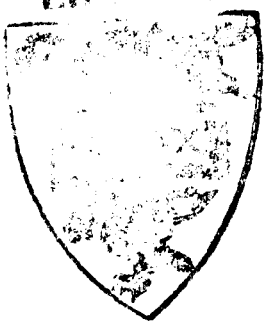

Ph.D. THESIS

1991

U N I V E R S I T Y O F L I V E R P O O L
DEPARTMENT OF CIVIL ENGINEERING

LOCAL HYDRODYNAMIC FORCE COEFFICIENTS FROM FIELD DATA AND PROBABILISTIC ANALYSIS OF OFFSHORE STRUCTURES EXPOSED TO RANDOM WAVE LOADING

Thesis submitted in accordance with
the requirements of the University of Liverpool
for the degree of Doctor of Philosophy

by

G. Najafian, M.Eng

December, 1991

To all those who are actively in search of the truth

SUMMARY

This study is composed of two parts:

Wave Loading on Flexible Cylinders

The objective of this study was to assess the suitability of the relative motion form of Morison's equation in describing random wave loading on flexible cylinders. The data base for this study was eleven 17-minute runs taken from an experimental programme on wave loading on and the response of a flexible (compliant) cylinder at Christchurch Bay, UK (1987). Furthermore, different methods of determining Morison's coefficients from the analysis of wave load data have been critically assessed.

Both probabilistic (method of moments) and time-domain methods have been used in derivation of Morison's coefficients. It has been shown that higher order moments of water particle kinematics needed in the method of moments must be calculated based on the assumption that water particle kinematics are Gaussian distributed. The use of observed values of these higher order moments leads to unstable results.

It has been proved that the Least Square Error Method leads to predicted forces with smaller variances than those of the observed forces. A new method, the Maximum Correlation Method, has been introduced which has all the advantages of the Least Square Error Method but leads to predicted forces with variances equal to those of the observed forces. In this study, there were cases where C_d and C_m from the Maximum Correlation Method were larger than those of the Least Square Error Method by as much as 50%.

C_d and C_m values for design purposes have been suggested. It has been shown that C_m values decrease with increasing values of acceleration parameter (ratio between the standard deviations of the cylinder and water particle accelerations).

The extreme peaks of the predicted forces are lower than those of the observed forces by as much as 40%. However, applying the predicted forces to the cylinder, it was observed that the predicted and observed extreme peaks of response are in reasonable agreement. The overall conclusion of this study is that the relative motion form of Morison's equation with appropriate C_d and C_m values can adequately describe the response of an offshore structure exposed to random wave loading.

Probabilistic Analysis of Offshore Structures

The probability distribution of the response of a jacket-type offshore structure exposed to random wave loading is of Pierson-Holmes type, which is fully defined by its second and fourth statistical moments. These moments are functions of different combinations of nodal forces, which, in turn (according to Morison's equation) are functions of the (Gaussian-distributed) wave-induced water particle kinematics at the nodes. The existing model (Burrows, 1983) is based on the analytical solutions to these expectations. However, due to excessive computer run-time, only a coarse model of the structure can be used in the analysis (say 40 nodes). The purpose of this study was to reduce the computer run-time by introducing appropriate approximations so that a more refined model of the structure can be used in the analysis.

Two different models have been developed for reducing the computer run-time. The polynomial approximation model reduces the computer run time

by about 28 times in comparison with Burrows' model (analytical solutions) while the reduction for the force-correlation model is about 1000 times. As a result, the number of nodes can be increased from 40 (in Burrows' model) to 85 and 200 nodes, respectively. For the test structures used in this study, the maximum level of inaccuracy in the kurtosis (fourth moment) was below 3% and 11% for the first and second models, respectively. In view of uncertainties in the input data to the model (such as environmental conditions, Morison's coefficients, etc.) these levels of inaccuracy are not significant.

ACKNOWLEDGEMENTS

I would like to express my sincere thanks to God for his continuous help and guidance throughout the course of study leading to this thesis. I do not claim that I have seen his helping hand in a physical sense; however, I have felt it. I am most grateful to Him. Very special thanks are also due to Mr. G.R.N. Jamieson, who was always ready to offer genuine help in every possible way. I would also like to thank Professor B. O'Connor, the Head of the Civil Engineering Department, who treated me and other students of the department as his friends.

Many thanks are due to Mrs Susan Zarywacz, who produced the typescript and to Mrs Barbara Cotgreave, who produced the drawings to a very tight deadline. I am also indebted to the Overseas Research Studentship Scheme for providing partial financial support for this study.

TABLE OF CONTENTS

NOTATION

The following is the list of important parameters in the main text. Where notation differs in the Appendices, parameters are defined where they first appear.

a_d^2	Contribution of the drag force to the variance of the observed force.
a_e^2	Error coefficient in the Least Square Error Method.
a_i^2	Contribution of the inertia force to the variance of the observed force.
[c]	Matrix of cross-covariances.
C_a	Added mass coefficient.
C_d	Drag coefficient.
C_m	Inertia coefficient.
$C_{x,y}( )$	Cross-covariance function.
d	Water depth.
D	Cylinder diameter.
$D(\omega,\theta)$	Spreading function.
E[ ]	Expected value operator.
E_1 to E_{24}	Abbreviations for expectations.
f_v	Vortex-shedding frequency.
f_s	Cylinder's natural frequency.
F_d	Drag component of Morison's force.
F_i	Inertia component of Morison's force.
F_r	Relative force, Equations (9.17c) and (9.17d).
g	Gravitational constant.
$G_{xx}(\omega)$	One-sided spectral density function of random process x(t).
$G_{x,y}(\omega)$	Cross-spectrum between x and y.
H	Wave height.
$H_{1/3}$	Significant wave height.
H_s	Significant wave height.
k	Wave number = $2\pi/L$.
K	Keulegan-Carpenter Number, Equation (9.1a).
$\hat{k}_d$	$\rho DL/2$.
$\hat{k}_i$	$\rho\pi D^2L/4$.
k_d	$C_d\ \hat{k}_d$.

k_i	$C_m \hat{k}_i$.
L	Cylinder length.
m_n	nth spectral moment.
$p(\ )$	Probability density function (pdf).
$P(\ )$	Cumulative probability distribution (cdf).
$Q(\ )$	Probability of exceedence.
r	Cylinder displacement.
$\dot{r}$	Cylinder velocity.
$\ddot{r}$	Cylinder acceleration.
R_e	Reynolds Number.
$R_{xx}(\ )$	Auto-correlation function of x(t).
$R_{xy}(\ )$	Cross-correlation function of x(t) and y(t).
S	Strouhal Number.
S_i	Flexibility coefficient due to load at node i.
t	Time.
T	Wave period or time duration.
T_z	Mean zero up-crossing period.
u	Water particle velocity in the x direction.
$\dot{u}$	Water particle acceleration in the x direction.
u_r	Relative velocity $u - \dot{r}$.
$\dot{u}_r$	Relative acceleration $\dot{u} - \ddot{r}$.
$\bar{u}$	Current component in the x direction.
v	Water particle velocity in the y direction.
$\dot{v}$	Water particle acceleration in the y direction.
$x_{2i-1} =$	$(0.50\ \rho D C_d L)_i^{1/2} u_i$.
$x_{2i} =$	$(\rho C_m L * \pi D^2/4)_i \dot{u}_i$.
y	Response.
z	Elevation above mean water level.
β	Frequency parameter, Equation (7.22).
β_f	Kurtosis of force.
Γ_h	Horizontal depth attenuation factor, Equation (3.64).
Γ_w	Vertical depth attenuation factor, Equation (3.65).
ϵ	Spectral bandwidth.
η	Water surface elevation with respect to mean water level.
ν	Kinematic viscosity.
ρ	Fluid density.
$\rho_{x,y}$	Central correlation coefficient between x and y, Equation (9.46b).

$\rho_{x,y}$ [a]	Absolute correlation coefficient between x and y, Equation (9.46a).
σ	Standard deviation.
σ^2	Variance.
τ	Time lag.
ω	Wave frequency = $2\pi/T$.
ω_p	Peak frequency.
φ	Phase angle.

Symbols

$(\bar{})$	Mean value.
$(\ )_{rms}$	Root mean square.
$(\ )_o$	Observed.

Chapter 1

Introduction

1.1 GENERAL INFORMATION

Offshore structures are used for many different purposes such as ocean energy extraction, navigational aid, microwave transmission, mining the ocean floor, and a few even serve as resort hotels. These, however, constitute a small percentage of the many thousands of offshore structures in operation round the world; the great majority of these structures are used in exploration, drilling, production, storage and transportation of oil and gas.

Exploration drilling is done from carefully positioned ships or mobile platforms. In contrast, production and storage operations involve more permanent structures. Concrete gravity platforms and steel jacket-type offshore structures are used for depths up to 250 and 360 metres respectively. Steel compliant towers, which are stabilised by guy lines anchored to the sea floor, are economical for depths between 300 and 750 metres. For deeper waters, tension-leg platforms, semi-submersible platforms and ship-controlled submerged systems are suitable (Wilson, 1984).

Among these different types of permanent structures, jacket or template types are most common. There were about 2000 of these units by 1980, some of them in deep waters. The tallest one was the ten-legged, 380m high Cognac unit located in the Gulf of Mexico in a water depth of 305m. 59000 tons of steel was used in its manufacture. Although some of these structures are in deep waters, the majority are in depths less than 90m.

A jacket structure consists of a prefabricated steel substructure and a prefabricated steel deck sitting on top of the substructure. The

substructure extends from the sea floor to above the water surface and is composed of vertical or slightly inclined tubular legs with K or X type tubular cross braces. The deck is supported by pipe piles driven through the legs of the substructure to the sea floor. The piles not only support the deck but also fix the structure to the sea floor against lateral loading (Dawson, 1983).

1.2 ANALYSIS AND DESIGN OF OFFSHORE STRUCTURES

Offshore structures can fail due to foundation failure, or the failure of individual load-carrying members of the substructure. The latter can be due to fatigue, resulting from stress reversals associated with the passage of each wave, or due to first excursion, i.e. due to the encounter of loads larger than the design loads. Therefore, these structures must be designed against both fatigue and first excursion failures.

The design of an (offshore) structure progresses through the following stages:

1. Select a preliminary design to satisfy the functional requirements of the structure based on experience.
2. Determine the external loads on the structure.
3. Analyse the structure to calculate the structural response, e.g. internal forces, stresses, displacements, etc.
4. Modify the structure so that it can safely and economically carry the external and internal loads.
5. Return to step 2 and repeat the process until no modification is required.

As observed, determination of (external) loading and structural analysis are key functions in the process of the design of a structure. This thesis is a contribution to these two key functions with regard to offshore structures as further explained in Sections 1.3 and 1.4.

1.3 WAVE LOADING ON FLEXIBLE CYLINDERS

For an offshore structure, wind, wave, current, gravity, earthquake, and the forces associated with the transportation and installation of the structure at its intended site, are all important sources of (external) loading. However, in most cases, the most important load is due to wind generated waves. Therefore, the accurate estimation of wave loading on cylindrical components of an offshore structure is a major design consideration.

The majority of steel offshore structures are jacket ones in water depths of less than 90m. The fundamental frequency of these structures is considerably larger than characteristic wave frequencies so that these structures can be treated as rigid structures and hence wave loading on individual members can be calculated assuming that each member is a fixed rigid cylinder. However, elements of these structures and their associated systems, such as riser arrays, may have natural frequencies in the same range as wave frequencies. For these elements, oscillations along the predominant wave direction and transverse to it may build up, which in turn may modify the wave loading on them.

For deeper water applications, the cost of scaling up jacket structures are prohibitive and consequently, there is a tendency for these structures to be either much more flexible jacket ones or compliant structures which are not rigidly attached to the sea bed. In both

cases, the movement of the structure is significant and the effect of this movement on wave loading on individual cylindrical members must be considered. Apart from the motion of complete structures, individual members may respond dynamically to wave loading, as was the case for fixed, rigid structures.

In view of the above discussion, it is clear that research on wave loading on both fixed and flexible cylinders is of great value in the safe and economical design of offshore structures.

Extensive small scale experiments have been conducted to study the mechanism of wave loading on cylindrical members and the effect of flexibility of members on that mechanism. However, there exists a major problem in the extrapolation of the results to full-scale conditions, where for example Reynolds numbers are much higher than those attainable in conventional laboratory experiments. Although some attempt has been made to do laboratory experiments with high Reynolds numbers (Chaplin, 1988a and 1988b; Bearman et al, 1985), it is fair to say that at present, one cannot simulate all aspects of real sea conditions, such as directionality, randomness, high Reynolds numbers, etc. in the laboratory.

Several major field experiments have been completed to study wave loading on rigid cylinders. One can refer to the Ocean Test Structure (1976-1977) (Haring et al, 1979) and Christchurch Bay Tower (1976-1982) (Bishop et al, 1980) experiments. However, no similar experiments directed to wave loading on flexible cylinders had been undertaken at the time of commencement of the present work.

However, in 1987, a joint government and industry project was established to carry out an experimental programme on the wave loading on and dynamic response of a flexible (compliant) vertical cylinder in real sea conditions. British Maritime Technology Limited (BMT) took responsibility for the manufacture and operation of the flexible cylinder. The Department of Civil Engineering at the University of Liverpool was commissioned to carry out analysis of data for this project and the work undertaken by the writer forms part of this thesis. In particular, the adequacy of the relative motion form of Morison's equation (Morison et al, 1950) in describing wave loading on flexible cylindrical members has been investigated and suitable values of drag and inertia coefficients for design purposes have been recommended. Particular attention has been given to different methods of obtaining the coefficients. Unsuitable common methods in the literature have been identified, and a new method has been introduced.

1.4 PROBABILISTIC ANALYSIS OF FIXED JACKET-TYPE OFFSHORE STRUCTURES EXPOSED TO RANDOM WAVE LOADING

Comparison of Probabilistic and Deterministic Methods

There are two distinct approaches to the analysis and design of offshore structures. One is deterministic, the other probabilistic.

In the deterministic design, the long-term distribution of wave heights is needed for both fatigue and first excursion failure analysis. The distribution is obtained from the convolution of the short-term distributions of wave heights and the long-term distribution of sea states or wave conditions (Battjes, 1970). The structure is exposed to regular waves with specified heights and periods and the response is calculated. For fatigue analysis, the response (stress range) is needed

for the entire range of wave heights, while for the first excursion failure analysis, the response is obtained for extreme conditions characterised by the '50 year' or '100 year' design wave. Several suitable periods are considered for each wave height.

In probabilistic methods, the long-term distribution of the response peaks is required. The distribution is obtained from the convolution of the short-term distributions of the response peaks with the long-term distribution of sea states, in a manner similar to that of the wave heights. Each short-term sea state is characterised by an appropriate water surface elevation spectrum, covering a wide range of frequencies. For fatigue analysis, the entire range of stress ranges (which are closely associated with stress peaks) is divided into a number of intervals and the damage due to each interval is calculated. The total damage is the sum of the damages due to all the intervals. For first excursion failure analysis, the '50 year' or '100 year' response peak is generally adopted as the basis of design.

The deterministic method fails to take account of the random nature of sea waves and hence has serious shortcomings when applied in design. For example, it is known that a particular regular wave does not lead to the maximum for all responses, on all parts of the structure. In other words, one particular response variable may be larger under regular wave A, while another response variable may be larger under regular wave B. Consequently, in the deterministic method, the risks are associated with the environmental conditions, i.e. one can calculate the probability that the '50 year' design wave will be exceeded at least once during the service life of the structure; however, one cannot convert this into the risk of failure for

individual members. In fact, every member will have a different unknown probability of failure.

In contrast, probabilistic methods do take account of the random nature of the sea. Thus, they are more appropriate for the design of offshore structures. In these methods, risk is associated with the response itself, and hence members can be designed so that they will all have equal risks of failure during the service life of the structure, (Inglis et al, 1985).

Probability Distribution of Response

The short-term distribution of response peaks is required in probabilistic methods. This obviously depends on the short-term distribution of Morison-type nodal loads. Assuming that water particle kinematics are Gaussian distributed, the probability distribution of the nonlinear Morison loading is of Pierson-Holmes type (Pierson and Holmes, 1965) and is fully expressed by its first four statistical moments. In the absence of current, the first and third moments are zero, and hence the distribution is defined by its second and fourth order statistical moments.

Due to the linear nature of the relationship between response and loading (for fixed offshore structures which do not respond dynamically to the wave loading), it is expected that the probability distribution of the response would be similar to that of the wave loading. Tickell (1977) confirmed the above expectation by analysing experimental and real ocean data. Therefore, in the absence of current, the distribution of response is fully defined by its second and fourth order statistical moments.

Determination of the Probability Distribution of Response in Time, Spectral or Probability Domain

Probabilistic analysis of structures can be attempted in the spectral, time or probability domains. The spectral analysis leads to the short-term frequency spectrum of response. Then, it is assumed that the response is Gaussian-distributed, and hence is fully defined by its second moment, which is equal to the area under the spectrum. But, this assumption is not justified due to the nonlinear nature of Morison loading. As stated before, the real distribution is of Pierson-Holmes type, which has higher probability of exceedence in its tails (thicker tails) compared to an equivalent (same variance) Gaussian distribution. Therefore, the Gaussian assumption leads to the underestimation of extreme peaks of response when the drag component of Morison loading is significant. On the positive side, the method can be applied to dynamic structures.

In the time domain, the Morison-type nodal loads are calculated from simulated water particle kinematics (Borgman, 1969b). The analysis of the structure leads to a time history of response, whose first 4 moments can be determined directly. However, in order to get stable results, long records are needed (typically in excess of 10,000 time steps); therefore, the computer run-time is prohibitive (Burrows, 1982). On the positive side, the method takes account of the non-linearity of Morison loading and is applicable to dynamic structures and the presence of currents leads to no difficulty.

Finally, the method can be applied in the probability domain. In this method, the 2nd and 4th order statistical moments of response are calculated in terms of the variances and cross-covariances of water

particle kinematics at different nodes, which are then used to establish the probability distribution of the response. Following this approach, Burrows (1977, 1979, 1983) produced a novel probabilistic model.

The model is only applicable to rigid structures, i.e. to structures whose fundamental natural frequencies are well above the frequency range of the waves, and hence inertia forces due to dynamic effects are negligible. This, however, is not a serious drawback since, as stated before, the great majority of these structures are in water depths less than 90m, and do not respond dynamically to wave loading. Nevertheless, the use of the model is limited due to excessive computer run-time. In present application, the structure must be idealised by a relatively small number of nodes (say 40), which is not enough for adequately representing the continuous loading on the structure. It has been the aim of this study to find ways of reducing the computer run-time substantially so that the model can be applied in the design of real structures with many nodes.

Reduction in computer run-time has herein been accomplished in two different ways. The polynomial approximation method reduces the computer run-time by about 28 times; hence the number of nodes can be increased from 40 to about 85. The inaccuracies are less than 3%. The force correlation method reduces the computer run-time by more than 1000 times so that the number of nodes can be increased to about 200 nodes. The inaccuracies are less than 11%. It should be emphasised that the above two models, in their present form, do not account for the presence of current or the intermittency of wave loading in the splash zone, as is the case with Burrows' model.

1.5 OUTLINE OF THE TEXT

The technical aspects of the compliant cylinder (its structure and instrumentation) together with the basic properties of wave records used in the Christchurch Bay Tower Project are discussed in Chapter 2.

Chapter 3 describes the short-term properties of sea waves while Chapter 4 is concerned with the evaluation of the short-term properties of wave records used in this study. Derivation of long-term properties of sea waves from their short-term properties are discussed in Chapter 5.

The data supplied by BMT included the cylinder displacements; however, in the relative motion form of Morison's equation, it is the cylinder kinematics which are required. Furthermore, due to cylinder movement, the perforated balls, used in measuring water particle kinematics were mounted on the small rigid column of the tower, which is some 12m distance from the complaint cylinder. Therefore, it was necessary to predict water particle kinematics at the cylinder by shifting (translating) them from their point of measurement to the cylinder axis. These two topics are discussed in Chapter 6.

Chapter 7 is concerned with fluid loading on submerged cylinders. In the first part, ideal fluid loading on cylinders is discussed while the second part is devoted to real fluid loading on both rigid and flexible cylinders. The spectral and probabilistic properties of in-line wave loading is described in Chapter 8.

Chapter 9 is devoted to the derivation of Morison's coefficients from the Christchurch Bay data. The performance of the relative motion form

of Morison's equation in predicting the in-line forces is investigated by comparing the predicted and observed forces in both probability and time domains. Furthermore, different methods of analysis of the data are critically assessed; shortcomings of some of these methods are discussed and alternative new methods are recommended.

Probabilistic analysis of fixed jacket-type offshore structures is the subject of study in Chapter 10. The two methods for reducing the computer run-time are described. Furthermore, by applying the models to a few sample structures, it is shown that they are reliable.

The main conclusions of this thesis are discussed in Chapter 11.

Appendix A is devoted to the study of an ambiguity in the cylinder displacement. The source of the problem and its effect on the cylinder displacement is fully described. The effect of this error on the derived Morison's coefficients is discussed in Chapter 9 and it is shown that the effect is negligible. Methods of analysis of random data is presented in Appendix B, which is taken from Burrows (1982). Finally, Appendix C is concerned with sampling variability due to the finite-length of the records used in Christchurch Bay data analysis.

Chapter 2

Technical Aspects of and Data Base for Christchurch Bay Tower Compliant Cylinder Project

INTRODUCTION

This chapter is devoted to the technical aspects of the compliant cylinder project together with a brief description of the data base collected for the experimental study of random wave loading on the compliant cylinder. Section 2.1 is devoted to general information about the tower and environmental conditions at its site. Section 2.2 is concerned with the structure of the cylinder. Instruments used for data gathering and the resulting data base are briefly discussed in Sections 2.3 and 2.4, respectively.

2.1 GENERAL INFORMATION

The compliant cylinder was mounted on BMT's test tower, a small offshore structure built purposely for the study of wave induced forces on cylinders in real sea conditions at a suitably large scale. As shown in Figure 2.1, the tower is composed of a large central column of 2.80m diameter and a small rigid column of 0.48m diameter on which velocity measurement probes are mounted. Figure 2.2 shows the position of the compliant (flexible) cylinder with respect to the tower. The tower is deployed in Christchurch Bay, Hampshire, off the South Coast of England, (Figure 2.3) in a water depth of approximately 9m.

The highest waves at Christchurch Bay occur when winds blow from the southwest, due to the long fetch along the English Channel in that direction. Several storms occur every winter, during which the wave heights can reach as high as 15m in deep waters near Christchurch Bay; however, the shoaling water of Christchurch Bay Ledge attenuates waves at the tower, so that the maximum wave height is approximately 7m. In storm conditions, significant wave heights are often in the range of 2.5-3m and zero-crossing periods are in the range of 5 to 7 seconds.

Tidal currents can be up to 0.60m/s and are almost perpendicular to predominant wave directions (Tickell et al, 1989; Bishop, 1982).

2.2 THE STRUCTURE OF THE COMPLIANT CYLINDER

The smooth cylinder is composed of two concentric cylinders. The inner fibreglass tube is continuous over the entire length of the cylinder (12.197m), but the outside cylinder with a diameter of 0.480m is divided into 6 sections which can be locked together by means of five hydraulic joints. The joints are activated by telemetered signals from a shore station. A diagram of the cylinder is shown in Figure 2.4.

Each section of the outer cylinder is mounted to the inner core tube by two thin diaphragms at its ends. When the outer sections are not connected to each other, they contribute mass but little bending stiffness; this leads to the lowest natural frequency (F6=0.46Hz). When two adjacent sections are locked together, there are three diaphragms between the core tube and the combined section and consequently the deflections of the core tube within the section are small. Therefore, the bending stiffness of the overall cylinder is increased leading to a higher natural frequency. Progressive locking of more sections lead to higher natural frequencies. When all the sections are locked together, the maximum natural frequency (F1=1.69Hz) is obtained (Bishop et al, 1982).

At each end of the cylinder there is a triangular array of links which incorporate three force transducers. This system provides for the measurement of total shear force and also gives effective pin jointing at the ends of the cylinder, that is, the system provides horizontal

constraint but vertical and rotational freedom (Bishop, 1988; Tickell and Burrows, 1988).

2.3 INSTRUMENTATION

There are three measurement stations along the length of the cylinder, known as Levels 2, 3 and 4, as shown in Figure 2.4. At each station, there is a force sleeve (ring) with three force transducers. The measured force consists of the hydrodynamic force and an inertia force due to cylinder acceleration. There are accelerometers at each measurement station. The measured acceleration is composed of two components: one due to horizontal cylinder acceleration and the other due to gravity (Bishop, 1988). The structure of the force sleeve, the derivation of hydrodynamic forces from measured forces, and the derivation of cylinder accelerations and displacements from measured accelerations (as done by BMT) are fully discussed in Appendix A.

Water particle kinematics have been measured by perforated ball instruments, at the same depth as the force rings. However, due to the cylinder movement, the perforated balls could not be mounted on the cylinder itself. Thus, they were retained on the small rigid column of the tower, which is some 12m distance from the compliant cylinder (Figure 2.2).

The perforated ball instruments were of 100mm diameter. The instrument measures the force exerted on the ball by water particle kinematics in two orthogonal directions, via strain gauges at the root of the cantilever on which the ball is mounted (Bishop et al, 1984; Shipway, 1984). The force on the ball is used to derive both the particle

velocity and acceleration through laboratory calibrated drag and inertia coefficients. Bishop (1979) has fully described the method.

Water surface elevation data were obtained from a wave buoy some 100m distance from the tower. There were also two capacitance wave gauges at a position near the test cylinder which unfortunately malfunctioned during the measurement period (Bishop, 1988).

2.4 DATA BASE

Various transducers were monitored during the experiments conducted during the winter of 1987 and the data have been recorded on magnetic tape. BMT preprocessed the instrument readings and supplied the data in the form of 41 data channels, as listed in Table 2.1. Each data record consists of 13816 data points at a sampling interval of 0.075472 seconds. All the time series have been subject to BMT quality checking routines.

BMT selected 11 data sets or runs for analysis. The basic properties of these runs are given in Table 2.2. The table includes the estimated damped natural frequencies which were obtained from displacement spectra. For the purposes of the present study, Runs 01, 08, 13, 15 and 23 were selected for more detailed analysis and discussion. These cover the cylinder in its most rigid condition (Run 01), an intermediate frequency setting (Run 08) and three runs for the cylinder in its most flexible condition (Runs 13, 15 and 23).

Throughout this report, the data records have been referred by their filenames, e.g. storm.13.chan.16. This refers to the data in channel 16 (hydrodynamic force at level 3, X direction) for Run number 13. The

word 'storm' only refers to the number of data set not to separate storm events. In fact, all the data were taken during two separate winter storms which occurred on the 6th February and 27th March 1987.

TABLE 2.1.
DATA CHANNELS AND UNITS (TICKELL AND BURROWS, 1989)

Basic Data

Digitising Frequency	f_s = 13.25Hz
Time Step	Δt = 0.075472 secs
Sample Size (Max)	N = 13816
Sample Duration	T_s = 1042.7 secs
Force Sleeve Diameter	D = 480mm
Force Sleeve Length	ι = 535mm
Seawater Density	ρ = 1025 kg/m^3
Structural Steel Density	ρ_s = 7700 kg/m^3

Channel Numbers

01 Accelerometer Buoy (η, m)

02 X Top Shear (T_x, KN)
03 Y Top Shear (T_y, KN)

04 X Force Level 2 (F_{x2}, KN)
05 Y Force Level 2 (F_{y2}, KN)

06 X Accelerometer Measurements Level 2 ($\ddot{r}_{x2}$, g)
07 Y Accelerometer Measurements Level 2 ($\ddot{r}_{y2}$, g)

08 X Displacement Level 2 (r_{x2}, m)
09 Y Displacement Level 2 (r_{y2}, m)

10 X Particle Velocity Level 2 (u_2, m/s)
11 Y Particle Velocity Level 2 (v_2, m/s)
12 Z Particle Velocity Level 2 (w_2, m/s)

13 X Particle Acceleration Level 2 ($\dot{u}_2$, m/s^2)
14 Y Particle Acceleration Level 2 ($\dot{v}_2$, m/s^2)
15 Z Particle Acceleration Level 2 ($\dot{w}_2$, m/s^2)

16 X Force Level 3 (F_{x3}, KN)
17 Y Force Level 3 (F_{y3}, KN)

TABLE 2.1.
DATA CHANNELS AND UNITS (CONTINUED)

18 X Accelerometer Measurements Level 3 ($\ddot{r}_{x3}$, g)

19 Y Accelerometer Measurements Level 3 ($\ddot{r}_{y3}$, g)

20 X Displacement Level 3 (r_{x3}, m)

21 Y Displacement Level 3 (r_{y3}, m)

22 X Particle Velocity Level 3 (u_3, m/s)

23 Y Particle Velocity Level 3 (v_3, m/s)

24 Z Particle Velocity Level 3 (w_3, m/s)

25 X Particle Acceleration Level 3 ($\dot{u}_3$, m/s^2)

26 Y Particle Acceleration Level 3 ($\dot{v}_3$, m/s^2)

27 Z Particle Acceleration Level 3 ($\dot{w}_3$, m/s^2)

28 X Force Level 4 (F_{x4}, KN)

29 Y Force Level 4 (F_{y4}, KN)

30 X Accelerometer Measurements Level 4 ($\ddot{r}_{x4}$, g)

31 Y Accelerometer Measurements Level 4 ($\ddot{r}_{y4}$, g)

32 X Displacement Level 4 (r_{x4}, m)

33 Y Displacement Level 4 (r_{y4}, m)

34 X Particle Velocity Level 4 (u_4, m/s)

35 Y Particle Velocity Level 4 (v_4, m/s)

36 Z Particle Velocity Level 4 (w_4, m/s)

37 X Particle Acceleration Level 4 ($\dot{u}_4$, m/s^2)

38 Y Particle Acceleration Level 4 ($\dot{v}_4$, m/s^2)

39 Z Particle Acceleration Level 4 ($\dot{w}_4$, m/s^2)

40 X Bottom Shear (B_x, KN)

41 Y Bottom Shear (B_y, KN)

Run Number	Day & Time	Water Depth (m)	Surface Elevation Standard Deviation (m)	Level	Mean Velocity (m/s)		Frequency Setting	Estimated Damped Natural Frequency (Hz)
					x	y		
01*	37 10.33	9.21	0.343	2	0.22	0.41	F1	1.69
				3	0.14	0.44		
				4	0.12	0.44		
02	37 10.56	9.24	0.351	2	0.22	0.44	F2	1.27
				3	0.18	0.48		
				4	0.14	0.48		
06	37 12.27	9.28	0.402	2	0.26	0.42	F6	0.46
				3	0.17	0.47		
				4	0.15	0.48		
07	37 12.50	9.28	0.428	2	0.26	0.41	F5	0.49
				3	0.17	0.47		
				4	0.15	0.48		
08*	37 13.11	9.27	0.395	2	0.22	0.41	F4	0.73
				3	0.16	0.46		
				4	0.14	0.47		
09	37 13.34	9.27	0.380	2	0.19	0.41	F3	0.93
				3	0.13	0.46		
				4	0.10	0.49		

TABLE 2.2.
BASIC PROPERTIES OF DATA SAMPLES (TICKELL AND BURROWS, 1989)

.../continued

Run Number	Day & Time	Water Depth (m)	Surface Elevation Standard Deviation (m)	Level	Mean Velocity (m/s)		Frequency Setting	Estimated Damped Natural Frequency (Hz)
					x	y		
13*	86 9.26	10.25	0.863	2	-0.01	0.01	F6	0.46
				3	-0.05	-0.02		
				4	-0.05	-0.04		
14	86 9.55	10.20	0.930	2	-0.09	-0.02	F6	0.46
				3	-0.14	-0.07		
				4	-0.14	-0.08		
15*	86 10.30	10.15	0.998	2	-0.13	-0.12	F6	0.47
				3	-0.19	-0.23		
				4	-0.21	-0.22		
16	86 11.30	9.95	0.929	2	-0.10	-0.25	F6	0.48
				3	-0.28	-0.35		
				4	-0.31	-0.33		
23*	86 17.00	9.60	0.949	2	0.45	0.46	F6	0.49
				3	0.14	0.55		
				4	0.16	0.58		

TABLE 2.2.
BASIC PROPERTIES OF DATA SAMPLES (TICKELL AND BURROWS, 1989)

Notes i) Water depths, surface elevation, standard deviations and mean velocities given by BMT.
ii) Mean velocities refer to mean values of time series - values given for Level 2 may be subject to intermittent submergence.
iii) Estimated damped natural frequencies are derived from the displacement spectra.
iv) *Run numbers selected for detailed studies

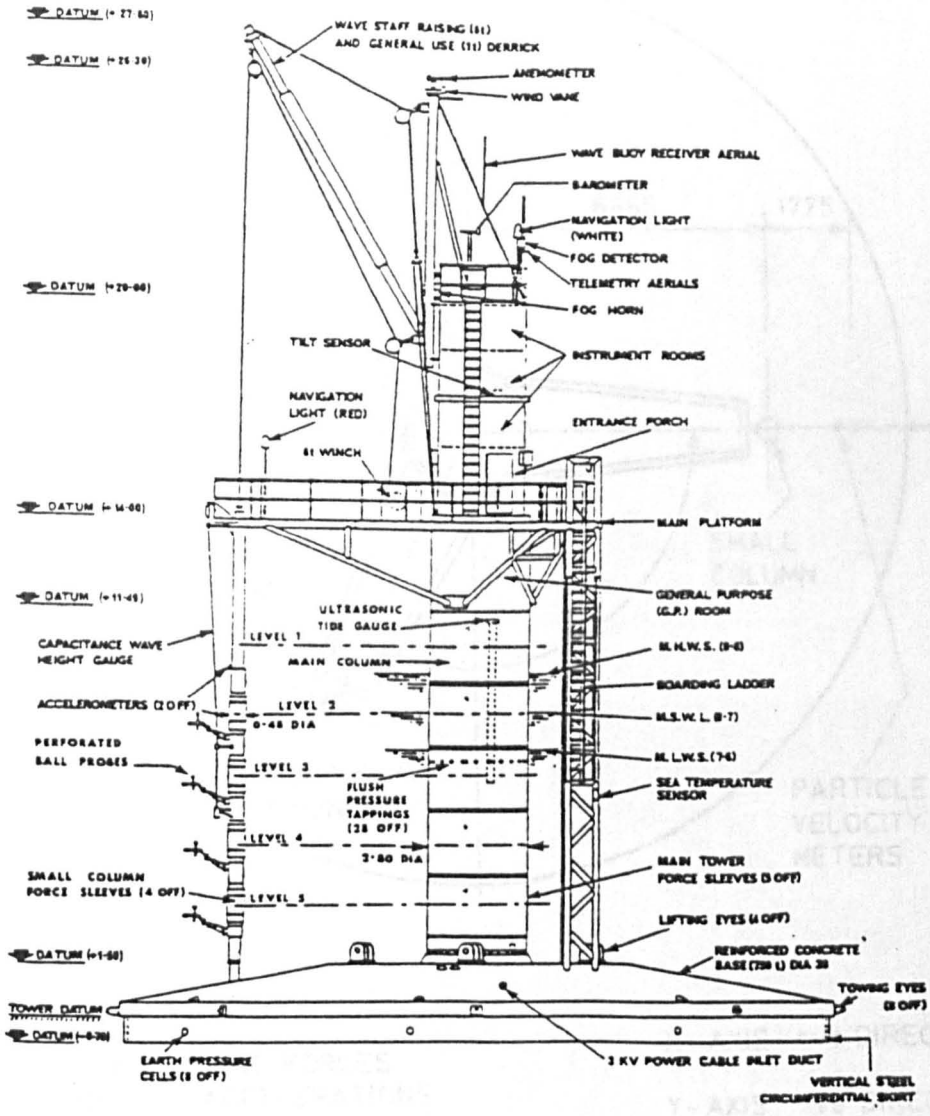

FIGURE 2.1. CHRISTCHURCH BAY TOWER, ELEVATION VIEW

(dimensions in m)

(Tickell and Burrows, 1989)

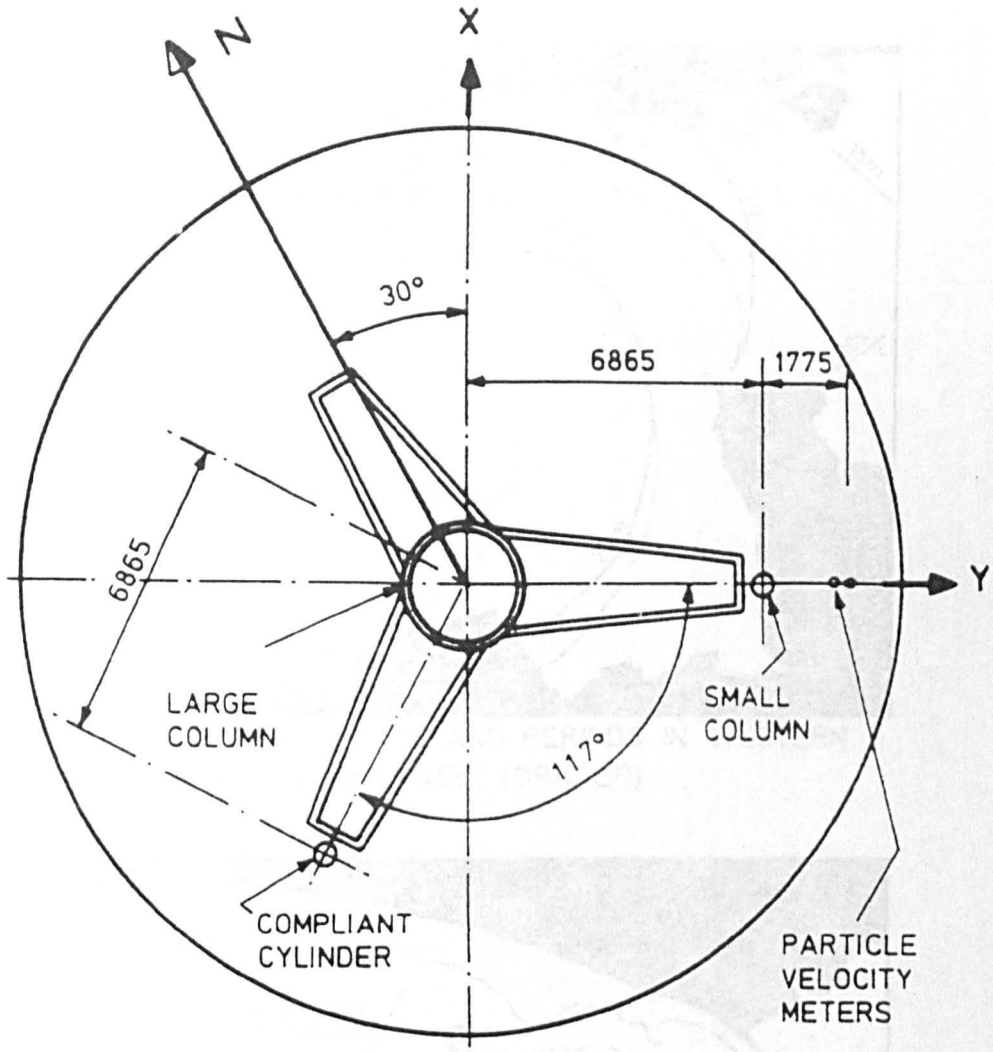

NOTE:-

ALL INSTRUMENT FORCES VELOCITIES, ACCELERATIONS ETC. ARE REFERRED TO THE TOWER X, Y, and Z AXES GIVEN HERE.

X-AXIS +ve DIRECTION

Y-AXIS +ve DIRECTION

Z-AXIS +ve UPWARDS

FIGURE 2.2. CHRISTCHURCH BAY TOWER, PLAN VIEW

(dimensions in mm)

(Tickell and Burrows, 1989)

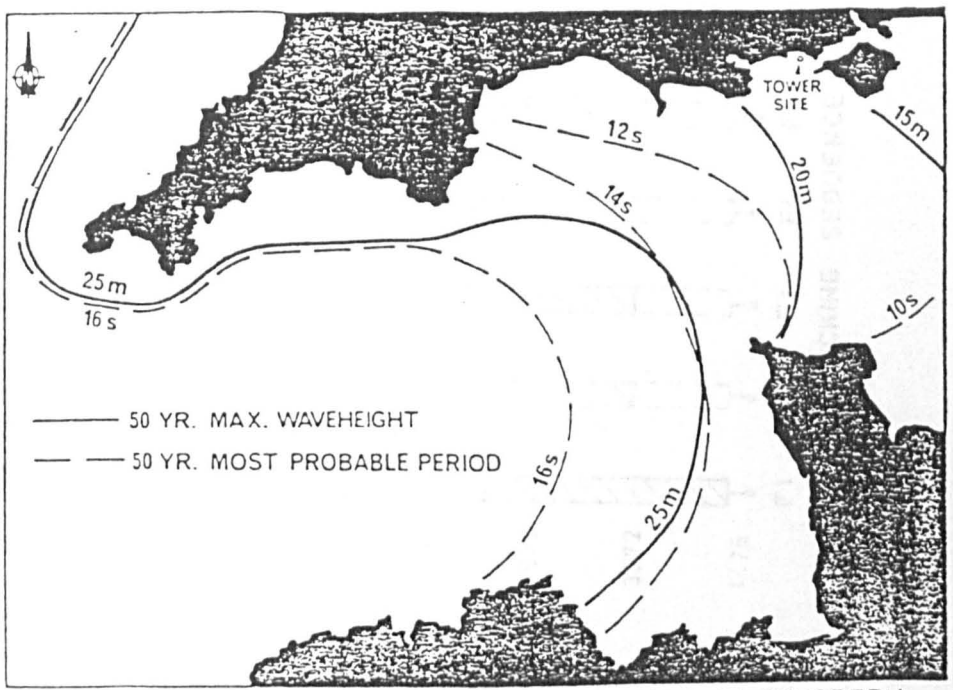

ESTIMATED STORM WAVEHEIGHTS AND PERIODS IN WESTERN ENGLISH CHANNEL (DRAPER)

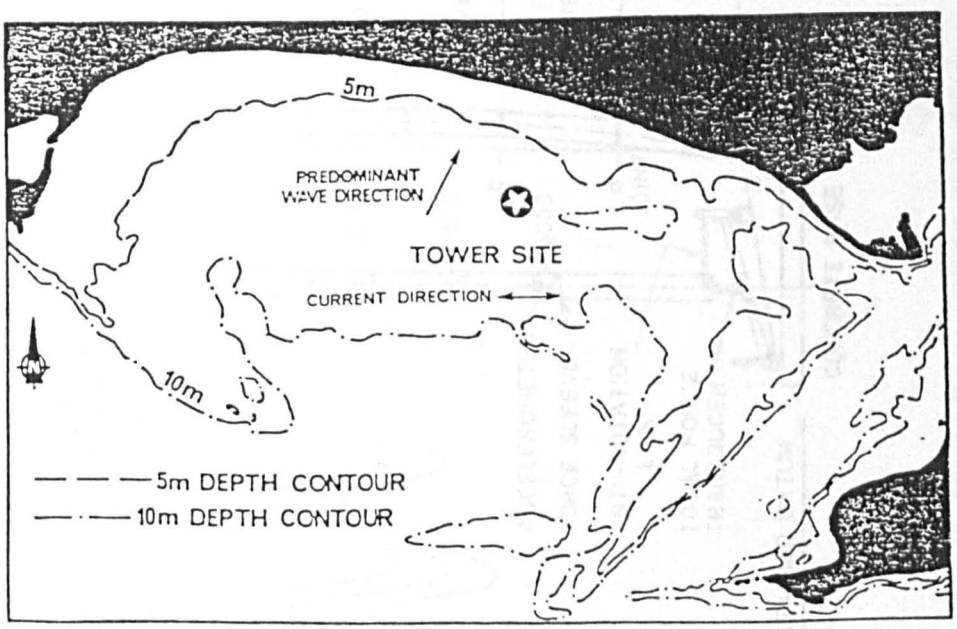

SITING OF TOWER IN CHRISTCHURCH BAY

FIGURE 2.3. SITE OF CHRISTCHURCH BAY TOWER.

(Bishop, 1982)

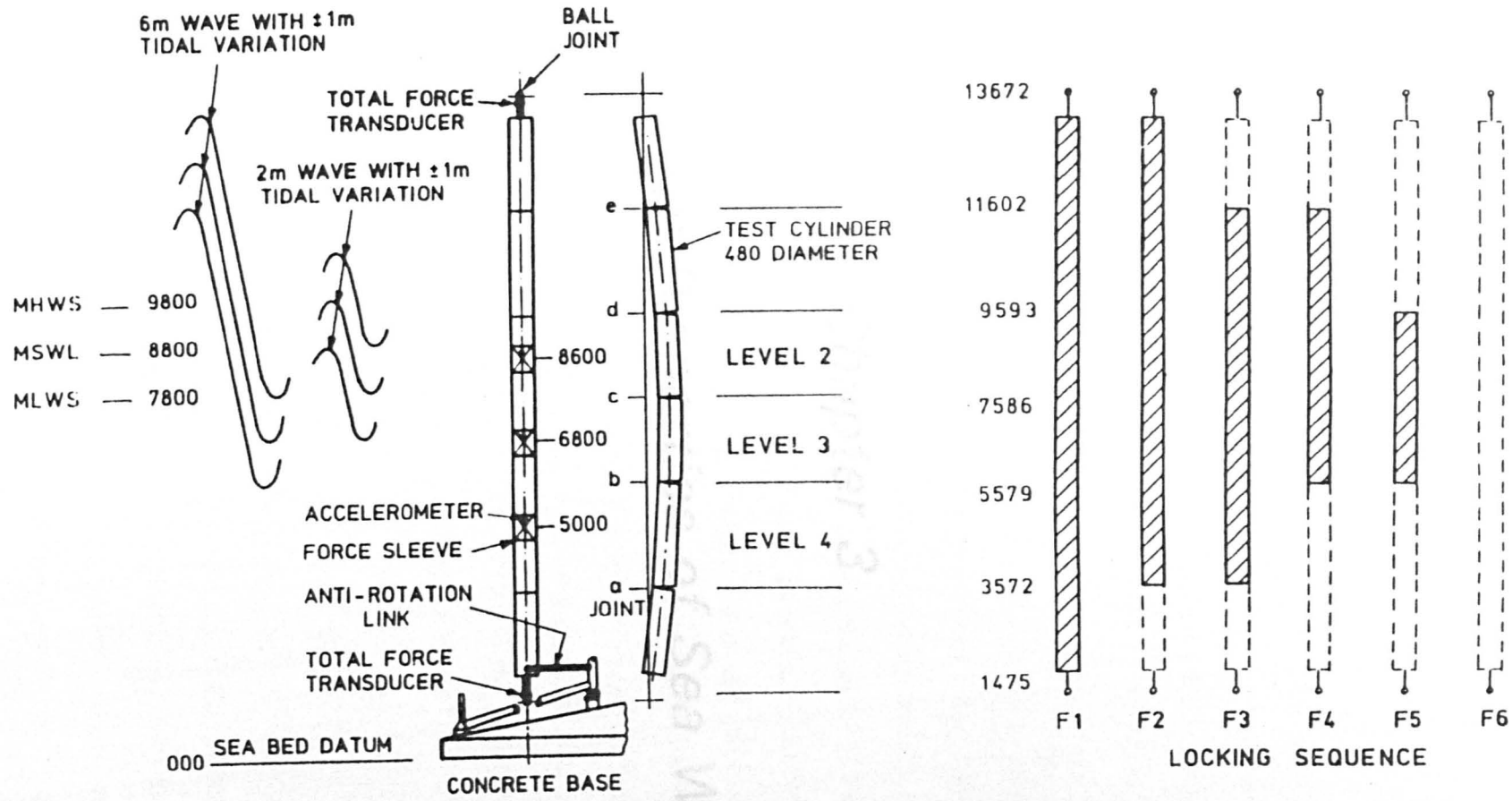

FIGURE 2.4. CHRISTCHURCH BAY TOWER COMPLIANT CYLINDER

(Levels in mm)

(Tickell and Burrows, 1989)

Chapter 3

Short-term Properties of Sea Waves

INTRODUCTION

This chapter is devoted to the study of short-term properties of sea waves based on Linear Random Wave Theory (LRWT). The study of LRWT is required for both subjects of this thesis as will be explained below:

a) In the probabilistic analysis of offshore structures to be discussed in Chapter 10, the frequency spectra of water particle kinematics at different nodes and the cross-spectra between pairs of water particle kinematics are established according to Linear Random Wave Theory.

   Furthermore, The basic idea in the probabilistic analysis of offshore structures is to determine the probabilistic properties of the force and response from the known probabilistic properties of water particle kinematics. It is, therefore, necessary as a prerequisite to investigate the probabilistic properties of water surface elevation and water particle kinematics based on LRWT. The probabilistic properties of force and response will then be determined by establishing how the probabilistic properties of water particle kinematics will be transformed by the nonlinear drag component of Morison's equation (the latter part is the subject of study in Chapter 8).

b) In the analysis of Christchurch Bay data, measured water particle kinematics have been used in deriving Morison's coefficients. However, one must appreciate that in practice, the designer will almost certainly use LRWT to predict water particle kinematics from a given water surface elevation spectrum. The predicted kinematics are then used in conjunction with Morison's equation

to predict random hydrodynamic forces. It is, therefore, necessary to consider the performance of LRWT in more detail and in particular, its capability in predicting the spectral properties of water particle kinematics must be assessed. LRWT itself will be discussed in this chapter and its performance with regard to Christchurch Bay data will be examined in the following chapter.

Section 3.1 is devoted to the description of water surface elevation according to LRWT. The probabilistic properties of water surface elevation are the subject of study in Section 3.2. Section 3.3 is concerned with the derivation of spectra and cross-spectra of water particle kinematics from water surface elevation spectrum. Section 3.4 discusses frequency spectra commonly used in specifying sea states (or wave conditions). These spectra are used as inputs to the probabilistic model.

3.1 DESCRIPTION OF WATER SURFACE ELEVATION BASED ON LINEAR RANDOM WAVE THEORY

A random process is stationary if its probability structure across the ensemble of its realisations is independent of the time origin. In other words, the statistical behaviour of a stationary random process does not change with time. If the mean, the standard deviation and the variance spectrum are the only statistical properties of the process which are invariant with time, then it is said to be stationary in the wide sense.

A stationary random process is ergodic if the temporal averages taken along any single realisation of the process are the same as the

ensemble averages. In particular, the mean, the standard deviation and the variance spectrum are the same. Physically, ergodicity implies that one realisation is typical of all the possible realisations of the process so that a measured realisation (Figure 3.1) contains all the statistical information of that process.

If a random process depends on both space and time, ergodicity implies that the process is homogenous, too. A homogenous process is similar to a stationary process except that its statistical behaviour is independent of the space origin, i.e. the statistical behaviour of a homogenous random process does not vary with space.

Over long periods of time and large distances, the sea surface is not stationary and homogenous, that is, storms vary in severity from time to time and from place to place. However, over a short period of time and small distances, the sea surface can be assumed stationary and homogenous. The time scale for stationarity is about a few hours. Typically, water surface records are obtained every three hours for a period of 10 to 20 minutes. The short-term spectral and probabilistic properties of ocean waves are obtained from these wave records.

Short-term properties of sea waves are generally studied on the basis of Linear Random Wave Theory (LRWT). With the exception of some nonlinear behaviour, LRWT has successfully explained most properties of real sea waves and hence its use can be justified for most engineering purposes. According to this theory, short-crested sea waves can be modelled as the sum of a large number of progressive 'linear' waves (Figure 3.2) of different amplitudes travelling in different directions with random phases (Borgman, 1969a) and can be expressed as

$$\eta(x,y,t) = \sum_m\sum_n a_{mn}\cos\{k_m[x\cos(\theta_n) + y\sin(\theta_n)] - \omega_m t - \alpha_{mn}\}$$
$$= \sum_m\sum_n a_{mn}\cos(x_{mn}) \qquad (3.1)$$

In the above equation, η is water surface elevation, measured from mean water level. x and y are the coordinates of a point in the horizontal plane, and t is the time. a_{mn} is the amplitude of the wave with frequency ω_m and direction θ_n (measured anti-clockwise from the x axis). α_{mn} is a random phase uniformly distributed between 0 and 2π. In the absence of current, the wave number k_m is related to wave frequency by

$$\omega_m^2 = gk_m\tanh(k_m d) \qquad (3.2)$$

where d and g are the water depth and the gravitational constant, respectively. It can be shown that $\eta(x,y,t)$ is a stationary, homogenous and ergodic random process (Price et al, 1974).

The mean and the variance of η are

$$\bar{\eta} = 0 \qquad (3.3)$$
$$\sigma_\eta^2 = \sum_m\sum_n a_{mn}^2/2 \qquad (3.4)$$

In the limit, the variance is

$$\sigma_\eta^2 = \int_0^\infty \int_{-\pi}^{\pi} G_{\eta\eta}(\omega,\theta)\,d\omega\,d\theta \qquad (3.5)$$

where $G_{\eta\eta}(\omega,\theta)$ is the one-sided directional spectral density function, defined as

$$G_{\eta\eta}(\omega,\theta) = \lim_{\Delta\omega \text{ and } \Delta\theta\to 0} \left(\frac{a_{mn}^2}{2\Delta\omega\Delta\theta} \right) \qquad (3.6)$$

in which $a_{mn}^2/2$ is the water surface variance due to wave components in the small rectangular element ($\Delta\omega$*$\Delta\theta$) centred at point (ω,θ).

Equation (3.6) can be rewritten as

$$a_{mn} \approx [2G_{\eta\eta}(\omega,\theta)\Delta\omega\Delta\theta]^{1/2} \tag{3.7}$$

In words, the directional wave spectrum represents the manner in which the variance of the water surface elevation is distributed with respect to frequency and direction.

The profiles of the sea waves represented by Equation (3.1), change from place to place and from time to time. However, at a fixed point such as (x_0,y_0), the wave record is a function of time only, and can be broken down into its sinusoidal components, i.e.

$$\eta = \eta(t) = \sum_m a_m \cos(\omega_m t - \alpha_m) \tag{3.8}$$

From Equation (3.1), the wave profile at point (x_0,y_0) is

$$\eta = \eta(x_0,y_0,t) = \sum_m \{\sum_n a_{mn}\cos[k_m (x_0\cos(\theta_n) + y_0\sin(\theta_n)) - \omega_m t - \alpha_{mn}]\} \tag{3.9}$$

Comparison of Equations (3.8) and (3.9) reveals that

$$a_m\cos(\omega_m t - \alpha_m) = \sum_n a_{mn}\cos[k_m (x_0\cos(\theta_n) + y_0\sin(\theta_n)) - \omega_m t - \alpha_{mn}] \tag{3.10}$$

Based on the above equation, the wave component with frequency ω_m in Equation (3.8) is not a physical reality but the result of mathematical manipulation of all the waves with frequency ω_m travelling in all different directions. Nevertheless, it can be imagined as an equivalent long-crested wave with frequency ω_m travelling in the mean direction of propagation.

Equating the variance of both sides of Equation (3.10) results in

$$a_m^2/2 = \sum_n a_{mn}^2/2 \tag{3.11a}$$

or

$$a_m^2 = \sum_n a_{mn}^2 \tag{3.11b}$$

According to Equation (3.11a), $a_m^2/2$ is the contribution of all the waves with frequency ω_m, regardless of their direction, to the variance of water surface elevation.

Substituting Equation (3.11a) into Equation (3.4) gives

$$\sigma_\eta^2 = \sum_m a_m^2/2 \tag{3.12}$$

In the limit, when m approaches infinity, σ_η^2 will be

$$\sigma_\eta^2 = \int_0^\infty G_{\eta\eta}(\omega)d\omega \tag{3.13}$$

where $G_{\eta\eta}(\omega)$ is the one-sided uni-directional frequency spectrum, or simply frequency spectrum, of the water surface elevation. Frequency spectra can be expressed in terms of circular frequency, f, rather than angular frequency $\omega = 2\pi f$. The relationship between the two is

$$G_{\eta\eta}(f) = 2\pi G_{\eta\eta}(\omega) \tag{3.14}$$

The amplitude of the uni-directional wave component a_m, is related to water surface frequency spectrum according to the following equation

$$a_m = [2G_{\eta\eta}(\omega)\Delta\omega]^{1/2} \tag{3.15}$$

Comparing Equations (3.13) and (3.5) leads to the relationship between the uni-directional and directional wave spectra

$$G_{\eta\eta}(\omega) = \int_{-\pi}^{\pi} G_{\eta\eta}(\omega,\theta)d\theta \tag{3.16}$$

It is convenient to express the directional spectrum in terms of the uni-directional wave spectrum and a spreading function, denoted by $D(\omega,\theta)$

$$G_{\eta\eta}(\omega,\theta) = D(\omega,\theta) * G_{\eta\eta}(\omega) \tag{3.17}$$

Integrating both sides of the above equation with respect to θ and replacing $\int G_{\eta\eta}(\omega,\theta)d\theta$ by $G_{\eta\eta}(\omega)$, leads to

$$\int_{-\pi}^{\pi} D(\omega,\theta)d\theta = 1 \tag{3.18}$$

3.2 SHORT-TERM PROBABILISTIC PROPERTIES OF SEA WAVES

Definition of Wave Height and Wave Period

The most commonly used definitions of wave heights and periods are based on the zero up-crossing method. The wave height H is taken to be the elevation range between the highest crest and the lowest trough within successive up-crossings of the mean water level. The zero crossing period $\acute{T}_z$ is, then, taken to be the time between successive up-crossings of the mean water level.

In addition to zero crossing period, the crest, the peak and the mean spectral periods are also mentioned in the literature (Price and Bishop, 1974; Tickell and Burrows, 1989). The crest period $\acute{T}_c$ is defined as the time interval between two successive crests. The peak and the mean spectral periods are related to the frequency spectrum. The peak period T_p is associated with the peak of the spectrum and is obtained

by reciprocating the peak frequency. The mean spectral period $\bar{T}_1$ is the reciprocal of the mean frequency $\bar{\omega}$. The peak and the mean spectral periods are not physical quantities and cannot be related to individual waves.

Spectral Bandwidth

A stationary random process can be classified as a broad-band or a narrow-band process depending on the nature of its frequency spectrum (Figure 3.4). In a narrow-band process, the width over which the ordinates are significant is substantially less than the central frequency within the band. The frequency spectrum of a broad-band process has significant values over a wide range of frequencies.

The spectral bandwidth ϵ is a measure of the width of the spectrum and is defined as

$$\epsilon = \left(1 - \frac{m_2^2}{m_0 m_4}\right)^{1/2} \tag{3.19}$$

where m_n is the nth moment of the frequency spectrum

$$m_n = \int_0^\infty \omega^n \, G_{\eta\eta}(\omega) d\omega \tag{3.20}$$

It can be shown (Sarpkaya and Isaacson, 1981) that ϵ is limited between zero and one. For a narrow-band process, ϵ approaches zero; for a broad-band process it approaches one.

Water Surface Elevation Distribution

According to the central limit theorem, water surface elevation is a mean zero Gaussian-distributed function as shown in Figure 3.3 (Pierson, 1955). Hence, its probability density function is

$$p_\eta(x) = \frac{1}{\sqrt{2\pi}\,\sigma_\eta} \exp\left[-\frac{x^2}{2\sigma_\eta^2}\right] \tag{3.21}$$

and its cumulative distribution function is

$$P_\eta(x) = \text{prob}[\eta \leq x] = \int_{-\infty}^{x} p(\epsilon)d\epsilon \tag{3.22}$$

Statistical and Probabilistic Properties of Wave Crests

Assuming that water surface elevation is Gaussian distributed, the probability density function of its crest elevations (η_{max}) is given by Cartwright and Longuet-Higgins (1956). Defining the normalised crest elevation A as η_{max}/σ_η, the distribution is

$$p_A(x) = \frac{\epsilon}{\sqrt{2\pi}} \exp\left(-\frac{x^2}{2\epsilon^2}\right) + (1 - \epsilon^2)^{1/2} \, x \exp\left(-\frac{x^2}{2}\right) * \left(0.50 + \text{erf}\left[\frac{(1 - \epsilon^2)^{1/2}}{\epsilon} x\right]\right) \tag{3.23}$$

where

$$\text{erf}(x) = \frac{2}{\sqrt{\pi}} \int_0^x \exp(-t^2)dt \tag{3.24}$$

The mean and the root mean square of the peak elevations are respectively given by

$$\bar{\eta}_{max} = \sqrt{\pi/2}\,(1 - \epsilon^2)^{1/2}\,\sigma_\eta \tag{3.25}$$

and

$$(\eta_{max})_{rms} = (2 - \epsilon^2)^{1/2}\,\sigma_\eta \tag{3.26}$$

The proportion of negative crests (crests below the mean water level) out of all crests is denoted by r and is related to ϵ by the equation

$$r = \tfrac{1}{2}\left[1 - (1 - \epsilon^2)^{1/2}\right] \tag{3.27}$$

Therefore, one can estimate r by counting the numbers of positive and negative crests of a given record and hence calculate ϵ from Equation (3.27) rewritten as

$$\epsilon = \left[1 - (1 - 2r)^2\right]^{1/2} \tag{3.28}$$

Alternatively, one can estimate the mean crest period T_c and the mean zero crossing period T_z of a given record and calculate ϵ from

$$\epsilon = \left[1 - (T_c/T_z)^2\right]^{1/2} \tag{3.29}$$

For a broad-band spectrum ($\epsilon \approx 1$), crest elevations are Gaussian distributed; therefore there are as many crests below the mean water level as there are above it. The pdf is

$$p_A(x) = \frac{1}{\sqrt{2\pi}} \exp\left(-\frac{x^2}{2}\right) \tag{3.30}$$

For a narrow-band spectrum ($\epsilon \approx 0$), crest elevations are Rayleigh distributed (Figure 3.5), so that there will be no crests below the mean water level. The probability and cumulative density functions are, respectively

$$p_A(x) = x \exp(-x^2/2) \tag{3.31}$$

and

$$p_A(x) = 1 - \exp(-x^2/2) \tag{3.32}$$

The pdf of crest elevations for different values of ϵ are shown in Figure 3.6.

Statistical and Probabilistic Properties of Wave Heights

Defining the wave height as twice the elevation crest ($H = 2\eta_{max}$), then its pdf, cdf and probability of exceedence for the case of a narrow-band process are, respectively

$$p_H(h) = \frac{h}{4\sigma_\eta^2} \exp\left(-\frac{h^2}{8\sigma_\eta^2}\right) \tag{3.33}$$

$$P_H(h) = 1 - \exp\left(-\frac{h^2}{8\sigma_\eta^2}\right) \tag{3.34}$$

$$Q_H(h) = 1 - p_H(h) = \exp\left(-\frac{h^2}{8\sigma_\eta^2}\right) \tag{3.35}$$

Strictly speaking, the above distribution is only applicable to a narrow-band process; however, it has been observed that for processes with $\epsilon \leq 0.80$, the Rayleigh distribution is a relatively good approximation (Ochi, 1973).

The various statistics of wave heights can be obtained from the above distribution. The following expresses the relationship between the probability of exceedence and the corresponding wave height, obtained from Equation (3.35)

$$h = 2\sqrt{2}\,\sigma_\eta \sqrt{\text{Ln}\left(\frac{1}{Q_H(h)}\right)} \tag{3.36}$$

Therefore, 10% of the wave heights are $\geq 4.29\sigma_\eta$, 5% $\geq 4.90\sigma_\eta$, 1% $\geq 6.07\sigma_\eta$, 0.1% $\geq 7.43\sigma_\eta$, and 0.01% $\geq 8.58\sigma_\eta$.

The mean, the root-mean-square, and the standard deviation of the wave heights are, respectively

$$\bar{H} = E[H] = \int_0^\infty h p_H(h) dh = 2.51\sigma_\eta \tag{3.37}$$

$$H_{rms} = (E[H^2])^{1/2} = \sqrt{\int_0^\infty h^2 p_H(h) dh} = \sqrt{8}\,\sigma_\eta = 2.83\,\sigma_\eta \tag{3.38}$$

$$\sigma_H = 1.31\,\sigma_\eta \tag{3.39}$$

$H_{1/n}$ is defined as the average height of the highest (1/n)th of the wave heights, and is equal to

$$H_{1/n} = \{\sqrt{8Ln(n)} + n\sqrt{2\pi}[1 - erf(\sqrt{Ln(n)})]\} * \sigma_\eta \tag{3.40}$$

From the above relationship, one can obtain

$$H_{1/2} = 1.42\bar{H} = 3.55\,\sigma_\eta \tag{3.41}$$

$$H_{1/3} = 1.60\bar{H} = 4.00\,\sigma_\eta \tag{3.42}$$

$$H_{1/10} = 2.03\bar{H} = 5.09\,\sigma_\eta \tag{3.43}$$

$$H_{1/100} = 2.66\bar{H} = 6.68\,\sigma_\eta \tag{3.44}$$

$H_{1/3}$ or alternatively H_s is called the significant wave height and is one of the parameters used to describe a sea state. That is why the wave height distribution is commonly expressed in terms of H_s rather than σ_η

$$p_H(h) = \frac{4h}{H_s^2} \exp\left(-\frac{2h^2}{H_s^2}\right) \tag{3.45}$$

and

$$P_H(h) = 1 - \exp\left(-\frac{2h^2}{H_s^2}\right) \tag{3.46}$$

Consider many wave records, all with the same significant wave height and the same number of waves N. The largest wave height of each record, H_N, is different from record to record and hence is a random variable. Its distribution in comparison to the wave height distribution is shown in Figure 3.7 and is called the extreme value distribution.

The expected value of the largest wave height in N waves is (Price and Bishop, 1974)

$$E[H_{max,N}] = H_{rms}\left[\sqrt{Ln(N)} + \frac{0.2886}{\sqrt{LN(N)}}\right] \tag{3.47}$$

For N > 100, it becomes

$$E[H_{max,N}] = 0.707H_s\sqrt{Ln(N)} \tag{3.48}$$

For N = 1000 and 10,000, the results are

$$E[H_{max,1000}] = 1.86H_s \tag{3.49}$$

and

$$E[H_{max,10,000}] = 2.15H_s \tag{3.50}$$

The cdf of $H_{max,N}$ is (Houmb, 1981)

$$P_{Hmax,N}(x) = \exp\left[-N\exp\left(-\frac{2x^2}{H_s^2}\right)\right] \tag{3.51}$$

Choosing N = 10,000 and $H_{max,N}/H_s = 3$, results in

$$P_{Hmax,10,000}(3H_s) = 0.999848 \tag{3.52}$$

which shows that the highest wave height in a record of approximately one day length will rarely exceed three times of the significant wave height.

The most probable maximum wave height to be encountered in N waves, corresponds to the mode of the extreme wave height distribution. It is only slightly smaller than the expected maximum wave height and for large values of N the two coincide (Longuet-Higgins, 1952).

Strictly speaking, the Rayleigh distribution of wave heights is only valid for narrow-band spectra. For the case of broad-band spectra, Longuet-Higgins (1980) has modified the distribution of wave heights by replacing H_{rms} with $0.925\sqrt{8}\,\sigma_\eta$ rather than $\sqrt{8}\sigma_\eta$. This leads to

$$p_H(h) = \frac{h}{3.41\sigma_\eta^2} \exp\left(-\frac{h^2}{6.84\sigma_\eta^2}\right) \tag{3.53}$$

or in terms of H_s

$$p_H(h) = \frac{4.69h}{H_s^2} \exp\left(-\frac{2.34h^2}{H_s^2}\right) \tag{3.54}$$

This distribution is referred to as the modified Rayleigh distribution. The cumulative distribution function and the probability of exceedence are, respectively

$$P_H(h) = 1 - \exp\left[-\frac{2.34h^2}{H_s^2}\right] \tag{3.55}$$

and

$$Q_H(h) = \exp\left[-\frac{2.34h^2}{H_s^2}\right] \tag{3.56}$$

Therefore, 10% of the wave heights are $\geq 3.97\sigma_\eta$, 5% $\geq 4.53\sigma_\eta$, 1% $\geq 5.61\sigma_\eta$, 0.1% $\geq 6.87\sigma_\eta$, and 0.01% $\geq 7.94\sigma_\eta$.

For the modified Rayleigh distribution, $H_{1/n}$ is

$$H_{1/n} = 0.925\ \{\sqrt{8Ln(n)} + n\sqrt{2}\pi[1 - erf(\sqrt{Ln(n)})]\} * \sigma_\eta \tag{3.57}$$

The modified Rayleigh distribution is more accurate than the standard Rayleigh distribution in predicting the probabilities associated with higher waves (Tickell et al, 1987).

Statistical and Probabilistic Properties of Wave Periods

The distribution of individual wave periods is narrower than that of the wave heights, that is, the spread lies mainly in the range of 0.50 to 2.0 times the mean wave period. However, the distribution becomes broader when wind waves and swell coexist. When this occurs, the period distribution is bi-modal, with two peaks corresponding to the mean periods of the wind waves and swell. This is one of the reasons that the wave distribution does not follow a universal distribution law. Therefore, relatively little effort has been devoted to the study of wave period distribution in comparison to the extensive research done on the distribution of wave heights. Discussion of the existing models for the wave period distribution and the bivariate distributions of the wave height and period is beyond the scope of this work.

The mean zero-crossing, crest and spectral periods are related to the frequency spectrum by the following equations, respectively

$$T_z = 2\pi\sqrt{m_0/m_2} \tag{3.58}$$

$$T_c = 2\pi\sqrt{m_2/m_4} \tag{3.59}$$

$$T_m = 2\pi(m_0/m_1) \tag{3.60}$$

where m_n is defined in Equation (3.20).

3.3 DESCRIPTION OF WATER PARTICLE KINEMATICS

Velocity Components (u, v, w)

According to Linear Random Wave Theory, the wave profile of Equation (3.1) is associated with the following horizontal and vertical wave particle velocities at point (x,y,z), with z being the elevation relative to still water level (Figure 3.2).

$$u(x,y,z,t) = \sum_m\sum_n a_{mn}\ \omega_m\ \Gamma_{hm}\ \cos(\theta_n)\cos(x_{mn}) \tag{3.61}$$

$$v(x,y,z,t) = \sum_m\sum_n a_{mn}\ \omega_m\ \Gamma_{hm}\ \sin(\theta_n)\cos(x_{mn}) \tag{3.62}$$

$$w(x,y,z,t) = \sum_m\sum_n a_{mn}\ \omega_m\ \Gamma_{wm}\ \sin(x_{mn}) \tag{3.63}$$

where u, v, and w are water particle velocities in the x, y and z directions, respectively. Γ_{hm} and Γ_{wm}, the horizontal and vertical depth attenuation factors, are

$$\Gamma_{hm} = \cosh[k_m(z+d)]/\sinh(k_m d) \tag{3.64}$$

and

$$\Gamma_{wm} = \sinh[k_m(z+d)]/\sinh(k_m d) \tag{3.65}$$

If there is current, appropriate mean velocities are added to Equations (3.61) and (3.62) to obtain the total velocities in the horizontal plane.

Acceleration components ($\dot{u}$, $\dot{v}$, $\dot{w}$)

Only the local accelerations are considered in the present study; therefore, accelerations will be the time derivative of the velocities, that is

$$\dot{u}(x,y,z,t) = \sum_m\sum_n a_{mn}\ \omega_m^2\ \Gamma_{hm}\ \cos(\theta_n)\sin(x_{mn}) \tag{3.66}$$

$$\dot{v}(x,y,z,t) = \sum_m\sum_n a_{mn}\ \omega_m^2\ \Gamma_{hm}\ \sin(\theta_n)\sin(x_{mn}) \tag{3.67}$$

$$\dot{w}(x,y,z,t) = -\sum_m\sum_n a_{mn}\ \omega_m^2\ \Gamma_{wm}\ \cos(x_{mn}) \tag{3.68}$$

Auto and cross-spectra of water particle kinematics

The various auto and cross-spectra densities for particle kinematics may be derived from their time domain expressions, in terms of the water surface elevation spectrum (Borgman, 1977), that is

$$G_{uu}(\omega) = G_{\eta\eta}(\omega) * \omega^2\ \Gamma_h^2 \int_{-\pi}^{\pi} D(\omega,\theta)\cos^2(\theta)d\theta \tag{3.69}$$

$$G_{vv}(\omega) = G_{\eta\eta}(\omega) * \omega^2\ \Gamma_h^2 \int_{-\pi}^{\pi} D(\omega,\theta)\sin^2(\theta)d\theta \tag{3.70}$$

$$G_{ww}(\omega) = G_{\eta\eta}(\omega) * \omega^2\ \Gamma_w^2(\omega) \tag{3.71}$$

$$G_{\dot{u}\dot{u}}(\omega) = \omega^2 G_{uu}(\omega) \tag{3.72}$$

For uni-directional waves along the x axis, the above equations reduce to

$$G_{uu}(\omega) = G_{\eta\eta}(\omega) * \omega^2\ \Gamma_h^2 \tag{3.73}$$

$$G_{ww}(\omega) = G_{\eta\eta}(\omega) * \omega^2\ \Gamma_w^2 \tag{3.74}$$

Cross-spectral density functions are, in general, complex functions in the form

$$G_{xy}(\omega) = C_{xy}(\omega) - iQ_{xy}(\omega) \tag{3.75}$$

where C_{xy} and Q_{xy} are the coincident and quadrature components of the cross-spectrum and i is $\sqrt{-1}$. For example, the cross-spectrum between u_1 and $\dot{w}_2$ is (subscripts 1 and 2 refer to points (x_1,y_1,z_1) and (x_2,y_2,z_2), respectively)

$$C_{u1,\dot{w}2}(\omega) = -G_{\eta\eta}(\omega) * \omega^3 \Gamma_{h1}\Gamma_{w2} \int_{-\pi}^{\pi} D(\omega,\theta)\cos(\theta)\cos(\Delta\varphi)d\theta \tag{3.76}$$

and

$$Q_{u1,\dot{w}2}(\omega) = -G_{\eta\eta}(\omega) * \omega^3 \Gamma_{h1}\Gamma_{w2} \int_{-\pi}^{\pi} D(\omega,\theta)\cos(\theta)\sin(\Delta\varphi)d\theta \tag{3.77}$$

where $\Delta\varphi$, the phase shift between u_1 and $\dot{w}_2$, is

$$\Delta\varphi = k[(x_2-x_1)\cos(\theta) + (y_2-y_1)\sin(\theta)] \tag{3.78}$$

For uni-directional waves along the x axis, the above equations reduce to

$$C_{u1,\dot{w}2}(\omega) = - G_{\eta\eta}(\omega) * \omega^3 \Gamma_{h1}\Gamma_{w2} \cos(\Delta\varphi) \tag{3.79}$$

and

$$Q_{u1,\dot{w}2}(\omega) = - G_{\eta\eta}(\omega) * \omega^3 \Gamma_{h1}\Gamma_{w2} \sin(\Delta\varphi) \tag{3.80}$$

where

$$\Delta\varphi = k(x_2-x_1) \tag{3.81}$$

Probability distribution

According to the central limit theorem, water particle kinematics are Gaussian distributed. In general, due to the presence of current, the velocities are not mean-zero; therefore, a typical probability density function (pdf) is (Figure 3.3)

$$p(r) = \frac{1}{\sqrt{2\pi}\,\sigma_r} \exp\left[-\frac{(r-\bar{r})^2}{2\sigma_r^2}\right] \tag{3.82}$$

where $\bar{r}$ is the mean and σ_r is the variance of the random process such that

$$\sigma_r^2 = \int_0^\infty G_{rr}(\omega)d\omega \tag{3.83}$$

The joint pdf for two Gaussian random variables r and s is

$$p(r,s) = \frac{1}{2\pi(1-\rho_{r,s}^2)^{1/2}} \exp\left\{ - \frac{1}{2(1-\rho_{rs}^2)} \left[\frac{(r - \bar{r})^2}{\sigma_r^2} + \frac{(s - \bar{s})^2}{\sigma_s^2} - \frac{2\rho_{r,s}(r - \bar{r})(s - \bar{s})}{\sigma_r\sigma_s} \right] \right\} \tag{3.84}$$

where $\bar{r}$ and $\bar{s}$ are the mean values of r and s, σ_r^2 and σ_s^2 are the variance of r and s and $\rho_{r,s}$ is the correlation coefficient defined as

$$\rho_{r,s} = \frac{E[(r-\bar{r})(s-\bar{s})]}{\sigma_r\sigma_s} \tag{3.85}$$

Expectations Required in the Probabilistic Model

In the probabilistic model to be discussed in Chapter 10, the correlation coefficients and hence the expected values of water particle kinematics at different nodes are required. Foster (1967) has derived these expressions for uni-directional waves along the x axis. A complete list of the expectations of water particle kinematics at points 1 and 2 follows. (Points 1 and 2 have coordinates (x_1,z_1) and (x_2,z_2), respectively).

$$E[\dot{u}_1 u_2] = \int_{-\infty}^{\infty}\int_{-\infty}^{\infty} \dot{u}_1 u_2 p(\dot{u}_1 u_2)d\dot{u}_1 du_2$$

$$= - \int_0^\infty \Gamma_{h1}\Gamma_{h2}\sin(\Delta\varphi)\omega^3 G_{\eta\eta}(\omega)d\omega \tag{3.86}$$

$$E[\dot{u}_1 w_2] = \int_0^\infty \Gamma_{h1}\Gamma_{w2}\cos(\Delta\varphi)\omega^3 G_{\eta\eta}(\omega)\,d\omega \tag{3.87}$$

$$E[\dot{w}_1 u_2] = -\int_0^\infty \Gamma_{w1}\Gamma_{h2}\cos(\Delta\varphi)\omega^3 G_{\eta\eta}(\omega)\,d\omega \tag{3.88}$$

$$E[\dot{w}_1 \dot{w}_2] = -\int_0^\infty \Gamma_{w1}\Gamma_{w2}\sin(\Delta\varphi)\omega^3 G_{\eta\eta}(\omega)\,d\omega \tag{3.89}$$

$$E[u_1 u_2] = \int_0^\infty \Gamma_{h1}\Gamma_{h2}\cos(\Delta\varphi)\omega^2 G_{\eta\eta}(\omega)\,d\omega \tag{3.90}$$

$$E[w_1 w_2] = \int_0^\infty \Gamma_{w1}\Gamma_{w2}\cos(\Delta\varphi)\omega^2 G_{\eta\eta}(\omega)\,d\omega \tag{3.91}$$

$$E[u_1 w_2] = \int_0^\infty \Gamma_{h1}\Gamma_{w2}\sin(\Delta\varphi)\omega^2 G_{\eta\eta}(\omega)\,d\omega \tag{3.92}$$

$$E[w_1 u_2] = -\int_0^\infty \Gamma_{w1}\Gamma_{h2}\sin(\Delta\varphi)\omega^2 G_{\eta\eta}(\omega)\,d\omega \tag{3.93}$$

$$E[\dot{u}_1 \dot{u}_2] = \int_0^\infty \Gamma_{h1}\Gamma_{h2}\cos(\Delta\varphi)\omega^4 G_{\eta\eta}(\omega)\,d\omega \tag{3.94}$$

$$E[\dot{w}_1 \dot{w}_2] = \int_0^\infty \Gamma_{w1}\Gamma_{w2}\cos(\Delta\varphi)\omega^4 G_{\eta\eta}(\omega)\,d\omega \tag{3.95}$$

$$E[\dot{u}_1 \dot{w}_2] = \int_0^\infty \Gamma_{h1}\Gamma_{w2}\sin(\Delta\varphi)\omega^4 G_{\eta\eta}(\omega)\,d\omega \tag{3.96}$$

$$E[\dot{w}_1 \dot{u}_2] = -\int_0^\infty \Gamma_{w1}\Gamma_{h2}\sin(\Delta\varphi)\omega^4 G_{\eta\eta}(\omega)\,d\omega \tag{3.97}$$

$$E[u_1 \dot{u}_2] = \int_0^\infty \Gamma_{h1}\Gamma_{h2}\sin(\Delta\varphi)\omega^3 G_{\eta\eta}(\omega)\,d\omega \tag{3.98}$$

$$E[w_1 \dot{w}_2] = \int_0^\infty \Gamma_{w1}\Gamma_{w2}\sin(\Delta\varphi)\omega^3 G_{\eta\eta}(\omega)\,d\omega \tag{3.99}$$

$$E[u_1\dot{w}_2] = -\int_0^\infty \Gamma_{h1}\Gamma_{w2}\cos(\Delta\varphi)\omega^3 G_{\eta\eta}(\omega)d\omega \tag{3.100}$$

$$E[w_1\dot{u}_2] = \int_0^\infty \Gamma_{w1}\Gamma_{h2}\cos(\Delta\varphi)\omega^3 G_{\eta\eta}(\omega)d\omega \tag{3.101}$$

$$E[u_1^2] = \sigma_u^2 = \int_0^\infty \Gamma_{h1}^2\omega^2 G_{\eta\eta}(\omega)d\omega \tag{3.102}$$

$$E[\dot{u}_1^2] = \sigma_{\dot{u}1}^2 = \int_0^\infty \Gamma_{h1}^2\omega^4 G_{\eta\eta}(\omega)d\omega \tag{3.103}$$

$$E[w_1^2] = \sigma_{w1}^2 = \int_0^\infty \Gamma_{w1}^2\omega^2 G_{\eta\eta}(\omega)d\omega \tag{3.104}$$

$$E[\dot{w}_1^2] = \sigma_{\dot{w}1}^2 = \int_0^\infty \Gamma_{w1}^2\omega^4 G_{\eta\eta}(\omega)d\omega \tag{3.105}$$

where, as before Γ_h and Γ_w refer to the horizontal and vertical depth attenuation factors, and $\Delta\varphi$ is the phase shift as follows

$$\Gamma_{h1} = \cosh[k(z_1 + d)]/\sinh(kd) \tag{3.106}$$

$$\Gamma_{h2} = \cosh[k(z_2 + d)]/\sinh(kd) \tag{3.107}$$

$$\Gamma_{w1} = \sinh[k(z_1 + d)]/\sinh(kd) \tag{3.108}$$

$$\Gamma_{w2} = \sinh[k(z_2 + d)]/\sinh(kd) \tag{3.109}$$

$$\Delta\varphi = k(x_2 - x_1) \tag{3.110}$$

and d is the water depth.

3.4 MODEL WAVE SPECTRA

Wind-generated waves are formed by the transfer of energy from the wind to the sea. The spectral shape of the resulting waves depends on the wind speed (strength), the duration, i.e. the time during which the wind blows over the water surface, and the fetch, which is the distance over which the wind blows.

As shown in Figures 3.8 and 3.9, the wave intensity increases with the wind speed, duration and fetch. However, there is a limit to the growth of waves due to instability of the higher waves which dissipate their energy through wave breaking. When this equilibrium condition, in which the rates of energy transfer and energy dissipation are equal, is reached, the sea is referred to as fully developed.

Figure 3.10 shows the effect of the increase in duration on a sea exposed to a steady wind of 30 knots. Two effects are observed: (1) The area under the spectrum becomes larger, (2) The peak of the spectrum moves towards lower frequencies. Both processes continue until the sea becomes fully developed. The shift towards lower frequencies occurs because high frequency waves develop more rapidly than the low frequency ones and hence they achieve a steady state earlier (Price and Bishop, 1974).

Several frequency spectra have been proposed to describe a particular sea state. Some of them refer to the condition of a fully developed sea; among them, the Pierson-Moskowitz spectrum is most commonly used. Others refer to the condition of developing seas; among them, the JONSWAP spectrum is most often employed.

Pierson-Moskowitz Wave Spectrum

Analysis of extensive wave data relating to fully-developed sea conditions in the North Atlantic by Pierson and Moskowitz (1964), led to the following semi-empirical wave spectrum.

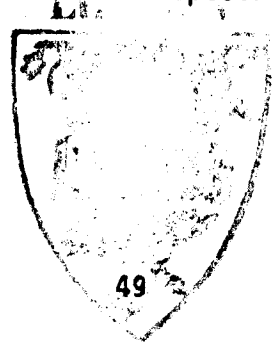

$$G_{\eta\eta}(\omega) = \frac{\alpha g^2}{\omega^5} \exp\left[-\beta\left(\frac{\omega_0}{\omega}\right)^4\right] \qquad (3.111)$$

where $\alpha = 0.0081$, $\beta = 0.74$, $g = 9.81 m/sec^2$, $\omega_0 = g/u_w$ and u_w is the wind speed in m/sec at a height of 19.5m above mean water level.

Setting the first derivative of Equation (3.111) equal to zero, the peak of the spectrum ω_p is

$$\omega_p = (0.8\beta)^{1/4}\omega_o \approx 0.877\omega_o \qquad (3.112)$$

and the spectral peak is

$$G_{\eta\eta}(\omega_p) = \frac{\alpha g^2 \exp(-5/4)}{(0.8\beta)^{5/4}} * \left(\frac{1}{\omega_0}\right)^5 \approx 0.430\omega_0^{-5} \qquad (3.113)$$

Sarpkaya and Isaacson (1981) have normalised Equation (3.111) by dividing both sides of the equation by the spectral peak $G_{\eta\eta}(\omega_p)$, that is

$$\frac{G_{\eta\eta}(\omega)}{G_{\eta\eta}(\omega_p)} = \exp\left(\frac{5}{4}\right)\left(\frac{\omega}{\omega_p}\right)^{-5} \exp\left[-\frac{5}{4}\left(\frac{\omega}{\omega_p}\right)^{-4}\right] \qquad (3.114)$$

Figure 3.11 represents the variation of the normalised spectrum in terms of the normalised frequency.

Applying Equations (3.42) and (3.58) to the Pierson-Moskowitz spectrum, the relationship between H_s and T_z with the wind speed can be obtained as

$$H_s = \frac{2u_w^2}{g}\left(\frac{\alpha}{\beta}\right)^{1/4} \qquad (3.115)$$

and

$$T_z = \frac{2\pi u_w}{g}\left(\frac{1}{\beta\pi}\right)^{1/4} \tag{3.116}$$

The above two relationships can be used to relate the wind speed to H_s, to T_z or to H_s/T_z, as follows:

$$u_w = (H_s)^{1/2} * \left(\frac{g}{2}\right)^{1/2} * \left(\frac{\beta}{\alpha}\right)^{1/4} \approx 6.84\sqrt{H_s} \tag{3.117}$$

$$u_w = T_z * \frac{g\beta^{1/4}}{2\pi^{3/4}} \approx 1.93T_z \tag{3.118}$$

$$u_w = \left(\frac{\pi^3\beta}{\alpha}\right)^{1/4} * \frac{H_s}{T_z} \approx 24.32 * \frac{H_s}{T_z} \tag{3.119}$$

Therefore, the P - M spectrum can be described in terms of H_s, T_z or the combination of H_s and T_z. However, since the long-term properties of H_s are understood much better than the long-term properties of T_z, the P - M spectrum is commonly expressed in terms of H_s as suggested by ITTC (The International Towing Tank Conference). The spectrum is described as

$$G_{\eta\eta}(\omega) = \frac{\alpha g^2}{\omega^5} \exp\left(\frac{-3.11}{H_s^2}\ \omega^{-4}\right) \tag{3.120}$$

The spectral peak is

$$G_{\eta\eta}(\omega_p) = 0.25 \exp\ (-\ 5/4)\ H_s^{5/2} \tag{3.121}$$

at a peak frequency of

$$\omega_p = 1.26\sqrt{H_s} \tag{3.122}$$

JONSWAP Wave Spectrum

The JONSWAP spectrum is a modification to P - M spectrum to account for the effect of fetch restrictions. The main characteristic of this spectrum is its enhanced peak compared to that of P - M spectrum, as shown in Figure 3.12. The spectrum is a five parameter function, expressible as (Wilson, 1984).

$$G_{\eta\eta}(\omega) = \left\{ \frac{\alpha g^2}{\omega^5} \exp\left[-\frac{5}{4}\left(\frac{\omega}{\omega_p}\right)^{-4} \right] \right\} * \gamma_p^{\left[\exp\left(-\frac{(\omega-\omega_p)^2}{2\sigma^2\omega_p^2}\right)\right]} \qquad (3.123)$$

where ω_p is the peak frequency in terms of radians/sec and σ is

$$\sigma = \begin{cases} \sigma_a = 0.07 \text{ for } \omega \leq \omega_p \\ \sigma_b = 0.09 \text{ for } \omega > \omega_p \end{cases} \qquad (3.124)$$

γ_p is the shape factor, defined as the ratio of the peak spectral density to that of the corresponding P - M spectrum. When $\gamma_p = 1$, the spectrum reduces to P - M spectrum. The mean of γ_p has been found to be 3.3. α and ω_p are fetch dependent; their best estimates are

$$\omega_p = 2\pi(3.5)(g/u_w)(gx_f/u_w^2)^{-0.33} \qquad (3.125)$$

and

$$\alpha = \begin{cases} 0.076(gx_f/u_w^2)^{-0.22} \\ \text{or} \\ 0.0081 \quad \text{whichever is the smaller} \end{cases} \qquad (3.126)$$

X_f is the fetch length and u_w is the wind speed at a height of 10m above the mean sea level.2

FIGURE 3.1. REALISATION OF A RANDOM PROCESS x(t)
(SARPKAYA and ISAACSON, 1981)

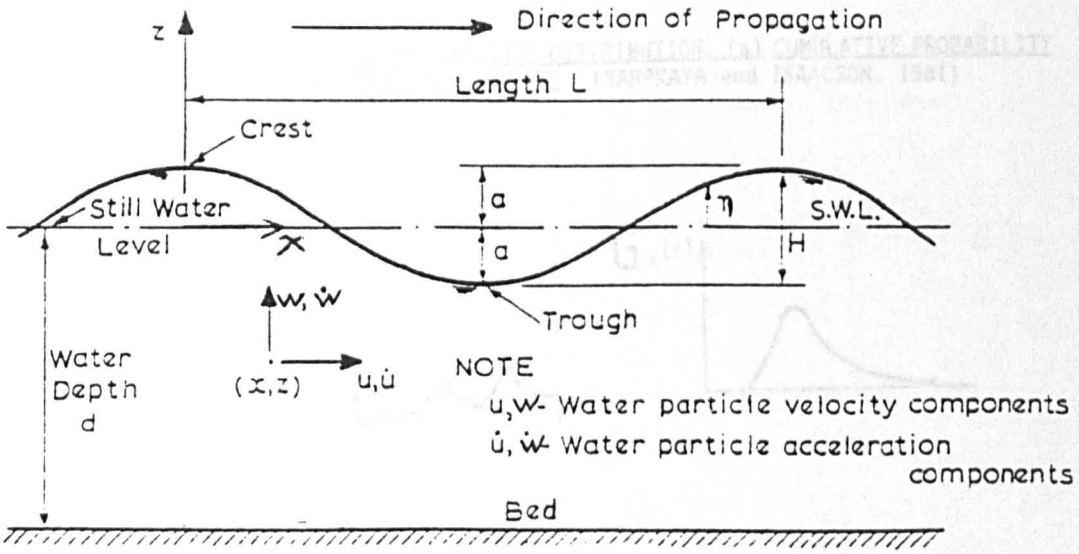

FIGURE 3.2. DEFINITION SKETCH FOR A PROGRESSIVE LINEAR WAVE
(Burrows, 1982)

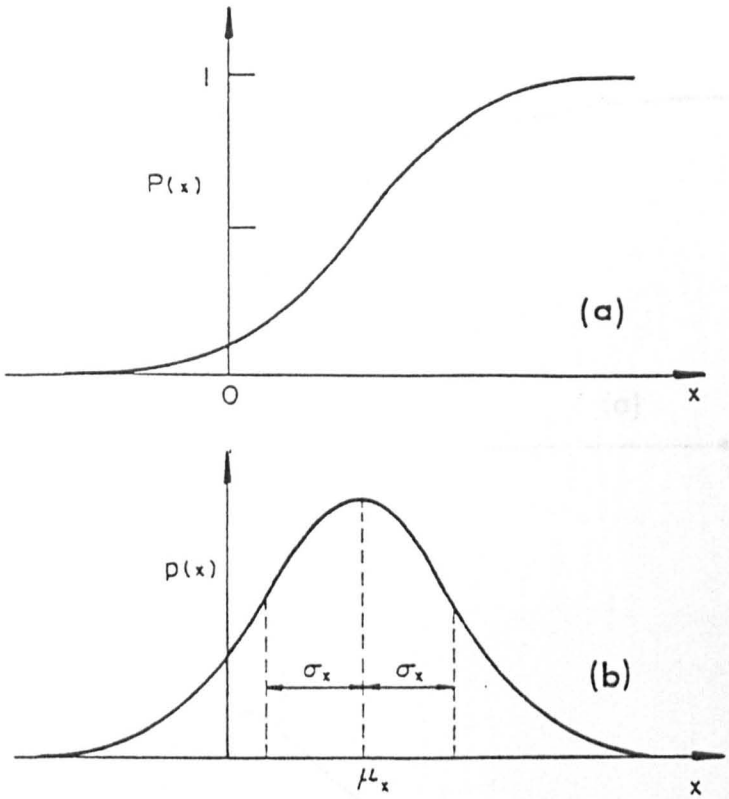

FIGURE 3.3. THE GAUSSIAN PROBABILITY DISTRIBUTION. (a) CUMULATIVE PROBABILITY (b) PROBABILITY DENSITY (SARPKAYA and ISAACSON, 1981)

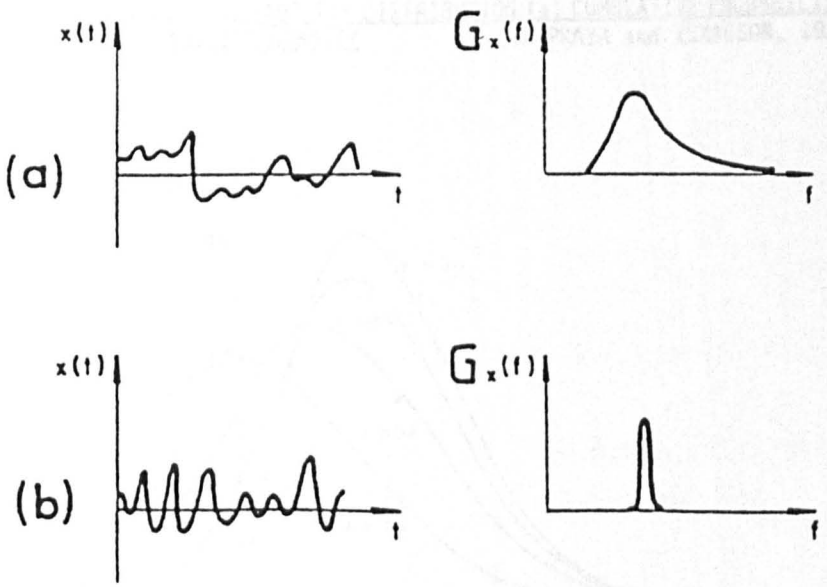

FIGURE 3.4. EXAMPLES OF RANDOM PROCESSES. (a) BROAD-BAND, (b) NARROW-BAND (SARPKAYA and ISAACSON, 1981)

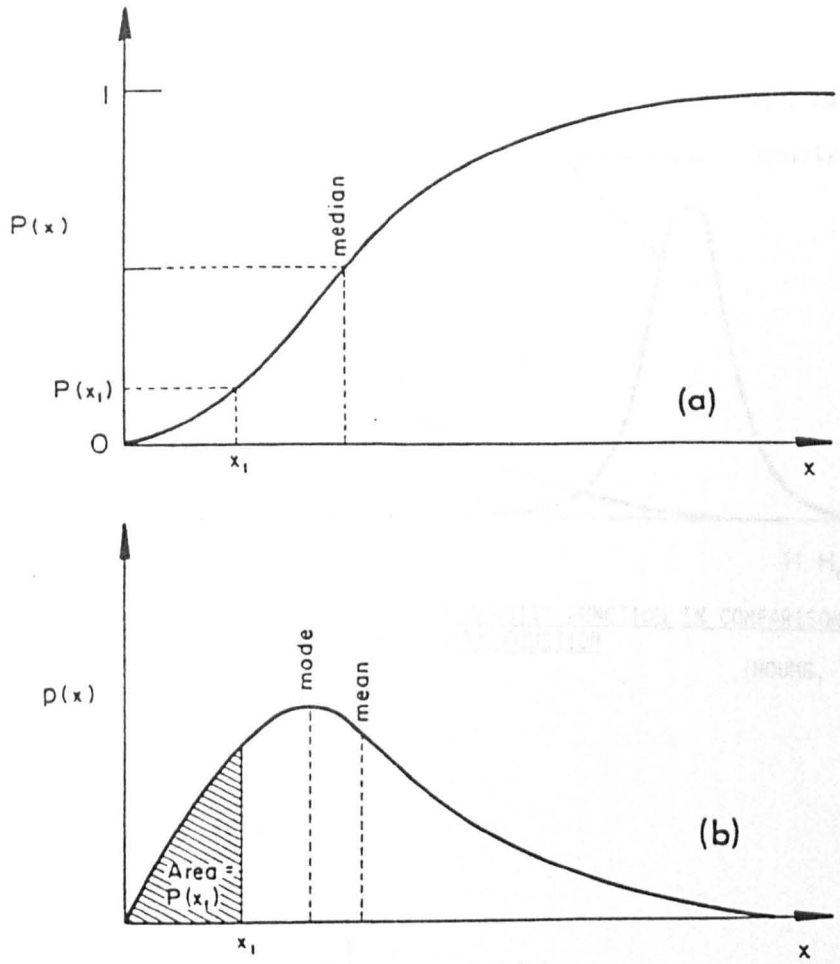

FIGURE 3.5. THE RAYLEIGH PROBABILITY DISTRIBUTION (a) CUMULATIVE PROBABILITY, (b) PROBABILITY DENSITY (SARPKAYA and ISAACSON, 1981)

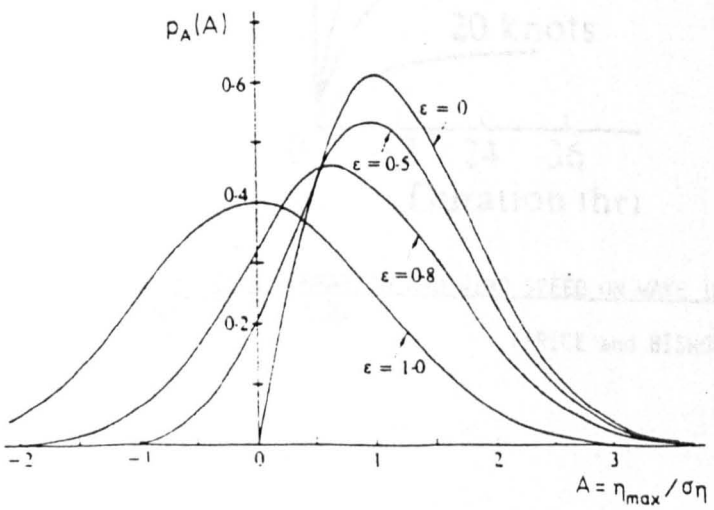

FIGURE 3.6. PROBABILITY DENSITY FUNCTION OF NORMALISED CREST ELEVATIONS FOR DIFFERENT VALUES OF THE SPECTRAL BAND WIDTH (PRICE and BISHOP, 1974)

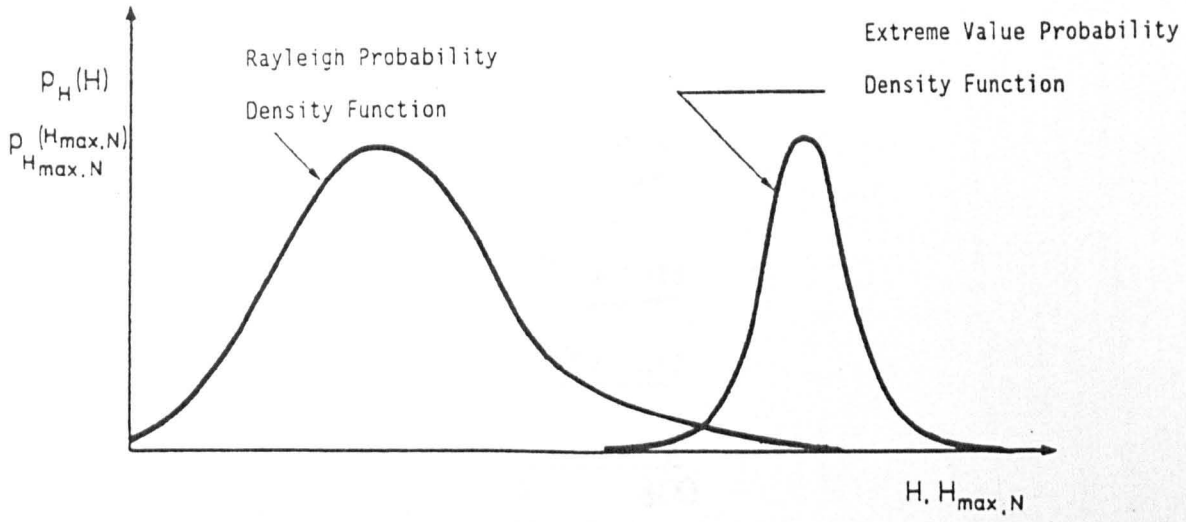

FIGURE 3.7. EXTREME VALUE PROBABILITY DENSITY FUNCTION IN COMPARISON WITH RAYLEIGH PROBABILITY DENSITY FUNCTION

(HOUMB, 1981)

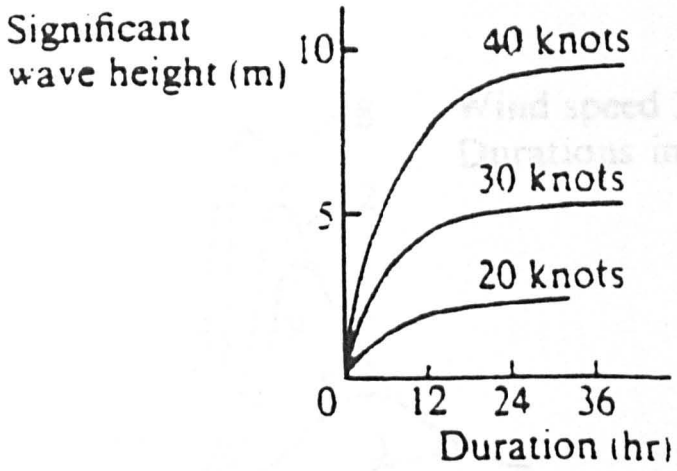

FIGURE 3.8 THE EFFECT OF DURATION AND WIND SPEED ON WAVE INTENSITY CHARACTERISED BY H_s

(PRICE and BISHOP, 1974)

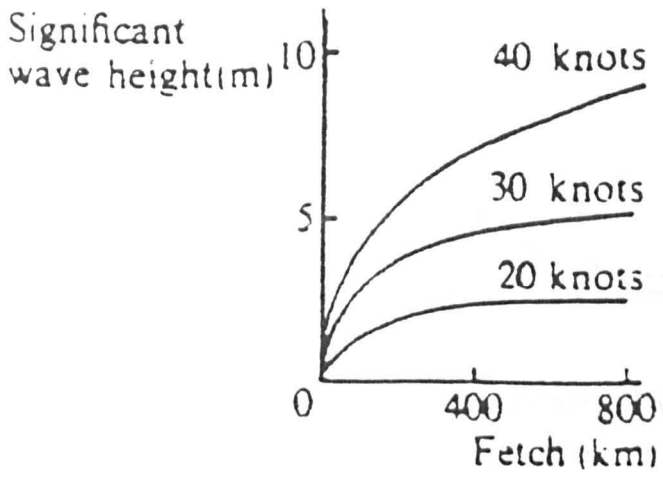

FIGURE 3.9 THE EFFECT OF FETCH AND WIND SPEED ON WAVE INTENSITY CHARACTERISED BY H.

(PRICE and BISHOP, 1974)

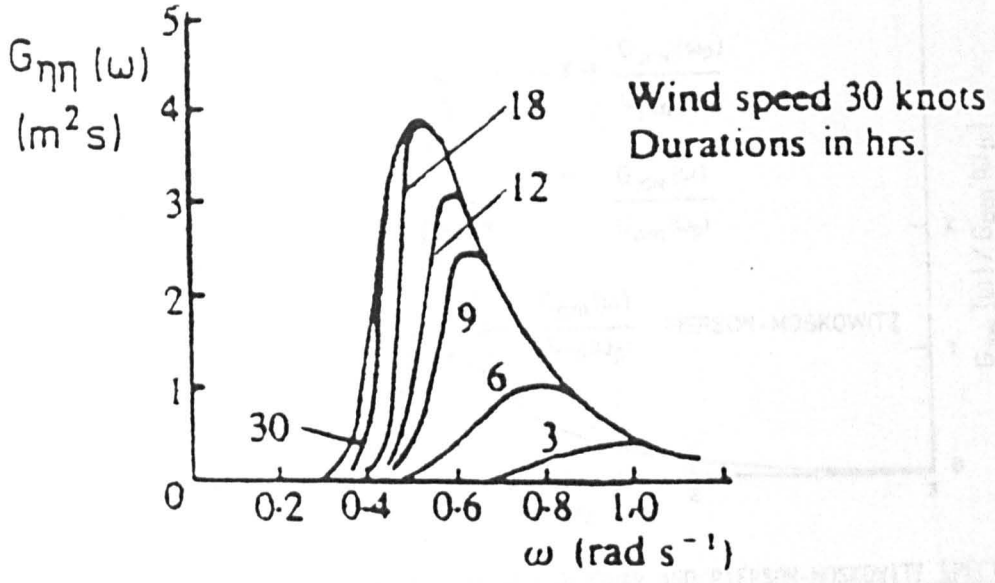

FIGURE 3.10. THE GROWTH OF THE SPECTRUM WITH INCREASING DURATION

(PRICE AND BISHOP, 1974)

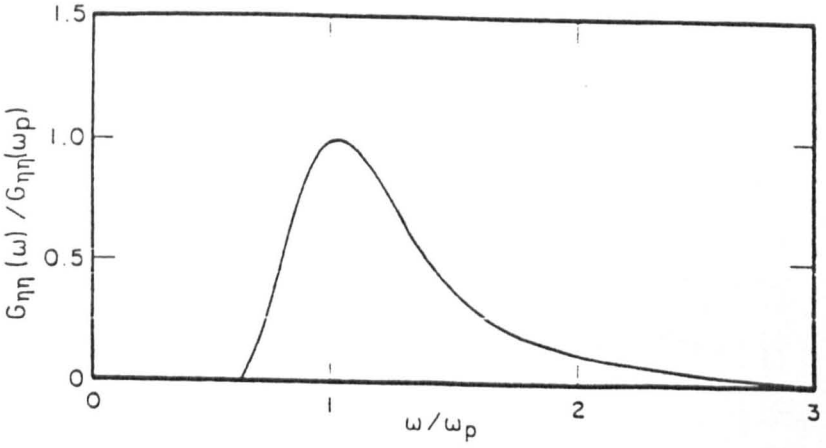

FIGURE 3.11. NORMALISED PIERSON-MOSKOWITZ SPECTRUM IN TERMS OF NORMALISED FREQUENCY
(SARPKAYA and ISAACSON, 1981)

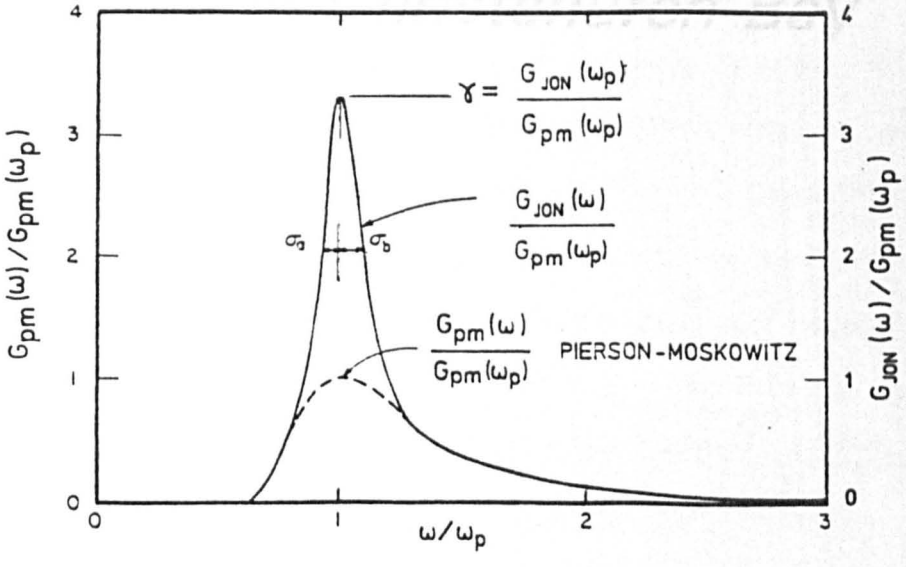

FIGURE 3.12. COMPARISON OF THE JONSWAP AND PIERSON-MOSKOWITZ SPECTRA
(SARPKAYA and ISAACSON, 1981)

Chapter 4

Short-Term Properties of Wave Records at Christchurch Bay

INTRODUCTION

This chapter is devoted to the study of wavefield conditions at Christchurch Bay so that the performance of the relative motion form of Morison's equation in predicting wave forces from water particle kinematics can be assessed. Of paramount importance, in this respect, is the study of wave directionality, predominant wave direction and currents. Furthermore, in the method of moments to be discussed in Chapter 9, C_d and C_m values have been determined based on the assumption that water particle kinematics are Gaussian distributed. It is, therefore, necessary to investigate the validity of this assumption, too. These are the minimum requirements for the analysis of Christchurch Bay data. However, in addition to the above minimum requirements, it is also desirable to establish the spectral and probabilistic properties of water surface elevation and water particle kinematics for the following reasons:

a) The theoretical effect of the nonlinear drag term of the Morison loading on the spectral and probabilistic properties of water particle kinematics is the subject of study in Chapter 8. On the other hand, the spectral and probabilistic properties of the observed wave forces at Christchurch Bay are determined in Chapter 9. Therefore, it is desirable to establish the spectral and probabilistic properties of water particle kinematics so that the performance of Morison's equation in the spectral and probability domains can be assessed. In other words, comparing the spectral and probabilistic properties of wave forces and the associated water particle kinematics, one can make comments on how closely the observed spectral and probabilistic properties of

wave forces can be predicted by the application of Morison's equation to water particle kinematics.

b) In the analysis of Christchurch Bay data, measured water particle kinematics have been used in deriving Morison's coefficients. However, one must appreciate that in practice, the designer will almost certainly use Linear Random Wave Theory (LRWT) to predict water particle kinematics from a given water surface elevation spectrum. The predicted kinematics are then used in conjunction with Morison's equation to predict random hydrodynamic forces. It is, therefore, necessary to consider the performance of LRWT in more detail and in particular, its capability in predicting the spectral properties of water particle kinematics from the water surface elevation spectrum must be assessed.

c) The model developed for the probabilistic analysis of offshore structures, is based on the following assumptions 1) Linear Random Wave Theory can successfully predict the spectral properties of water particle kinematics from the water surface elevation spectrum. 2) Water particle kinematics are Gaussian-distributed, as predicted by LRWT. 3) Morison's equation can successfully predict the probabilistic properties of wave forces from the known probabilistic properties of water particle kinematics. The study of spectral and probabilistic properties of water particle kinematics and wave forces at Christchurch Bay can be used in assessing the validity of these assumptions with regard to Christchurch Bay data.

Sections 4.1 and 4.2 of this chapter are devoted to the study of the spectral and probabilistic properties of water surface elevation and water particle kinematics, respectively. Although wave height of itself is not a primary variable in the probabilistic theory of wave loading, it is a very useful one by which to investigate the general behaviour of the seas. Therefore, the opportunity has been taken herein to compare the observed statistical and probabilistic properties of the wave heights of the Christchurch Bay records with their corresponding theoretical counterparts. The results of this study are also included in Section 4.1.

Sections 4.3 and 4.4 are concerned with the predominant wave direction and wave directionality, respectively. It will be shown that to a first degree of approximation, the waves can be considered to be uni-directional. Currents are the subject of study in Section 4.5. Finally, the performance of LRWT in predicting the spectral and probabilistic properties of water particle kinematics from the spectral and probabilistic properties of water surface elevation is studied in Section 4.6. Section 4.7 is devoted to the conclusions of this study.

4.1 SPECTRAL, STATISTICAL AND PROBABILISTIC PROPERTIES OF WATER SURFACE ELEVATION

The basic statistics for water surface elevation are given in Table 4.1. As observed, all the data sets are drawn from two distinct sea state intensities; that is, Runs 01, 02, 06, 07, 08 and 09, collected on 6th February 1987, have a significant wave height of $H_s \approx 1.5$m and Runs 13, 14, 15, 16 and 23, collected on 27th March 1987, have a significant wave height of $H_s \approx 3.75$m, where $H_s = 4\sigma_\eta$ (Equation (3.42)). From now on, the two sea states will be referred to as the low-

intensity and high-intensity sea states, and are characterised by the dimensionless numbers of three and eight, which are the approximate ratios between their corresponding significant wave heights and the cylinder diameter.

Mean zero-crossing, mean crest and mean spectral periods, calculated from appropriate moments of the water surface elevation spectrum according to Equations (3.58), (3.59) and (3.60), are listed in Columns 8, 9 and 10 of Table 4.1, respectively. In addition, the mean zero-crossing periods calculated directly from the time series are given in column 5. There is the general degree of agreement that might be expected from these period statistics. The calculated mean zero-crossing periods for low- and high-intensity runs are about 3.5 and 7.0 seconds, respectively.

Furthermore, the spectral band-widths calculated from Equation (3.29) are given in Column 11. Its value for the low-intensity runs is about 0.80 and for the high-intensity runs is about 0.85, indicating that water surface elevations are not strictly narrow-banded.

Water surface elevation and wave height probability distributions together with plots of surface elevation spectra for a typical low-intensity run (Run 01) and a typical high-intensity run (Run 15) are represented in Figures 4.1 to 4.8. A comparison of the two frequency spectra shows that the low-intensity run is slightly more energetic than the high-intensity run for frequencies above 0.40Hz. The important frequency range for Run 01 is up to 0.40Hz and for Run 15 is up to 0.20Hz.

With regard to logarithmic plots of spectra, it should be noted that small-amplitude, high-frequency components are due to numerical errors in digitizing the data and also due to round off errors in numerical calculations. Therefore, they should not be interpreted as the presence of real low-amplitude, high-frequency waves. Furthermore, it should be noted that the frequency spectra, cumulative distribution functions, and other statistics used in this study, are calculated from finite-length records and hence are subject to sampling variability. 95% confidence bands for typical spectral plots, cdf plots, and statistics have been established according to Sections C.5, C.6 and C.4 of Appendix C, respectively.

According to Linear Random Wave Theory (LRWT), water surface elevation is Gaussian-distributed. Figure 4.6 shows that the cdf of water surface elevation for Run 15 is outside the 95% confidence band of the theoretical Gaussian distribution. Furthermore, with reference to Columns 6 and 7 of Table 4.1, skewness and kurtosis for Run 15 are 0.37 and 3.00, respectively. The 95% confidence bands for these two statistics are $0.17 < \lambda < 0.57$ and $2.59 < \beta < 3.41$ (refer to Section C.4.2). The theoretical values of λ and β for a Gaussian-distributed random variable are zero and three, respectively. As such, the theoretical value of kurtosis is within its associated 95% confidence band; however, that of skewness is not. Therefore, both cdf plots and skewness values indicate (at a significance level of 5%) that water surface elevation for Run 15 is not a sample record from a Gaussian-distributed random process.

The situation for Run 01 is different. Figure 4.2 shows that the cdf of water surface elevation is within the 95% confidence band of the

theoretical Gaussian distribution. From Table 4.1 (Columns 6 and 7), the values of skewness and kurtosis are 0.07 and 2.94 and the corresponding 95% confidence bands are $-0.09 < \lambda < 0.23$ and $2.61 < \beta < 3.27$. Both ranges cover their corresponding theoretical values. It can therefore be concluded that there is no statistical reason to reject the Gaussian hypothesis (at the 5% significance level). In other words, it can be assumed that water surface elevation for Run 01 is a sample record from a Gaussian-distributed random process. It should be noted that the above approach investigates the validity of the Gaussian assumption for Run 01 in isolation from other runs. One can reach a different conclusion if all the records are used in assessing the validity of the Gaussian assumption.

With reference to Column 6 of Table 4.1, it is observed that the skewness values are positive for all the runs and generally speaking increase with increasing H_s. If each run was a sample record from a Gaussian-distributed random process, then skewness values should fluctuate about zero because of sampling variability. The fact that they are all positive, indicates that the sampling variability alone cannot explain the deviation of skewness from its theoretical value of zero. In fact, the deviation is consistent with finite-amplitude effects which give rise to higher crest elevations compared to trough elevations.

Overall, there is no doubt that the water surface elevation cannot be exactly Gaussian-distributed due to physical factors. For example, the Gaussian model predicts very large excursions of the water surface from the mean water level, albeit with low probability. In reality these excursions are limited by wave breaking and nonlinear interactions

between waves. When a sample record such as Run 01 is investigated in isolation from other records, the genuine deviation from the Gaussian model and the sampling variability get mixed up and one cannot differentiate between the two. The correct interpretation for the case of Run 01 is that there is some genuine deviation between the probability distribution of the random process represented by Run 01 and the corresponding theoretical Gaussian distribution; However, the deviation is small so that it can be explained by the sampling variability alone.

In conclusion, both low-intensity and high-intensity runs (represented by Runs 01 and 15, respectively) deviate from their corresponding theoretical Gaussian distributions. However, for low-intensity runs, the deviation is small so that the sampling variability alone can explain the deviation; In contrast, for high-intensity runs, the deviation is large so that it cannot be explained by the sampling variability alone.

Crests and Waveheights

Examination of Figures 4.3 and 4.7 shows that crests are more or less Gaussian distributed, as expected for random processes with high spectral bandwidths ($\epsilon \approx 0.8$). However, comparison of Figure 4.2 with 4.3 and 4.6 with 4.7 shows that the deviation between water surface elevations and associated theoretical Gaussian distributions in Figures 4.2 and 4.6 are reproduced in Figures 4.3 and 4.7 for water surface elevation crests.

Figures 4.4 and 4.8 show that wave heights are in reasonable agreement with Rayleigh distribution. Three different theoretical Rayleigh

distributions are plotted based on range data (wave height) mean, range data standard deviation, and basic signal (water surface elevation) standard deviation (Equations (3.34), (3.37) and (3.39)). While the distribution based on the mean of the wave heights are in closer agreement with the observed data for Run 01, examination of similar probability plots for other runs shows that this is not a general trend. Furthermore, it should be noted that due to the relatively small number of peaks and wave heights (in the order of a few hundreds), peaks and wave height values with low probability of exceedence (say 1%) are subject to significant sampling variability and hence their departure from their theoretical distributions should not necessarily be taken as evidence for the significant departure of the underlying population distribution from their corresponding theoretical distributions.

Wave height statistics are presented in Table 4.2, where the upper 5% and 10% quantiles are calculated from Rayleigh distribution (Equation 3.46) with $H_s = 4\sigma_\eta$ and are compared, as ratios, with their corresponding observed values (Columns 4 and 5). Furthermore, the ratio between the observed maximum wave height and the expected maximum wave height (Equation 3.48) is given in column 6. Since all these ratios are less than one, it is clear that Rayleigh distribution slightly overestimates the extreme wave height statistics. The level of overestimation is typical of data sets from other sites (Tickell et al, 1987). The above ratios when calculated from the modified Rayleigh distribution (Equation (3.56)) are given in Columns 7, 8 and 9, and offer an improvement over those calculated from Rayleigh distribution.

In addition, for the maximum wave height of each record, the zero-crossing period, T_{max}, and the crest height to wave height ratio, η_c/H_{max}, are given in Columns 10 and 11. This ratio is greater than 0.50 for all runs (except for Runs 02 and 06), which may be due to finite amplitude effects.

Also included in Table 4.2, are estimates of the percentage exposure of the centreline of Level 2 force sleeve, based on the assumption that water surface elevation is Gaussian distributed. For example, for Run 23, the water depth and σ_η are 9.60m and 0.948m, respectively. The centreline of Level 2 has an elevation of 8.60m, or it is 1.00m below mean water level. This distance is equivalent to -1.055 σ_η. The probability of η being less that -1.055 σ_η is 0.147. Therefore, 14.7% of the time, the centreline of the force sleeve at Level 2 is above water surface. The intermittency at Level 2 can introduce bias in estimates of mean current and hydrodynamic forces at this level. Hence, Morison coefficients obtained from the analysis of data at Level 2 must be treated cautiously.

4.2 SPECTRAL AND PROBABILISTIC PROPERTIES OF WATER PARTICLE KINEMATICS

Low-Intensity Runs

Figures 4.9 to 4.11 show the autospectra of the three components of the velocity in the x, y and z directions (u,v,w) at Level 3 for Run 01. The spectra is multi-modal, which can be due to the presence of a residual swell in the 15-17 second range in addition to a higher frequency local sea. Other low-intensity runs have similar spectral shapes.

Figures 4.12 to 4.14 represent the cumulative distribution of the three velocity components at Level 3 for Run 01. The probability distributions show some departure from Gaussian behaviour.

Values of skewness and kurtosis for the three velocity components of low-intensity runs are given in Table 4.3. The x components are all negatively skewed while the vertical components (except for Run 06) are all positively skewed. The kurtoses are all well above 3.0, indicating some departure from Gaussian distribution.

Values of skewness and kurtosis for acceleration components are given in Table 4.4. The x and z components are all positively skewed and the kurtoses are all well above 3.0 and are higher than those for the velocity components.

High-Intensity Runs

The autospectra of the velocity components at Level 3 for Run 15 are shown in Figures 4.15 to 4.17. Other runs in this group have similar spectral shapes. The cdf of the velocity components are shown in Figures 4.18 to 4.20. The agreement of this data with Gaussian distribution is greater than that for Run 01 despite greater severity and hence expected increase in finite amplitude effects.

Values of skewness and kurtosis for the three velocity components of the high-intensity runs are given in Table 4.5. The x and the z components (except for Run 14) are all positively skewed and have a kurtosis of less than 3.0 (except for Run 16).

Values of skewness and kurtosis for acceleration components are given in Table 4.6. The x components are all positively skewed while the z components are all negatively skewed. The kurtoses of the x components (except for Run 13) and all the z components are above 3.0, and are higher than those for the velocity components; however, they are less than those of the low-intensity runs.

Are Water Particle Kinematics Gaussian Distributed?

Examination of the probability plots for water particle velocities, together with skewness and kurtosis values for both velocities and accelerations, shows that the departure of water particle kinematics from their associated theoretical Gaussian distributions is statistically significant (at 5% significance level); that is, the cdfs of water particle kinematics lie outside the 95% confidence bands. Therefore, strictly speaking, the answer to the question of the validity of Gaussian distribution assumption for water particle kinematics is negative. However, the real question is whether the Gaussian distribution is a good approximation to the true distributions of the water particle kinematics at Christchurch Bay. The answer to this question is that it depends on the ultimate application of the results, which in the case of this study is the calculation of Morison's coefficients from the method of moments assuming that water particle kinematics are Gaussian distributed. Should the Gaussian distribution be a poor approximation to the real distribution, then the resultant C_d and C_m values from the method of moments should show great variation from record to record and from level to level. As will be demonstrated in Chapter 9, the results of this study show that C_d values for high-intensity runs are reasonably constant, and that C_m values, though of greater variability, show good correlation with the

acceleration parameter for both low-intensity and high-intensity runs. C_d values for low-intensity runs are unstable; however, that is because these runs are inertia dominated and hence are ill-conditioned for determination of C_d values.

The overall conclusion of this section is that there is genuine deviation between the observed probability distribution for water particle kinematics and their theoretical Gaussian distributions; however, the Gaussian distribution can be considered as a good approximation for the purpose of calculating Morison's coefficients from the method of moments.

4.3 PREDOMINANT WAVE DIRECTION

The component of wave induced horizontal velocity on an axis making an angle of θ with the x axis is

$$\hat{u} = (u - \bar{u})\cos\theta + (v - \bar{v})\sin\theta \tag{4.1}$$

in which u and v are the x and y components of the water particle velocity and $\bar{u}$ and $\bar{v}$ are the x and y components of the current. Note that $\bar{u}$ and $\bar{v}$ are

$$\bar{u} = E[u] \tag{4.2}$$

$$\bar{v} = E[v] \tag{4.3}$$

where E[.] is the expectation operator.

The predominant wave direction is then defined as the direction for which $E[\hat{u}^2]$ is maximum. From Equation (4.1), the following relationships are obtained

$$E[\hat{u}] = E[(u - \bar{u})]\cos\theta + E[(v - \bar{v})]\sin\theta = 0 \tag{4.4}$$

and

$$E[\hat{u}^2] = E[(u - \bar{u})^2]\cos^2\theta + E[(v - \bar{v})^2]\sin^2\theta + \sin 2\theta\, E[(u - \bar{u})(v - \bar{v})] \quad (4.5)$$

or

$$E[\hat{u}^2] = \sigma_{\hat{u}}^2 = \cos^2\theta\, \sigma_u^2 + \sin^2\theta\, \sigma_v^2 + \sin 2\theta\, \rho_{u,v}\, \sigma_u\, \sigma_v \quad (4.6)$$

where σ is the standard deviation and $\rho_{u,v}$ is the correlation coefficient between u and v, defined as $\rho_{u,v} = E[u - \bar{u})\ (v - \bar{v})]/\sigma_u\, \sigma_v$.

$E[\hat{u}^2]$ is maximum or minimum when its first derivative with respect to θ is zero. Thus, the predominant wave direction, $\bar{\theta}$, is the solution to the following equation.

$$\frac{dE[\hat{u}^2]}{d\theta} = -\sin 2\theta\, \sigma_u^2 + \sin 2\theta\, \sigma_v^2 + 2\cos 2\theta\, \rho_{u,v}\, \sigma_u\, \sigma_v = 0 \quad (4.7)$$

which after simplification reduces to

$$\tan(2\bar{\theta}) = \frac{2\rho_{u,v}\, \sigma_u\, \sigma_v}{\sigma_u^2 - \sigma_v^2} = \frac{2\rho_{u,v} * \sigma_v/\sigma_u}{1 - (\sigma_v/\sigma_u)^2} = \alpha \quad (4.8)$$

or

$$2\bar{\theta} = \arctan(\alpha) + k\pi \qquad k = 0,1,2,3,.....$$

Thus

$$\bar{\theta} = \tfrac{1}{2}\,\mathrm{Arctan}(\alpha) + k\pi/2 \quad (4.9)$$

The above equation leads to 4 angles round a circle, i.e.

$$\theta_1 = \tfrac{1}{2}\,\mathrm{Arctan}(\alpha)$$

$$\theta_2 = \theta_1 + \pi/2$$

$$\theta_3 = \theta_1 + \pi$$

$$\theta_4 = \theta_1 + 3\pi/2 \quad (4.10)$$

Two of the above angles (180° apart) lead to the maximum and the other two lead to the minimum of $E[\hat{u}^2]$. The two angles which lead to the maximum of $E[\hat{u}^2]$ can be identified by direct substitution of the above angles into Equation (4.5). However, there is an ambiguity in that it is not clear which of the two angles which lead to the maximum of $E[\hat{u}^2]$ is the true predominant wave direction. This ambiguity is resolved by knowing from the physical knowledge of the site that the predominant wave direction is close to the positive direction of the x axis.

The wave component velocity on a direction making an angle of $(\pi/2 + \theta)$ with the x axis is denoted by $\hat{v}$ and is equal to

$$\hat{v} = (u - \bar{u})\cos(\pi/2 + \theta) + (v - \bar{v})\sin(\pi/2 + \theta) = -(u - \bar{u})\sin\theta + (v - \bar{v})\cos\theta \qquad (4.11)$$

From Equations (4.1) and (4.11), $\hat{u}.\hat{v}$ will be

$$\hat{u}.\hat{v} = \cos2\theta(u - \bar{u})(v - \bar{v}) - \tfrac{1}{2}\sin2\theta\,[(u - \bar{u})^2 + (v - \bar{v})^2] \qquad (4.12)$$

Taking expectations from both sides of the above relationship results in

$$E[\hat{u}.\hat{v}] = \cos2\theta\,\rho_{u,v}\,\sigma_u\,\sigma_v - \tfrac{1}{2}\sin2\theta\,(\sigma_u^2 - \sigma_v^2) \qquad (4.13)$$

Setting $E[\hat{u}.\hat{v}]$ equal to zero, leads to the following equation

$$\mathrm{Tan}2\theta = \frac{2\rho_{u,v}\,\sigma_u\,\sigma_v}{\sigma_u^2 - \sigma_v^2} \qquad (4.14)$$

which is identical to Equation (4.8). Therefore, for the predominant wave direction, $\bar{\theta}$, the following properties hold true.

$E[\hat{u}^2]$ is maximum

$E[\hat{v}^2]$ is minimum

$$E[\hat{u}\hat{v}] = \rho_{\hat{u},\hat{v}} = 0$$

Where $\hat{u}$ and $\hat{v}$ are defined by Equations (4.1) and (4.11), respectively.

The predominant wave direction for each run, together with $\rho_{u,v}$, σ_u, σ_v and σ_v/σ_u are presented in Table 4.7. Some of the results for Level 2 must be treated with caution due to intermittency at this level. There is a consistency in the estimated predominant wave direction and this is very close to the x axis of the tower. The ratio σ_v/σ_u is about 0.3, indicating that the sea states are not strongly short-crested. The average predominant wave direction for Levels 3 and 4 has been taken as the predominant wave direction for that run. The results are presented in Table 4.8.

It is worth noting that in Equation (4.8), it is possible to replace u and v with $\dot{u}$ and $\dot{v}$ and calculate predominant wave directions based on water particle accelerations. The results are only marginally different from those in Table 4.7 and hence are not presented.

4.4 WAVE DIRECTIONALITY

As stated in Chapter 3, it is convenient to express the directional spectrum, $G_{\eta\eta}(\omega,\theta)$, in terms of the uni-directional wave spectrum and a spreading function, denoted by $D(\omega,\theta)$. Thus

$$G_{\eta\eta}(\omega,\theta) = D(\omega,\theta) * G_{\eta\eta}(\omega) \qquad (4.15)$$

Integrating both sides of the above equation with respect to θ and replacing $\int_{-\pi}^{\pi} G_{\eta\eta}(\omega,\theta)d\theta$ by $G_{\eta\eta}(\omega)$, leads to

$$\int_{-\pi}^{\pi} D(\omega,\theta)d\theta = 1 \qquad (4.16)$$

According to the above equation, the spreading function shows the directional distribution of the water surface variance (wave energy) at any frequency.

Calculation of the spreading function

At any particular frequency, $D(\omega,\theta)$ is a function of θ only and its truncated Fourier series is

$$D(\omega,\theta) = 1/2\pi + \sum_{k=1}^{n} a_k(\omega)\cos(k\theta) + b_k(\omega)\sin(k\theta) \tag{4.17}$$

The term $1/2\pi$ is the mean of $D(\theta)$ over the range $-\pi$ to $+\pi$ and ensures that Equation (4.16) is satisfied.

Fourier coefficients up to n=2 (a_1, b_1, a_2, b_2) can be calculated from the auto and cross-spectra of the three orthogonal velocity components (van Heteren et al, 1988).

$$a_1(\omega) = \frac{Q_{uw}(\omega)}{\pi[C_{ww}(\omega)(C_{uu}(\omega) + C_{vv}(\omega))]^{1/2}} \tag{4.18}$$

$$b_1(\omega) = \frac{Q_{vw}(\omega)}{\pi[C_{ww}(\omega)(C_{uu}(\omega) + C_{vv}(\omega)]^{1/2}} \tag{4.19}$$

$$a_2(\omega) = \frac{C_{uu}(\omega) - C_{vv}(\omega)}{\pi[C_{uu}(\omega) + C_{vv}(\omega)]} \tag{4.20}$$

$$b_2(\omega) = \frac{2C_{uv}(\omega)}{\pi[C_{uu}(\omega) + C_{vv}(\omega)]} \tag{4.21}$$

where in general, the cross-spectrum between x and y is

$$G_{xy}(\omega) = C_{xy}(\omega) - iQ_{xy}(\omega) \tag{4.22}$$

Fourier coefficients up to n=4 were calculated by Mitsuyasu (1975); however, that requires measurements such as wave slope and wave curvature which were not available in the present study.

The truncated Fourier series (Equation 4.17) does not necessarily provide a good fit to the spreading function since, for example, it can lead to negative values for some directions. To provide a better approximation, weighting coefficients w_n are introduced into Equation (4.17) in the following form.

$$D(\omega,\theta) = 1/2\pi + \sum_{k=1}^{n} w_k(\omega)[a_k(\omega)\cos(k\theta) + b_k(\omega)\sin(k\theta)] \qquad (4.23)$$

However, this weighted or smoothed form of the spreading function leads to overly broad estimates of $D(\omega,\theta)$. This has resulted in the use of parametric spreading functions, such as the full circle cosine-power spreading function used in this study.

Cosine-power spreading function

The full circle cosine-power function is defined as (Mitsuyasu et al., 1975),

$$D(\omega,\theta) = C(s)\cos^{2s}\left(\frac{\theta - \bar{\theta}}{2}\right) \qquad |\theta - \bar{\theta}| \leq \pi \qquad (4.24)$$

Where $\bar{\theta}$ is the mean wave direction and s, the spreading parameter, determines the broadness of the spreading, as shown in Figure 4.21. C(s) is a normalising function and ensures that Equation 4.16 is satisfied, and is given by

$$C(s) = \frac{2^{2s-1}}{\pi}\,\frac{\Gamma^2(s+1)}{\Gamma(2s+1)} = \frac{1}{2\sqrt{\pi}}\,\frac{\Gamma(s+1)}{\Gamma(s+\frac{1}{2})} \qquad (4.25)$$

Where Γ is the Gamma function. In general, both $\bar{\theta}$ and s are functions of ω.

This parametric form may be fitted to the Fourier representation of the spreading function (Equation 4.17) in terms of the calculated Fourier coefficients (Equations 4.18 to 4.21) using the expressions given by Mitsuyasu et al (1975).

$$\tan \bar{\theta}_1 = b_1/a_1 \tag{4.26}$$

$$s_1 = c_1/(1-c_1) \tag{4.27}$$

where

$$c_1 = \pi[a_1^2 + b_1^2]^{\frac{1}{2}} \tag{4.28}$$

or

$$\tan 2\bar{\theta}_2 = b_2/a_2 \text{ (mod } 180°) \tag{4.29}$$

$$s_2 = \frac{1 + 3c_2 + [c_2^2 + 14c_2 + 1]^{\frac{1}{2}}}{2(1 - c_2)} \tag{4.30}$$

where

$$c_2 = \pi\,[a_2^2 + b_2^2]^{\frac{1}{2}} \tag{4.31}$$

If the cosine-power spreading function was a perfect fit to the measured (real) spreading function, $\bar{\theta}_1 = \bar{\theta}_2$ and $s_1 = s_2$; however, in general, $\bar{\theta}_1 \neq \bar{\theta}_2$ and $s_1 \neq s_2$.

Table 4.9 gives the cosine power parameters for Run 01 and Run 23 derived from Level 3 and Level 4 particle velocities, while Table 4.10 gives similar results for Run 13 and Run 15. The data for Run 08 is shown in Figure 4.22. The mean directions ($\bar{\theta}_1$ and $\bar{\theta}_2$) at frequencies near the peak of the spectra are in agreement with those quoted in

Table 4.7. The mean direction at other frequencies is generally within 5 - 10° of the overall direction except for Run 15 where there are some shifts at high frequency.

As is commonly found, the spreading function is narrow (high s values) at the peak of $G_{\eta\eta}(\omega)$ and then broadens in the tail of the spectra.

Overall, the data can, to a first degree of approximation, be treated as long-crested.

4.5 CURRENTS

Currents can be normalised in two different ways:

a) By dividing the current magnitude by the cylinder diameter times its natural frequency, i.e.

$$r_1 = \frac{\sqrt{\bar{u}^2 + \bar{v}^2}}{D^* f_n} \tag{4.32}$$

This parameter is known as the current reduced velocity.

b) By dividing the current magnitude by the standard deviation of the horizontal component of the wave-induced velocity, i.e.

$$r_2 = \left(\frac{\bar{u}^2 + \bar{v}^2}{\sigma_u^2 + \sigma_v^2} \right)^{1/2} \tag{4.33}$$

Where $\bar{u}$ and σ_u are the mean and S.D of the water particle velocity in the x direction. $\bar{v}$ and σ_v refer to similar entities in the y direction.

Low-Intensity Runs

Current magnitude and direction (measured clockwise from x axis as shown in Figure 2.2) together with values of r_1 and r_2 are given in Table 4.11. The values of r_2 are scattered about 1.6 indicating that current is significant with respect to wave-induced velocities. Current direction is about 70° from x axis (predominant wave direction) and therefore can be considered as being almost transverse to the predominant wave direction.

High-Intensity Runs

Similar information as Table 4.11 are represented in Table 4.12 for high-intensity runs. r_2 has a maximum of 0.6 indicating that current for high-intensity runs is not as significant as it is for low-intensity runs with respect to wave induced velocities. Current direction changes; however, with the exception of Run 23, it is in the opposite direction to wave propagation. For Run 23, the current is almost transverse to the predominant wave direction so that the particle velocity meters are almost in the shadow of the large column; hence, the measured value of the current is expected to be somewhat different from its real value at the compliant cylinder position (refer to Figure 2.2). Another point to be noted is that for this run the current magnitude is larger than that for other high-intensity runs.

4.6 PERFORMANCE OF LINEAR RANDOM WAVE THEORY (LRWT)

Water surface elevation and water particle kinematics have not been measured at the same point at Christchurch Bay (refer to Chapter 2). Therefore, it is not possible to assess the performance of LRWT (in predicting water particle kinematics from given records of water surface elevation) in the time domain. However, since water surface

elevation and the associated water particle kinematics are assumed to be stationary and homogeneous random processes, it is possible to study the performance of the theory in both spectral and probability domains.

Spectral Domain

Performance of LRWT in the spectral domain can be assessed by comparing the observed and predicted transfer functions between water surface elevation (η) and water particle velocity in the predominant wave direction (u).

The observed transfer function between η and u is defined as

$$|H_{\eta u}(\omega)| = |G_{\eta u}(\omega)|/G_{\eta\eta}(\omega) \tag{4.34a}$$

Where $G_{\eta u}(\omega)$ is the cross-spectrum between η and u (refer to Section 3.3). The theoretical value of the above transfer function in the case of directional seas is (Borgman, 1977).

$$|H_{\eta u}(\omega)| = \omega\, \Gamma_h(\omega) \int_{-\pi}^{\pi} D(\omega,\theta)\, \cos(\theta)\, d\theta \tag{4.34b}$$

Where $D(\omega,\theta)$ is the spreading function and Γ_h is the horizontal depth attenuation factor given by Equation (3.64). That is,

$$\Gamma_h = \cosh[k(z + d)]/\sinh(kd) \tag{4.34c}$$

According to Equation (4.34b), the transfer function is dependent on the spreading function, the value of which cannot be determined accurately. In order to remove the uncertainty regarding the appropriate spreading function, the following method was adopted for assessing the performance of LRWT.

According to Equations (3.69) and (3.70), the following relationships exists between the auto-spectra of horizontal water particle kinematics and water surface elevation spectrum.

$$G_{uu}(\omega) = G_{\eta\eta}(\omega) * \omega^2 \Gamma_h^2 \int_{-\pi}^{\pi} D(\omega,\theta) \cos^2\theta \, d\theta \tag{4.35}$$

and

$$G_{vv}(\omega) = G_{\eta\eta}(\omega) * \omega^2 \Gamma_h^2 \int_{-\pi}^{\pi} D(\omega,\theta) \sin^2\theta \, d\theta \tag{4.36}$$

Adding Equations (4.34) and (4.35) and replacing $\int_{-\pi}^{+\pi} D(\omega,\theta) \, d\theta$ by one, leads to

$$G_{uu}(\omega) + G_{vv}(\omega) = G_{\eta\eta}(\omega) * \omega^2 \Gamma_h^2 \int_{-\pi}^{\pi} D(\omega,\theta)[\cos^2\theta + \sin^2\theta] \, d\theta$$

$$= G_{\eta\eta}(\omega) * \omega^2 \Gamma_h^2 \int_{-\pi}^{\pi} D(\omega,\theta) \, d\theta$$

$$= G_{\eta\eta}(\omega) * \omega^2 \Gamma_h^2 \tag{4.37}$$

or

$$G_{\eta\eta}(\omega) = \frac{1}{\omega^2 \Gamma_h^2} * [G_{uu}(\omega) + G_{vv}(\omega)] \tag{4.38}$$

which when combined with Equation (4.36), yields

$$G_{\eta\eta}(\omega) = \frac{\sinh^2 (kd)}{\omega^2 \cosh^2 [k(z+d)]} \; [G_{uu}(\omega) + G_{vv}(\omega)] \tag{4.39}$$

The above relationship can be used to calculate $G_{\eta\eta}(\omega)$ from $G_{uu}(\omega)$ and $G_{vv}(\omega)$. On the other hand, to calculate $G_{uu}(\omega)$ and $G_{vv}(\omega)$ from $G_{\eta\eta}(\omega)$, it is necessary to establish the spreading function accurately. Therefore, it is preferable to calculate $G_{\eta\eta}(\omega)$ from the auto-spectra of horizontal water particle kinematics and compare it with the observed water

surface elevation spectrum. Alternatively, $G_{\eta\eta}(\omega)$ can be obtained from the following relationship (Equation 3.71).

$$G_{ww}(\omega) = G_{\eta\eta}(\omega) * \omega^2 \Gamma_w^2(\omega) \tag{4.40}$$

where Γ_w is the vertical depth attenuation factor. After replacing Γ_w from Equation (3.65), the above equation can be rewritten as

$$G_{\eta\eta}(\omega) = \frac{\sinh^2 (kd)}{\omega^2 \sinh^2 [k(z + d)]} G_{ww}(\omega) \tag{4.41}$$

Figure 4.23 shows the comparison between the observed surface elevation spectrum for Run 13 and that predicted from Equation (4.39) at Level 3. Table 4.13 gives further comparison of observed and predicted (from Equation 4.39) surface elevation spectra for Runs 01, 08, 15 and 23. For Run 01, predictions based on Level 4 are smaller than predictions based on Level 3, while the opposite is true for Run 15, though for this run the differences are very small compared to the peak spectral value. Figure 4.24 shows the comparison between the observed surface elevation spectrum for Run 15 and those predicted from vertical velocity spectra (Equation 4.41) at all levels. It is noted that data for Level 4 leads to a consistent underestimation of the surface elevation spectrum.

In addition to the above procedure, the performance of LRWT in the spectral domain can be checked in the following way, too. Dividing Equation (4.41) by (4.39) and taking the square root of the resultant, a measure of the performance of linear random wave theory is obtained in terms of a function $Z(\omega)$ where,

$$Z(\omega) = \left[\frac{G_{ww}(\omega)}{[G_{uu}(\omega) + G_{vv}(\omega)] \tanh^2 (kd)} \right]^{1/2} \qquad (4.42)$$

According to LRWT, $Z(\omega)$ must be unity for all frequencies. Values of Z are presented in Table 4.14 over the relevant range of frequencies. The largest departures occur in the high frequency tails of the spectra and in general, the data at Level 3 shows smaller discrepancies than those for Level 4.

The above results show that there are differences between the observed velocity spectra and those predicted from the observed surface elevation spectrum using linear wave theory. Tickell and Burrows (1989) have offered a number of possible explanations for these differences though they could not identify any clear cause. These factors include:

(1) **Instrument/Calibration Errors**

The perforated ball systems have been in use for some time and the final version of the BMT algorithm for interpreting the three force measurements, in terms of the velocities and accelerations, has been as well proven as any other monitoring system. Spectral values given in Table 4.13 show both over and underestimation in comparison with the observed spectra which is not consistent with a system bias. It should also be recalled that the measurement of surface elevation being used is from an accelerometer buoy which is some 100m remote from the site and subject to its own set of system characteristics.

(2) Current Interactions

Simple calculations will show that no Doppler shift effect, due to currents, applied to the depth attenuation factors could alone explain the differences seen in the spectra in Table 4.13.

(3) Interference Effects

particle velocity meters are supported on the rigid small column and are approximately three diameters to one side in a line orthogonal to the predominant wave direction. It is not clear, from the data collected in the present programme, that any of the discrepancy can be explained through interference effects. It is of course recognised that, by virtue of the presence of the tower base, the seabed is not a horizontal plane. This is unlikely to produce diffraction effects in the longer period components ($f < 0.15$Hz, say). Waves above $f = 0.3$Hz are effectively in deep water and unaffected by the base. Simple calculations show that, for waves in the range $0.15 < f < 0.3$Hz, an effective decrease in water depth would lead to increases in the predicted horizontal particle velocity spectra and decreases in the corresponding vertical spectra of typically 5-10%.

(4) Nonlinear Hydrodynamics

The existence of finite-amplitude effects has already been noted in terms of non-zero skewnesses of the kinematics. However, while weak nonlinear random wave theories do produce peaky crests and flat troughs, they do not deal with wind shear effects on the horizontal asymmetry of wave profiles. It was considered to be beyond the scope of the present study to pursue finite-amplitude modifications to the predicted kinematics.

Overall, the combination of the above-mentioned factors together with measurement errors and the shortcomings of LRWT itself can be considered as the cause of the discrepancies between the observed and predicted water particle velocity spectra. However, with the exception of Run 23, the differences are not consistent; that is, there are some overestimations and some underestimations so that the variance of the observed and the predicted velocities are expected to be in good agreement.

The case of Run 23 deserves special consideration in that the predicted water surface elevation is consistently above the observed values over the important frequency range, i.e. 0.0 to 0.2Hz. As a result, the variance of the predicted water surface elevation is about 15% higher than that of the observed water surface elevation. This implies that water particle velocities (and hence accelerations) predicted by the application of LRWT to the observed water surface elevation record, will be of lower variance in comparison with the observed kinematics (predicted/observed = 0.87). This is important because, as will be shown in Chapter 9, the total force coefficient for Run 23 is smaller than those for other high-intensity runs (and in particular, than that for Run 16 which has the same Keulegan-Carpenter No. as Run 23) by about the same factor, without any clear reason (refer to Table 9.2). One possible explanation would be that somehow, the measured kinematics for Run 23 are overestimated.

Probability Domain

The cdfs of water particle velocities are expected to follow the same trend as those of their corresponding water surface elevations in view of the linear nature of the transformation between the two. Examination

of skewness values for water surface elevation and water particle velocities (Tables 4.1, 4.3, and 4.5) shows that with the exception of Run 16, $\lambda_u < \lambda_\eta$. According to LRWT, $\lambda_u \approx \lambda_\eta$ after accounting for sampling variability. Therefore, it seems that in this study, $(\lambda_u)_{LRWT} > (\lambda_u)_{Observed}$. This implies that generated velocities (through the use of LRWT) underpredict extreme negative velocities and/or overpredict the extreme positive ones (also compare Figure 4.12 with 4.2, and 4.18 with 4.6). This conclusion is in agreement with the results of Tickell et al, 1976 (Figures 3.9 and 3.10) who came to the same conclusion from analysis of 1976 Christchurch Bay data.

The skewness of water particle accelerations are in better agreement with those of their corresponding water surface elevations and generally speaking are closer to their theoretical value of zero. This is not surprising as extreme values of velocity (positive or negative) will result in both large positive and negative accelerations. Therefore, accelerations are expected to be more symmetrical than the skewed velocities which gave rise to them, in the first place.

In contradiction with LRWT, the kurtoses of water particle velocities in the case of low-intensity runs are consistently smaller than those of their associated water surface elevations (except for Run 09) and the reverse is true for high-intensity runs. Kurtoses of water particle accelerations are consistently higher than those of water particle velocities. Again this is expected because of the asymmetries in the distributions of water particle velocities. As was previously mentioned, high extreme values of velocity (positive or negative) lead to high positive and negative accelerations with the overall effect that $\beta_{acceleration} > \beta_{velocity}$.

Overall, the results of this investigation shows that there are some discrepancies between the probabilistic properties of the observed kinematics and those predicted by LRWT. The same factors as those mentioned for the discrepancies in the spectral domain can be responsible for the discrepancies in the probability domain.

Is Linear Random Wave Theory Useable?

The results of the above study in both spectral and probability domains show that there are some discrepancies between the spectral and probabilistic properties of the observed water particle kinematics and those predicted by the application of LRWT to water surface elevation records. The discrepancy is partly accounted for by the shortcomings of LRWT itself, partly by measurement errors, and partly by reasons mentioned by Tickell and Burrows (1989), though at this stage, it is not possible to quantify the effect of any of the above-mentioned factors. Overall, though these differences are not insignificant, they are not excessive, either. Furthermore, these differences are more or less of a random nature, so that there are some overestimations and some underestimations. It is, therefore, expected that the discrepancies do balance each other out, so that the variances of the water particle kinematics and the resultant forces and responses can be established with reasonable accuracy. Therefore, the application of LRWT in the design of offshore structures, in view of its simplicity and in view of uncertainties in other important parameters used in the design of offshore structures (such as the water surface elevation spectrum and Morison's coefficients) is justifiable. However, the author believes that it is always good practice to corroborate the results of such a study with other methods (which inevitably have their own shortcomings). If the results are significantly different, then the

cause of the differences must be established. If that proves impossible, the design, then, must be based on the most conservative results.

With regard to the analysis of Christchurch Bay data, LRWT has been used in shifting water particle kinematics from their point of measurement to the cylinder axis assuming that the waves are uni-directional. Furthermore, water particle kinematics have been assumed to be Gaussian-distributed in calculating Morison's coefficients from the method of moments. The second assumption was fully discussed in Section 4.2 and its use for the purpose of the method of moments was justified. The shifting of water particle kinematics will be fully discussed in Chapter 6. In Chapter 9, it will be shown that phase shift errors introduced because of the shortcomings of LRWT and also because of the uni-directionality assumption, do not have a significant adverse effect on the calculated Morison's coefficients.

4.7 Conclusions

This chapter was devoted to the study of wave conditions at Christchurch Bay. The following conclusions have been made.

1. The eleven data sets have been divided into two groups, low-intensity runs with a significant wave height of $H_s \approx 1.5$m and high-intensity runs with a significant wave height of $H_s \approx 3.75$m. The mean zero-crossing periods for the low- and high-intensity runs are about 3.5 and 7.0 seconds, respectively.

2. While close to Gaussian distribution, the surface elevation time series show departures consistent with finite amplitude effects.

3. As expected, the deviations between the cdfs of water surface elevations and their associated theoretical Gaussian distributions are reproduced in the cdfs of water surface elevation crests.

4. Level 2 is subject to intermittent exposure and hence the results associated with this level must be treated cautiously.

5. The Rayleigh distribution based on significant wave height ($H_s = 4\sigma_\eta$) can lead to an overestimation of 7 to 14% for the upper 5% quantile of the wave heights at Christchurch Bay. The modified Rayleigh distribution (incorporating the factor 0.925) provides an improved fit.

6. There are statistically significant differences between the observed probability distributions of water particle kinematics and their associated theoretical Gaussian distributions. However, the Gaussian assumption leads to stable C_d and C_m values from the method of moments, so that it can be considered as a good approximation to the true distribution of water particle kinematics for the purpose of determining Morison's coefficients from the method of moments.

7. The predominant wave direction is very close to the X axis of the tower.

8. Near the peak of the wave spectrum, the sea is almost long-crested with high powers of s in the full circle cosine-power spreading function ($12 < s < 24$). At twice the peak frequency,

the sea is more short-crested with s in the range of 2 to 6. Overall, to a first degree of approximation, the waves can be considered to be uni-directional.

9. The results of this investigation show that there are statistically significant discrepancies between the spectral and probabilistic properties of the observed kinematics and those predicted by the application of LRWT to their corresponding water surface elevation records. The discrepancies can be attributed to several factors such as measurement errors and the shortcomings of LRWT itself. However, the discrepancies are not excessive and are more or less of a random nature, so that in view of its simplicity, the application of LRWT to the design of offshore structures is justifiable in most circumstances.

10. The case of Run 23 deserves special consideration. This is because the total force coefficient for this run is smaller than those for other high-intensity runs (and in particular than that for Run 16, which is of the same Keulegan-Carpenter No.), without any clear reason. Run 23 is different from other high-intensity runs in the following points. These points may prove useful in offering possible explanations for this apparent observed discrepancy in Chapter 9.

a) Water depth for Run 23 is lower than that for other high-intensity runs. Consequently, the percentage of Level 2 exposure for this run is higher (15% against an average of 5%; refer to Table 4.2).

b) With the exception of Run 23, the current is in the opposite direction to wave propagation for high-intensity runs. For run 23, the current is almost transverse to the predominant wave direction, so that the particle velocity meters are almost in the shadow of the large column. Hence, the measured value of the current is expected to be somewhat different from its real value at the compliant cylinder position. Another point to be noted is that the current magnitude for this run is larger than that for other high-intensity runs (Table 4.12).

c) Water particle velocities (and hence accelerations) predicted by the application of LRWT to the observed water surface elevation record, are of lower variance in comparison with the measured kinematics (predicted/observed = 0.87). On the other hand, the force coefficient for this run are smaller than that for Run 16 by about the same factor. One possible explanation for the discrepancy is that somehow, the measured kinematics for this run are overestimated.

(1) Run No	(2) Water Depth (d m)	(3) Surface Elevn. (σ_η m)	(4) Sig. Height (H_s m)	(5) Zero-crossing Period (T_z sec)	(6) Skewness (λ)	(7) Kurtosis (β)	(8) Spectral Periods (sec) (T_z)	(9) (T_c)	(10) (T_m)	(11) Spectral Band-width (ϵ)
01	9.21	0.345	1.38	3.2	0.07	2.94	3.7	2.3	4.2	0.78
02	9.24	0.352	1.41	3.4	0.09	2.86	3.7	2.3	4.2	0.78
06	9.28	0.403	1.61	3.9	0.10	3.40	4.2	2.4	4.8	0.82
07	9.28	0.429	1.72	3.2	0.07	2.89	4.3	2.5	5.0	0.81
08	9.27	0.395	1.58	4.1	0.07	2.85	4.2	2.5	4.8	0.80
09	9.27	0.374	1.50	3.9	0.27	3.19	4.3	2.5	5.0	0.81
13	10.25	0.859	3.44	6.4	0.22	2.99	6.5	3.4	7.4	0.85
14	10.20	0.933	3.73	6.8	0.36	3.00	6.7	4.3	7.4	0.77
15	10.15	0.991	3.96	8.1	0.37	3.00	7.4	3.8	8.6	0.86
16	9.95	0.936	3.74	6.6	0.11	2.62	7.5	4.1	8.5	0.84
23	9.60	0.948	3.80	8.2	0.37	2.81	7.5	3.6	8.6	0.88

TABLE 4.1.
BASIC SURFACE ELEVATION STATISTICS (TICKELL AND BURROWS, 1989)

Run Number	Significant Height	% Exposure Level 2	Rayleigh Distribution			Modified Rayleigh Distribution			Maximum Height Properties	
			Quantile Height Ratios		Maximum Height Obs/Th	Quantile Height Ratios		Maximum Height Obs/Th	T_{max}(sec)	η_c/H_{max}
			(Obs/Th)5%	(Obs/Th)10%		(Obs/Th)5%	(Obs/Th)10%			
(1)	(2)	(3)	(4)	(5)	(6)	(7)	(8)	(9)	(10)	(11)
01	1.38	3.6	0.93	0.93	0.87	1.00	1.00	0.94	5.1	0.69
02	1.41	3.5	0.87	0.83	0.79	0.94	0.90	0.85	5.1	0.49
06	1.61	4.5	0.94	0.87	0.93	1.01	0.94	1.00	6.0	0.48
07	1.72	6.0	0.89	0.84	0.90	0.96	0.91	0.97	5.3	0.57
08	1.58	4.5	0.91	0.93	0.86	0.98	1.00	0.93	4.8	0.56
09	1.50	3.6	0.90	0.86	0.92	0.97	0.93	1.00	9.2	0.59
13	3.44	2.7	1.00	0.96	0.89	1.08	1.04	0.96	9.6	0.56
14	3.73	4.5	0.99	0.92	0.88	1.07	1.00	0.95	12.7	0.58
15	3.96	5.5	0.93	0.95	0.86	1.00	1.03	0.93	9.8	0.61
16	3.74	7.5	0.93	0.88	0.86	1.00	0.95	0.93	9.4	0.54
23	3.80	14.7	0.96	0.99	0.86	1.04	1.07	0.93	8.2	0.54

TABLE 4.2.
WAVE HEIGHT AND EXPOSURE STATISTICS (TICKELL AND BURROWS, 1989)

Run Nº	Skewness			Kurtosis		
	u	v	w	u	v	w
01	-0.43	-0.27	0.15	3.86	3.89	4.37
02	-0.36	0.19	0.20	3.57	3.33	4.08
06	-0.49	-0.04	-0.01	3.57	3.38	4.27
07	-0.40	0.03	0.08	3.24	3.42	3.65
08	-0.36	-0.02	0.03	3.48	3.87	4.34
09	-0.26	0.36	0.35	2.95	3.51	3.68

TABLE 4.3.
VALUES OF SKEWNESS AND KURTOSIS FOR VELOCITY COMPONENTS OF LOW-INTENSITY RUNS (LEVEL 3)

Run Nº	Skewness			Kurtosis		
	$\dot{u}$	$\dot{v}$	$\dot{w}$	$\dot{u}$	$\dot{v}$	$\dot{w}$
01	0.13	0.19	0.24	4.36	5.23	4.61
02	0.23	0.24	0.26	3.98	3.83	4.22
06	0.14	0.05	0.28	3.85	3.62	4.90
07	0.20	0.03	0.18	3.63	3.74	4.05
08	0.15	-0.04	0.07	3.89	4.36	4.14
09	0.35	0.10	0.28	3.80	4.68	3.90

TABLE 4.4.
VALUES OF SKEWNESS AND KURTOSIS FOR ACCELERATION COMPONENTS OF LOW-INTENSITY RUNS (LEVEL 3)

Run Nº	Skewness			Kurtosis		
	u	v	w	u	v	w
13	0.02	0.04	0.08	2.24	3.39	2.72
14	0.02	0.03	-0.05	2.54	2.93	2.87
15	0.22	-0.09	0.05	2.40	3.03	2.81
16	0.41	0.17	0.01	2.60	3.13	3.27
23	0.22	-0.10	0.21	2.24	2.87	2.94

TABLE 4.5.
VALUES OF SKEWNESS AND KURTOSIS FOR VELOCITY COMPONENTS OF HIGH-INTENSITY RUNS (LEVEL 3)

Run Nº	Skewness			Kurtosis		
	$\dot{u}$	$\dot{v}$	$\dot{w}$	$\dot{u}$	$\dot{v}$	$\dot{w}$
13	0.06	-0.20	-0.04	2.78	3.73	3.14
14	0.01	0.00	-0.19	3.26	3.64	3.30
15	0.10	-0.28	-0.32	3.11	3.29	3.69
16	0.19	-0.22	-0.54	3.57	3.46	4.03
23	0.21	0.18	-0.28	3.48	3.58	4.00

TABLE 4.6.
VALUES OF SKEWNESS AND KURTOSIS FOR ACCELERATION COMPONENTS OF HIGH-INTENSITY RUNS (LEVEL 3)

Run Nº	Level	σ_u m/sec	σ_v m/sec	$\frac{\sigma_v}{\sigma_u}$	$\rho_{u,v}$	$\bar{\theta}$ "degrees"
	2	0.313	0.145	0.46	-0.24	- 7.8
01	3	0.293	0.092	0.31	-0.13	- 2.5
	4	0.232	0.070	0.30	0.05	1.1
	2	0.336	0.138	0.41	-0.19	- 5.2
02	3	0.296	0.090	0.30	-0.10	- 1.9
	4	0.231	0.081	0.35	0.07	1.5
	2	0.349	0.146	0.42	-0.23	- 6.5
06	3	0.357	0.100	0.28	-0.21	- 3.6
	4	0.286	0.088	0.31	0.06	1.1
	2	0.369	0.150	0.41	-0.34	- 9.2
07	3	0.390	0.109	0.28	-0.26	- 4.4
	4	0.325	0.092	0.28	-0.01	- 0.1
	2	0.363	0.138	0.38	-0.26	- 6.6
08	3	0.342	0.103	0.30	-0.24	- 4.5
	4	0.270	0.080	0.30	-0.01	- 0.2
	2	0.365	0.140	0.38	-0.34	- 8.6
09	3	0.348	0.108	0.31	-0.26	- 5.1
	4	0.278	0.087	0.31	-0.24	- 4.7
	2	0.777	0.309	0.40	-0.41	-10.6
13	3	0.740	0.231	0.31	-0.23	- 4.5
	4	0.694	0.208	0.30	-0.23	- 4.3
	2	0.797	0.350	0.44	-0.38	-11.2
14	3	0.767	0.263	0.34	-0.19	- 4.2
	4	0.718	0.241	0.34	-0.17	- 3.6
	2	0.843	0.358	0.42	-0.36	-10.1
15	3	0.823	0.252	0.31	0.01	- 0.1
	4	0.776	0.233	0.30	0.02	0.3
	2	0.815	0.396	0.49	-0.37	-12.5
16	3	0.871	0.279	0.32	-0.17	- 3.5
	4	0.820	0.256	0.31	-0.17	- 3.3
	2	0.822	0.339	0.41	-0.30	- 8.2
23	3	0.998	0.329	0.33	-0.15	- 3.1
	4	0.954	0.309	0.32	-0.12	- 2.6

TABLE 4.7.
PREDOMINANT WAVE DIRECTIONS FOR ALL RUNS AND ALL LEVELS

Run Number	Predominant Wave Direction (Degrees)
01	-0.7
02	-0.2
06	-1.2
07	-2.2
08	-2.3
09	-4.9
13	-4.4
14	-3.9
15	0.1
16	-3.4
23	-2.8

TABLE 4.8.
PREDOMINANT WAVE DIRECTIONS

Frequency (Hz)	RUN 01							
	Level 3				Level 4			
	$\bar{\theta}_1^o$	s_1	$\bar{\theta}_2^o$	s_2	$\bar{\theta}_1^o$	s_1	$\bar{\theta}_2^o$	s_2
0.065	1	2	- 8	7	- 1	3	- 5	9
0.097	- 4	1	- 6	5	- 6	1	- 2	5
0.129	- 6	9	- 5	16	- 1	11	0	14
0.162	- 4	9	- 3	9	- 3	9	- 3	9
0.194	- 1	13	0	10	3	17	2	13
0.226	6	8	8	7	3	6	6	6
0.259	- 3	8	- 1	5	0	6	3	6
0.291	5	6	5	3	11	4	11	4
0.323	9	6	8	4	11	2	9	3
0.356	8	3	5	3	19	1	10	3

Frequency (Hz)	RUN 23							
	Level 3				Level 4			
	$\bar{\theta}_1^o$	s_1	$\bar{\theta}_2^o$	s_2	$\bar{\theta}_1^o$	s_1	$\bar{\theta}_2^o$	s_2
0.065	- 4	7	- 5	9	2	2	- 1	8
0.097	- 5	10	- 5	9	- 3	7	- 4	10
0.129	- 3	13	- 3	11	- 3	8	- 5	11
0.162	- 2	9	- 1	7	- 1	8	- 3	8
0.194	4	4	6	3	- 1	3	- 1	3
0.226	4	2	10	3	- 4	2	4	3
0.259	- 1	1	10	2	4	1	2	2
0.291	11	1	6	2	4	1	9	2

TABLE 4.9.
COSINE-POWER SPREADING FUNCTION PARAMETERS FOR RUN 01 AND RUN 23
(TICKELL AND BURROWS, 1989)

Frequency (Hz)	RUN 13					
	Level 2		Level 3		Level 4	
	$\bar{\theta}_1^o$	s_1	$\bar{\theta}_1^o$	s_1	$\bar{\theta}_1^o$	s_1
0.058	-16	3	-7	5	-10	4
0.071	-10	12	-4	16	- 4	12
0.084	-10	19	-4	27	- 5	15
0.097	- 9	25	-3	35	- 3	18
0.110	-10	16	-4	24	- 2	16
0.123	-12	15	-5	23	- 4	16
0.136	-15	9	-8	12	- 6	9
0.149	-15	8	-8	10	- 7	8
0.162	- 7	7	-1	10	1	8
0.175	- 7	7	0	10	2	9
0.188	-10	6	-1	8	0	8
0.201	- 9	4	-2	6	- 1	6

Frequency (Hz)	RUN 15							
	Level 3				Level 4			
	$\bar{\theta}_1^o$	s_1	$\bar{\theta}_2^o$	s_2	$\bar{\theta}_1^o$	s_1	$\bar{\theta}_2^o$	s_2
0.032	-13	1	-15	4	- 5	-	-18	3
0.065	- 4	11	- 4	15	- 3	10	- 3	15
0.097	1	18	1	10	1	14	2	9
0.129	0	23	0	9	0	20	0	9
0.162	- 3	10	- 3	5	- 2	10	- 2	5
0.194	2	5	6	2	4	5	8	2
0.226	- 3	4	-31	5	- 1	4	- 2	2
0.259	14	1	-47	-	- 1	2	-64	1
0.291	- 9	2	-22	1	- 1	-	-29	2
0.323	-15	1	-65	2	-10	1	-27	1
0.356	-10	1	-58	1	-11	2	-11	2

TABLE 4.10.
COSINE-POWER SPREADING FUNCTION PARAMETERS FOR RUN 13 AND RUN 15
(TICKELL AND BURROWS, 1989)

Run Nº	Level	Current Magnitude (m/sec)	Current Direction (Degrees)	r_1	r_2
	2	0.47	62	0.57	1.35
01	3	0.46	72	0.56	1.50
	4	0.46	75	0.56	1.89
	2	0.49	63	0.81	1.36
02	3	0.51	69	0.83	1.65
	4	0.50	73	0.83	2.05
	2	0.49	59	2.24	1.30
06	3	0.50	71	2.28	1.36
	4	0.50	73	2.26	1.67
	2	0.49	57	2.08	1.23
07	3	0.50	70	2.10	1.22
	4	0.50	73	2.14	1.49
	2	0.47	61	1.34	1.21
08	3	0.48	71	1.38	1.35
	4	0.49	73	1.40	1.74
	2	0.46	64	1.02	1.17
09	3	0.48	73	1.06	1.31
	4	0.50	77	1.13	1.72

TABLE 4.11.
CURRENT FOR LOW-INTENSITY RUNS

Run Nº	Level	Current Magnitude (m/sec)	Current Direction (Degrees)	r_1	r_2
13	2	0.01	146	0.06	0.02
	3	0.05	203	0.24	0.07
	4	0.06	216	0.28	0.09
14	2	0.09	191	0.41	0.10
	3	0.15	206	0.70	0.19
	4	0.17	208	0.76	0.22
15	2	0.18	224	0.79	0.19
	3	0.30	230	1.34	0.35
	4	0.30	226	1.34	0.38
16	2	0.27	247	1.17	0.30
	3	0.45	231	1.96	0.49
	4	0.45	227	1.96	0.53
23	2	0.64	46	2.71	0.72
	3	0.57	76	2.45	0.55
	4	0.60	75	2.55	0.60

TABLE 4.12.
CURRENT FOR HIGH-INTENSITY RUNS

Frequency (Hz)	RUN 01			RUN 08		RUN 15			RUN 23	
	Observed	Level 3	Level 4	Observed	Level 3	Observed	Level 3	Level 4	Observed	Level 3
0.032	0.006	0.154	0.117	0.014	0.119	0.558	0.760	0.772	0.487	2.707
0.065	0.322	0.572	0.442	0.382	0.605	5.978	4.161	4.024	8.020	10.410
0.097	0.087	0.174	0.121	0.130	0.256	9.254	8.538	8.631	8.050	9.411
0.129	0.507	0.504	0.427	0.782	0.759	5.764	7.099	7.219	4.750	5.360
0.162	0.578	0.450	0.396	1.177	0.986	2.514	2.540	2.696	3.450	3.761
0.194	0.295	0.376	0.370	0.547	0.454	1.461	1.466	1.628	1.160	1.696
0.226	0.323	0.300	0.264	0.549	0.479	1.041	0.723	0.846	0.878	0.832
0.259	0.375	0.209	0.208	0.380	0.302	0.551	0.425	0.556	0.374	0.434
0.291	0.252	0.126	0.139	0.214	0.187	0.181	0.244	0.398	0.229	0.260
0.323	0.221	0.119	0.125	0.135	0.085	0.149	0.137	0.337	0.113	0.257
0.356	0.150	0.066	0.075	0.066	0.075	0.093	0.112	0.471	0.044	0.193

TABLE 4.13.
SURFACE ELEVATION SPECTRA BASED ON TOTAL HORIZONTAL VELOCITY SPECTRA ($G_{\eta\eta}$ m^2/Hz)
(TICKELL AND BURROWS, 1989)

Frequency	RUN 01		RUN 08	RUN 15		RUN 23
(Hz)	Level 3	Level 4	Level 3	Level 3	Level 4	level 3
0.065	0.976	1.240	1.030	1.056	1.018	0.972
0.097	1.057	1.262	0.803	0.949	0.869	0.827
0.129	0.909	0.908	0.817	0.968	0.873	0.827
0.162	0.862	0.804	0.824	0.972	0.837	0.827
0.194	0.817	0.784	0.823	0.965	0.845	0.905
0.226	0.788	0.759	0.814	1.021	0.866	0.821
0.259	0.879	0.744	0.798	0.773	0.674	0.918
0.291	0.859	0.771	0.830	0.972	0.785	0.928
0.323	0.800	0.771	0.875	1.002	0.713	0.867
0.356	0.834	0.717	0.644	0.890	0.562	0.768

TABLE 4.14.
HORIZONTAL/VERTICAL TRANSFORM FACTOR Z
(TICKELL AND BURROWS, 1989)

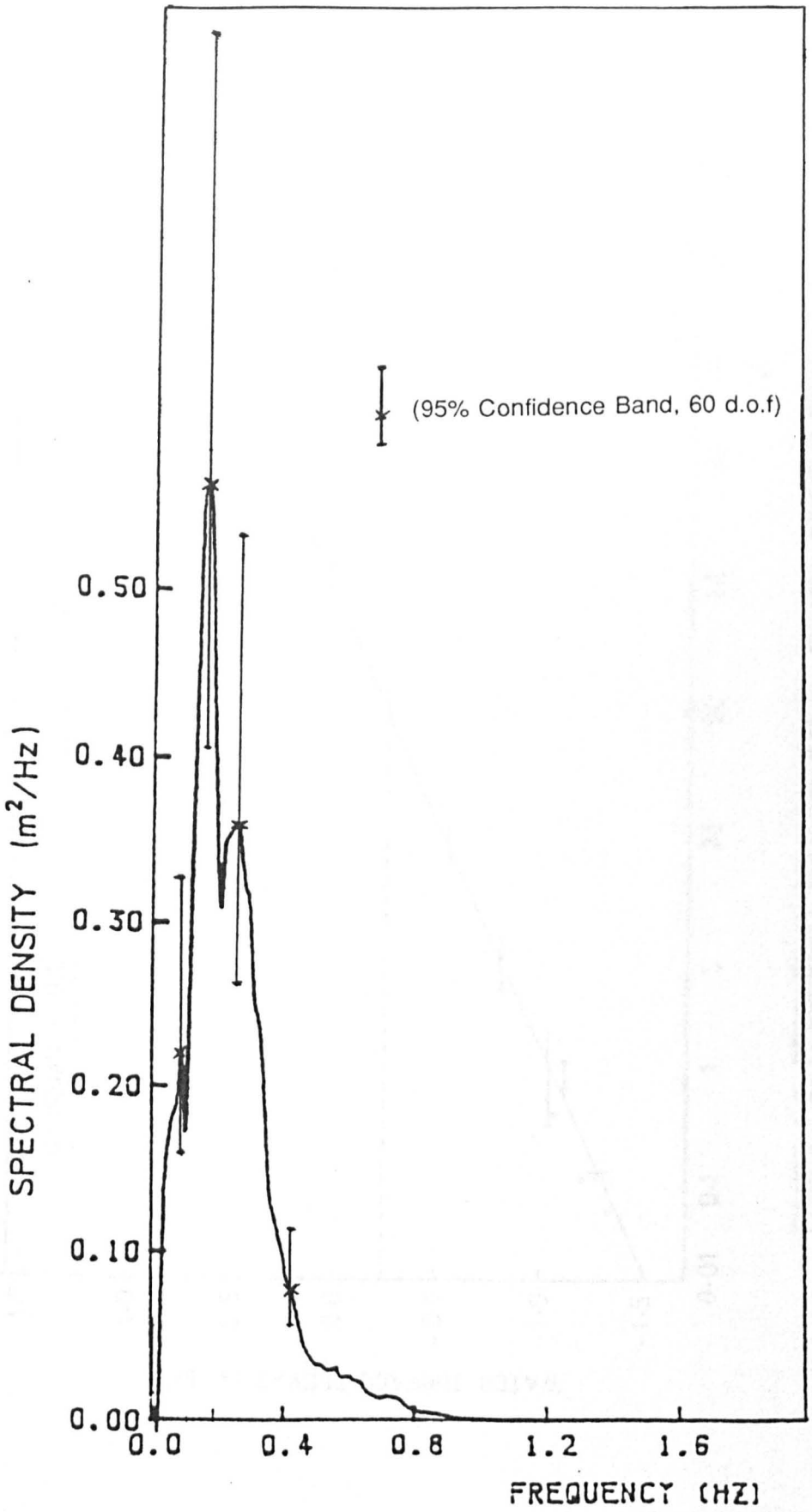

FIGURE 4.1. WATER SURFACE ELEVATION FREQUENCY SPECTRUM FOR RUN 01

(Tickell and Burrows, 1989)

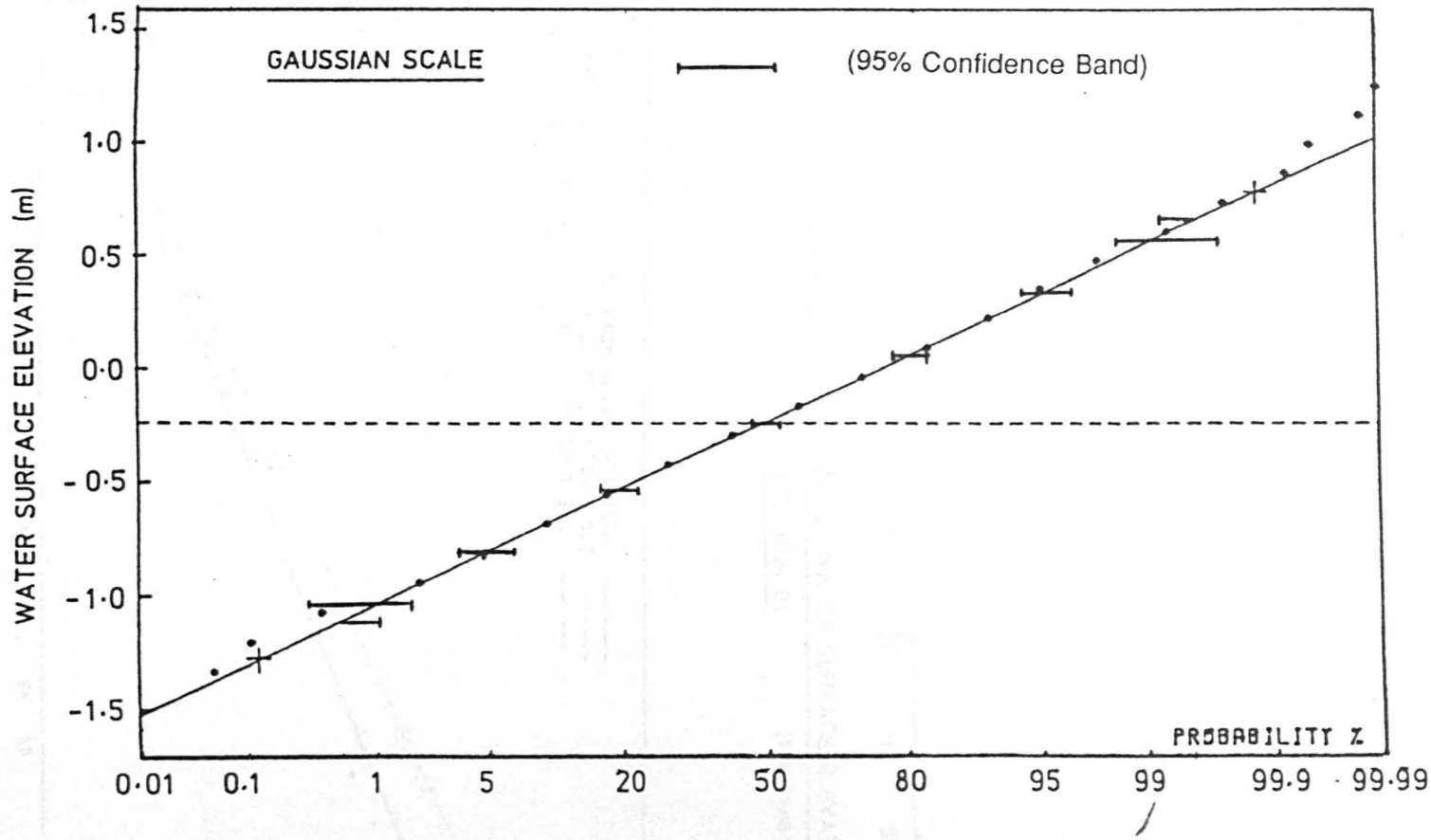

FIGURE 4.2. PROBABILITY DISTRIBUTION OF WATER SURFACE ELEVATION FOR RUN 01. (Tickell and Burrows, 1989)

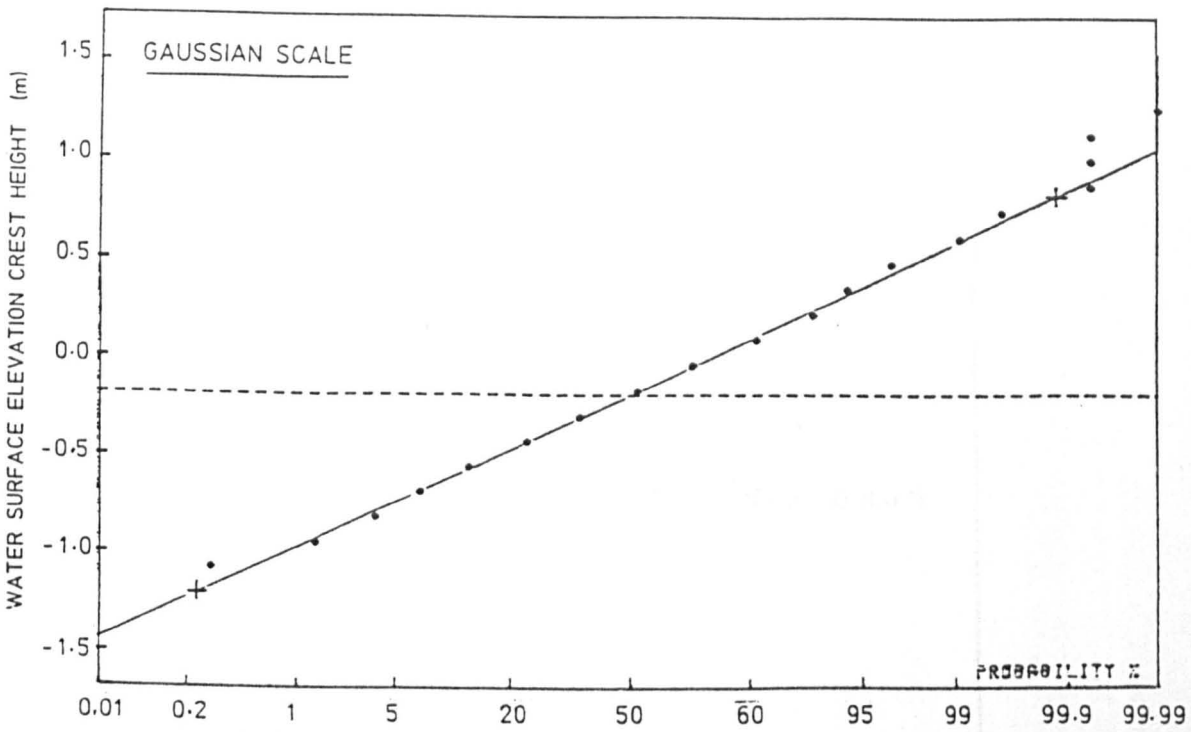

FIGURE 4.3. PROBABILITY DISTRIBUTION OF WATER SURFACE ELEVATION CRESTS FOR RUN 01. (Tickell and Burrows, 1989)

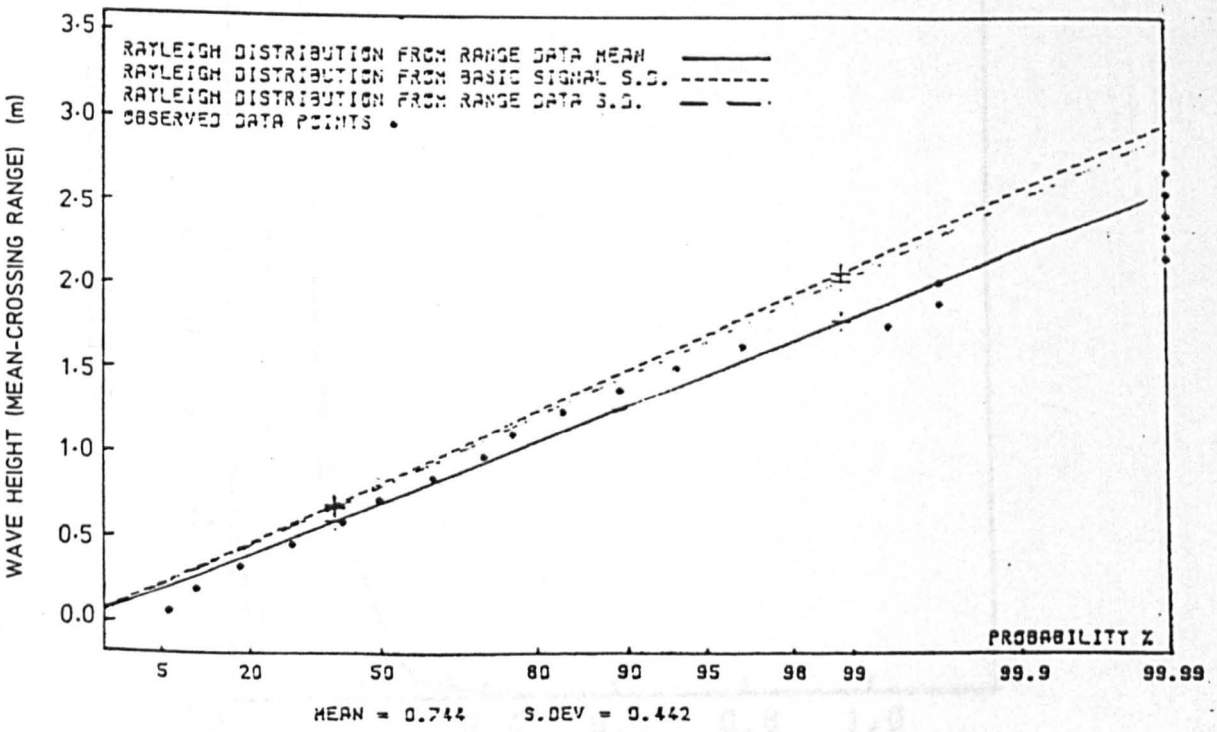

FIGURE 4.4 PROBABILITY DISTRIBUTION OF WAVE HEIGHTS FOR RUN 01.

(Tickell and Burrows, 1989)

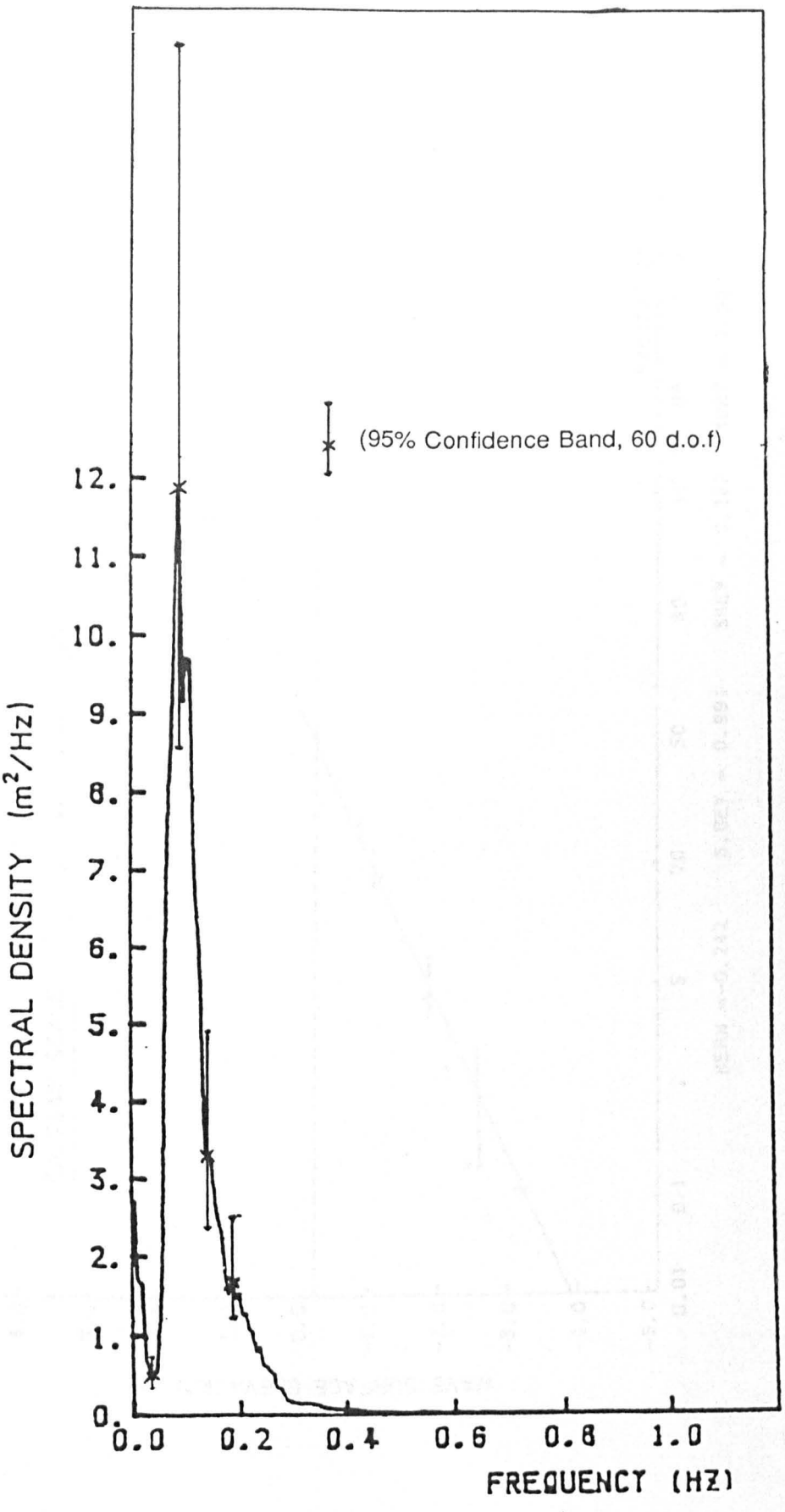

FIGURE 4.5. WATER SURFACE ELEVATION FREQUENCY SPECTRUM FOR RUN 15

(Tickell and Burrows, 1989)

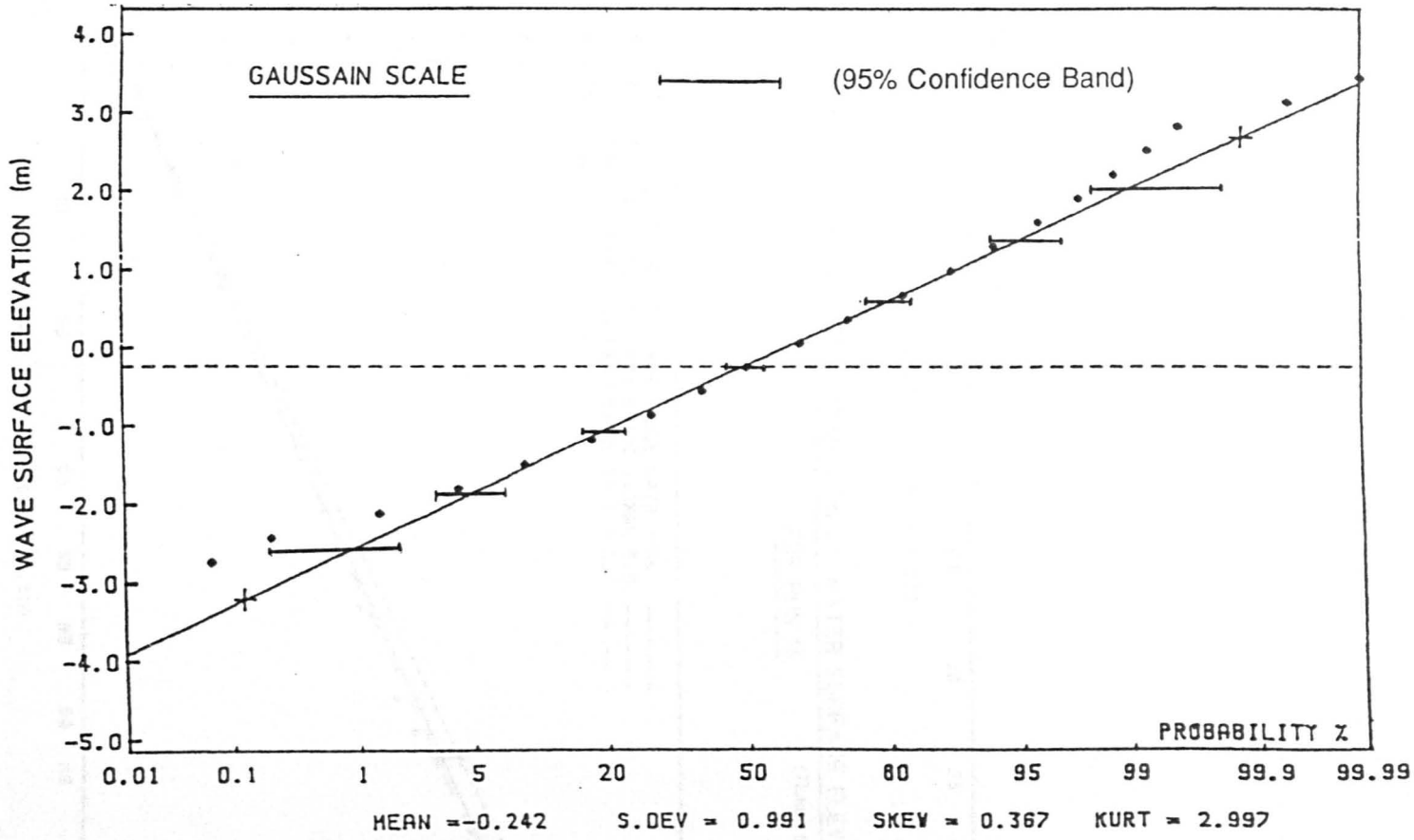

FIGURE 4.6. PROBABILITY DISTRIBUTION OF WATER SURFACE ELEVATION FOR RUN 15

(Tickell and Burrows, 1989)

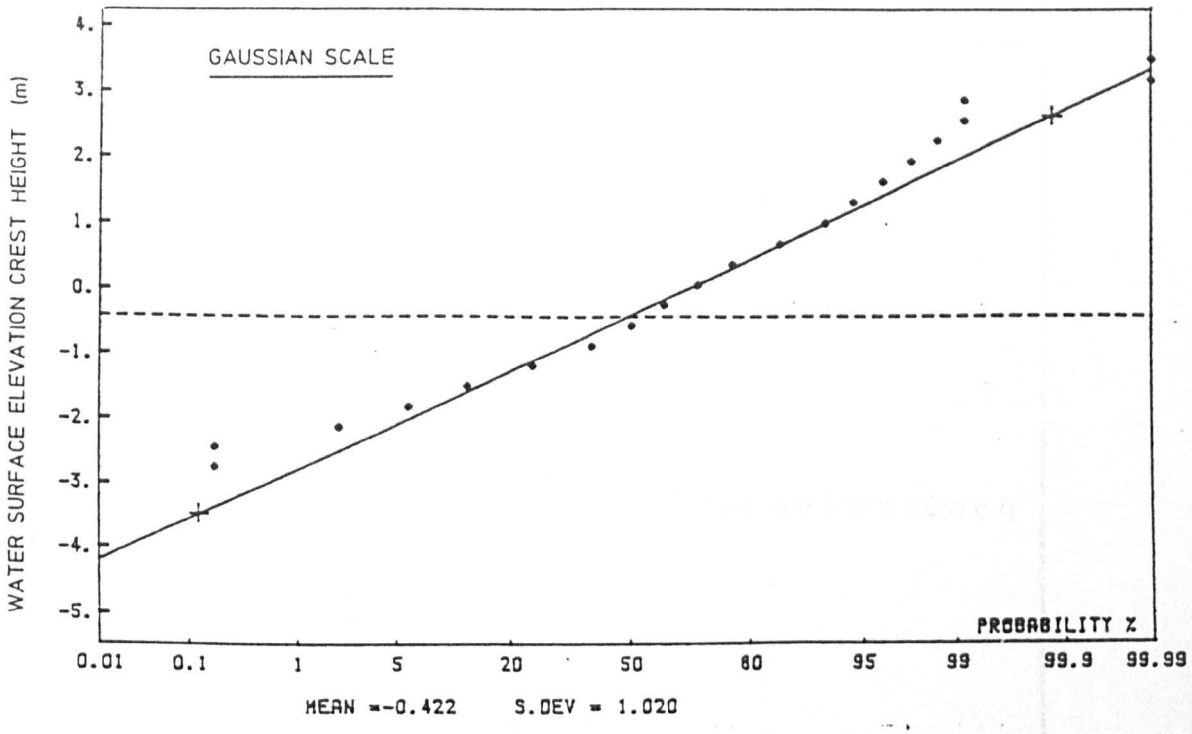

FIGURE 4.7. PROBABILITY DISTRIBUTION OF WATER SURFACE ELEVATION CRESTS FOR RUN 15. (Tickell and Burrows, 1989)

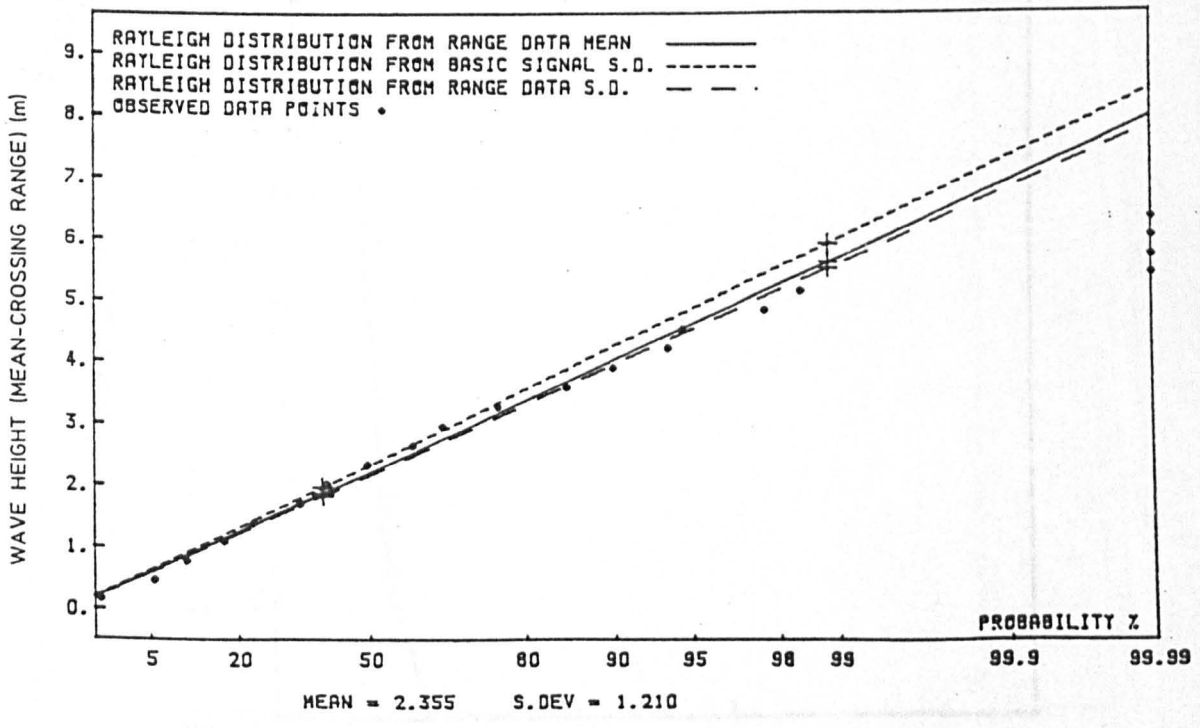

FIGURE 4.8. PROBABILITY DISTRIBUTION OF WAVE HEIGHTS FOR RUN 15 (Tickell and Burrows, 1989)

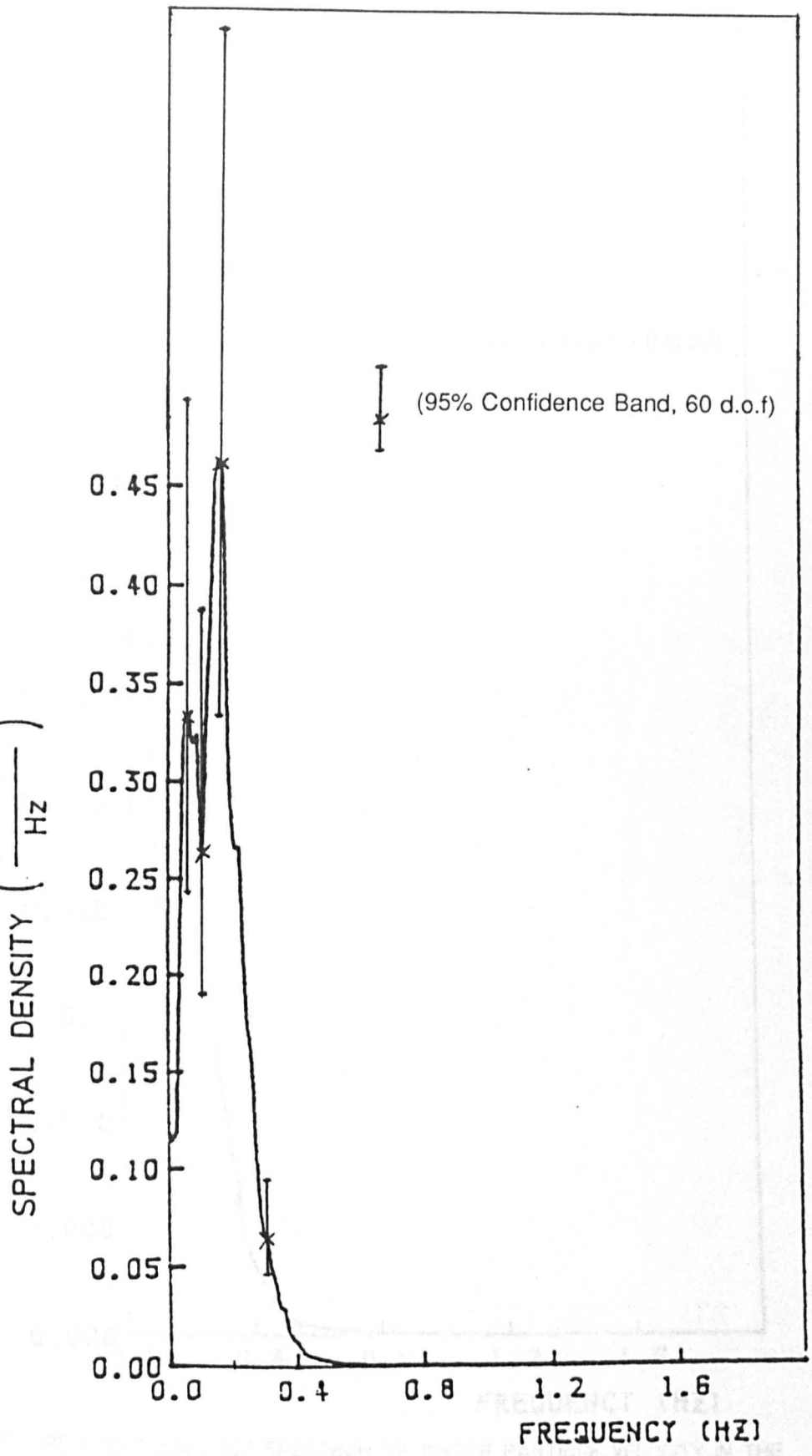

FIGURE 4.9. FREQUENCY SPECTRUM OF WATER PARTICLE VELOCITY IN THE x DIRECTION AT LEVEL 3 FOR RUN 01.

(Tickell and Burrows, 1989)

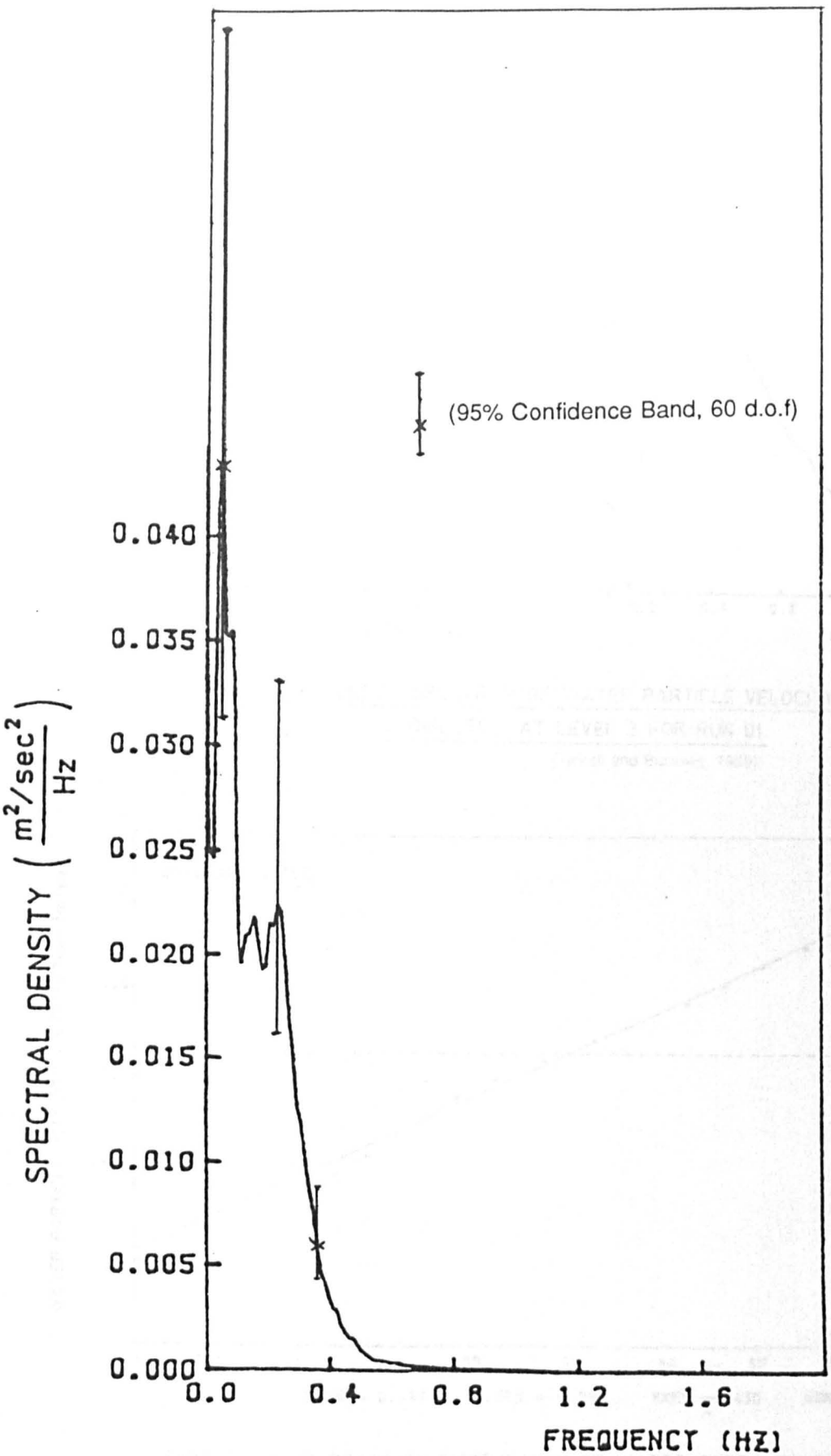

FIGURE 4.10. FREQUENCY SPECTRUM OF WATER PARTICLE VELOCITY IN THE y DIRECTION AT LEVEL 3 FOR RUN 01.

(Tickell and Burrows, 1989)

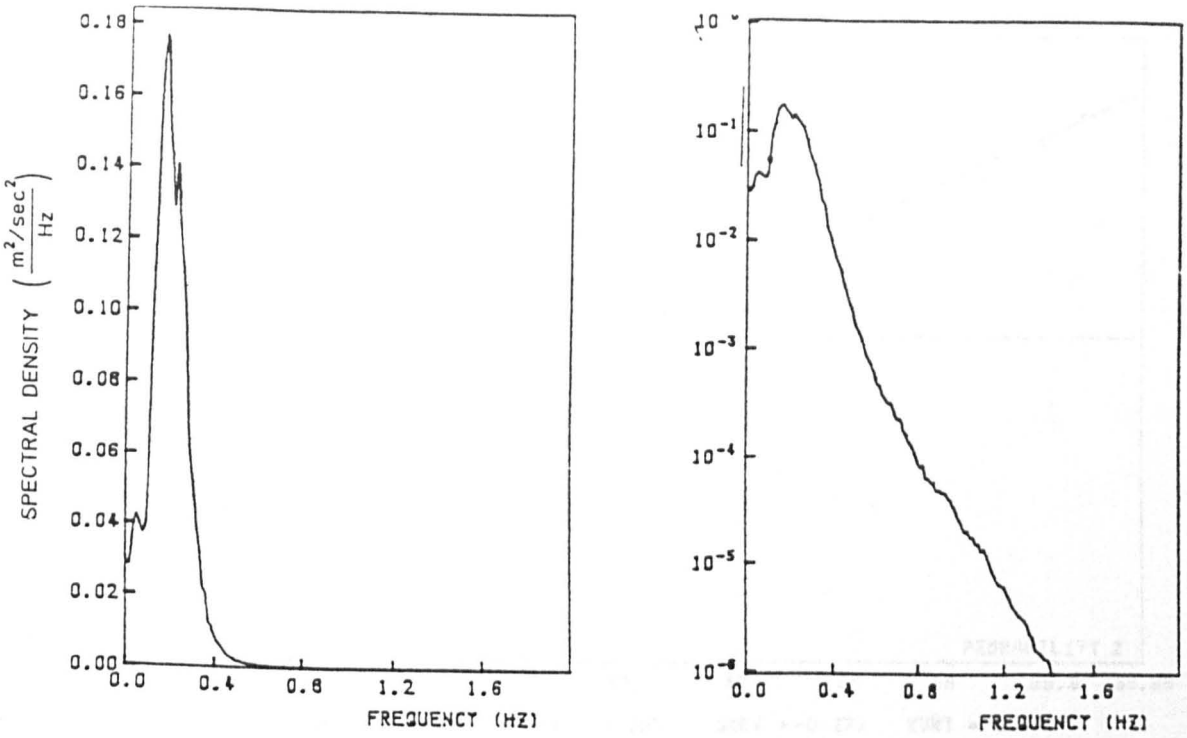

FIGURE 4.11. FREQUENCY SPECTRUM OF WATER PARTICLE VELOCITY IN THE z DIRECTION AT LEVEL 3 FOR RUN 01

(Tickell and Burrows, 1989)

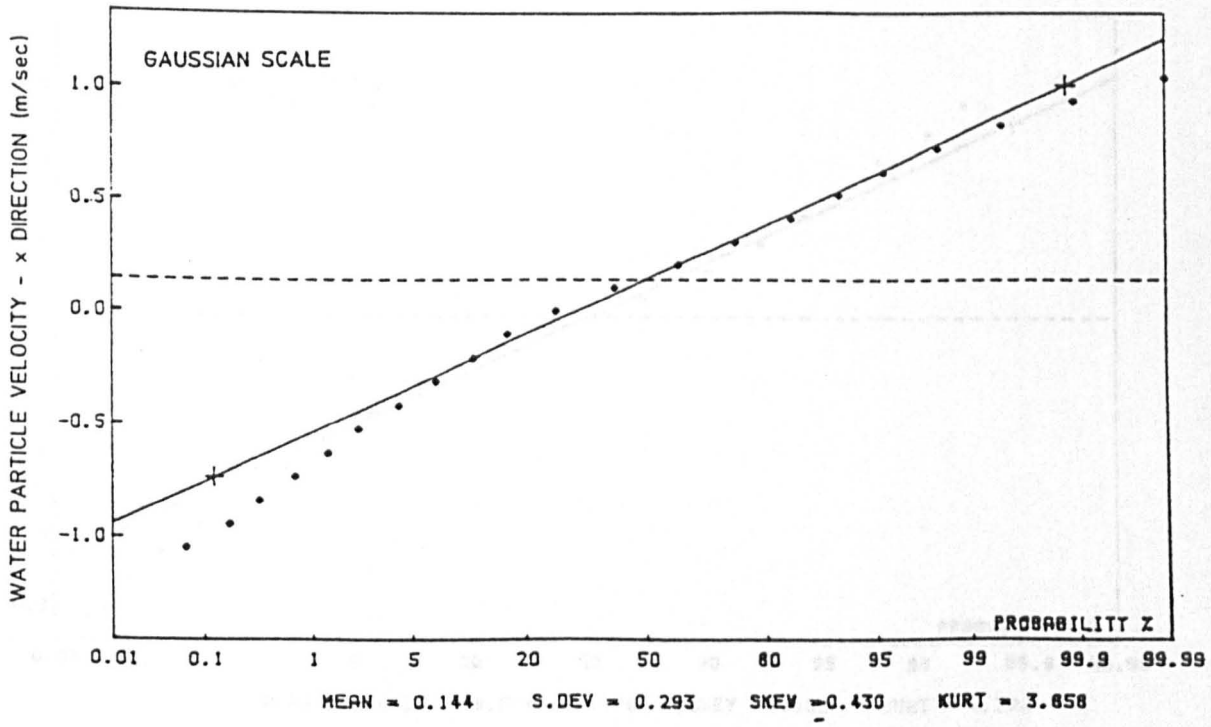

FIGURE 4.12. PROBABILITY DISTRIBUTION OF WATER PARTICLE VELOCITY IN THE x DIRECTION AT LEVEL 3 FOR RUN 01

(Tickell and Burrows, 1989)

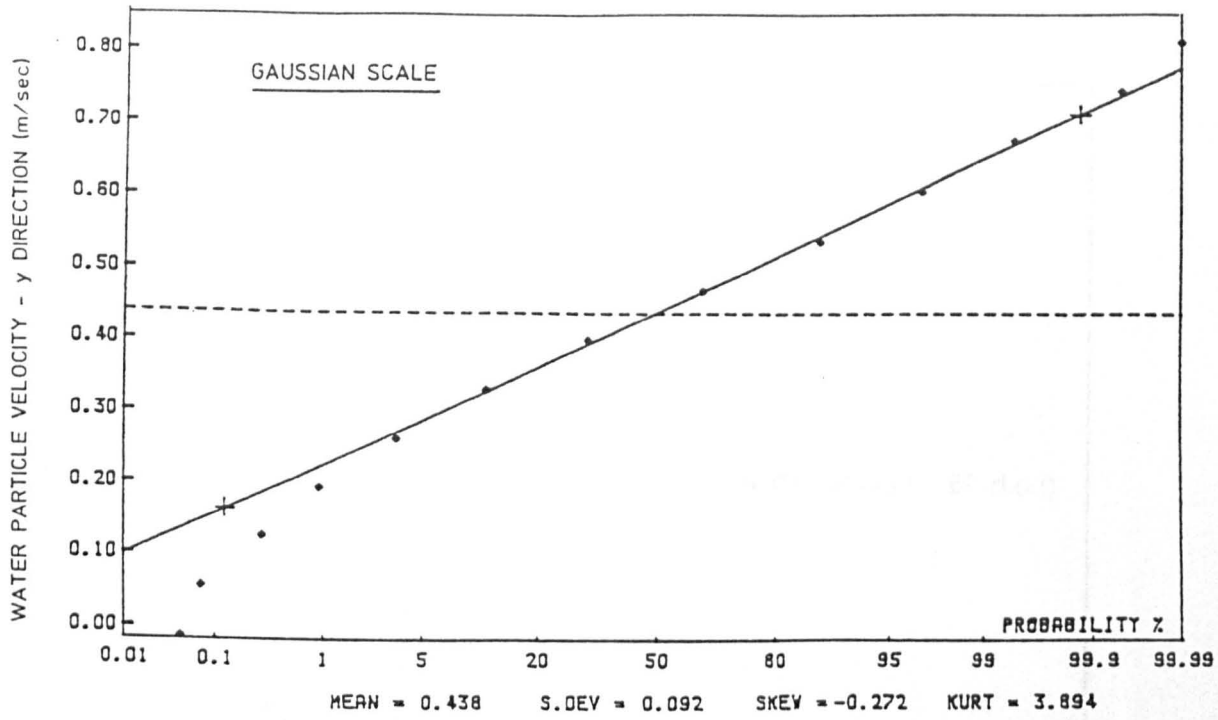

FIGURE 4.13. PROBABILITY DISTRIBUTION OF WATER PARTICLE VELOCITY IN THE y DIRECTION AT LEVEL 3 FOR RUN 01

(Tickell and Burrows, 1989)

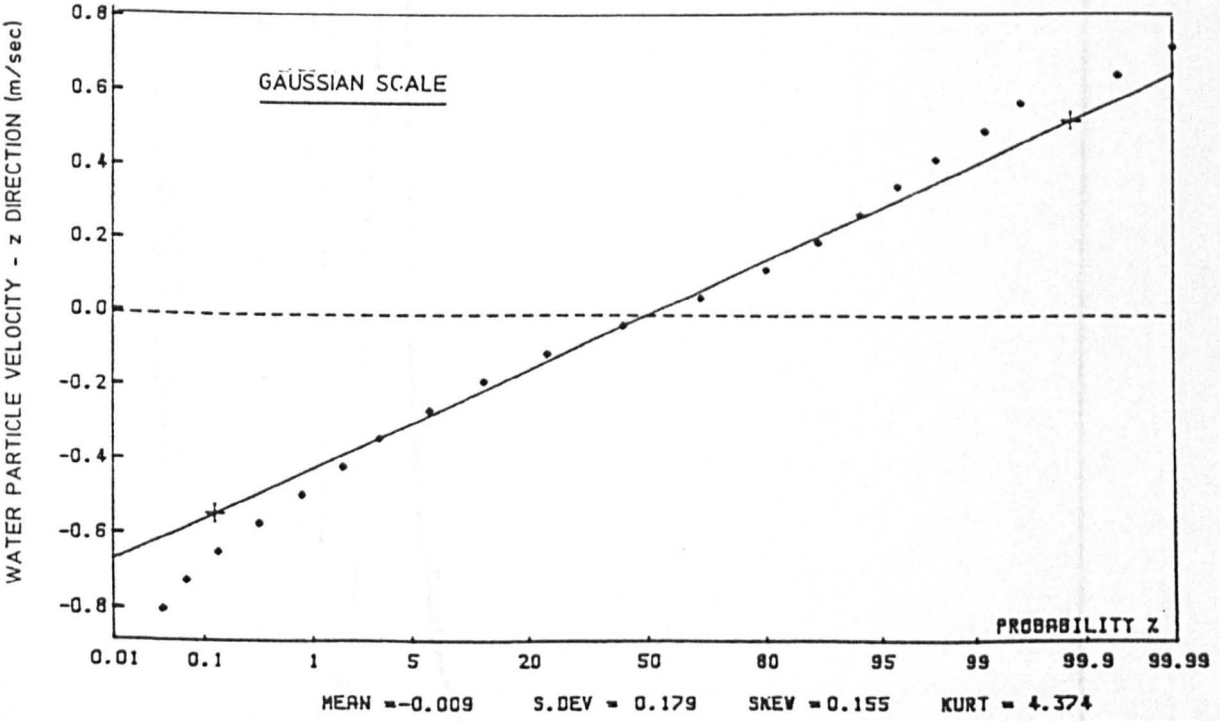

FIGURE 4.14. PROBABILITY DISTRIBUTION OF WATER PARTICLE VELOCITY IN THE z DIRECTION AT LEVEL 3 FOR RUN 01

(Tickell and Burrows, 1989)

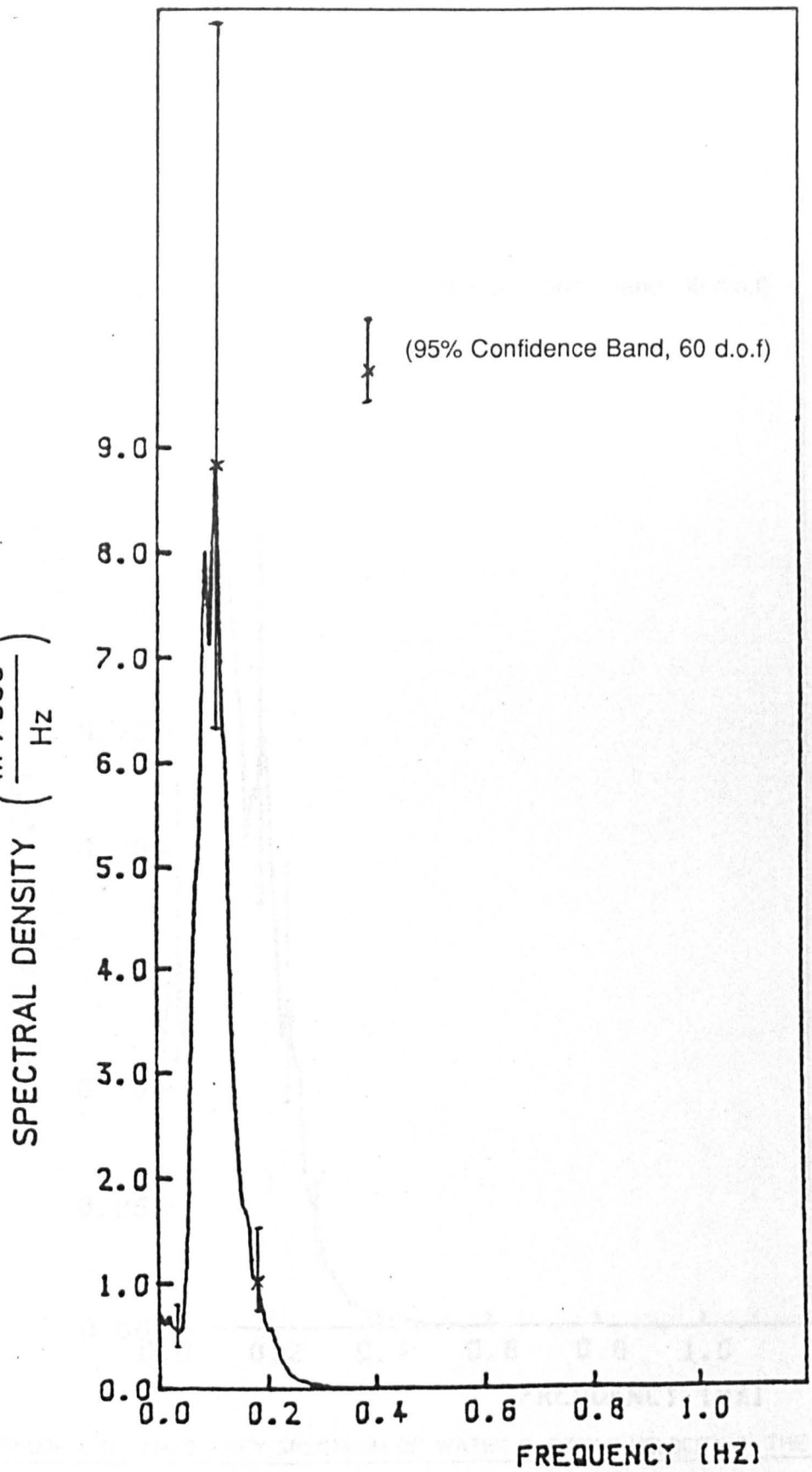

FIGURE 4.15. FREQUENCY SPECTRUM OF WATER PARTICLE VELOCITY IN THE x DIRECTION AT LEVEL 3 FOR RUN 15.

(Tickell and Burrows, 1989)

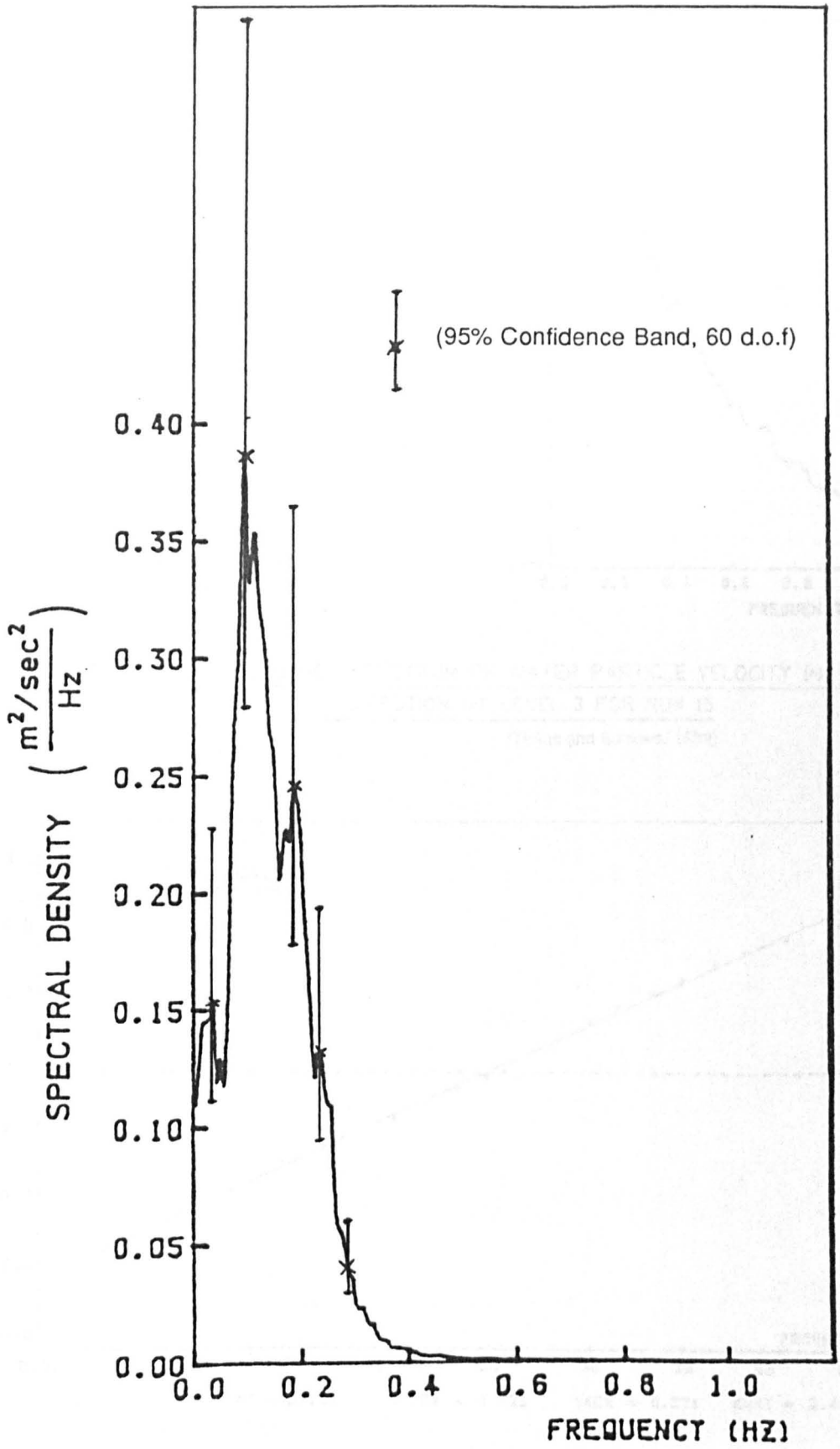

FIGURE 4.16. FREQUENCY SPECTRUM OF WATER PARTICLE VELOCITY IN THE y DIRECTION AT LEVEL 3 FOR RUN 15.

(Tickell and Burrows, 1989)

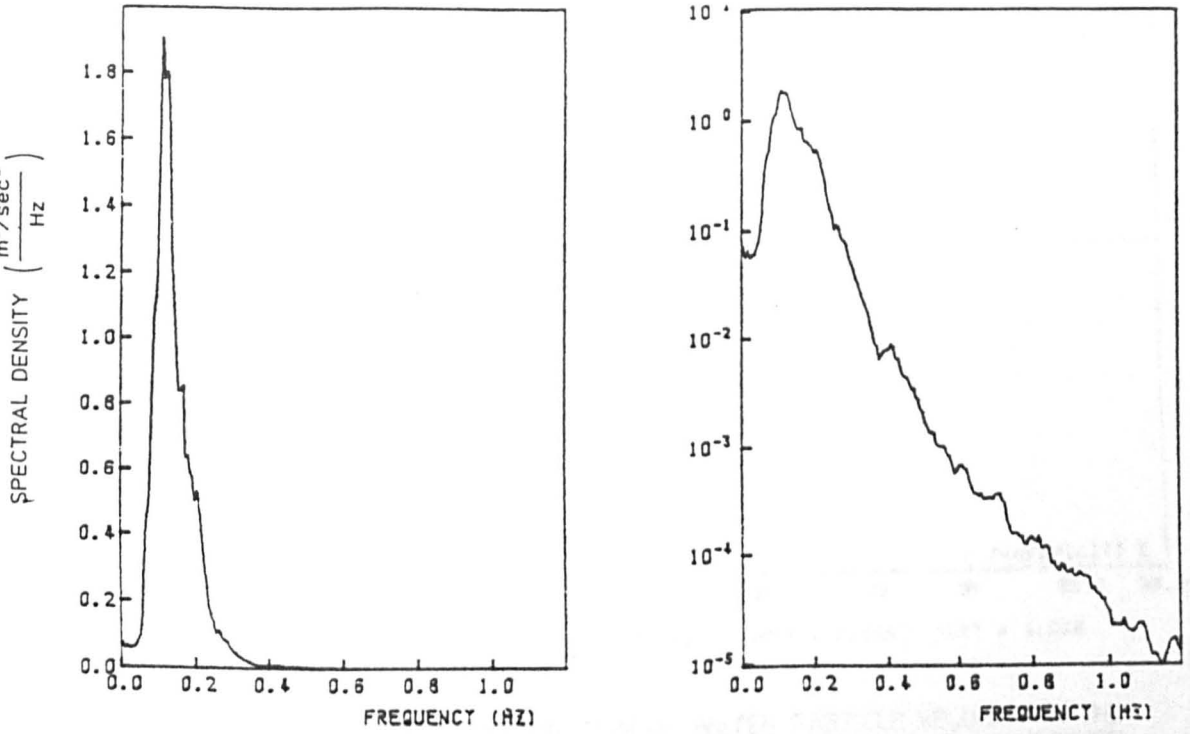

FIGURE 4.17. FREQUENCY SPECTRUM OF WATER PARTICLE VELOCITY IN THE z DIRECTION AT LEVEL 3 FOR RUN 15

(Tickell and Burrows, 1989)

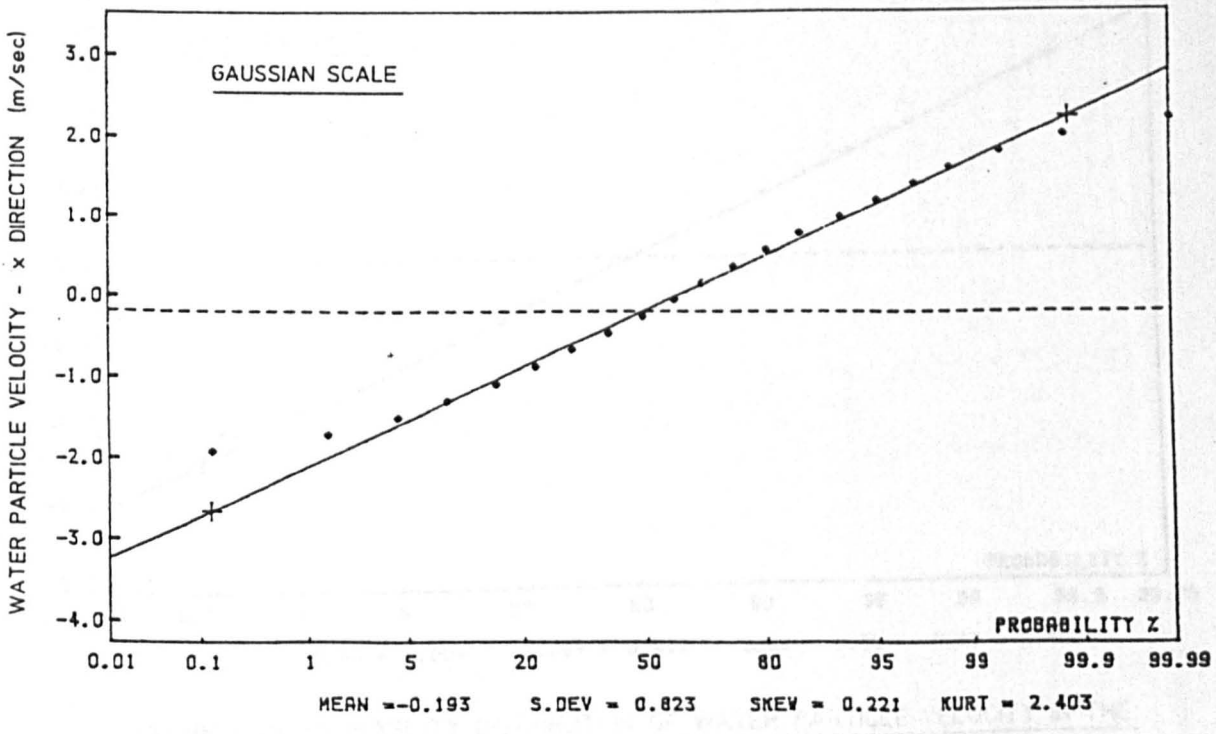

FIGURE 4.18. PROBABILITY DISTRIBUTION OF WATER PARTICLE VELOCITY IN THE x DIRECTION AT LEVEL 3 FOR RUN 15

(Tickell and Burrows, 1989)

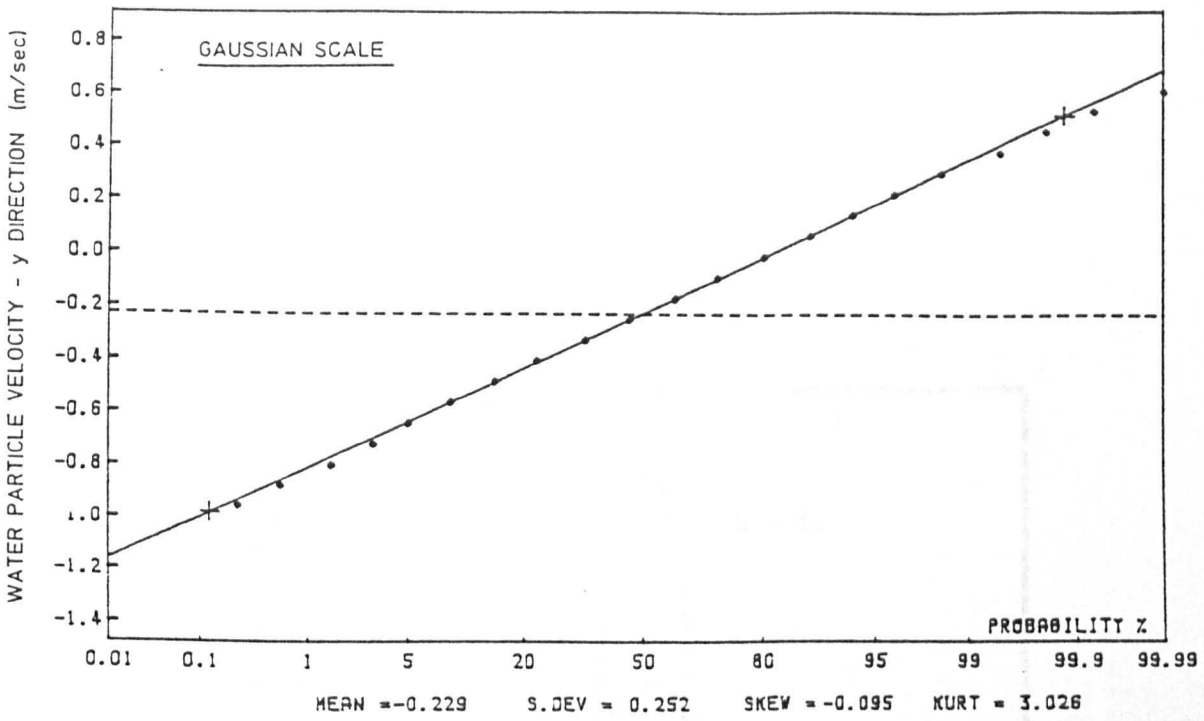

FIGURE 4.19. PROBABILITY DISTRIBUTION OF WATER PARTICLE VELOCITY IN THE y DIRECTION AT LEVEL 3 FOR RUN 15.

(Tickell and Burrows, 1989)

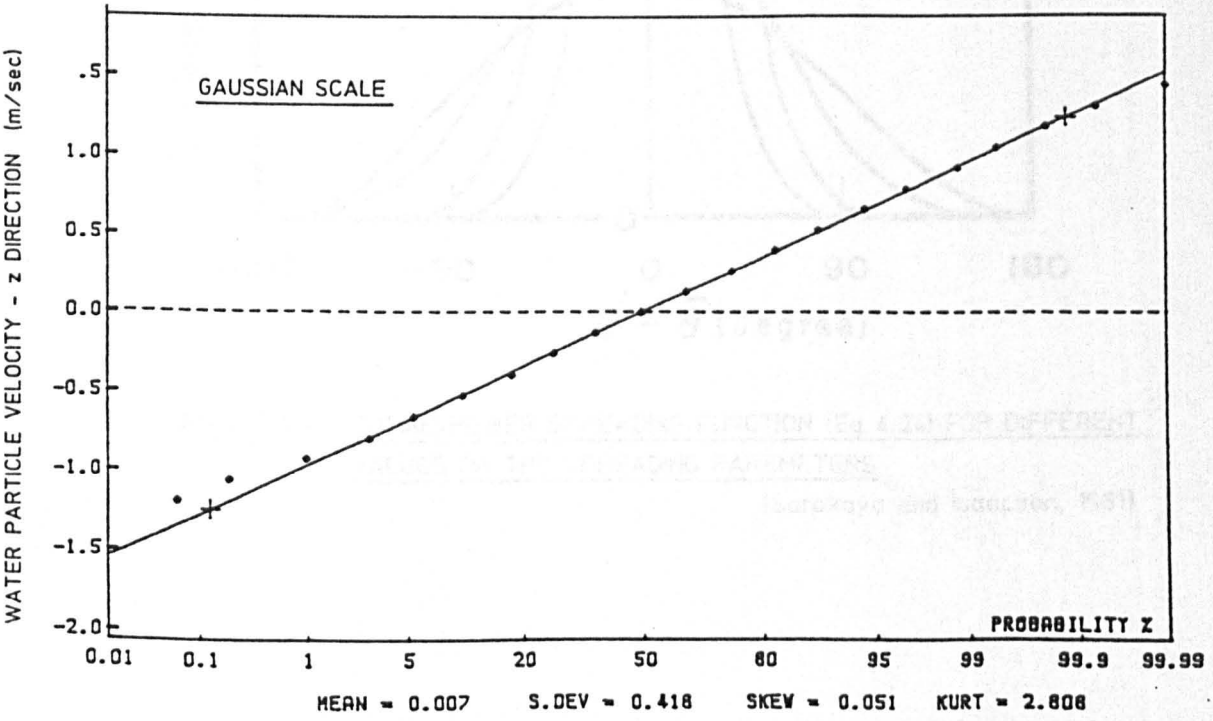

FIGURE 4.20. PROBABILITY DISTRIBUTION OF WATER PARTICLE VELOCITY IN THE z DIRECTION AT LEVEL 3 FOR RUN 15

(Tickell and Burrows, 1989)

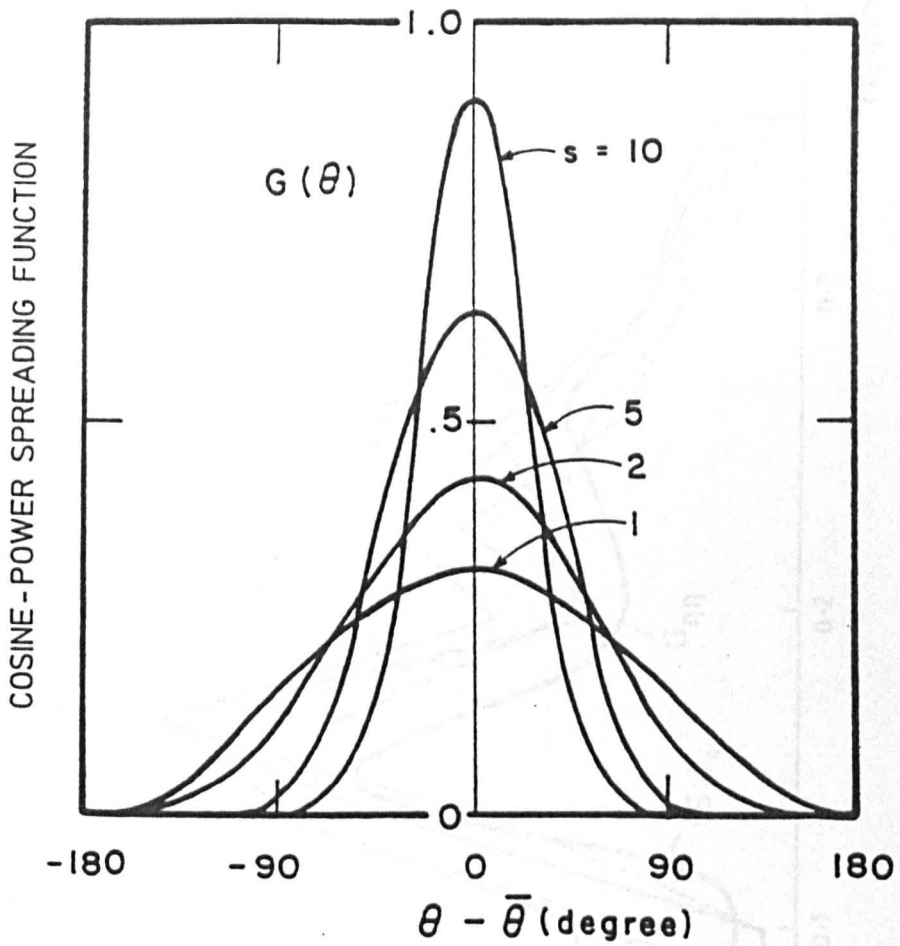

FIGURE 4.21. COSINE-POWER SPREADING FUNCTION (Eq. 4.24) FOR DIFFERENT VALUES OF THE SPREADING PARAMETERS

(Sarpkaya and Isaacson, 1981)

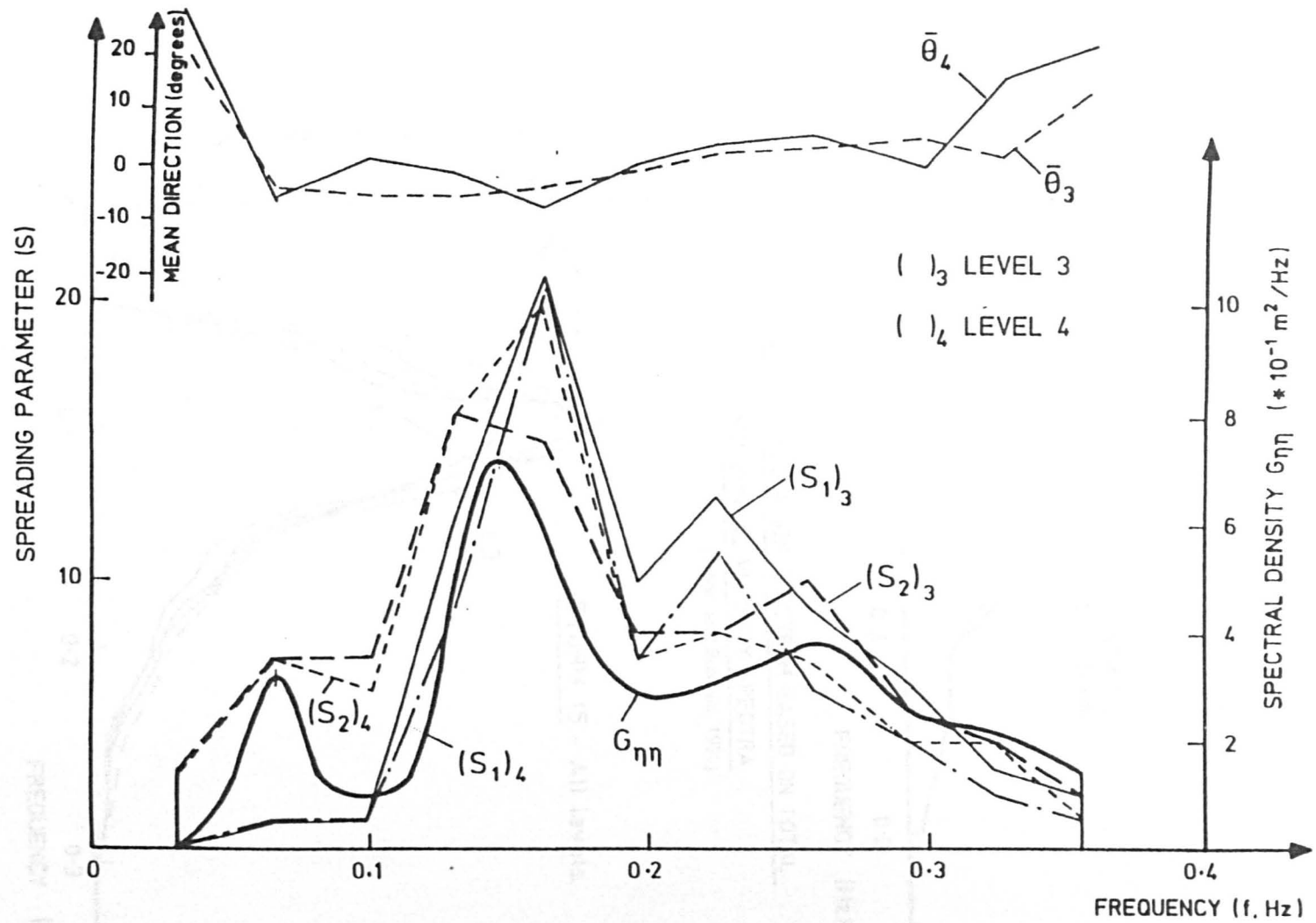

FIGURE 4.22. DIRECTIONAL PROPERTIES STORM ϕ 8

(Tickell and Burrows, 1989)

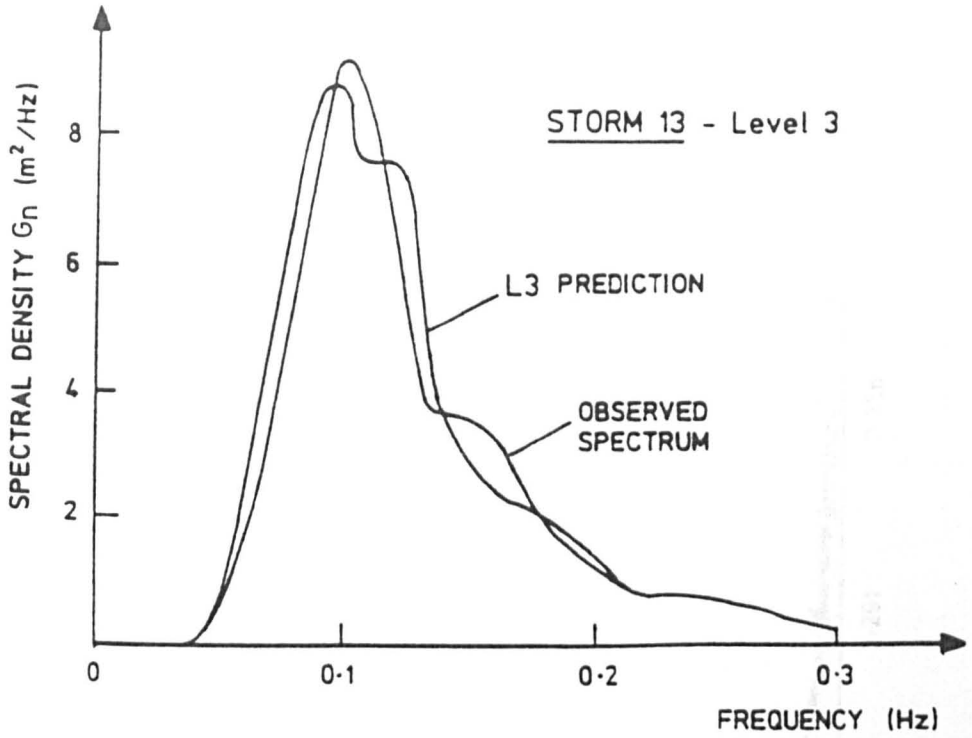

FIGURE 4.23. SURFACE ELEVATION SPECTRUM BASED ON TOTAL HORIZONTAL VELOCITY SPECTRA

(Tickell and Burrows, 1989)

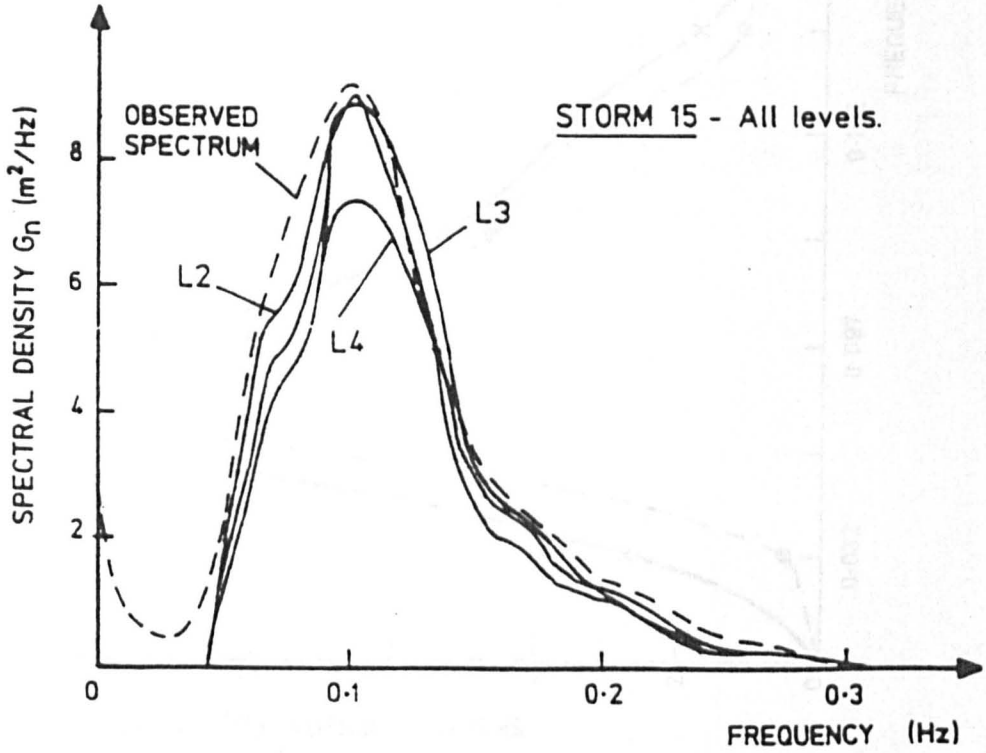

FIGURE 4.24. SURFACE ELEVATION SPECTRUM BASED ON VERTICAL VELOCITY SPECTRA

(Tickell and Burrows, 1989)

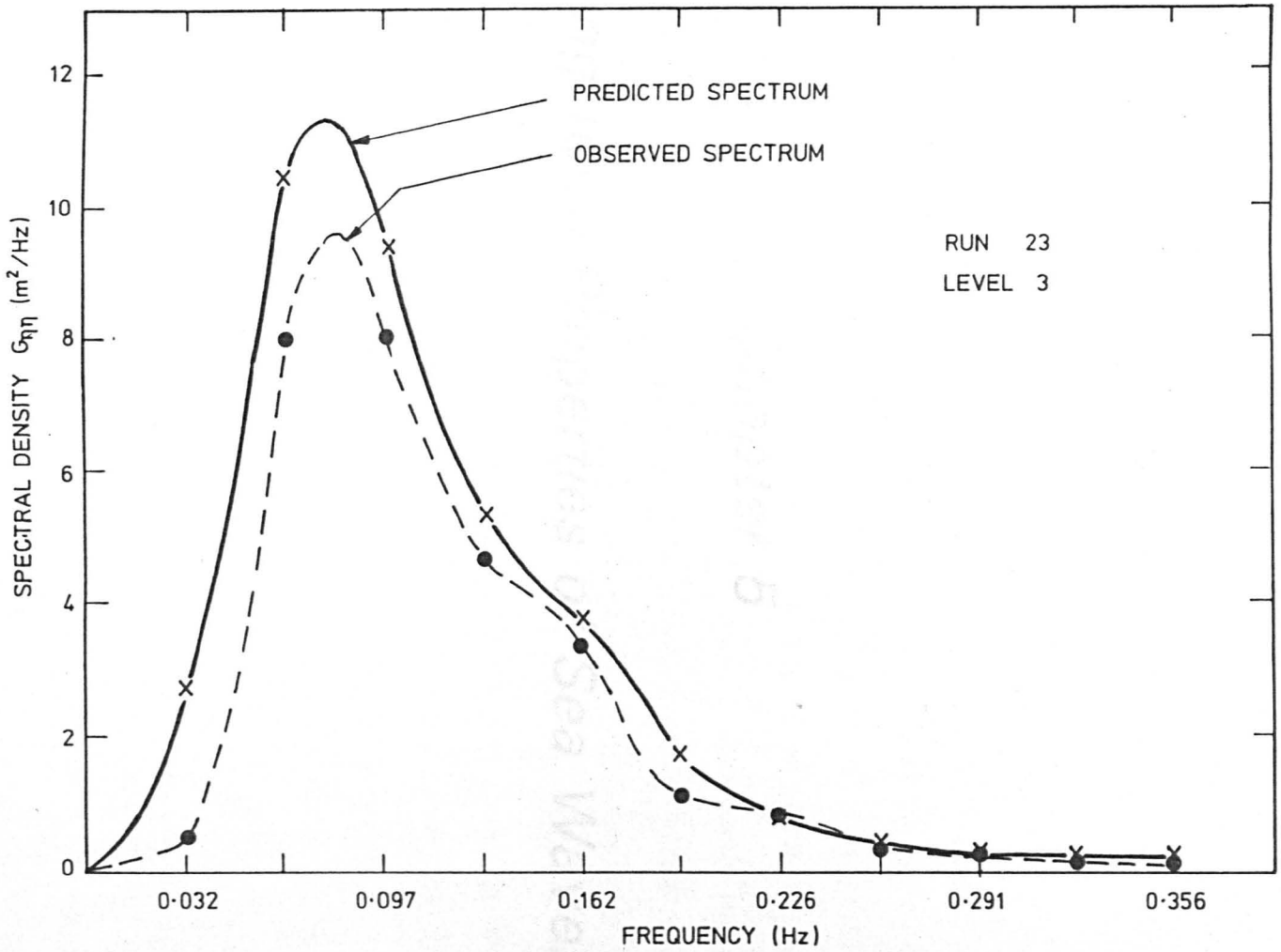

FIGURE 4.25. SURFACE ELEVATION SPECTRUM BASED ON TOTAL HORIZONTAL VELOCITY SPECTRA.

Chapter 5

Long-term Properties of Sea Waves

INTRODUCTION

There are two distinct approaches to the design of offshore structures: deterministic and probabilistic. One of the two subjects of this thesis, is the probabilistic analysis of fixed jacket-type offshore structures exposed to random wave loading. Deterministic and probabilistic methods are different in that the former is based on the long-term distribution of wave heights while the latter, on the long-term distribution of response peaks.

Chapter 8 is concerned with the short-term probability distribution of response while Chapter 10 is devoted to efficient ways of establishing that probability distribution. The determination of the short-term distribution of the response peaks from the short-term distribution of the response itself, is the subject of study in Section 8.3. On the other hand, the derivation of long-term distribution of response peaks from its short-term distribution, is similar to the derivation of long-term distribution of waveheights from its corresponding short-term distribution (which was discussed in Chapter 3). For this reason, the methodology for derivation of long-term distribution of waveheights is fully described herein. A brief discussion of the properties of the long-term distribution of response peaks will be presented in Section 8.4.

Offshore structures must be designed against both fatigue and first-excursion failures. First excursion failure analysis is based on extreme events. In the deterministic approach, an extreme wave height such as the '50 year' or '100 year' design wave height is used, while in the probabilistic approach, the '50 year' or '100 year' response peak is computed. There is a small probability that these extreme

events will be exceeded during the service life of the structure. This is referred to as the probability of encounter or the risk of failure.

The relationship between the risk of failure, the service life of the structure, and the probability of exceedence for the design waveheight (or the design response peak) will be established in Section 5.1. Knowing the probability of exceedence, the design waveheight can be determined from the long-term distribution of the waveheights.

The long-term distribution of the waveheights is obtained by convoluting the short-term distributions of the waveheights with the long-term distribution of sea states or wave conditions. Therefore, before the long-term distribution of the waveheights can be established, one must determine the long-term distribution of the sea states from a few years measurement. This is the subject of study in Section 5.2. The determination of the long-term distribution of waveheights by convoluting their short-term distributions with the long-term distribution of sea states is studied in Section 5.3. Knowing the long-term distribution of waveheights and the risk of failure, the design waveheight can be determined.

5.1 PROBABILITY OF ENCOUNTER

The probability of encounter or risk of failure has a clear interpretation; therefore, it is preferable to base the design on an acceptable level of risk of failure rather than on an extreme event which does not offer a clear interpretation. Of course, the two are interrelated so that knowing one of them, the other can be calculated.

The 'r-year' wave height H_r is defined as the wave height which is equalled or exceeded on average once every r years.

Let M' be the average number of waves per year, then $M'*r$ will be the average number of waves per r years. From the definition of the 'r-year' wave height, the probability of a wave height being equal to or greater than H_r is

$$\text{prob}\{H \geq H_r\} = 1/M'*r \tag{5.1}$$

or

$$\text{prob}\{H < H_r\} = 1 - 1/M'*r \tag{5.2}$$

Let L years be the service life of a structure; then the expected number of waves during this period is $M'*L$. Since the probability of an individual wave height being less than H_r is $1- 1/M'*r$, then, assuming that all the wave heights are statistically independent, the probability of all the wave heights (or the extreme wave height) in L years being smaller than H_r is

$$\begin{aligned}\text{prob}\{\text{extreme } H < H_r \text{ during the service life}\} &= (1 - 1/M'*r)^{M'*L} \\ &= (1 - 1/M'*r)^{M'*r*L/r} \\ &= [(1 - 1/M'*r)^{M'*r}]^{L/r}\end{aligned} \tag{5.3}$$

Since $1/(M'*r)$ is a very small number, the quantity in square brackets will approach e^{-1}. Hence,

$$\text{prob}\{\text{extreme } H < H_r \text{ during the service life}\} = (e^{-1})^{L/r} = \exp(-L/r) \tag{5.4}$$

Thus, the probability of encountering at least one wave height greater than or equal to the 'r-year' wave height during the service life of the structure is

$$E_p = \text{prob}\{\text{at least one } H \geq H_r \text{ during the service life}\}$$
$$= 1 - \exp(-L/r) \qquad (5.5)$$

Therefore, for example, in order to keep the risk of failure below 10%, the design return period must be greater than 10 times the service life of the structure.

In some publications (Borgman, 1963), E_p has been derived in a different way. The argument goes like this.

$$\text{prob}\{\text{at least one } H \geq H_r \text{ during a one-year period}\} = 1/r \qquad (5.6)$$

Therefore,

$$\text{prob}\{\text{extreme } H < H_r \text{ during a one-year period}\} = 1 - 1/r \qquad (5.7)$$

and

$$\text{prob}\{\text{extreme } H < H_r \text{ during L years}\} = (1 - 1/r)^L \qquad (5.8)$$

consequently,

$$E_p = \text{prob}\{\text{at least one } H \geq H_r \text{ during L years}\} = 1 - (1 - 1/r)^L \qquad (5.9)$$

Equation (5.9) approaches Equation (5.5) most of the time, but for example assume that the analysis is based on the 'one-year' wave height, i.e. $r = 1$, then from Equation (5.9), $E_p = 1$. This means that the probability of the 'one-year' wave height being exceeded in a period longer than one year is 1, which obviously cannot be true. Equation (5.5) gives a probability of 0.63. It is Equation (5.6) which is flawed. During a one-year period, the 'r-year' wave height can be exceeded 0, 1, 2, 3,.....times. 1/r is the mean of the associated

probability distribution, not the probability of 'r-year' wave height being exceeded at least one time.

Sarpkaya and Isaacson (1981) suggest that Equation (5.9) is correct and that Equation (5.5) is a good approximation to it. In my opinion, it is Equation (5.5) which is correct and Equation (5.9) can be considered as an approximation to it. For the two equations to be equal, the following identity must hold true.

$$1 - 1/r = \exp(- 1/r) \tag{5.10}$$

The following table compares the values of (1 - 1/r) and exp(- 1/r).

r	1 - 1/r	exp(- 1/r)
1	0	0.37
2	0.50	0.61
3	0.72	0.67
4	0.78	0.75
5	0.82	0.80
10	0.90	0.90

As observed, for the larger return periods ($r \geq 10$), the two quantities approach each other. Therefore, in practical design both methods are equivalent.

5.2 SCATTER DIAGRAM AND ITS EXTRAPOLATION

The long-term distribution of wave heights is obtained by convoluting the short-term distribution of wave heights with the long-term distribution of sea states or wave conditions (Battjes, 1970). As previously mentioned, over short periods of time (a few hours), the sea surface can be assumed stationary. Over longer periods, however, storms

vary in severity; therefore, in the long-term, the sea surface is not stationary. To represent the major long-term characteristics of sea waves, typically water surface records are obtained every 3 hours for a period of 10 to 20 minutes. Each record is considered to represent a sample from a short-term stationary sea state and is normally reduced to two representative parameters, H_s and T_z. Furthermore, the expected maximum wave height $E[H_{max}]$ can be computed for each three hour observation.

In addition to H_s and T_z, a complete representation of the long-term properties of sea waves requires the short-term mean direction of the waves as well as their directionality. However, due to difficulty in measuring wave directions, the wave climate or distribution of sea states is normally described by means of a scatter diagram giving the joint probability of occurrence of pairs of H_s and T_z, as shown in Figure 5.1. The wave scatter diagram is usually obtained by direct measurements.

A scatter diagram obtained from a short period of measurement (one year, for example) does not cover all the sea states possible at the site and hence does not lead to a reliable long-term distribution of wave heights. If one uses the measured scatter diagram, it means that the wave climate is repeated exactly at intervals equal to the measurement period; consequently, sea state conditions of greater intensity (and of greater return period) than those measured are not accounted for.

Trial calculations have shown that scatter diagrams should cover the average occurrence of sea states over a duration which is at least 10 times as long as the service life of the structure (Inglis et al,

1985). Since such a long data base is not available, one must simulate it by extrapolating the observed wave scatter diagram.

The first step in extrapolating the wave scatter diagram is to establish the long-term distribution of significant wave heights. Knowing this distribution, the procedure for extrapolating the diagram is straightforward and is nicely described by Inglis et al, (1985). Figure 5.2 (taken from Inglis (1985)) covers the procedure through an example in which a measured 6-year scatter diagram is extrapolated to a 1000-year scatter diagram.

Distribution of H_s

The long-term distribution of H_s has not been derived by theoretical means. However, trial and error has shown that the best fits are obtained by the Weibull or Gumbel (extreme value type I) distributions. In effect, the marginal distribution of H_s, obtained from the scatter diagram, is compared with various theoretical probability distributions until a reasonable fit is obtained. The distribution of H_s is then assumed to follow this distribution.

It is usually the observed and theoretical cumulative distributions which are compared. Based on the scatter diagram, the observed cumulative distribution of H_s is

$$\text{prob}\{H_s \leq H_{sn}\} = \sum_{i=1}^{n} \frac{W_i}{W + 1} \qquad (5.11)$$

where

$W_i = \sum_{\text{all } j} W_{ij}$

W_{ij} = number of occurrences in scatter diagram class (i,j)

$W = \sum_{all\ i} \sum_{all\ j} W_{ij}$

H_{sn} = upper limit of H_s in class i = n

The reason for using (W+1) rather than W is that the use of W assigns a probability of 1.0 to the upper bound of the observed significant wave heights which is not appropriate because it implies that higher values of H_s are not possible. By using (W+1), the probability assigned to the highest observed value of H_s will be less than one and therefore, there will be room for extrapolation of the data.

The data is then fitted to a theoretical probability distribution, i.e. the parameters of the distribution are chosen so that the best fit between the observed and the theoretical distribution is obtained. These parameters are determined by one of the following methods (Sarpkaya and Isaacson, 1981).

a) Graphical estimation ('eye' fitting)

b) Method of least squares

c) Method of moments

d) Method of maximum likelihood

Probability papers are used to check how good a theoretical probability distribution fits the observed data. These papers are constructed so that the cumulative probability distribution is plotted as a straight line on the papers. The goodness of fit is judged by how close the observed cumulative distribution follows a straight line on the paper, as shown in Figure 5.3.

In establishing the long-term distribution of significant wave heights, the following points must be considered:

1. Measurements of H_s taken over any finite interval of time are random samples from the complete population of H_s. Through the techniques of extrapolation, one tries to estimate the distribution of the population from analysis of the limited amount of data available. However, it must be recognised that the distribution of such short-term data samples from infinite populations are subject to sampling errors. In particular, it is inevitable that higher intensity sea state occurrences will vary considerably from year to year.

2. If the yearly variability is limited to the extreme events, then mathematical methods of fitting data such as the method of moments are more suitable than the graphical fitting method because the latter tends to place more emphasis on the upper range data points in comparison to mathematical methods. However, if the wave climate variability from sample to sample is not restricted to extreme sea states, but there is variability in lower and middle ranges of H_s, then the one-year record length is too short and high degrees of uncertainty are inevitable (Nolte, 1973). Therefore, an adequate data base is essential for establishing the long-term distribution of H_s.

3. When such a data base is not available, the wave height data may be obtained by hindcasting from meteorological data. Hindcast data are established from past weather information using wind data as input to a wave generating model.

4. There will be a physical limit to the values of H_s recorded at any location which depends upon the limiting wind speed, and its

duration and the fetch available for the generation of the sea states of extreme severity. Clearly, extrapolation of H_s beyond this physical limit would be meaningless.

5.3 LONG-TERM DISTRIBUTION OF WAVE HEIGHTS

As stated before, the long-term distribution of wave heights is obtained by convoluting the short-term distribution of wave heights with the long-term distribution of sea states or wave conditions. For each short-term sea state (H_{si}, T_{zj}), the probability of exceedence of individual wave heights is

$$Q_H(h|H_{si},T_{zj}) = \exp[-2(h/H_{si})^2] \tag{5.12}$$

and the average number of waves per unit time is

$$E[N|H_{si},T_{zj}] = 1/T_{zj} \tag{5.13}$$

Therefore, the average number of waves per unit time with $H \geq h$, $N(h)$, would be

$$E[N(h)|H_{si},T_{zj}] = (1/T_{zj}) * \exp[-2(h/H_{si})^2] \tag{5.14}$$

Now, the proportion of time for which sea states are in class (i,j) is W_{ij}/W, where W_{ij} and W are defined as before. Thus, the unconditional average number of waves per unit time, associated with class (i,j) is

$$\begin{aligned} E[N(h)]_{i,j} &= E[N(h)|H_{si},T_{zj}] * W_{ij}/W \\ &= (1/T_{zj}) * \exp[-2(h/H_{si})^2] * W_{ij}/W \end{aligned} \tag{5.15}$$

The expected number of waves per unit time with $H \geq h$, for all the sea states is

$$\begin{aligned} E[N(h)] &= \sum_i \sum_j E[N(h)]_{i,j} \\ &= (1/W) * \sum_i \exp[-2(h/H_{si})^2] \sum_j W_{ij}/T_{zj} \end{aligned} \tag{5.16}$$

and the expected number of waves per unit time for all heights is obtained by setting h=0 in the above equation.

$$E[N(0)] = (1/W) * \sum_i \sum_j W_{ij}/T_{zj} \tag{5.17}$$

Finally, the long-term probability of exceedence is

$$Q_{LT,H}(h) = prob_{LT}\{H \geq h\} = E[N(h)]/E[N(0)]$$

$$= \frac{\sum_i \exp[-2(h/H_{si})^2] * \sum_j W_{ij}/T_{zj}}{\sum_i \sum_j W_{ij}/T_{zj}} \tag{5.18}$$

and the long-term cdf is

$$P_{LT,H}(h) = prob_{LT}\{H < h\}$$

$$= 1.0 - \frac{\sum_i \exp[-2(h/H_{si})^2] \sum_j W_{ij}/T_{zj}}{\sum_i \sum_j W_{ij}/T_{zj}} \tag{5.19}$$

The above expression is then fitted to a suitable probability distribution such as Weibull 2 parameter or Gumbel (extreme value type I) distributions. The extreme events (such as the '100 year' wave height) are then obtained by extrapolating the theoretical distributions.

Figure 5.4 shows the sensitivity of the long-term distribution of wave heights to the extrapolation of significant wave height.

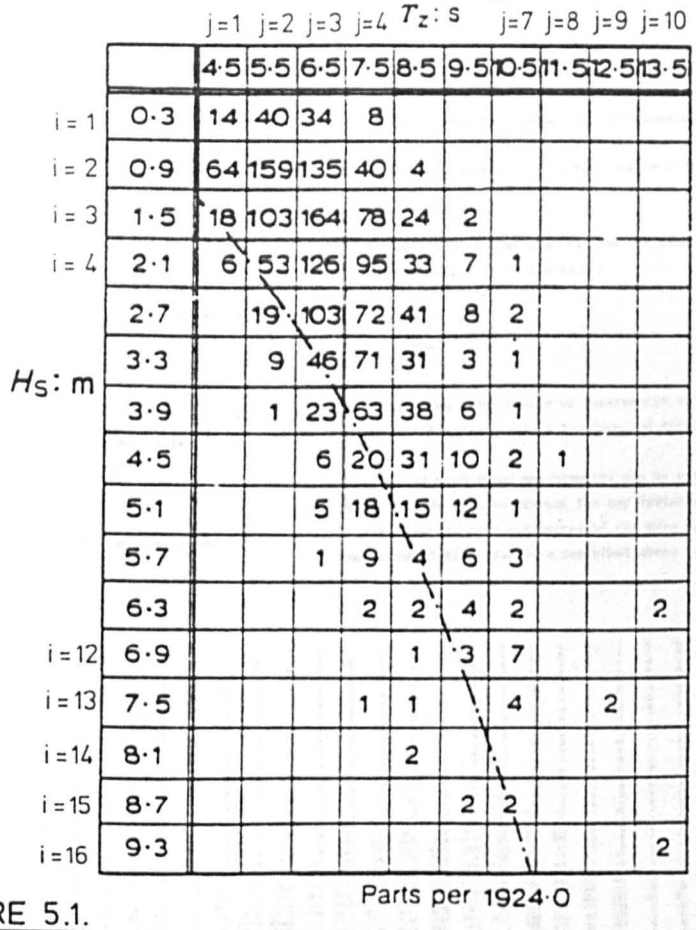

FIGURE 5.1.

Typical bivariate histogram of significant wave height H_S and mean zero crossing period T_z for one year

(Burrows, 1989)

Appendix: Engineering procedure to construct an extrapolated long duration wave scatter diagram.

The procedure to obtain a wave scatter diagram covering a period which is long compared to the structure's service life is in essence fairly straight forward. The example to be considered concerns the Northern North Sea where wave measurements have been made over a six-year period. This data base can be presented as a wave scatter diagram normalised on a total of 1000 observations as is usually done, or by giving the actual number of observations totalling 16042. If the data base is to be extrapolated to give a wave scatter diagram which is representative of the wave climate over, say, 1000 years, for example, the following steps are necessary.

1) Plot the cumulative probability distribution $P(H_s \leq H_s^*)$ for the available observations on Weibull scales.

2) Determine the parameters A, B and C of the three parameter Weibull distribution

$$P(H_s \leq H_s^*) = 1 - \exp\left(-\left(\frac{H_s^* - A}{B}\right)^C\right)$$

which fits the data best.

3) Calculate $P(H_s \leq H_s^*)$ for a range of values of H_s^* in excess of the largest H_s in the observations using the above Weibull distribution.

4) The total number of observations in 1000 years, based on one observation every three hours, is 1000 (years) * 365.2425 (average number of days per year) * 8 (observations per day) = 2921940.

5) The number of occurrences in 1000 years smaller than or equal to H_s^* is then

$$n(H_s \leq H_s^*) = 2921940\ P(H_s \leq H_s^*)$$

rounded to the nearest integer value.

6) The number of occurrences of each H_s^*-value chosen is thus

$$n(H_s^*) = n_1\ (H_s \leq (H_s^* + \delta)) - n_2\ (H_s \leq (H_s^* - \delta))$$

where δ is half the difference between two adjacent H_s^*-values. The number $n(H_s^*)$ is assigned to the middle of the classes thus formed.

7) Sum all numbers of occurrences $n(H_s^*)$ for H_s^*-values exceeding the highest H_s in the actual observations; this sum is n_T.

8) The number of occurrences $n(H_s^*)$ from step 6, which is added by extrapolation, are next associated with an estimated mean wave period T_z, for example by assuming a constant wave steepness relationship for these high sea states. Alternatively, they may be distributed around this period.

9) The number of actual observations for each (H_s, T_z) pair is finally scaled up by the factor

$$\frac{2921940 - n_T}{16042}$$

to make the total number of occurrences of the 1000-year scatter diagram equal to the required total 2921940.

If required wind speed measurements can be used to adjust the measured wave data to correct for any deviations from the average weather over the period of the wave measurement before the extrapolation procedure described above is carried out.

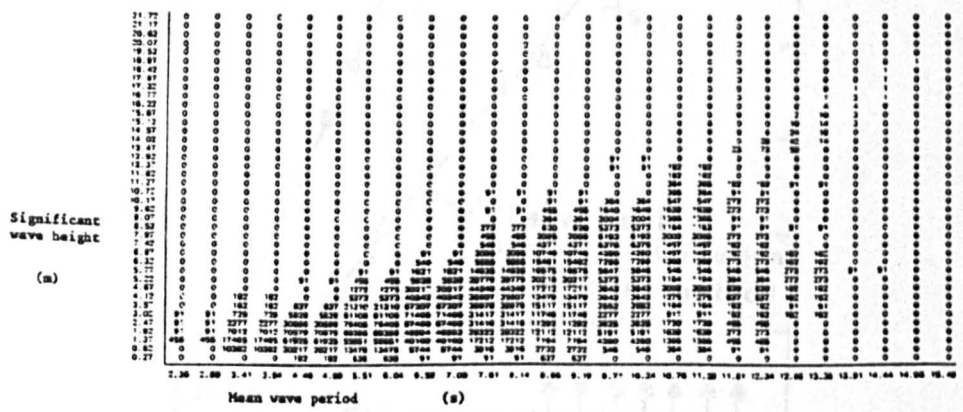

Fig. A.1. 1000 year Northern-North Sea wave scatter diagram

FIGURE 5 2 EXTRAPOLATION OF AN OBSERVED WAVE SCATTER DIAGRAM

(Inglis et al, 1985)

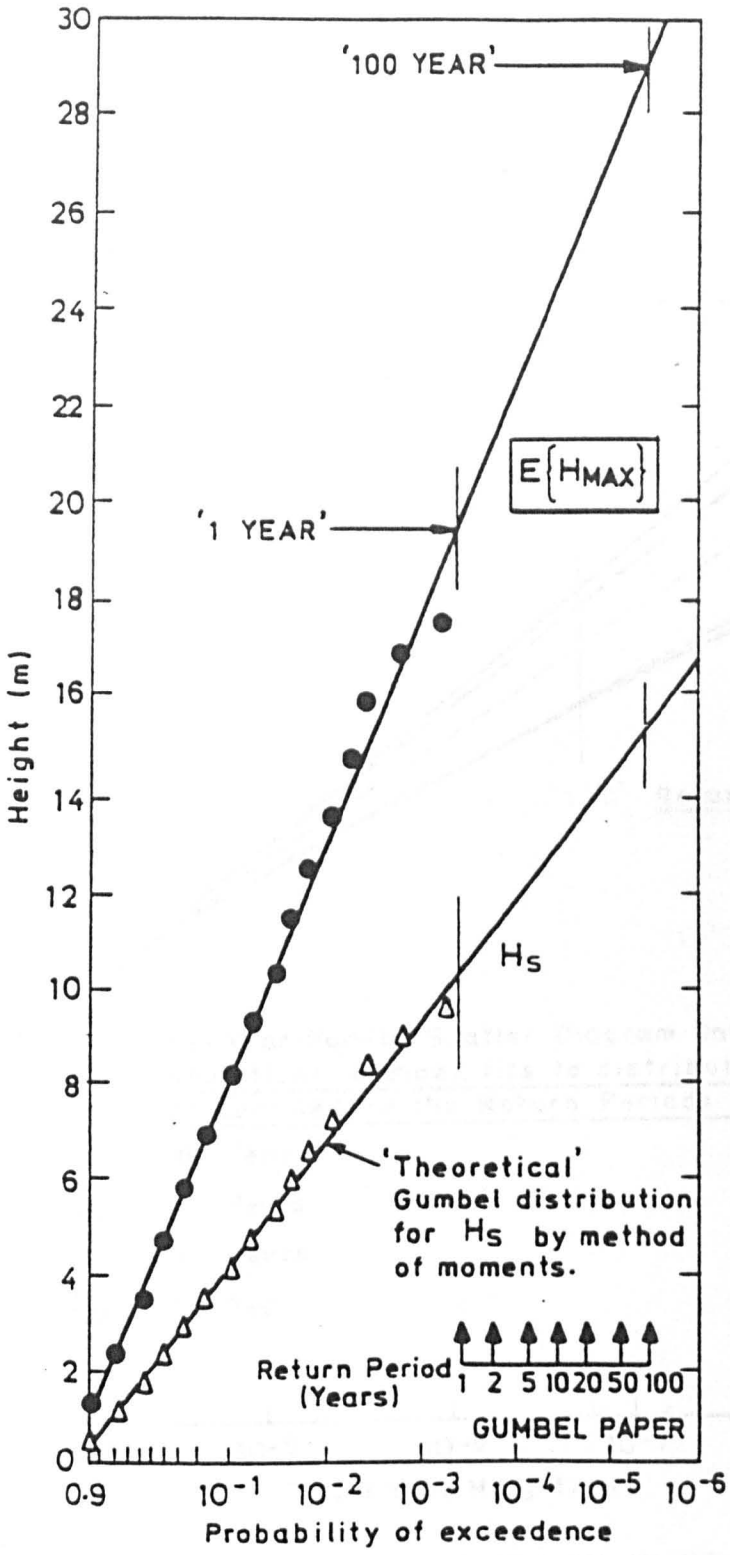

FIGURE 5.3 CDF's OF H_S AND E $\{H_{MAX}\}$

(Burrows, 1989)

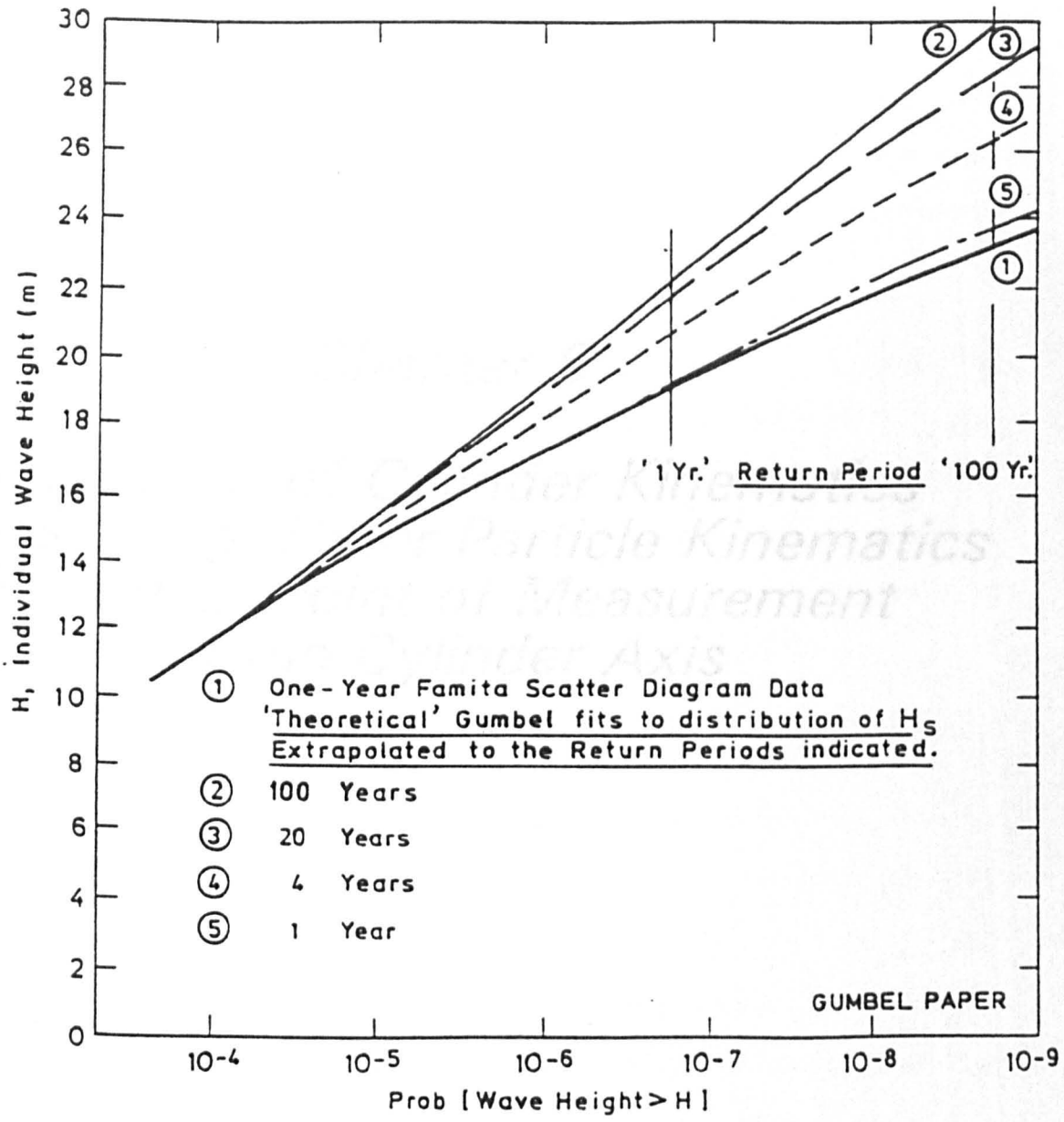

FIGURE 5.4. CDF OF INDIVIDUAL WAVE HEIGHT
(Burrows, 1989)

Chapter 6

Calculation of Cylinder Kinematics and Shifting Water Particle Kinematics from their Point of Measurement to the Cylinder Axis

INTRODUCTION

Before proceeding with the derivation of Morison coefficients, the following steps must be taken:

1. The data supplied by BMT included cylinder displacements in the x and y directions; however, in the relative motion form of Morison's equation, the cylinder velocity and acceleration (i.e. the first and second derivatives of displacement with respect to time) are required. Finite-Difference and Fourier methods have been employed in derivation of the cylinder kinematics (velocity and acceleration) from cylinder displacement.

2. Due to cylinder movement, the perforated balls, used in measuring water particle kinematics, were mounted on the small rigid column of the tower, which is some 12m distance from the compliant cylinder. Therefore, it is necessary to predict water particle kinematics at the cylinder by shifting (translating) them from their point of measurement to the cylinder axis.

6.1 CYLINDER KINEMATICS

6.1.1 FINITE DIFFERENCE METHOD

The cylinder displacement is known at intervals of $\Delta t = 0.075472$ seconds and is denoted by r_s, where subscript s refers to time $t_s = s\Delta t$ with $s = 0,1,.....,N - 1$. In the Finite-Difference method, the successive derivatives of r at time t_s are obtained in terms of the values of r at that point and a few neighbouring points. To ensure accuracy, especially as regard to the second order derivative, fourth order equations, which approximate the derivatives of a function at a point in terms of the values of the function at that point and four neighbouring points, were applied.

Central difference equations, in which two of the neighbouring points are before r_s and the other two are after r_s, were applied to all points except the first two and the last two points. That is,

$$\dot{r}_s = \frac{1}{12\Delta t}(r_{s-2} - 8r_{s-1} + 8r_{s+1} - r_{s+2}) \qquad (6.1)$$

$$s = 2,3,\ldots,N-3$$

$$\ddot{r}_s = \frac{1}{12\Delta t^2}(-r_{s-2} + 16r_{s-1} - 30r_s + 16r_{s+1} - r_{s+2}) \qquad (6.2)$$

where $\dot{r}$ and $\ddot{r}$ are the first and second derivatives of r with respect to time.

For s = 0 fully-forward difference equations, in which all the neighbouring points are after point r_s were used. Hence,

$$\dot{r}_s = \frac{1}{12\Delta t}(-25r_s + 48r_{s+1} - 36r_{s+2} + 16r_{s+3} - 3r_{s+4}) \qquad (6.3)$$

$$\ddot{r}_s = \frac{1}{12\Delta t^2}(35r_s - 104r_{s+1} + 114r_{s+2} - 56r_{s+3} + 11r_{s+4}) \qquad (6.4)$$

For s = 1, semi-forward difference equations, in which only one of the neighbouring points is before r_s and the remaining three are after r_s, were used.

$$\dot{r}_s = \frac{1}{12\Delta t}(-3r_{s-1} - 10r_s + 18r_{s+1} - 6r_{s+2} + r_{s+3}) \qquad (6.5)$$

$$\ddot{r}_s = \frac{1}{12\Delta t^2}(11r_{s-1} - 20r_s + 6r_{s+1} + 4r_{s+2} - r_{s+3}) \qquad (6.6)$$

For s = N - 2, semi-backward difference equations, in which three of the four neighbouring points are before r_s, were applied.

$$\dot{r}_s = \frac{1}{12\Delta t} (- r_{s-3} + 6r_{s-2} - 18r_{s-1} + 10r_s + 3r_{s+1}) \tag{6.7}$$

$$\ddot{r}_s = \frac{1}{12\Delta t^2} (- r_{s-3} + 4r_{s-2} + 6r_{s-1} - 20r_s + 11r_{s+1}) \tag{6.8}$$

And finally, for s = N - 1, fully-backward difference equations, in which all the four neighbouring points are before r_s, were used.

$$\dot{r}_s = \frac{1}{12\Delta t} (3r_{s-4} - 16r_{s-3} + 36r_{s-2} - 48r_{s-1} + 25r_s) \tag{6.9}$$

$$\ddot{r}_s = \frac{1}{12\Delta t^2} (11r_{s-4} - 56r_{s-3} + 114r_{s-2} - 104r_{s-1} + 35r_s) \tag{6.10}$$

Figures 6.1 and 6.2 show sample time series of cylinder velocity and acceleration obtained by this method for Level 2 of Run 15.

Derivation of Central Difference Equations

In this section, central difference equations are derived. Other equations are derived in a similar manner.

In general, the central difference equations are of the following form

$$\dot{r}_s = Ar_{s-2} + Br_{s-1} + Cr_s + Dr_{s+1} + Er_{s+2} \tag{6.11}$$

$$\ddot{r}_s = Pr_{s-2} + Qr_{s-1} + Sr_s + Tr_{s+1} + Ur_{s+2} \tag{6.12}$$

According to Taylor's theorem

$$r(t+h) = r(t) + h.\dot{r}(t) + 1/2\ h^2.\ddot{r}(t) + 1/6\ h^3.r^{(3)}(t) + 1/24\ h^4\ r^{(4)}(t) + O(h^5) \tag{6.13}$$

Where $r^{(3)}$ and $r^{(4)}$ are the third and fourth order derivatives of r and $O(h^5)$ contains terms with h^5 and higher powers of h. Setting $t = t_s$ and replacing h with $-2\Delta t$, $-\Delta t$, 0, Δt, and $2\Delta t$ respectively, the following values of r are obtained.

$$r_{s-2} = r_s - 2\Delta t\dot{r}_s + 2\Delta t^2\ddot{r}_s - 8/6\Delta t^3 r_s^{(3)} + 16/24 \Delta t^4 r_s^{(4)} + O(\Delta t^5) \quad (6.14)$$

$$r_{s-1} = r_s - \Delta t\dot{r}_s + 1/2\Delta t^2\ddot{r}_s - 1/6\Delta t^3 r_s^{(3)} + 1/24\Delta t^4 r_s^{(4)} + O(\Delta t^5) \quad (6.15)$$

$$r_s = r_s \quad (6.16)$$

$$r_{s+1} = r_s + \Delta t\dot{r}_s + 1/2\Delta t^2\ddot{r}_s + 1/6\Delta t^3 r_s^{(3)} + 1/24\Delta t^4 r_s^{(4)} + O(\Delta t^5) \quad (6.17)$$

$$r_{s+2} = r_s + 2\Delta t\dot{r}_s + 2\Delta t^2\ddot{r}_s + 8/6\Delta t^3 r_s^{(3)} + 16/24\Delta t^4 r_s^{(4)} + O(\Delta t^5) \quad (6.18)$$

Substituting from Equations (6.14) to (6.18) for r_{s-2}, r_{s-1}, r_s, r_{s+1}, and r_{s+2} into Equations (6.11) and (6.12), leads to

$$\dot{r}_s = (A + B + C + D + E)r_s + \Delta t(-2A - B + D + 2E)\dot{r}_s + \Delta t^2(2A + 1/2B + 1/2D + 2E)\ddot{r}_s + \Delta t^3(-4/3A - 1/6B + 1/6D + 4/3E)r_s^{(3)} + \Delta t^4(2/3A + 1/24B + 1/24D + 2/3E)r_s^{(4)} + O(\Delta t^5) \quad (6.19)$$

and

$$\ddot{r}_s = (P + Q + S + T + U)r_s + \Delta t(-2P - Q + T + 2U)\dot{r}_s + \Delta t^2(2P + 1/2Q + 1/2T + 2U)\ddot{r}_s + \Delta t^3(-4/3P - 1/6Q + 1/6T + 4/3U)r_s^{(3)} + \Delta t^4(2/3P + 1/24Q + 1/24T + 2/3U)r_s^{(4)} + O(\Delta t^5) \quad (6.20)$$

If the above relationships are to be correct for all values of s, then similar terms on both sides of the equations must be equal. Hence

$$\begin{cases} A + B + C + D + E = 0 \\ -2A - B + D + 2E = \dfrac{1}{\Delta t} \\ 2A + 1/2B + 1/2D + 2E = 0 \\ -4/3A - 1/6B + 1/6D + 4/3E = 0 \\ 2/3A + 1/24B + 1/24D + 2/3E = 0 \end{cases} \tag{6.21}$$

and

$$\begin{cases} P + Q + S + T + U = 0 \\ -2P - Q + T + 2U = 0 \\ 2P + 1/2Q + 1/2T + 2U = \dfrac{1}{\Delta t^2} \\ -4/3P - 1/6Q + 1/6T + 4/3U = 0 \\ 2/3P + 1/24Q + 1/24T + 2/3U = 0 \end{cases} \tag{6.22}$$

Solving the above two sets of linear equations, yields

$$\begin{cases} A = \dfrac{1}{12\Delta t} \\ B = -\dfrac{8}{12\Delta t} \\ C = 0 \\ D = \dfrac{8}{12}\Delta t \\ E = -\dfrac{1}{12}\Delta t \end{cases} \tag{6.23}$$

and

$$\begin{cases} P = -\dfrac{1}{12\Delta t^2} \\ Q = \dfrac{16}{12\Delta t^2} \\ S = -\dfrac{30}{12\Delta t^2} \\ T = \dfrac{16}{12\Delta t^2} \\ U = \dfrac{-1}{12\Delta t^2} \end{cases} \tag{6.24}$$

Equations (6.5) and (6.6) are obtained, by replacing the values of the above coefficients into Equations (6.11) and 6.12), respectively.

6.1.2 FOURIER METHOD

If x(t) is a periodic function with period T, then it is always possible to write (Newland, 1975)

$$x(t) = x_0 + \sum_{K=1}^{\infty} [a_k \cos(\omega_k t) + b_k \sin(\omega_k t)] \tag{6.25}$$

Where

$$\omega_k = \frac{2\pi k}{T} \tag{6.26}$$

$$a_k = \frac{2}{T} \int_0^T x(t) \cos(\omega_k t)\, dt \tag{6.27}$$

$$b_k = \frac{2}{T} \int_0^T x(t) \sin(\omega_k t)\, dt \tag{6.28}$$

$$x_o = \frac{1}{T} \int_0^T x(t)\, dt \tag{6.29}$$

Using complex notation, Equations (6.27) and (6.28) can be combined into a single equation by defining

$$x_k = a_k - ib_k \tag{6.30}$$

Then,

$$x_k = \frac{2}{T} \int_0^T x(t) \exp(-i\omega_k t)\, dt \tag{6.31}$$

and

$$x(t) = x_o + \sum_{k=1}^{\infty} \text{Real}\,[x_k \exp(i\omega_k t)] \tag{6.32}$$

where Real(c) refers to the real part of the complex number c. x_k are known as the Fourier coefficients of the periodic function x(t).

If the maximum frequency present in x(t) corresponds to k=m, then

$$x(t) = x_o + \sum_{k=1}^{m} [a_k \cos(\omega_k t) + b_k \sin(\omega_k t)] \tag{6.33}$$

Now consider the case when x(t) is only known at equally spaced intervals of Δt. In other words, x(t) is represented by the Discrete series $\{x_s\}$ where subscript s refers to the time $t_s = s\Delta t$ and s=0,1,.....,N-1. In this case the maximum measurable frequency is known as the folding or Nyquist frequency and is equal to

$$\omega_{nyq} = \omega_{k=N/2} = \frac{2\pi(N/2)}{T} = \frac{2\pi(N/2)}{N.\Delta t} = \frac{\pi}{\Delta t} \tag{6.34}$$

or

$$f_{nyq} = \frac{1}{2\Delta t} \tag{6.35}$$

In practice, Δt must be small enough so that the Nyquist frequency is well above (say at least 2 times) the maximum frequency present in the signal x(t).

From Equation (6.31), the Fourier coefficients of the discrete series $\{x_s\}$ will be

$$x_o = \frac{1}{N} \sum_{s=0}^{N-1} x_s \tag{6.36}$$

$$x_k = \frac{2}{N} \sum_{s=0}^{N-1} x_s \exp[-i(2\pi ks/N)]$$

$$k = 1,2,.....,(N/2 - 1) \tag{6.37}$$

$$x_{N/2} = \frac{1}{N} \sum_{s=0}^{N-1} x_s \exp(-is\pi) = \frac{1}{N} \sum_{s=0}^{N-1} x_s \cos(s\pi) \tag{6.38}$$

Any typical value x_s of the series $\{x_s\}$ is given by the inverse equation

$$x_s = x_o + \sum_{k=1}^{N/2} \text{Real } [x_k \exp(i2\pi ks/N)]$$

$$s = 0,1,.....,(N-1) \tag{6.39}$$

Note that for $s < 0$ or $s > (N-1)$, the series repeats itself so that $x_{N+s} = x_{-N+s} = x_s$

Fast Fourier Algorithms (FFT) were used to break down the cylinder displacement, r(t), into its frequency components, i.e.

$$r(t) = r_o + \sum_{k=1}^{N/2} [a_k \cos(\omega_k t) + b_k \sin(\omega_k t)] \tag{6.40}$$

The cylinder velocity and acceleration are obtained by taking the first and the second order derivatives of r(t) with respect to time, i.e.

$$\dot{r}(t) = \sum_{k=1}^{N/2} [-a_k \omega_k \sin(\omega_k t) + b_k \omega_k \cos(\omega_k t)] \tag{6.41}$$

and

$$\ddot{r}(t) = \sum_{k=1}^{N/2} [-a_k \omega^2_k \cos(\omega_k t) - b_k \omega^2_k \sin(\omega_k t)] \quad (6.42)$$

The cylinder velocity and acceleration are then obtained by an inverse Fourier Transform of the above equations. Cylinder velocity and acceleration for Level 2 of Run 15 are shown in Figures 6.3 and 6.4, respectively and are in full agreement with those obtained from the Finite Difference method shown in Figures 6.1 and 6.2.

Practical Considerations in the Fourier Method

In FFT, the number of elements in a sequence must be an integer power of 2. If this is not the case, it is common practice to add zeros to the tail of the sequence so that the number of data points is increased to the nearest integer power of 2. For example, the number of data points in the cylinder displacement series $\{r_n\}$ is N = 13816 which is higher than 2^{13} = 8192 but less than 2^{14} = 16384. Therefore, 2568 zero points need to be added to the tail of the sequence so that the number of data points in the signal is increased to 2^{14} = 16384 points. Alternatively, as was the case with this study, L = 1284 zeros can be added to both the beginning and the end of the sequence.

Using FFT algorithms, Fourier coefficients of r(t) were calculated. Fourier coefficients of $\dot{r}(t)$ and $\ddot{r}(t)$ were then obtained from Equations (6.41) and (6.42) and subsequently an inverse Fourier transform yielded the values of $\dot{r}(t)$ and $\ddot{r}(t)$. The results were satisfactory except that as shown in Figures 6.5 and 6.6, there were very large-amplitude, high-frequency fluctuations at the vicinity of time t=0. These high-frequency fluctuations are almost certainly due to the sudden jumps from r_{N-1} to $r_N = 0$ and from $r_{-1} = 0$ to r_0 (Figure 6.7-a). As a result of

these sudden jumps, high-frequency, low-amplitude oscillations are introduced in the signal r(t). However, these low-amplitudes are greatly magnified because of their high frequency, when the first and second order derivatives are calculated.

Furthermore, the cylinder kinematics at the first and the last two points (points 0,1,N-2,N-1) deserve special attention. Since these kinematics are dependent on the cylinder displacement in the vicinity of the above mentioned points, adding zeros to the beginning and the end of the series results in unreliable values of kinematics at these points.

The above mentioned problems were solved in the following manner.

a) L = 1284 non-zero points were added to both the beginning and the end of the sequence (r_s), as will be described below. The new sequence is (r_s) with s = -L,....., -1,0,1,.....,N + L - 1 (Figure 6.7-b).

b) In Discrete Fourier analysis, the sequence (r_s) repeats itself for s > N + L - 1, so that $r_{N+L} = r_{-L}$ and $r_{N+L}^{(n)} = r_{-L}^{(n)}$ where $r^{(n)}$ stands for the nth order derivative of r. Therefore the values of r_{N+L-1} and r_{-L} must not be far apart. In other words, there must not be a sudden jump from r_{N+L-1} to r_{-L}. Furthermore, since it is intended to calculate the first and the second order derivatives of r, $\acute{r}_{N+L-1}$ and $\acute{r}_{N+L-1}$ must also be close to $\acute{r}_{-L}$ and $\acute{r}_{-L}$, respectively.

c) To avoid distorting the values of the kinematics at points 0 and 1, r_{-1} and r_{-2} were calculated from the following relationships.

$$r_{-1} = 5r_0 - 10r_1 + 10r_2 - 5r_3 + r_4 \tag{6.43}$$

$$r_{-2} = 15r_0 - 40r_1 + 45r_2 - 24r_3 + 5r_4 \tag{6.44}$$

Substituting for r_{-1} and r_{-2} from the above equations into Equations (6.1) and (6.2) (Central-Difference Equations) with s = 0 and 1, leads to

$$\begin{cases} \dot{r}_0 = \dfrac{1}{12\Delta t}(-25r_0 + 48r_1 - 36r_2 + 16r_3 - 3r_4) & (6.45) \\ \ddot{r}_0 = \dfrac{1}{12\Delta t^2}(35r_0 - 104r_1 + 114r_2 - 56r_3 + 11r_4) & (6.46) \end{cases}$$

and

$$\begin{cases} \dot{r}_1 = \dfrac{1}{12\Delta t}(-3r_0 - 10r_1 + 18r_2 - 6r_3 + r_4) & (6.47) \\ \ddot{r}_1 = \dfrac{1}{12\Delta t^2}(11r_0 - 20r_1 + 6r_2 + 4r_3 - r_4) & (6.48) \end{cases}$$

which are the same as the fully-forward and semi-forward equations (Equations 6.3 - 6.6) used in calculation of the kinematics at points 0 and 1 in the finite-difference method.

d) Similarly, to avoid distorting the values of kinematics at points N - 2 and N - 1, r_N and r_{N+1} were calculated from the following relationships

$$r_N = r_{N-5} - 5r_{N-4} + 10r_{N-3} - 10r_{N-2} + 5r_{N+1} \quad (6.49)$$

$$r_{N+1} = 5r_{N-5} - 24r_{N-4} + 45r_{N-3} - 40r_{N-2} + 15r_{N-1} \quad (6.50)$$

when these values of r_N and r_{N+1} are replaced into the central-difference equations for s = N - 2 and s = N - 1, they lead to the semi-backward and fully-backward equations used in calculation of the kinematics at points N - 2 and N - 1 in the finite difference method.

e) The first L - 2 points are the mirror image of r_{-1} to r_{L-4} with respect to a vertical line at point r_{-2} (Figure 6.7b). Therefore,

$$r_{-2-j} = r_{-2+j}$$

$$j = 1,2,.....,L - 2 \quad (6.51)$$

f) Similarly, the last L - 2 points are the mirror image of r_{N-L+3} to r_N with respect to a line at point r_{N+1} (Figure 6.7b). Therefore,

$$r_{N+1+j} = r_{N+1-j}$$

$$j = 1,2,.....,L - 2 \quad (6.52)$$

g) The resultant time series (r_s) s = - L,....,-1,0,1,...., N + L - 1 is multiplied by the weighting coefficients (w_s) defined as (Figure 6.7c)

$$\{W_s\} = \begin{cases} \left[\dfrac{L + s}{L - 2}\right]^3 & \text{for } s = -L,.....,-3 \\ 1 & \text{for } s = -2,-1,0,.....,N+1 \\ \left[\dfrac{N + L - 1 - s}{L - 2}\right]^3 & \text{for } s = N+2,.....,N+L-1 \end{cases} \quad (6.53)$$

so that

$$r_{-L} = \acute{r}_{-L} = \bar{r}_{-L} = r_{N+L-1} = \acute{r}_{N+L-1} = \bar{r}_{N+L-1} = 0$$

In other words, between the values of r_{-L} and r_{N+L-1}, $\acute{r}_{-L}$ and $\acute{r}_{N+L-1}$, $\bar{r}_{-L}$ and $\bar{r}_{N+L-1}$ there is no sudden jump. Therefore, high-frequency oscillations will not be introduced in the series.

Figure 6.8a shows that when zeros were added to the beginning and end of the series, high frequency oscillations build up in the vicinity of time = 0. In contrast when the above mentioned procedure is followed, high frequency oscillations are absent, as shown in Figure 6.8b.

6.2 SHIFTING WATER PARTICLE KINEMATICS IN THE PRESENCE OF CURRENT

6.2.1 WAVE-CURRENT INTERACTION

Consider a train of regular waves (wave length L, height H) travelling on a steady horizontally and vertically uniform current. The current velocity is c and its component in the direction of wave propagation, x, is $\bar{u} = c \cos\alpha$ (Figure 6.9). According to linear Wave theory, water surface elevation and water particle kinematics as observed by a stationary observer are (Hedges, 1987)

$$\eta = \frac{H}{2} \cos(kx - \omega_a t) \tag{6.54}$$

$$u = \bar{u} + \frac{H}{2} (\omega_a - k\bar{u}) \Gamma_h \cos(kx - \omega_a t) \tag{6.55}$$

$$v = \bar{v} = c \sin\alpha \tag{6.56}$$

$$w = \frac{H}{2} (\omega_a - k\bar{u}) \Gamma_v \sin(kx - \omega_a t) \tag{6.57}$$

$$\dot{u} = \frac{H}{2} (\omega_a - k\bar{u})^2 \Gamma_h \sin(kx - \omega_a t) \tag{6.58}$$

$$\dot{w} = - \frac{H}{2} (\omega_a - k\bar{u})^2 \Gamma_v \cos(kx - \omega_a t) \tag{6.59}$$

Where Γ_h and Γ_v are the horizontal and vertical depth attenuation factors (Equations (3.64) and (3.65)), $k = 2\pi/L$ is the wave number, $\omega_a = 2\pi/T_a$ and T_a is the apparent wave period (wave period as measured by the stationary observer). The apparent angular frequency, ω_a, is related to wave number by

$$\omega_a = \sqrt{gk\tanh(kd)} + k\bar{u} \tag{6.60}$$

or

$$T_a = \frac{2\pi}{\sqrt{gk\tanh(kd)} + k\bar{u}} \tag{6.61}$$

6.2.2 SHIFTING THE KINEMATICS

The above equations show that water surface elevation and its associated water particle kinematics are all of the form

$$f(x,t) = \bar{f} + \rho \cos(kx - \omega_a t) \tag{6.62}$$

where $\bar{f}$ is the mean of f and ρ is the amplitude of the sinusoidal function. At an arbitrary point x_1, $g(x_1,t) = f(x_1,t) - \bar{f}$ is a function of time only. That is

$$g(x_1,t) = f(x_1,t) - \bar{f} = \rho \cos(kx_1 - \omega_e t) \tag{6.63}$$

in which kx_1 is a fixed phase angle. Expanding the cosine term, $g(x_1,t)$ can be written as

$$g(x_1,t) = a_{x1} \cos(\omega_e t) + b_{x1} \sin(\omega_e t) \tag{6.64}$$

where

$$\begin{cases} a_{x1} = \rho \cos(kx_1) \\ b_{x1} = \rho \sin(kx_1) \end{cases} \tag{6.65}$$

Using complex notation, a_{x1} and b_{x1} can be combined into a single complex number by defining

$$A = a_{x1} - ib_{x1} = \rho \exp(-ikx_1) \tag{6.66}$$

A is the complex Fourier coefficient of $g(x_1,t)$. Knowing A, $g(x_1,t)$ can be calculated by the process of inverse Fourier transform. Similarly, at point $x_2 = x_1 + \Delta x$ the Fourier coefficient B is

$$B = \rho \exp(-ikx_2) = \rho \exp[-k(x_1 + \Delta x)] = \rho \exp(-ikx_1)$$
$$\exp(-ik\Delta x) = A \exp(-ik\Delta x) \tag{6.67}$$

Therefore, the Fourier coefficient of the sinusoidal wave at point x_2 can be obtained by multiplying its Fourier coefficient at point x_1 by $\exp(-ik\Delta x)$ where $k\Delta x$ is the phase shift.

In a random wave field, the discretised measured kinematics at point x_1 (N points at Δt apart) can be broken down into its harmonic components

through FFT. For example, the horizontal component of water particle velocity is

$$u_{x1} - \bar{u} = \sum_{j=1}^{N/2} \rho_j \cos(k_j x_1 - \omega_{aj} t) \tag{6.68}$$

The wave number, k_j, for each harmonic can be obtained from Equation (6.60) where

$$\omega_{aj} = \frac{2\pi j}{T} \qquad j = 1,2,.....,N/2 \tag{6.69}$$

and $T = N\Delta t$ is the length of the recorded signal.

To obtain the kinematics at point x_2, the Fourier coefficients at point x_1, A_j, are multiplied by $\exp(-ik_j\Delta x)$ where Δx is the shift along the direction of wave propagation. Thus

$$B_j = A_j \exp(-ik_j \Delta x) \qquad j = 1,2,.....,N/2 \tag{6.70}$$

Knowing B_j, $(u - \bar{u})$ at point x_2 can be calculated by inverse Fourier transform. Note that the current component $\bar{u}$ does not change from point x_1 to point x_2.

Results

The shifting distance depends on wave direction but is of the order of 6m for the predominant direction. The phase shift can only be achieved by approximating the sea as long-crested in the predominant direction. Previous discussion of the directional properties of the seas suggests that this might not be unreasonable for those components in the most energetic part of the spectrum with wave lengths of 60-120m, where the shift is a fraction of the wave length. It is recognised that the phase

of shorter components, where the directional spread is greater and the wave length is shorter, will not be accurately transformed.

Figures 6.10 to 6.15 show sample time series of the observed and translated velocities and accelerations at Level 2 and Level 3. Checks have been made to ensure that the general character of the time series, their variances and cross-correlations are reasonably maintained through the shifting process.

6.2.3 PRACTICAL CONSIDERATIONS IN SHIFTING THE KINEMATICS

6.2.3.1 The Effect of Current on Wave Period

1) Examination of Equation (6.61) shows that when $\bar{u} \geq 0$, T_a is always positive and that for large values of k, T_a approaches zero. For a wave with a particular wave length, wave period in the presence of current, T_a, is less than the wave period in the absence of current (Figure 6.16).

2) Figure 6.17 shows the variation of the apparent wave period with k for the case of a negative current. Equation (6.61) shows that the apparent wave period is infinity when

$$\sqrt{gk\tanh(kd)} + k\bar{u} = 0 \qquad (6.71)$$

Dividing the above equation by k and taking $\bar{u}$ to the right hand side of the equation, leads to

$$\sqrt{(g/k)\tanh(kd)} = -\bar{u} \qquad (6.72)$$

The left hand side of the above equation is equal to the celerity of individual waves. Therefore, when the celerity of the individual waves is equal and opposite to that of the current,

the apparent wave period is infinity, i.e. the waves are stagnant for the stationary observer (Hedges, 1987).

3) Figure 6.17 shows that for negative currents, the apparent wave period has a minimum. The wave number leading to the minimum of T_a, can be obtained by setting the first derivative of Equation (6.61) equal to zero. That is T_a is minimum when

$$g \tanh(kd) + \frac{gkd}{\cosh^2(kd)} + 2\bar{u}\sqrt{gk\tanh(kd)} = 0 \qquad (6.73)$$

Dividing the above equation by 2tanh(kd) and replacing 2sinh(kd) cosh(kd) by sinh(2kd), results in

$$\frac{1}{2}\left[1 + \frac{2kd}{\sinh(2kd)}\right] = -\bar{u}\sqrt{\frac{k}{g\tanh(kd)}} \qquad (6.74)$$

Multiplying the above equation throughout by $\sqrt{(g/k)\tanh(kd)}$, gives

$$\frac{1}{2}\left[1 + \frac{2kd}{\sinh(2kd)}\right]\sqrt{(g/k)\tanh(kd)} = -\bar{u} \qquad (6.75)$$

The left hand side of the above equation is equal to the group velocity of the waves and therefore, it can be concluded that the apparent wave period T_a is minimum when the group velocity is equal and opposite to the current velocity (Hedges, 1987).

For deep water conditions (d/L > 0.5), tanh(kd) ≈ 1 and cosh(kd) would be large so that from Equation (6.73), T_a is minimum when

$$k = \frac{g}{4\bar{u}^2} \qquad (6.76)$$

Combining Equations (6.76) and (6.61) leads to the minimum value of T_a for deep water conditions in the presence of negative currents

$$(T_a)_{min} = \frac{8\pi |\bar{u}|}{g} \tag{6.77}$$

4) The above discussion shows that for negative currents, the wave number can be divided into three distinct regions (Figure 6.17).

Region (a) - Long waves (small k) where both the celerity of individual waves and group velocity are larger than $|\bar{u}|$. Therefore, individual waves and wave group as a whole propagate upstream.

Region (b) - Short waves where the celerity of individual waves is larger than $|\bar{u}|$, but the group velocity is smaller. Therefore, individual waves propagate upstream while the wave group as a whole is swept downstream.

Region (c) - Very short waves (large k) where both the celerity of individual waves and group velocity are smaller than $|\bar{u}|$. Thus, individual waves and wave group as a whole are swept downstream and that is why the apparent period is negative for these short waves.

Figure 6.17 shows that there are two possible solutions for periods greater than the minimum apparent wave period. However, virtually all waves of engineering interest have group velocities which are greater than any current velocities likely to be

encountered (Hedges, 1987). Consequently, only solutions in Region (a) need be considered in practice.

5) In this study, the minimum value of $\bar{u}$ is -0.31 m/sec for Run 16 at Level 4. From Equation (6.76), the wave number that leads to the minimum apparent wave period is

$$k = \frac{g}{4\bar{u}^2} = 25.52 m^{-1}$$

or

$$L = 0.246 m$$

The water depth is approximately 10m so that d/L > 40 and hence deep water conditions are satisfied. Therefore, in this study, Equation (6.77) can be used to calculate the minimum apparent wave period for all the runs with negative currents. The largest value of $(T_a)_{min}$ is for Run 16 at Level 4.

$$\text{Maximum } [(T_a)_{min}] = \frac{8\pi|\bar{u}|}{g} = 0.79 \text{ sec}$$

Which corresponds to a frequency of 1.27Hz. While this is well above the important range of frequencies for all the runs, it is less than the Nyquist frequency of 6.6Hz. Ideally, harmonics with periods smaller than $(T_a)_{min}$ should not exist at all. However, the amplitudes of these harmonics though small are not zero. In this study, harmonics with periods greater than $(T_a)_{min}$ were phase-shifted, but those with smaller periods were not. However, these harmonics have not been eliminated because their elimination results in a shifted signal which has a smaller standard deviation in comparison with the unshifted signal.

6.2.3.2 Solving the Dispersion Equation

Deep Water Condition

For deep water conditions, ($d/L \geq 0.50$), $\tanh(kd) \approx 1$ and Equation (6.60) reduces to

$$\omega_a = \sqrt{gk} + k\bar{u} \tag{6.78}$$

Taking $k\bar{u}$ to the left hand side of the above equation and raising both sides to the second power, results in

$$\bar{u}^2k^2 - (2\bar{u}\omega_a + g)k + \omega_a^2 = 0 \tag{6.79}$$

Solving this quadratic equation, gives

$$k = \frac{\omega_a^2}{g}\left(\frac{1 + 2\alpha \pm \sqrt{1 + 4\alpha}}{2\alpha^2}\right) \tag{6.80}$$

where α is a dimensionless entity defined as

$$\alpha = \frac{\bar{u}\omega_a}{g} \tag{6.81}$$

Equation (6.80) offers two solutions; however, for positive currents, there is only one acceptable solution. Equation (6.78) shows that $\omega_a - k\bar{u}$ must be positive. Substituting from Equation (6.80) for k in Equation (6.78), yields

$$\omega_a - k\bar{u} = \omega_a\left(\frac{-1 \mp \sqrt{1 + 4\alpha}}{2\alpha}\right)$$

That solution of k with positive square term results in a negative value for $\omega_a - k\bar{u}$. It is therefore concluded that for positive currents, the only acceptable solution is

$$k = \frac{\omega_a^2}{g}\left(\frac{1 + 2\alpha - \sqrt{1 + 4\alpha}}{2\alpha^2}\right) \tag{6.82}$$

For negative currents, $(T_a)_{min}$ is calculated from Equation (6.77). For larger values of T_a, there are two solutions. However, as previously discussed, only the longer wave (smaller k) is of engineering interest. Therefore, for both negative and positive currents, the following solution is adopted

$$k = \frac{\omega_a^2}{g}\left(\frac{1 + 2\alpha - \sqrt{1 + 4\alpha}}{2\alpha^2}\right) \tag{6.83}$$

The above equation is indeterminate for $\alpha = 0$ ($\bar{u} = 0$) and for small values of α (small $\bar{u}$ and large T_a), the problem of accuracy arises because $(1 + 2\alpha)$ and $\sqrt{1 + 4\alpha}$ will be very close to each other. From Taylor's series, the power series expansion of $\sqrt{1 + 4\alpha}$ is

$$\sqrt{1 + 4\alpha} = 1 + 2\alpha - 2\alpha^2 + 4\alpha^3 - 10\alpha^4 \tag{6.84}$$

Combining Equations (6.83) and (6.84) leads to

$$k = \frac{\omega_a^2}{g}(1 - 2\alpha + 5\alpha^2) \tag{6.85}$$

For $|\alpha| < 0.01$, the above equation gives accurate results. For larger values of α Equation (6.83) is used. Note that for $\alpha = 0$ ($\bar{u} = 0$), $k = \omega_a^2/g$ which is the solution to Equation (6.78) when $\bar{u}$ is equal to zero.

Shallow Water Condition

When $d/L < 0.50$, there is no analytical solution to Equation (6.60). The wave number k is the root of function f(k) defined as

$$f(k) = \sqrt{gk\tanh(kd)} + k\bar{u} - \omega_a \tag{6.86}$$

Newton-Raphson numerical technique was used to solve the above equation. In this technique, the initial estimate of the root k_0 is successively improved in the following manner.

$$k_{n+1} = k_n - \frac{f(k_n)}{\acute{f}(k_n)} \tag{6.87}$$

where $\acute{f}(k_n)$ is the first order derivative of $f(k_n)$ with respect to k, and is equal to,

$$\acute{f}(k) = \frac{g\tanh(kd) + \dfrac{gkd}{\cosh^2(kd)}}{2\sqrt{gk\tanh(kd)}} + \bar{u} \tag{6.88}$$

The iterative process is repeated until sufficient accuracy is achieved. The initial estimate, k_0, can be taken as the wave number for deep-water conditions obtained from Equations (6.83) or (6.85). Since for a given period, the wave length in deep water is always larger than the wave length in shallow water, k_0 serves as a lower bound to the solution of Equation (6.86). Furthermore, since for negative currents, there are two possible solutions, the choice of k_0 as the initial estimate ensures that the iterative process converges to the solution with the larger wave length, i.e. the solution in Region (a) of Figure 6.17.

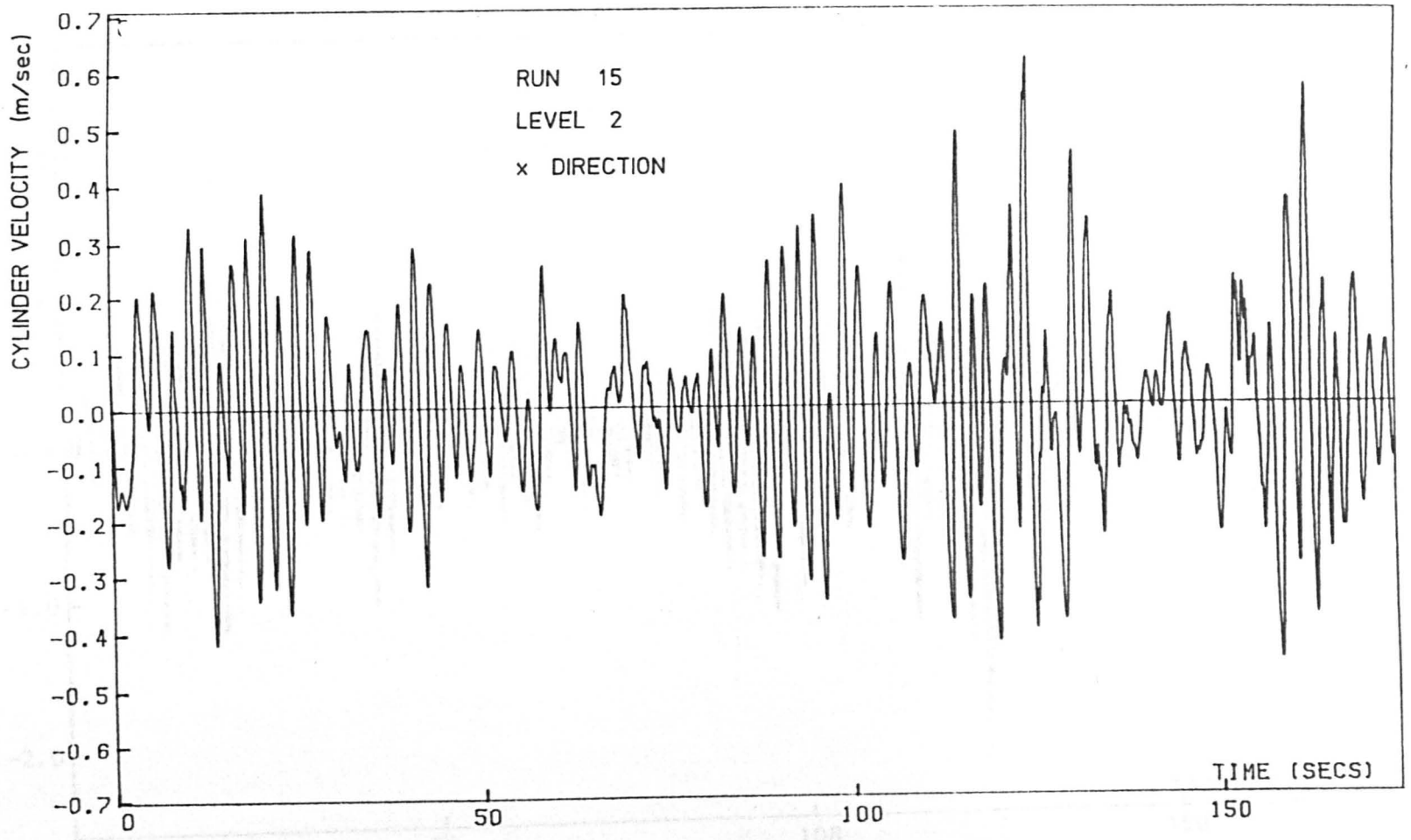

FIGURE 6.1. CYLINDER VELOCITY FROM FINITE-DIFFERENCE METHOD

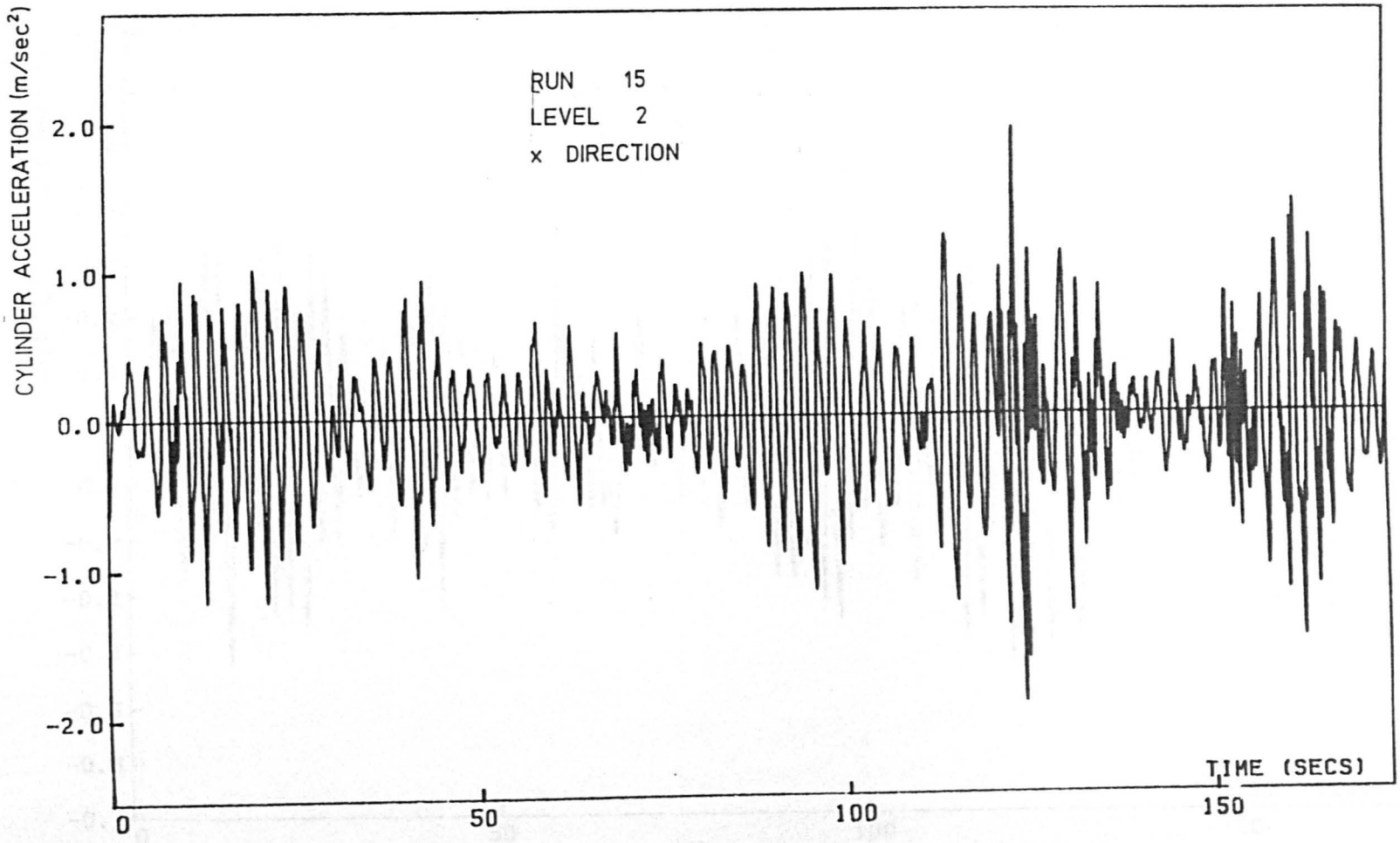

FIGURE 6.2. CYLINDER ACCELERATION FROM FINITE-DIFFERENCE METHOD

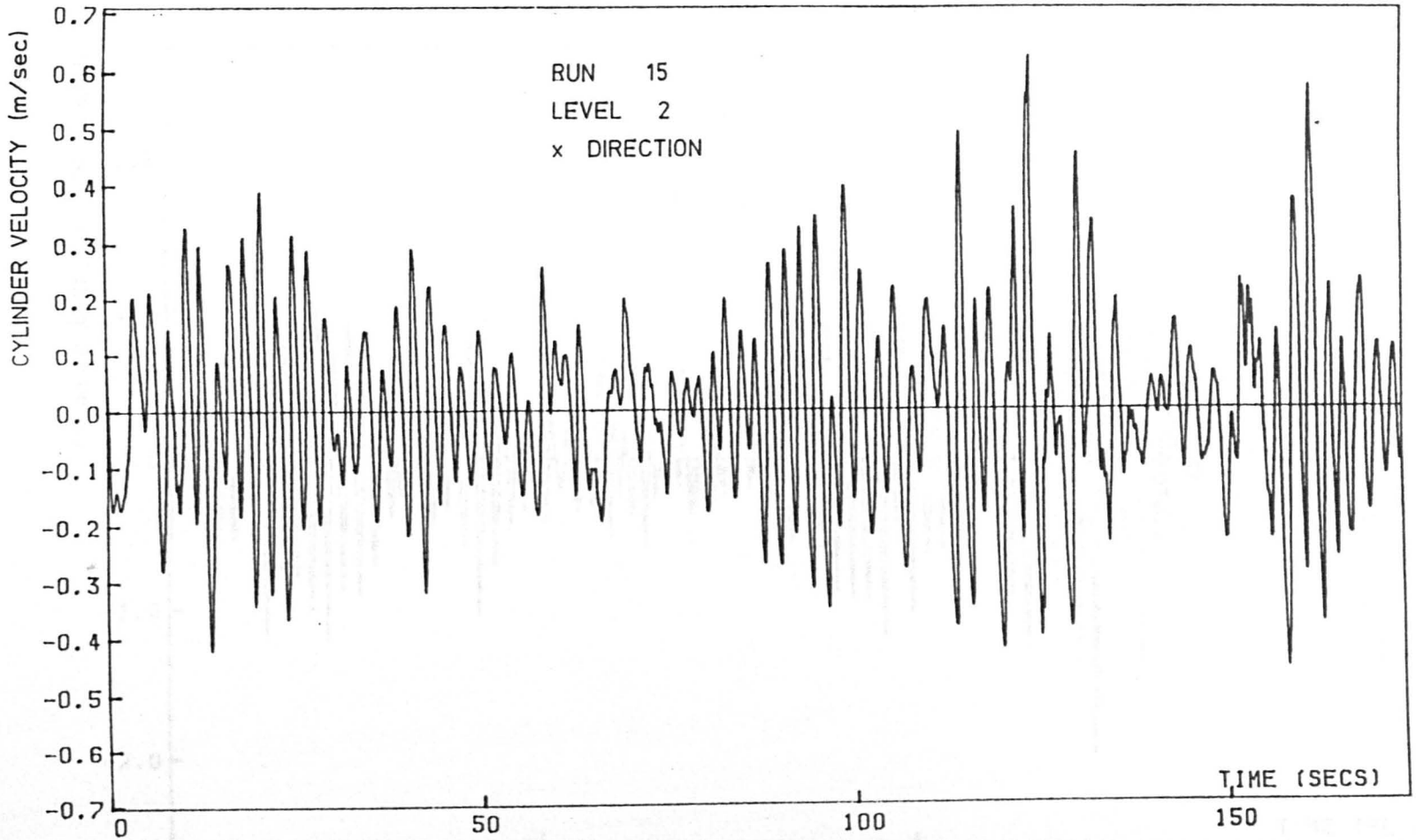

FIGURE 6.3. CYLINDER VELOCITY FROM FOURIER METHOD

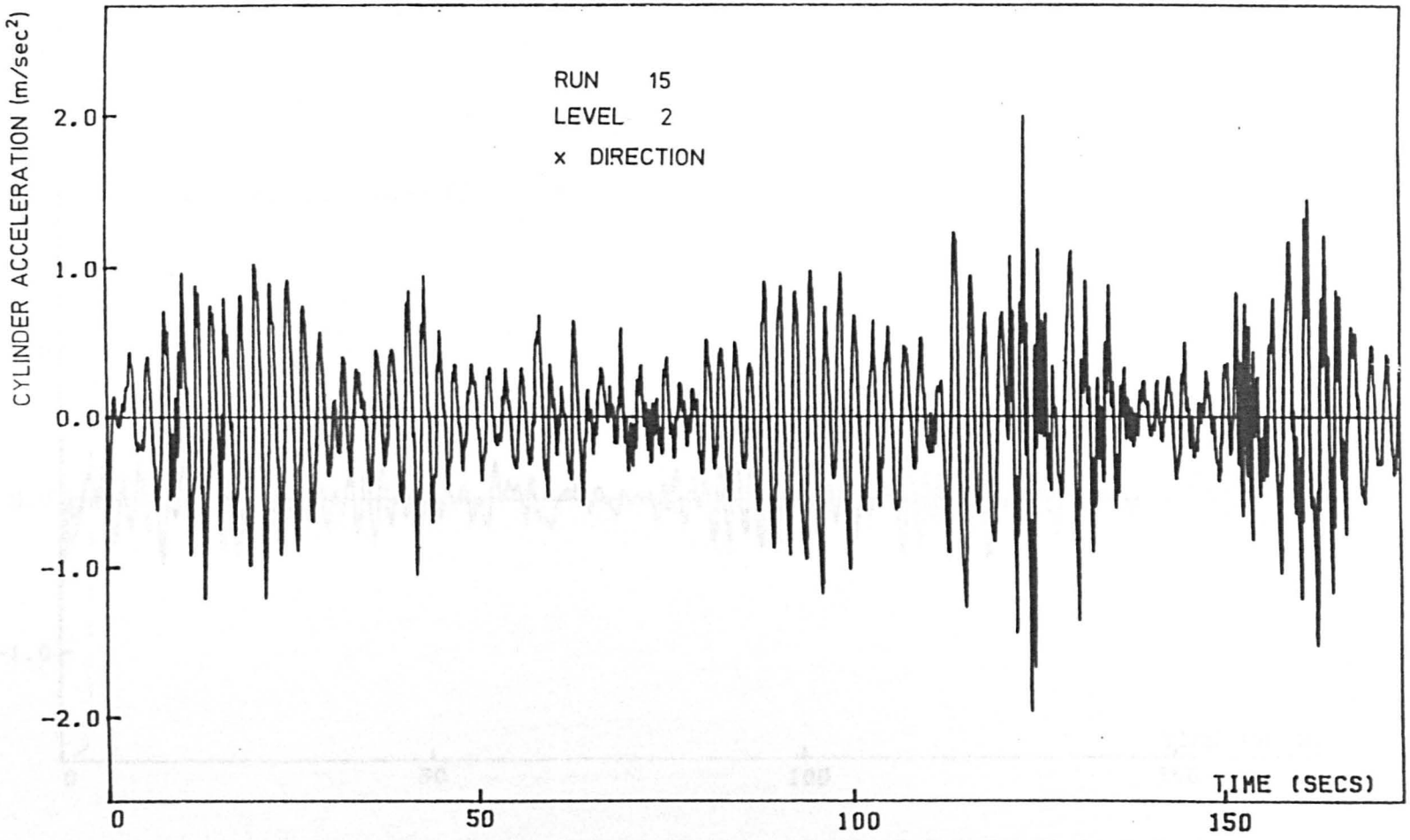

FIGURE 6.4. CYLINDER ACCELERATION FROM FOURIER METHOD

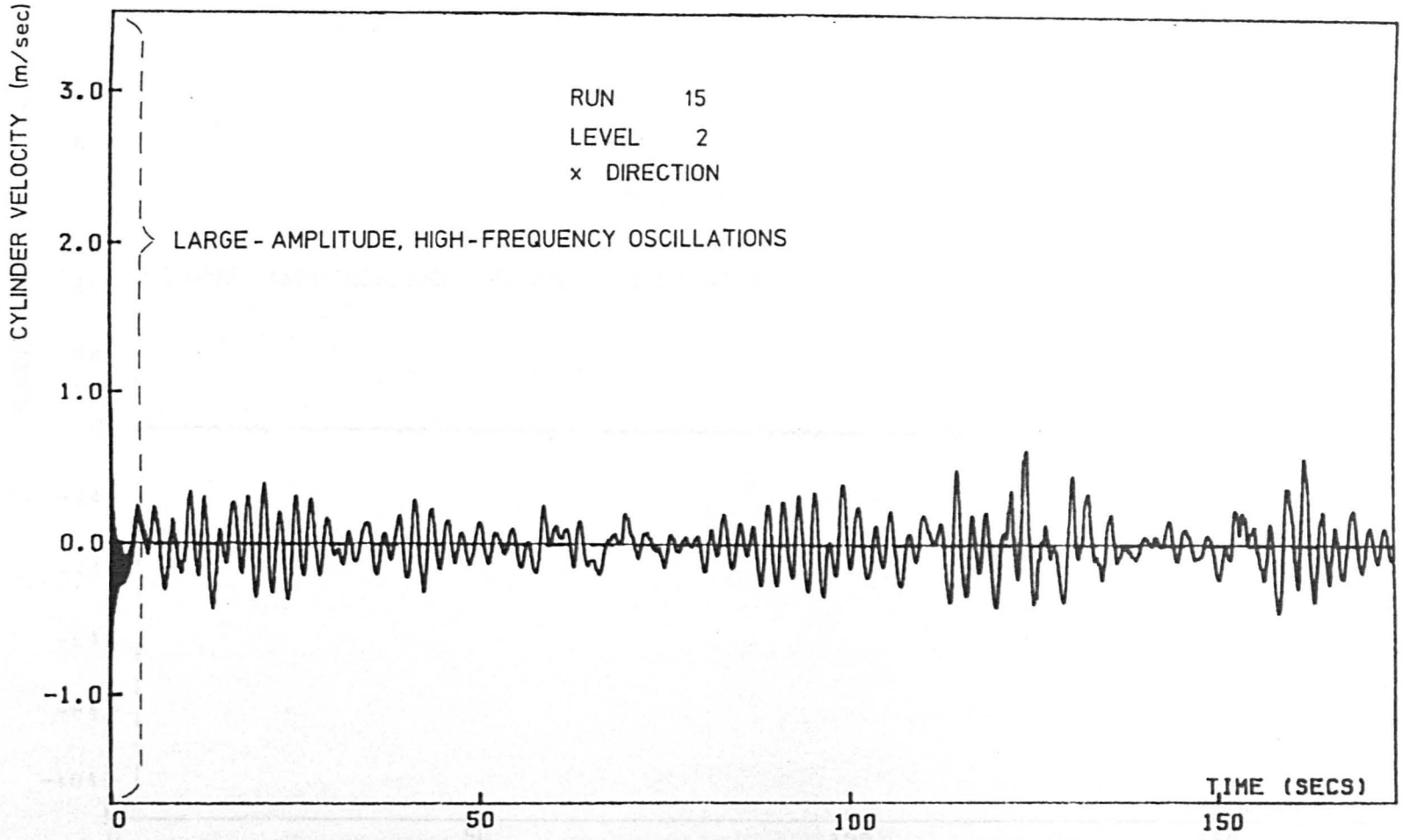

FIGURE 6.5. LARGE-AMPLITUDE, HIGH FREQUENCY OSCILLATIONS AT THE VICINITY OF TIME t = o FOR CYLINDER VELOCITY RESULTING FROM FOURIER METHOD

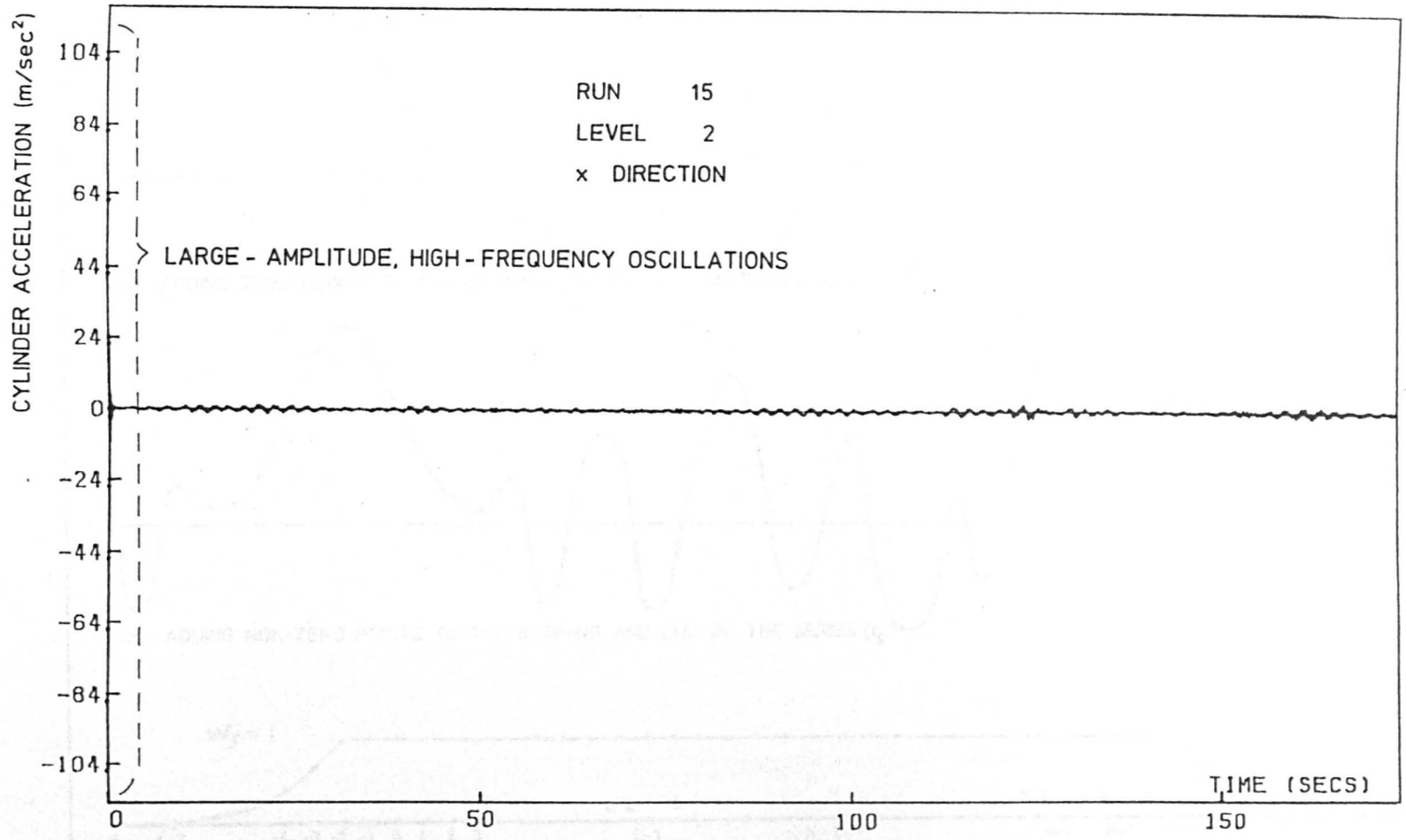

FIGURE 6.6. LARGE-AMPLITUDE, HIGH-FREQUENCY OSCILLATIONS AT THE VICINITY OF TIME t = o FOR CYLINDER ACCELERATION RESULTING FROM FOURIER METHOD

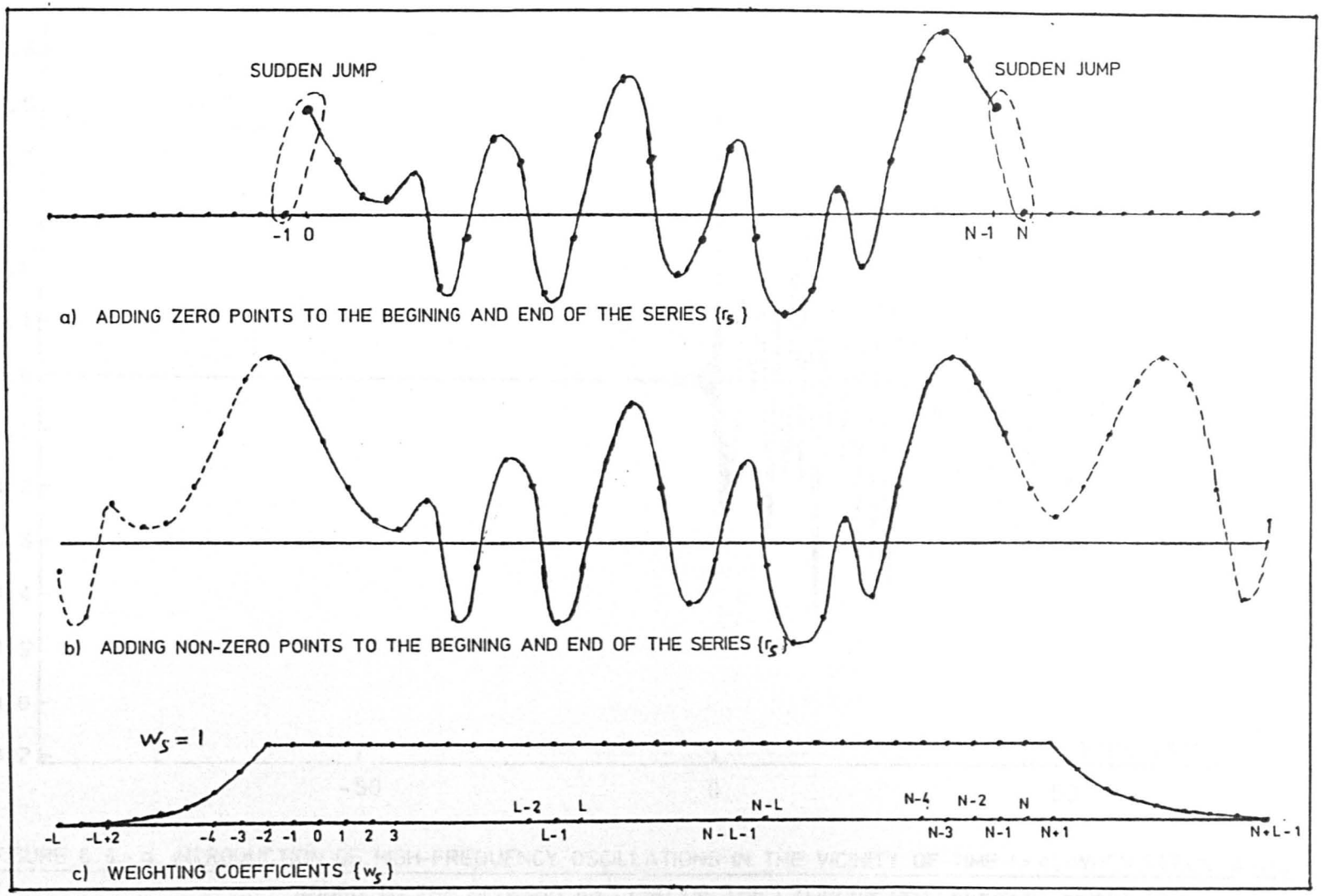

FIGURE 6.7. ADDITION OF POINTS TO THE BEGINING AND END OF THE SERIES {r_s} $s=0,1,\ldots,N-1$

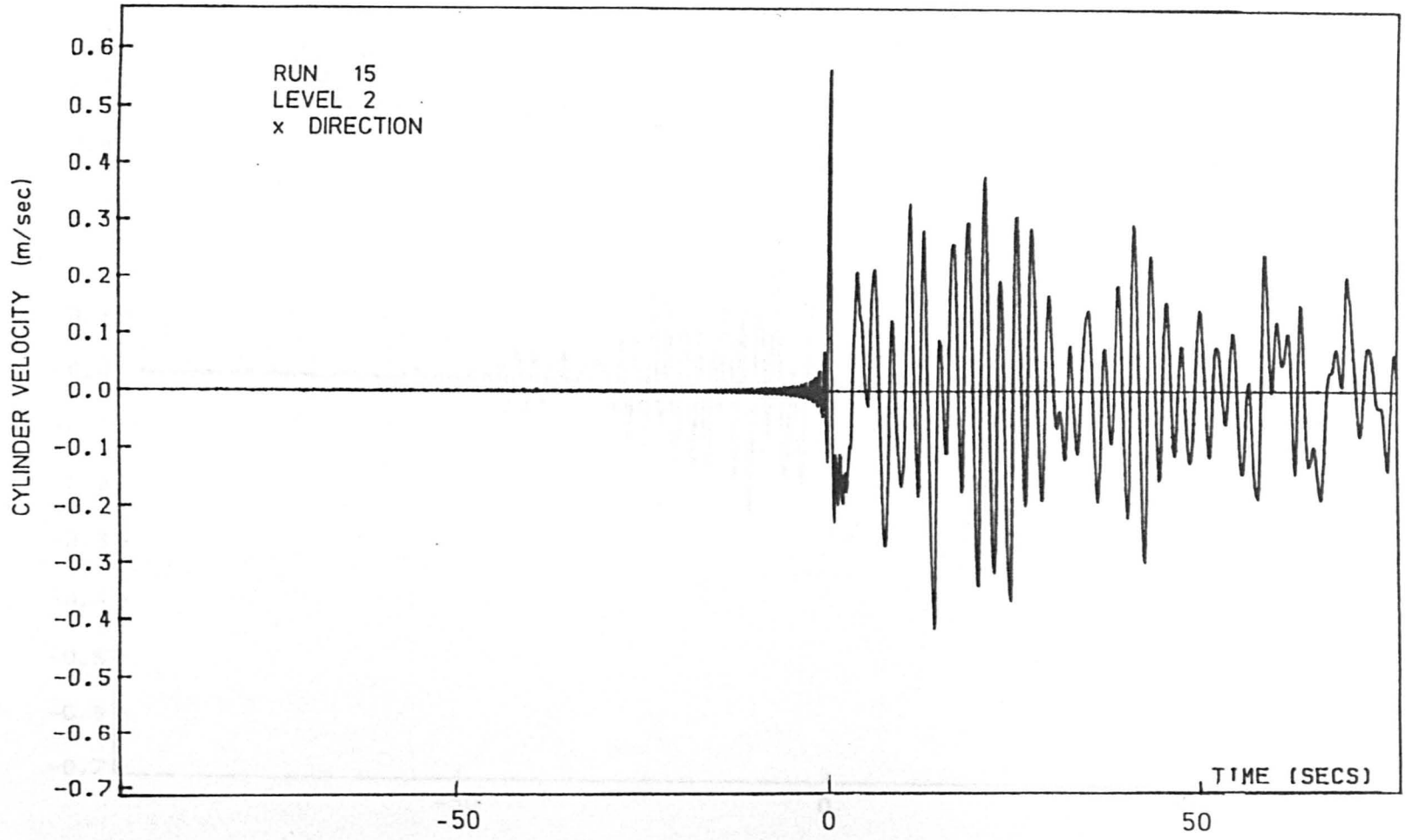

FIGURE 6.8 - a. INTRODUCTION OF HIGH-FREQUENCY OSCILLATIONS IN THE VICINITY OF TIME t = o, WHEN ZEROS WERE ADDED TO THE BEGINING AND END OF THE CYLINDER DISPLACEMENT SERIES $\{r_s\}$

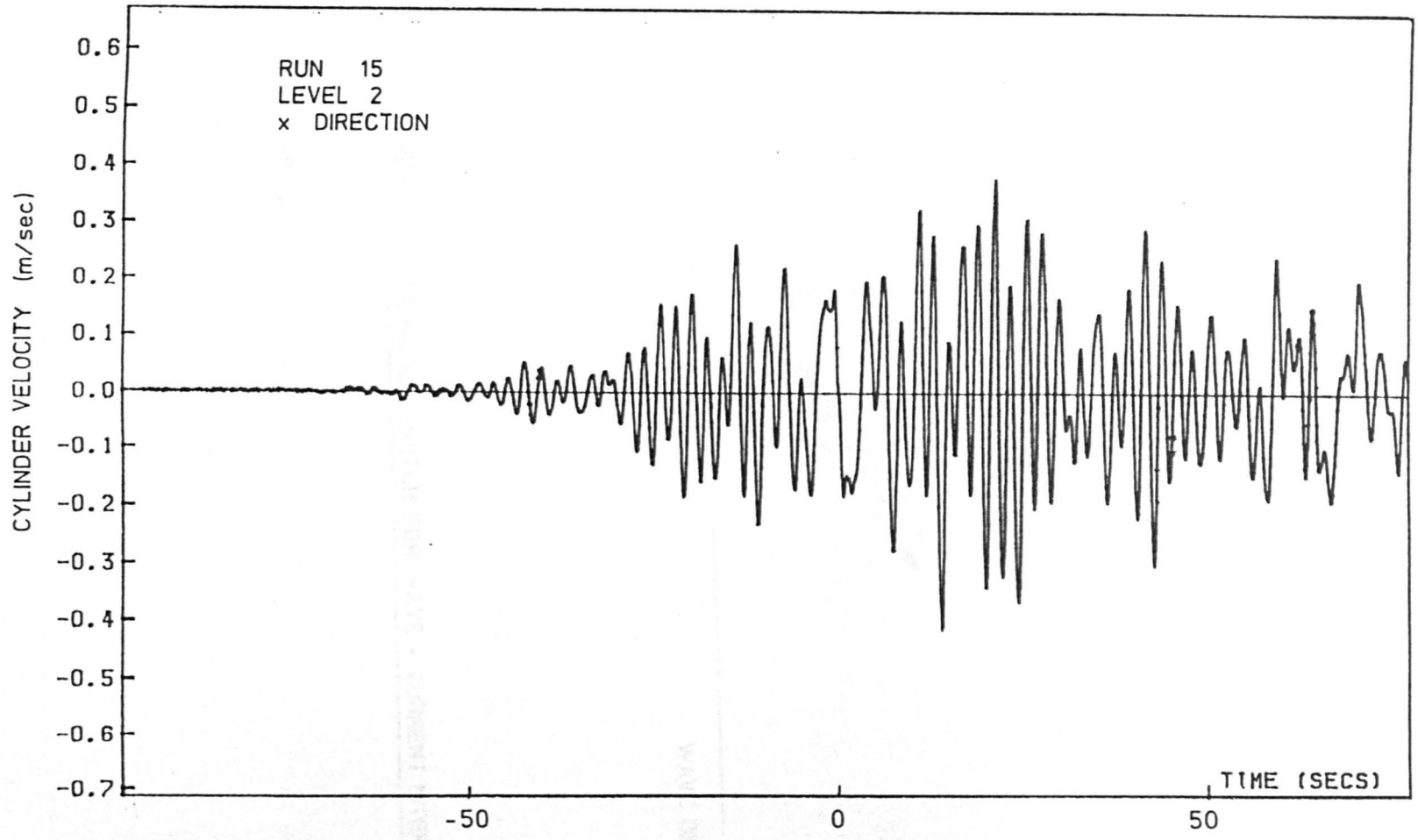

FIGURE 6.8-b ABSENCE OF HIGH-FREQUENCY OSCILLATIONS IN THE VICINITY OF TIME t = o, WHEN NON-ZERO POINTS WERE ADDED TO THE BEGINING AND END OF THE CYLINDER DISPLACEMENT SERIES $\{r_s\}$

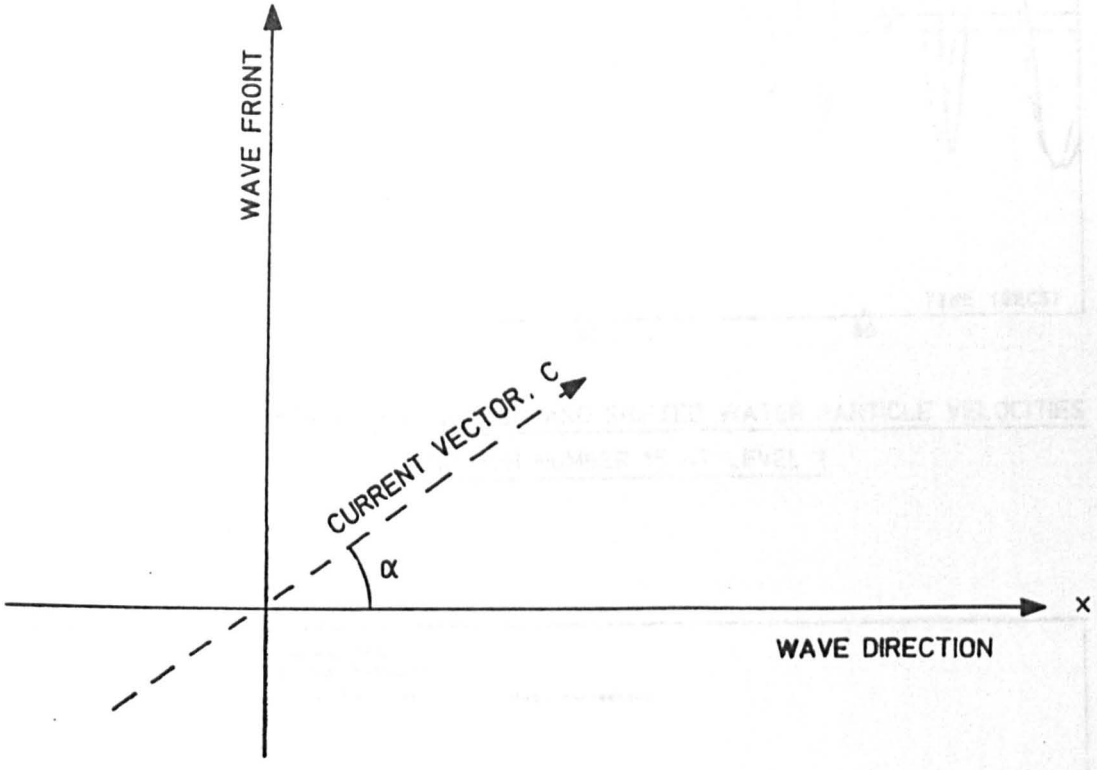

FIGURE 6.9. DEFINITION SKETCH FOR WAVE - CURRENT INTERACTION

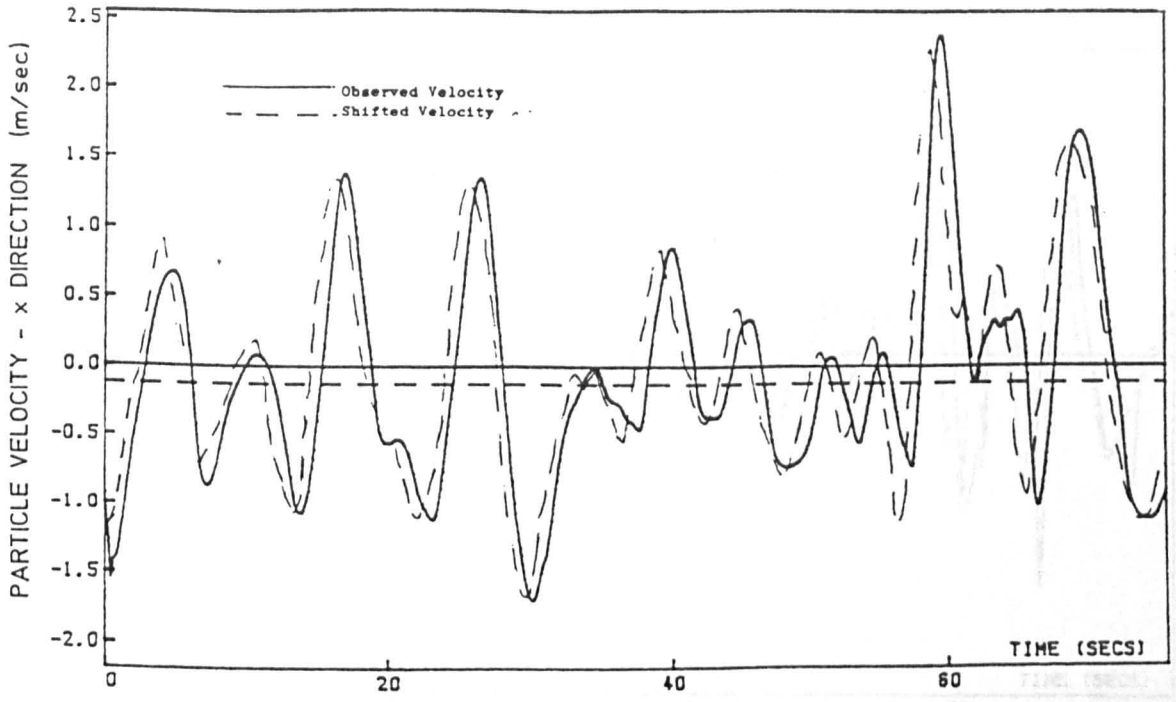

FIGURE 6.10. COMPARISON OF OBSERVED AND SHIFTED WATER PARTICLE VELOCITIES FOR RUN NUMBER 15 AT LEVEL 2

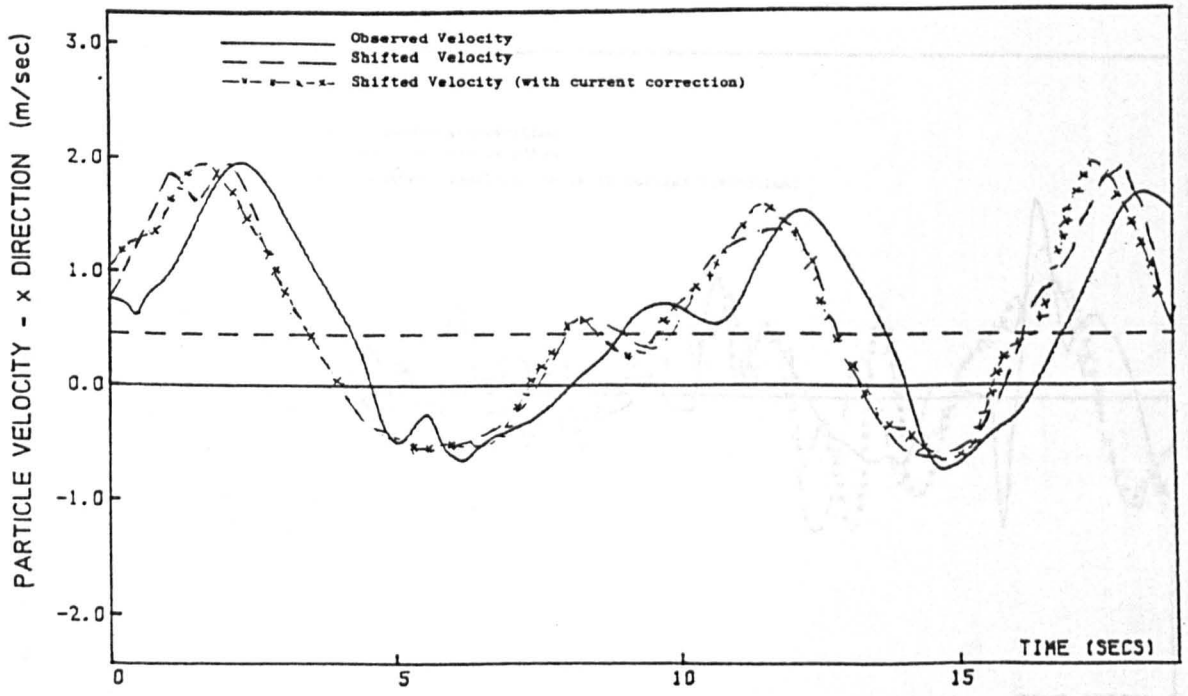

FIGURE 6.11. COMPARISON OF OBSERVED AND SHIFTED WATER PARTICLE VELOCITIES FOR RUN NUMBER 23 AT LEVEL 2

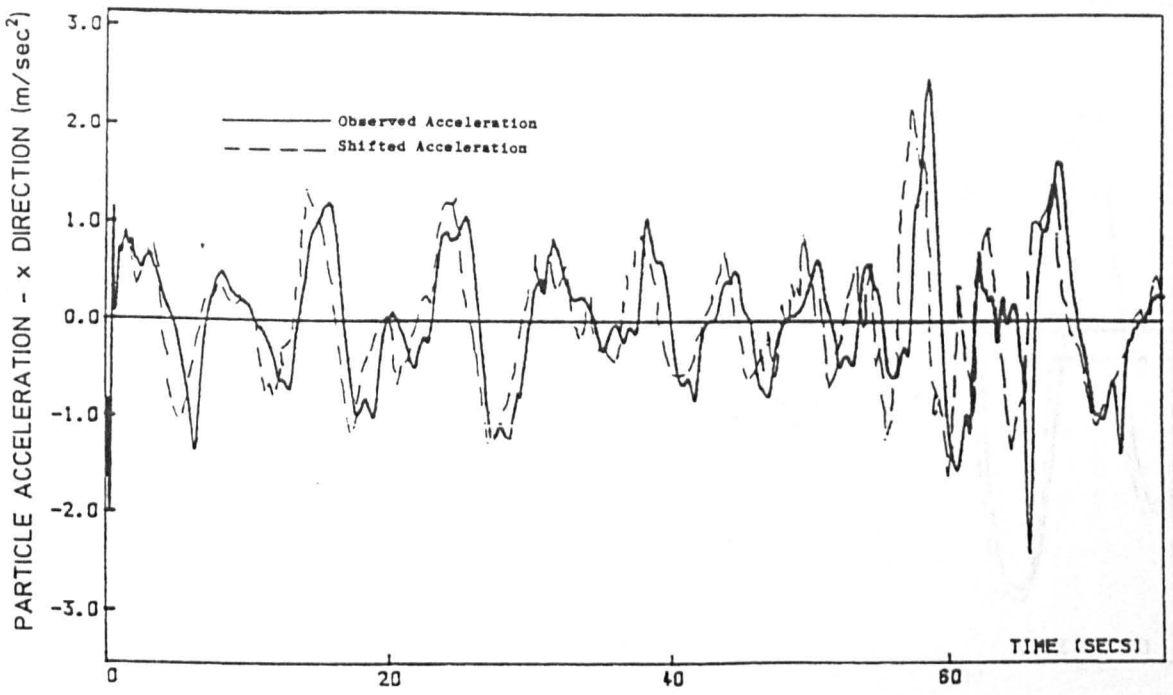

FIGURE 6.12. COMPARISON OF OBSERVED AND SHIFTED WATER PARTICLE ACCELERATIONS FOR RUN NUMBER 15 AT LEVEL 2

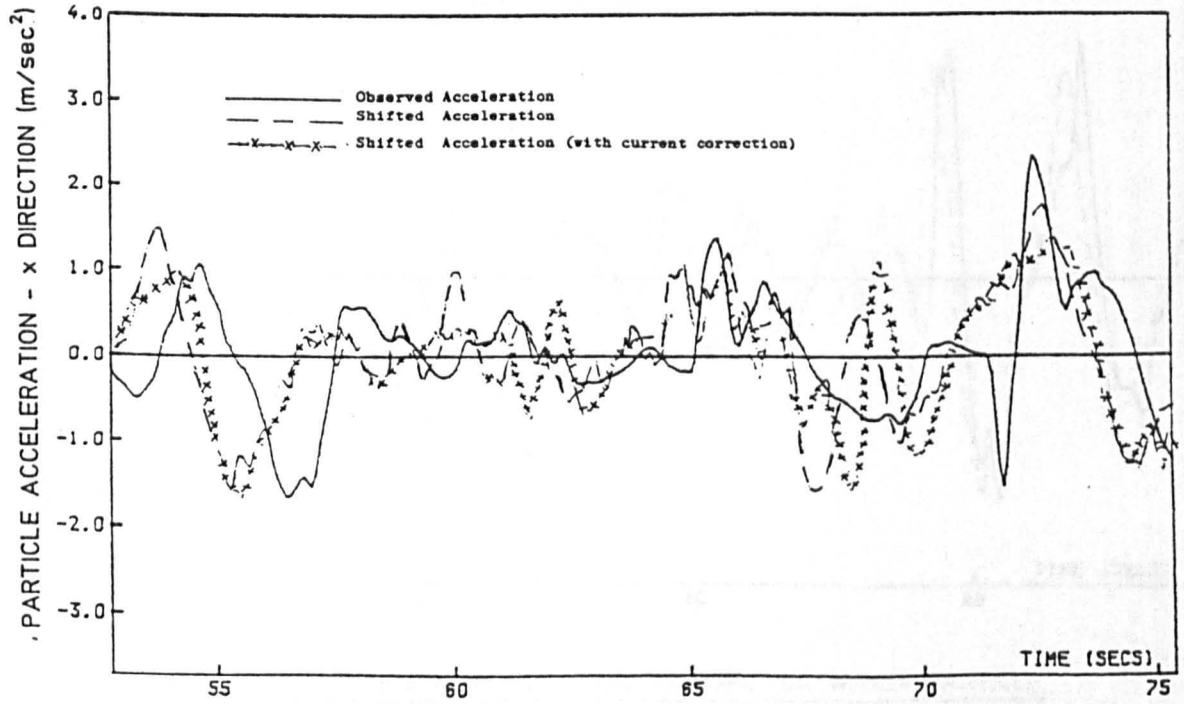

FIGURE 6.13. COMPARISON OF OBSERVED AND SHIFTED WATER PARTICLE ACCELERATIONS FOR RUN NUMBER 23 AT LEVEL 2

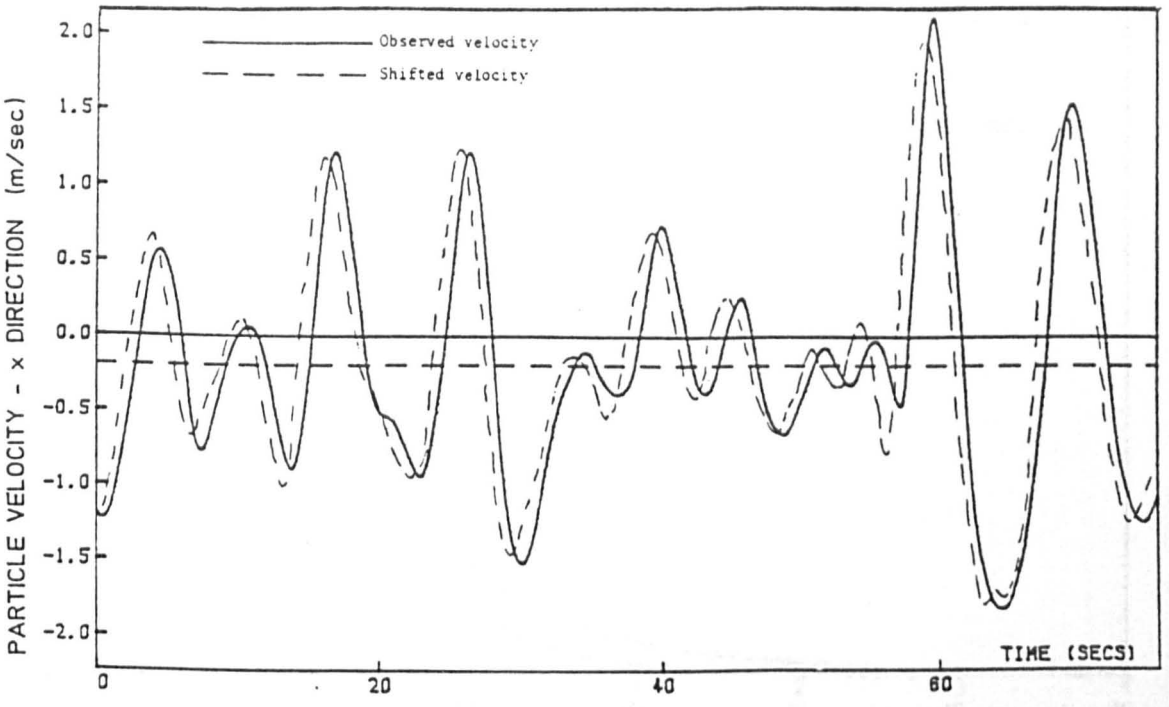

FIGURE 6.14. COMPARISON OF OBSERVED AND SHIFTED WATER PARTICLE VELOCITIES FOR RUN NUMBER 15 AT LEVEL 3

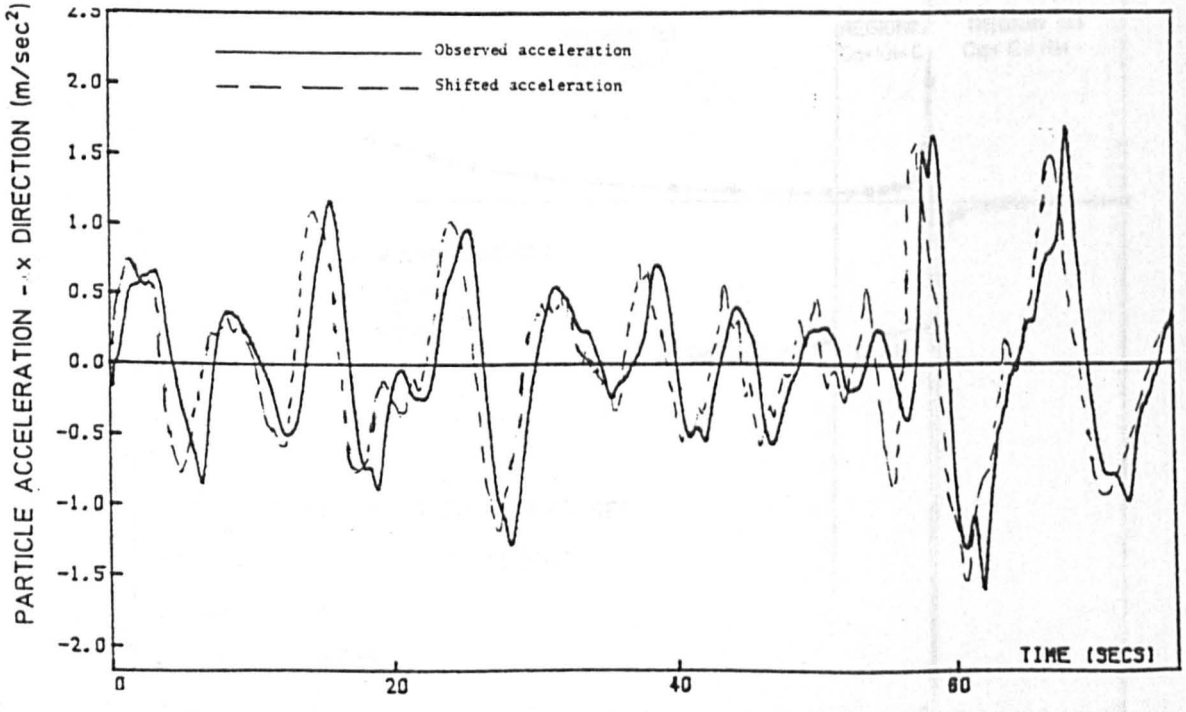

FIGURE 6.15. COMPARISON OF OBSERVED AND SHIFTED WATER PARTICLE ACCELERATIONS FOR RUN NUMBER 15 AT LEVEL 3

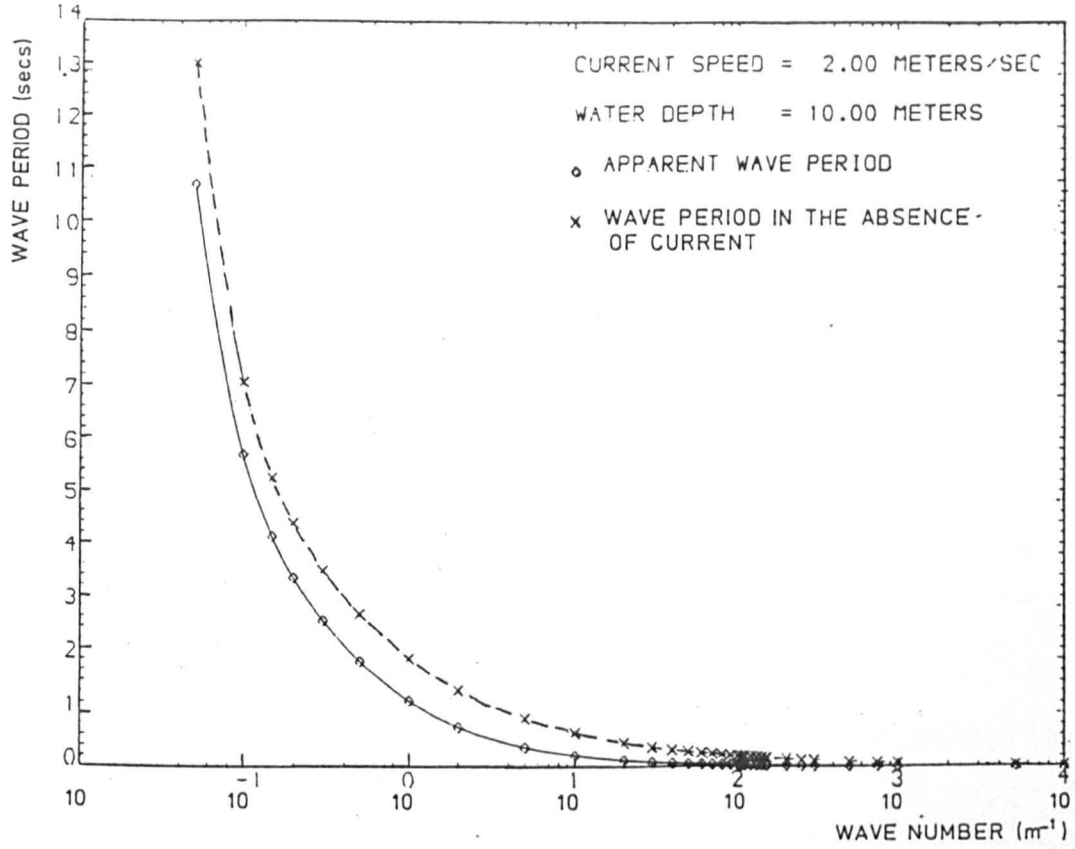

FIGURE 6.16. EFFECT OF POSITIVE CURRENT ON WAVE PERIOD

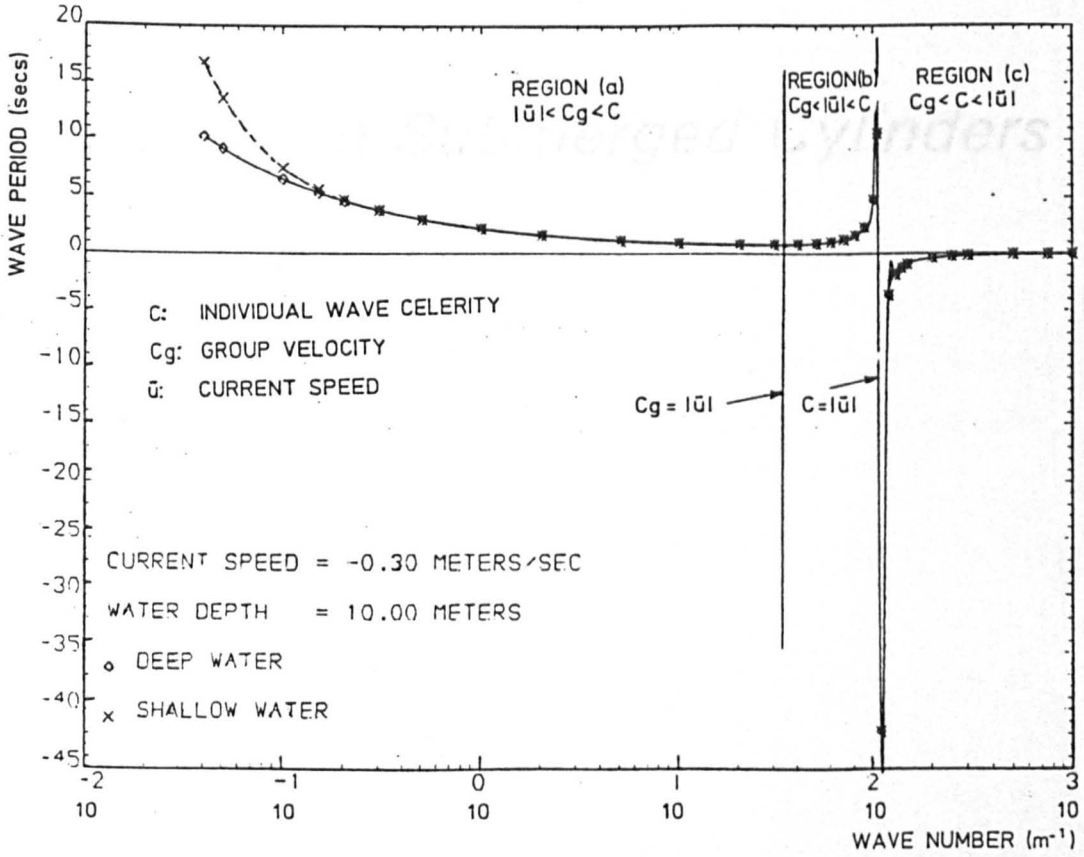

FIGURE 6.17. EFFECT OF NEGATIVE CURRENT ON WAVE PERIOD

Chapter 7

Fluid Loading on Submerged Cylinders

INTRODUCTION

The most-widely accepted approach to the problem of predicting wave loads on submerged members of an offshore structure with characteristic dimensions much smaller than the wave length (D/L < 1/5) is due to Morison et al (1950). The method is based on the assumption that the total force exerted by the fluid is composed of two parts: a drag force due to water particle velocity, similar to drag on a body subjected to a steady flow of a real (viscous) fluid; and an inertial force due to water particle acceleration, analogous to that on a body subjected to a uniformly-accelerated flow of an ideal (inviscid) fluid. That is, the horizontal force per unit length on a vertical cylindrical member of diameter D is

$$F = F_d + F_i = 0.50\ \rho D\ C_d\ u|u| + \frac{\pi D^2}{4}\ \rho\ C_m\ \dot{u} \qquad (7.1)$$

where

F_d and F_i are the drag and inertial components of fluid loading

C_d and C_m are empirical drag and inertia coefficients

ρ is the fluid density

u and $\dot{u}$ are the undisturbed horizontal components of water particle velocity and acceleration at the centre of the cylinder.

For simplicity, the Morison equation is usually written in the following form

$$F = k_d\ u|u| + k_i\ \dot{u} \qquad (7.2)$$

In which, k_d and k_i are defined as

$$k_d = C_d\ \hat{k}_d = 0.50\ \rho D * C_d \qquad (7.3)$$

$$k_i = C_m \hat{k}_i = \frac{\pi D^2}{4} \rho * C_m \tag{7.4}$$

The vertical component of fluid loading is negligible. It must be noted that Morison loading does not account for lift (transverse) force which can be important in some cases.

Note that in the general case of an inclined cylinder, the Morison loading can be written as

$$F = 0.50 \rho C_d A_p u|u| + \rho C_m \bar{V} \dot{u} \tag{7.5}$$

where u and $\dot{u}$ are components of water particle kinematics in a plane normal to the cylinder axis. A_p is the projected area of the cylinder per unit length on a plane perpendicular to u, and $\bar{V}$ is the volume of the cylinder per unit length.

The main purpose of this chapter is twofold:

a) To study the mechanism which gives rise to wave loading on submerged bodies, mostly the result of small-scale experiments in the laboratory. In this regard, Section 7.1 has been devoted to the study of ideal fluid loading on fixed submerged cylinders, where the origin of inertia loading is studied. Section 7.2 is concerned with real (viscous) fluid loading on fixed submerged cylinders where the effect of separation on fluid loading is emphasized. Finally, the effect of flexibility of cylinders on fluid loading is studied in Section 7.3.

b) To report large-scale experiments, conducted either in laboratory or in real ocean environment, so that the results of the present

Christchurch Bay project can be compared with the results of other large-scale investigations. Section 7.4 has been devoted to this topic.

The reference for the contents of this chapter, unless otherwise notified, is Sarpkaya and Isaacson (1981).

7.1 IDEAL FLUID LOADING ON FIXED SUBMERGED CYLINDERS

For analysis purposes, it is frequently assumed that a fluid is non-viscous (inviscid). With zero viscosity the shear stress is always zero, even if the fluid is in motion. If it is also assumed that the fluid is incompressible, it is then called an ideal fluid. If a body of ideal fluid, initially at rest, is brought into motion, it flows without vorticity because it does not experience any shear stress. This is said to be irrotational flow. For a uniform (steady or non-steady) irrotational flow past a circular cylinder (Figures 7.1 and 7.2), the velocity at the surface of the cylinder, necessarily tangent to it, can be obtained from potential theory. That is

$$V_\theta = 2u \sin\theta \tag{7.6}$$

where u is the ambient flow velocity.

The above equation shows that at $\theta = 180°$, the fluid particles come to rest. In other words, there is a stagnation point at $\theta = 180°$. The velocity then gradually increases until at $\theta = 90°$ it reaches its maximum of two times the ambient flow velocity. From $\theta = 90°$ to 0° degrees, the velocity gradually decreases until it comes to rest at $\theta = 0°$ (another stagnation point). Therefore, from $\theta = 180°$ to 90°, the flow is accelerating (favourable pressure gradient) while from $\theta = 90°$

to 180°, the flow is decelerating (adverse pressure gradient). For a steady ($du/dt = 0$) uniform flow, the pressure on the cylinder is equal to

$$P = 0.5\,\rho u^2\,(1 - 4\sin^2\theta) \tag{7.7}$$

Equation (7.7) shows that there is pressure variation round the cylinder, with pressure being maximum at stagnation points and minimum at $\theta = 90°$. However, due to symmetry of pressure distribution with respect to x and y axes, the components of force in both directions are zero. In other words, no drag force or lift force act on the cylinder. The important point to be noticed is that for the case of an irrotational, ideal fluid past a cylinder, there is pressure recovery behind the cylinder; that is, the pressure decreases from 180° to 90° but increases from 90° to 0° and that the pressure at 180° and 0° are equal.

For an unsteady ($du/dt \neq 0$) uniform flow, the (dynamic) pressure on the cylinder surface is

$$P = 0.5\,\rho u^2\,(1 - 4\sin^2\theta) - \rho D\cos\theta\,\frac{du}{dt} \tag{7.8}$$

where du/dt is the total undisturbed acceleration of the ambient flow. The pressure distribution is composed of two terms. The first term is the same as the pressure distribution for a uniform, steady flow and as discussed before, due to symmetry, it does not lead to any drag or lift. However, the second term which accounts for the ambient flow acceleration is only symmetric with respect to x axis. Therefore, the component of force in the y direction (lift force) will be zero, but the component of force in the x direction is

$$F = 2\pi\rho \frac{D^2}{4} \frac{du}{dt} \tag{7.9}$$

The above force, which exist only when the acceleration of the ambient flow is not zero, is referred to as the inertia force, and is equal to two times the mass of the fluid displaced by the cylinder times the ambient flow acceleration. This force acts in the direction of the acceleration vector, regardless of the instantaneous flow direction. The inertia force can be considered as the sum of two components:

1) The Froude-Krylov Force: The basic assumption in the calculation of this force is that the fluid pressure is completely undisturbed by the presence of the cylinder. In other words, it is the force which in the absence of the cylinder would accelerate at du/dt the volume of fluid it displaces, namely $\rho\pi(D^2/4)$ (du/dt).

2) The Added-Mass Force: This force results from the disturbance in the flow field caused by the presence of the cylinder. The force is represented by the Froude-Krylov force on a certain added mass of the fluid. The added mass coefficient, C_a, is defined as the ratio between the added mass and the fluid mass displaced by the cylinder. The added mass coefficient depends on the shape of the body. Its value for a sphere and a long cylinder is 0.50 and 1.0, respectively. The inertia coefficient, C_m, is defined as

$$C_m = 1 + C_a \tag{7.10}$$

Thus, the inertia force, F_i, is

$$F_i = C_m * (\text{Displaced Fluid Mass}) * \frac{du}{dt} = 2\pi\rho \frac{D^2}{4} \frac{du}{dt} \quad (7.11)$$

Figure 7.3 shows the values of C_m for circular cylinders of different length to diameter ratios (Wilson, 1984).

If a cylinder with a mass per unit length of m_o is moving at an acceleration of du/dt in a fluid otherwise at rest, the total force acting on the cylinder is

$$\text{Total force} = (\text{body mass} + \text{added mass}) * \frac{du}{dt} \quad (7.12)$$

As regard to the physical meaning of the added mass it has been shown that the motion of a body in an inviscid fluid is always accompanied by a fluid-mass transport and that this mass is the added mass which unveils itself only if the body is accelerated.

7.2 REAL FLUID LOADING ON FIXED SUBMERGED CYLINDERS

7.2.1 STEADY UNIFORM FLOW PAST A CYLINDER

Boundary Layer

Since the fluid cannot slip over the surface of solid boundaries, there is a steep velocity gradient from zero velocity (on the boundary surface) to the external flow velocity in a thin layer called the boundary layer (Figure 7.4). This velocity gradient sets up near the boundary shear forces that reduce the flow relative to the boundary. For fluids having relatively small viscosity (such as water), the effect of internal friction (shear forces) in the fluid is appreciable only in the boundary layer. The flow outside the boundary layer can be considered as an ideal or potential flow.

The boundary layer is very thin at the upstream end of a streamlined body at rest in an otherwise uniform flow. As this layer moves along the body, the continual action of shear stress tends to slow down additional fluid particles, causing the thickness of the boundary layer to increase with distance from the upstream point. The flow in the layer is also subjected to a pressure gradient, determined from the potential flow, that increases the fluid particle velocity in the layer if the pressure decreases downstream (favourable pressure gradient) and decreases the particle velocities if the pressure increases downstream (adverse pressure gradient).

For smooth upstream boundaries, the boundary layer starts out as a laminar boundary layer in which the fluid particles move in smooth layers. As the laminar boundary layer increases in thickness, it becomes unstable and finally transforms into a turbulent boundary layer in which the fluid particles move in haphazard paths, although their velocity has been reduced by the action of shear stresses at the boundary. When the boundary layer has become turbulent, there is still a very thin layer next to the boundary that has laminar motion. It is called the laminar sub-layer.

If a flat plate is placed at rest in an otherwise uniform flow, the thickness of the boundary layer, as long as it is laminar, is (Streeter et al, 1979)

$$\delta = \frac{4.65x}{\sqrt{R_x}} \tag{7.13}$$

Where $R_x = ux/\nu$ is a Reynolds number based on the distance x from the leading edge of the plate; u is the flow velocity and ν is the fluid

kinematic viscosity. This equation shows that δ increases as the square root of the distance from upstream end of the plate for a laminar boundary layer. For a turbulent boundary layer, the thickness is

$$\delta = 0.37x/R_x^{1/5} \tag{7.14}$$

That is, the thickness increases as $x^{4/5}$. Therefore, the thickness increases more rapidly in the case of a turbulent boundary layer.

When the Reynolds number for the plate reaches a value between 500,000 and 1,000,000, the boundary layer becomes turbulent. Figure 7.5 indicates the growth and transition from laminar to turbulent boundary layer. The critical Reynolds number depends upon the initial turbulence of the fluid stream, the upstream edge of the plate, and the plate roughness.

Separation

Along a flat plate, the thickness of the boundary layer increases in the downstream direction, regardless of the length of the plate, when the pressure gradient remains zero. A favourable pressure gradient tends to reduce the thickness of the boundary layer, while on the other hand, an adverse pressure gradient causes the boundary layer to grow rapidly. The adverse pressure gradient and the boundary shear decrease the momentum in the boundary layer, and if both act over a sufficient distance, they cause the boundary layer to come to rest (Figure 7.6). The boundary streamline must leave the boundary at the point where it has come to rest, leading to a phenomenon called separation. Downstream from this point the adverse pressure gradient causes backflow near the wall. The region downstream from the streamline that separates from the boundary is known as the wake. As a result of separation, the pressure

recovery in the wake is incomplete, leading to a drag force. The drag force can be expressed in terms of a drag coefficient C_d times the stagnation pressure $\rho u^2/2$ times the projected area of the body on a plane perpendicular to the flow. That is

$$\text{Drag} = C_d \frac{\rho u^2}{2} * \text{projected area} \tag{7.15}$$

Streamlined bodies are so designed that the separation point occurs as far downstream along the body as possible (Figure 7.7). If separation can be avoided, the boundary layer remains thin and the pressure recovery will be almost complete along the body. Then, the drag is only due to shear stress in the boundary layer, called skin friction. When there is separation, the pressure is not recovered in the wake, and a pressure drag results. Reduction of wake size reduces the pressure drag on a body. In general, the drag force is due to both skin friction and pressure drag.

Uniform Flow Past a Circular Cylinder

As was seen for the case of an ideal flow past a circular cylinder, over the front face of the cylinder the external velocity (that outside the boundary layer) increases towards the widest section of the cylinder and thereafter decreases. As long as the flow is accelerating, the favourable pressure gradient maintains the forward flow in the boundary layers. However, downstream of the widest section of the cylinder, the adverse pressure gradient causes the boundary layer to leave the surface of the cylinder altogether, separated from it by a region of recirculating flow (wake). The separated boundary layer retains initially its characteristic high velocity gradient and consequent shear stress but gradually diffuses into the surrounding

fluid. It provides a route for the vorticity generated in the attached portion of the boundary layers to be fed into the wake. From a cylinder there are of course two separated boundary layers carrying vorticity of opposing sense of rotation.

For a Reynolds number of the order of 1000, the flow is predominantly laminar, though the wake may degenerate into turbulence some distance from the cylinder. As R_e is increased the transition to turbulence gradually approaches the cylinder, finally moving up the separated boundary layers even to the separation points and beyond. When the transition to turbulence coincides with the separation point at a Reynolds number of about 5×10^5, the flow undergoes first a laminar separation, followed by a reattachment to the cylinder, and then a turbulent separation. As previously discussed, a turbulent boundary layer over a solid surface is able to remain attached beneath an unfavourable pressure gradient longer than a laminar one because of the high-momentum transfer in the turbulent boundary layer. Consequently, as soon as the region of turbulence envelopes the separation points, they move rearwards to form a narrower wake leading to smaller drag (drag crisis). With further increases in R_e, the attached boundary layers become turbulent progressively earlier, until around $R_e = 10^7$, they are immediately turbulent from the stagnation point. Over this trans-critical range, the separation points move somewhat upstream to form a slightly larger wake and hence larger drag.

The drag force is conveniently expressed in terms of the drag coefficient C_d defined as

$$C_d = \frac{\text{drag force per unit length}}{1/2\ \rho u^2 D} \qquad (7.16)$$

Where D is the cylinder diameter, Figure 7.8 shows the variation of C_d with Reynolds number. At very low Reynolds numbers the drag is dominated by the effects of skin friction and hence C_d is inversely proportional to R_e. For $R_e > 1000$, however, the form (pressure) drag is much larger than the skin friction so that the skin friction contribution is insignificant.

Uniform Flow Past a Sphere

Flow around a sphere is an excellent example of the effect of separation on drag. For Reynolds numbers less than one, ($R_e = VD/\nu$ with D and V, the diameter and the velocity of sphere in fluid, respectively) the flow is laminar everywhere. Stokes's Law gives the drag force for this case. For large Reynolds numbers, the flow may be considered potential flow except in the boundary layer and the wake. The boundary layer forms at the forward stagnation point and is generally laminar.

Figure 7.9 shows the photographs of two spheres dropped into water at 25 ft/sec (Streeter et al, 1979). In (a), separation occurs in the laminar boundary layer that forms along the smooth surface and causes a very large wake with a resulting large pressure drag. In (b), the nose of the sphere, roughened by sand glued to it, induced an early transition to turbulent boundary layer before separation occurred. The high-momentum transfer in the turbulent boundary layer delayed the separation so that the wake size is substantially reduced, resulting in a total drag on the sphere, less than half that occurring in (a).

A plot of drag coefficient against Reynolds number for smooth spheres is shown in Figure 7.10. The sudden drop in the drag coefficient at a Reynolds number of about 5×10^5 shows that the shift to turbulent boundary layer before separation occurs by itself at a sufficiently large Reynolds number. The exact Reynolds number for the sudden shift depends upon the smoothness of the sphere and the turbulence in the fluid stream. Note that the sudden drop in the drag coefficient does not occur for the disk (flat plate), where the separation points are always fixed at the edge of the plate.

Vortex Shedding

The separated boundary layers, or 'free shear layers' do not remain stationary downstream of the cylinder. Each one has a strong tendency to curl up in the direction of the vorticity it is transporting and form a concentration of rotation (a vortex). In doing so it occupies much of the wake area and draws the other shear layer across the rear face of the cylinder. Ultimately its supply of vorticity is cut off by interference from fluid of opposite sense of rotation, and the fully-formed vortex is swept downstream leaving the other shear layer room to begin growing the next one. Consequently, much of the vorticity generated on the cylinder passes downstream not in a continuous stream but in the form of concentrated packets (vortices) of different sense of rotation shed alternately from both sides of the cylinder.

The vortex shedding frequency, f_v, (equal to the number of vortex pairs per unit time) can be determined from the following empirical relationship.

$$f_v = \frac{Su}{D} \tag{7.17}$$

Where S is a dimensionless constant called Strouhal number. The Strouhal number is about 0.20 for a large range of sub-critical Reynolds number. The vortex shedding at critical Reynolds number is rather irregular with an average Strouhal number of about 0.40. At higher Reynolds numbers the shedding becomes more regular, and the Strouhal number is about 0.30.

Because of the growth and shedding of alternate vortices, the rear wake of the cylinder, bounded by the free shear layers, oscillates from side to side like the tail of a swimming fish (Figure 7.11). As a result, unsteady forces in-line and perpendicular to the flow (and cylinder axis) is felt by the cylinder. In the in-line direction there will be one force cycle for each vortex shed, i.e. the in-line force has a frequency of $2f_v$. In the transverse direction, each vortex gives rise to only half a cycle in the transverse (lift) force, i.e. the transverse force has a frequency of f_v. The magnitudes of these forces are normally non-dimensionalised in the same way as the mean drag (Equation 7.16) to define coefficients of fluctuating lift C_{fl} and fluctuating drag C_{fd}. These coefficients are very sensitive to external disturbances. Typical values for cylinders in two-dimensional wind or water tunnel flow are $C_{fl} \approx 0.2 - 1.0$ and $C_{fd} \approx 0.1$.

The oscillatory nature of unsteady lift and drag gives rise to the possibility of resonance if a natural frequency of the cylinder is close to f_v or $2f_v$. Vortex-induced vibrations will be discussed later in this chapter.

7.2.2 TIME-VARYING FLOW PAST A CYLINDER

7.2.2.1 Impulsively-Started Flow and Uniformly-Accelerated Flow

The separation of boundary layers and formation of a wake behind a bluff body gives rise to a form drag and also significant changes in the inertia forces. It must be recognised that the drag and inertia forces are interdependent and time-dependent for real viscous fluids past bluff bodies. In other words, the velocity dependent drag is not the same as that for the steady flow of a viscous fluid and the acceleration dependent inertial resistance is not the same as that of the unsteady flow of an ideal fluid. The drag and inertia coefficients obtained for unseparated unsteady flows are not applicable to occurrences in which the duration of flow in one direction is long enough and the body form blunt enough for separation to occur.

If a circular cylinder starts impulsively from rest to a constant velocity, v, the distance covered until separation begins is $S \approx 0.351C$, where C is the radius of the cylinder. The separation begins at rear stagnation point. For a uniformly-accelerating circular cylinder the separation distance is 0.52C. The measured drag and lift coefficients for an impulsively-started flow are shown in Figures 7.12 and 7.13, respectively. The growth and motion of vortices at the initial stages of the flow for different values of vt/C (obtained from numerical simulation through the use of discrete vortex modelling) is shown in Figure 7.14 (Sarpkaya and Shoaff, 1979).

Figure 7.12 shows that the drag coefficient in the initial stages (vt/C = 4) of an impulsively-started flow can exceed its steady value by as much as 30 percent. In the early periods of the flow, vorticity is slow to diffuse and therefore accumulates rapidly in the close vicinity of

the cylinder. The growing vortex soon reaches unstable proportions and separates from its shear layer; however, the growth of the vortices are so rapid that the vortices become much larger than their quasi-steady-size before separation. This leads to the observed large drag coefficient. Shortly after the onset of asymmetry, the drag coefficient decreases sharply and the lift coefficient begins to increase. Therefore, in impulsively-started flow, a drag overshoot occurs at about $S/D \approx 2$ ($vt/C = 4$) because of the rapid accumulation of vorticity in the two symmetrically growing vortices (see Figure 7.14), where S is the distance travelled by the cylinder or the displacement of the ambient flow, i.e. $S = vt$. For a uniformly-accelerating flow, the displacement of the ambient flow is $0.5vt$, where v is the velocity at time t. The variation of the drag and inertia coefficients with relative displacement in uniformly-accelerated flow is shown in Figure 7.15. The drag overshoot occurs at $S/D = 2.5$ and is milder in comparison with the impulsively-started flow. This is because the rate of accumulation of vorticity is not as large. For all other flows whose velocity is an arbitrary function of time, the drag overshoot may range from 10 percent (uniformly-accelerating flow) to about 30 percent (impulsively-started flow). The inter-relationship between the drag and inertia coefficients in uniformly-accelerated flow is shown in Figure 7.16.

7.2.2.2 Harmonically Oscillating (Bodies) Flows

Planar oscillatory flow provides a two dimensional idealisation of the conditions present under waves. It ignores several important effects, including the three dimensionality of wave flows due to orbital motion of water particles and the exponential decay of water particle velocities with depth, etc. Nevertheless, planar oscillatory flow does

reproduce the periodic conditions which are the most important characteristic of wave induced flow. The assumption in this section is that the oscillations are of large amplitude so that the separation of flow plays an important role.

There are several fundamental differences between the harmonically oscillating flow and the unidirectional flow. When a cylinder is subjected to a harmonic flow normal to its axis, in addition to accelerating and decelerating to zero, the flow changes direction as well during each cycle. Consequently, the wake reverses from the downstream to upstream side whenever the flow changes sign and the separation points undergo large excursions. The boundary layer over the cylinder may change from fully laminar to partially or fully turbulent states and the Reynolds number may range from sub-critical to post-supercritical over a given cycle.

In steady flow, the near wake is dominated to a large degree by the newest generation of vortices. In periodic flow, however, as a result of sweeping back of vortices, the body is surrounded by a cluster of young and old generations of vortices. The formation, growth and motion of the new vortices strongly affect and are affected by the older vortices which have survived diffusion and dissipation. The transverse force is partly due to the shedding of the newest vortices, as in steady flow, and partly due to the older vortices returning to the body which gave rise to their existence in the first place. These phenomena lead to incalculable changes in the pressure distribution on the cylinder indicating that the force coefficients can be determined only experimentally.

Keulegan-Carpenter Number

An important dimensionless parameter in oscillatory flow is the Keulegan-Carpenter number, K, given by

$$K = \frac{u_m T}{D} \qquad (7.18)$$

in which u_m is the maximum ambient flow velocity and T is the period of the motion. Keulegan-Carpenter number is related to the relative amplitude of water particle motion, through the following relationship.

$$K = 2\pi \left(\frac{A}{D}\right) \qquad (7.19)$$

Where A is the amplitude of water particle motion. The Keulegan-Carpenter number gives an indication of the relative significance of drag and inertia loading. For example, in planar oscillatory flow, in which the ambient motion is simply backwards and forwards along a straight line with $u = u_m \cos 2\pi t/T$, the ratio of magnitudes of drag and inertia forces from Morison's equation is

$$\frac{\text{drag}}{\text{inertia}} = \frac{C_d}{\pi^2 C_m} K \qquad (7.20)$$

Reynolds number

For an oscillating flow, the Reynolds number is defined as

$$R_e = \frac{u_m D}{\nu} \qquad (7.21)$$

where u_m is the maximum ambient flow velocity and ν is the kinematic viscosity. Since u_m appears in both K and R_e, Sarpkaya introduced a new parameter which is defined as the ratio between the Reynolds number and

the Keulegan-Carpenter number and is referred to as the frequency parameter. That is

$$\beta = R_e/K = \frac{D^2}{\nu T} \tag{7.22}$$

Experimental Values of C_d and C_m

Physical considerations and simple dimensional analysis show that C_d and C_m are not only dependent on the Keulegan-Carpenter number, the Reynolds number, and the relative roughness, but also they are time dependent, i.e. even when all the above parameters are fixed, the Morison coefficients are changing with time in a given cycle. However, the use of instantaneous values of C_d and C_m is not practical and hence it is the time-averaged (constant) values of C_d and C_m which are invariably used for design purposes.

The results of experiments conducted by Sarpkaya (1976a) in a u-shaped vertical water tunnel are shown in Figures 7.17 to 7.21. The variation of C_d and C_m with Keulegan-Carpenter number, for several values of the frequency parameters are shown in Figures 7.17 and 7.18, respectively. It is observed that at small Keulegan-Carpenter numbers (say less than 5), C_m is close to its ideal flow value of 2. For larger values of K ($K > 12$), C_d decreases with K, while C_m increases. Furthermore, it is observed that C_m increases with frequency parameter while C_d decreases. The same data are shown as functions of R_e for different values of K in Figures 7.19 and 7.20. These figures show that within the range of Reynolds numbers encountered, C_d decreases with increasing R_e to a value of about 0.50 (depending on K) and then gradually rises to a constant value of about 0.65 (post-supercritical value). The inertia coefficient

increases with increasing R_e, reaches a maximum and then gradually approaches a value of about 1.85.

Figure 7.19 shows that the drag coefficient for a cylinder in harmonically oscillating flow is not always larger than that for the steady flow at the same Reynolds number. Stokes has shown that for an unseparated flow about an oscillating sphere, the drag coefficient is always larger than its corresponding steady-state value. However, according to Figure 7.19, for K = 100, for example, C_d for the oscillating flow is smaller than its steady-state value for R_e between 60,000 and 400,000. The reason for this is believed to be the earlier transition to turbulence in the boundary layers for an oscillating flow in comparison with the steady-state flow. Furthermore, Figures 7.17 to 7.20 show that C_d and C_m follow different trends with respect to R_e and K, i.e. in a general sense, whenever C_d increases, C_m decreases and vice versa. Figure 7.21 shows a plot of C_m versus C_d for different values of K.

Transverse (lift) Force and the Strouhal Number

The transverse force acting on smooth and sand-roughened cylinders were measured by Sarpkaya (1976a) for a wide range of Keulegan-Carpenter numbers and Reynolds numbers, and relative roughness. Figures 7.22 and 7.23 show the lift coefficient defined by C_L = (lift force)/ $(0.5\rho LDu^2_m)$ as a function of K (for various values of β) and as a function of R_e (for various values of K). The results show that C_L(max) reaches its maximum value in the vicinity of K = 12 and decreases sharply with increasing K.

As previously mentioned, the lift force is due to alternating pressure gradient across the wake, which in turn is due to the asymmetry of the strength and position of the vortices. The minimum value of K at which lift or the asymmetry in the vortices develop is between 4 - 5. The maximum asymmetry is in the neighbourhood of K = 12.

The alternating nature of the transverse force is as important as its magnitude. The relative frequency of the transverse force, f_r, defined as the frequency of the transverse force divided by the frequency of the oscillatory flow, is shown in Figure 7.24 for a smooth cylinder. It is apparent that f_r is not constant but increases with K and R_e. It should be noted that the frequency of vortex shedding is not constant in a given cycle and that it also changes from cycle to cycle. Figure 7.24 is based on the maximum frequency in a given cycle defined as the reciprocal of the shortest interval between two maxima. A point on each line represents the maximum value of K for a given R_e and f_r. In other words, a line such as $f_r = 4$ means that the alternating force does not contain frequencies larger than $f_r = 4$ for K and R_e values in the region to the left of the line. Odd values of f_r such as $f_r = 3$, 5, etc., are not shown to keep the figure relatively simple.

It should be noted that the frequency of vortex shedding is not a pure multiple of the flow oscillation frequency. Relative frequency, as an integer, is a measure of the number of vortices actually shed during a cycle. However, there are vortices which do not break away from their shear layers before the flow is reversed because they are not fully-developed and dissipate when the flow reverses. This is particularly true for f_r in the neighbourhood of 2 or 3. The fractional shedding of vortices for values of K between 5 and 15 leads to incalculable changes

in the flow pattern and hence in the in-line and transverse forces. For small values of K, two vortices begin to develop at the start of the cycle in one direction; however, due to various reasons the vortices will acquire different strengths. As the flow reverses, the larger of the vortices is swept past the cylinder but the weaker one dissipates partly due to turbulent diffusion. As a result of the single shedding, the in-line force becomes asymmetrical. Furthermore, the vortex which is swept away plays an important role in the formation of the new vortices when the flow reverses its direction. The dominant vortex establishes, by its sense of rotation, a preferred location for the generation of a new dominant vortex. The new vortex and the one convected downstream may form a pair, increase the transverse pressure gradient and thus give rise to significant lift forces. The evolution of vortices for various ranges of Keulegan-Carpenter number are shown in Figure 7.25.

The vortex shedding frequency can be expressed in terms of Strouhal number defined as $S = f_v D/u_m = f_r/K$. Sarpkaya's experiments (1976a) have shown that for f_r larger than about 3, the Strouhal number remains reasonably constant at 0.22. Strouhal number depends on both R_e and K and for very large values of R_e (post-supercritical region) it rises to about 0.3. Its average value based on all vortices shed during a given cycle was found to be between 0.14 and 0.16.

Instantaneous Values of Force Coefficients

Sarpkaya calculated the instantaneous values of $C_d(\theta)$ and $C_m(\theta)$ ($\theta = 2\pi t/T$) by solving a set of Morison type equations written at $\theta = \theta_n$ and $\theta = \theta_n + \Delta\theta$ assuming that $C_d(\theta)$ and $C_m(\theta)$ remain constant in the interval $\Delta\theta$ ($\Delta\theta \approx 3$ degrees). The results of this study showed that for

intermediate values of K (for β less than about 2500), C_d and C_m vary significantly during a given cycle (Figure 7.26). It can therefore be concluded that the Morison's equation with time-averaged C_d and C_m gives a poor estimate of the loading on a cylinder for intermediate values of K. However, for K smaller that 8 (inertia dominated) and larger than 20 (drag dominated) the difference between C_d and $C_d(\theta)$ and C_m and $C_m(\theta)$ rapidly diminishes and the instantaneous force is accurately predicted by the linear-quadratic sum with constant coefficients.

7.2.2.3 Wave Forces on Cylinders

In waves the flow field surrounding the cylinder is always three-dimensional. According to linear wave theory, deep water waves have circular orbits rather than the planar-harmonic motion previously discussed. The effect of the tangential component of water particle velocity on a cylinder is to destabilise the boundary layer and thus lower the critical Reynolds number. In the ocean environment, a cylindrical member will experience the integral effect of a mixture of wavelets of many frequencies also having a directional spread. Furthermore, the decay of wave-induced water particle kinematics with depth makes vortex shedding and pressure distribution along the cylindrical pile less correlated. Fortunately, these effects lead to forces which are smaller than those calculated based on plane-harmonic flow. It can therefore be concluded that the use of force coefficients obtained from plane-harmonic flow experiments in the design of offshore structures are conservative.

The influence of current on wave loading is taken into account by adding the current vectorially to the wave-induced water particle velocity in the absence of current. Morison's equation then becomes

$$F = \frac{1}{2}\rho D C_d (u + \bar{u})|u + \bar{u}| + \frac{\pi}{4}\rho D^2 C_m \dot{u} \qquad (7.23)$$

Where $\bar{u}$ represents the current velocity and u and $\dot{u}$ are the horizontal components of wave-induced kinematics. The above procedure is a simplified approach to the problem of wave loading on cylinders in the presence of currents. A more rigorous method must account for the wave current interactions. If the current is in the direction of wave propagation, the wave amplitude decreases and its length increases. If the current opposes the wave, the wave becomes steeper and its length decreases. Further discussion of this subject is beyond the scope of this Thesis.

The most important point to be considered is that in the design of offshore structures water particle kinematics must be calculated according to a particular wave theory and that the choice of wave theory affects the values of Morison's coefficients. Therefore, in practice Morison's coefficients must be calibrated against a particular wave theory and only be used in conjunction with kinematics obtained from that particular theory. In other words, the drag and inertia coefficients obtained through the use of one method should not be compared with those obtained through the use of another one.

Furthermore, Sarpkaya and Isaacson (1981) suggest that the Reynolds number and the Keulegan-Carpenter number be defined as

$$R_e = \frac{(u_m + \bar{u})D}{\nu} \qquad (7.24)$$

and

$$K = \frac{(u_m + \bar{u})T}{D} \tag{7.25}$$

where u_m is the amplitude (maximum) of the horizontal component of wave-induced water particle velocity.

7.3 REAL FLUID LOADING ON FLEXIBLE SUBMERGED CYLINDERS

7.3.1 WAVE-INDUCED IN-LINE LOADING

If a structural member is dynamically responsive, then fluid loading on the member can be written in terms of relative velocities and accelerations between the fluid $(u,\dot{u})$ and the structure $(\dot{r},\ddot{r})$. That is

$$F = C_d \rho \frac{D}{2}(u - \dot{r})|u - \dot{r}| + \rho \frac{\pi D^2}{4}\dot{u} + C_a \rho \frac{\pi D^2}{4}(\dot{u} - \ddot{r}) \tag{7.26}$$

Where the first term on the right hand side of the above equation is the drag force, the second term is the Froude-Krylov force and the third term is the added-mass force. The Froude-Krylov force is due to undisturbed pressure field and therefore does not depend upon the pile motion. The above equation can be rewritten as

$$F = C_d \rho \frac{D}{2}(u - \dot{r})|u - \dot{r}| + C_m \rho \frac{\pi D^2}{4}\dot{u} - C_a \rho \frac{\pi D^2}{4}\ddot{r} \tag{7.27}$$

The equation of motion for a single-degree of freedom system with mass M, damping coefficient C and stiffness K can be written as

$$M\ddot{r} + C\dot{r} + Kr = F(t) \tag{7.28}$$

Where F(t), the fluid loading on the mass M (assumed to be a cylinder), is given by Equation (7.27). Combining Equations (7.27) and (7.28) results in

$$(M + C_a \rho \frac{\pi D^2}{2}) \ddot{r} + C\dot{r} + Kr = C_d \rho \frac{D}{2} (u - \dot{r})|u - \dot{r}| + C_m \rho \frac{\pi D^2}{4} \dot{u} \quad (7.29)$$

The drag term can be approximated by (Penzien, 1976)

$$(u - \dot{r})|u - \dot{r}| = u|u| - 2E[|u|]\dot{r} \quad (7.30)$$

Where $E[|u|]$ is the time average of the absolute value of the water particle velocity.

Substituting Equation (7.30) into Equation (7.29), gives

$$(M + C_a \rho \frac{\pi D^2}{4}) \ddot{r} + [C + C_d \rho D E[|u|]]\dot{r} + Kr = C_d \rho \frac{D}{2} u|u| + C_m \rho \frac{\pi D^2}{4} \dot{u} \quad (7.31)$$

The term $C_d \rho D E[|u|]$ which is added to the viscous damping, C, in the above equation is frequently referred to as the fluid damping. Knowing the values of C_d and C_m and the flow field, r can be obtained by solving Equation (7.31).

It should be noted that the lift force is not considered in the dynamic analysis of the full structure. This is justifiable partly because of phase shifts in lift forces acting on various members and partly because of the relatively high frequency of vortex shedding. However, it is emphasised that for individual members as well as for tube bundles, the periodic lift can be very important and may give rise to in-line and/or transverse oscillations.

7.3.2 VORTEX-INDUCED OSCILLATIONS

Flexible Cylinders in Currents

A flexible pile in a steady current will respond dynamically to the unsteady drag and the fluctuating transverse forces. The motions of the pile in many cases modify the force and one may therefore talk about hydro-elastic oscillations. A most important feature of hydro-elastic oscillations is the so called 'lock-in' or synchronisation phenomenon (Figures 7.27 and 7.28). When lock-in occurs, the cylinder takes control of vortex shedding in apparent violation of the Strouhal relationship, i.e. the frequencies of vortex shedding and the body oscillation collapse into a single frequency close to the natural frequency of the body.

Lock-in occurs when the fluid velocity is increased beyond that for which $f_v = f_s$, in which f_s is the resonant frequency of the structure and f_v is the vortex shedding frequency. Then the resonant motions of the pile from side to side will slow down the vortex shedding process, keeping the vortex shedding frequency 'locked at' or 'synchronised' with the resonant frequency of the pile. Thus while the vortex shedding frequency (or the frequency of transverse force) for a rigid pile would increase with the velocity according to the Strouhal relationship, the flexible cylinder will have large amplitude motions at $f_v = f_s$ for a range of velocities. Eventually when the velocity is too high, the large amplitude pile motions suddenly stop and the vortex shedding frequency jumps up to that of the fixed pile at the same velocity (Figure 7.27).

The most important parameter with regard to synchronisation is the reduced velocity defined as

$$u_r = \frac{u}{f_s D} = \frac{1}{S} * \frac{f_v}{f_s} \qquad (7.32)$$

Where as before S is the Strouhal number and f_s is the natural frequency of the cylinder. f_v is the number of vortex pairs shed per unit time. For alternative vortex shedding, the in-line force will have a frequency of $2f_v$ and the transverse force a frequency of f_v. Therefore, one must expect resonance in the transverse direction at $u_r = S^{-1}$ and for the in-line direction at $u_r = 0.5S^{-1}$. For sub-critical flow, $S^{-1} = 5$ and therefore, one expects resonance in the transverse direction at about $u_r = 5$ and in the in-line direction at $u_r = 2.5$. However, in view of the lock-in phenomenon, resonance continues for u_r appreciably larger than that.

Experiments have shown that in-line oscillations occur within two adjacent regions (Figures 7.28 and 7.29). The first is in the range of $1.25 < u_r < 2.5$, with maximum amplitudes (about 0.2D) occurring at $u_r = 2.1$. The second region extends from $u_r = 2.7$ to $u_r = 3.8$ with maximum amplitude at $u_r = 3.2$. The first instability region is accompanied by symmetric vortex shedding, which become aligned in an alternate vortex street within a short distance downstream. Oscillations are at the cylinder's natural frequency; however, the vortex shedding frequency continues to be governed approximately by the Strouhal relationship (Figure 7.28). The second unstable region of the in-line motion and the first (and only) unstable region of cross-flow direction (Figure 7.29) are accompanied by alternate vortex shedding and 'lock-in' occurs. The frequency of vortex shedding remains constant throughout the lock-in range, being equal to the cylinder's natural frequency for cross-flow

motion and one-half of the natural frequency for in-line motion (King, 1977).

For a circular cylinder with large L/D, synchronisation begins with $f_v \approx f_s$ and ends at $f_v/f_s = 1.4$. The maximum amplitude occurs near the middle of the range. At the end of the lock-in range, vortex shedding frequency jumps to that governed by the Strouhal relationship, but the cylinder continues to oscillate at $f_c \approx f_s$, where f_c is the cylinder oscillation frequency. This is true at both ends of the lock-in range and shows that the response is not a simple forced vibration at the exciting natural Strouhal frequency.

The correlation length increases rapidly with amplitude. The increase of the correlation length in smooth flow is much larger than in turbulent flow. In smooth flow the correlation length is estimated by numerical extrapolation to increase from about 3.5D to 40D for $R_e = 19{,}000$ in the range $0.05 < A/D < 0.1$, (A is the amplitude of cylinder oscillation). In turbulent flow, it is again estimated to vary from about 2.5D to 10D in the same A/D range. The rate of increase is steeper than linear but does not show any abrupt change which would indicate a sudden development of the lock-in once a threshold amplitude is achieved.

Flexible Cylinders in Waves

Rajabi (1979) conducted experiments with spring-mounted smooth and rough cylinders undergoing sustained oscillations in a harmonically oscillating flow in a u-shaped water tunnel. The results indicate that an elastically-mounted cylinder may sustain synchronised oscillations when the reduced velocity $u_r = u_m/f_sD$ is in the range of 5 to 7.5, with

maximum response at $u_r \approx 5$. Synchronised oscillations occurred at an average Strouhal number of 0.16.

7.4 LARGE-SCALE EXPERIMENTS

Small-scale experiments have greatly increased our understanding of the mechanism of wave loading on circular cylinders. However, the experiments are in the range of low Reynolds number (subcritical) and hence the results cannot be used for design purposes where Reynolds number are in the post-critical regime. In the 1980's, however, several research programmes were initiated to study wave loading at large scale with Reynolds numbers large enough to represent post-critical conditions.

Chaplin's Work

Chaplin (1988a) conducted experiments in which a smooth cylinder was driven along a straight line in a large tank of water. The Random Planar Motion mechanism (RPM), on which the experiments were carried out, was built in the Marine Technology Laboratory of the University of Liverpool for the purpose of moving a cylinder through a tank of water with a regular or random oscillatory motion. The general arrangement of the RPM is shown in Figure 7.30. The cylinder under test was bolted beneath a mounting frame which was suspended above a large tank of water (7.0m diameter and 1.3m deep). The mounting frame could be driven up to 1.0m in any horizontal direction from its central position by two computer-controlled hydraulic winches.

Driving the cylinder with a simple harmonic motion along a straight line generates conditions which correspond to those produced in naturally-oscillating U-tubes. However, unlike the U-tube experiments,

in which there are a very narrow range of available frequencies, the RPM could be programmed to oscillate at constant magnitude, but over a wide range of periods. By keeping the amplitude of motion fixed while T changes, different Reynolds numbers for the same K values were obtained.

Two smooth plastic cylinders, of diameters 160 mm and 315 mm, were used in the experiments. For each experiment, the rig executed 5 oscillations from rest, and then at least 30 oscillations were recorded. The sequence of at least 30 cycles were phase-averaged in order to obtain the mean force and displacement records.

The above experiments were conducted for K = 6, 10, 14 and 20. The largest period was about 15 seconds. The results, shown in Figure 7.31, indicates that the root-mean-square in-line force coefficient, $C_{f(rms)}$, does not vary significantly with the Reynolds number. $C_{f(rms)}$ is defined in terms of the in-line force per unit length (including a Froude-Krylov force) and the rms velocity, U_{rms}, that is

$$C_{f(rms)} = F_{in(rms)}/(0.5\rho DU_{rms}^2)$$

The variation of $C_{f(rms)}$ with the Keulegan-Carpenter No. is shown in Figure 7.32a and is in very good agreement with the results from a vertical cylinder in waves at similar Reynolds numbers by Bearman et al, 1985, shown in Figure 7.32b.

Morison's coefficients were derived for each cycle of oscillation , and their mean and S.D were computed over the whole sequence of 30 or so cycles.

The variation of C_d and C_m with Re at Keulegan-Carpenter No. of 10 (inertia-dominated) and 20 (drag-inertia regime) are shown in Figure 7.33. The results are in good agreement with Sarpkaya's (1976b) data from U-tube experiments. The lines through each point extend up and down by a distance corresponding to the standard deviation of the coefficient.

Bearman's Work on a Rigid Cylinder

Bearman et al (1985) conducted experiments on a smooth rigid vertical cylinder of 0.50m diameter in the large Delta flume at the Delft Hydraulics Laboratory. This facility is 230m long, 5m wide and 7m deep, and is equipped with a programmable, hydraulically driven, piston type wavemaker, which can generate waves with periods between 3 and 10 seconds and with heights up to about 2 meters. The aim of the experiments was to study wave loading at high Reynolds number under controlled laboratory conditions. For these experiments the Reynolds number was in the range $1.46*10^5 < Re < 5*10^5$.

Both regular and random waves were used in the study. Each regular wave test lasted for about 15 minutes and usually the passage of more than 100 waves was recorded. One random wave test was done on the cylinder with a duration of 189 minutes. For regular waves, C_d and C_m were calculated on a wave by wave basis and averaged over the length of the record (100 or so waves). In order to compare regular and random waves, 16 individual waves were chosen from the random test. First, the 11 waves which gave the highest maximum or minimum in-line forces were chosen. Then the Keulegan-Carpenter No. range was extended by 5 additional waves with smaller values of K=UT/D (where U is the

fundamental component of the horizontal velocity for an individual wave).

The variation of root-mean-square in-line force coefficients with Keulegan-Carpenter No. is shown in Figure 7.32b. There is very good agreement between force coefficients from regular and random waves.

Values of C_d and C_m for regular waves are plotted against Keulegan-Carpenter No. in Figure 7.34. At Keulegan-Carpenter No. between 10 and 20, C_d is about 0.60 and C_m is in the range 1.45 to 1.65. The force coefficients did not show any significant variation with Reynolds number.

Bearman's Work on the Compliant Cylinder

Before the compliant cylinder (described in Chapter 2) was mounted at Christchurch Bay, some wave loading measurements were done for regular waves in the delta flume. The flume is 7m deep over most of its length, but has a 9.5m deep section, where the 12.2m long cylinder was mounted. Tests were done for the cylinder in both F6 mode (most flexible) and F1 mode (most rigid) conditions. C_d and C_m values were calculated for each wave and then averaged for all but the first few waves over runs lasting about 15 minutes. Reynolds numbers were in the range of $2*10^5$ to $5.5*10^5$. In-line force coefficients were calculated as before.

In the F1 mode, displacements of the cylinder were never more than a few percent of a diameter and the C_d and C_m values were found to agree well with the earlier results for a fixed, smooth cylinder. Displacements recorded in the F6 mode, defined as the ratio of rms displacement divided by cylinder diameter reached values as high as 0.30 to 0.40 in both in-line and transverse directions. The largest

displacements in both directions occurred when the cylinder oscillation frequency was an integer multiple of wave frequency.

The root-mean-square in-line force coefficient for F6 mode is plotted in Figure 7.35, and the curve for F1 mode is shown for comparison. In general, the loading is 15 to 20% higher when the cylinder is responding but around K=7.5, the loading is increased by as much as 50%.

The variation of C_d and C_m with Keulegan-Carpenter No. (F6 mode) is shown in Figure 7.36. Comparison of Figure 7.36 with Figure 7.34 shows that C_m values have not been significantly affected by the cylinder's response; However, C_d values at low Keulegan-Carpenter No. have been significantly increased. The average C_d for K vales between 10 and 20 is 0.70. Another point to be noted is that C_d values for station 4 (deeper station) are consistently lower than those for Level 3.

Second Christchurch Bay Tower Project

The tower (Figure 2.1) has been described in Section 2.1. The 2.8m diameter vertical member is in the inertia regime while the small column (0.48m diam.) is in the drag-inertia regime. Measurements (winter 1982) were done at four different levels known as Levels 2, 3, 4 and 5. However, due to intermittency at Level 2, the results have been presented for other levels only (Bishop and Shipway, 1984). A total of sixty-nine 20-minute records were analysed. About half of the analysed records were in the high wave group with water surface elevation standard deviation greater than 0.40m ($H_s > 1.6$m).

Keulegan-Carpenter numbers and total force coefficients were calculated using the expressions due to Bishop (Equations 9.1a and 9.3a). The variation of total force coefficient with Keulegan-Carpenter No. is shown in Figure 7.37. As observed, the total force coefficient decreases with increasing depth of immersion. C_d and C_m values as a function of Keulegan-Carpenter No. are shown in Figure 7.38. There is considerable scatter in the data for K values between 10 and 30; C_m is about 1.8 and C_d is about 0.75. For smaller values of K, C_m is about 2.0 and C_d values are unreliable because the forces are strongly inertia dominated. The coefficients do not show a trend with Reynolds number.

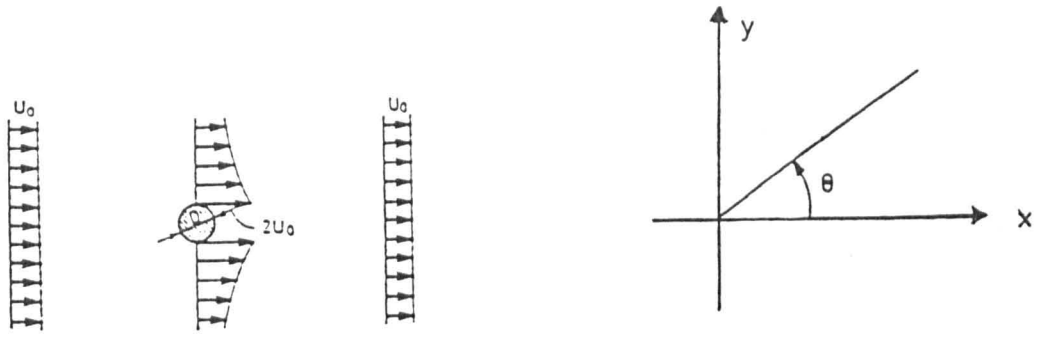

FIGURE 7.1. DEFINITION SKETCH FOR FLUID LOADING ON A SUBMERGED CYLINDER

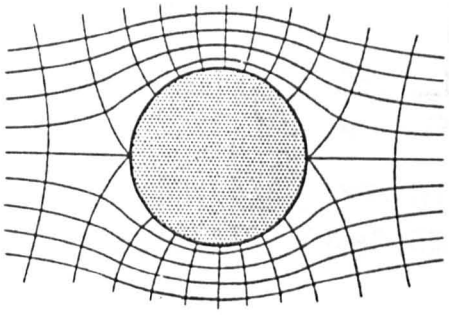

FIGURE 7.2. EQUIPOTENTIAL LINES AND STREAMLINES FOR IDEAL FLOW AROUND A CIRCULAR CYLINDER. (Streeter, 1979)

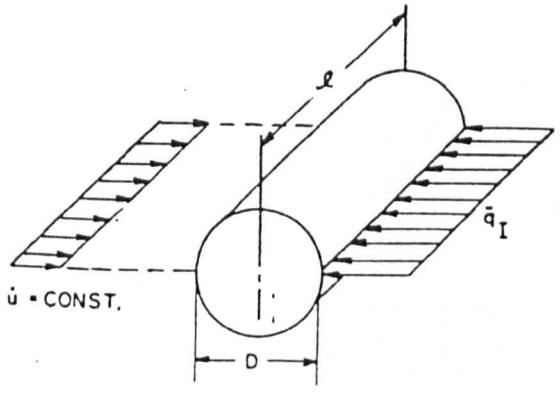

ℓ/D	C_M
1.2	1.62
2.5	1.78
5.0	1.90
9.0	1.96
∞	2

FIGURE 7.3. A RIGID, STATIONARY CYLINDER IN AN IDEAL ACCELERATING FLUID. (Wilson, 1984)

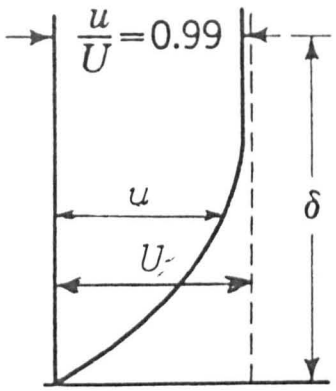

FIGURE 7.4. DEFINITION OF BOUNDARY LAYER THICKNESS (Streeter, 1979)

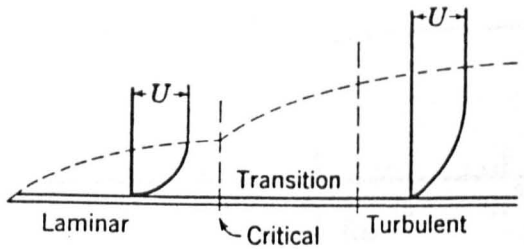

FIGURE 7.5. BOUNDARY LAYER GROWTH (THE VERTICAL SCALE IS GREATLY ENLARGED) (Streeter, 1979)

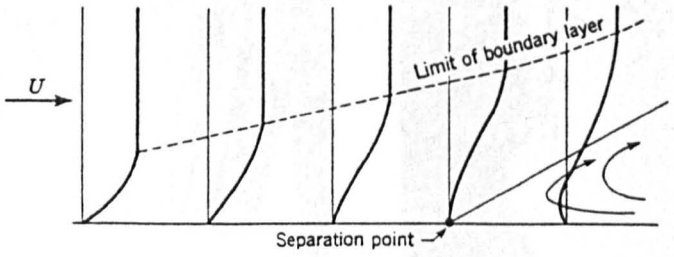

FIGURE 7.6. SEPARATION DUE TO COMBINED EFFECT OF ADVERSE PRESSURE GRADIENT AND BOUNDARY SHEAR. (Streeter, 1979)

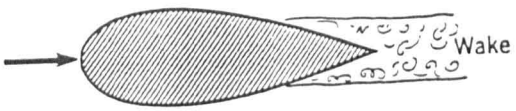

FIGURE 7.7. REDUCTION OF WAKE SIZE FOR STREAMLINE BODIES (Streeter, 1979)

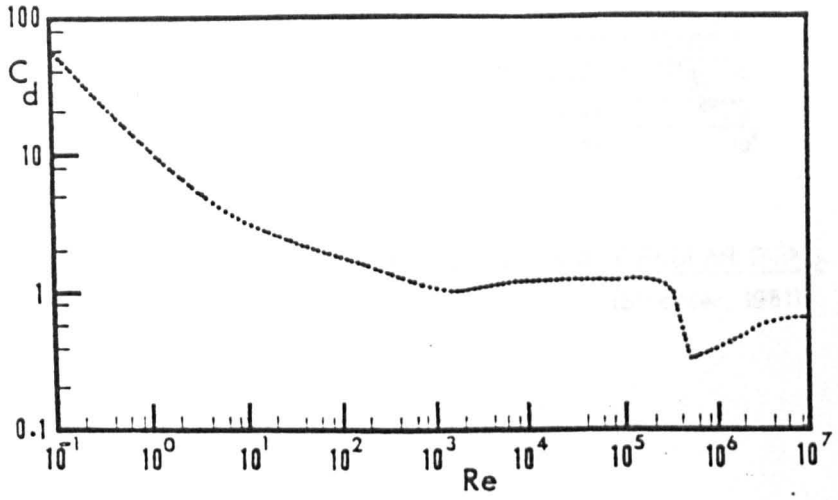

FIGURE 7.8. VARIATION OF DRAG COEFFICIENT WITH REYNOLDS No. FOR A CIRCULAR CYLINDER. (Sarpkaya and Isaacson, 1981)

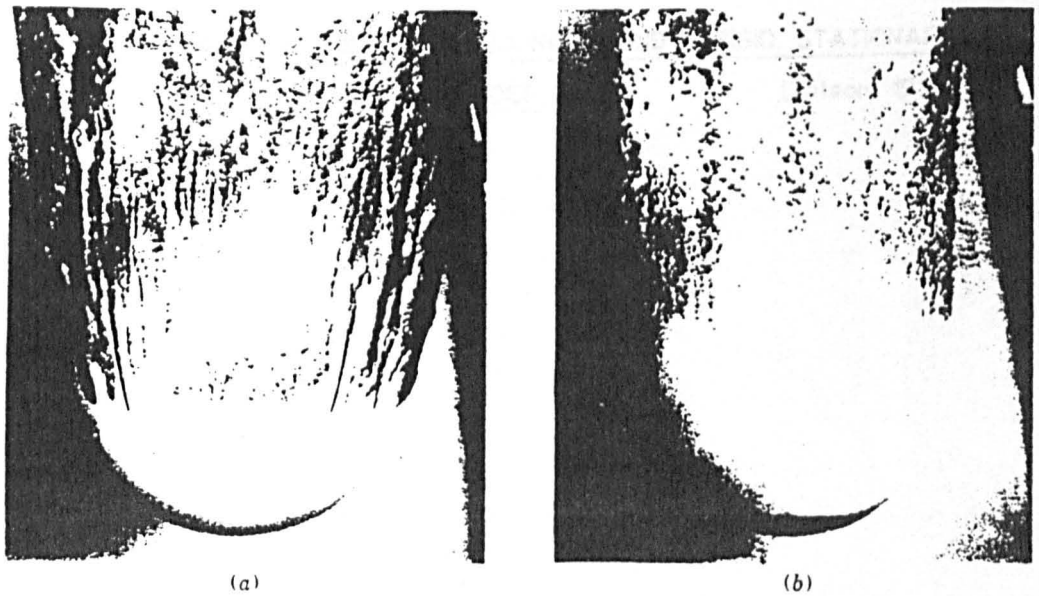

FIGURE 7.9. Shift in separation point due to induced turbulence: (*a*) 8.5-in bowling ball, smooth surface, 25 ft/s entry velocity into water; (*b*) same except for 4-in-diameter patch of sand on nose. (*Official U.S. Navy photograph made at Navy Ordnance Test Station, Pasadena Annex.*)

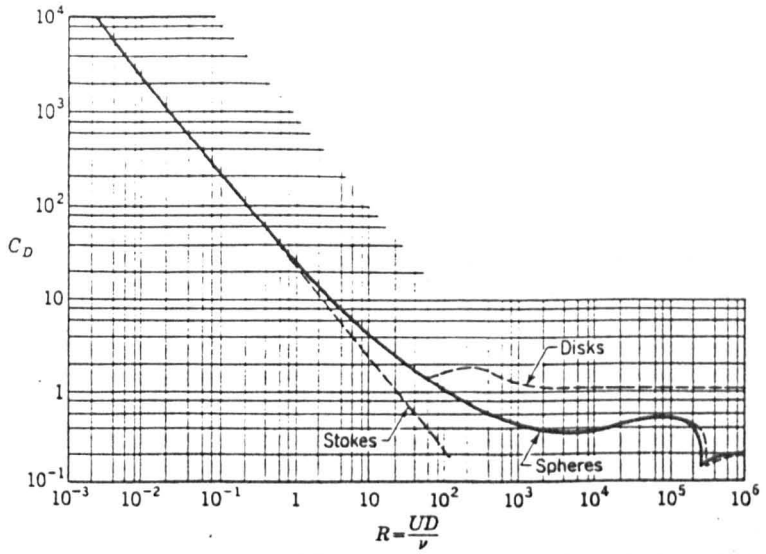

FIGURE 7.10. DRAG COEFFICIENTS FOR SPHERES AND CIRCULAR DISKS.
(Streeter, 1981)

FIGURE 7.11. PERIODIC VORTICES TRAILING BEHIND A RIGID, STATIONARY CYLINDER. (Wilson, 1984)

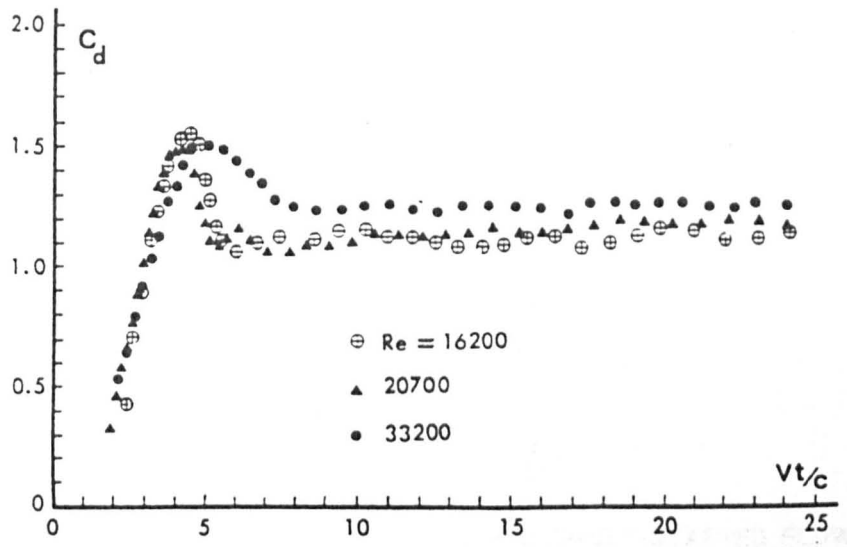

FIGURE 7.12. MEASURED DRAG COEFFICIENT AS A FUNCTION OF Vt/c FOR IMPULSIVELY - STARTED FLOW. (Sarpkaya and Isaacson, 1981)

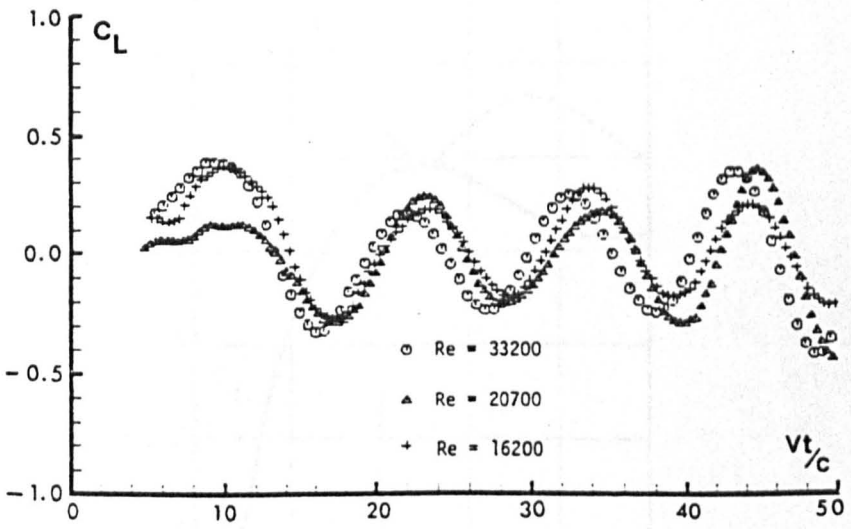

FIGURE 7.13. MEASURED LIFT COEFFICIENT AS A FUNCTION OF Vt/c FOR IMPULSIVELY-STARTED FLOW (Sarpkaya and Isaacson, 1981)

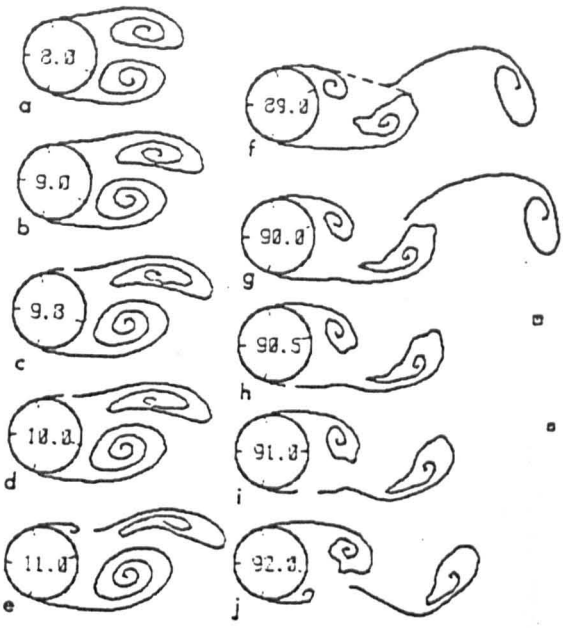

FIGURE 7.14. EVOLUTION OF WAKE IN IMPULSIVELY-STARTED FLOW FOR DIFFERENT VALUES OF Vt/c

(Sarpkaya and Shoaff, 1979)

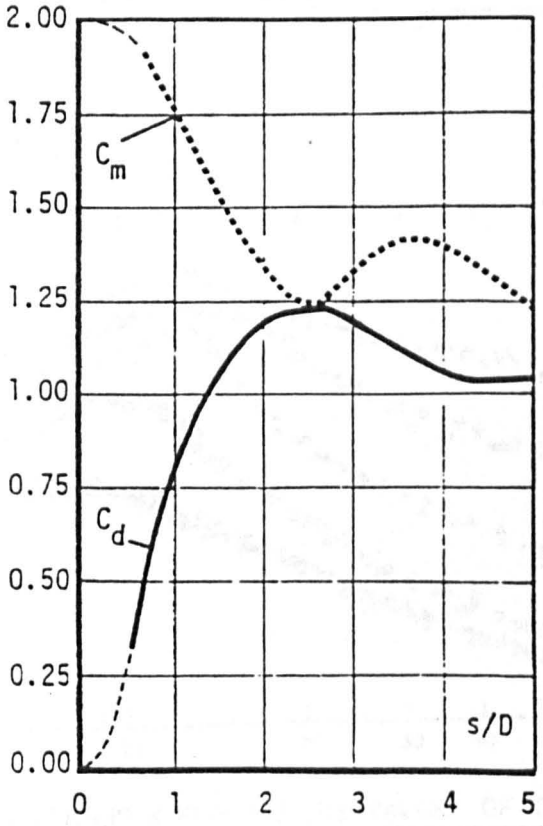

FIGURE 7.15. VARIATION OF THE DRAG AND INERTIA COEFFICIENTS WITH RELATIVE DISPLACEMENT IN UNIFORMLY-ACCELERATED FLOW (Sarpkaya and Isaacson, 1981)

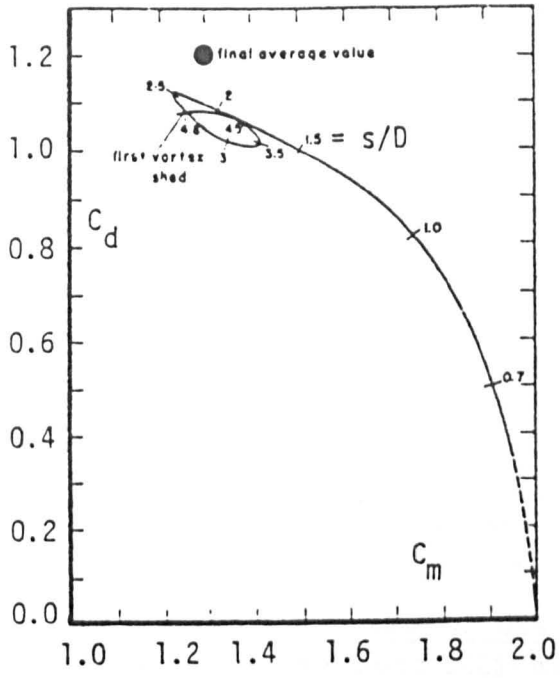

FIGURE 7.16. THE INTER-RELATIONSHIP BETWEEN THE DRAG AND INERTIA COEFFICIENTS FOR UNIFORMLY-ACCELERATED FLOW

(Sarpkaya and Isaacson, 1981)

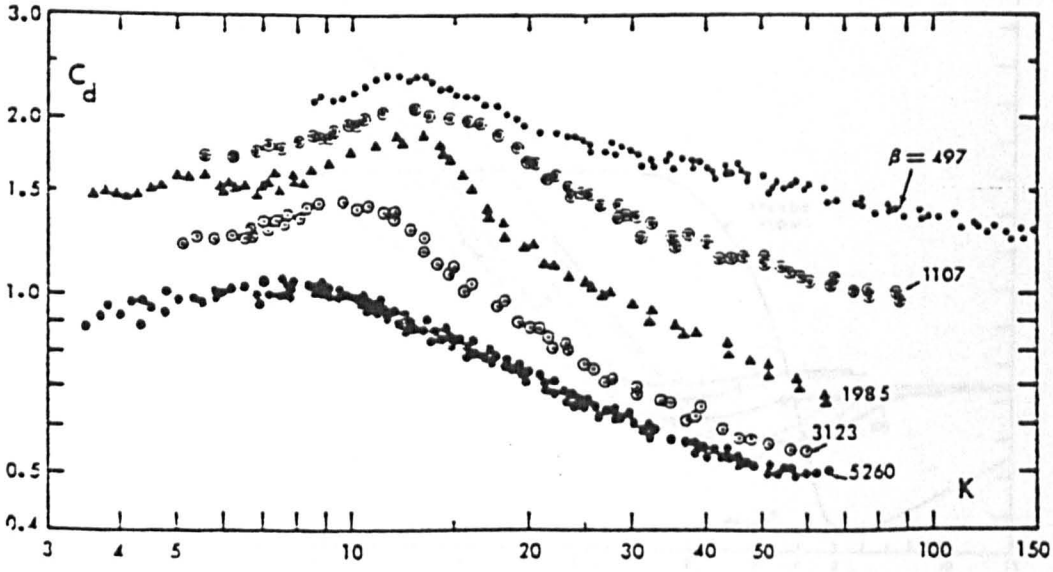

FIGURE 7.17. C_d VERSUS K FOR VARIOUS VALUES OF THE FREQUENCY PARAMETER FOR HARMONICALLY OSCILLATING FLOW

(Sarpkaya, 1976a)

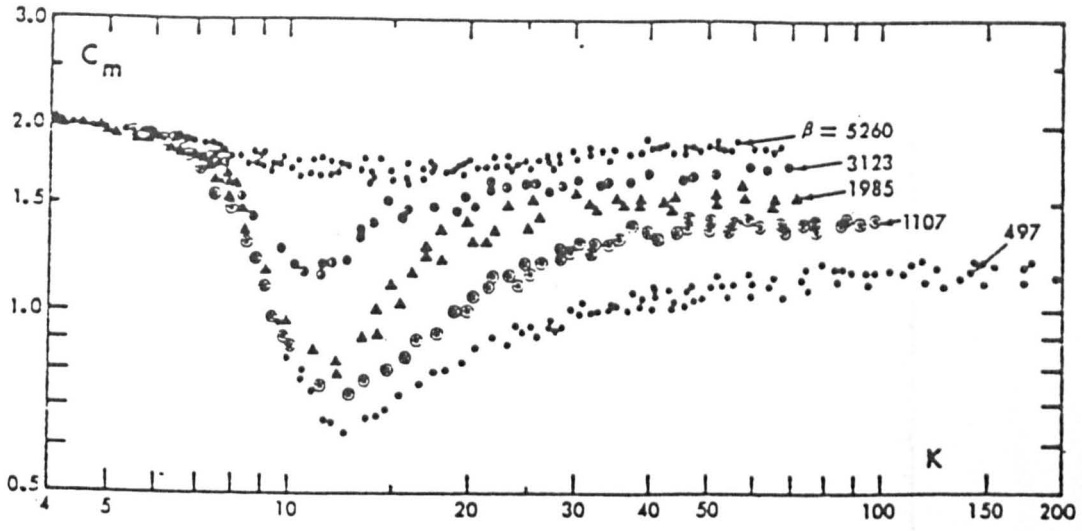

FIGURE 7.18. C_m VERSUS K FOR THE VARIOUS VALUES OF THE FREQUENCY PARAMETER FOR HARMONICALLY OSCILLATING FLOW (Sarpkaya, 1976d)

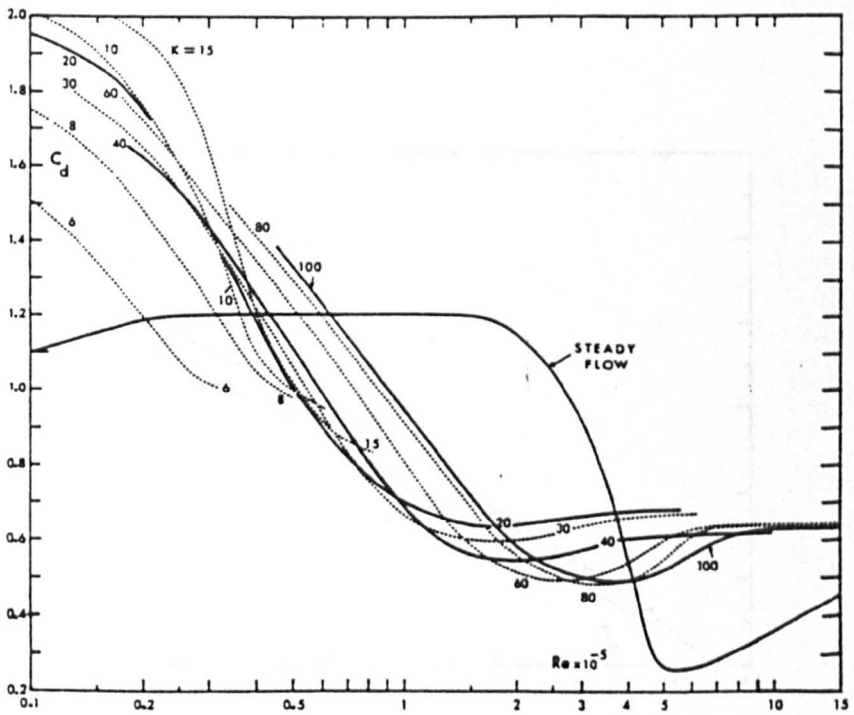

FIGURE 7.19. C_d VERSUS REYNOLDS NUMBER FOR VARIOUS VALUES OF K FOR HARMONICALLY-OSCILLATING FLOW (Sarpkaya, 1976d)

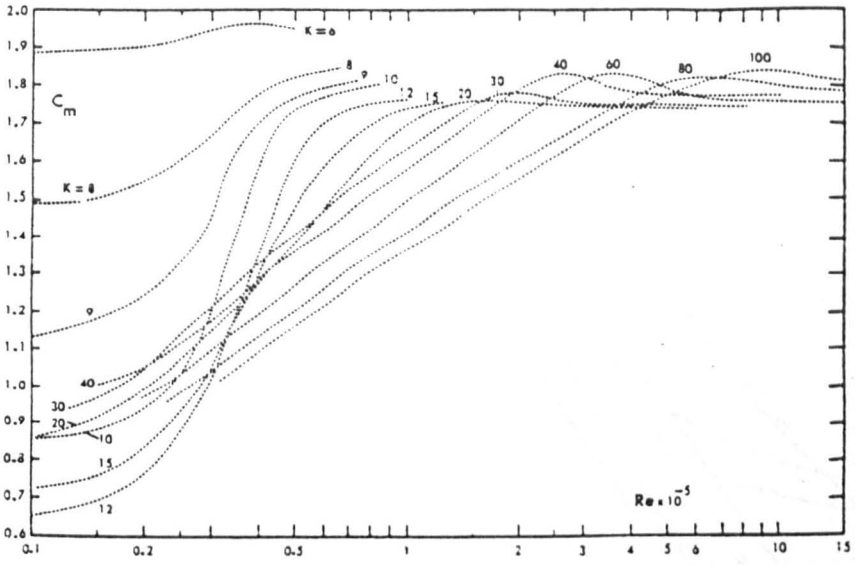

FIGURE 7.20. C_m VERSUS REYNOLDS NUMBER FOR VARIOUS VALUES OF K FOR HARMONICALLY-OSCILLATING FLOW

(Sarpkaya, 1976d)

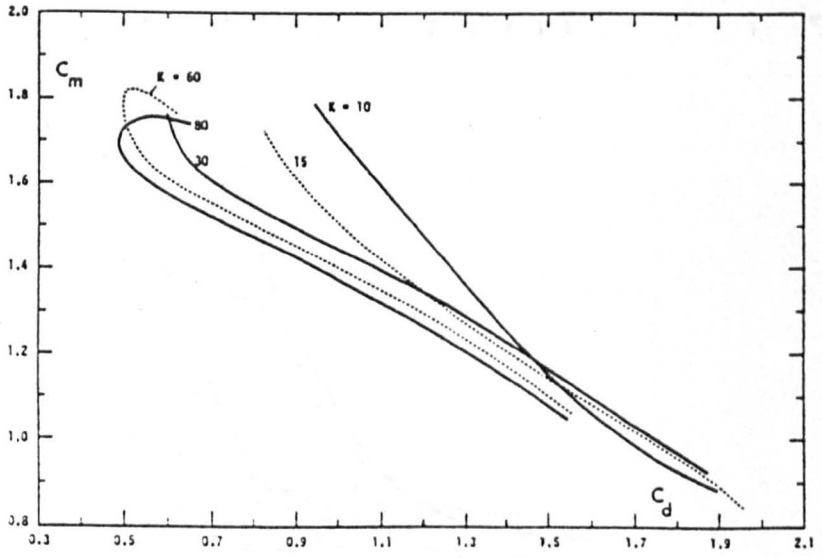

FIGURE 7.21. VARIATION OF C_m WITH C_d FOR VARIOUS VALUES OF K FOR HARMONICALLY-OSCILLATING FLOW

(Sarpkaya, 1976d)

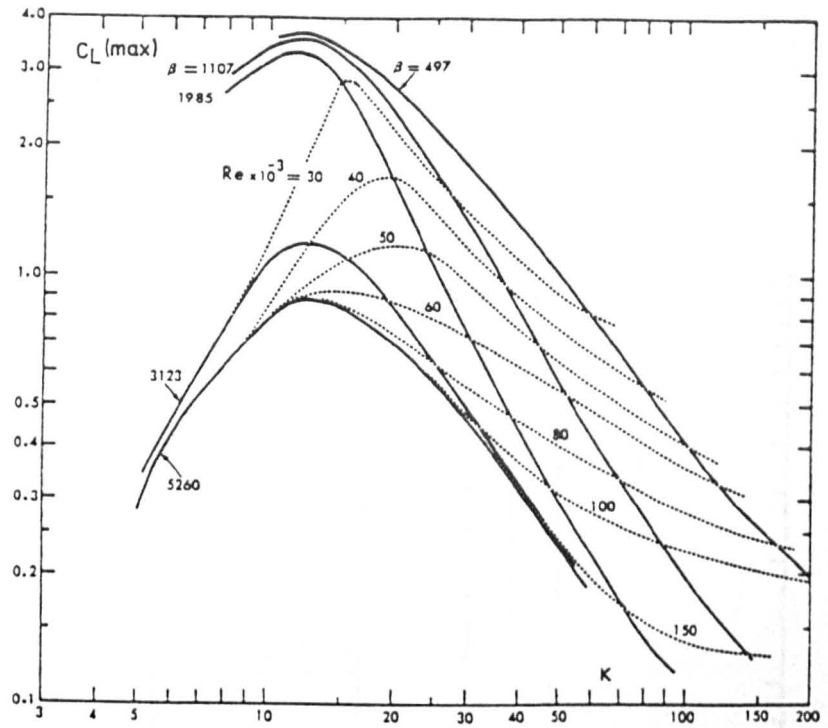

FIGURE 7.22. LIFT COEFFICIENT VERSUS K FOR VARIOUS VALUES OF THE REYNOLDS NUMBER AND THE FREQUENCY PARAMETER FOR HARMONICALLY-OSCILLATING FLOWS (Sarpkaya, 1976a)

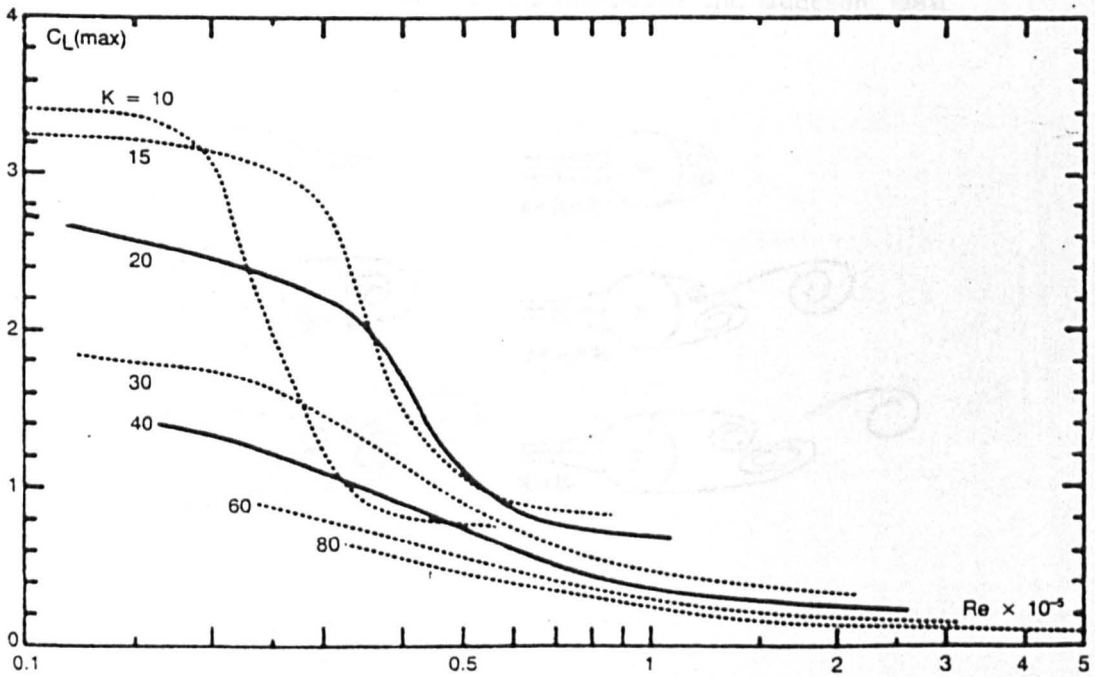

FIGURE 7.23. LIFT COEFFICIENT VERSUS REYNOLDS NUMBER FOR VARIOUS VALUES OF K FOR HARMONICALLY-OSCILLATING FLOWS (Sarpkaya, 1976a)

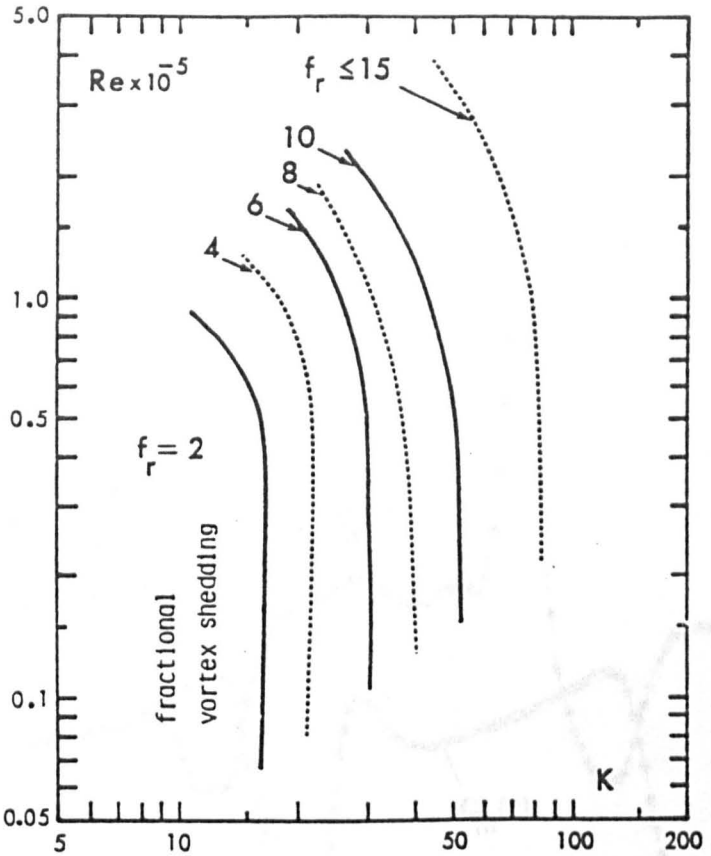

FIGURE 7.24. RELATIVE FREQUENCY OF VORTEX SHEDDING AS A FUNCTION OF K AND Re FOR HARMONICALLY-OSCILLATING FLOWS. (Sarpkaya and Isaacson, 1981)

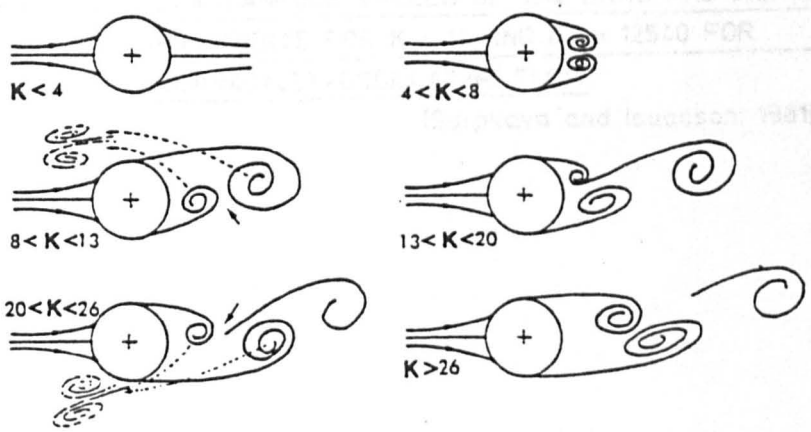

FIGURE 7.25. EVOLUTION OF VORTICES IN VARIOUS RANGES OF THE KEULEGAN - CARPENTER NUMBER (Sarpkaya and Isaacson, 1981)

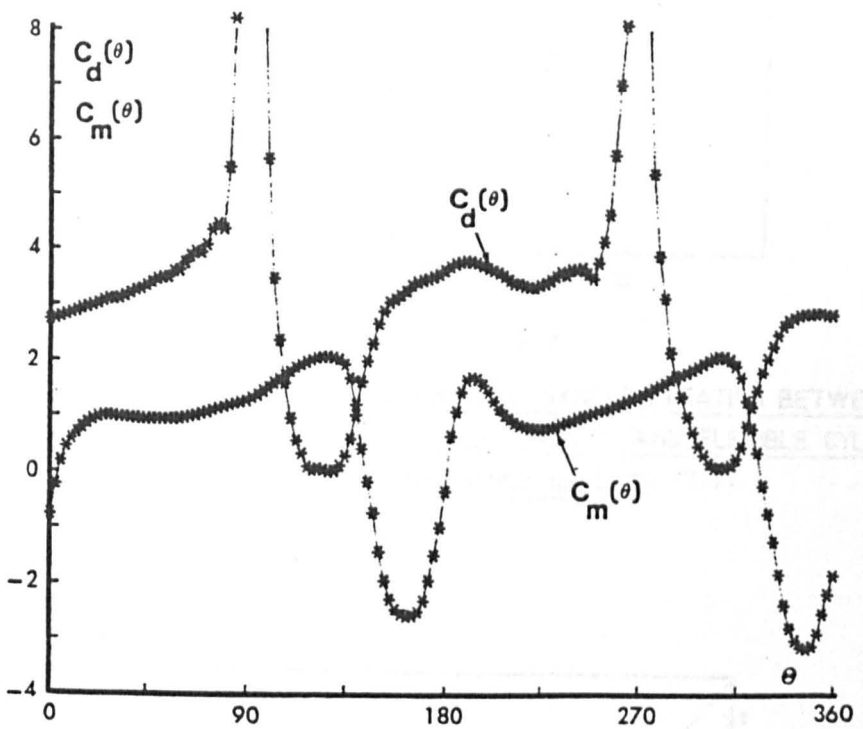

FIGURE 7.26. INSTANTANEOUS VALUES OF THE DRAG AND INERTIA COEFFICIENTS FOR K = 12 AND R_e = 12540 FOR HARMONICALLY-OSCILLATING FLOW.

(Sarpkaya and Isaacson, 1981)

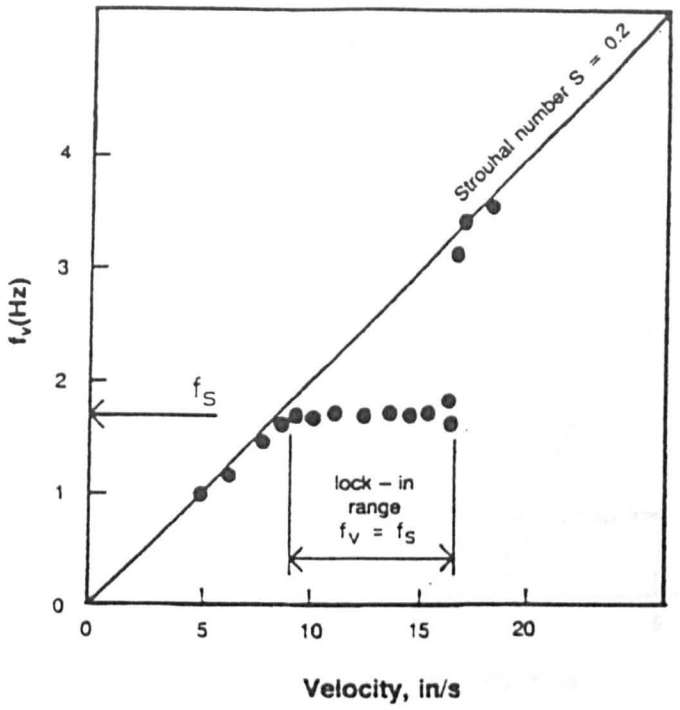

FIGURE 7.27. CROSS-FLOW RESONANCE: SYNCHRONIZATION BETWEEN VORTEX SHEDDING FREQUENCY f_v AND FLEXIBLE CYLINDER FREQUENCY f_s. (King, 1977)

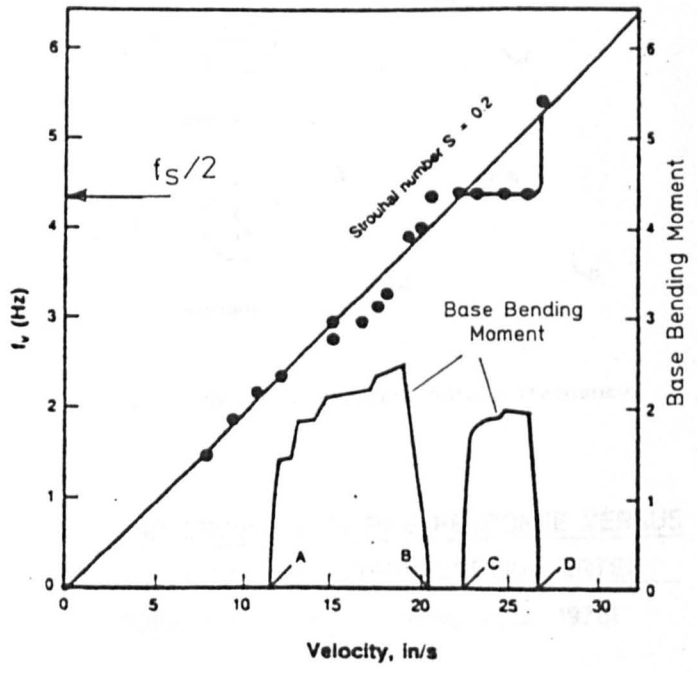

FIGURE 7.28. SELF-EXCITED VIBRATIONS IN THE IN-LINE DIRECTION.

TWO REGIONS: A-B SYMMETRIC VORTEX SHEDDING-NO SYNCHRONIZATION
C-D ALTERNATE VORTEX SHEDDING - SYNCHRONIZATION
(King, 1977)

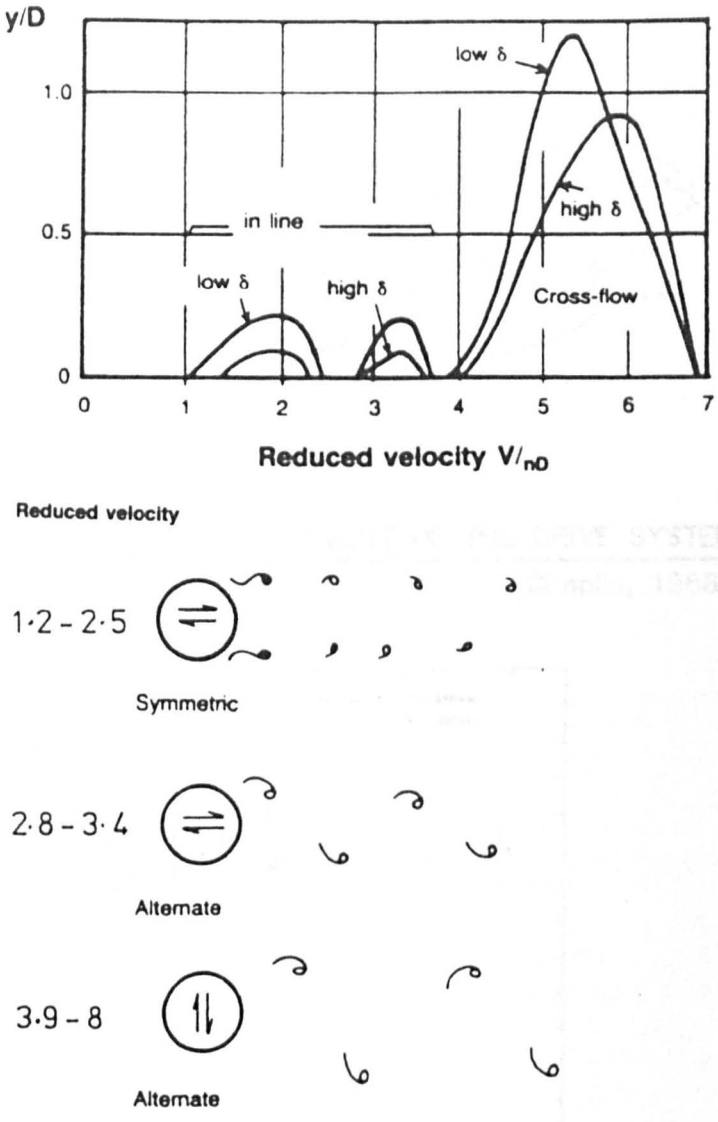

δ: measure of damping; n: cylinder's natural frequency

FIGURE 7.29. IN-LINE AND CROSS FLOW PILE RESPONSE VERSUS REDUCED VELOCITY AND CORRESPONDING VORTEX SHEDDING PATTERNS (King, et al 1976)

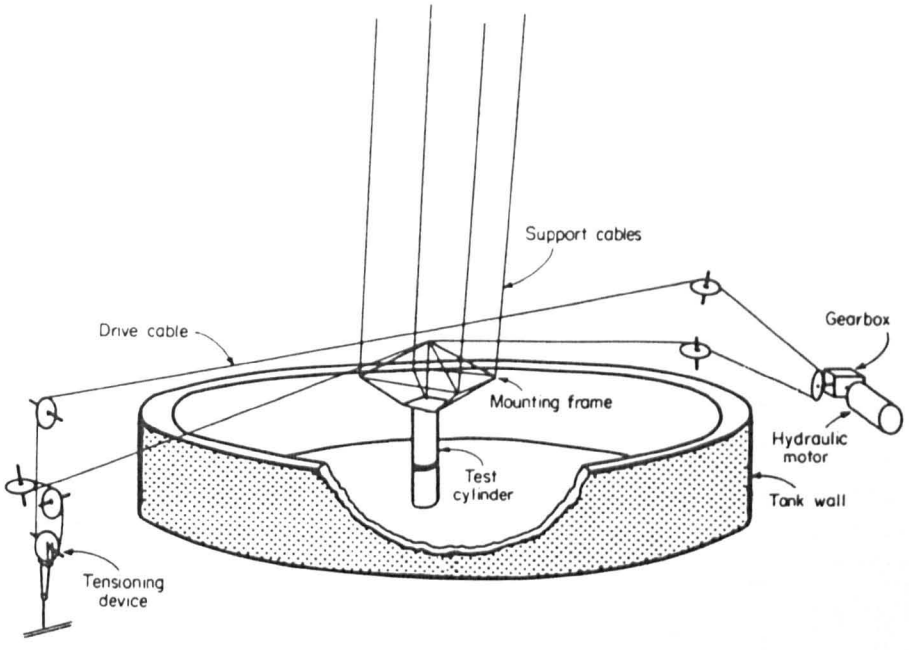

FIGURE 7.30 GENERAL ARRANGEMENT OF THE DRIVE SYSTEM (Chaplin, 1988a)

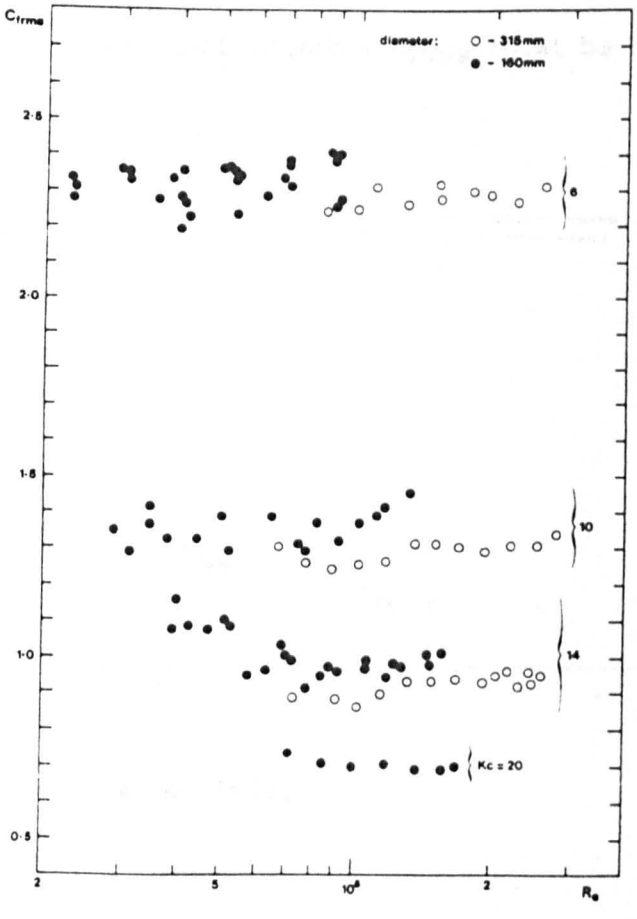

FIGURE 7.31 ROOT-MEAN-SQUARE IN-LINE FORCE COEFFICIENT VERSUS REYNOLDS NUMBER (Chaplin, 1988a)

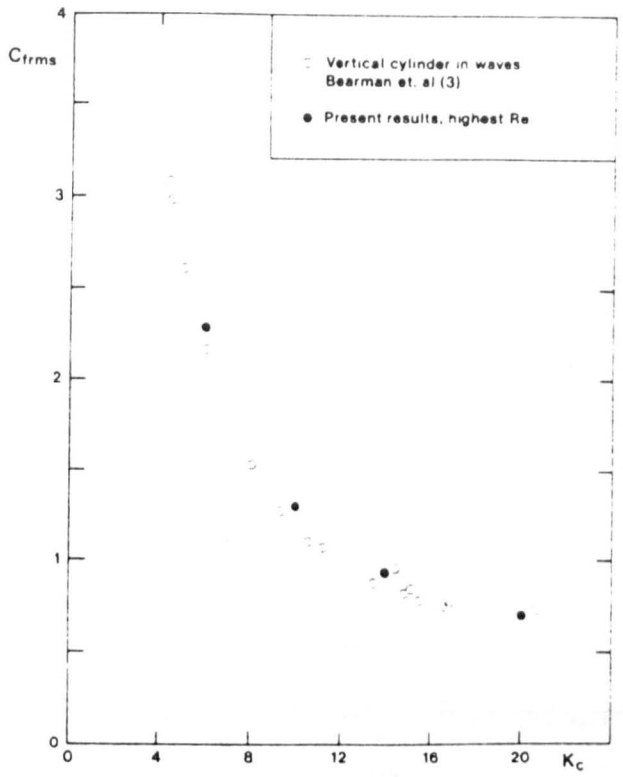

(a) (Chaplin,1988a)
Note: it seems that Chaplin's C_{frms} must be multiplied by 2

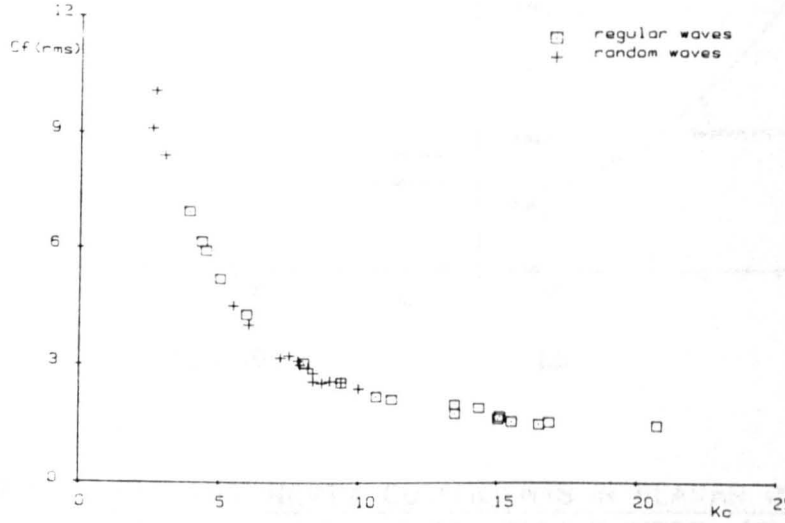

(b) (Bearman et al, 1985)

FIGURE 7.32 ROOT-MEAN-SQUARE IN-LINE FORCE COEFFICIENT AS A FUNCTION OF KEULEGAN-CARPENTER NUMBER

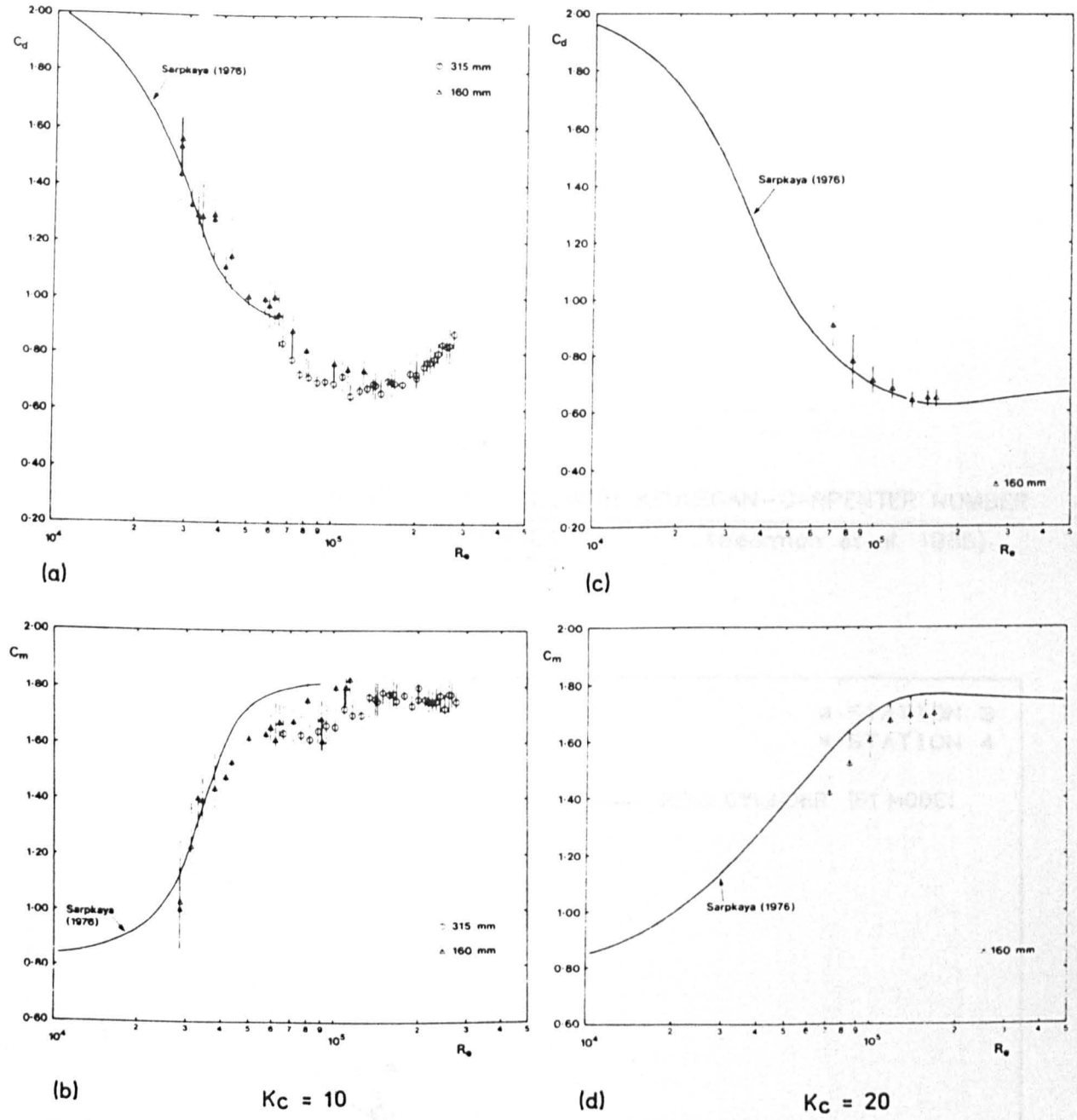

FIGURE 7.33. DRAG AND INERTIA COEFFICIENTS IN PLANAR OSCILLATORY FLOW AS A FUNCTION OF REYNOLDS NUMBER (Chaplin, 1988a)

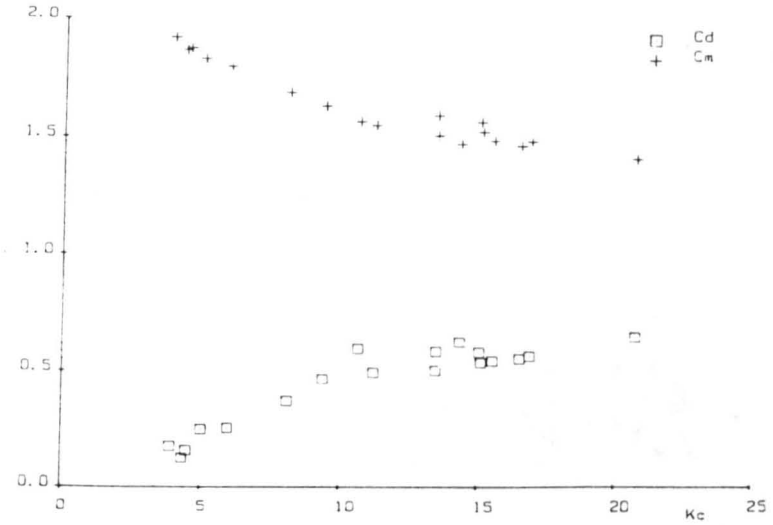

FIGURE 7.34 VARIATION OF C_d AND C_m WITH KEULEGAN–CARPENTER NUMBER FOR A RIGID CYLINDER (Bearman et al, 1985)

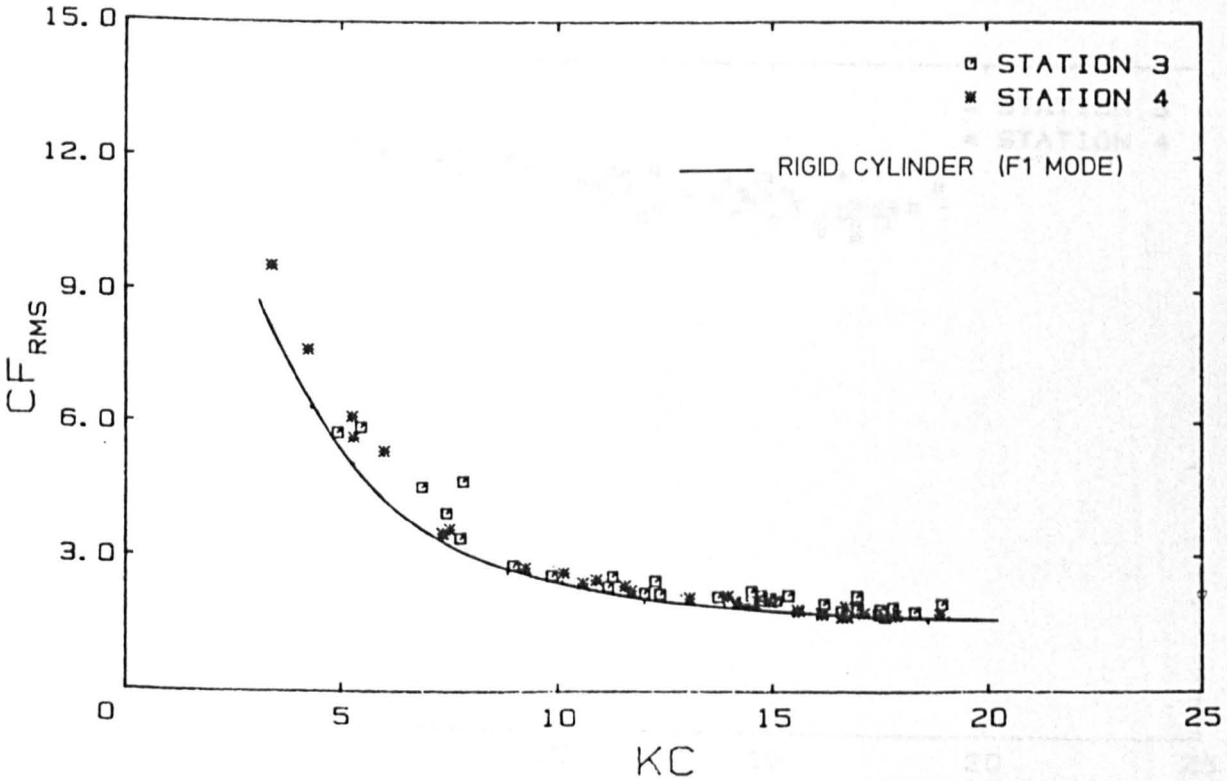

FIGURE 7.35 VARIATION OF IN–LINE TOTAL FORCE COEFFICIENT WITH K_c FOR THE FLEXIBLE CYLINDER (F6 MODE) (Bearman,1988)

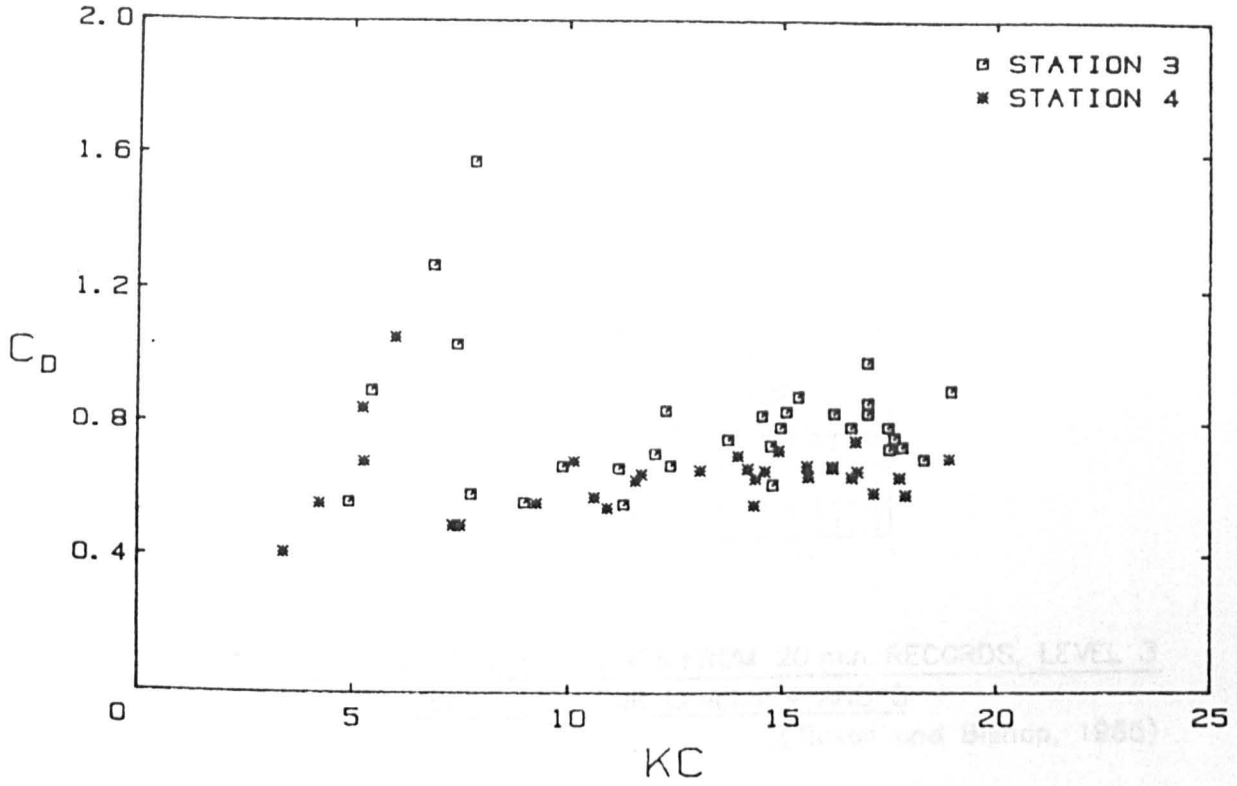

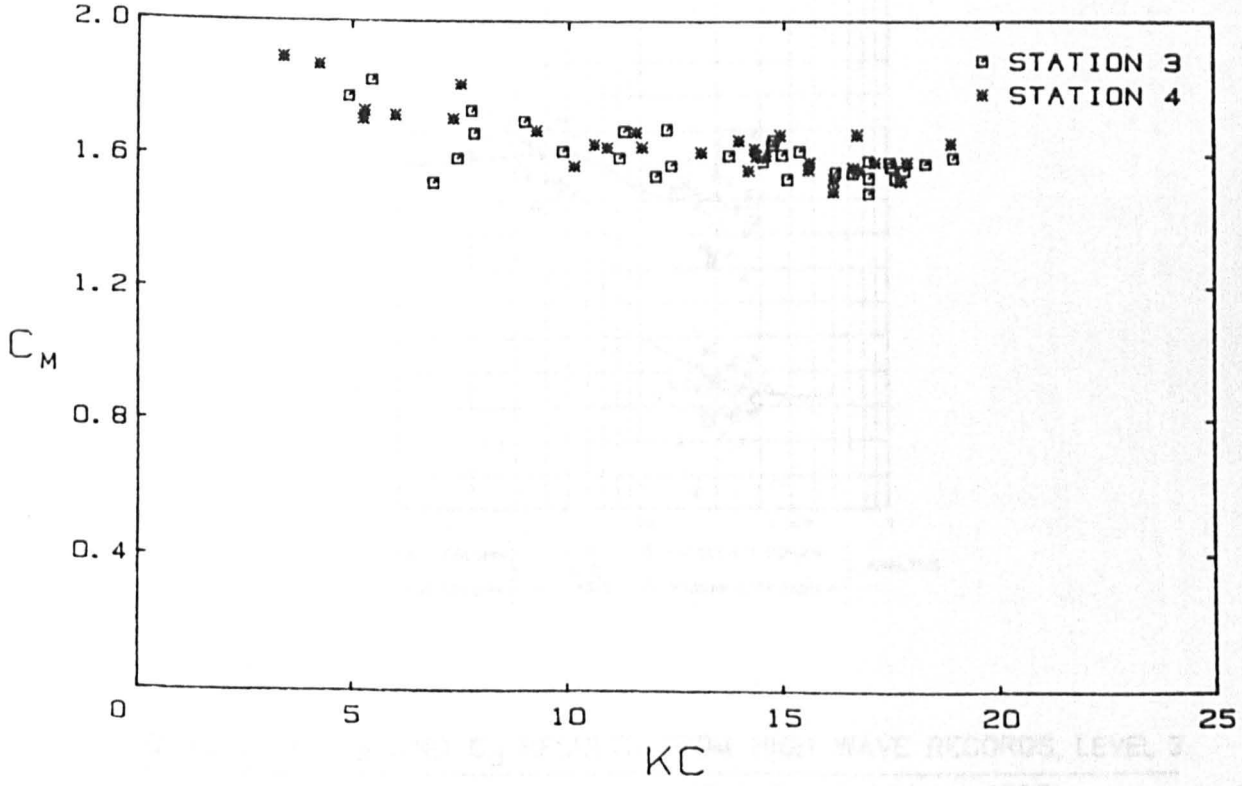

FIGURE 7.36 VARIATION OF C_d AND C_m WITH K_c FOR THE FLEXIBLE CYLINDER (F6 MODE) (Bearman, 1988)

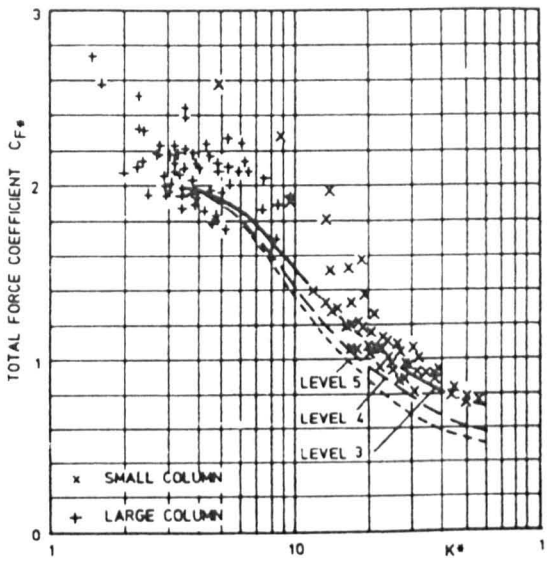

FIGURE 7.37 TOTAL FORCE COEFFICIENTS FROM 20 min. RECORDS, LEVEL 3 ALSO MEAN LINES FOR LEVELS 4 AND 5

(Tickell and Bishop, 1985)

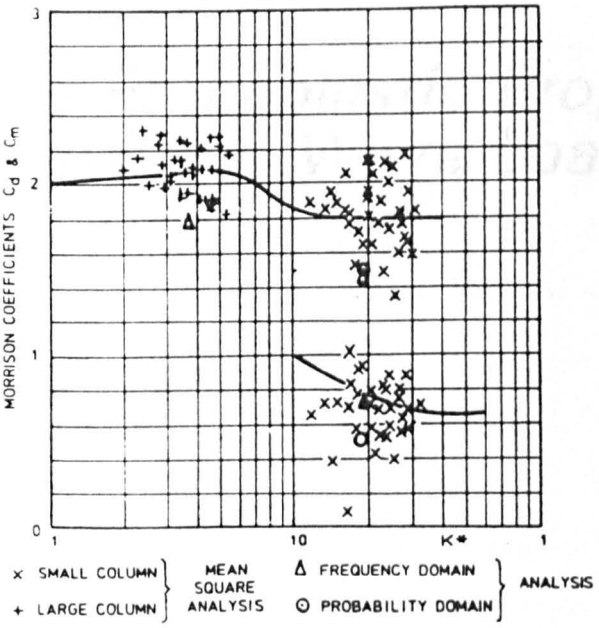

FIGURE 7.38 C_m AND C_d RESULTS FROM HIGH WAVE RECORDS, LEVEL 3.

(Tickell and Bishop, 1985)

Chapter 8

Spectral and Probabilistic Properties of Morison-Type Wave Loading

INTRODUCTION

This chapter is devoted to the study of spectral and probabilistic properties of Morison-type wave loading. In this regard, it should be noted that probabilistic properties of the response are similar to those of wave forces due to the linear nature of the relationship between the response and loading (for fixed offshore structures which do not respond dynamically to wave loading). The study of the spectral and probabilistic properties of wave loading is required for both parts of this thesis as will be explained below:

a) With regard to the Christchurch Bay project, the spectral and probabilistic properties of measured forces and their peaks will be established in Chapter 9. On the other hand, the spectral and probabilistic properties of water particle kinematics were established in Chapter 4. In this chapter, the theoretical effect of the nonlinear drag component of force on both spectral and probabilistic properties of water particle kinematics are studied. This paves the way for the assessment of the performance of Morison's equation in predicting the spectral and probabilistic properties of forces from the spectral and probabilistic properties of their associated water particle kinematics in Chapter 9.

b) With regard to the probabilistic analysis of offshore structures, the ultimate goal is to establish the long-term distribution of the response peaks. This is obtained by the convolution of the short-term distribution of the response peaks with the long-term distribution of the sea-states, as was explained in Chapter 5. The short-term properties of the peaks are obviously dependent on

the short-term properties of the force (or response) itself. Therefore, for the purpose of the probabilistic analysis of offshore structures, one has to study the short-term probability distributions of both the response and its peaks.

Section 8.1 is devoted to the probabilistic properties of the force itself. Section 8.2 is concerned with the short-term probability distribution of the peaks, while the short-term probability distribution of the extreme peak is the subject of study in Section 8.3. Section 8.4 is devoted to a brief discussion of the long-term distribution of the peaks. Finally, the relationship between the spectral properties of the force and water particle kinematics are established in Section 8.5.

8.1 SHORT-TERM PROBABILITY DISTRIBUTION OF MORISON-TYPE WAVE LOADING

8.1.1 UNIDIRECTIONAL SEAS

No Current

According to Morison's equation, wave loading per unit length on a vertical cylinder exposed to unidirectional waves can be expressed as

$$F = k_i \dot{u} + k_d u|u| \tag{8.1}$$

where all the variables are defined as in Chapter 7, and u and $\dot{u}$ are assumed to be Gaussian-distributed according to Linear Random Wave Theory. The probability distribution of force may be found in terms of the joint distribution of u and $\dot{u}$ by the method of transformation of variables (Pierson and Holmes, 1965). The general procedure for the transformation of variables is as follows (Papoulis, 1965).

Let W and X be functions of two random variables Y and Z. That is

$$W = f_1 (Y, Z) \tag{8.2}$$

and

$$X = f_2 (Y, Z) \tag{8.3}$$

For given values of W and X, i.e., W_o and X_o, let there be m pairs of roots for Equations (8.2) and (8.3), (i.e. Y_i, Z_i, i=1, m), then

$$p_{W,X} (W_o, X_o) = \sum_{i=1}^{m} \frac{p_{Y,Z} (Y_i, Z_i)}{|\text{Det } J[Y_i, Z_i]|} \tag{8.4}$$

$p_{W,X}(W_o, X_o)$ is the joint probability density function of W and X and Det J is the determinant of the Jacobian matrix defined as

$$J(Y,Z) = \begin{bmatrix} \frac{\partial f_1}{\partial Y} & \frac{\partial f_1}{\partial Z} \\ \frac{\partial f_2}{\partial Y} & \frac{\partial f_2}{\partial Z} \end{bmatrix} \tag{8.5}$$

Now in the case of Morison's equation, the joint pdf of u and $\dot{u}$ is known, from Linear Random Wave Theory, to be a mean-zero Gaussian pdf.

$$p(u,\dot{u}) = \frac{1}{2\pi\sigma_u\sigma_{\dot{u}}} \exp[-\frac{1}{2} (\frac{u^2}{\sigma_u^2} + \frac{\dot{u}^2}{\sigma_{\dot{u}}^2})] \tag{8.6}$$

where σ_u and $\sigma_{\dot{u}}$ are the standard deviations of water particle velocity and acceleration, respectively. In order to map between the u, $\dot{u}$ probability space and the force space, it is necessary to introduce a dummy variable such as

$$G = u \tag{8.7}$$

Then

$$p(F,G) = \frac{p(u,\dot{u})}{|\text{Det } J|} \tag{8.8}$$

where

$$J = \begin{bmatrix} 2k_d|u| & k_i \\ 1 & 0 \end{bmatrix} \tag{8.9}$$

Thus

$$|\text{Det } J| = k_i \tag{8.10}$$

and

$$p(F,G) = \frac{1}{2\pi k_i \sigma_u \sigma_{\dot{u}}} \exp\left[-\frac{1}{2} \left(\frac{u^2}{\sigma_u^2} + \frac{\dot{u}^2}{\sigma_{\dot{u}}^2}\right)\right] \tag{8.11}$$

The dummy variable G may be removed by integration with respect to G = u, leading to the following expression for the pdf of force (Tickell, 1977)

$$p(F) = \int_{-\infty}^{+\infty} p(F,G)dG = \frac{1}{2\pi k_i \sigma_u \sigma_{\dot{u}}} \int_{-\infty}^{+\infty} \exp\left[-\frac{1}{2}\left(\frac{u^2}{\sigma_u^2} + \frac{\dot{u}^2}{\sigma_{\dot{u}}^2}\right)\right]du \tag{8.12}$$

where

$$\dot{u} = (F - k_d\, u|u|)/k_i \tag{8.13}$$

The pdf given by Equation (8.12) will be referred to as Pierson/Holmes (P/H) distribution. In the absence of current, the odd-valued absolute moments of force are all zero. That is

$$E[F^{2j-1}] = 0 \quad , J = 1, 2, \ldots \tag{8.14}$$

The second and fourth moments are given by

$$\mu_2 = m_2 = E[F^2] = k_i\, \sigma_{\dot{u}}^2 + 3k_d^2\, \sigma_u^4 = \sigma_F^2 \tag{8.15}$$

and

$$\mu_4 = m_4 = E[F^4] = 3k_i^4 \sigma_{\dot{u}}^4 + 18k_i^2 k_d^2 \sigma_{\dot{u}}^2 \sigma_u^4 + 105k_d^4 \sigma_u^8 \tag{8.16}$$

Morison's equation can be rewritten as

$$F = x_1 + x_2|x_2| \tag{8.17}$$

where $x_1 = k_i\dot{u}$ and $x_2 = \sqrt{k_d}\, u$ are Gaussian random variables. Then the pdf of force will be

$$p(F) = \frac{1}{2\pi\sigma_{x1}\sigma_{x2}} \int_{-\infty}^{+\infty} \exp\left[-\frac{1}{2}\left(\frac{x_1^2}{\sigma_{x1}^2} + \frac{x_2^2}{\sigma_{x2}^2}\right)\right]dx_2 \tag{8.18}$$

where

$$x_1 = F - x_2|x_2| \tag{8.19}$$

The second and the fourth statistical moments of the above distribution are

$$\mu_2 = E[F^2] = \sigma_{x1}^2 + 3\sigma_{x2}^4 \tag{8.20a}$$

and

$$\mu_4 = E[F^4] = 3\sigma_{x1}^4 + 18\sigma_{x1}^2 \sigma_{x2}^4 + 105\sigma_{x2}^8 \tag{8.20b}$$

Knowing μ_2 and μ_4, the above two equations may be solved simultaneously for σ_{x1} and σ_{x2}. That is

$$\sigma_{x2}^2 = \left(\frac{E[F^4] - 3E[F^2]^2}{78}\right)^{1/4} = \left(\frac{\beta - 3}{78}\right)^{1/4} * \left(E[F_2^2]\right)^{1/2} \tag{8.21a}$$

and

$$\sigma_{x1}^2 = E[F^2] - 3\sigma_{x2}^4 = E[F^2] - 3E[F_2^2]\sqrt{\frac{\beta - 3}{78}} = \left(1 - 3\sqrt{\frac{\beta - 3}{78}}\right) * E[F^2] \tag{8.21b}$$

where β is the kurtosis of force defined as $\beta = \mu_4/\mu_2^2$

σ_{x1} and σ_{x2} are then used in Equation (8.18) to define the probability density function of the force. Therefore, in the absence of current, the pdf of force is fully defined by its second and fourth order statistical moments.

The pdf of force is clearly not of a Gaussian form which is fully defined by its second moment. A typical pdf and cumulative distribution function (cdf) are shown in Figure 8.1, compared with the Gaussian forms with the same variance. It is clear that in such a case, the level of force with a given probability of exceedence is higher in the tails of the distribution than would be predicted from a Gaussian form.

As previously mentioned the ratio of μ_4 to μ_2^2 is known as the kurtosis and is denoted by β

$$\beta = \frac{\mu_4}{\mu_2^2} \tag{8.22}$$

Substituting for μ_4 and μ_2 from Equations (8.20-a) and (8.20-b) leads to

$$\beta = 3 + \frac{78}{[3 + \frac{k_i^2 \sigma_{\dot{u}}^2}{k_d^2 \sigma_u^4}]^2} \tag{8.23}$$

Hence, for inertia dominated loading ($k_i \sigma_{\dot{u}} >> k_d \sigma_u^2$), $\beta \rightarrow 3.0$ (Gaussian distribution) and for drag dominated loading ($k_d \sigma_u^2 >> k_i \sigma_{\dot{u}}$), $\beta \rightarrow 11.67$. Therefore, the kurtosis serves as a measure of the importance of the nonlinear drag term and the higher the value of the kurtosis, the more marked is the departure of the force distribution from Gaussian distribution, as shown in Figure 8.2.

With Current

In the presence of a current $\bar{u}$, the pdf of force will be

$$p(F) = \frac{1}{2\pi\sigma_{x1}\sigma_{x2}} \int_{-\infty}^{+\infty} \exp\left\{-\frac{1}{2}\left[\frac{x_1^2}{\sigma_{x1}^2} + \frac{(x_2 - \bar{x}_2)^2}{\sigma_{x2}^2}\right]\right\} dx_2 \tag{8.24}$$

where

$$\begin{cases} x_2 = \sqrt{k_d}\,(u + \bar{u}) \text{ (u is the wave-induced horizontal velocity)} & (8.25) \\ x_1 = k_i\,\dot{u} = F - x_2|x_2| & (8.26) \\ \sigma_{x1} = k_i\,\sigma_{\dot{u}} & (8.27) \\ \sigma_{x2} = \sqrt{k_d}\,\sigma_u & (8.28) \\ \bar{x}_2 = \sqrt{k_d}\,\bar{u} & (8.29) \end{cases}$$

When current is not zero, the odd-valued statistical moments are no longer zero, i.e. $E[F] \neq 0$, $E[F^3] \neq 0$ and the pdf is skewed to the right or left depending on the sense of the current. The first four statistical moments of force are (Borgman, 1967)

$$m_1 = E[F] = 2\sigma_{x2}^2\,[\gamma Z(\gamma) + (\gamma^2 + 1)\,Q(\gamma)] \tag{8.30}$$

$$m_2 = E[F^2] = \sigma_{x2}^4\,[3 + 6\gamma^2 + \gamma^4) + \sigma_{x1}^2 \tag{8.31}$$

$$\begin{aligned} m_3 = E[F^3] &= 2\gamma Z(\gamma)[(\gamma^4 + 14\gamma^2 + 33)\,\sigma_{x2}^6 + 3\,\sigma_{x1}^2\,\sigma_{x2}^2] \\ &+ 2Q(\gamma)[(\gamma^6 + 15\gamma^4 + 45\gamma^2 + 15)\,\sigma_{x2}^6 + 3(\gamma^2 + 1) \\ &\sigma_{x1}^2\,\sigma_{x2}^2] \end{aligned} \tag{8.32}$$

$$\begin{aligned} m_4 = E[F^4] &= \sigma_{x2}^8\,(\gamma^8 + 28\gamma^6 + 210\gamma^4 + 420\gamma^2 + 105) \\ &+ 6\sigma_{x1}^2\,\sigma_{x2}^4\,(\gamma^4 + 6\gamma^2 + 3) + 3\sigma_{x1}^4 \end{aligned} \tag{8.33}$$

where

$$\gamma = \frac{\bar{x}_2}{\sigma_{x2}} = \frac{\bar{u}}{\sigma_u} \tag{8.34}$$

$$Z(\gamma) = \frac{1}{\sqrt{2\pi}} \exp\left(-\frac{\gamma^2}{2}\right) \tag{8.35}$$

and

$$Q(\gamma) = \int_0^{\gamma} Z(Y)\, dY \tag{8.36}$$

The pdf and cdf can be calculated once σ_{x1}, σ_{x2} and $\gamma = \bar{x}_2/\sigma_{x2}$ are known and these can be found from the solution of any 3 of the four equations giving the first four statistical moments of force. That is why the distribution of force in the presence of current is sometimes referred to as a PH3 distribution.

8.1.2 SHORT-CRESTED SEAS

When a vertical pile is subjected to a short-crested sea, there will be forces in two orthogonal directions in the horizontal plane, as shown in Figure 8.3. According to Morison's equation, the horizontal components of force per unit length are (note that lift forces have not been included),

$$F_x = k_i \dot{u} + k_d u (u^2 + v^2)^{1/2} \tag{8.37}$$

$$F_y = k_i \dot{v} + k_d v (u^2 + v^2)^{1/2} \tag{8.38}$$

Tickell and Elwany (1979) have derived the joint probability distribution of F_x and F_y in the absence of current. They rewrote Equations (8.37) and (8.38) in the following form.

$$F_x = \psi_1 + \psi_3 (\psi_3^2 + \psi_4^2)^{1/2} \tag{8.39}$$

$$F_y = \psi_2 + \psi_4 (\psi_3^2 + \psi_4^2)^{1/2} \tag{8.40}$$

in which $\psi_1 = k_i\dot{u}$; $\psi_2 = k_i\dot{v}$; $\psi_3 = \sqrt{k_d}\, u$ and $\psi_4 = \sqrt{k_d}\, v$.

Following the method of transformation of variables, the joint pdf of F_x and F_y is

$$p(F_x,F_y) = \int_{-\infty}^{+\infty}\int_{-\infty}^{+\infty} \frac{\exp[-\{\psi\}\{\mu\}^{-1}\{\psi\}^T/2]}{4\pi^2\sqrt{\text{Det }\mu}}\, d\psi_3\, d\psi_4 \tag{8.41}$$

where in evaluating the above integral,

$$\psi_1 = F_x - \psi_3\,(\psi_3^2 + \psi_4^2)^{1/2} \tag{8.42}$$

$$\psi_2 = F_y - \psi_4\,(\psi_3^2 + \psi_4^2)^{1/2} \tag{8.43}$$

$$\{\psi\} = \{\psi_1,\ \psi_2,\ \psi_3,\ \psi_4\} \tag{8.44}$$

$\{\psi\}^T$ is the transpose of $\{\psi\}$ and the matrix μ consists of the second moments of $\{\psi\}$. That is

$$\mu = \begin{bmatrix} C_{11} & C_{12} & C_{13} & C_{14} \\ C_{21} & C_{22} & C_{23} & C_{24} \\ C_{31} & C_{32} & C_{33} & C_{34} \\ C_{41} & C_{42} & C_{43} & C_{44} \end{bmatrix} \tag{8.45}$$

where

$$C_{ij} = E[\psi_i\ \psi_j] \tag{8.46}$$

The pdf is of Pierson/Holmes type and is fully defined when m_{20}, m_{11}, m_{40}, m_{31} and m_{22} are known, where $m_{kl} = E[F_x^k F_y^l]$. Tickell and Elwany (1979) compared the cdf of simulated force data in a directional sea with their theoretical distribution and found it to be satisfactory, as shown in Figure 8.4. Figure 8.4 also shows $P(F_x)$ obtained by introducing the theoretical second and fourth moment of force (m_{20} and m_{40}) into the expression for the distribution of force for a long-crested sea (Equations (8.18) to (8.20)) and found it to be in very good agreement

with the theoretical distribution. Therefore, the theoretical distribution of force in the predominant wave direction can be obtained by calculating the second and fourth order moments of force component in the predominant wave direction in conjunction with Equations (8.18) to (8.20).

Finally, it should be noted that Tickell (1977) has demonstrated by analysis of prototype data that the distribution of structural response (stress, displacement) is similar to that of wave loading. In other words, structural response follows P/H distribution (Figure 8.5). Hence, the content of this chapter with regard to the probabilistic properties of wave loading is also valid for the probabilistic properties of structural response.

8.2 THE PROBABILITY DISTRIBUTION OF PEAK FORCES

In design applications it is the probabilistic distribution of the peak and extreme values of either load or response, rather than the basic variate, that are of most importance. Distribution of peak values may be transformed into the pdfs of stress range required in fatigue analyses to check the long-term integrity of structures and they also form the input to the distribution of extreme values necessary for the assessment of risk of first excursion failure.

The theory covering the probability structure of the peaks of random variables is given by Lin (1967). A positive peak (maximum or crest) on the time history of F(t) corresponds to the condition of zero slope, $\dot{F}(t) = 0$, and $\ddot{F}(t) \leq 0$, where $\dot{F}$ and $\ddot{F}$ are the first and second order derivatives of F, respectively. Using this criteria, Lin has shown that

$E[M(q)]$, the number of positive peaks per unit time of magnitude greater than or equal to a force level $F = q$, is

$$E[M(q)] = -\int_{q}^{\infty}\int_{-\infty}^{0} \ddot{F}\, p(F, \dot{F} = 0, \ddot{F})\, d\ddot{F}\, dF \tag{8.47}$$

where $p(F, \dot{F}, \ddot{F})$ is the joint probability distribution of force and its two first derivatives. The total number of positive peaks, $E[M_T]$ is obtained by setting $q = -\infty$. That is

$$E[M_T] = -\int_{-\infty}^{\infty}\int_{-\infty}^{0} \ddot{F}\, p(F, \dot{F} = 0, \ddot{F})\, d\ddot{F}\, dF \tag{8.48}$$

The cumulative peak distribution, $P_p(q)$, can then be determined from

$$P_p(q) = 1 - \frac{E[M(q)]}{E[M_T]} \tag{8.49}$$

The above distribution is referred to as the wide-band peak distribution as opposed to the narrow-band peak distribution obtained from the assumption of a narrow-band force.

The joint pdf of force and its two derivatives needed in Equations (8.47) and (8.48) can be obtained in the following manner (Tickell, 1977). Differentiation of Morison's equation with respect to time leads to the following relationships.

$$F = k_d\, u|u| + k_i\, du/dt \tag{8.50}$$

$$\dot{F} = 2k_d|u|\, du/dt + k_i d^2u/dt^2 \tag{8.51}$$

$$\ddot{F} = 2k_d|u|\, d^2u/dt^2 + 2k_d\, (du/dt)^2\, \mathrm{sign}(u) + k_i\, d^3u/dt^3 \tag{8.52}$$

The method of transformation of variables can be used to obtain the pdf of $(F) = (F, \dot{F}, \ddot{F}, G)$, where $G = u$ is an auxiliary variable $G = u$, from

the pdf of $\{u\} = \{u, du/dt, d^2u/dt^2, d^3u/dt^3\}$. The variables $\{u\}$ are jointly Gaussian distributed with the following distribution

$$p(u,du/dt, d^2u/dt^2, d^3u/dt^3) = \frac{1}{4\pi^2\sqrt{Det[\mu]}} \exp\left[-\frac{1}{2}\{u\}[\mu]^{-1}\{u\}^T\right] \tag{8.53}$$

where $\{u\}^T$ is the transpose of $\{u\}$ and $[\mu]$ is the square matrix of cross-covariances

$$[\mu] = \begin{bmatrix} m_0 & 0 & -m_2 & 0 \\ 0 & m_2 & 0 & -m_4 \\ -m_2 & 0 & m_4 & 0 \\ 0 & -m_4 & 0 & m_6 \end{bmatrix} \tag{8.54}$$

where

$$m_j = \int_0^\infty \omega^j G_{uu}(\omega)\, d\omega$$

the determinant of the Jacobian matrix needed in derivation of pdf of $\{F\}$ is k_i^3. Therefore,

$$p(F, \dot{F}, \ddot{F}, u) = \frac{p(u)}{k_i^3} \tag{8.55}$$

and the pdf of F, $\dot{F}$, $\ddot{F}$ is obtained by integrating out the auxiliary variable $G = u$. Therefore,

$$p(F, \dot{F} = 0, \ddot{F}) = \frac{1}{4\pi^2\sqrt{Det[\mu]}\, k_i^3} \int_{-\infty}^{+\infty} \exp\left[-\frac{1}{2}\{u\}[\mu]^{-1}\{u\}^T\right] du \tag{8.56}$$

where in evaluating Equation (8.56)

$$\frac{du}{dt} = (F - k_d\, u|u|)/k_i \tag{8.57}$$

$$d^2u/dt^2 = - (2k_d|u|du/dt)/k_i \tag{8.58}$$

$$d^3u/dt^3 = [\dot{F} - 2k_d|u|d^2u/dt^2 - 2k_d(du/dt)^2 \text{ sign}(u)]/k_i \tag{8.59}$$

The peak distribution thus derived is referred to as wide-band peak distribution and is applicable to time series with a general bandwidth form. It therefore includes the occurrence of peaks below mean level for a wide-band (wb) spectrum. It is obvious that the wb peak distribution is computationally very demanding. The peak distribution can be simplified if one assumes that the force is narrow-banded. Tickell (1977) has shown by analysis of prototype data that the assumption has little effect on the distribution of force peaks.

For a narrow-banded process, each threshold crossing with positive slope leads to a single positive peak and all positive peaks (maxima) have positive magnitudes. Under these conditions, the peak distribution may be simplified to

$$P_p(q) = 1 - \frac{E[N^+(q)]}{E[N^+(0)]} \tag{8.60}$$

where $E[N^+(q)]$ is the number of upward threshold crossings of $F = q$.

Lin (1967) has shown that the number of upward crossings of a threshold level $F = q$, $E[N^+(q)]$, is

$$E[N^+(q)] = \int_0^\infty \dot{f}\, p(F = q, \dot{F})\, d\dot{f} \tag{8.61}$$

substituting the above equation into Equation (8.60) leads to

$$P_p(F = q) = 1 - \frac{\int_0^\infty \dot{F}\, p(F = q, \dot{F})\, d\dot{F}}{\int_0^\infty \dot{F}\, p(F = 0, \dot{F})\, d\dot{F}} \qquad (8.62)$$

This distribution, referred to as 'type 1' narrow-band distribution, is simpler than the wide band distribution because it does not involve the second order derivative of force. The 'type 1' narrow-band distribution can be obtained in terms of the joint pdf of u, ú, ü, in a manner similar to the wide band distribution and is not repeated here.

If F and $\dot{F}$ are assumed to be statistically independent, a simplified expression results, termed the 'type 2' narrow-band peak distribution. The joint pdf of F and $\dot{F}$ under the independence assumption is

$$p(F, \dot{F}) = p(F)\, p(\dot{F}) \qquad (8.63)$$

Replacing this equation into Equation (8.62), yields

$$P_p\,(F = q) = 1 - \frac{p(F = q)}{p(F = 0)} \qquad (8.64)$$

The great advantage of the 'type 2' approximation is that it represents a considerable reduction in computational effort over the 'type 1' approach, requiring only the P/H probability densities for its evaluation.

A standardised plot of the 'type 2' peak distributions is shown in Figure 8.6. The plots are made on Rayleigh paper since the narrow-band Gaussian process ($\beta = 3.0$) has peak values following the Rayleigh pdf.

Comparison of Theoretical Peak Distributions with Prototype Data

Tickell (1977) has compared the peak distributions of the prototype stress records with 'type 2' narrow-band theoretical distribution (Figure 8.7). The fact that the stress records are not narrow-banded is obvious since peaks were identified below the mean value of the stress. In addition to the 'type 2' distribution, the theoretical peak distribution for a wide-band Gaussian process and the Rayleigh distribution, which results from a narrow-band Gaussian process, have been plotted. The Rayleigh and the 'type 2' distributions do not compare favourably with the observed behaviour at low stress levels due to their narrow-band assumption which leads to positive peaks only. However, the 'type 2' distribution approaches the observed distribution at higher levels. Both the Rayleigh and wide-band peak distributions, arising from the assumption of a Gaussian distribution for the basic stress, significantly underestimate peak values with low probability of exceedence (say less than 1%).

In fatigue calculations, it is the probability distribution of the stress range which is required. Tickell (1977) compared prototype cumulative distribution range with its theoretical distribution. The prototype stress range was defined as the magnitude of the stress reversal measured from the highest peak to the lowest trough between two successive upward zero-crossings. The theoretical stress range was defined based on the narrow-band assumption that each value of positive peak is associated with a negative trough of equal magnitude between successive upcrossings, that is, stress range = 2 * peak. As demonstrated in Figure (8.8), the results showed that the non-Gaussian stress range provides a much better fit to the data than the Rayleigh

distribution resulting from the assumption that force is Gaussian distributed.

Comparison of Theoretical Peak Distributions with Simulated Force Data

In addition to the comparison of prototype data with the above mentioned theoretical peak distributions, Tickell (1977) compared simulated wave force data based on Morison's equation with these theoretical models. His results, shown in Figures 8.9 to 8.11, revealed that the 'type 1' narrow-band approximation gives a satisfactory distribution when compared with the full wide-band model for all degrees of non-linearity. The 'type 2' narrow-band approximation gives a reasonable estimate of the approximation when the kurtosis is low, say less than 4.5. However, at higher values of kurtosis, the 'type 2' distribution underestimates the high stress levels but still it is much better than the Rayleigh distribution resulting from the linearisation of the drag term. It should be noted that a modification was introduced in the case of wide-band model. That is the cdf was obtained for positive peaks only by setting the lower limit of the first integral in Equation (8.48) equal to zero rather than minus infinity.

8.3 THE PROBABILITY DISTRIBUTION OF EXTREME PEAKS

The distribution of extreme peaks is derived from the distribution of peaks by applying the theory of Gumbel. If all the peaks in a record are assumed to be independent then, the probability of all the peaks (or the extreme peak) in a record of N peaks, to be smaller than the given value is

$$P_{ep}(F) = [P_p(F)]^N \qquad (8.65)$$

This distribution may be used to assess the risk of exceedence of a particular level of F during a period of exposure equivalent to the passage of N cycles for application in first-excursion failure analysis.

The pdf of the extreme force is obtained by differentiating Equation (8.65) with respect to F. That is

$$p_{ep}(F) = \frac{dP_{ep}(F)}{dF} = N[P_p(F)]^{N-1}\, p_p(F) \tag{8.66}$$

and the expected value of extreme peak force, $E[F_{max}]$, is obtained as

$$E[F_{max}] = \int_0^\infty F p_{ep}(F)\, dF \tag{8.67}$$

For a given duration, the number of peaks, N, can be estimated using the spectral moments of force in the same way as was done for wave processes (Equation (3.58)).

Tickell calculated the extreme peak statistics for a 1.0m diameter member for a storm with assumed durations ranging from 1 hour to 12 hours (Figure 8.12). These statistics include the expected value of the extreme peak, $E[F_{max}]$, based on the three theoretical models for the non-Gaussian distribution of force (wb, nb1, nb2). For comparison, the same statistic was also calculated assuming that the force was Gaussian distributed. Furthermore, the peak force which would occur during the passage of an equivalent deterministic wave is shown. The wave height was taken to be the expected maximum wave height for the duration considered and the wave period was taken to be the expected zero-crossing period. Stoke's fifth order wave theory was used to compute

the fluid kinematics. The extreme peak with one percent probability of exceedence during the storm duration is also given. The following comments about the accuracy of these extreme events with very low probability of exceedence are worthy of report here.

The number of peaks in a 10 hour storm is in the order of several thousands. Let us assume that there are 5000 peaks in that duration. Then, the cdf of the extreme peak would be

$$P_{ep}(F) = [P_p(F)]^{5000} \tag{8.68}$$

A probability of exceedence of 0.01 for the extreme peak requires that $P_p(F)^{5000} = 0.99$ or $P_p(F) = 0.999998$. In other words, the probability of exceedence of the peak force itself is $2*10^{-6}$. The problem is that there is no firm evidence that the theoretical distributions are valid at these very low levels of probability of exceedence. Tickell has demonstrated that the theoretical distributions are valid up to a probability of exceedence of at least 0.01 (Figure 8.5). Of course, it is understood that practically it is very difficult if not impossible to verify the theoretical distributions against prototype data for very low values of probability of exceedence, as that requires very long records and even then the question of stationarity of the record would be raised. The above comments are only meant to serve as a caution against the use of the extreme values obtained from probabilistic methods without a thorough examination. The author intuitively believes that the extreme events with very low probability of exceedence can be conservative because the underlying probability distribution assigns a very small but non-zero probability to events which are physically impossible. In view of the above comments, extreme events predicted from 'type 2' narrow-band distribution, which are somewhat smaller than

those predicted from the 'type 1' narrow-band distribution, may be closer to the real value of these extreme events.

8.4 LONG-TERM PROBABILITY DISTRIBUTION OF FORCE (RESPONSE) PEAKS

The long-term probability distribution of peaks is obtained by convoluting the short-term distribution of the peaks with the long-term distribution of sea states or wave conditions in a similar way to that of the wave heights discussed in Chapter 5 (Tickell et al, 1976). Tickell's results indicate that for drag dominated cases, the 'type 2' long-term distribution is somewhat smaller than the 'type 1' distribution at low values of probability of exceedence. However, in view of the considerable reduction in computer run-time, the use of the 'type 2' distribution is recommended except for cases where the load (response) is strongly drag dominated. The long-term probability distribution of extreme peaks required in the first-excursion failure analysis of a structure is derived from the long-term distribution of peaks according to Gumbel's theory as was the case for the short-term distribution of extreme peaks. That is

$$P_{epLT}(F) = [P_{PLT}(F)]^N \tag{8.69}$$

where N is the total number of peaks.

8.5 FORCE SPECTRUM

The spectrum of force can be derived by first obtaining its auto correlation function. The force and the auto correlation function are, respectively

$$F(t) = k_d\, u(t)|u(t)| + k_i\, \dot{u}(t) \tag{8.70}$$

and

$$R_{FF}(\tau) = E[F(t)F(t+\tau)] = k_d^2 E[u(t)|u(t)|*u(t+\tau)|u(t+\tau)|] + k_i^2 E[\dot{u}(t)\dot{u}(t+\tau)] + k_d k_i E[u(t)|u(t)|\dot{u}(t+\tau)] + k_d k_i E[u(t+\tau)|u(t+\tau)|\dot{u}(t)] \quad (8.71)$$

Assuming that water particle kinematics are Gaussian distributed the expectations in the above equation are (Borgman, 1967)

$$E[u(t)|u(t)|*u(t+\tau)|u(t+\tau)|] = G[\rho_{uu}(\tau)] * \sigma_u^4 \quad (8.72)$$

where

$$\rho_{uu}(\tau) = \frac{E[u(t)u(t+\tau)]}{\sigma_u^2} = \frac{R_{uu}(\tau)}{\sigma_u^2} \quad (8.73)$$

and

$$G(r) = \frac{1}{\pi}[(4r^2 + 2)\sin^{-1}(r) + 6r\sqrt{1 - r^2}] \quad (8.74)$$

$$E[u(t)|u(t)|\dot{u}(t+\tau)] = \frac{4}{\sqrt{2\pi}} * \rho_{u,\dot{u}}(\tau) * \sigma_u^2 \sigma_{\dot{u}} \quad (8.75)$$

$$E[u(t+\tau)|u(t+\tau)|\dot{u}(t)] = \frac{4}{\sqrt{2\pi}} * \rho_{\dot{u},u}(\tau) * \sigma_u^2 \sigma_{\dot{u}} \quad (8.76)$$

Borgman (1967) has shown that $\rho_{u,\dot{u}}(\tau) = -\rho_{\dot{u},u}(\tau)$; therefore Equation (8.71) can be rewritten as

$$R_{FF}(\tau) = k_d^2 \sigma_u^4 G[R_{uu}(\tau)/\sigma_u^2] + k_i^2 R_{\dot{u}\dot{u}}(\tau) \quad (8.77)$$

The function G(r) may be expressed as a power series in r; that is

$$G(r) = \frac{1}{\pi}\left(8r + \frac{4}{3}r^3 + \frac{1}{15}r^5 + \ldots\ldots\right) \quad (8.78)$$

The spectrum of the wave force is the Fourier Transform of the auto correlation function.

$$G_{FF}(\omega) = \frac{2}{\pi} \int_0^{\infty} R_{FF}(\tau) \cos(\omega\tau)\, d\tau \tag{8.79}$$

There is no closed-form solution for the above integral. However, by approximating G(r) with the first term of the expansion series, that is, by assuming that G(r) is equal to the following linear function of r

$$G(r) \approx \frac{8r}{\pi} \tag{8.80}$$

Then $R_{FF}(\tau)$ from Equation (8.77) will be

$$R_{FF}(\tau) = \frac{8}{\pi} k_d^2 \sigma_u^2 R_{uu}(\tau) + k_i^2 R_{\dot{u}\dot{u}}(\tau) \tag{8.81}$$

which leads to the following approximation for the force spectrum

$$G_{FF}(\omega) \approx \frac{8}{\pi} k_d^2 \sigma_u^2 G_{uu}(\omega) + k_i^2 G_{\dot{u}\dot{u}}(\omega) \tag{8.82}$$

The above expression for the force spectrum can be obtained by linearising the drag component in the Morison's equation (Borgman, 1972). That is by assuming

$$u|u| \approx cu \tag{8.83}$$

The coefficient c is obtained by minimising the expected value of the square of the error term, where the error term is

$$\Delta = u|u| - cu \tag{8.84}$$

Raising both sides of the above equation to the second power leads to

$$\Delta^2 = u^4 + c^2u^2 - 2cu^2|u| \tag{8.85}$$

Therefore

$$E[\Delta^2] = E[u^4] + c^2E[u^2] - 2cE[u^2|u|] \tag{8.86}$$

The above expectation is minimum when

$$\frac{dE[\Delta^2]}{dc} = 0 \tag{8.87}$$

from which it follows that

$$\frac{dE[\Delta^2]}{dc} = 2cE[u^2] - 2E[u^2|u|] = 0 \tag{8.88}$$

or

$$c = \frac{E[u^2|u|]}{E[u^2]} = \frac{\sqrt{8/\pi} * \sigma_u^3}{\sigma_u^2} = \sqrt{8/\pi} * \sigma_u \tag{8.89}$$

Hence, the linearised form of the Morison's equation is (Borgman, 1972)

$$\hat{F} = \sqrt{8/\pi}\, k_d\, \sigma_u\, u + k_i\, \dot{u} \tag{8.90}$$

The above expression, leads to an autocorrelation function and frequency spectrum as in Equations (8.81) and (8.82).

The force spectra resulting from the linearisation of the drag component fit the measured field force spectra quite well and it is therefore valid to use the linearised form of Morison's equation in the Frequency domain. However, the coefficient derived by Borgman (1972) underestimates the variance of the loading. The variances of the nonlinear and the linearised form of Morison's loading are respectively,

$$\sigma_F^2 = 3k_d^2\, \sigma_u^4 + k_i^2\, \sigma_{\dot{u}}^2 \tag{8.91}$$

and

$$\sigma_f^2 = \frac{8}{\pi} k_d^2 \sigma_u^4 + k_i^2 \sigma_{\dot{u}}^2 \tag{8.92}$$

which leads to the following difference between the two variances

$$\sigma_F^2 - \sigma_f^2 = (3 - \frac{8}{\pi}) k_d^2 \sigma_u^4 \approx 0.454 \, k_d^2 \sigma_u^4 \tag{8.93}$$

The underestimation of variance as a result of linearisation is

$$\frac{\sigma_F^2 - \sigma_f^2}{\sigma_F^2} = \frac{0.454 k_d^2 \sigma_u^4}{3 k_d^2 \sigma_u^4 + k_i^2 \sigma_{\dot{u}}^2} \tag{8.94}$$

The underestimation is most significant when the force is drag dominated. The maximum possible value for the underestimation of variance is

$$[\frac{\sigma_F^2 - \sigma_f^2}{\sigma_F^2}]_{max} = \frac{0.454}{3} = 0.15 \tag{8.95}$$

The criterion used for the derivation of the linearisation coefficient, i.e. minimisation of the error term is not justifiable. That criterion means that if one wishes to use the linear form of Morison's equation in the time domain, then the coefficient $c = \sqrt{8/\pi}$ minimises the expected value of the square of the error term. However, the linear form of Morison's equation is not used in the time domain, as it is inaccurate. The linearisation technique is used only in the frequency domain, and as such, the best criterion to be used is to ensure that the variance of the nonlinear drag term and the linearised drag term are equal, i.e.

$$E[u^4] = c^2 \sigma_u^2 E[u^2] \tag{8.96}$$

which leads to

$$c^2 = 3 \tag{8.97}$$

Therefore, the force spectrum would be

$$G_{FF}(\omega) = 3k_d^2 \sigma_u^2 G_{uu}(\omega) + k_i^2 G_{\dot{u}\dot{u}}(\omega) \tag{8.98}$$

The use of the coefficient $c^2 = 8/\pi$ rather than $c^2 = 3$, causes a consistent overestimation of the drag coefficient by 8.5%, when spectral methods are used in derivation of Morison's coefficients. The reason for this is explained below. If the drag coefficient obtained by using $c^2 = 8/\pi$ and $c^2 = 3$ are denoted by $\acute{k}_d$ and k_d, respectively, then equating the variance of the drag term in both cases results in

$$3k_d^2 \sigma_u^2 G_{uu}(\omega) = \frac{8}{\pi} \acute{k}_d^2 \sigma_u^2 G_{uu}(\omega) \tag{8.99}$$

or

$$\frac{\acute{k}_d}{k_d} = (3\pi/8)^{1/2} = 1.085 \tag{8.100}$$

As will be fully discussed in Chapter 9, the important criteria for determining parameters when a function is approximated by another function in the analysis of random processes is that (a) the correlation coefficient between the two functions is maximised and (b) the variances of the two functions will be equal. In linearising the drag term, $u|u|$ is replaced by cu. Assuming that u is Gaussian distributed, the correlation coefficient between $u|u|$ and cu is

$$\rho_{u|u|,cu} = \frac{E[u|u| * cu]}{\sqrt{E[u^4]} \cdot \sqrt{E[c^2u^2]}} = \frac{c\sqrt{8/\pi}\,\sigma_u^3}{\sqrt{3\sigma_u^4} * \sqrt{c^2\sigma_u^2}} = \sqrt{8/3\pi} \approx 0.921 \qquad (8.101)$$

The correlation coefficient is independent of c. Therefore, there is no preference between different values of c as far as the correlation coefficient is concerned. However, equating the variances of $u|u|$ and cu leads to $c = \sqrt{3}$ as was previously discussed.

Finally, the following point deserves attention. Assuming that u is a sinusoidal function of time, then $u|u|$ (drag component) contains components at odd multiples of the fundamental frequency. The contribution to the mean-square drag component arising from components at the fundamental frequency and at the third and fifth harmonics are 96.1%, 3.8% and 0.1%, respectively (Sarpkaya and Isaacson, 1981). As a result of linearisation of the drag term, the odd harmonics are omitted. This point must be considered when the third harmonic can excite one of the natural frequencies of a structure.

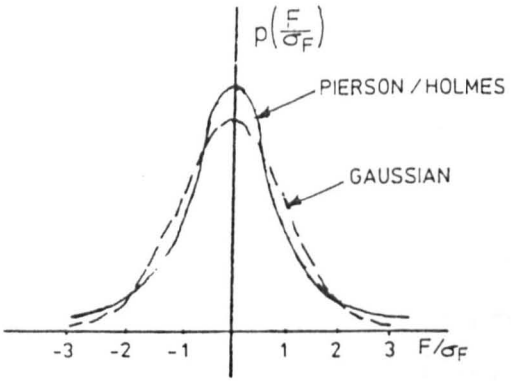

a) Probability density function of normalized Morison's wave force.

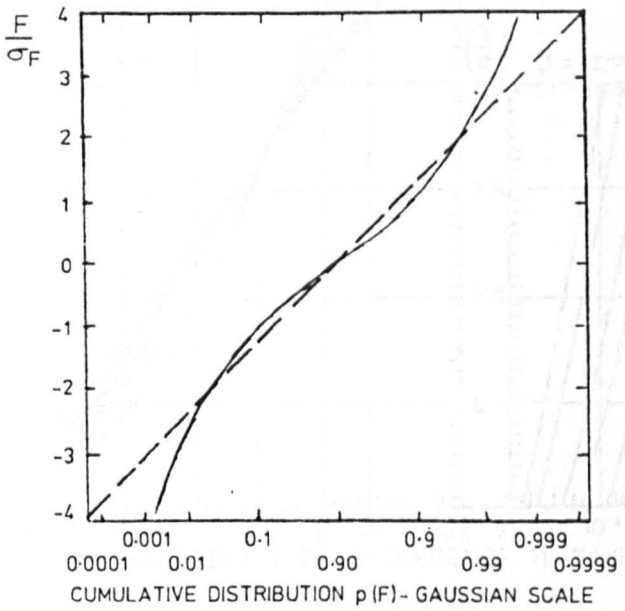

b) Cumulative distribution function of normalized Morison's wave force.

FIGURE 8.1. COMPARISON OF PIERSON HOLMES AND GAUSSIAN DISTRIBUTIONS WITH THE SAME VARIANCE.

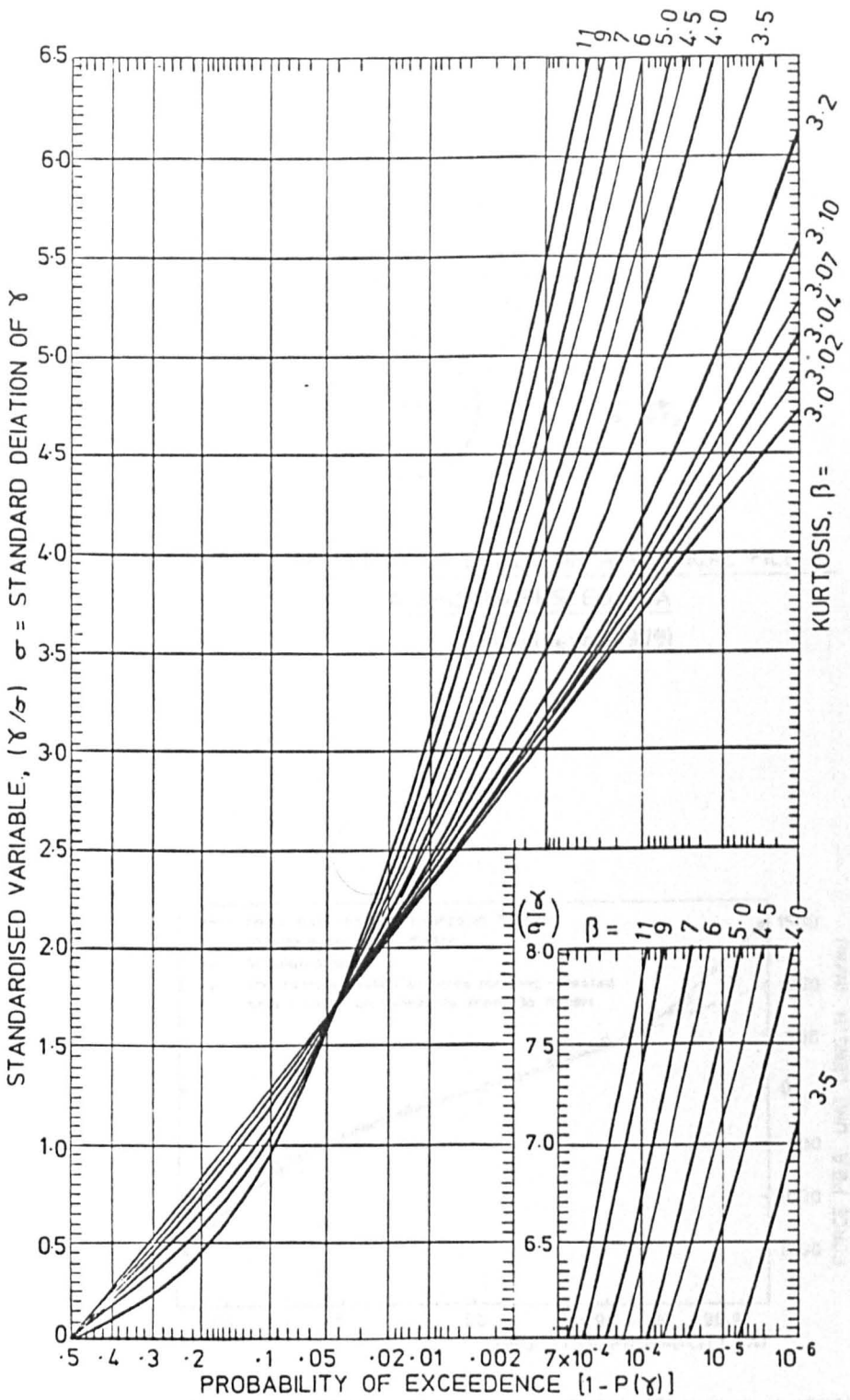

FIGURE 8.2. STANDARDISED MEAN-ZERO SYMMETRICAL PIERSON-HOLMES CUMULATIVE DISTRIBUTION FUNCTIONS FOR VARIOUS VALUES OF KURTOSIS. (Burrows, 1978)

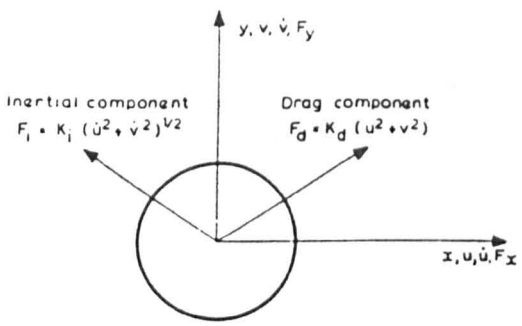

FIGURE 8.3. COMPONENTS OF FORCE ON A VERTICAL PILE IN A SHORT-CRESTED SEA (Tickell et al, 1979)

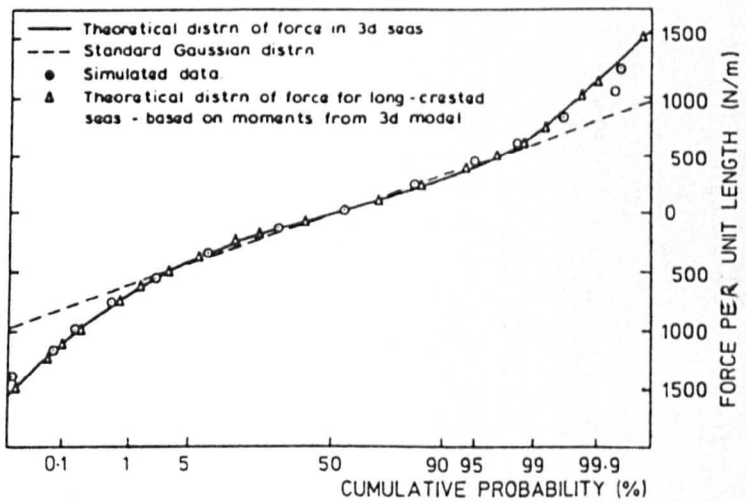

FIGURE 8.4. MARGINAL DISTRIBUTION OF FX. (Tickell et al, 1979)

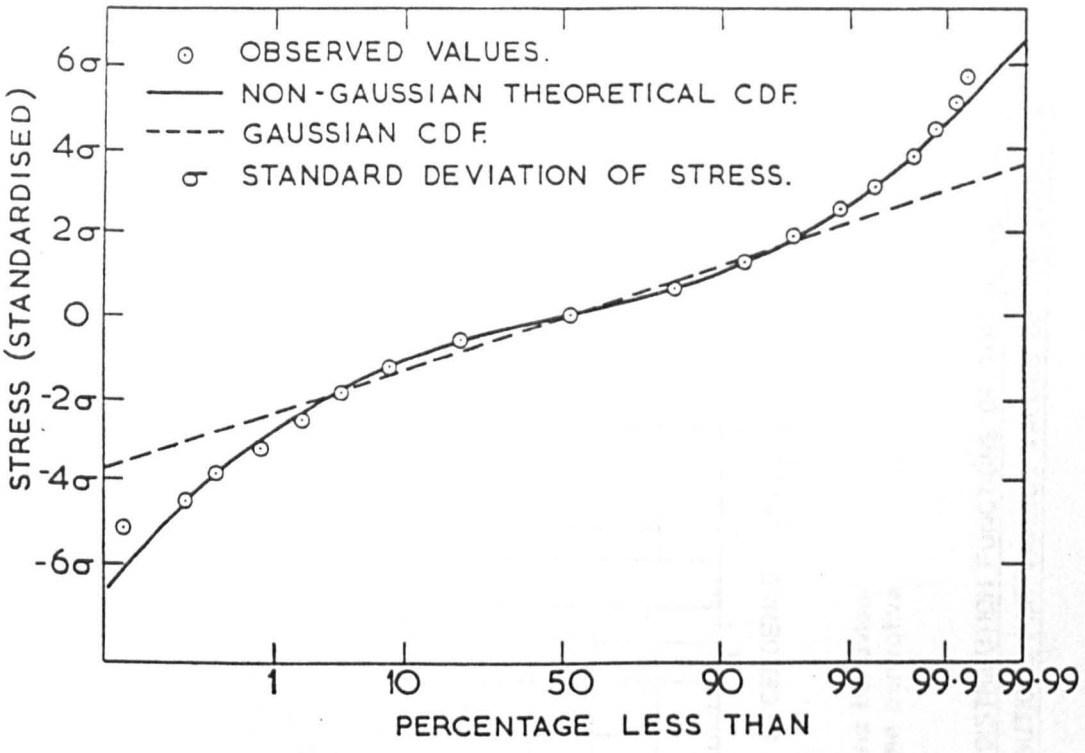

FIGURE 8.5. CDF. OF BENDING STRESS MEASURED IN A MEMBER OF A NORTH SEA PLATFORM. (Tickell, 1977)

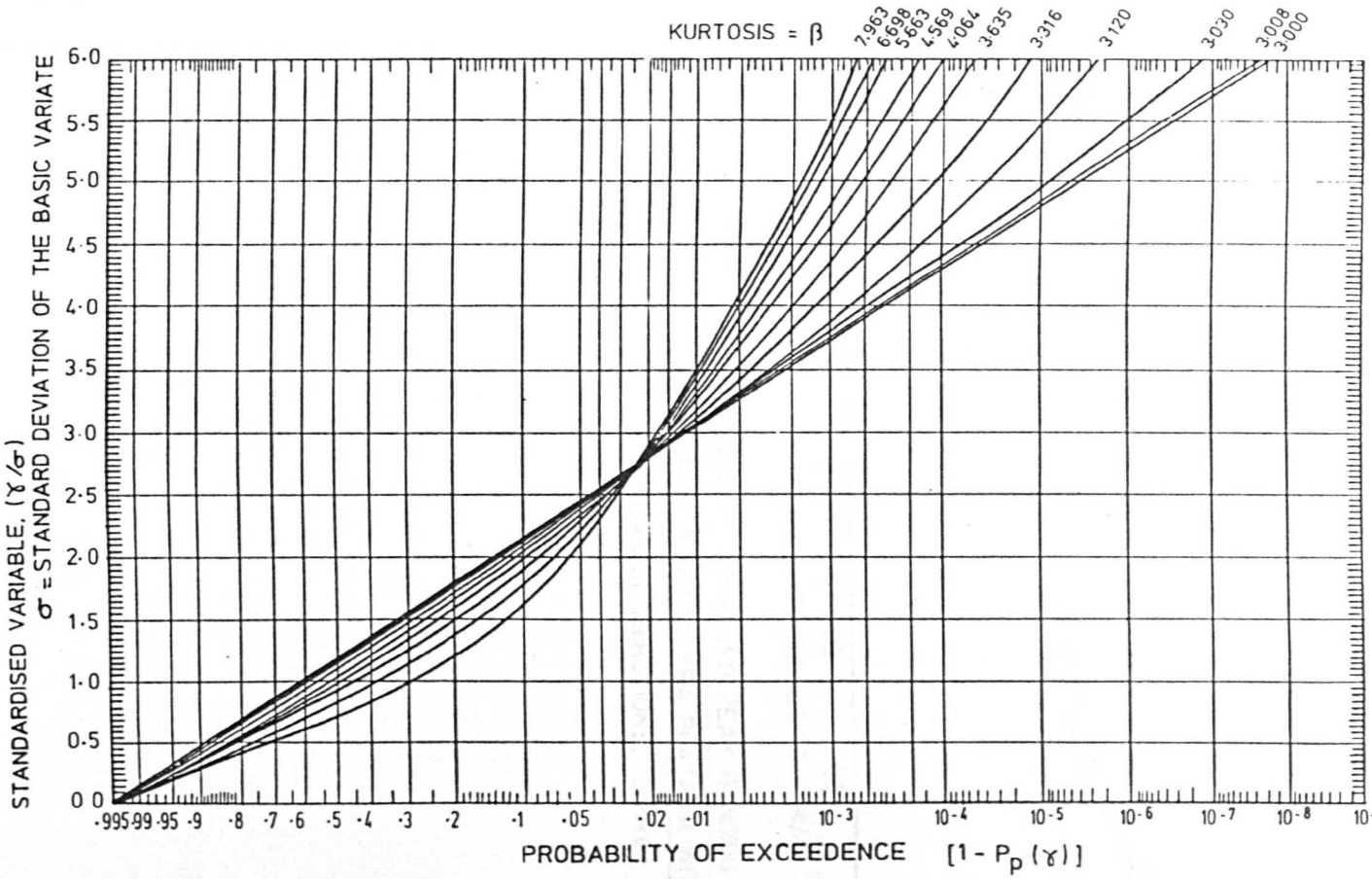

Variable assumed to follow narrow-band behaviour statistically independent of its first time derivative
Narrow-band Type 2 distribution.

FIGURE 8.6. STANDARDISED PLOTS OF CUMULATIVE DISTRIBUTION FUNCTIONS OF THE PEAKS OF MEAN-ZERO SYMMETRICAL PIERSON-HOLMES DISTRIBUTIONS FOR VARIOUS VALUES OF THE BASIC VARIATE KURTOSIS. (Burrows, 1978).

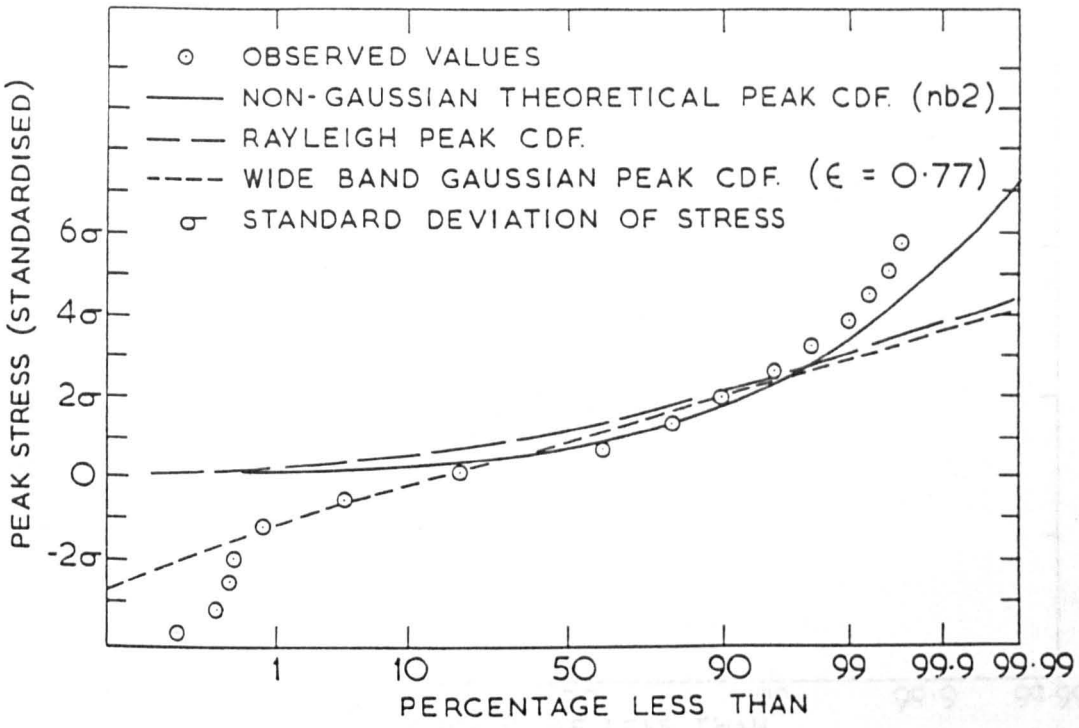

FIGURE 8.7. COMPARISON OF OBSERVED PEAK BENDING STRESSES MEASURED ON A NORTH SEA PLATFOM WITH THEORETICAL PEAK DISTRIBUTIONS. (Tickell, 1977)

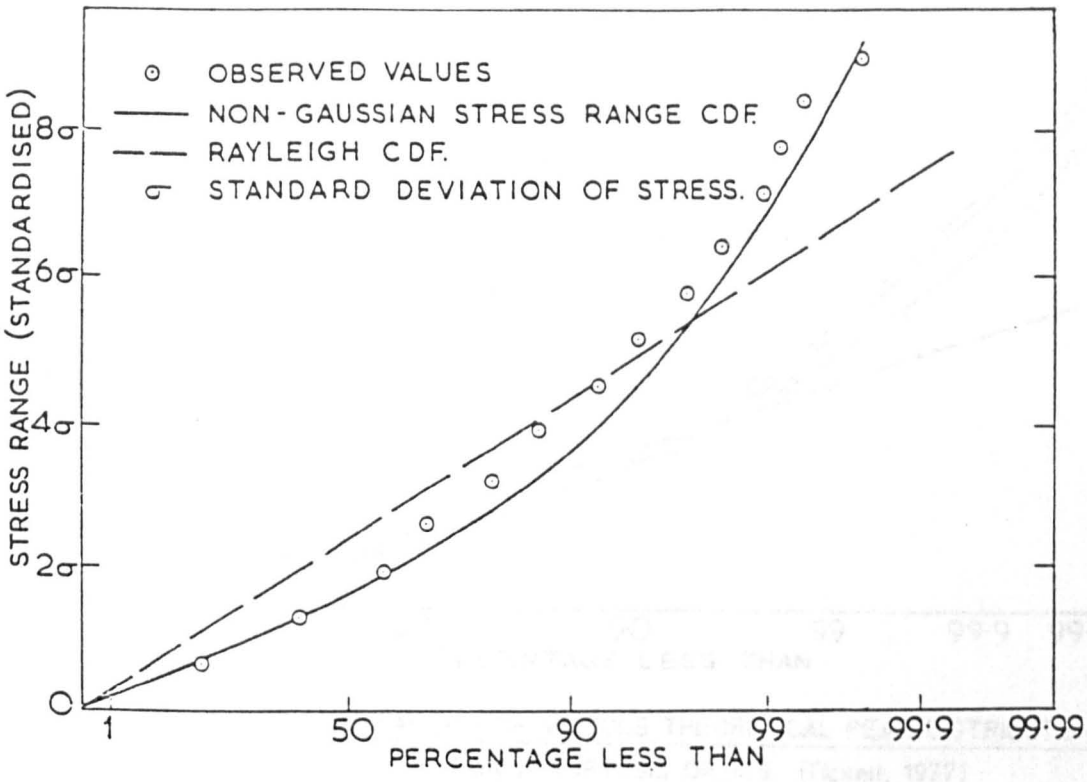

FIGURE 8.8. THE OBSERVED AND THEORETICAL CDF. OF STRESS RANGE FOR THE PROTOTYPE DATA. (Tickell, 1977)

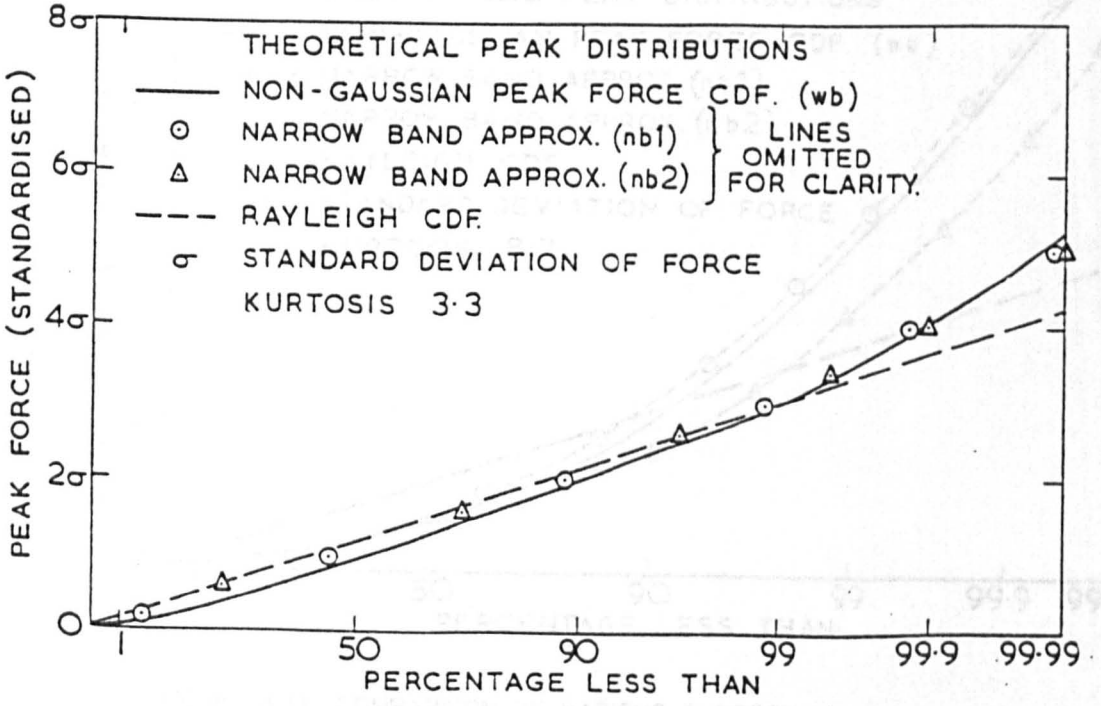

FIGURE 8.9. COMPARISON OF VARIOUS THEORETICAL PEAK FORCE DISTRIBUTIONS FOR A KURTOSIS OF 3.3. (Tickell, 1977)

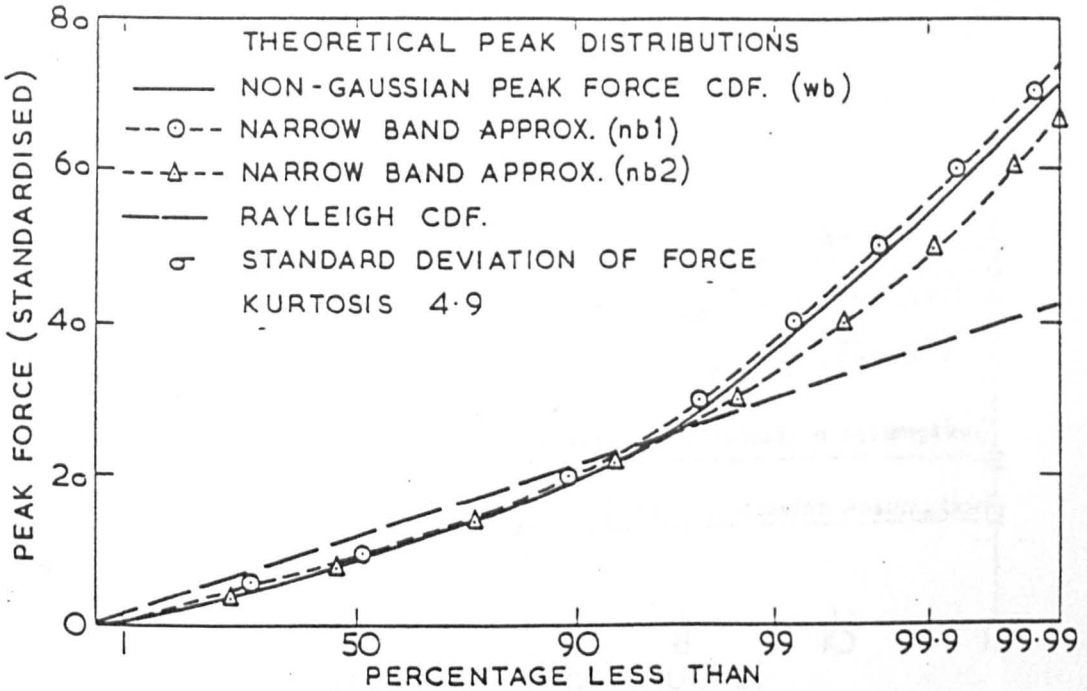

FIGURE 8.10. COMPARISON OF VARIOUS THEORETICAL PEAK DISTRIBUTIONS FOR A KURTOSIS OF 4.9. (Tickell, 1977)

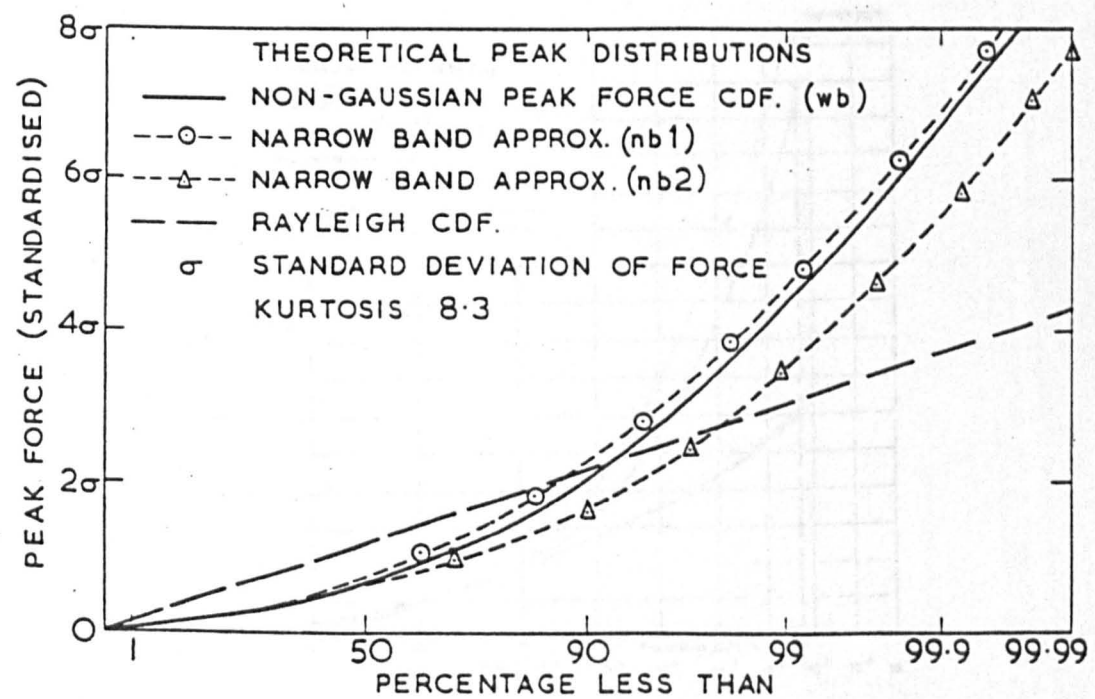

FIGURE 8.11. COMPARISON OF VARIOUS THEORETICAL PEAK DISTRIBUTIONS FOR A KURTOSIS OF 8.3. (Tickell, 1977)

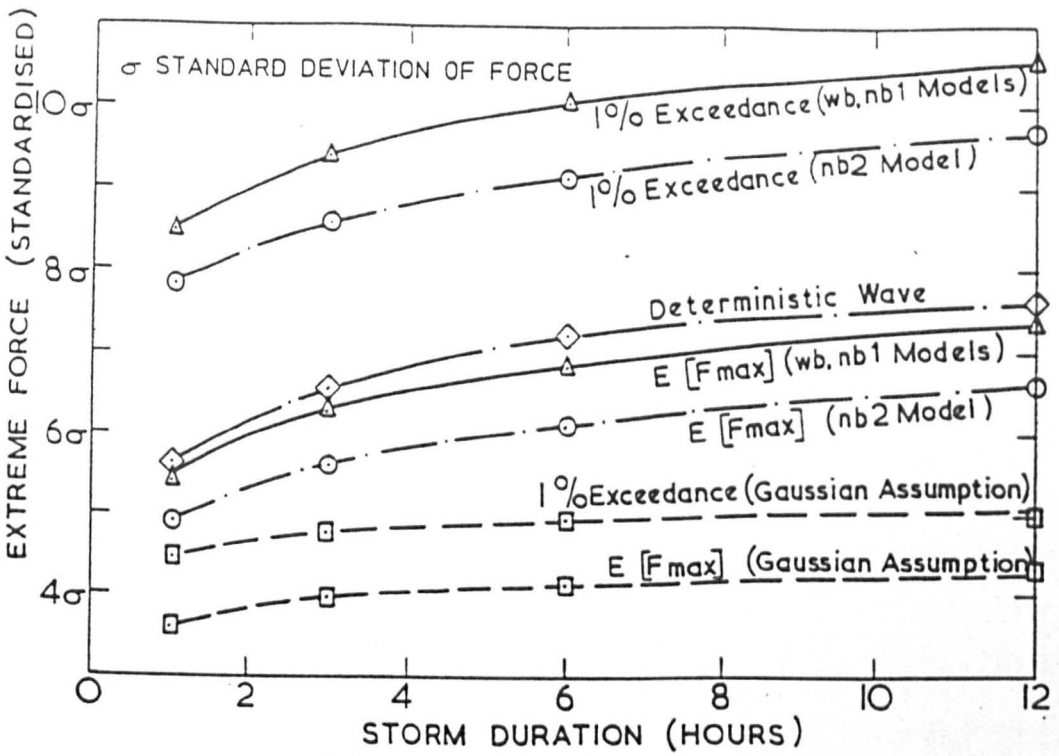

FIGURE 8.12. VARIATION OF EXTREME STATISTICS FOR VARIOUS THEORETICAL MODELS AND STORM DURATIONS. (Tickell, 1977)

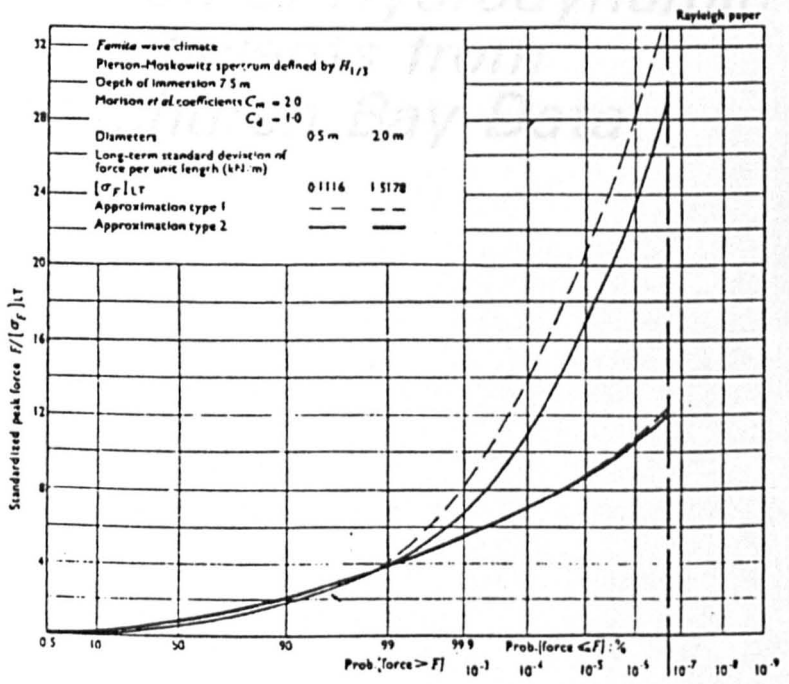

FIGURE 8.13. COMPARISON OF LONG-TERM PROBABILITY DISTRIBUTIONS OF PEAK FORCE DERIVED FROM NARROW-BAND APPROXIMATIONS TYPE 1 AND 2 FOR THE SHORT-TERM DISTRIBUTION OF PEAK FORCE. (Tickell et al, 1976)

Chapter 9

Determination of Hydrodynamic Coefficients from Christchurch Bay Data

INTRODUCTION

This chapter discusses the suitability of the relative motion form of Morison's equation in describing the in-line random wave loading on the flexible cylinder at Christchurch Bay.

Spectral and probabilistic properties of the observed forces together with the basic hydrodynamic parameters and total force coefficients are discussed in Section 9.1. Sections 9.2 and 9.3 are devoted to the determination of Morison's coefficients via probabilistic and time-domain methods, respectively. In respect of the latter, the Least Square Error method of fitting has been critically assessed; its shortcomings in the analysis of stochastic processes have been identified and a new method, termed maximum correlation method, has been introduced. The effect of sampling variability on these coefficients has been discussed in Appendix C, where it is shown that the effect is not significant.

The success of the relative motion form of Morison's equation can best be judged by the goodness of fit between the observed and predicted forces. This is covered in Section 9.4. However, even a perfect fit between the observed and predicted forces does not mean that the relative motion form of Morison's equation is a successful model for predicting random wave loading on flexible cylinders. Of paramount importance is the stability of C_d and C_m values from one run to another one. In this context, stability means that either Morison's coefficients must be relatively constant, or alternatively, their variation must be predictable in terms of their dependence on basic hydrodynamic coefficients or some other parameters. This led to the introduction of a new parameter, which was termed the acceleration

parameter. The stability of Morison's coefficients is discussed in Section 9.5. Section 9.6 is devoted to the comparison of the results of this study with previous relevant work (which was discussed in Section 7.4). The variation of C_d and C_m values for individual large waves in each run is presented in Section 9.7.

Finally, although the main objective of this study was the investigation of in-line forces, brief discussions of in-line cylinder response, and transverse force and response are included in Sections 9.8 and 9.9, respectively.

9.1 GENERAL CONSIDERATIONS

9.1.1 BASIC HYDRODYNAMIC PARAMETERS

Hydrodynamic loads on cylindrical members are known to be related to the values of parameters such as Reynolds number (R_e), Keulegan-Carpenter number (K) and roughness. Data in this study refers to only smooth cylinder condition; hence the latter effect is omitted. Furthermore, reduced velocity is known to be an important parameter for the case of flexible cylinders. The definition of these parameters for a random wave environment is not firmly established, that is, several different definitions for these parameters have been mentioned in the literature. In this study, the parameters have been calculated using the expressions due to Bishop (1980), so that the results of this study can be compared with those of the previous rigid cylinder studies at the Tower. Therefore

$$K = \frac{7.255}{D} * \left[\frac{E[u^4]}{E[\dot{u}^2]} \right]^{1/2} \qquad (9.1a)$$

$$R_e = \frac{1.28D}{\nu} * [E[u^4]]^{1/4} \qquad (9.1b)$$

$$u_r = \frac{1.28}{f_e \cdot D} * [E[u^4]]^{1/4} \qquad (9.1c)$$

where ν is the kinematic viscosity of sea water ($\nu = 1.43*10^{-6}$ m^2/sec), f_e is the cylinder natural frequency and other variables are as previously defined. If a monochromatic linear wave is considered in calculating $E[u^4]$ and $E[\dot{u}^2]$, then the more familiar forms of K and R_e are obtained. The values of these parameters for both low-intensity and high-intensity runs are given in Table 9.1. These calculations are based on both the observed absolute moments for $E[u^4]$ and $E[\dot{u}^2]$ and theoretical absolute moments by assuming that u is Gaussian distributed. In both cases, the effect of current has been included. The values of the parameters obtained from observed and theoretical values of $E[u^4]$ are in reasonable agreement.

Low-Intensity Runs

The Keulegan-Carpenter number is in the range $8.5 < K < 11.9$ and hence, it is expected that the in-line force is inertia-dominated. The Reynolds number lies in the range $1.5*10^5 < R_e < 2.7*10^5$; therefore the shear layers are expected to be turbulent under the effect of three-dimensional flow, which in turn leads to low and high values of drag and inertia coefficients, respectively. The reduced velocity varies between 0.6 to 3.4, with the result that cylinder synchronisation ('lock-in' effect) is not highly probable as synchronisation for flexible cylinders in waves occurs when the reduced velocity is in the range of 5 to 7.5 with maximum response at $u_r \approx 5$ (Rajabi, 1979).

High-Intensity Runs

The Keulegan-Carpenter number is in the range $20.8 < K < 36.9$, so that the in-line force is in the drag-inertia regime. The Reynolds number lies in the range $3.6*10^5 < R_e < 5.7*10^5$; therefore, the shear layers are turbulent, drag coefficient is expected to be low and inertia coefficient is expected to be high. The reduced velocity ranges from 4.9 to 7.2; hence synchronisation can be expected.

9.1.2 TOTAL FORCE COEFFICIENTS

In-line and transverse force coefficients are respectively defined as (Bearman, 1988):

$$C_{Frms} = \frac{F_{rms}}{\hat{k}_d \, u_{rms}^2} \tag{9.2a}$$

and

$$C_{lrms} = \frac{F_{lrms}}{\hat{k}_d \, u_{rms}^2} \tag{9.2b}$$

where F_{rms}, F_{lrms} and u_{rms} refer to the root mean square of the in-line force, transverse force, and the in-line water particle velocity, respectively, and

$$\hat{k}_d = \rho DL/2 \tag{9.2c}$$

with L being the length of the force sleeve.

Bishop (1988) has defined the in-line and transverse force coefficients in the following way

$$C_{Frms}^{*} = \frac{F_{rms}}{\hat{k}_d(E[u^4] + (\pi D/2)^2 E[\dot{u}^2])^{1/2}} \tag{9.3a}$$

and

$$C_{Irms}^{*} = \frac{F_{Irms}}{\hat{k}_d(E[u^4] + (\pi D/2)^2 E[\dot{u}^2])^{1/2}} \qquad (9.3b)$$

The form of the above equations is such that C^* will tend to C_m for inertia-dominated situations and tend to C_d for drag-dominated situations.

Bearman's and Bishop's force coefficients for the present study are presented in Table 9.2 and are plotted against Keulegan-Carpenter number in Figures 9.1 and 9.2. The transverse force coefficients are about 0.75 times the in-line force coefficients indicating that the transverse force is significant. As expected, the force coefficients decrease with increasing Keulegan-Carpenter number as the drag component becomes more significant. Force coefficients for low-intensity runs are more widely scattered than those for high-intensity runs.

9.1.3 SPECTRAL AND PROBABILISTIC PROPERTIES OF IN-LINE AND TRANSVERSE FORCES

9.1.3.1 Basic Statistical Parameters

Values of skewness and kurtosis for both low-intensity and high-intensity runs, together with the ratio of σ_{Fy}/σ_{Fx} are given in Table 9.3.

Low-Intensity Runs

The values of skewness for in-line forces are small and fluctuate about zero, while their values for transverse forces are higher and are mainly positive. With the exception of Run 06, the skewness of the in-

line forces (at Level 3) are between those of the in-line water particle velocities and accelerations (refer to Tables 4.3 and 4.4) but are closer to the skewness values for accelerations. This is expected because these runs are inertia-dominated and hence are mostly affected by acceleration components. The effect of the drag component is expected to be small; however, the velocities have large negative skewnesses and hence, their effect on reducing the skewness values for the forces are not insignificant.

The kurtoses for the in-line forces are close to 3 and are occasionally smaller than 3. From a theoretical point of view, Kurtosis cannot be less than 3; however, for records of finite length, this is possible due to sampling variability. Overall, the small values of kurtosis indicate that the in-line forces are inertia-dominated. Values of kurtosis for transverse forces are higher than their equivalents for in-line forces.

The kurtoses of the in-line forces, against expectation, are systematically smaller than those of water particle kinematics (refer to Tables 4.3 and 4.4). According to Morison's equation, while the kurtoses of these inertia-dominated in-line forces must be between those of the water particle velocities and accelerations, they should be closer to the kurtoses for accelerations. However, it should be noted that Morison's equation offers only an approximation to the fluid loading on submerged cylinders because it does not account for the effect of vortex shedding, etc. Therefore, some discrepancy between the properties of Morison-type forces and observed forces are expected. Measurement errors in hydrodynamic forces and water particle kinematics can also contribute to the above-mentioned discrepancy.

The ratio between the standard deviations of the transverse and in-line forces are greater than 0.50, indicating that transverse forces are significant.

High-Intensity Runs

The values of skewness for in-line forces are all positive and relatively large, which could be due to finite amplitude effects. Their values for transverse forces are also large but they are negative. The skewness of the associated water particle kinematics are all positive but are smaller than those of the in-line forces (refer to Tables 4.5 and 4.6). The drag component of force is expected to have a higher value of skewness than that of water particle velocity. However, the skewness of in-line forces are significantly higher than those of water particle kinematics so that some deviation from theoretical predictions are suspected.

The kurtoses for in-line forces are all above 3 and larger than those for the low-intensity runs, which is expected in view of the fact that drag forces are more significant for high-intensity runs. Values of kurtosis for transverse forces are all well above 3 and are higher than those for in-line forces. They are also larger than their equivalents for low-intensity runs. the kurtoses of in-line forces are significantly greater than those of water particle kinematics (refer to Tables 4.5 and 4.6). This is consistent with theory as the high-intensity runs are in the drag-inertia regime and hence are expected to have kurtoses values greater than the associated water particle kinematics.

Conclusion

At least in a qualitative sense, the predictions of Morison's equation with respect to skewness and kurtoses values of the in-line forces are correct. The exceptions are the kurtoses of the in-line forces for low-intensity runs which are consistently smaller than those of water particle kinematics.

9.1.3.2 Spectral Properties

Run 01

Figures 9.3 to 9.6 show sample time series and spectra for the x and y components of force for Run 01. The major variance for both in-line and transverse components is restricted to $0 < f < 0.4$Hz as was the case with the water surface elevation spectrum; however, the spectra show a very small contribution at the cylinder natural frequency, too. The contribution at the cylinder natural frequency in the in-line direction is about 2 times as large as that in the transverse direction. The spectral peak for F_y is at a higher frequency than that for F_x, which is expected due to the presence of higher frequencies in the y components of water particle kinematics.

According to Morison's equation, the frequency spectra of in-line forces are expected to be similar to those of water particle kinematics, except that due to the nonlinear drag component, there is a small contribution to the variance of the in-line forces at about three times the peak spectral density of the associated water particle velocities (refer to the last paragraph of Chapter 8). The comparison of the in-line frequency spectrum with that of the water particle velocity (Figure 4.9) shows that the general shape of the two spectra are the same; however the contribution of frequencies between 0.40 to

0.80 Hz is more significant for the in-line force. This could partly be due to the amplification of higher frequencies in the acceleration spectrum in comparison with the water particle velocity spectrum and partly due to the nonlinear drag component.

Run 08

The spectra are shown in Figures 9.7 and 9.8 and are strongly multi-modal as was the case for water particle kinematics. The spectra include a component at the cylinder natural frequency (0.73Hz), which are of equal magnitude in both x and y directions.

Run 13

The spectra shown in Figures 9.9 and 9.10, are noticeably different from the previous sets as the transverse force is dominated by the component at the natural frequency (0.46Hz). The contribution to variance at the cylinder natural frequency in the transverse direction is about 5 times as large as that in the in-line direction. Examination of water particle kinematics' spectra reveals that transverse wave components at this frequency are somewhat smaller than the in-line ones. This clearly shows that a mechanism different from Morison's equation is responsible for the excitation at the cylinder frequency in the transverse direction. This could be due to synchronisation which is possible in view of a reduced velocity of about 5.5 (Rajabi, 1979). In addition to the peaks at the cylinder natural frequency, there are three other peaks at the wave frequency, at twice and three times the wave frequency which could be due to vortex shedding. This is because the Keulegan-Carpenter number is above 20 and hence up to a maximum of four vortices per cycle are possible (Figure 7.24).

Run 15

Figures 9.11 to 9.14 show sample time series and spectra for the x and y components of force for Run 15. The spectra are more or less similar to those of Run 13.

Again, comparing Figure 9.13 with Figure 4.11, it is observed that the general shape of the two spectra are the same; however, the contribution of frequencies between 0.2 to 0.4 Hz to the variance of the in-line force is more significant than their contribution to the variance of the associated water particle velocity. The reasons are similar to those mentioned for Run 01.

Run 23

The spectra for both in-line and transverse forces are shown in Figures 9.15 and 9.16. The spectra are more or less similar to those of Runs 13 and 15. It should be noted, however, that the contribution to variance at the cylinder natural frequency in the transverse direction is only about two times as large as the contribution in the in-line direction. That is, the contribution in the x direction for this run is somewhat larger than Runs 13 and 15 while the contribution in the y direction is somewhat smaller. The increased contribution in the in-line direction can be explained by the fact that water particle velocity is more energetic at this frequency in comparison with Runs 13 and 15. The reduced contribution in the transverse direction could be due to a reduced velocity of about 6.8 which is further away from 5.0 (maximum synchronisation) in comparison with Runs 13 and 15, which have reduced velocities of 5.3 and 5.7, respectively.

Conclusion

At least in a qualitative sense, the performance of Morison's equation in the frequency domain is good. In other words, Morison's equation can be used in predicting the spectral properties of the in-line forces from the spectral properties of water particle kinematics.

9.1.3.3 Probabilistic Properties

Low-Intensity Runs

Figures 9.17 and 9.18 show cumulative probability distributions for a typical low-intensity run (Run 01) for in-line and transverse forces, respectively. The distributions are approximately Gaussian as is expected for the case of inertia-dominated loads (low kurtosis). Figure 9.17 shows that the deviation of the negative tail from the Gaussian distribution is more marked than that of the positive tail. Examination of the probability distribution of water particle velocity (Figure 4.12) shows that this is the result of a similar deviation in the cdf of water particle velocity.

The crests distributions, shown in Figures 9.19 and 9.20 are also of Gaussian form, indicating that the forces are not narrow-banded. The distribution of mean-crossing ranges (equivalent to wave heights for water surface elevation) are in reasonable agreement with the Rayleigh distribution (Figures 9.21 and 9.22). As was the case with water particle kinematics, three different theoretical Rayleigh distributions are plotted based on range data mean, range data standard deviation and basic signal (in-line or transverse hydrodynamic force) standard deviation.

High-Intensity Runs

Figures 9.23 and 9.24 show cumulative distributions of in-line and transverse forces for Run 13. The non-Gaussian behaviour is evident in both cases. Pierson-Holmes 3 parameter distribution (PH3) have also been fitted to the data and offer a much better fit than the Gaussian distribution.

The analysis can be taken a further stage to develop narrow-band 'type 2' approximations for the crest and trough distributions of force (Tickell, 1977). This distribution can then be used to predict the extremes of the force. A comparison between predicted and observed maximum and minimum for the forces are shown in Figures 9.23 and 9.24 (Tickell and Burrows, 1989). The same narrow-band approximation for peak distributions may be used to form the probability distribution of the mean-crossing ranges of the force variables. The distribution plotted on Rayleigh distribution papers are shown in Figures 9.25 and 9.26. The non-Rayleigh PH3 distributions gives a better fit to the data in comparison with the Rayleigh distribution arising from the assumption that the force variables are narrow-banded and Gaussian distributed. It should be noted that the sample size for mean-crossing ranges is relatively small (about 300) and therefore range data values with low probability of exceedence (say less than 1%) are subject to significant sampling variability and hence their departures from their theoretical distributions should not necessarily be taken as evidence for the significant departure of the underlying population distribution from their corresponding theoretical distributions.

Similar plots for Run 15 are shown in Figures 9.27 to 9.32 and show similar characteristics to those for Run 13.

Examination of Figure 9.27 shows that the positive tail of the distribution follows the theoretical P/H distribution. On the other hand, the negative tail is closer to the Gaussian distribution. This seems to be against theoretical expectations which predict a P/H distribution. However, a closer examination of the cdf of water particle velocity (Figure 4.18) reveals that this is due to the departure of the negative tail of the water particle velocity from the Gaussian distribution. In effect, both tails of the water particle velocity have been pushed toward values of higher magnitude as the result of the nonlinear drag component, in agreement with theory.

Examination of Figure 9.29 indicates that the force crests follow the same trend as those of the basic variate itself.

Conclusion

At least in a qualitative sense, Morison's equation is capable of predicting the probabilistic properties of the in-line forces from the probabilistic properties of the associated water particle kinematics.

9.2 DERIVATION OF DRAG AND INERTIA COEFFICIENTS VIA PROBABILISTIC METHODS

As was fully discussed in Chapter 6, the water particle kinematics had to be shifted from their point of measurement at the small rigid column to the compliant cylinder by assuming that waves were uni-directional and that linear random wave theory is correct. The above process cannot be accurate due to the short-crestedness of the waves and finite-amplitude effects; hence the relative velocity and acceleration needed in the study of the relative motion form of Morison's equation are not error free. However, by ignoring the cylinder movement, i.e. by

assuming that the cylinder is rigid and motionless and by resorting to probabilistic methods, one can avoid the shifting problem. Because of this reason and also in order to evaluate the effect of cylinder motion on the coefficients, it was decided to perform the probabilistic methods for both rigid and flexible cylinder cases.

9.2.1 RIGID CYLINDER CASE

9.2.1.1 Derivation of Morison's Coefficients

According to Morison's equation, in-line wave loading can be written as

$$F = k_d\, u|u| + k_i\dot{u} \tag{9.4a}$$

The above form of Morison's equation is based on the resolved part of the kinematics in the predominant wave direction (x axis). However, recognising that the drag and inertia components of force are along the water particle velocity and acceleration vectors respectively, Morison's equation for a short-crested sea should be written as

$$F = k_d u\, (u^2 + v^2)^{1/2} + k_i\dot{u} \tag{9.4b}$$

where u and v are the in-line and transverse components of water particle velocity, respectively. In this section, both forms of Morison's equation have been explored and the resultant coefficients have been compared. It is noted that by setting v = 0 in Equation (9.4b), Equation (9.4a) is obtained.

Drag and inertia coefficients can be determined by forming the second and fourth order statistical moments of Morison's force and equating them to their corresponding observed values. Once the Morison's coefficients have been determined, the resultant first and third

moments of the predicted force can be compared with their corresponding observed values through the following non-dimensionalised error terms.

$$E_1 = (m_{10} - m_1)/\sigma_{F0} \tag{9.5a}$$

$$E_3 = (\mu_{30} - \mu_3)/\sigma_{F0}^3 \tag{9.5b}$$

Where m_1, μ_3 and σ_F refer to the first absolute moment, third central moment and the standard deviation of force, respectively. Subscript '0' indicates an observed value. It is noted that E_3 refers to the difference between the skewness of the observed and predicted forces.

In general, the first four statistical moments of force can be written as

$$m_1 = E[F] = \alpha_{13} (k_d) + \alpha_{14} (k_i) \tag{9.6a}$$

$$m_2 = E[F^2] = \alpha_1 (k_d^2) + \alpha_2 (k_i^2) + \alpha_3 (k_d k_i) \tag{9.6b}$$

$$m_3 = E[F^3] = \alpha_9 (k_d^3) + \alpha_{10} (k_i^3) + 3\alpha_{11} (k_d^2 k_i) + 3\alpha_{12} (k_d k_i^2) \tag{9.6c}$$

$$m_4 = E[F^4] = \alpha_4 (k_d^4) + \alpha_5 (k_i^4) + \alpha_6 (k_d^2 k_i^2) + 2\alpha_7 (k_d^3 k_i) + 2\alpha_8 (k_d k_i^3) \tag{9.6d}$$

Where α_1 to α_{14} are algebraic sums of expectations of different combinations of water particle kinematics. Their values for both short-crested form (Equation (9.4b)) and uni-directional form (Equation (9.4a)) of Morison's equation are given in Table 9.4. (It should be noted that since the predominant wave direction is a few degrees apart from the x axis, α coefficients were calculated by writing the short-crested form of Morison's equation in the following form

$$F = k_d (u \cos \varphi + v \sin \varphi) (u^2 + v^2)^{1/2} + k_i (\dot{u} \cos \varphi + \dot{v} \sin \varphi)$$

where φ refers to the angle between the predominant wave direction and the x axis. The α coefficients turn out to be functions of 97 different combinations of water particle kinematics. However, Morison's equations derived from the assumption of $\varphi = 0$, are only very slightly different from those based on the real values of predominant wave directions. Therefore, for simplicity, α coefficients for the case of $\varphi = 0$ are only mentioned here).

The statistical moments of Table 9.4 can either be calculated from water particle kinematics data directly or by assuming that they are independent Gaussian-distributed random variables. The independence assumption is justified by recognising that $\rho_{u,v} = 0$ (because the predominant wave direction is very close to the x axis, Table 4.7) and values of $\rho_{\dot{u},v}$ have been checked and are small (less than 0.25 with higher values mostly at Level 2 which may have some bias due to intermittency). Therefore, overall, four different methods can be used in calculating α coefficients, namely:

Method 1. Directional form of Morison's equation with all statistical moments estimated from the data.

Method 2. Directional form of Morison's equation but using high order moments calculated on a Gaussian assumption.

Method 3. Estimating Morison coefficients from the resolved part of the force and kinematics in the predominant wave direction and using observed values of high order moments.

Method 4. As method 3 but using high order moments from assumed Gaussian relationships.

Once the values of α coefficients are known, C_d and C_m are determined by solving the set of two non-linear equations given in (9.6b) and (9.6d).

α Coefficients for Methods 2 and 4

Calculation of statistical moments of Gaussian distributed random variables will be fully discussed in Chapter 10. The closed-form solutions for the expectations needed in α coefficients are herein presented. It should be noted that due to the assumed mutual independence of u, $\dot{u}$ and v, the following relationship holds true.

$$E[f(u, \dot{u}, v) = f_1(u)\ f_2(\dot{u})\ f_3(v)] = E[f_1(u)]\ .\ E[f_2(\dot{u})]\ .\ E[f_3(v)] \tag{9.7}$$

In calculating the required expectations of water particle kinematics, u and v were normalised in the following way

$$u = \sigma_u\ (x + \gamma) \tag{9.8a}$$

$$v = \lambda\sigma_u(y + \beta) \tag{9.8b}$$

where

$$x = \frac{u - \bar{u}}{\sigma_u} \tag{9.8c}$$

$$y = \frac{v - \bar{v}}{\sigma_v} \tag{9.8d}$$

$$\gamma = \frac{\bar{u}}{\sigma_u} \tag{9.8e}$$

$$\beta = \frac{\bar{v}}{\sigma_v} \tag{9.8f}$$

$$\lambda = \frac{\sigma_v}{\sigma_u} \tag{9.8g}$$

It should be noted that x and y are two independent mean-zero Gaussian random variables with standard deviations of unity, and therefore their joint probability density function is

$$p(x,y) = p(x)\ p(y) = \frac{1}{2\pi} \exp\left(-\frac{x^2}{2}\right) * \exp\left(-\frac{y^2}{2}\right) \tag{9.9}$$

The following expectations have closed-form solutions

$$E[\dot{u}] = 0$$

$$E[\dot{u}^3] = 0$$

$$E[\dot{u}u|u|] = E[\dot{u}]E[u|u|] = 0$$

$$E[\dot{u}u\sqrt{u^2 + v^2}] = E[\dot{u}]E[u\sqrt{u^2 + v^2}] = 0$$

$$E[\dot{u}u^5\sqrt{u^2 + v^2}] = E[\dot{u}]E[u^5\sqrt{u^2 + v^2}] = 0$$

$$E[\dot{u}u^3v^2\sqrt{u^2 + v^2}] = E[\dot{u}]E[u^3v^2\sqrt{u^2 + v^2}] = 0$$

$$E[\dot{u}u^5|u|] = E[\dot{u}]E[u^5|u|] = 0$$

$$E[\dot{u}^3u\sqrt{u^2 + v^2}] = E[\dot{u}^3]E[u\sqrt{u^2 + v^2}] = 0$$

$$E[\dot{u}^3u|u|] = E[\dot{u}^3]E[u|u|] = 0$$

$$E[\dot{u}u^4] = E[\dot{u}]E[u^4] = 0$$

$$E[\dot{u}u^2v^2] = E[\dot{u}]E[u^2v^2] = 0$$

$$E[\dot{u}^2] = \sigma_{\dot{u}}^2$$

$$E[\dot{u}^4] = 3\sigma_{\dot{u}}^4$$

$$E[u^4] = (3 + 6\gamma^2 + \gamma^4)\ \sigma_u^4$$

$$E[u^8] = (105 + 420\gamma^2 + 210\gamma^4 + 28\gamma^6 + \gamma^8)\ \sigma_u^8$$

$$E[u^2v^2] = E[u^2]\ .\ E[v^2] = \lambda^2\sigma_u^4\ (1 + \gamma^2)(1 + \beta^2)$$

$$E[u^6v^2] = E[u^6]\ .\ E[v^2] = \lambda^2\sigma_u^8\ (15 + 45\gamma^2 + 15\gamma^4 + \gamma^6)(1 + \beta^2)$$

$$E[u^4v^4] = E[u^4] \cdot E[v^4] = \lambda^4\sigma_u^8 (3 + 6\gamma^2 + \gamma^4)(3 + 6\beta^2 + \beta^4)$$

$$E[u^4\dot{u}^2] = E[u^4]E[\dot{u}^2]$$

$$E[u^2v^2\dot{u}^2] = E[u^2v^2]E[\dot{u}^2] \qquad (9.10)$$

The expectations listed below do not have closed-form solutions and hence have been calculated by numerical integration as will be discussed in Chapter 10.

$$E[u|u|] = E[(x + \gamma)|x + \gamma|]$$

$$E[u^5|u|] = \sigma_u^6 E[(x + \gamma)^5|x + \gamma|]$$

$$E[\dot{u}^2u|u|] = E[\dot{u}^2]E[u|u|]$$

$$E[u\sqrt{u^2 + v^2}] = \sigma_u^2 E[(x + \gamma)\sqrt{(x + \gamma)^2 + \lambda^2(y + \beta)^2}]$$

$$E[\dot{u}^2u\sqrt{u^2 + v^2}] = E[\dot{u}^2]E[u\sqrt{u^2 + v^2}]$$

$$E[u^5\sqrt{u^2 + v^2}] = \sigma_u^6 E[(x + \gamma)^5\sqrt{(x + \gamma)^2 + \lambda^2(y + \beta)^2}]$$

$$E[u^3v^2\sqrt{u^2+v^2}] = \lambda^2\sigma_u^6 E[(x+\gamma)^3(y + \beta)^2\sqrt{(x + \gamma)^2 + \lambda^2(y + \beta)^2}] \qquad (9.11)$$

9.2.1.2 Results and Discussion

Values of Morison's coefficients derived from the four different methods are presented in Table 9.5. Examination of these values lead to the following observations.

1. Solution to the non-linear system of equations resulting from these methods were not obtainable in the case of Methods 1 and 3 for all low-intensity runs and in the case of Methods 2 and 4 for some of the low-intensity runs, i.e. Runs 02, 07 and 09 at Levels 3 and 4. The mathematical reason for this is now explained

   Solving Equations (9.6b) and (9.6d) for Morison's coefficients for Method 4 ($\alpha_6 = 6\alpha_1\alpha_2$ due to Gaussian assumption) leads to

$$C_d = \frac{1}{\hat{k}_d} * \left[\frac{m_{40} - 3m_{20}^2}{\alpha_4 - 3\alpha_1^2} \right]^{1/4} \tag{9.12a}$$

$$C_m = \frac{1}{\hat{k}_i} * \left[\frac{m_{20} - \alpha_1 C_d^2 \hat{k}_d^2}{\alpha_2} \right]^{1/2} \tag{9.12b}$$

The above equations can be simplified to

$$C_d = \frac{1}{\hat{k}_d} * \sqrt{\frac{m_{20}}{\alpha_1}} * a_d \tag{9.13a}$$

$$C_m = \frac{1}{\hat{k}_i} * \sqrt{\frac{m_{20}}{\alpha_2}} * a_i \tag{9.13b}$$

Where

$$a_d = \left[\frac{\frac{m_{40}}{m_{20}^2} - 3}{\frac{\alpha_4}{\alpha_1^2} - 3} \right]^{1/4} \tag{9.13c}$$

and

$$a_i = \left[1 - \left[\frac{\frac{m_{40}}{m_{20}^2} - 3}{\frac{\alpha_4}{\alpha_1^2} - 3} \right]^{1/2} \right]^{1/2} \tag{9.13d}$$

When current is negligible ($\bar{u} = 0$), a_d and a_i, reduce to

$$a_d = 0.583 * (\beta_f - 3)^{1/4} \tag{9.14a}$$

$$a_i = \sqrt{1 - 0.34\sqrt{\beta_f - 3}} \tag{9.14b}$$

Where β_f is the kurtosis of the in-line force. Introducing the above relationships into Equations (9.13a) and (9.13b), replacing $\hat{k}_d$ and $\hat{k}_i$ by their real numerical values, and substituting for α_1

and α_2 from Table 9.4 and Equations (9.10), Morison's coefficients from Method 4 (for this particular study when current is negligible) will be

$$C_d = 2.56 * (\beta_f - 3)^{1/4} * \frac{\sigma_f}{\sigma_u^2} \qquad (9.15a)$$

and

$$C_m = 10.08 * \sqrt{1 - 0.34\sqrt{\beta_f - 3}} * \frac{\sigma_f}{\sigma_{\dot{u}}} \qquad (9.15b)$$

Examination of the above equations shows that for C_d and C_m to exist, the kurtosis of force must be above 3. Referring to Table 9.3, it is observed that when there is no solution for C_d and C_m, kurtosis of the in-line force is less than 3.

2. Morison's coefficients derived from Method 1 are only slightly different from those derived from Method 3. Drag coefficient is consistently smaller while the inertia coefficient does not show a consistent trend. Comparison of the results of Methods 2 and 4 show that both drag and inertia coefficients from Method 2 are slightly smaller than those derived from Method 4. The difference is more noticeable for low-intensity runs where there is a significant transverse current (high value of r_2 defined in Section 4.5). Overall, it can be concluded that the assumption of uni-directionality does not lead to significant errors in the probabilistic properties of the force. It is recommended that slightly higher (about 2%) values of C_d and C_m be used when in-line forces are calculated based on the resolved part of water particle kinematics in the predominant wave direction.

3. Morison's coefficients derived from Methods 2 and 4 are more stable than those derived from Methods 1 and 3. This is because high order moments (such as $E[u^8]$) calculated from finite data samples are very unstable and can vary significantly from one data sample to another. The values of these high order moments are very much dependent on the extreme events in the data sample. The extreme events themselves can vary significantly from one record to another and hence high order moments tend to be very unstable. The reason that the Gaussian assumption leads to higher stability for high order moments is that they become a function of the standard deviation, which is a very stable parameter (since its value is influenced by all the data points, though more significantly by the higher ones). An example of the instability of high order moments and its effect on C_d and C_m can be provided by comparing the results of Runs 13 and 14, presented in the following Table. These two runs are very similar with a time delay of only half an hour between them. The current and water depth is only slightly different. It is therefore expected that C_d and C_m values for the two runs to be only slightly different. This is the case for Method 4; in contrast, Method 3 shows significant variation caused by the instability of high order moments.

Level	Run No	σ_u	Method 3				Method 4			
		m/sec	C_d	C_m	$E[u^4]$	$E[u^8]$	C_d	C_m	$E[u^4]$	$E[u^8]$
2	13	0.78	1.26	1.44	0.83	3.64	0.72	2.26	1.09	13.99
	14	0.80	1.09	1.82	1.03	6.83	0.76	2.29	1.24	17.89
3	13	0.74	1.18	1.28	0.68	2.40	0.66	2.18	0.91	9.56
	14	0.77	0.89	1.87	0.95	6.86	0.66	2.22	1.11	14.26
4	13	0.69	1.04	1.29	0.52	1.40	0.52	2.04	0.71	5.80
	14	0.72	0.85	1.63	0.73	3.80	0.58	2.05	0.87	8.73

4. Coefficients a_d and a_i, introduced in Equations (9.13a) and (9.13b), are measures of the contribution of the drag and inertia components of force to the total force variance, respectively. That is

$$a_d^2 = \frac{C_d^2 \hat{k}_d^2 \alpha_1}{m_{20}} = \frac{C_d^2 \hat{k}_d^2 E[u^4]}{m_{20}} = \frac{E[F^2_{drag}]}{E[F^2_{total}]} \qquad (9.16a)$$

and

$$a_i^2 = \frac{C_m^2 \hat{k}_i^2 \alpha_2}{m_{20}} = \frac{C_m^2 \hat{k}_i^2 E[\dot{u}^2]}{m_{20}} = \frac{E[F^2_{inertia}]}{E[F^2_{total}]} \qquad (9.16b)$$

For Method 4, where u and $\dot{u}$ are independent Gaussian distributed random variables, $E[F_{drag} \cdot F_{inertia}] = 0$, and therefore the following relationship holds true.

$$a_d^2 + a_i^2 = 1 \qquad (9.16c)$$

The values of a_d^2 and a_i^2 for Method 4 are given in Table 9.5. It is observed that low-intensity runs are inertia dominated while the high-intensity runs are in the drag-inertia regime.

5. The values of C_d are high for low-intensity runs but it must be considered that the low-intensity runs are inertia dominated and hence are not well-conditioned for the determination of C_d (Dean, 1976). As an illustration, the value of kurtosis for Run 01 at Level 3 is 3.3. Considering that kurtosis is subject to sampling variability, the true value of kurtosis for the random process from which Run 01 is only one sample, could be (say) 3.1. As a result of this change, a_d (Equation 9.14a) will reduce from 0.43 to 0.33, which is equivalent to a reduction of about 25% in a_d and hence C_d. In contrast, as a result of the same change in kurtosis, a_i will change from 0.90 to 0.94, which is equivalent to an increase of only 4% in a_i and hence C_m.

6. C_m values are higher than one might have anticipated but the implications of the dynamic response on the coefficients are not covered in the results of Table 9.5. It will be shown in the next section that the analysis of the relative motion form of Morison's equation leads to lower values of C_m.

7. There is a consistent reduction in C_d in moving from Level 2 to Level 4. It must be stressed that Level 2 is subject to some intermittent exposure which could affect the values of C_d and C_m. The difference between C_d for Level 3 and Level 4 are not so marked though they do show a consistent trend to reduce (with the exception of Run 07 which shows an increase). Previous studies at Christchurch Bay Tower have shown the same feature (Bishop, 1984; Tickell et al, 1982). The mathematical reason for this feature is the reduction of kurtosis from Level 2 to Level 4 (Table 9.3).

8. Coefficients E_1 and E_3, the measures of errors of the first and third moments given in Equations (9.5a) and (9.5b), do not give a consistent quantitative method for selection between Methods 1, 2, 3 and 4. Their values for Method 4 are presented in Table 9.5.

Conclusion

In view of the above discussion, it is clear that Methods 2 and 4 are preferable to Methods 1 and 3 due to the stability of their results. While Method 4 is simpler than Method 2 due to the assumption of uni-directionality, the difference between the results of the two Methods is insignificant. It can therefore be concluded that Method 4 is preferable to the other methods. Consequently, only Method 4 was used in the probabilistic study of the relative motion form of Morison's equation, which follows in the next section.

9.2.2 FLEXIBLE CYLINDER CASE

9.2.2.1 Derivation of Morison's Coefficients

The relative motion form of Morison's equation can be written as (Equation 7.27),

$$F = k_d (u - \dot{r})|u - \dot{r}| + k_i \dot{u} - C_a \hat{k}_i \ddot{r} \qquad (9.17a)$$

where F refers to the in-line wave loading on the flexible cylinder, $\dot{r}$ and $\ddot{r}$ refer to the cylinder kinematics and $\hat{k}_i$ is defined as

$$\hat{k}_i = \rho\pi D^2 L/4 = k_i/C_m \qquad (9.17b)$$

Subtracting $\hat{k}_i \ddot{r}$ from both sides of Equation (9.17a), leads to

$$F_r = F - \hat{k}_i \ddot{r} = k_d(u - \dot{r})|u - \dot{r}| + k_i \dot{u} - \hat{k}_i(1 + C_a)\ddot{r} \quad (9.17c)$$

where F_r is referred to as the relative force. Noting that $\hat{k}_i(1 + C_a) = k_i$, the relative motion form of Morison's equation simplifies to

$$F_r = k_d (u - \dot{r})|u - \dot{r}| + k_i (\dot{u} - \ddot{r}) \quad (9.17d)$$

The above relationship can be rewritten as

$$F_r = k_d u_r|u_r| + k_i \dot{u}_r \quad (9.18a)$$

where u_r and $\dot{u}_r$ refer to the relative velocity and acceleration respectively and are defined as

$$u_r = u - \dot{r} \quad (9.18b)$$

$$\dot{u}_r = \dot{u} - \ddot{r} \quad (9.18c)$$

It is noted that Equation (9.18a) is of the same form as Equation (9.4a) and therefore by calculating F_r, u_r and $\dot{u}_r$, the methods used in deriving Morison's coefficients for the rigid cylinder case can be used in deriving the coefficients for the flexible cylinder case, too. As previously discussed, Method 4 is preferable to the other three methods; hence only Method 4 was applied in this section.

9.2.2.2 Effect of Shifting Water Particle Kinematics on Morison's Coefficients

As was fully discussed in Chapter 6, the shifting process was conducted by breaking down the water particle kinematics into its harmonic components and then phase shifting each component to the cylinder centre by assuming that the waves were uni-directional along the predominant wave direction. As a result of this assumption, the

calculated phase shifts are only approximate with the high frequency harmonics being less accurate for two reasons, a) at high frequencies the sea is more short-crested than at low frequencies, b) the wave lengths of the high frequency components are shorter and hence the phase shift is larger. Consequently, the Fourier series of the calculated water particle kinematics are accurate in terms of the amplitude of the harmonics (i.e. the shifting process does not alter the frequency spectra of the shifted kinematics) but are not error free in terms of the phase shifts. It is the intention of this section to show that the phase shift errors have only a marginal effect on the (calculated) values of Morison's coefficients.

According to Equation (9.15), it is the variance of the relative kinematics which are used in determination of Morison's coefficients. Therefore, it is necessary to investigate the effect of the phase shift errors on the variance of the kinematics. From Equation (9.18b), the variance of the relative velocity is

$$E[u_r^2] = E[u^2] + E[\dot{r}^2] - 2E[u.\dot{r}) = \bar{u}^2 + \sigma_u^2 + \sigma_t^2 - 2\rho_{u,t}\,\sigma_u\,\sigma_t \qquad (9.19)$$

With the exception of the correlation coefficient between water particle velocity and cylinder velocity ($\rho_{u,t}$), all the terms in the above relationship are independent of the phase shift and hence are not affected by phase shift errors. That is

$$\sigma_u^2 = \sum_{i=1}^{n} \lambda_i^2 \qquad (9.20)$$

Where λ_i is the amplitude of the ith harmonic of water particle velocity. Therefore, it remains to investigate the effect of phase

shift errors on the correlation coefficients between the particle and relative kinematics.

Limit on the Correlation Coefficient Between Two Random Processes with Known Frequency Spectra

In general, the correlation coefficient between two random processes x and y is limited to

$$|\rho_{x,y}| \leq 1 \tag{9.21}$$

However, when the frequency spectra of the two processes are known, one can put tighter limits on the correlation coefficient. That is

$$|\rho_{x,y}| \leq \frac{\int_0^\infty \sqrt{G_{xx}(f)G_{yy}(f)}\,df}{\sigma_x\,\sigma_y} = \frac{\int_0^\infty \sqrt{G_{xx}(f)G_{yy}(f)}\,df}{\left[\int_0^\infty G_{xx}(f)df * \int_0^\infty G_{yy}(f)df\right]^{1/2}} \tag{9.22}$$

As far as the author is aware, the above is a new relationship, which can prove very useful in the analysis of random processes as will be demonstrated.

In general, the cross-spectrum between x and y is

$$G_{xy}(f) = C_{xy}(f) - iQ_{xy}(f) = |G_{xy}(f)|\exp(-i\Delta\varphi(f)) \tag{9.23a}$$

Where C_{xy} and Q_{xy} are referred to as the coincident and quadrature spectral density functions, respectively. $|G_{xy}(f)|$ is the amplitude of the one-sided cross-spectrum and $\Delta\varphi(f)$ is the phase difference between y and x at frequency (f). That is

$$|G_{xy}(f)| = [C^2_{xy}(f) + Q^2_{xy}(f)]^{1/2} \tag{9.23b}$$

and

$$\Delta\varphi(f) = \varphi_y(f) - \varphi_x(f) = \tan^{-1}\left[\frac{Q_{xy}(f)}{C_{xy}(f)}\right] \qquad (9.23c)$$

The cross-correlation function is related to the cross-spectrum through the following relationship.

$$\begin{aligned} R_{xy}(\Gamma) &= \text{Real}\left[\int_0^\infty G_{xy}(f)\,\exp(i2\pi f\Gamma)df\right] = \\ &= \int_0^\infty C_{xy}(f)\,\cos(2\pi f\Gamma)df = \\ &= \int_0^\infty |G_{xy}(f)|\,\cos\Delta\varphi(f)\,\cos(2\pi f\Gamma)df \end{aligned} \qquad (9.24)$$

The expected value of x times y is

$$E[x.y] = R_{xy}(0) = \int_0^\infty C_{xy}(f)df = \int_0^\infty |G_{xy}(f)|\,\cos\Delta\varphi(f)df \qquad (9.25a)$$

The above relationship shows that E[x,y] and hence $\rho_{x,y}$ is dependent on the phase shift between x and y at each frequency. The maximum of E[x.y] is obtained when $\cos\Delta\varphi(f)$ is equal to one for all frequencies and the minimum is obtained when the cosine is equal to minus one for all frequencies. Therefore

$$|E[x.y]| \leq \int_0^\infty |G_{xy}(f)|df \qquad (9.25b)$$

On the other hand, the following relationship exists between $|G_{xy}(f)|$, $G_{xx}(f)$ and $G_{yy}(f)$

$$|G_{xy}(f)|^2 = \gamma_{xy}^2(f)\,G_{xx}(f)\,G_{yy}(f) \qquad (9.26a)$$

Where $\gamma_{xy}^2(f)$ is called the coherence function and is always less than or equal to unity (Bendat and Piersol, 1971). (The coherence function is equal to unity for all frequencies only when y is the response from

a linear, noise-free system, with x being the only input). Consequently, Equation (9.26a) can be written as

$$|G_{xy}(f)|^2 \leq G_{xx}(f)\ G_{yy}(f) \tag{9.26b}$$

Combining Equations (9.26a) and (9.25b) leads to

$$\begin{aligned} |E[x.y]| &\leq \int_0^\infty |\gamma_{xy}(f)| \sqrt{G_{xx}(f)\ G_{yy}(f)}\ df \\ &\leq \int_0^\infty \sqrt{G_{xx}(f)\ G_{yy}(f)}\ df \end{aligned} \tag{9.27}$$

The limit on the correlation coefficient is obtained from the definition of the correlation coefficient, that is

$$|\rho_{x,y}| = \frac{|E[x.y]|}{\sigma_x\ \sigma_y} \leq \frac{\int_0^\infty |\gamma_{xy}(f)| \sqrt{G_{xx}(f)\ G_{yy}(f)}\ df}{\sigma_x\ \sigma_y} \tag{9.28}$$

Considering that the variance, σ^2, is equal to the area under the frequency spectrum, the above relationship can be written as

$$|\rho_{x,y}| \leq \frac{\int_0^\infty |\gamma_{xy}(f)| \sqrt{G_{xx}(f)\ G_{yy}(f)}df}{[\int_0^\infty G_{xx}(f)df * \int_0^\infty G_{yy}(f)df]^{1/2}} \leq \frac{\int_0^\infty \sqrt{G_{xx}(f)\ G_{yy}(f)}df}{[\int_0^\infty G_{xx}(f)df * \int_0^\infty G_{yy}(f)df]^{1/2}} \tag{9.29}$$

Which is the same as Equation (9.22).

Examination of the above relationship reveals that $|\rho_{xy}|$ can be equal to unity only when the frequency spectra of x and y are linearly related. This is an obvious conclusion because $|\rho_{xy}|$ is equal to one only when x and y are linearly related and if two processes are linearly related, their frequency spectra will be linearly related, too. Of more relevance to this study is the observation that if the

important frequency range of x is different from the important frequency range of y, then their correlation coefficient will always be close to zero. If the two frequency ranges are exclusive of each other, then the correlation coefficient will be equal to zero.

Furthermore, when the frequency spectra of x and y are exclusive of each other, then the frequency spectrum of $z = x \pm y$ is simply the sum of x and y frequency spectra. That is

$$G_{zz}(f) = G_{xx}(f) + G_{yy}(f) \tag{9.30}$$

The reason for the above relationship is that

$$R_{zz}(\Gamma) = E[z(t)z(t+\Gamma)] = R_{xx}(\Gamma) + R_{yy}(\Gamma) \pm R_{xy}(\Gamma) \pm R_{yx}(\Gamma) \tag{9.31}$$

Substituting Equation (9.26a) into Equation (9.24), yields

$$R_{xy}(\Gamma) = \text{REAL}\left[\int_0^\infty |\gamma_{xy}(f)| \sqrt{G_{xx}(f)\, G_{yy}(f)}\, \cos(2\pi f \Gamma) df\right] \tag{9.32}$$

When the x and y frequency spectra are exclusive of each other, $G_{xx}(f) * G_{yy}(f)$ will always be zero and hence $R_{xy}(\Gamma) = 0$. As a result, Equation (9.31) reduces to

$$R_{zz}(\Gamma) = R_{xx}(\Gamma) + R_{yy}(\Gamma) \tag{9.33}$$

Taking Fourier Transforms from both sides of the above equation leads to Equation (9.30). It is also clear that

$$\sigma_z^2 = \sigma_x^2 + \sigma_y^2 \tag{9.34}$$

Finally, it should be obvious that changing the phase angles of x and y when they have exclusive frequency spectra does not have any effect

on the above conclusions since frequency spectra are always independent of the phase angles.

Accuracy of the Variance of the Relative Kinematics

The relevance of the above discussion to this study becomes clear when it is noted that the cylinder natural frequency is well above the important frequency range for both low-intensity and high-intensity runs. Therefore, it is expected that correlation coefficients between water particle and cylinder kinematics be close to zero and hence insensitive to phase angle errors resulting from the shifting process.

As an example, the frequency spectra for water particle acceleration, cylinder acceleration and relative acceleration for Run 13 are shown in Figure 9.33. It is evident that the spectra of water particle and cylinder accelerations are exclusive and that the frequency spectrum of the relative acceleration is just the sum of the two frequency spectra. Therefore, phase angle errors have only a very small effect on the variance of the relative acceleration. Similar plots for water particle and cylinder velocity are shown in Figure 9.34. It is observed that the important frequency range for cylinder and water particle velocity is different, though there is a contribution to cylinder velocity at the wave frequency range. However, the variance of the cylinder velocity at the wave frequency range is by far smaller than the variance of water particle velocity and hence the effect of phase angle errors would be negligible. Comparison of the frequency spectra of the water particle velocity and the relative velocity spectra shows that the effect of the cylinder velocity on the variance of the relative velocity is small.

For interest, the frequency spectrum of $u_r|u_r|$ is shown in Figure 9.35 in comparison with the frequency spectrum of u_r. As observed, the two spectra are strikingly similar, and that is why the linearisation technique is so successful in the frequency domain. It was proved in Chapter 8 (Equation (8.101)) that the correlation coefficient between u_r and $u_r|u_r|$, assuming that u_r is Gaussian distributed, is 0.921. It is, therefore, inevitable that the spectra of u_r and $u_r|u_r|$ be very similar; otherwise, such a high correlation coefficient would be impossible. In general, a high correlation coefficient between two random processes x and y implies two things a) their frequency spectra are of similar shape, b) in the important frequency range, the phase angle difference between the processes are small. On the other hand, if the correlation coefficient between the two processes is small, it can be because of one or both of the following reasons a) the important frequency range of the two processes are not the same, b) the phase angle difference at the important frequency range is close to 90°. If the low correlation coefficient is due to the difference in phase angles, then its value would be very sensitive to any operation, such as shifting, that involves a change in the phase angles. On the other hand, if the low correlation coefficient is due to having different frequency ranges, then a change in the phase angles, would not have any effect on the correlation coefficient.

The overall conclusion of this section is that the inaccuracies in the phase angles of water particle kinematics due to shifting have a very small effect on the variance of the water particle kinematics because the frequency spectra of water particle and cylinder kinematics have different important frequency ranges and hence the correlation coefficients between them would not be affected by the process of

shifting. This, in turn, leads to the conclusion that the results of the method of moments for the flexible cylinder assumption, which are presented in the next section, are reliable.

9.2.2.3 Results and Discussion

Values of C_d, C_m, E_1, E_3, a_d^2 and a_i^2 are given in Table 9.6. Furthermore, for ease of discussion, the results of the rigid and flexible cylinder assumptions are compared in Table 9.7. Examination of these results lead to the following conclusions.

1. The C_m values have reduced for all runs in comparison with the rigid cylinder case. The reduction for the high-intensity runs, where the cylinder is at its most flexible mode, is in the range of 15% to 30%. For Runs 07 and 06 and in particular for Run 06, the reduction is more substantial. It should be noted that the cylinder is at its most flexible mode for these two low-intensity runs. The reduction for Run 01, as expected, is insignificant because the cylinder is at its most rigid mode and hence the response is small. The change in C_d values are less significant. With the exception of Run 16 at Levels 3 and 4, there is a slight reduction in C_d for the high-intensity runs. For Runs 07 and 06, and in particular for Run 06, the change is more substantial. For Run 01, the reduction is insignificant. The mathematical reasons for the above observations are now explained.

   Approximate values for Morison's coefficients can be obtained through Equations (9.15a) and (9.15b). The details of the calculations for both flexible and rigid cylinder cases are presented in Table 9.8 for Runs 13 and 23. Also included in the

table, are the results of the exact solutions which are only slightly different from the approximate solutions. For Run 13, C_m for the flexible cylinder is 76% of C_m for the rigid cylinder (Column 13). This ratio is the result of the multiplication of three different ratios given in Columns 6, 7 and 11; that is 0.76 = 0.974 * 0.994 * 0.782. The first coefficient is due to the difference of the kurtosis of the relative force and the hydrodynamic force. The second coefficient is due to the change in the standard deviation of the relative force and the hydrodynamic force. The third coefficient, which accounts for the major part of the difference between the C_m values, comes from the fact that the standard deviation of the relative acceleration is about 28% larger than that of the water particle acceleration (Column 9). The reason for this is shown in Figure 9.33, where it is observed that the variance of the relative acceleration is the sum of the variances of the water particle acceleration and cylinder acceleration. It is therefore concluded that the main reason for the substantial reduction in C_m values for the flexible cylinder in comparison with the rigid cylinder is that the variance of the cylinder acceleration is added to the variance of the water particle acceleration to form the variance of the relative acceleration. Table 9.8 also includes similar calculations for Run 23. The reason for more substantial reduction in C_m for Run 06 is that the cylinder is highly responsive and that the ratio between the variance of the cylinder acceleration and water particle acceleration is larger in comparison with other runs. The difference in C_d values are in the order of 5% and are much less significant than those for the C_m values. This can be explained by the fact that the variance of

the cylinder velocity is very small in comparison with the variance of water particle velocity as shown in Figure 9.34. Therefore, the standard deviation of the relative velocity is only slightly larger than the standard deviation of the water particle velocity. (i.e. 5% for Run 13 and 3% for Run 23). This in turn leads to relatively small changes in C_d values.

2. As was the case for the rigid cylinder study, a_d^2 generally decreases with increasing depth of immersion, reflecting the slightly greater rate of decay with depth for the drag force.

3. As was the case for the rigid cylinder study, low-intensity runs are inertia dominated and hence are not well-conditioned for the determination of C_d values, which are high most of the time.

4. There is a consistent reduction in both C_d and C_m values from Level 2 to Level 4. The mathematical reason for this observation is that though σ_{Fr}, σ_{ur} and $\sigma_{\dot{u}r}$ all decrease with depth, the rate of decrease is larger for σ_{Fr} so that $\sigma_{Fr}/\sigma_{ur}^2$ and $\sigma_{Fr}/\sigma_{\dot{u}r}$ decrease with depth, too, which leads to a reduction in C_d and C_m values according to Equations (9.15a) and (9.15b). The physical reason behind this observation is not known.

5. It is believed that the cylinder displacement (as supplied by BMT and after its sign was reversed) has the right sign at the wave frequency range but the wrong sign at cylinder's natural frequency range (refer to Appendix A). The wrong sign is equivalent to a phase shift of 180°; however, it was previously shown that the standard deviations of the relative kinematics are

insensitive to phase angle errors because the frequency spectra of the cylinder and water particle kinematics are exclusive of each other. Therefore, σ_{u_r} and $\sigma_{\dot{u}_r}$ are reliable. The effect of the sign error on the standard deviation of the relative force is now investigated.

The frequency spectra of the hydrodynamic force and the relative force are compared in Figure 9.36. As observed, the major difference between the two spectra is that the bump at the cylinder's natural frequency has been removed from the spectrum of the relative force. However, examination of Equations (9.17a) and (9.17c) reveals that the relative force must have a larger bump (amplitude) at the cylinder's natural frequency. This, on its own, is a strong evidence for the assertion that the cylinder's response close to it's natural frequency has the incorrect sign. If the sign was right, then the area under the bump would have doubled rather than being removed. Therefore, the calculated σ_{F_r} is less than its real value leading to reduced values for C_d and C_m. However, the area under the bump is very small, therefore the overall effect is negligible. As shown in Column 7 of Table 9.8, the removal of the bump has caused 0.5% reduction in σ_{F_r}, hence, real σ_{F_r} is expected to be larger than σ_F by about 0.5%. Overall, real σ_{F_r} is expected to be about 1% larger than the calculated σ_{F_r}; hence, C_d and C_m should be increased by about 1%, which is negligible.

As regard to the effect of the sign error, it cannot be quantified on the kurtosis. An error in the kurtosis will change the balance between the C_d and C_m. The C_d and C_m values presented

in Table 9.8 are not unusual. It can therefore be hoped that the value of kurtosis has not been significantly affected as a result of the incorrect sign.

6. Values of E_1 and E_3 for the rigid and flexible cylinder assumptions are compared in Table 9.7(c). Against expectation, these coefficients are higher for the flexible cylinder assumption. This is believed to be the consequence of the incorrect sign previously discussed.

9.3 DERIVATION OF DRAG AND INERTIA COEFFICIENTS IN THE TIME DOMAIN FOR THE RELATIVE MOTION FORM OF MORISON'S EQUATION

In this section, the Least Square Method and Bearman's Method (Bearman, 1988) will be used for derivation of Morison's coefficients. The two methods will be criticised and a new method, which will be termed the Maximum Correlation method for the purposes of this study, will be introduced.

9.3.1 LEAST SQUARE ERROR METHOD

This technique is based on the minimisation of the sum of the square errors ($\sum e$) between the observed force (F_o) and the predicted Morison force (F) over all or part of the data set. Considering that $F_r = F - \hat{k}_i \ddot{r}$, the error term is

$$e = F_o - F = F_o - (F_r + \hat{k}_i \ddot{r}) = (F_o - \hat{k}_i \ddot{r}) - F_r = F_{ro} - F_r \qquad (9.35a)$$

where F_{ro} is referred to as the relative observed force and is a known quantity. Substituting for F_r from Equation (9.18a) leads to

$$e = F_{ro} - C_d \hat{k}_d u_r|u_r| - C_m \hat{k}_i \dot{u}_r \qquad (9.35b)$$

Raising both sides of the above equation to the second power and taking expectations, gives

$$E[e^2] = C_d^2 \hat{k}_d^2 z_1 + 2C_d C_m \hat{k}_d^2 \hat{k}_i^2 z_2 - 2C_d \hat{k}_d^2 z_3 + C_m^2 \hat{k}_i^2 z_4 - 2C_m \hat{k}_i z_5 + z_6 \tag{9.36}$$

where

$$\begin{aligned} z_1 &= E[u_r^4] \\ z_2 &= E[\dot{u}_r \cdot u_r|u_r|] \\ z_3 &= E[F_{ro} \cdot u_r|u_r|] \\ z_4 &= E[\dot{u}_r^2] \\ z_5 &= E[F_{ro} \cdot \dot{u}_r] \\ z_6 &= E[F_{ro}^2] \end{aligned} \tag{9.37}$$

The expected value of the error term will be minimum when both of the following conditions are met. That is when

$$\frac{\partial(E[e^2])}{\partial C_d} = 2z_1 \hat{k}_d C_d + 2z_2 \hat{k}_d \hat{k}_i C_m - 2\hat{k}_d z_3 = 0 \tag{9.38a}$$

and

$$\frac{\partial(E[e^2])}{\partial C_m} = 2z_2 \hat{k}_d \hat{k}_i C_d + 2z_4 \hat{k}_i^2 C_m - 2\hat{k}_i z_5 = 0 \tag{9.38b}$$

The simultaneous solution of the above equations, leads to the following relationships for Morison's coefficients

$$C_d = \frac{1}{\hat{k}_d} * \frac{z_3 z_4 - z_2 z_5}{z_1 z_4 - z_2^2} \tag{9.39a}$$

$$C_m = \frac{1}{\hat{k}_i} * \frac{z_1 z_5 - z_2 z_3}{z_1 z_4 - z_2^2} \tag{9.39b}$$

The expected value of the error term is obtained by substituting for C_d and C_m from the above equations into Equation (9.36). That is

$$E[e^2] = z_6 - \frac{z_1 z_3^2 z_4^4 + 2z_2^3 z_3 z_5 + 2z_1^2 z_4 z_5^2 - z_1^2 z_2^2 z_5^2 - 2z_1 z_2 z_3 z_4 z_5}{z_1 z_4 - z_2^2} \tag{9.39c}$$

Assuming that relative velocity and relative acceleration are Gaussian distributed, then they would be statistically independent ($\rho_{u_r,\dot{u}_r} = 0$). Thus

$$z_2 = E[\dot{u}_r . u_r|u_r|] = E[\dot{u}_r] \; . \; E[u_r|u_r|] = 0 \tag{9.40}$$

and C_d, C_m and $E[e^2]$ will reduce to,

$$C_d = \frac{1}{\hat{k}_d} * \frac{z_3}{z_1} \tag{9.41a}$$

$$C_m = \frac{1}{\hat{k}_i} * \frac{z_5}{z_4} \tag{9.41b}$$

$$E[e^2] = z_6 - \frac{z_3^2}{z_1} - \frac{z_5^2}{z_4} \tag{9.41c}$$

It should be noted that the second and third terms on the right hand side of Equation (9.41c) are the mean square of the drag and inertia forces, respectively. That is

$$E[F_d^2] = C_d^2 \hat{k}_d^2 \, E[u_r^4] = \frac{z_3^2}{z_1^2} * z_1 = \frac{z_3^2}{z_1} \tag{9.42a}$$

and

$$E[F_i^2] = C_m^2 \hat{k}_i^2 E[\dot{u}_r^2] = \frac{z_5^2}{z_4^2} * z_4 = \frac{z_5^2}{z_4} \tag{9.42b}$$

Therefore, Equation (9.41c) can be written as

$$E[e^2] = E[F_{ro}^2] - E[F_d^2] - E[F_i^2] \tag{9.43a}$$

or

$$E[F_{ro}^2] = E[F_d^2] + E[F_i^2] + E[e^2] = E[F_r^2] + E[e^2] \tag{9.43b}$$

Dividing both sides of the above equation by $E[F_{ro}^2]$, leads to

$$\frac{E[F_d^2]}{E[F_{ro}^2]} + \frac{E[F_i^2]}{E[F_{ro}^2]} + \frac{E[e^2]}{E[F_{ro}^2]} = 1 \tag{9.43c}$$

or

$$a_d^2 + a_i^2 + a_e^2 = 1 \tag{9.44a}$$

where

$$a_d^2 = z_3^2/(z_1 z_6) \tag{9.44b}$$

$$a_i^2 = z_5^2/(z_4 z_6) \tag{9.44c}$$

Combining Equations (9.44b) and (9.44c) with Equations (9.41a) and (9.41b), respectively, yields

$$C_d = \frac{1}{\hat{k}_d} * (z_6/z_1)^{1/2} * a_d \tag{9.44d}$$

$$C_m = \frac{1}{k_i} * (z_6/z_4)^{1/2} * a_i \tag{9.44e}$$

As before a_d^2 and a_i^2 are measures of the contribution of the drag and inertia components of force to the mean square of the observed relative force. The third term (a_e^2) is referred to as the error coefficient and

is a measure of the goodness of fit between the predicted and the observed forces. Equation (9.44a) carries a simple but very important message. It indicates that all the variance of the observed force cannot be accounted by drag and inertia components of force. If it could, then a_e^2 would be zero, which is possible only if Morison's equation was an exact relationship. In other words, the variance of the observed force is composed of three components a) the variance of the drag force, b) the variance of the inertia force, c) the variance of the error term. Consequently, Least Square Error Method results in a predicted force which always has a smaller variance than the observed force. This observation is very important in the study of random processes where the variance is a very important parameter and all the extreme statistics are expressed in terms of multiples of the standard deviation. It is obvious that the larger the value of a_e^2, the smaller the variance of the predicted force.

Therefore, the Least Square Error Method is good in spectral analysis because the fit between the spectra of the observed and predicted forces is expected to be good. On the other hand, its application in the time domain is not recommended because the agreement between the observed and predicted forces in the time domain is relatively poor. In particular, it is expected that Morison's coefficients from the analysis of long records in the time domain would be smaller than those obtained from the analysis of the same data in the spectral domain. It is now intended to identify those parameters which affect the value of the error coefficient.

Coefficients z_1 to z_6 from Equation (9.37) can be written as

$$z_1 = E[u^4]$$

$$z_2 = 0$$

$$z_3 = \overset{(a)}{\rho}_{Fro,ur|ur|} * (E[F_{ro}^2])^{1/2} * (E[(u_r|u_r|)^2])^{1/2} = \overset{(a)}{\rho}_{Fro,ur|ur|} * (z_1 z_6)^{1/2}$$

$$z_4 = E[\dot{u}_r^2]$$

$$z_5 = \overset{(a)}{\rho}_{Fro,\dot{u}r} * (E[F_{ro}^2])^{1/2} * (E[\dot{u}_r^2])^{1/2} = \overset{(a)}{\rho}_{Fro,\dot{u}r} * (z_4 z_6)^{1/2}$$

$$z_6 = E[F_{ro}^2] \qquad (9.45)$$

where $\overset{(a)}{\rho}_{x,y}$ is the absolute correlation coefficient defined as

$$\overset{(a)}{\rho}_{x,y} = \frac{E[x.y]}{x_{rms} \cdot y_{rms}} \qquad (9.46a)$$

as opposed to the (central) correlation coefficient which is equal to

$$\rho_{x,y} = \frac{E[(x - \bar{x})(y - \bar{y})]}{\sigma_x \ \sigma_y} \qquad (9.46b)$$

Substituting for the above z values into Equation (9.44b) and (9.44c), a_d^2 and a_i^2 will become

$$a_d^2 = (\overset{(a)}{\rho}_{Fro,ur|ur|})^2 \qquad (9.47a)$$

$$a_i^2 = (\overset{(a)}{\rho}_{Fro,\dot{u}r})^2 \qquad (9.47b)$$

Thus, from Equation (9.44a)

$$a_e^2 = 1 - (\overset{(a)}{\rho}_{Fro,ur|ur|})^2 - (\overset{(a)}{\rho}_{Fro,\dot{u}r})^2 \qquad (9.47c)$$

It was previously shown that for a Gaussian distributed random variable such as x, the correlation coefficient between x and x|x| is very high ($\rho_{x,x|x|} = 0.921$); it can therefore be concluded that $\rho_{Fro,ur|ur|}$ is high

only when $\rho_{Fro,ur}$ is high and vice versa. Consequently, in a qualitative sense, if the correlation coefficients between the force and at least one of the water particle kinematics is high, then from Equation (9.47c), a_e^2 will be small, the fit between the predicted and observed forces will be good and C_d and C_m values would not be significantly underestimated. On the other hand, if the correlation coefficient between the force and both water particle velocity and acceleration is low, then a_e^2 will be large, a_d^2 and a_i^2 will be small and from Equations (9.44d) and (9.44e), C_d and C_m will be small, too. The following relationships give further insight into the Least Square Error Method.

Multiplying, both sides of Equation (9.35b) by $\dot{u}_r$ and taking expectations leads to

$$E[e.\dot{u}_r] = E[F_{ro}.\dot{u}_r] - C_d \hat{k}_d E[\dot{u}_r * u_r|u_r|] - C_m \hat{k}_i E[\dot{u}_r^2] \tag{9.48}$$

Combining the above equation with Equations (9.37), (9.41a) and (9.41b), and considering that $z_2 = 0$, results in

$$E[e.\dot{u}_r] = z_5 - \frac{z_3}{z_1} * z_2 - \frac{z_5}{z_4} * z_4 = 0 \tag{9.49a}$$

Similarly, one can show that

$$E[e.u_r|u_r|] = 0 \tag{9.49b}$$

$$E[e.F_r] = 0 \tag{9.49c}$$

$$E[e.F_{ro}] = z_6 - \frac{z_3^2}{z_1} - \frac{z_5^2}{z_4} = E[e^2] \tag{9.49d}$$

and

$$\overset{(a)}{\rho}_{Fro,e} = \frac{E[F_{ro} \cdot e]}{(E[F_{ro}^2])^{1/2} * (E[e^2])^{1/2}} = \frac{E[e^2]}{(E[F_{ro}^2])^{1/2} * (E[e^2])^{1/2}}$$

$$= \left(\frac{E[e^2]}{E[F_{ro}^2]}\right)^{1/2} = a_e \qquad (9.49e)$$

Therefore, from Equation (9.47c)

$$(\overset{(a)}{\rho}_{Fro,ur|ur|})^2 + (\overset{(a)}{\rho}_{Fro,\dot{u}r})^2 + (\overset{(a)}{\rho}_{Fro,e})^2 = 1 \qquad (9.49f)$$

Where F_r and F_{ro} refer to the predicted and observed relative forces, respectively. The above equations indicate that the correlation coefficients between the error term on one hand and $u_r|u_r|$, $\dot{u}_r$ and F_r is zero. In other words, the observed force is composed of three components. The first part is in correlation with $u_r|u_r|$ and forms the drag component; the second part is in correlation with $\dot{u}_r$ and forms the inertia component and finally, the third part is neither correlated with $u_r|u_r|$, nor with $\dot{u}_r$ and hence forms the error term.

Finally, considering that $F_{ro} = F_r + e$, $E[F_{ro} \cdot F_r]$ will be

$$E[F_{ro}.F_r] = E[F_r^2] + E[e.F_r] \qquad (9.50a)$$

However, according to Equation (9.49c), $E[e.F_r] = 0$, therefore

$$E[F_{ro}.F_r] = E[F_r^2] \qquad (9.50b)$$

or

$$\overset{(a)}{\rho}_{Fro,Fr} = \frac{E[F_{ro}.F_r]}{(E[F_{ro}^2])^{1/2} * (E[F_r^2])^{1/2}} = \left(\frac{E[F_r^2]}{E[F_{ro}^2]}\right)^{1/2} \qquad (9.50c)$$

From Equation (9.43b), $E[F_r^2] = E[F_{ro}^2] - E[e^2]$. Consequently

$$\overset{(a)}{\rho}_{Fro,Fr} = \left(\frac{E[F_{ro}^2] - E[e^2]}{E[F_{ro}^2]} \right)^{1/2} = (1 - a_e^2)^{1/2} = (a_d^2 + a_i^2)^{1/2} \qquad (9.50d)$$

Combining the above equation with Equation (9.47c), leads to

$$\overset{(a)}{\rho}_{Fro,Fr} = [(\overset{(a)}{\rho}_{Fro,ur|ur|})^2 + (\overset{(a)}{\rho}_{Fro,\dot{u}r})^2]^{1/2} \qquad (9.50e)$$

As expected, Equation (9.50d) shows that the larger the error coefficient, a_e^2, the smaller the correlation coefficient between the observed and the predicted forces. The correlation coefficient can only be equal to one only when the error coefficient is equal to zero.

Comment on the Least Square Error Method

Least Square Error Method is a very powerful and valuable method of analysis. However, its results must be interpreted correctly. The error coefficient indicates what fraction of the total variance of the observed force cannot be accounted for by terms containing $u_r|u_r|$ and $\dot{u}_r$. At this stage, three options are available.

1. Trying to improve Morison's equation by introducing new terms or changing its form so that the error coefficient will reduce. This path has not been successful and it is generally believed that the present form of Morison's equation is the best one can expect for years to come.

2. Ignoring the error term altogether. This is what has happened without being noticed. It leads to a predicted force with a smaller variance than that of the observed force, with all the implications that it may have. For example, extreme statistics

which are expressed in terms of multiples of the standard deviation of the predicted force may be underestimated.

3. The third and the best option is to accept the present form of Morison's equation but changing the philosophy behind the method of analysis by determining Morison's coefficients such that a) the variances of the observed and predicted forces are equal, b) the correlation coefficient between the observed and predicted forces are maximum. This method will be investigated in Section 9.3.3.

Alternative Forms of Least Square Error Method

The difference between the observed and predicted forces in the neighbourhood of maximum forces may be further minimised by defining the error term in the following way

$$e = w\,(F_{ro} - F_r) \tag{9.51a}$$

where w is a weighting factor. In the present study, w was set to $|F_{ro}|^{k/2}$ for various integer values of k. If k = 0, then the error term becomes the same as the standard error term, defined in Equation (9.35a). Higher values of k put greater weight on errors at the higher levels of force. Substituting for F_r from Equation (9.18a) yields

$$e = |F_{ro}|^{k/2} * (F_{ro} - C_d\hat{k}_d\, u_r|u_r| - C_m\hat{k}_i\dot{u}_r) \tag{9.51b}$$

Raising both sides of the above equation to the second power and taking expectations, gives

$$E[e^2] = C_d^2\hat{k}_d^2T_1 + 2C_dC_m\hat{k}_d\hat{k}_iT_2 - 2C_d\hat{k}_dT_3 + C_m^2\hat{k}_i^2T_4 - 2C_m\hat{k}_iT_5 + T_6 \tag{9.51c}$$

where

$$T_1 = E[|F_{ro}|^k * u_r^4]$$

$$T_2 = E[|F_{ro}|^k * \dot{u}_r * u_r|u_r|]$$

$$T_3 = E[|F_{ro}|^k * F_{ro} * u_r|u_r|]$$

$$T_4 = E[|F_{ro}|^k * \dot{u}_r^2]$$

$$T_5 = E[|F_{ro}|^k * F_{ro} * \dot{u}_r]$$

$$T_6 = E[|F_{ro}|^k * F_{ro}^2] \qquad (9.51d)$$

The expected value of the error term will be minimum when its partial derivatives with respect to both C_d and C_m are zero. The resulting equations are similar to Equations (9.38a) and (9.38b) except that z coefficients are replaced with T coefficients. Solving these equations leads to the following values of C_d and C_m similar to Equations (9.39a) and (9.39b).

$$C_d = \frac{1}{\hat{k}_d} * \frac{T_3T_4 - T_2T_5}{T_1T_4 - T_2^2} \qquad (9.51e)$$

$$C_m = \frac{1}{\hat{k}_i} * \frac{T_1T_5 - T_2T_3}{T_1T_4 - T_2^2} \qquad (9.51f)$$

The expected value of the error term is obtained by substituting for C_d and C_m from the above equations into Equation (9.51c). That is

$$E[e^2] = T_6 - \frac{T_1T_3^2T_4^2 + 2T_2^3T_3T_5 + 2T_1T_4^2T_5^2 - T_1T_2^2T_5^2 + 2T_1T_2T_3T_4T_5}{T_1T_4 - T_2^2} \qquad (9.51g)$$

The unit of $E[e^2]$ is force to the power of $(k + 2)$. The error coefficient is then defined as

$$a_e^2 = \frac{(E[e^2])^{2/(k+2)}}{E[F_{ro}^2]} \qquad (9.51h)$$

So that a_e^2 is non-dimensional and is comparable with the error coefficient defined for the standard least square error technique.

An alternative way of reducing the difference between the observed and predicted forces in the neighbourhood of maximum forces is by eliminating those points which are below a threshold level, Th (i.e. by attempting a least square fit to the large amplitude sections of the force time series). The error term is therefore defined as

$$e = H(|F_{ro}| - Th) \cdot (F_{ro} - F_r) \qquad (9.52)$$

with H(x) as a Heavyside function such that H(x) = 0 for x < 0, otherwise H(x) = 1. In this way, all the data points for which F_{ro} lies in a band from -Th to +Th will be eliminated from the analysis; hence the error term is dependent on the differences between the observed and predicted forces at higher levels of force.

9.3.2 BEARMAN'S METHOD

Bearman (1988) refers to a simpler system of equations arising from the regular wave studies at de Voorst. According to Equation (9.18a), the relative observed force is estimated by

$$F_{ro} \approx C_d\hat{k}_d\, u_r|u_r| + C_m\hat{k}_i\dot{u}_r \qquad (9.53)$$

multiplying the above equation throughout first by u_r and then by $\dot{u}_r$ and taking expectations gives

$$E[F_{ro} \cdot u_r] = C_d\hat{k}_d\, E[|u_r|^3] + C_m\hat{k}_i\, E[u_r \cdot \dot{u}_r] \qquad (9.54a)$$

$$E[F_{ro} \cdot \dot{u}] = C_d\hat{k}_d\, E[|u_r|u_r|\dot{u}_r|] + C_m\hat{k}_i\, E[\dot{u}_r^2] \qquad (9.54b)$$

Solving the above set of equations for C_d and C_m leads to

$$C_d = \frac{1}{\hat{k}_d} * \frac{\beta_3\beta_5 - \beta_2\beta_6}{\beta_1\beta_5 - \beta_2\beta_4} \qquad (9.55a)$$

$$C_m = \frac{1}{\hat{k}_i} * \frac{\beta_3\beta_4 - \beta_1\beta_6}{\beta_2\beta_4 - \beta_1\beta_5} \qquad (9.55b)$$

where

$$\beta_1 = E[|u_r|^3]$$

$$\beta_2 = E[u_r \cdot \dot{u}_r]$$

$$\beta_3 = E[F_{ro} \cdot u_r]$$

$$\beta_4 = E[u_r|u_r|\dot{u}_r]$$

$$\beta_5 = E[\dot{u}_r^2]$$

$$\beta_6 = E[F_{ro} \cdot \dot{u}_r] \qquad (9.55c)$$

As for the case of the Least Square Error Method, if relative velocity and acceleration are assumed to be Gaussian distributed, then β_2 and β_4 will be zero. Therefore, Equations (9.55a) and (9.55b) will reduce to

$$C_d = \frac{1}{\hat{k}_d} * \frac{\beta_3}{\beta_1} \qquad (9.56a)$$

$$C_m = \frac{1}{\hat{k}_i} * \frac{\beta_6}{\beta_5} \qquad (9.56b)$$

Examination of the above relationships reveals that C_d and C_m depend on the correlation coefficients between the observed force and the relative velocity and acceleration, respectively. As was shown for the Least Square Error Method, this leads to a predicted force with a smaller variance than the observed force. While the Least Square Method

has an error term with a clear interpretation associated with it, Bearman's method lacks such a measure of error. Its use for short records of regular waves where the error is expected to be small is justifiable; however, for the study of long records of random data where the error is expected to be large, the least square error technique offers a more robust method of analysis. Comparison of Equations (9.56b) and (9.41b) shows that the two methods result in identical values of C_m; however, the relationships for the drag coefficients are not the same; therefore, some discrepancy between C_d values from the two methods are expected.

9.3.3 MAXIMUM CORRELATION METHOD

In this method, Morison's coefficients are determined so that a) the variances of the observed and predicted forces are equal, and b) the correlation coefficients between the observed and the predicted forces are maximum. It should be noted that Morison's equation offers only an approximation to the fluid loading on submerged cylinders because it does not account for the effect of vortex shedding, etc. and hence the predicted forces can never fit the observed forces perfectly. In other words, no method of determination of Morison's coefficients will result in a perfect fit between the observed and predicted forces.

According to Equation (9.18a), the relative motion form of Morison's equation is

$$F_r = C_d \hat{k}_d \, u_r |u_r| + C_m \hat{k}_i \, \dot{u}_r \qquad (9.57a)$$

Raising both sides of the above equation to the second power and taking expectations, gives

$$E[F_r^2] = C_d^2 \hat{k}_d^2 z_1 + C_m^2 \hat{k}_i^2 z_4 + 2C_d C_m \hat{k}_d \hat{k}_i z_2 \qquad (9.57b)$$

where the z coefficients are the same as those introduced in the Least Square Error Method (Equation 9.37). Recognising that $E[F_r^2] = E[F_{ro}^2] = z_6$ and that $z_2 = 0$ (Equation 9.40), the above equation will reduce to

$$C_d^2 \hat{k}_d^2 \, z_1 + C_m^2 \hat{k}_i^2 \, z_4 = z_6 \qquad (9.58a)$$

or

$$C_m = \frac{1}{\hat{k}_i} * \left(\frac{z_6 - C_d^2 \hat{k}_d^2 \, z_1}{z_4} \right)^{1/2} \qquad (9.58b)$$

Multiplying Equation (9.57a) throughout by F_{ro} and taking expectations yields

$$E[F_{ro} \, . \, F_r] = C_d \hat{k}_d \, z_3 + C_m \hat{k}_i \, z_5 \qquad (9.59a)$$

The correlation coefficient would then be

$$\overset{(a)}{\rho}_{Fro,fr} = \frac{E[F_{ro} \, . \, F_r]}{(E[F_{ro}^2])^{1/2} * (E[F_r^2])^{1/2}} = C_d \hat{k}_d * \frac{z_3}{z_6} + C_m \hat{k}_i * \frac{z_5}{z_6} \qquad (9.59b)$$

The correlation coefficient is maximum when $E[F_{ro} \, . \, F_r]$ is maximum. Substituting Equation (9.58b) into Equation (9.59a), results in

$$E[F_{ro} \, . \, F_r] = C_d \hat{k}_d \, z_3 + z_5 * \left(\frac{z_6 - C_d^2 \hat{k}_d^2 \, z_1}{z_4} \right)^{1/2} \qquad (9.59c)$$

The above is maximum when its first derivative with respect to C_d is zero. The solution to the resultant equation is

$$C_d = \frac{1}{\hat{k}_d} * z_3 * \left[\frac{z_4 z_6}{z_1(z_1 z_5^2 + z_3^2 z_4)} \right]^{1/2} = \frac{1}{\hat{k}_d} * \frac{z_6}{z_1} * a_d \qquad (9.60a)$$

Substituting the above equation into Equation (9.58b), gives

$$C_m = \frac{1}{\hat{k}_i} * z_5 * \left[\frac{z_1 z_6}{z_4(z_1 z_5^2 + z_3^2 z_4)} \right]^{1/2} = \frac{1}{\hat{k}_i} * \frac{z_6}{z_4} * a_i \qquad (9.60b)$$

where, as before, a_d^2 and a_i^2 are measures of the contribution of the drag and inertia components of force to the mean square of the observed force. That is

$$a_d^2 = \frac{E[F_d^2]}{E[F_{ro}^2]} = \frac{C_d^2 \hat{k}_d^2 z_1}{z_6} = \frac{z_3^2 z_4}{z_1 z_5^2 + z_3^2 z_4} \qquad (9.61a)$$

and

$$a_i^2 = \frac{E[F_i^2]}{E[F_{ro}^2]} = \frac{C_m^2 \hat{k}_i^2 z_4}{z_6} = \frac{z_1 z_5^2}{z_1 z_5^2 + z_3^2 z_4} \qquad (9.61b)$$

so that as expected

$$a_d^2 + a_i^2 = 1 \qquad (9.61c)$$

The correlation coefficient is obtained by substituting Equations (9.60a) and (9.60b) into Equation (9.59b). That is

$$\rho^{(a)}_{Fro,Fr} = \left[\frac{z_1 z_5^2 + z_3^2 z_4}{z_1 z_4 z_6} \right]^{1/2} \qquad (9.62)$$

Substituting from Equation (9.45) into Equations (9.61a), (9.61b) and (9.62), leads to

$$a_d^2 = \frac{(\rho^{(a)}_{Fro,ur|ur|})^2}{(\rho^{(a)}_{Fro,ur|ur|})^2 + (\rho^{(a)}_{Fro,\dot{u}r})^2} \tag{9.63a}$$

$$a_i^2 = \frac{(\rho^{(a)}_{Fro,\dot{u}r})^2}{(\rho^{(a)}_{Fro,ur|ur|})^2 + (\rho^{(a)}_{Fro,\dot{u}r})^2} \tag{9.63b}$$

and

$$\rho^{(a)}_{Fro,Fr} = [(\rho^{(a)}_{Fro,ur|ur|})^2 + (\rho^{(a)}_{Fro,\dot{u}r})^2]^{1/2} \tag{9.63c}$$

The correlation coefficient is a measure of the goodness of fit between the observed and predicted forces.

Relationship Between Maximum Correlation Method and Least Square Error Method

As was the case for the Least Square Error Method, the error term is defined as

$$e = F_{ro} - F_r \tag{9.64a}$$

Raising both sides of the above equation to the second power, taking expectations and noting that for Maximum Correlation Method $E[F_{ro}^2] = E[F_r^2]$, one obtains

$$E[e^2] = 2*(E[F_{ro}^2] - E[F_{ro} \cdot F_r]) \tag{9.64b}$$

In Maximum Correlation Method, $E[F_{ro} \cdot F_r]$ is maximised; however, the above equation shows that maximising $E[F_{ro} \cdot F_r]$ is equivalent to minimising $E[e^2]$ since $E[F_{ro}^2]$ is fixed. Thus, the Maximum Correlation Method is equivalent to a restrained form of the Least Square Error

Method. That is, it is equivalent to minimising $E[e^2]$, subject to the condition that $E[F_r^2] = E[F_{ro}^2]$.

The error coefficient can then be obtained by dividing Equation (9.46b) by $E[F_{ro}^2]$. That is

$$\acute{a}_e^2 = \frac{E[e^2]}{E[F_{ro}^2]} = 2\,(1 - \overset{(a)}{\rho}_{Fro,Fr}) \tag{9.64c}$$

According to the above equation, $\acute{a}_e^2$ will be zero only when $\overset{(a)}{\rho}_{Fro,Fr} = 1$, which means a perfect match between the observed and predicted forces.

Comparison of the Maximum Correlation and the Standard Least Square Error Methods

Comparison of Equations (9.63a) and (9.50e) shows that the correlation coefficients between the observed and predicted forces for both methods are identical. That means that the predicted force from the two methods are in perfect correlation. In other words, there is a linear relationship between the predicted forces from the two methods. This can be rigorously proved by calculating the ratios between the Morison's coefficients from the two methods. Dividing Equations (9.60a) and (9.60b) by Equations (9.41a) and (9.41b), respectively, leads to

$$\frac{(C_d)_m}{(C_d)_I} = \frac{(C_m)_m}{(C_m)_I} = \left[\frac{Z_1 Z_4 Z_6}{Z_1 Z_5^2 + Z_3^2 Z_4}\right]^{1/2} = \left[\frac{1}{\dfrac{Z_3^2}{Z_1 Z_6} + \dfrac{Z_5^2}{Z_4 Z_6}}\right]^{1/2} \tag{9.65a}$$

Substituting Equations (9.44b) and (9.44c) into the above equation gives

$$\frac{(C_d)_m}{(C_d)_I} = \frac{(C_m)_m}{(C_m)_I} = \left(\frac{1}{a_d^2 + a_i^2}\right)^{1/2} \tag{9.65b}$$

Combining Equation (9.44a) with Equation (9.65b), results in

$$\frac{(C_d)_m}{(C_d)_I} = \frac{(C_m)_m}{(C_m)_I} = \left(\frac{1}{1 - a_e^2}\right)^{1/2} = MF \tag{9.66}$$

Therefore, the predicted forces from the two methods are related by

$$(F_r)_m = (F_r)_I * MF \tag{9.67a}$$

where MF is a magnification factor defined by

$$MF = \left(\frac{1}{1 - a_e^2}\right)^{1/2} \tag{9.67b}$$

and a_e^2 is the error coefficient of the Least Square Error Method.

9.3.4 GENERAL COMMENT ON DIFFERENT METHODS

Equating the second moments of the observed and predicted forces will result in Equation (9.58a). That is

$$C_d^2 \hat{k}_d^2 z_1 + C_m^2 \hat{k}_i^2 z_4 = z_e \tag{9.68a}$$

where the z coefficients are defined in Equation (9.37). Dividing both sides of the above equation by z_e will lead to

$$\frac{C_d^2}{\left(\frac{z_e}{\hat{k}_d \sqrt{z_1}}\right)^2} + \frac{C_m^2}{\left(\frac{z_e}{\hat{k}_i \sqrt{z_4}}\right)^2} = 1 \tag{9.68b}$$

or,

$$\frac{C_d^2}{a^2} + \frac{C_m^2}{b^2} = 1 \tag{9.68c}$$

where

$$a = \frac{z_6}{\hat{k}_d \sqrt{z_1}} \tag{9.68d}$$

and

$$b = \frac{z_6}{\hat{k}_i \sqrt{z_4}} \tag{9.68e}$$

Equation (9.68c) is the equation of an ellipse as shown in the following figure. It should be obvious that C_d and C_m values which are inside the ellipse will lead to predicted forces with smaller variances than the observed force; C_d and C_m values on the ellipse will lead to forces with variances equal to that of the observed force. Those C_d and C_m values which lie out of the ellipse, will lead to forces with higher variances than that of the observed force. It is suggested that whatever method is used in determination of C_d and C_m values, if the resultant point is not on the ellipse, it should be connected to the origin and its intersection with the ellipse should be taken as the desired solution. In this way, the discrepancy in the reported C_d and C_m values from different experiments is expected to be reduced.

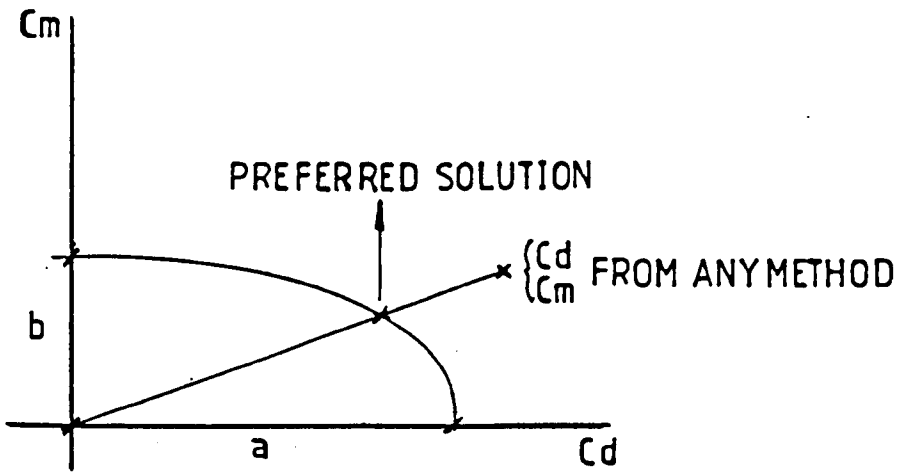

9.3.5 EFFECT OF SHIFTING WATER PARTICLE KINEMATICS ON THE VALUES OF C_d AND C_m

According to Equations (9.47a) and (9.47b), a_d and a_i and hence C_d and C_m depend on the correlation coefficients between the observed force and water particle kinematics. Therefore, it is necessary to investigate the effect due to shifting on these correlation coefficients. As previously discussed, shifting involves a change in the phase angles of different harmonics of water particle kinematics. Consequently, the phase angles of the harmonics of the shifted kinematics are not error free. The problem therefore reduces to the investigation of the effect of these phase angle inaccuracies on the correlation coefficients between observed forces and the shifted kinematics.

Consider two random signals x and y which have been broken down into their harmonic components in the following way

$$x = \sum_{k=1}^{N/2} \lambda_k \cos(\omega_k t - \varphi_k) \tag{9.69a}$$

and

$$y = \sum_{k=1}^{N/2} \acute{\lambda}_k \cos(\omega_k t - \acute{\varphi}_k) \tag{9.69b}$$

It can readily be shown that

$$E[xy] = \sum_{k=1}^{N/2} \lambda_k \acute{\lambda}_k \cos(\Delta\varphi_k) \tag{9.70a}$$

where

$$\Delta\varphi_k = \varphi_k - \acute{\varphi}_k \tag{9.70b}$$

Differentiation of Equation (9.70a) with respect to the phase angles, leads to

$$d(E[xy]) = - \sum_{k=1}^{N/2} \lambda_k \acute{\lambda}_k \sin(\Delta\varphi_k)\, d(\Delta\varphi_k) \tag{9.71}$$

If x and y are highly correlated, then $\Delta\varphi_k$ would be close to zero; $\sin(\Delta\varphi_k)$ would be small and hence d(E[xy]) would be small, too. On the other hand, the first derivative of y, $\dot{y}$, is 90° out of phase with y; therefore, phase angle differences for x and $\dot{y}$ would be close to 90°; $\rho_{x,\dot{y}}$ would be small and d(E[x,y]) would be large since $\sin(\Delta\varphi_k)$ will be close to one. If the force is drag dominated, then $\rho_{Fr,ur}$ is high but $\rho_{Fr,\dot{u}r}$ is small. Therefore phase angle inaccuracies have a much more significant effect on $\rho_{Fr,\dot{u}r}$ and hence on C_m. On the other hand, if the force is inertia dominated, $\rho_{Fr,\dot{u}r}$ is high but $\rho_{Fr,ur}$ is small. Therefore the phase angle inaccuracies have a much more significant effect on $\rho_{Fr,ur}$ and hence on C_d. It should be noted that the above comments are valid for low frequencies, where the error in the phase angles are expected to be in the order of a few degrees. For high frequencies where the shifting distance is several times the wave length and wave

directionality is more significant, the phase angle errors are large and both $\rho_{Fr,ur}$ and $\rho_{Fr,\dot{u}r}$ and hence both C_d and C_m values are unreliable. It was therefore decided to investigate the effect of filtering out all the high frequencies from the three terms of Equation (9.53), i.e. F_{ro}, $u_r|u_r|$ and $\dot{u}_r$. It must be noted that high frequency harmonics must be eliminated from $u_r|u_r|$ rather than u_r itself because if the high frequency harmonics are eliminated from u_r, then $u_r|u_r|$ will have some high frequency components due to the non-linear nature of the operation. For the low-intensity runs, the important frequency range is from 0.1Hz to 0.30Hz and therefore frequencies out of this range were eliminated. For high-intensity runs, the important frequency range is up to 0.20Hz and hence frequencies above this level were filtered. As was previously discussed, it is believed that there is a sign error in cylinder response at high frequencies. Therefore, removing the high-frequency harmonics has the extra advantage of ensuring that C_d and C_m values are not affected by this error.

9.3.6 RESULTS AND DISCUSSION

The results of the standard Least Square Error Method (k = 0, Th = 0) for both unfiltered and filtered data are presented in Table 9.9. The results from the unfiltered data are unsatisfactory (high error coefficients); therefore other methods were only applied to the filtered data. Among the methods used are Bearman's method and the Maximum Correlation Method. Furthermore, the Least Square Error Method was also applied to the data points for which $|F_{ro}| \geq \sigma_{Fro}$ so that a better fit is obtained between the observed and predicted forces in the neighbourhood of maximum forces. The results of different methods are compared in Table 9.10. Examination of the results leads to the following conclusions.

1. In the case of low-intensity runs, the error coefficient for unfiltered data is very high ($0.53 < a_e^2 < 0.94$); consequently, both C_d and C_m are small. For filtered data, the error coefficient is smaller ($0.38 < a_e^2 < 0.66$) and $\rho_{Fro,Fr}$ is about 0.73. The inertia coefficient is in the reasonable range but C_d values are of poor quality even including a few negative ones. This is because low-intensity runs are inertia dominated and hence their correlation with water particle velocity is low. As was previously discussed, low correlation coefficients are sensitive to phase angle errors (introduced due to shifting) leading to unreliable C_d values.

2. The C_m values for filtered data are substantially higher than those for the unfiltered data for all the runs. The reason for this is now investigated.

Combining Equations (9.44e) and (9.47b), gives

$$C_m = \frac{1}{\hat{k}_i} * \left(\frac{E[F_{ro}^2]}{E[\dot{u}_r^2]} \right)^{1/2} * \overset{(a)}{\rho}_{Fro,\dot{u}r} \qquad (9.72a)$$

Assuming that current is negligible, as is the case for Run 13, then

$$C_m = \frac{1}{\hat{k}_i} * \frac{\sigma_{Fro}}{\sigma_{\dot{u}r}} * \rho_{Fro,\dot{u}r} \qquad (9.72b)$$

The details of the approximate calculations for both Levels 2 and 3 of Run 13 are presented in Table 9.11a. For comparison, the exact value of C_m from Equation (9.39b) is also included in

Column 10. For Level 2, C_m for filtered data is 56% larger than that of the unfiltered data (Column 9). This is the result of multiplication of three different ratios; that is, 1.56 = 0.863 * (1/0.714) * 1.289. The first and second coefficients account for the reduction in the standard deviations of the relative force and relative acceleration as a result of filtering, respectively, while the third coefficient refers to the increase in the correlation coefficient between relative force and relative acceleration due to filtering. The reason for the increase in correlation coefficient is two-fold, a) the process of shifting high-frequency components are less reliable; therefore, as a result of their removal, the correlation coefficient has increased, b) the cylinder response which has the wrong sign at high frequencies has been eliminated, leading to an increase in the correlation coefficient. The combined effect of the reduction in the standard deviations of the relative force and relative acceleration is an increase of 21% in C_m; that is, 0.863 * (1/0.714) = 1.21. This is because the reduction in the standard deviation of relative acceleration as a result of filtering is more substantial than that of the relative force (refer to Figures 9.33 and 9.36). Overall, two factors have contributed to the increase in C_m. $\sigma_{Fro}/\sigma_{\dot{u}r}$ has increased by 21% and $\rho_{Fro,\dot{u}r}$ has increased by 29%, leading to an increase of 56% in C_m.

3. For high-intensity runs, the C_d values for filtered data is somewhat higher than those for unfiltered data, though the difference is not as significant as the difference for C_m values. The reason is now investigated.

Combining Equation (9.44d) and (9.47a) leads to

$$C_d = \frac{1}{\hat{k}_d} * \left(\frac{E[F_{ro}^2]}{E[u_r^4]} \right)^{1/2} * \rho^{(a)}_{Fro,ur|ur|} \qquad (9.73a)$$

when current is negligible, the above relationship can be written as

$$C_d = \frac{1}{\hat{k}_d} * \frac{\sigma_{Fro}}{(E[u_r^4])^{1/2}} * \rho_{Fro,ur|ur|} \qquad (9.73b)$$

The details of calculations are presented in Table 9.11b. For Level 2, C_d for filtered data is 13% larger than that of the unfiltered data (column 9). This is the result of multiplication of 3 different ratios; that is, 1.13 = 0.863 * (1/0.922) * 1.209. The first and second coefficients account for the reduction in the standard deviations of the relative force and relative velocity as a result of filtering, respectively, while the third coefficient refers to the increase in the correlation coefficient between relative force and relative velocity due to filtering. The effect of filtering on $\rho_{Fro,\dot{u}r}$ is more than its effect on $\rho_{Fro,ur|ur|}$ because cylinder acceleration is a large part of relative acceleration while cylinder velocity is only a small part of relative velocity (compare Figures 9.33 and 9.34). Furthermore, as a result of filtering, $\sigma_{Fro}/(E[u_r^4])^{1/2}$ has reduced (0.936) while $\sigma_{Fro}/\sigma_{\dot{u}r}$ has increased (1.209). The above two points explain why the effect of filtering is much more pronounced on C_m values in comparison with its effect on C_d values.

4. The results of Bearman's method and the standard Least Square Error Method are close to each other. The reason that C_m values

are not exactly the same as theory suggests is that the results of the Least Square Error Method are based on the exact relationships (Equation (9.39)), while the results of Bearman's method were obtained from the simplified version of the relationships (Equation (9.56)).

5. When a threshold of $|F_{ro}| \geq \sigma_{Fro}$ is considered in the Least Square Error Method, both C_d and C_m increase (Table 9.10). The increase is more noticeable for low-intensity runs compared to high-intensity runs. The increase in C_d and C_m values shows that predicted forces due to standard Least Square Error Method underpredict the high forces. This will be demonstrated in a clearer way in the next section.

6. There is a trend for C_d values to reduce from Level 2 to Level 4 as was the case for the results of the method of moments.

7. The results of Maximum Correlation Method are higher than those of the Least Square Error Method (Table 9.10). The average increase is about 10% for high-intensity runs and 35% for low-intensity runs (based on Level 3 and Level 4 results).

9.4 THE GOODNESS OF FIT BETWEEN OBSERVED AND PREDICTED FORCES

Morison's coefficients have been determined by a number of different methods. Of cardinal importance at this stage is the question of how well any pair of C_d and C_m values in Morison's equation predict the forces actually observed. The degree of fit between observed and predicted forces are investigated in Figures 9.37 to 9.46 for Runs 01,

13 and 15 at Level 3. In addition, a statistical comparison is presented in Table 9.12.

The first section of the observed force (F_{ox}) time series is compared with that predicted using the derived Morison's coefficients and the shifted but unfiltered particle kinematics. In all cases there is a general agreement in phasing of the forces, however, the agreement is more noticeable for Runs 13 and 15 with a correlation coefficient of about 0.70 between the observed and predicted forces (Table 9.12) compared with Run 01 with a correlation coefficient of about 0.50. Examination of the time series plots shows that there are major force events where the observed and predicted force time histories agree closely but on the same plot there are similar events where the magnitude of predicted force can be in error by ± 100%. A review of the force and response time series in the corresponding transverse direction does not suggest a clear cause for such departures arising from strong vortex shedding.

Of great importance for design purposes is the comparison of observed and predicted peak forces. The comparison was done in the following way. The mean-crossing positive and negative maxima for each time series were identified and then rank-ordered for plotting (Figures 9.38, 9.40, etc.). It should be stressed that there is no guarantee that any particular rank-ordered observed and predicted peak values occurred in the same real time event. However, this engineering approach has some value in indicating whether a designer might over- or under-estimate a peak force in a given duration. If there were a perfect fit between the observed and predicted peak forces, then all the points would lie on the 45° perfect prediction line. To assist

explaining the degree of fit between the observed and predicted peak forces, the standard derivations and the kurtoses of the observed and predicted peak forces are presented in Table 9.12.

For Run 01, the standard deviation of the force predicted from the Least Square Error Method with k = 0, is only 2/3 of that of the observed force. Therefore, it is expected that both maxima and minima should be under-estimated (Figure 9.40). When k = 1, the standard deviation of the predicted force rises to 84% of that of the observed force. Therefore, some underestimation is expected. However, the kurtoses of the predicted force is 4.02 which is higher than that of the observed force (3.30). This partially compensates for the lower standard deviation of the predicted force. Overall, the fit is good, though the lowest minima is under-estimated. The method of moments give a good fit with a standard deviation of 96% of that of the observed force. The standard deviation and kurtosis of the force due to Maximum Correlation Method are slightly higher than those of the method of moments and hence slightly higher predicted peak forces are expected.

Runs 13 and 15 show similar trends. For Run 13, the standard deviation of the force predicted from Least Square Error Method with k = 0 is only 86% of that of the observed force. The kurtosis is also lower. Therefore, a significant under-estimation of the extreme peaks are expected (Figure 9.44). When k = 1, the standard deviation of the observed and predicted forces are close but the kurtoses of the predicted force is lower. Therefore, some under-estimation is expected (Figure 9.54). The results of Maximum Correlation Method are very close to that of Least Square with k = 1, therefore, a similar degree of under-estimation is expected. Both standard deviation and kurtosis are

under-estimated by the method of moments and hence significant under-estimation of the peaks are expected (Figure 9.44).

Overall the Maximum Correlation Method and the Least Square Error Method with k = 1 offer the best predictors, though even here, the extreme peaks of the high-intensity runs are underestimated by as much as 40%. As regard to the method of moments, it must be emphasised that since C_d and C_m values were obtained from a probabilistic analysis, the best procedure for assessing them is to form their 'type 2' narrow-band peak distribution and then calculate the extreme peaks as shown in Figures 9.23 and 9.27 for Runs 13 and 15, respectively. (Tickell and Burrows, 1989). It is observed that the extreme peaks with 1% probability of exceedence are always higher but in reasonable agreement with their associated observed extreme peaks.

Finally, it should be noted that the correlation coefficients between observed and predicted forces quoted in Table 9.12 are somewhat lower than their real values due to the sign error of the high-frequency components of the cylinder's response.

9.5 RECOMMENDED C_d AND C_m VALUES

Morison's coefficients have been determined in both probability and time domains. However, it should be remembered that the time domain results were obtained from the analysis of filtered time series whereas the method of moments values were determined from a fit to the observed moments including the high frequency components. Therefore, a direct comparison between the two sets of results is not justified. Furthermore, in the design of real structures, the entire frequency range including the high frequency components must be considered. It is

therefore desirable to adjust the time domain Morison's coefficients to the full frequency range. The adjustment can be done in the following way.

1. Calculate the C_m/C_d ratio for the results of the Least Square Error Method (k = 0) applied to the filtered data. Note that this ratio is the same for the results of the Maximum Correlation Method (Equation (9.66)).

2. Assume that this ratio would have been the same for the results of the full frequency range if they were not of poor quality due to the phase angle errors of the high frequency wave components and the sign error in the high frequency components of the cylinder's response.

3. Once the C_m/C_d ratio for the full frequency range data is known, C_d and C_m can be determined by equating the second moments of the observed and predicted forces (full-frequency range) which leads to Equation (9.58a). That is

$$C_d^2 \hat{k}_d^2 z_1 + C_m^2 \hat{k}_i^2 z_4 = z_6 \tag{9.74a}$$

where the z coefficients are defined in Equation (9.37). The above equation can be written as

$$C_d^2 \hat{k}_d^2 (z_1 + \alpha z_4) = z_6 \tag{9.74b}$$

in which

$$\alpha = \left(\frac{C_m \hat{k}_i}{C_d \hat{k}_d} \right)^2 \tag{9.74c}$$

is a known quantity. Equation (9.74b) leads to

$$C_d^2 \hat{k}_d^2 = \frac{z_6}{z_1 + \alpha z_4} = x^2 \tag{9.74d}$$

or

$$C_d = \frac{1}{\hat{k}_d} * x \tag{9.75a}$$

Substituting the above equation into Equation (9.74c), gives

$$C_m = \frac{1}{\hat{k}_i} * \sqrt{\alpha} * x \tag{9.75b}$$

The contribution of drag and inertia components of force to the total force variance will then be

$$a_d^2 = \frac{C_d^2 \hat{k}_d^2 z_1}{z_6} = \frac{1}{1 + \alpha(z_4/z_1)} \tag{9.75c}$$

and

$$a_i^2 = 1 - a_d^2 = \frac{C_m^2 \hat{k}_i^2 z_4}{z_6} = \frac{\alpha}{\alpha + (z_1/z_4)} \tag{9.75d}$$

The details of calculations are presented in Table 9.13. It is expected that the resultant C_d and C_m values would be close to the results of the Maximum Correlation Method applied to the full frequency data if they were error free.

As previously mentioned, C_d values for low-intensity runs obtained from the Least Square Error Method are unreliable; a few are even negative. Therefore, in the calculations presented in Table 9.13, whenever C_d values (for low-intensity runs) were less that 0.5, an assumed value of

0.5 was considered. Examination of a_d^2 and a_i^2 shows that the low-intensity runs are strongly inertia dominated and hence even large errors in C_d have only a relatively small effect on the predicted forces.

The resultant C_d and C_m values can now be compared with the results of the method of moments (Table 9.14). Similar comparisons for a_d^2 and a_i^2 are presented in Table 9.16. For high-intensity runs, the Maximum Correlation Method leads to higher C_d values in comparison with the method of moments (flexible) and consequently the C_m values are somewhat lower. This, in turn, means higher a_d^2 and lower a_i^2 for the Maximum Correlation Method (Table 9.15). For low-intensity runs, C_d and hence a_d^2 from the method of moments are higher than those from the Maximum Correlation Method.

At this stage, it is desirable to relate the C_d and C_m values with the basic hydrodynamic parameters presented in Table 9.1. Unfortunately, the resultant curves do not show a clear trend. However, the C_m values show a good correlation with $\sigma_f/\sigma_{\dot{u}}$ (i.e. the ratio between the standard deviations of the cylinder and water particle accelerations) referred to as the acceleration parameter. The values of this parameter are presented in Table 9.16 and the variation of C_m from different methods with this parameter is shown in Figures 9.55 to 9.57. As observed, there are a tendency for C_m values to decrease with increasing values of the acceleration parameter when the cylinder's response is considered in the derivation of Morison's coefficients. When the response is ignored, i.e. for the rigid cylinder assumption, the C_m

values show a tendency to increase with increasing values of the acceleration parameter.

For design purposes, the results of Figures 9.55 and 9.56 are combined in Figure 9.58 in which the larger of the C_m values from the method of moments and the Maximum Correlation Method are plotted against the acceleration parameter. It must be emphasised that these C_m values are only applicable when the basic hydrodynamic parameters are in the range of those shown in Table 9.1. and many more studies are necessary for the results to be used in the industry.

The acceleration parameter, itself, is dependent on the ratio between the wave frequency content and the cylinder's natural frequency. Therefore, it is expected that C_m values should decline with f_w/f_s where f_w is the most energetic wave frequency and f_s is the cylinder's natural frequency. The variation of C_m with this parameter is shown in Figure 9.59. Obviously, f_w/f_s gives an indication of the cylinder's response but the cylinder's response is dependent on the entire wave frequency content and therefore, the correlation of C_m with f_w/f_s is not a good as its correlation with $\sigma_r/\sigma_{\dot{u}}$. However, Figure 9.59 can be used for the first estimate of C_m which is then used to calculate the cylinder's response and hence $\sigma_r/\sigma_{\dot{u}}$. This value of the acceleration parameter can then be used to read a more exact C_m value from Figure 9.58. The iterative process continues until the difference between two successive C_m values is negligible.

As regard to the C_d values, for high-intensity runs, they do not show much variation. For Level 3, the average C_d from the method of moments

and the Maximum Correlation Method are 0.64 and 0.83, respectively. Similar results for Level 4 are 0.54 and 0.70, respectively. For low-intensity runs, the C_d values are not reliable; however, for design purposes a C_d value of 1.00 seems to be reasonably conservative. For high-intensity runs a C_d value in the range of 0.70 to 0.85 is recommended.

A parameter similar to the acceleration parameter, i.e. σ_t/u_{rms} is listed in Table 9.16. For high-intensity runs, this parameter shows little variation about 0.20. Perhaps, if the data base for this study was such that this parameter showed greater variation, then there would have been some correlation between C_d and σ_t/u_{rms}. However, the data base of this study does not allow such an investigation.

In summary, for this study (basic hydrodynamic parameters as given in Table 9.1) the C_m values are recommended to be read from Figure 9.58. For low-intensity runs, a C_d value of 1.00 and for high-intensity runs, C_d values in the range of 0.70 to 0.85 are recommended.

Special Case of Run 23

The total force coefficient for Run 23 (Table 9.2) is smaller than those for other high-intensity runs (and in particular than that for Run 16 which has almost the same Keulegan-Carpenter No. (Table 9.1) and acceleration parameter (Table 9.16) as Run 16). As a result, different methods of determination of C_d and C_m values lead to lower values of C_d and/or C_m for this run (Tables 9.6 and 9.13) in comparison with Run 16. The special case of Run 23 was discussed in Section 4.7 (conclusion No. 10). It was observed that water particle kinematics calculated from the

application of LRWT to the observed water surface elevation spectrum were of lower variance in comparison with the measured kinematics (predicted/measured = 0.87). Whether this is because of the shortcomings of LRWT or that somehow the measured water particle kinematics have been overestimated is not clear. However, if water particle kinematics predicted by LRWT are used in the determination of Morison's coefficients, the discrepancies between Run 23 and other high-intensity runs will be removed.

The Effect of Vortices on In-line Forces

It will be shown, in Section 9.9, that there is significant vortex shedding for both high-intensity and low-intensity runs, and that transverse forces are significantly affected by these vortices. It is expected that vortex-induced loads in the in-line direction do not correlate with water particle kinematics, and hence they do contribute to the lack of fit between the observed and predicted forces. The error coefficient in the Least Square Error method is a measure of the relative importance of that part of the observed force which does not correlate with water particle kinematics. The values of a_e^2 for filtered data (Table 9.9) shows that the error coefficient is significant for low-intensity runs. This can be interpreted as the sign of significant effect of vortices on the in-line forces. However, it should be considered that in this study, the shifted water particle kinematics are less accurate for low-intensity runs than those for high-intensity runs (due to the presence of higher frequencies and more severe directionality) and therefore part of the error coefficient is due to this source of inaccuracy. C_d and C_m values from the method of moments and the maximum correlation method do account for the effect of vortices in the in-line direction by equating the second moments of the

observed and predicted forces. However, the correlation coefficients between the observed and predicted forces will be less than unity due to the presence of vortex-induced loads and other effects which do not correlate with water particle kinematics (Table 9.12).

Bearman (1985) and Chaplin (1988a) have reported high lift coefficients for Keulegan-Carpenter numbers about 10; however, they have not made any comment on the effect of the vortices on the in-line forces.

9.6 COMPARISON WITH PREVIOUS STUDIES

In this section, the results of the present study are compared with those of previous studies (as discussed in Chapter 7). Special emphasis will be put on the results of large-scale experiments, which were the subject of study in section 7.4.

Total Force Coefficients

Comparison of Figures 7.37 and 9.1 shows that (Bishop's) total force coefficients from this study and the second Christchurch Bay Project (Tickell and Bishop, 1985) are in good agreement. It can therefore be concluded that the flexibility of the cylinder has not led to an increase in the force coefficients. This is in contrast with Bearman's (1988) experiments which showed an increase between 15% to 20% in the coefficients for the F6 mode in comparison with the rigid cylinder results.

On the other hand, comparison of Figures 7.32 and 7.35 with Figure 9.1 shows that Bearman's total force coefficients from this study are higher than those of Chaplin (1988a), Bearman et al (1985) and Bearman (1988). However, it should be noted that the definitions of Keulegan-

Carpenter No. in these studies are not the same. The Keulegan-carpenter numbers in this study have been calculated using the expressions due to Bishop (Equation (9.1a)), which is dependent on the fourth power of water particle velocity and as such leads to higher values of K compared with the normal definition of K for planar oscillatory flows (Equation 7.18). The above intuitive conclusion is confirmed by the results of the present study, which shows that Bearman's total force coefficient at K=25 is about 1.9 which is equal to Bearman's (1985) force coefficient at K=15. It is suggested that Bishop's K is replaced by a definition dependent on the second power of velocity. For example, the random velocity can be considered to be equivalent to a sinusoidal velocity with amplitude u_m and period T, u_m being determined so that the variance of the two signals are equal. T could be the mean zero-crossing period or any other suitable measure of the period (preferably one dependent on lower moments of the spectral density). Therefore, for the purpose of comparing the results of this study with other studies (apart from the second Christchurch Bay project), the Keulegan-Carpenter numbers are (rather arbitrarily) scaled down by about two-thirds.

Morison's Coefficients

The results of Bearman's (1988) experiments on the flexible cylinder (F6 mode) are shown in Figure 7.36. At Keulegan-Carpenter numbers between 10 and 20, C_d was found to lie in the range of $0.55 < C_d < 0.85$ and C_m in the range of $1.50 < C_m < 1.65$ for the cylinder in its most flexible mode (for Levels 3 and 4). This is in reasonable agreement with the results of this study where for the high-intensity runs, C_d is in the range of $0.68 < C_d < 0.86$ and C_m in the range of $1.40 < C_m < 1.54$ (Table 9.13). As observed, C_d values from this study are somewhat higher

and consequently C_m values are somewhat lower. It is therefore expected that both sets of C_d and C_m values will result in predicted forces with the same amount of variance. Bearman (1988) concluded that C_m values were not affected by the cylinder's response. This is in contrast with the results of this study which shows that C_m reduces with cylinder's response (Figures 9.55 and 9.56).

A C_m value of about 1.8 for Run 01 (most rigid mode, K=10) compares favourably with the results of the Second Christchurch Bay Project (Figure 7.38). Furthermore, with reference to Figure 7.20, it is observed that the inertia coefficient for this almost rigid cylinder is in good agreement with the results of small-scale experiments for a K value of 7 at higher Reynolds numbers. The C_d values for this inertia-dominated run are not reliable and hence comparison is avoided.

For Keulegan-Carpenter numbers of about 20, Chaplin (1988a) has C_d and C_m values about 0.70 and 1.70, respectively (Figure 7.33). C_d values are slightly smaller than the results of this study while C_m values are slightly higher. Results of Bearman (1985) with C_d = 0.60 and $1.40 < C_m < 1.60$ are in good agreement with the results of the present study though C_d values are somewhat lower. At lower values of K, C_m values of about 1.8 are reported by both Chaplin (1988a) and Bearman (1985), in good agreement with the results of the present study.

Overall, it can be concluded that C_d and C_m values from this study are in the range of values reported by other investigators. A further point to be noticed is that C_d values in this study decrease with increasing

depth of immersion in line with the Second Christchurch Bay results and Bearman's (1988) work in Delft Laboratory.

9.7 WAVE-BY-WAVE ANALYSIS OF IN-LINE LOADS

Morison's coefficients were also calculated for individual large waves from the standard Least Square Error Method applied to the filtered data. Large waves were defined as those for which the peak relative velocities were higher than 1.2 times the standard deviation of the relative velocity. Keulegan-Carpenter number was defined as $u_{max}.T/D$ where u_{max} was the average of the relative velocity at the trough and the crest of the relative velocity for the individual wave. T is the wave period and D is the cylinder diameter. The resultant Morison's coefficients are presented in Figure 9.60. The familiar "buckshot" scatter of the results is comparable with the scatter of the results reported from the study of the Exxon Ocean Test Structure (Heidman et al, 1979). The main reason behind the scatter is the striving of Morison's equation to minimise the phase differences between the observed and predicted forces. It does not reflect large uncertainties in the peak forces experienced in successive wave cycles (Starsmore, 1981). In other words, the use of fixed Morison's coefficients results in predicted forces for individual waves which are different from the observed forces in both magnitude and phase, however, the phase difference is more severe than the difference between the observed and predicted magnitudes.

9.8 IN-LINE CYLINDER'S RESPONSE

The study of cylinder's response is beyond the scope of this Thesis; however, for completeness and due to its relevance, the following is taken from Tickell and Burrows (1989).

Cylinder's response was calculated in the time-domain. The time-domain analysis for each sample was based on the observed surface elevation spectrum being used to generate realisations of complex Fourier components with uniformly-distributed, independent random phases, which were transformed to Fourier series for water particle velocities and accelerations using linear wave theory. The time series of (u, $\dot{u}$) were obtained by inverse Fourier transforms. The currents were added to the velocities. These long-crested simulations were performed for 6 load positions when the water depth was more than 10m and 5 load positions for lower water depths. Some 20 minutes of real time was considered for each case, corresponding to the durations of the measurement programme. The observed and predicted forces at Level 3 for Runs 01, 13 and 15 are compared in Table 9.17. A similar comparison for the in-line cylinder displacement is presented in Table 9.18.

The results of Table 9.17 shows that the standard deviations of the predicted forces are in good agreement with those of the observed forces. The agreement between the kurtoses are not as good but they are not far apart and that the extreme peaks are underestimated by up to 35% in the case of Run 13. However, the results of Table 9.18 shows that although extreme peaks are underestimated, this does not result in the underestimation of the extreme displacements, which are in reasonable agreement with extreme observed displacements. This is very encouraging as in the design, it is the responses which are the basis of design not the loads. One explanation for this phenomenon is that the extreme force peaks are not well correlated along the length of the cylinder, and as such they do not lead to corresponding extreme responses.

In the case of Run 01, the agreement between the kurtoses and hence the extremes of the predicted and observed displacements are very poor. A kurtosis of 9.14 for the displacement is very unusual as the forces are inertia-dominated and therefore, it is expected that the resultant responses must be nearly Gaussian distributed with a kurtosis close to three. It is possible that the observed response is unreliable because it is of very low magnitude. Furthermore, the author is not aware of any particular reason why the mean displacement for this run is not zero.

Figures 9.61 to 9.66 show the cumulative probability distributions for the in-line cylinder displacements and their corresponding mean-crossing ranges. For Runs 13 and 15, the agreement between observed and theoretical distributions are good while for Run 01, the agreement is very poor. (Observed moments of response have been used to derive the theoretical PH3 distributions). Furthermore, extreme events over the measurement period have been calculated and are compared with the time-domain and the observed extremes. It is observed that for Runs 13 and 15, the mean of the calculated extreme peaks are in good agreement with the observed extremes.

9.9 TRANSVERSE FORCE AND RESPONSE

Run 13

As was explained in Section 9.1.3.2, comparison of the frequency spectra of in-line and transverse forces for a typical high-intensity run such as Run 13 (Figures 9.9 and 9.10) reveals that at about the cylinder's natural frequency, transverse force is larger than the in-line force. Since the transverse wave components at this frequency are considerably smaller than the in-line ones (about 5 times), there

should be a mechanism different from Morison's equation for the excitation of the cylinder at its natural frequency. This could be due to synchronisation which is possible in view of a reduced velocity of about 5.5 (Rajabi, 1979). However, this does not mean that the large bump at the cylinder's natural frequency in Figure (9.10) is the same as the vortex-induced loading. What happens is that small transverse forces due to vortex shedding at the cylinder's natural frequency lead to large transverse responses because of large magnification factors at frequencies close to the natural frequency. This large response, according to the third term on the right hand side of Morison's equation (Equation (9.17a)), leads to a force which is due to structural accelerations. The bump at the cylinder's natural frequency is therefore due to this inertial reaction to cylinder's response. However, the underlying reason for the existence of the inertial reaction is vortex-shedding at cylinder's natural frequency (synchronisation). Further discussion of this subject is beyond the scope of this thesis. It is, however, emphasised that it is very important that the difference between the two loads (transverse force due to vortex shedding and the inertial reaction force) must be clearly understood as it has major design implications. (Refer to Tickell and Burrows, (1989) and future publications on the analysis of Christchurch Bay data).

Run 01

Tickell and Burrows (1989) showed that Morison loading due to the short-crestedness of the sea can only account for about half of the variance of the force in the y direction. This shows that the remaining half of the variance is due to vortex shedding. However, in view of the small value of the reduced velocity (Table 9.1), synchronisation does

not occur. Consequently, the inertial reaction at the cylinder's natural frequency is very small (Figure 9.6).

Sea State Intensity	Run No	Level	Keulegan-Carpenter Number		Reynolds Number $*10^{-5}$		Reduced Velocity	
			Real $E[u^4]$	Theoretical $E[u^4]$	Real $E[u^4]$	Theoretical $E[u^4]$	Real $E[u^4]$	Theoretical $E[u^4]$
Low-Intensity Runs	01	2	8.5	7.7	2.2	2.1	0.8	0.8
		3	8.6	8.6	1.8	1.8	0.7	0.7
		4	8.4	7.9	1.5	1.5	0.6	0.6
	02	2	8.8	8.4	2.3	2.2	1.1	1.1
		3	9.3	9.6	1.9	1.9	0.9	0.9
		4	8.6	8.7	1.5	1.5	0.7	0.7
	06	2	10.2	9.5	2.5	2.4	3.4	3.3
		3	10.6	11.1	2.2	2.2	2.9	3.0
		4	10.1	10.0	1.8	1.8	2.5	2.5
	07	2	11.1	9.9	2.7	2.5	3.4	3.2
		3	11.2	11.9	2.3	2.4	2.9	3.0
		4	11.1	11.0	2.0	2.0	2.5	2.5
	08	2	9.9	9.0	2.5	2.4	2.1	2.0
		3	9.7	9.9	2.1	2.1	1.8	1.8
		4	9.0	9.0	1.7	1.7	1.5	1.5
	09	2	9.2	9.0	2.4	2.4	1.6	1.6
		3	9.4	10.0	2.1	2.2	1.4	1.4
		4	8.7	9.0	1.7	1.7	1.1	1.1
High-Intensity Runs	13	2	20.8	23.8	4.1	4.4	5.5	5.9
		3	22.2	25.6	3.9	4.2	5.3	5.7
		4	21.4	25.0	3.6	3.9	4.9	5.3
	14	2	22.8	25.0	4.3	4.5	5.8	6.1
		3	25.7	27.9	4.2	4.4	5.7	5.9
		4	24.9	27.2	4.0	4.2	5.4	5.6
	15	2	24.0	26.8	4.6	4.9	6.0	6.3
		3	27.1	31.1	4.5	4.8	5.9	6.3
		4	26.3	30.6	4.2	4.5	5.6	6.0
	16	2	23.4	24.3	4.6	4.7	5.9	6.0
		3	31.4	36.5	4.8	5.2	6.2	6.7
		4	31.0	36.3	4.6	5.0	5.9	6.4
	23	2	32.0	29.2	5.5	5.3	7.0	6.7
		3	33.0	36.9	5.4	5.7	6.8	7.2
		4	32.1	36.3	5.1	5.4	6.5	6.9

TABLE 9.1
BASIC HYDRODYNAMIC PARAMETERS

(NOTE : CAUTION MUST BE EXERCISED WITH RESPECT TO RESULTS FOR LEVEL 2 DUE TO INTERMITTENT EXPOSURE)

Sea State Intensity	Run No	Level	Bearman's Coefficients		Bishop's Coefficients	
			In-line	Transverse	In-line	Transverse
Low-Intensity Runs	01	2	6.1	4.7	2.05	1.56
		3	4.5	3.3	1.57	1.16
		4	4.9	4.1	1.63	1.34
	02	2	5.2	4.2	1.84	1.47
		3	4.0	3.0	1.51	1.14
		4	4.5	3.8	1.62	1.36
	06	2	5.7	4.3	2.16	1.64
		3	4.8	3.9	1.93	1.56
		4	4.9	4.2	1.86	1.60
	07	2	4.9	3.6	1.89	1.38
		3	3.7	2.9	1.52	1.19
		4	4.0	3.2	1.57	1.26
	08	2	5.1	3.9	1.83	1.39
		3	3.9	2.9	1.46	1.09
		4	4.6	3.5	1.60	1.24
	09	2	5.0	4.0	1.72	1.39
		3	3.6	2.7	1.34	0.98
		4	4.3	3.4	1.48	1.16
High-Intensity Runs	13	2	2.2	1.6	1.16	0.83
		3	2.0	1.6	1.08	0.83
		4	1.9	1.4	0.98	0.72
	14	2	2.2	1.6	1.17	0.83
		3	2.0	1.5	1.05	0.79
		4	1.8	1.3	0.96	0.68
	15	2	2.1	1.6	1.14	0.83
		3	1.8	1.4	0.97	0.77
		4	1.6	1.2	0.88	0.63
	16	2	2.5	1.8	1.29	0.92
		3	1.7	1.2	0.91	0.67
		4	1.5	1.1	0.84	0.60
	23	2	1.9	1.6	1.03	0.86
		3	1.5	1.2	0.81	0.65
		4	1.3	1.0	0.73	0.56

TABLE 9.2
BEARMAN'S AND BISHOP'S TOTAL FORCE COEFFICIENTS

(NOTE : CAUTION MUST BE EXERCISED WITH RESPECT TO RESULTS FOR LEVEL 2 DUE TO INTERMITTENT EXPOSURE)

Sea State Intensity	Run No	Level	Skewness		Kurtosis		$\frac{\sigma_{Fy}}{\sigma_{Fx}}$
			F_x	F_y	F_x	F_y	
Low-Intensity Runs	01	2	-0.09	0.21	3.68	3.86	0.70
		3	0.06	0.33	3.30	3.46	0.54
		4	0.09	0.28	3.10	4.65	0.47
	02	2	0.05	0.27	3.33	4.42	0.72
		3	0.09	0.31	2.92	3.94	0.52
		4	0.03	0.11	2.79	3.18	0.45
	06	2	-0.04	0.16	3.54	4.75	0.70
		3	0.22	-0.09	3.40	7.98	0.69
		4	0.12	0.20	3.19	16.11	0.67
	07	2	-0.04	0.20	3.28	4.05	0.66
		3	0.14	0.29	3.16	5.20	0.66
		4	0.14	0.31	3.18	4.91	0.61
	08	2	-0.02	0.21	3.02	3.75	0.68
		3	0.05	0.38	2.90	4.20	0.56
		4	0.04	0.41	2.90	3.93	0.50
	09	2	-0.05	0.25	3.20	4.04	0.73
		3	-0.01	0.41	2.95	3.94	0.55
		4	-0.07	0.26	2.81	3.32	0.50
High-Intensity Runs	13	2	0.25	-0.26	3.88	4.39	0.74
		3	0.36	-0.30	3.91	5.42	0.79
		4	0.26	-0.42	3.55	8.24	0.76
	14	2	0.18	-0.24	4.09	4.75	0.74
		3	0.39	-0.28	4.07	4.35	0.78
		4	0.32	-0.56	3.92	6.94	0.73
	15	2	0.34	-0.15	5.32	4.12	0.72
		3	0.64	-0.35	4.62	4.52	0.77
		4	0.54	-0.55	4.42	6.45	0.70
	16	2	0.57	-0.51	5.19	6.79	0.72
		3	0.83	-0.35	5.70	5.42	0.73
		4	0.66	-0.38	4.57	6.89	0.70
	23	2	0.79	-0.12	4.43	4.95	0.69
		3	0.64	-0.21	4.29	6.06	0.66
		4	0.42	-0.02	4.30	7.64	0.60

TABLE 9.3
BASIC STATISTICAL PROPERTIES OF HYDRODYNAMIC FORCES

(NOTE : CAUTION MUST BE EXERCISED WITH RESPECT TO RESULTS FOR LEVEL 2 DUE TO INTERMITTENT EXPOSURE)

α Coefficients	Short-Crested Form of Morison's equation	Uni-directional Form of Morison's equation
α_1	$E[u^4] + E[u^2v^2]$	$E[u^4]$
α_2	$E[\dot{u}^2]$	$E[\dot{u}^2]$
α_3	$2E[u\dot{u}\sqrt{u^2 + v^2}]$	$2E[\dot{u}u\lvert u\rvert]$
α_4	$E[u^8] + 2E[u^6v^2] + E[u^4v^4]$	$E[u^8]$
α_5	$E[\dot{u}^4]$	$E[\dot{u}^4]$
α_6	$6E[u^4\dot{u}^2] + 6E[u^2v^2\dot{u}^2]$	$6E[u^4\dot{u}^2]$
α_7	$2E[u^5\dot{u}\sqrt{u^2 + v^2}] + 2E[u^3v^2\dot{u}\sqrt{u^2 + v^2}]$	$2E[\dot{u}u^5\lvert u\rvert]$
α_8	$2E[u\dot{u}^3\sqrt{u^2 + v^2}]$	$2E[\dot{u}^3u\lvert u\rvert]$
α_9	$E[u^5\sqrt{u^2 + v^2}] + E[u^3v^2\sqrt{u^2 + v^2}]$	$E[u^5\lvert u\rvert]$
α_{10}	$E[\dot{u}^3]$	$E[\dot{u}^3]$
α_{11}	$E[u^4\dot{u}] + E[u^2v^2\dot{u}]$	$E[u^4\dot{u}]$
α_{12}	$E[\dot{u}^2u\sqrt{u^2 + v^2}]$	$E[\dot{u}^2u\lvert u\rvert]$
α_{13}	$E[u\sqrt{u^2 + v^2}]$	$E[u\lvert u\rvert]$
α_{14}	$E[\dot{u}]$	$E[\dot{u}]$

TABLE 9.4
LIST OF WATER PARTICLE STATISTICAL MOMENTS
REQUIRED IN THE METHOD OF MOMENTS

Run No	Level	Method 1		Method 2		Method 3		Method 4					
		C_d	C_m	C_d	C_m	C_d	C_m	C_d	C_m	E_1	E_3	a_d^2	a_i^2
01	2	-	-	1.99	1.88	-	-	2.06	2.03	-0.27	-0.32	0.32	0.68
	3	-	-	1.10	1.65	-	-	1.16	1.75	-0.12	-0.06	0.20	0.80
	4	-	-	0.94	1.75	-	-	1.03	1.84	-0.06	0.03	0.13	0.87
02	2	-	-	1.40	1.92	-	-	1.46	2.01	-0.19	-0.09	0.22	0.78
	3	-	-	-	-	-	-	-	-	-	-	-	-
	4	-	-	-	-	-	-	-	-	-	-	-	-
06	2	-	-	1.77	2.22	-	-	1.82	2.35	-0.26	-0.24	0.29	0.71
	3	-	-	1.28	2.21	-	-	1.33	2.34	-0.14	0.07	0.23	0.77
	4	-	-	1.07	2.11	-	-	1.14	2.23	-0.11	0.03	0.17	0.83
07	2	-	-	1.27	2.15	-	-	1.29	2.22	-0.20	-0.16	0.20	0.80
	3	-	-	0.79	1.93	-	-	0.82	1.99	-0.09	0.06	0.15	0.85
	4	-	-	0.85	1.87	-	-	0.89	1.96	-0.08	0.05	0.16	0.84
08	2	-	-	0.62	2.25	-	-	0.63	2.26	-0.08	0.03	0.04	0.96
	3	-	-	-	-	-	-	-	-	-	-	-	-
	4	-	-	-	-	-	-	-	-	-	-	-	-
09	2	-	-	1.10	1.93	-	-	1.11	1.99	-0.14	-0.14	0.16	0.84
	3	-	-	-	-	-	-	-	-	-	-	-	-
	4	-	-	-	-	-	-	-	-	-	-	-	-
13	2	1.23	1.44	0.72	2.26	1.26	1.44	0.72	2.26	-0.04	0.26	0.31	0.69
	3	1.17	1.30	0.66	2.18	1.18	1.28	0.66	2.18	0.01	0.41	0.32	0.68
	4	1.02	1.33	0.52	2.04	1.04	1.29	0.52	2.04	-0.01	0.30	0.24	0.76
14	2	1.05	1.87	0.76	2.29	1.09	1.82	0.76	2.29	-0.01	0.28	0.35	0.65
	3	0.85	1.96	0.66	2.22	0.89	1.87	0.66	2.22	0.06	0.54	0.34	0.66
	4	0.82	1.70	0.58	2.04	0.85	1.63	0.58	2.05	0.04	0.47	0.31	0.69
15	2	1.20	1.29	0.87	2.05	1.22	1.38	0.87	2.06	0.00	0.57	0.50	0.50
	3	1.12	0.74	0.66	2.15	1.12	0.94	0.66	2.17	0.07	0.88	0.41	0.59
	4	1.03	0.64	0.57	1.99	1.04	0.80	0.58	2.00	0.05	0.78	0.37	0.63
16	2	0.81	2.56	0.96	2.24	0.87	2.48	0.97	2.26	-0.07	0.75	0.45	0.55
	3	-	-	0.68	2.02	-	-	0.68	2.07	0.10	1.28	0.52	0.48
	4	0.96	0.41	0.53	2.14	0.96	0.80	0.53	2.17	0.06	0.96	0.38	0.62
23	2	0.64	2.14	0.76	1.93	0.67	2.05	0.76	2.00	-0.16	0.32	0.49	0.51
	3	0.80	1.21	0.54	2.00	0.80	1.42	0.55	2.06	0.06	0.45	0.43	0.57
	4	0.75	0.83	0.48	1.79	0.76	1.15	0.49	1.85	0.05	0.23	0.41	0.59

TABLE 9.5
MORISON COEFFICIENTS FROM THE METHOD OF MOMENTS - RIGID CYLINDER CASE

(NOTE: CAUTION MUST BE EXERCISED WITH RESPECT TO RESULTS FOR LEVEL 2 DUE TO INTERMITTENT EXPOSURE)

Run No	Level	Method 4					
		C_d	C_m	E_1	E_3	a_d^2	a_i^2
01	2	2.06	2.01	-0.27	-0.32	0.32	0.68
	3	1.08	1.74	-0.11	-0.02	0.17	0.83
	4	1.06	1.78	-0.07	0.02	0.14	0.86
02	2	1.47	1.94	-0.19	-0.10	0.23	0.77
	3	-	-	-	-	-	-
	4	-	-	-	-	-	-
06	2	1.47	1.71	-0.23	-0.23	0.28	0.72
	3	1.11	1.29	-0.14	-0.01	0.29	0.71
	4	1.28	0.92	-0.16	-0.13	0.34	0.66
07	2	1.11	1.80	-0.18	-0.16	0.18	0.82
	3	0.32	1.53	-0.02	0.09	0.03	0.97
	4	0.51	1.25	-0.03	0.06	0.07	0.93
08	2	0.75	1.95	-0.11	-0.04	0.07	0.93
	3	-	-	-	-	-	-
	4	-	-	-	-	-	-
09	2	1.17	1.89	-0.14	-0.16	0.17	0.83
	3	-	-	-	-	-	-
	4	-	-	-	-	-	-
13	2	0.70	1.84	-0.03	0.32	0.35	0.65
	3	0.63	1.69	0.01	0.46	0.35	0.65
	4	0.55	1.49	-0.01	0.33	0.29	0.71
14	2	0.73	1.95	-0.00	0.36	0.38	0.62
	3	0.65	1.82	0.06	0.63	0.39	0.61
	4	0.56	1.61	0.04	0.46	0.32	0.68
15	2	0.84	1.72	0.00	0.65	0.53	0.47
	3	0.65	1.69	0.07	1.00	0.46	0.54
	4	0.56	1.48	0.05	0.81	0.40	0.60
16	2	0.91	1.87	-0.07	0.82	0.48	0.52
	3	0.70	1.49	0.11	1.51	0.62	0.38
	4	0.53	1.61	0.07	0.95	0.40	0.60
23	2	0.77	1.57	-0.18	0.29	0.53	0.47
	3	0.58	1.45	0.05	0.57	0.54	0.46
	4	0.51	1.27	0.03	0.28	0.49	0.51

TABLE 9.6.
MORISON COEFFICIENTS FROM THE
METHOD OF MOMENTS-FLEXIBLE CYLINDER CASE

(NOTE : CAUTION MUST BE EXERCISED WITH RESPECT TO RESULTS FOR LEVEL 2 DUE TO INTERMITTENT EXPOSURE)

Level		01		02		06		07		08		09		13		14		15		16		23	
		C_d	C_m	C_d	C_m	C_d	C_m	C_d	C_m	C_d	C_m	C_d	C_m	C_d	C_m	C_d	C_m	C_d	C_m	C_d	C_m	C_d	C_m
2	Rigid	2.06	2.03	1.46	2.01	1.82	2.35	1.29	2.22	0.63	2.26	1.11	1.99	0.72	2.26	0.76	2.29	0.87	2.06	0.97	2.26	0.76	2.00
	Flexible	2.06	2.01	1.47	1.94	1.47	1.71	1.11	1.80	0.75	1.95	1.17	1.89	0.70	1.84	0.73	1.95	0.84	1.72	0.91	1.87	0.77	1.57
3	Rigid	1.16	1.75	-	-	1.33	2.34	0.82	1.99	-	-	-	-	0.66	2.18	0.66	2.22	0.66	2.17	0.68	2.07	0.55	2.06
	Flexible	1.08	1.74	-	-	1.11	1.29	0.32	1.53	-	-	-	-	0.63	1.69	0.65	1.82	0.65	1.69	0.70	1.49	0.58	1.45
4	Rigid	1.03	1.84	-	-	1.14	2.23	0.89	1.96	-	-	-	-	0.52	2.04	0.58	2.05	0.58	2.00	0.53	2.17	0.49	1.85
	Flexible	1.06	1.78	-	-	1.28	0.92	0.51	1.25	-	-	-	-	0.55	1.49	0.56	1.61	0.56	1.48	0.53	1.61	0.51	1.27

(a)

TABLE 9.7.
COMPARISON OF THE RESULTS FOR THE RIGID AND FLEXIBLE CYLINDER ASSUMPTIONS (CONTINUED)

(NOTE : CAUTION MUST BE EXERCISED WITH RESPECT TO
RESULTS FOR LEVEL 2 DUE TO INTERMITTENT EXPOSURE)

Level		01		02		06		07		08		09		13		14		15		16		23	
		a_d^2	a_i^2	a_d^2	a_i^2	a_d^2	a_i^2	a_d^2	a_i^2	a_d^2	a_i^2	a_d^2	a_i^2	a_d^2	a_i^2	a_d^2	a_i^2	a_d^2	a_i^2	a_d^2	a_i^2	a_d^2	a_i^2
2	Rigid	0.32	0.68	0.22	0.78	0.29	0.71	0.20	0.80	0.04	0.96	0.16	0.84	0.31	0.69	0.35	0.65	0.50	0.50	0.45	0.55	0.49	0.51
	Flexible	0.32	0.68	0.23	0.77	0.28	0.72	0.18	0.82	0.07	0.93	0.17	0.83	0.35	0.65	0.38	0.62	0.53	0.47	0.48	0.52	0.53	0.47
3	Rigid	0.20	0.80	-	-	0.23	0.77	0.15	0.85	-	-	-	-	0.32	0.68	0.34	0.66	0.41	0.59	0.52	0.48	0.43	0.57
	Flexible	0.17	0.83	-	-	0.29	0.71	0.03	0.97	-	-	-	-	0.35	0.65	0.39	0.61	0.46	0.54	0.62	0.38	0.54	0.46
4	Rigid	0.13	0.87	-	-	0.17	0.83	0.16	0.84	-	-	-	-	0.24	0.76	0.31	0.69	0.37	0.63	0.38	0.62	0.41	0.59
	Flexible	0.14	0.86	-	-	0.34	0.66	0.07	0.93	-	-	-	-	0.29	0.71	0.32	0.68	0.40	0.60	0.40	0.60	0.49	0.51

(b)

TABLE 9.7.
COMPARISON OF THE RESULTS FOR THE RIGID AND FLEXIBLE CYLINDER ASSUMPTIONS (CONTINUED)

(NOTE : CAUTION MUST BE EXERCISED WITH RESPECT TO RESULTS FOR LEVEL 2 DUE TO INTERMITTENT EXPOSURE)

Level		01		02		06		07		08		09		13		14		15		16		23	
		E_1	E_3	E_1	E_3	E_1	E_3	E_1	E_3	E_1	E_3	E_1	E_3	E_1	E_3	E_1	E_3	E_1	E_3	E_1	E_3	E_1	E_3
2	Rigid	-0.27	-0.32	-0.19	-0.09	-0.26	-0.24	-0.20	-0.16	-0.08	-0.03	-0.14	-0.14	-0.04	0.26	-0.01	0.28	0.00	0.57	-0.07	0.75	-0.16	0.32
	Flexible	-0.27	-0.32	-0.19	-0.10	-0.23	-0.23	-0.18	-0.16	-0.11	-0.04	-0.14	-0.16	-0.03	0.32	-0.00	0.36	0.00	0.65	-0.07	0.82	-0.18	0.29
3	Rigid	-0.12	-0.06	-	-	-0.14	0.07	-0.09	0.06	-	-	-	-	0.01	0.41	0.06	0.54	0.07	0.88	0.10	1.28	0.06	0.45
	Flexible	-0.11	-0.02	-	-	-0.14	-0.01	-0.02	0.09	-	-	-	-	0.01	0.46	0.06	0.63	0.07	1.00	0.11	1.51	0.05	0.57
4	Rigid	-0.06	0.03	-	-	-0.11	0.03	-0.08	0.05	-	-	-	-	-0.01	0.30	0.04	0.47	0.05	0.78	0.06	0.96	0.05	0.23
	Flexible	-0.07	0.02	-	-	-0.16	-0.13	-0.03	0.06	-	-	-	-	-0.01	0.33	0.04	0.46	0.05	0.81	0.07	0.95	0.03	0.28

(c)

TABLE 9.7.
COMPARISON OF THE RESULTS FOR THE RIGID AND FLEXIBLE CYLINDER ASSUMPTION

(NOTE : CAUTION MUST BE EXERCISED WITH RESPECT TO
RESULTS FOR LEVEL 2 DUE TO INTERMITTENT EXPOSURE)

Run	Level		β	$(\beta - 3)^{1/4}$	$a_i = (1 - 0.34\sqrt{\beta - 3})^{1/2}$	σ_F	σ_u	$\sigma_{\dot{u}}$	$\frac{1}{\sigma_u^2}$	$\frac{1}{\sigma_{\dot{u}}}$	Approx. Value		Exact Value	
											C_d	C_m	C_d	C_m
(1)	(2)	(3)	(4)	(5)	(6)	(7)	(8)	(9)	(10)	(11)	(12)	(13)	(14)	(15)
13	3	Flexible	4.112	1.0269	0.8009	0.1455	0.7762	0.7157	1.6598	1.3972	0.63	1.64	0.63	1.69
		Rigid	3.911	0.9763	0.8219	0.1464	0.7396	0.5597	1.8281	1.7867	0.67	2.17	0.66	2.18
		Flexible / Rigid	1.051	1.052	0.974	0.994	1.049	1.279	0.908	0.782	0.95	0.76	0.95	0.77
23	3	Flexible	5.125	1.2074	0.7102	0.1910	1.0282	0.9177	0.9459	1.0897	0.56	1.49	0.58	1.45
		Rigid	4.289	1.0655	0.7834	0.1923	0.9978	0.7181	1.0044	1.3926	0.53	2.11	0.55	2.06
		Flexible / Rigid	1.195	1.133	0.9066	0.993	1.030	1.278	0.942	0.782	1.06	0.70	1.05	0.70

TABLE 9.8.
EXPLAINING THE DIFFERENCE BETWEEN MORISON'S COEFFICIENTS
DERIVED FROM THE RIGID AND FLEXIBLE CYLINDER ASSUMPTIONS

Run No	Level	Unfiltered				Filtered			
		C_d	C_m	a_e^2	ρ	C_d	C_m	a_e^2	ρ
01	2	0.13	0.56	0.937	0.25	0.34	1.56	0.66	0.58
	3	0.12	0.98	0.728	0.52	0.05	1.32	0.52	0.69
	4	0.13	1.29	0.545	0.67	0.04	1.53	0.41	0.77
02	2	0.17	0.68	0.884	0.34	0.02	1.44	0.60	0.63
	3	0.07	0.97	0.716	0.53	-0.12	1.28	0.54	0.68
	4	0.12	1.24	0.581	0.65	-0.19	1.53	0.45	0.74
06	2	0.55	0.72	0.817	0.43	0.78	2.03	0.42	0.76
	3	0.42	0.52	0.654	0.59	0.54	1.62	0.42	0.76
	4	0.42	0.68	0.573	0.65	0.58	1.57	0.44	0.75
07	2	0.56	0.72	0.783	0.47	0.75	1.92	0.44	0.75
	3	0.40	0.71	0.623	0.61	0.36	1.49	0.38	0.79
	4	0.39	0.75	0.5[illegible]8	0.67	0.31	1.57	0.37	0.79
08	2	0.38	0.69	0.806	0.44	0.44	1.70	0.48	0.72
	3	0.19	0.89	0.619	0.62	0.13	1.38	0.42	0.76
	4	0.23	1.03	0.530	0.69	0.11	1.58	0.36	0.80
09	2	0.29	0.67	0.863	0.37	0.32	1.45	0.54	0.68
	3	0.12	0.92	0.667	0.58	0.01	1.24	0.46	0.73
	4	0.11	1.09	0.573	0.65	-0.11	1.44	0.41	0.77
13	2	0.79	1.03	0.480	0.72	0.88	1.58	0.21	0.89
	3	0.76	0.94	0.441	0.75	0.83	1.46	0.19	0.90
	4	0.69	1.00	0.350	0.81	0.76	1.48	0.17	0.91
14	2	0.78	1.07	0.472	0.73	0.93	1.46	0.24	0.87
	3	0.73	1.02	0.406	0.77	0.79	1.43	0.18	0.91
	4	0.67	1.04	0.346	0.81	0.71	1.45	0.17	0.91
15	2	0.86	0.97	0.434	0.75	0.85	1.55	0.21	0.89
	3	0.75	0.94	0.376	0.79	0.78	1.48	0.17	0.91
	4	0.66	0.97	0.329	0.82	0.72	1.50	0.15	0.92
16	2	0.86	0.83	0.528	0.69	0.96	1.50	0.35	0.81
	3	0.74	0.91	0.358	0.80	0.79	1.37	0.16	0.92
	4	0.66	0.99	0.319	0.83	0.71	1.44	0.17	0.91
23	2	0.65	0.71	0.474	0.72	0.69	1.07	0.31	0.83
	3	0.69	0.56	0.363	0.80	0.73	0.86	0.16	0.92
	4	0.62	0.62	0.340	0.81	0.66	0.85	0.16	0.92

TABLE 9.9
MORISON'S COEFFICIENTS FROM STANDARD LEAST SQUARE ERROR METHOD

(NOTE : CAUTION MUST BE EXERCISED WITH RESPECT TO RESULTS FOR LEVEL 2 DUE TO INTERMITTENT EXPOSURE)

Level	Method of Analysis		01		02		06		07		08		09		13		14		15		16		23	
			C_d	C_m	C_d	C_m	C_d	C_m	C_d	C_m	C_d	C_m	C_d	C_m	C_d	C_m	C_d	C_m	C_d	C_m	C_d	C_m	C_d	C_m
2	Least Square Method	k = 0 Th = 0	0.34	1.56	0.02	1.44	0.78	2.03	0.75	1.92	0.44	1.70	0.32	1.45	0.88	1.58	0.93	1.46	0.85	1.55	0.96	1.50	0.69	1.07
		k = 0 $\lvert Th \rvert = \sigma_{Fro}$	0.59	2.12	0.12	1.93	1.14	2.71	0.99	2.60	0.62	2.25	0.46	1.95	1.04	1.74	0.99	1.67	1.04	1.66	1.05	1.61	0.72	1.20
	Bearman Method		0.32	1.56	*	1.44	0.73	2.04	0.78	1.94	0.42	1.70	0.32	1.45	0.89	1.54	0.86	1.52	0.93	1.43	1.01	1.52	0.71	1.11
	Max Correlation Method		0.58	2.68	0.03	2.28	1.02	2.67	1.00	2.57	0.61	2.36	0.47	2.14	0.99	1.78	1.07	1.67	0.96	1.74	1.19	1.86	0.83	1.29
3	Least Square Method	k = 0 Th = 0	0.05	1.32	*	1.28	0.54	1.62	0.36	1.49	0.13	1.38	0.00	1.24	0.83	1.46	0.79	1.43	0.78	1.48	0.79	1.37	0.73	0.86
		k = 0 $\lvert Th \rvert = \sigma_{Fro}$	0.09	1.74	*	1.74	0.77	2.00	0.39	1.85	0.19	1.72	*	1.64	0.93	1.62	0.86	1.61	0.89	1.56	0.88	1.52	0.76	0.93
	Bearman Method		*	1.32	*	1.29	0.39	1.59	0.28	1.48	*	1.38	*	1.24	0.84	1.42	0.80	1.45	0.80	1.40	0.82	1.35	0.75	0.87
	Max Correlation Method		0.07	1.91	*	1.89	0.71	2.13	0.46	1.89	0.17	1.81	0.00	1.69	0.92	1.62	0.87	1.58	0.86	1.62	0.86	1.49	0.80	0.94
4	Least Square Method	k = 0 Th = 0	0.04	1.53	*	1.53	0.58	1.57	0.31	1.57	0.11	1.58	*	1.44	0.76	1.48	0.71	1.45	0.72	1.50	0.71	1.44	0.66	0.85
		k = 0 $\lvert Th \rvert = \sigma_{Fro}$	0.08	1.88	*	1.97	0.75	1.92	0.29	1.89	0.10	1.89	*	1.87	0.82	1.66	0.76	1.66	0.79	1.56	0.81	1.62	0.69	0.93
	Bearman Method		*	1.53	*	1.54	0.43	1.55	0.27	1.56	*	1.58	*	1.44	0.76	1.44	0.73	1.47	0.72	1.42	0.72	1.42	0.68	0.86
	Max Correlation Method		0.05	1.99	*	2.06	0.78	2.10	0.39	1.98	0.14	1.98	*	1.87	0.83	1.62	0.78	1.59	0.78	1.63	0.78	1.58	0.72	0.93

TABLE 9.10
COMPARISON OF MORISON'S COEFFICIENTS FROM DIFFERENT METHODS IN THE TIME DOMAIN - FILTERED DATA

Note: * These Values are Negative

(NOTE : CAUTION MUST BE EXERCISED WITH RESPECT TO RESULTS FOR LEVEL 2 DUE TO INTERMITTENT EXPOSURE)

Run	Level	Status of Data	$\frac{1}{\hat{k}_i}$	σ_{Fro}	$\sigma_{\dot{u}r}$	$\frac{\sigma_{Fro}}{\sigma_{\dot{u}r}}$	$\rho_{Fro,\dot{u}r}$	Approximate C_m	Exact C_m
(1)	(2)	(3)	(4)	(5)	(6)	(7)	(8)	(9)	(10)
13	2	Filtered	10.08	0.1578	0.5868	0.2689	0.5661	1.53	1.58
		Unfiltered	10.08	0.1828	0.8218	0.2224	0.4391	0.98	1.03
		$\frac{\text{Filtered}}{\text{Unfiltered}}$	1.00	0.863	0.714	1.209	1.289	1.56	1.53
	3	Filtered	10.08	0.1319	0.5395	0.2445	0.5753	1.42	1.46
		Unfiltered	10.08	0.1455	0.7157	0.2033	0.4346	0.89	0.94
		$\frac{\text{Filtered}}{\text{Unfiltered}}$	1.00	0.907	0.754	1.203	1.324	1.59	1.55

(a)

TABLE 9.11
EXPLAINING THE DIFFERENCE BETWEEN THE RESULTS FROM THE STANDARD LEAST SQUARE ERROR METHOD FOR FILTERED AND UNFILTERED DATA a) C_m VALUES, b) C_d VALUES

Run	Level	Status of Data	$\frac{1}{\hat{k}_d}$	σ_{Fro}	$\sqrt{E[u_r^4]}$	$\frac{\sigma_{Fro}}{(E[u_r^4])^{1/2}}$	$\rho_{Fro,\dot{u}r\|ur\|}$	Approximate C_d	Exact C_d
(1)	(2)	(3)	(4)	(5)	(6)	(7)	(8)	(9)	(10)
13	2	Filtered	7.598	0.1578	0.9497	0.1662	0.6873	0.87	0.88
		Unfiltered	7.598	0.1828	1.0296	0.1775	0.5685	0.77	0.79
		$\frac{\text{Filtered}}{\text{Unfiltered}}$	1.00	0.863	0.922	0.936	1.209	1.13	1.11
	3	Filtered	7.598	0.1319	0.8626	0.1529	0.6997	0.81	0.83
		Unfiltered	7.598	0.1455	0.9017	0.1614	0.6098	0.75	0.76
		$\frac{\text{Filtered}}{\text{Unfiltered}}$	1.00	0.907	0.957	0.947	1.147	1.08	1.09

(b)

TABLE 9.11 (CONTINUED)
EXPLAINING THE DIFFERENCE BETWEEN THE RESULTS FROM THE STANDARD LEAST SQUARE ERROR METHOD FOR FILTERED AND UNFILTERED DATA a) C_m VALUES, b) C_d VALUES

Run	Level		S.D (KN)	Kurtosis	$\rho_{predicted, observed}$
01	3	Observed Force	0.0620	3.30	
		Least Square k = 0	0.0419	4.00	0.52
		Least Square k = 1	0.0521	4.02	0.51
		Max. Correlation Method	0.0604	4.00	0.52
		Methods of Moments	0.0595	3.95	0.48
13	3	Observed Force	0.146	3.91	
		Least Square k = 0	0.126	3.04	0.71
		Least Square k = 1	0.141	3.11	0.77
		Max. Correlation Method	0.140	3.04	0.71
		Methods of Moments	0.121	2.58	0.66
15	3	Observed Force	0.168	4.62	
		Least Square k = 0	0.145	3.69	0.77
		Least Square k = 1	0.161	3.77	0.71
		Max. Correlation Method	0.159	3.69	0.77
		Methods of Moments	0.141	3.13	0.72

TABLE 9.12
STATISTICAL COMPARISON OF OBSERVED AND PREDICTED FORCES

Run	Level	Least Square k = 0 Limited Frequency Range		$\alpha = \left(\frac{C_m \hat{k}_i}{C_d \hat{k}_d}\right)^2$	$x^2 = \frac{z_6}{z_1 + \alpha z_4}$	Max. Correlation Method Full Frequency Range		$a_d^2 = \frac{1}{1 + \alpha(z_4/z_1)}$	$a_i^2 = (1 - a_d^2)$
		C_d	C_m			$C_d = \frac{1}{\hat{k}_d} * x$	C_m		
01	2	0.50	1.56	5.531	0.01010	0.764	2.382	0.044	0.956
	3	0.50	1.32	3.960	0.00842	0.697	1.841	0.070	0.930
	4	0.50	1.53	5.321	0.00647	0.611	1.870	0.049	0.950
02	2	0.50	1.44	4.713	0.00960	0.745	2.144	0.057	0.943
	3	0.50	1.28	3.724	0.00860	0.704	1.804	0.084	0.916
	4	0.50	1.53	5.321	0.00665	0.620	1.897	0.050	0.949
06	2	0.78	2.03	3.849	0.00967	0.747	1.944	0.072	0.928
	3	0.54	1.62	5.114	0.00423	0.494	1.482	0.055	0.932
	4	0.58	1.57	4.163	0.00296	0.414	1.120	0.037	0.963
07	2	0.75	1.92	3.724	0.00961	0.745	1.907	0.083	0.916
	3	0.50	1.49	5.046	0.00442	0.505	1.504	0.070	0.930
	4	0.50	1.57	5.602	0.00281	0.403	1.266	0.042	0.958
08	2	0.50	1.70	6.569	0.00586	0.581	1.978	0.042	0.958
	3	0.50	1.38	4.328	0.00562	0.569	1.571	0.066	0.933
	4	0.50	1.58	5.674	0.00430	0.499	1.575	0.037	0.963
09	2	0.50	1.45	4.779	0.00831	0.693	2.008	0.057	0.943
	3	0.50	1.24	3.495	0.00712	0.641	1.590	0.085	0.915
	4	0.50	1.44	4.713	0.00583	0.580	1.670	0.050	0.950
13	2	0.88	1.58	1.832	0.01500	0.931	1.671	0.465	0.535
	3	0.83	1.46	1.758	0.01289	0.863	1.517	0.479	0.521
	4	0.76	1.48	2.155	0.00898	0.720	1.402	0.373	0.627
14	2	0.93	1.46	1.400	0.01754	1.006	1.580	0.594	0.406
	3	0.79	1.43	1.862	0.01253	0.851	1.540	0.559	0.441
	4	0.71	1.45	2.370	0.00885	0.715	1.460	0.447	0.553
15	2	0.85	1.55	1.889	0.01556	0.948	1.728	0.524	0.476
	3	0.78	1.48	2.046	0.01142	0.812	1.541	0.549	0.451
	4	0.72	1.50	2.466	0.00796	0.678	1.413	0.451	0.549
16	2	0.96	1.50	1.387	0.01964	1.064	1.664	0.592	0.408
	3	0.79	1.37	1.709	0.01194	0.830	1.440	0.645	0.355
	4	0.71	1.44	2.337	0.00858	0.704	1.428	0.527	0.473
23	2	0.69	1.07	1.366	0.01153	0.816	1.266	0.691	0.309
	3	0.73	0.86	0.789	0.01135	0.809	0.954	0.799	0.201
	4	0.66	0.85	0.943	0.00877	0.711	0.916	0.732	0.268

TABLE 9.13.
MORISON'S COEFFICIENTS FROM MAXIMUM CORRELATION METHOD - FULL FREQUENCY RANGE

(NOTE : CAUTION MUST BE EXERCISED WITH RESPECT TO RESULTS FOR LEVEL 2 DUE TO INTERMITTENT EXPOSURE)

Level	Methods	01		02		06		07		08		09		13		14		15		16		23	
		C_d	C_m	C_d	C_m	C_d	C_m	C_d	C_m	C_d	C_m	C_d	C_m	C_d	C_m	C_d	C_m	C_d	C_m	C_d	C_m	C_d	C_m
2	Method of Moments, Rigid	2.06	2.03	1.46	2.01	1.82	2.35	1.29	2.22	0.63	2.26	1.11	1.99	0.72	2.26	0.76	2.29	0.87	2.06	0.97	2.26	0.76	2.00
	Method of Moments, Flexible	2.06	2.01	1.47	1.94	1.47	1.71	1.11	1.80	0.75	1.95	1.17	1.89	0.70	1.84	0.73	1.95	0.84	1.72	0.91	1.87	0.77	1.57
	Full Frequency Maximum Correlation Method	0.76	2.38	0.74	2.15	0.75	1.94	0.75	1.91	0.58	1.98	0.69	2 01	0.93	1.67	1.00	1.58	0.95	1.73	1.06	1.66	0.82	1.27
3	Method of Moments, Rigid	1.16	1.75	-	-	1.33	2.34	0.82	1.99	-	-	-	-	0.66	2.18	0.66	2.22	0.66	2.17	0.68	2.07	0.55	2.06
	Method of Moments, Flexible	1.08	1.74	-	-	1.11	1.29	0.32	1.53	-	-	-	-	0.63	1.69	0.65	1.82	0.65	1.69	0.70	1.49	0.58	1.45
	Full Frequency Maximum Correlation Method	0.70	1.84	0.70	1.81	0.50	1.48	0.50	1.51	0.57	1.57	0.64	1.59	0.86	1.52	0.85	1.54	0.81	1.54	0.83	1.44	0.81	0.95
4	Method of Moments, Rigid	1.03	1.84	-	-	1.14	2.23	0.89	1.96	-	-	-	-	0.52	2.04	0.58	2.05	0.58	2.00	0.53	2.17	0.49	1.85
	Method of Moments, Flexible	1.06	1.78	-	-	1.28	0.92	0.51	1.25	-	-	-	-	0.55	1.49	0.56	1.61	0.56	1.48	0.53	1.61	0.51	1.27
	Full Frequency Maximum Correlation Method	0.61	1.87	0.62	1.90	0.41	1.12	0.40	1.27	0.50	1.58	0.58	1.67	0.72	1.40	0.71	1.46	0.68	1.41	0.70	1.43	0.71	0.92

TABLE 9.14
COMPARISON OF THE RESULTS OF MAXIMUM CORRELATION METHOD
WITH METHOD OF MOMENTS, BOTH FLEXIBLE AND RIGID ASSUMPTIONS

(NOTE : CAUTION MUST BE EXERCISED WITH RESPECT TO
RESULTS FOR LEVEL 2 DUE TO INTERMITTENT EXPOSURE)

Level	Methods	01		02		06		07		08		09		13		14		15		16		23	
		a_d^2	a_i^2	a_d^2	a_i^2	a_d^2	a_i^2	a_d^2	a_i^2	a_d^2	a_i^2	a_d^2	a_i^2	a_d^2	a_i^2	a_d^2	a_i^2	a_d^2	a_i^2	a_d^2	a_i^2	a_d^2	a_i^2
2	Method of Moments, Rigid	0.32	0.68	0.22	0.78	0.29	0.71	0.20	0.80	0.04	0.96	0.16	0.84	0.31	0.69	0.35	0.65	0.50	0.50	0.45	0.55	0.49	0.51
	Method of Moments, Flexible	0.32	0.68	0.23	0.77	0.28	0.72	0.18	0.82	0.07	0.93	0.17	0.83	0.35	0.65	0.38	0.62	0.53	0.47	0.48	0.52	0.53	0.47
	Full Frequency Maximum Correlation Method	0.04	0.96	0.06	0.94	0.07	0.93	0.08	0.92	0.04	0.96	0.06	0.94	0.46	0.54	0.59	0.41	0.52	0.48	0.59	0.41	0.69	0.31
3	Method of Moments, Rigid	0.20	0.80	-	-	0.23	0.77	0.15	0.85	-	-	-	-	0.32	0.68	0.34	0.66	0.41	0.59	0.52	0.48	0.43	0.57
	Method of Moments, Flexible	0.17	0.83	-	-	0.29	0.71	0.03	0.97	-	-	-	-	0.35	0.65	0.39	0.61	0.46	0.54	0.62	0.38	0.54	0.46
	Full Frequency Maximum Correlation Method	0.07	0.93	0.08	0.92	0.06	0.94	0.07	0.93	0.07	0.93	0.09	0.91	0.48	0.52	0.56	0.44	0.55	0.45	0.64	0.36	0.80	0.20
4	Method of Moments, Rigid	0.13	0.87	-	-	0.17	0.83	0.16	0.84	-	-	-	-	0.24	0.76	0.31	0.69	0.37	0.63	0.38	0.62	0.41	0.59
	Method of Moments, Flexible	0.14	0.86	-	-	0.34	0.66	0.07	0.93	-	-	-	-	0.29	0.71	0.32	0.68	0.40	0.60	0.40	0.60	0.49	0.51
	Full Frequency Maximum Correlation Method	0.05	0.95	0.05	0.95	0.04	0.96	0.04	0.96	0.04	0.96	0.05	0.95	0.37	0.63	0.45	0.55	0.45	0.55	0.53	0.47	0.73	0.27

TABLE 9.15
COMPARISON OF a_d^2 AND a_i^2 FROM MAXIMUM CORRELATION METHOD
WITH THOSE FROM THE METHOD OF MOMENTS, BOTH FLEXIBLE AND RIGID ASSUMPTIONS

(NOTE : CAUTION MUST BE EXERCISED WITH RESPECT TO
RESULTS FOR LEVEL 2 DUE TO INTERMITTENT EXPOSURE)

Run	Level	σ_r	$\sigma_{\dot{u}}$	$\frac{\sigma_r}{\sigma_{\dot{u}}}$	σ_t	u_{rms}	$\frac{\sigma_t}{u_{rms}}$
01	2	0.0549	0.477	0.12	0.0076	0.3823	0.020
	3	0.0535	0.320	0.17	0.0068	0.3262	0.021
	4	0.0487	0.220	0.22	0.0064	0.2613	0.025
02	2	0.0853	0.490	0.17	0.0137	0.4027	0.034
	3	0.0733	0.319	0.23	0.0117	0.3464	0.034
	4	0.0623	0.218	0.29	0.0104	0.2729	0.038
06	2	0.4210	0.499	0.84	0.1394	0.4341	0.32
	3	0.4160	0.365	1.14	0.1356	0.3943	0.34
	4	0.4859	0.267	1.82	0.1547	0.3205	0.48
07	2	0.3436	0.522	0.66	0.1003	0.4543	0.22
	3	0.2956	0.397	0.74	0.0883	0.4251	0.21
	4	0.3532	0.297	1.19	0.1001	0.3554	0.28
08	2	0.2309	0.516	0.45	0.0555	0.4265	0.13
	3	0.1832	0.374	0.49	0.0457	0.3782	0.12
	4	0.1809	0.264	0.69	0.0414	0.3042	0.14
09	2	0.0929	0.499	0.19	0.0204	0.4157	0.049
	3	0.0825	0.368	0.22	0.0168	0.3756	0.045
	4	0.0913	0.260	0.35	0.0173	0.2998	0.058
13	2	0.4348	0.662	0.66	0.1586	0.7772	0.20
	3	0.4226	0.560	0.75	0.1482	0.7411	0.20
	4	0.4864	0.507	0.96	0.1605	0.6963	0.23
14	2	0.3763	0.672	0.56	0.1411	0.8016	0.18
	3	0.3545	0.571	0.62	0.1286	0.7795	0.16
	4	0.4166	0.518	0.80	0.1372	0.7333	0.19
15	2	0.4364	0.712	0.61	0.1567	0.8528	0.18
	3	0.4150	0.600	0.69	0.1460	0.8450	0.17
	4	0.4871	0.554	0.88	0.1562	0.8042	0.19
16	2	0.4425	0.728	0.61	0.1573	0.8219	0.19
	3	0.4228	0.600	0.70	0.1482	0.9150	0.16
	4	0.4920	0.550	0.89	0.1583	0.8759	0.18
23	2	0.5730	0.770	0.74	0.1919	0.9351	0.21
	3	0.5591	0.718	0.78	0.1856	1.0076	0.18
	4	0.6407	0.670	0.96	0.2017	0.9664	0.21

TABLE 9.16.
STATISTICAL COMPARISON OF CYLINDER KINEMATICS
WITH WATER PARTICLE KINEMATICS

(NOTE : CAUTION MUST BE EXERCISED WITH RESPECT TO
RESULTS FOR LEVEL 2 DUE TO INTERMITTENT EXPOSURE)

Run No	Force	C_d	C_m	Standard Deviation (KN)	Skewness	Kurtosis	Maximum (KN)	Minimum (KN)
01	Predicted	0.80	1.75	0.0673	-0.01	3.02	0.236	-0.234
	Observed			0.0621	0.06	3.30	0.232	-0.329
13	Predicted	0.80	1.65	0.150	-0.07	3.33	0.579	-0.541
	Observed			0.146	0.36	3.91	0.900	-0.550
15	Predicted	0.80	1.65	0.167	-0.75	5.04	0.630	-0.798
	Observed			0.168	0.64	4.62	0.900	-0.670

TABLE 9.17.
COMPARISON OF THE IN-LINE FORCES
CALCULATED IN THE TIME DOMAIN WITH THE OBSERVED FORCES (LEVEL 3)

Run No	Cylinder Displacement	C_d	C_m	Standard Deviation (m)	Skewness	Kurtosis	Maximum (m)	Minimum (m)
01	Predicted	0.80	1.75	0.0024	-0.02	3.02	0.0093	-0.0085
	Observed			0.0024	-0.45	9.14	0.0290	-0.0110
13	Predicted	0.80	1.65	0.0786	-0.05	3.55	0.2960	-0.2922
	Observed			0.0810	0.09	3.04	0.3000	-0.2900
15	Predicted	0.80	1.65	0.0841	-0.58	4.70	0.3147	-0.3892
	Observed			0.0880	0.16	3.42	0.3400	-0.3200

TABLE 9.18.
COMPARISON OF THE IN-LINE CYLINDER DISPLACEMENTS
CALCULATED IN THE TIME DOMAIN WITH THE OBSERVED CYLINDER DISPLACEMENTS (LEVEL 3)

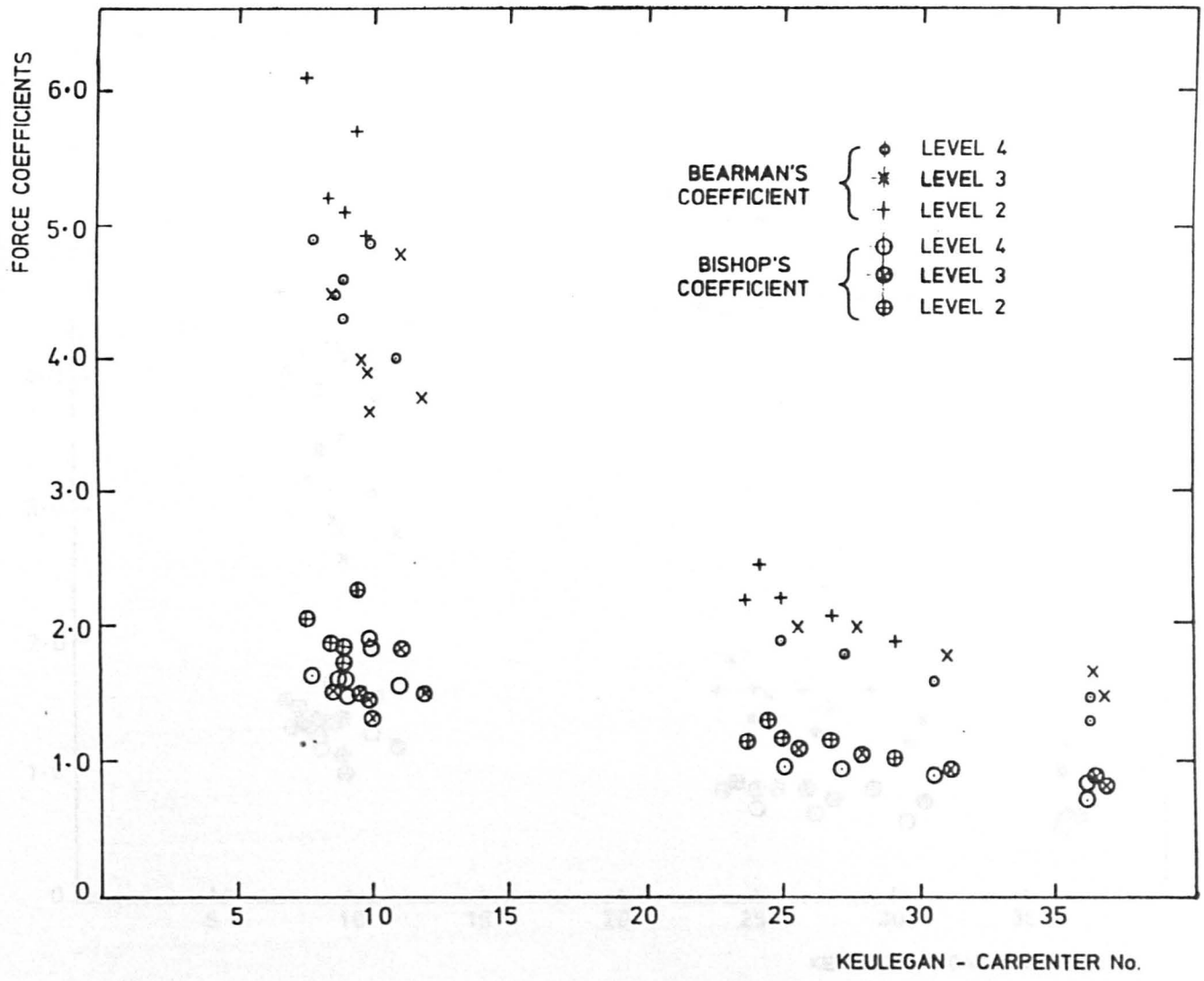

FIGURE 9.1. BEARMAN'S AND BISHOP'S FORCE COEFFICIENTS VERSUS KEULEGAN - CARPENTER No. FOR IN - LINE FORCES

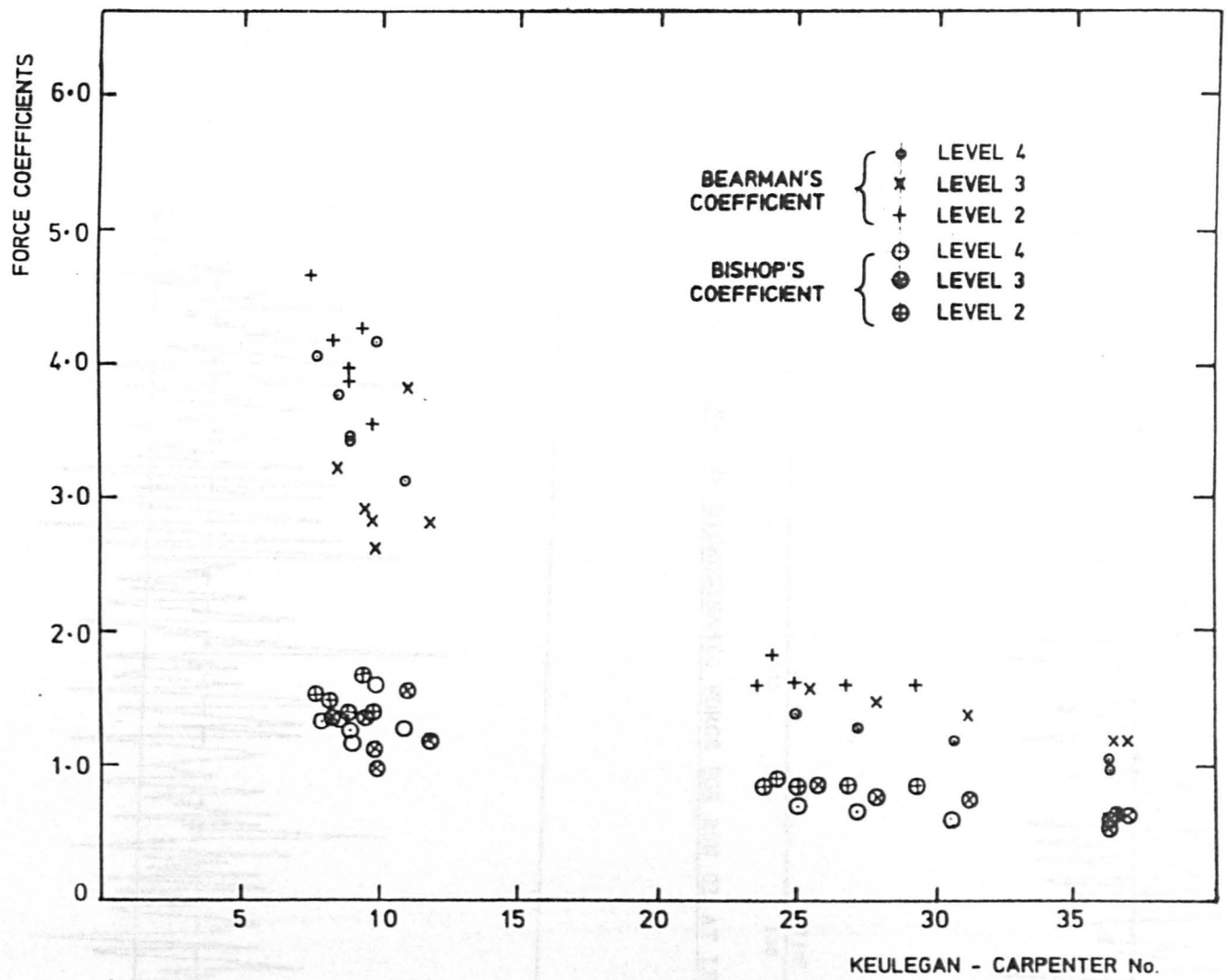

FIGURE 9.2 BEARMAN'S AND BISHOP'S FORCE COEFFICIENTS VERSUS KEULEGAN - CARPENTER No. FOR TRANSVERSE FORCES

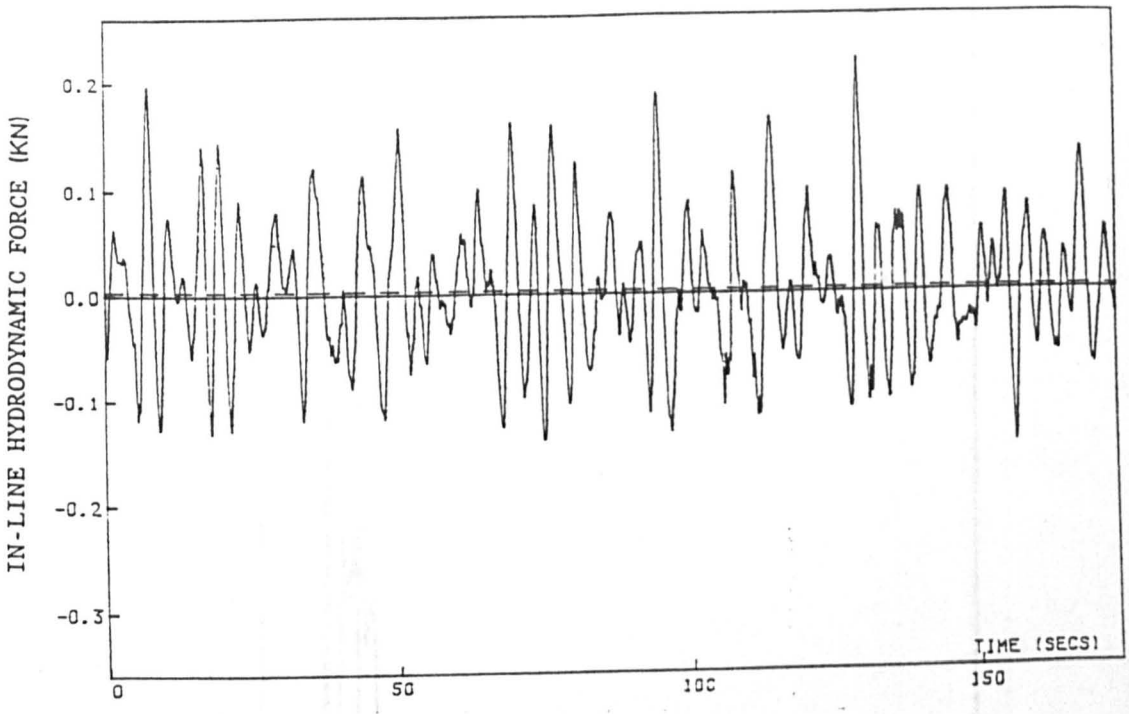

FIGURE 9.3. SAMPLE IN-LINE HYDRODYNAMIC FORCE FOR RUN 01 AT LEVEL 3

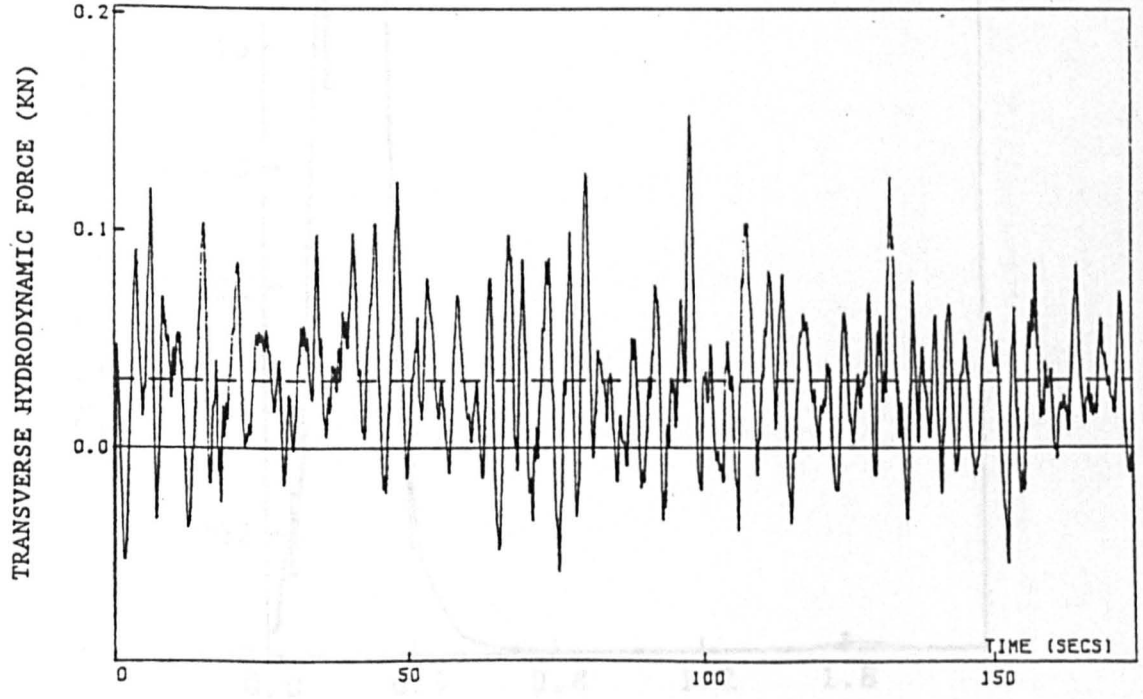

FIGURE 9.4. SAMPLE TRANSVERSE HYDRODYNAMIC FORCE FOR RUN 01 AT LEVEL 3

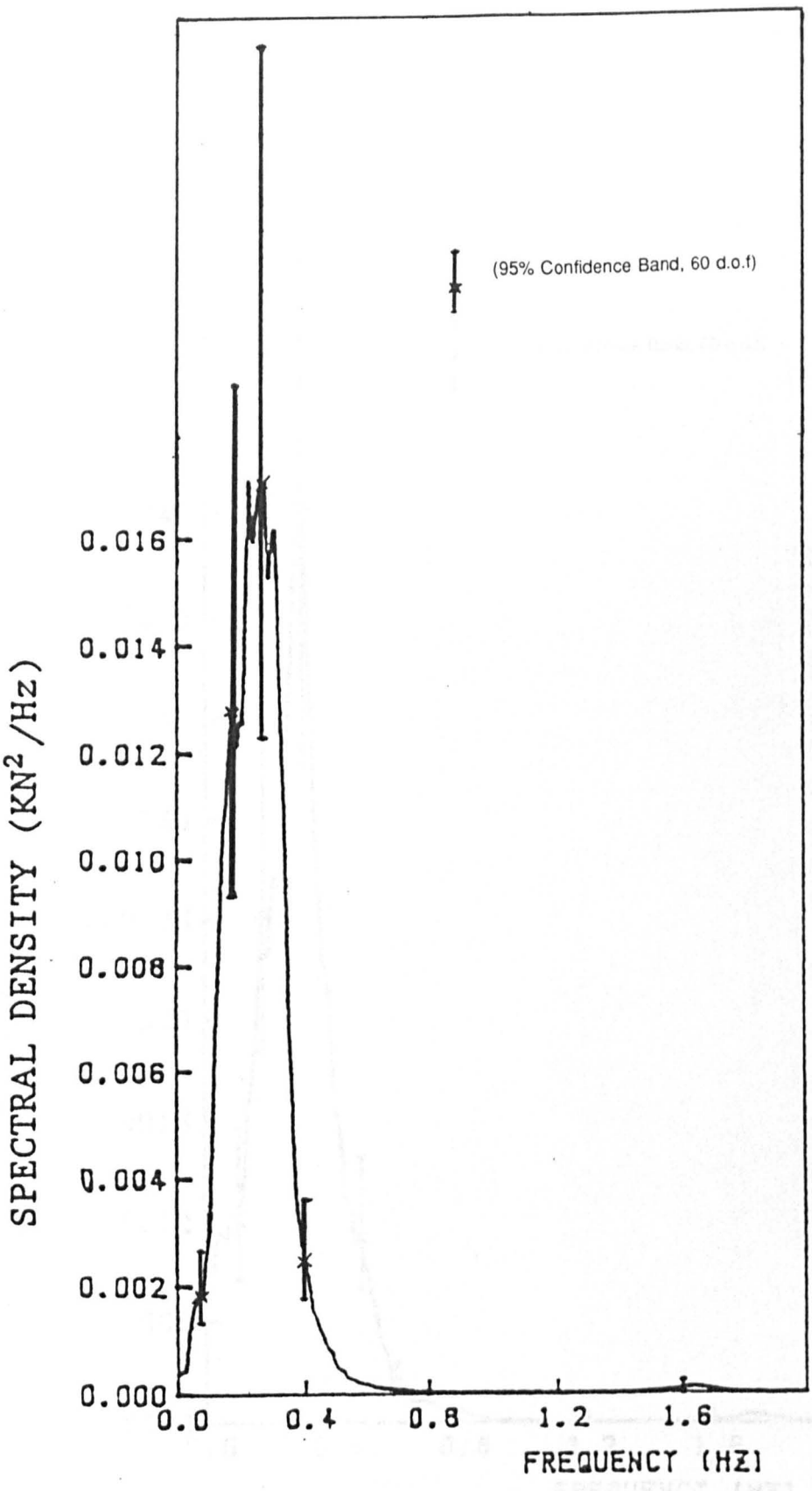

FIGURE 9.5. FREQUENCY SPECTRUM OF IN-LINE HYDRODYNAMIC FORCE AT LEVEL 3 FOR RUN 01 (Tickell and Burrows, 1989)

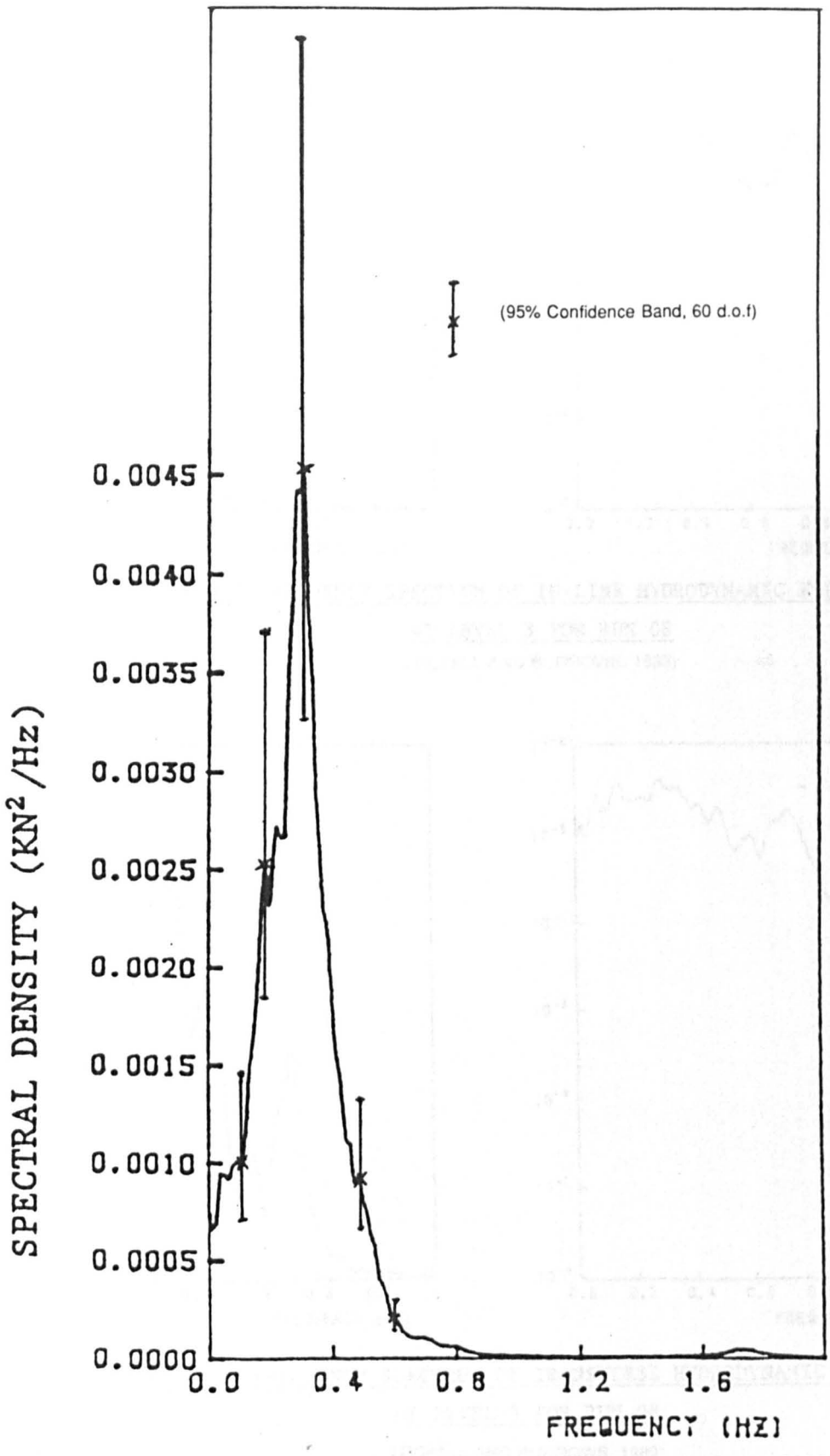

FIGURE 9.6. FREQUENCY SPECTRUM OF TRANSVERSE HYDRODYNAMIC FORCE AT LEVEL 3 FOR RUN 01 (Tickell and Burrows, 1989)

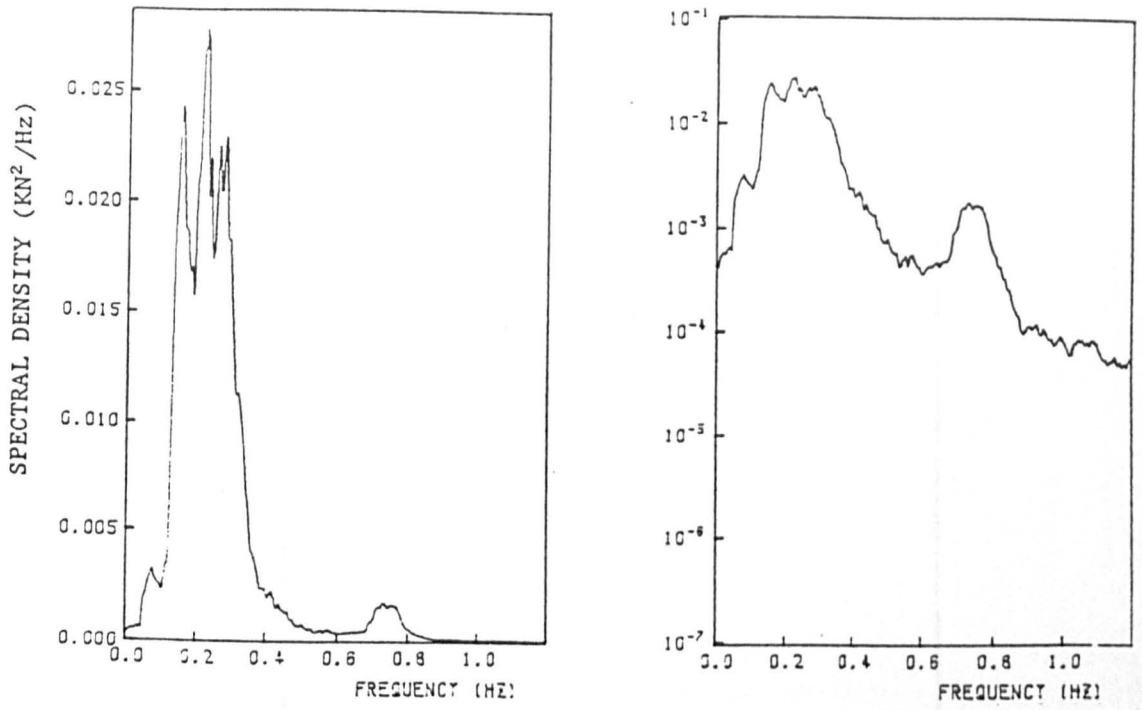

FIGURE 9.7 FREQUENCY SPECTRUM OF IN-LINE HYDRODYNAMIC FORCE AT LEVEL 3 FOR RUN 08

(TICKELL AND BURROWS, 1989)

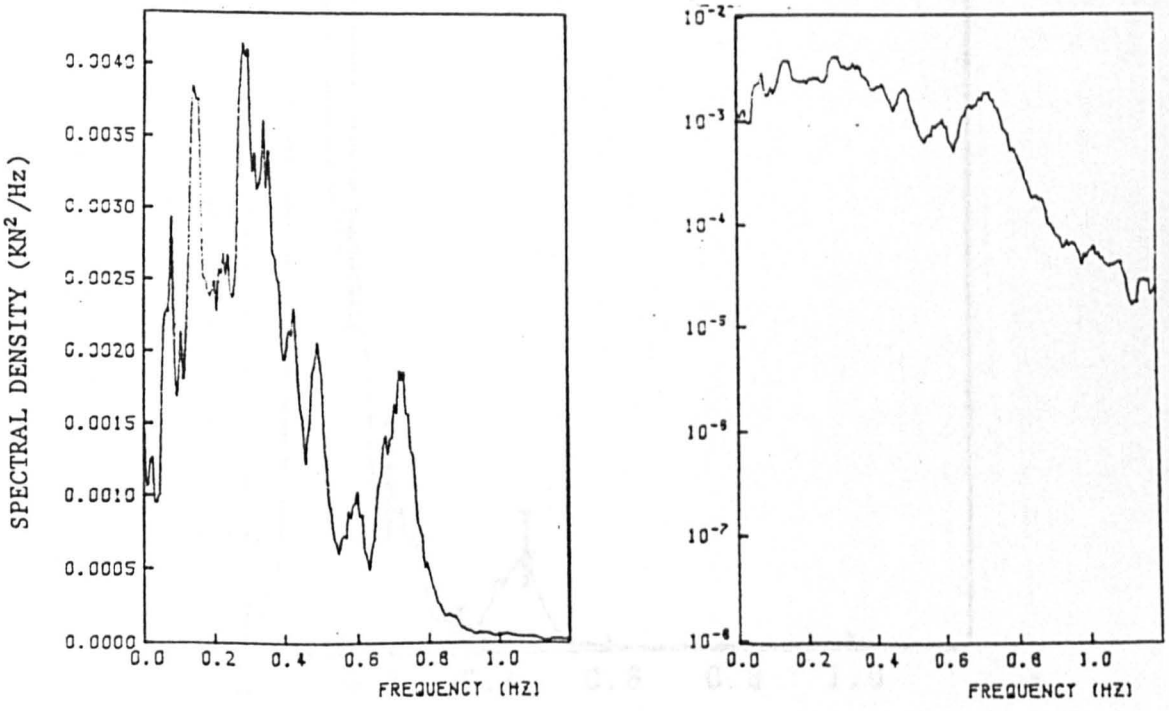

FIGURE 9.8. FREQUENCY SPECTRUM OF TRANSVERSE HYDRODYNAMIC FORCE AT LEVEL 3 FOR RUN 08

(TICKELL AND BURROWS, 1989)

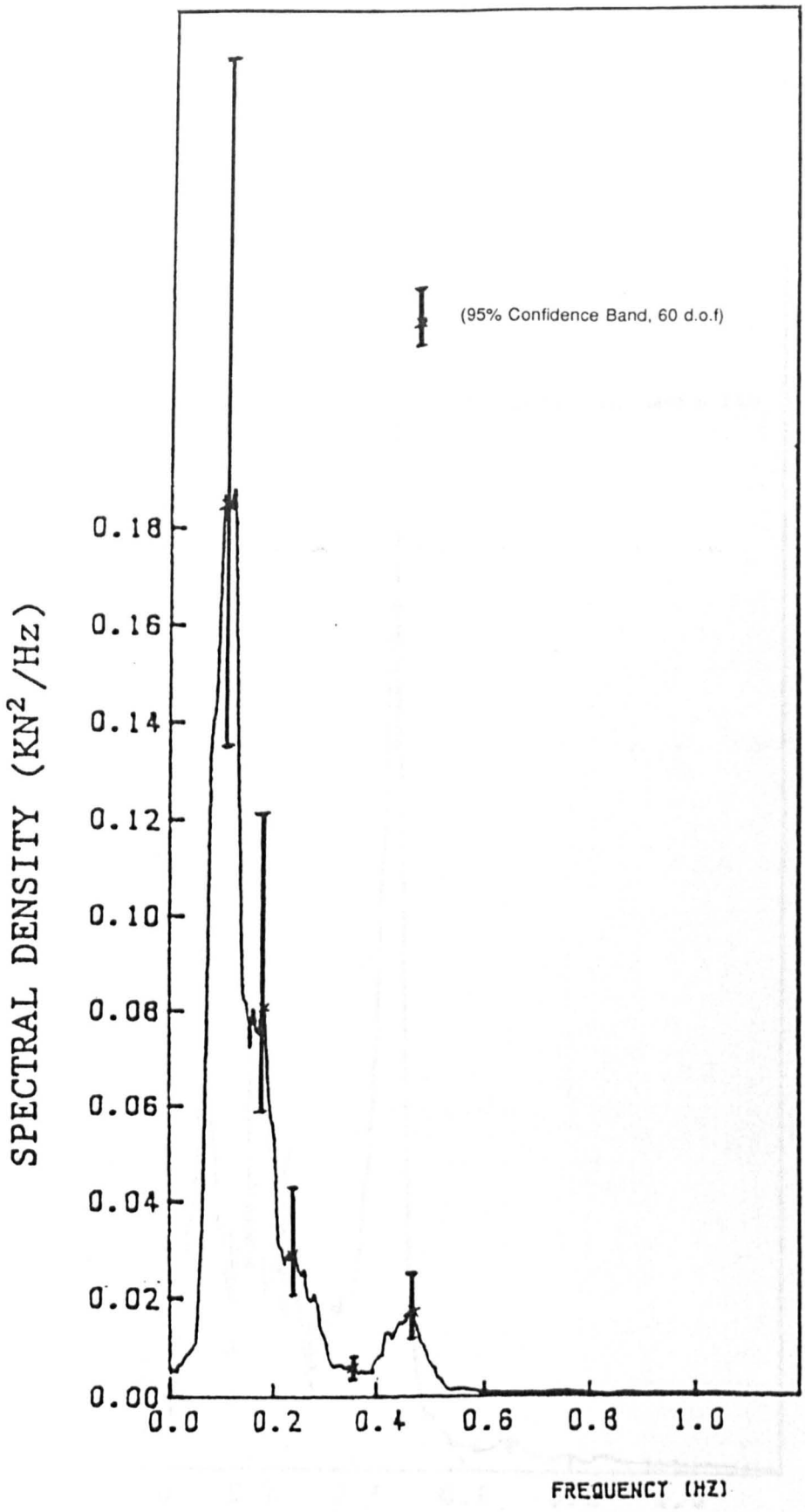

FIGURE 9.9. FREQUENCY SPECTRUM OF IN-LINE HYDRODYNAMIC FORCE AT LEVEL 3 FOR RUN 13 (Tickell and Burrows, 1989)

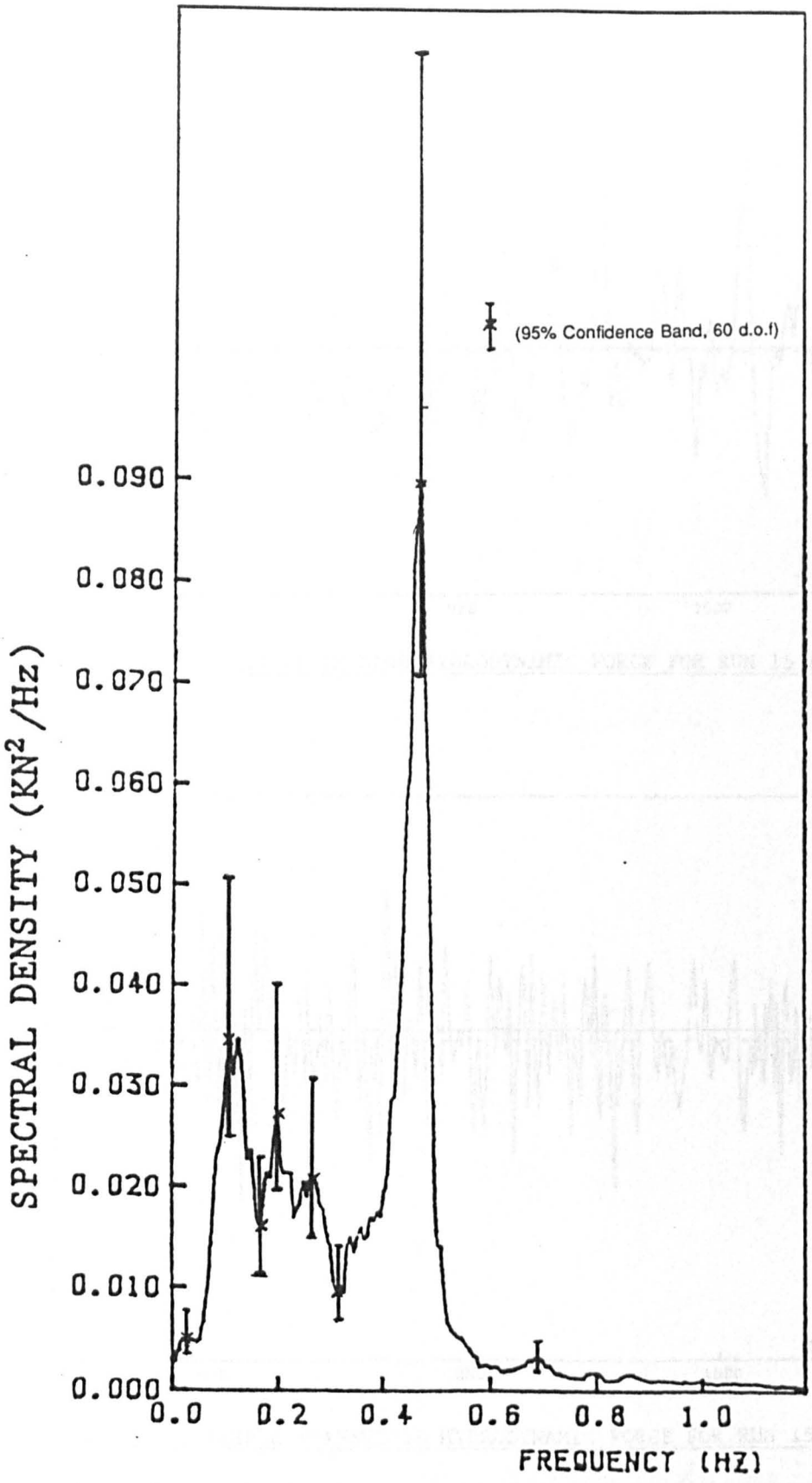

FIGURE 9.10. FREQUENCY SPECTRUM OF TRANSVERSE HYDRODYNAMIC FORCE AT LEVEL 3 FOR RUN 13 (Tickell and Burrows, 1989)

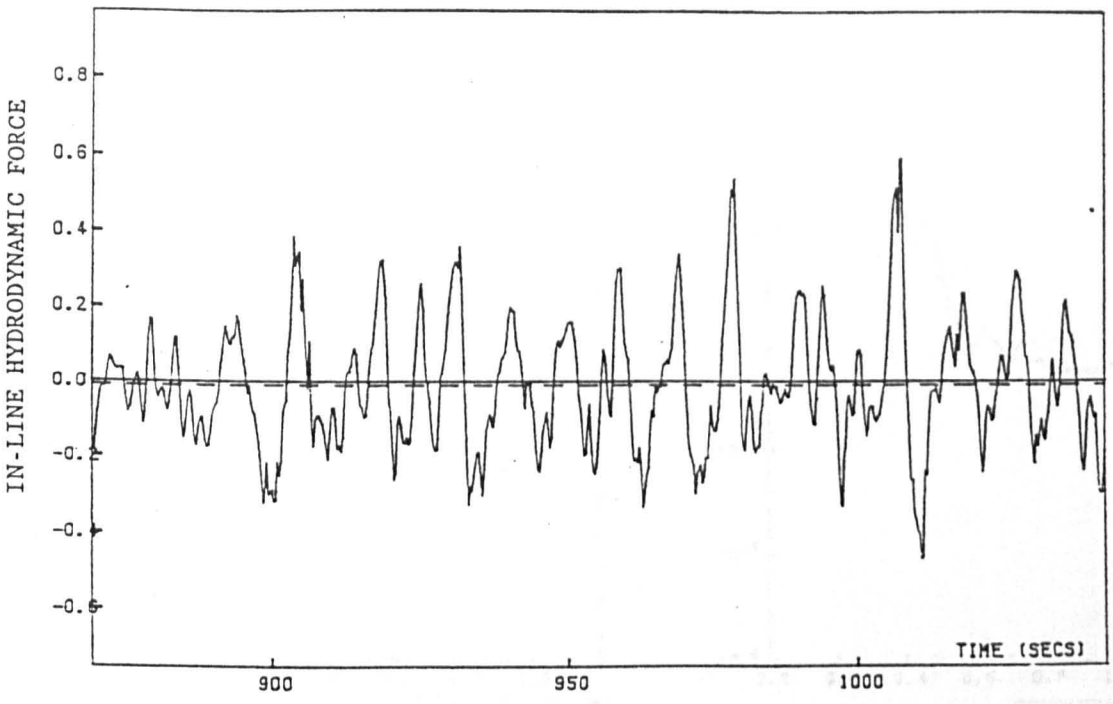

FIGURE 9.11. SAMPLE IN-LINE HYDRODYNAMIC FORCE FOR RUN 15 AT LEVEL 3

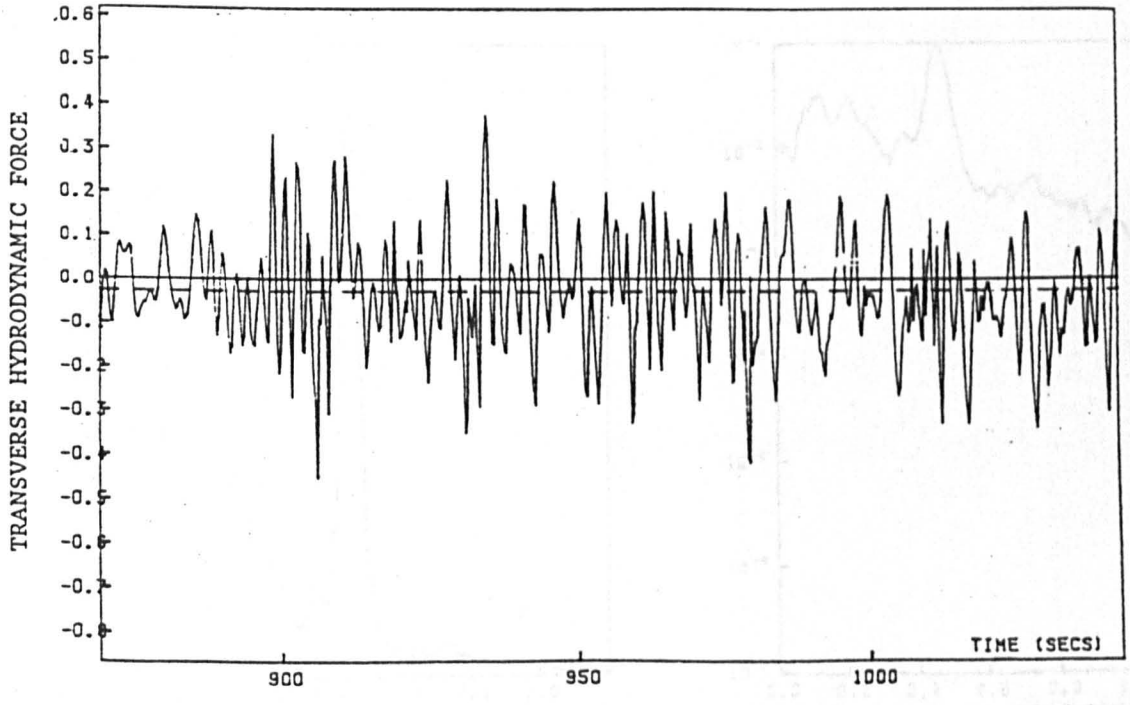

FIGURE 9.12. SAMPLE TRANSVERSE HYDRODYNAMIC FORCE FOR RUN 15 AT LEVEL 3

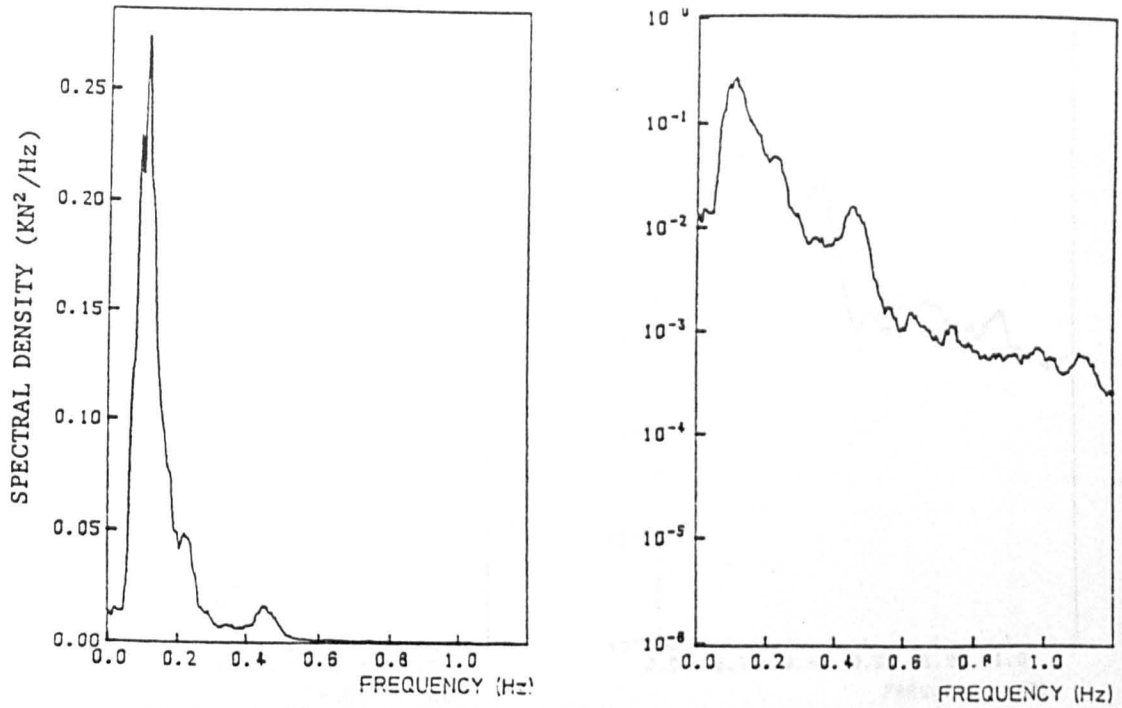

FIGURE 9.13. FREQUENCY SPECTRUM OF IN-LINE HYDRODYNAMIC FORCE AT LEVEL 3 FOR RUN 15

(TICKELL AND BURROWS, 1989)

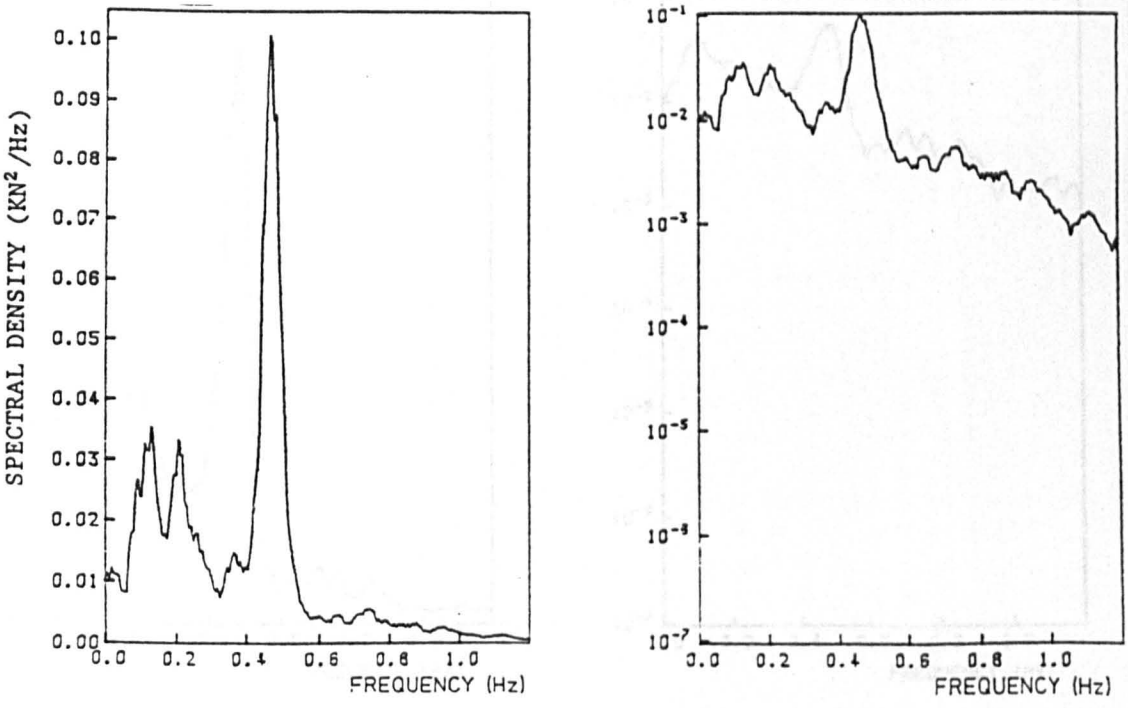

FIGURE 9.14. FREQUENCY SPECTRUM OF TRANSVERSE HYDRODYNAMIC FORCE AT LEVEL 3 FOR RUN 15

(TICKELL AND BURROWS, 1989)

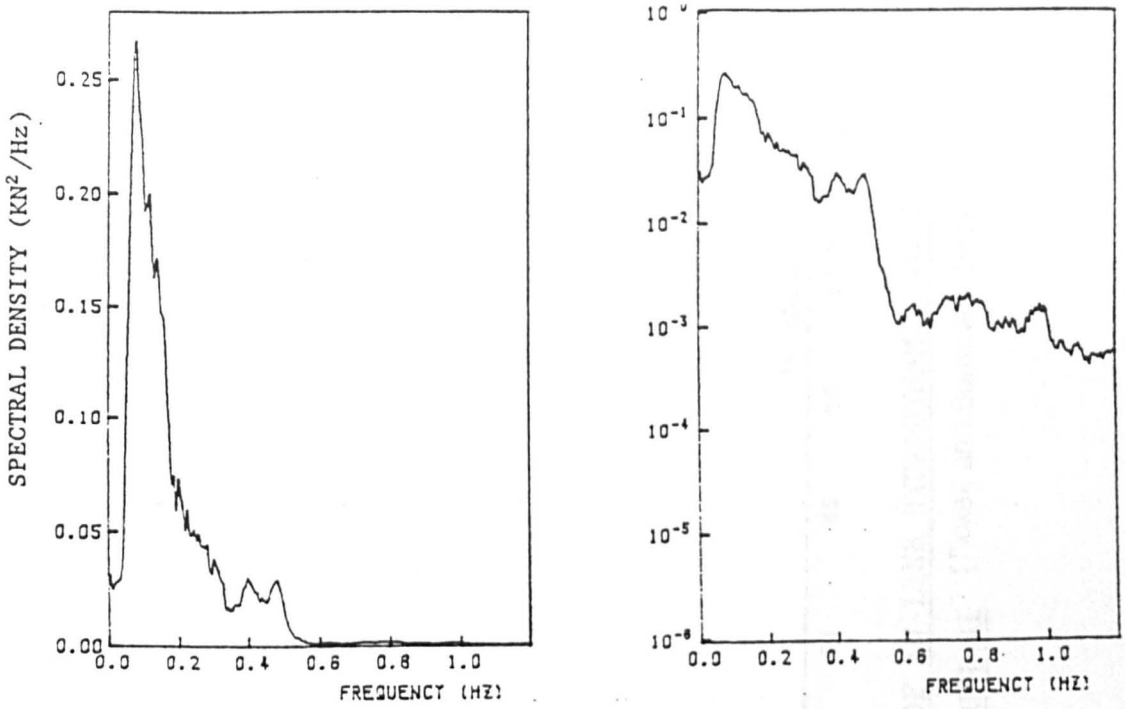

FIGURE 9.15. FREQUENCY SPECTRUM OF IN-LINE HYDRODYNAMIC FORCE AT LEVEL 3 FOR RUN 23

(TICKELL AND BURROWS, 1989)

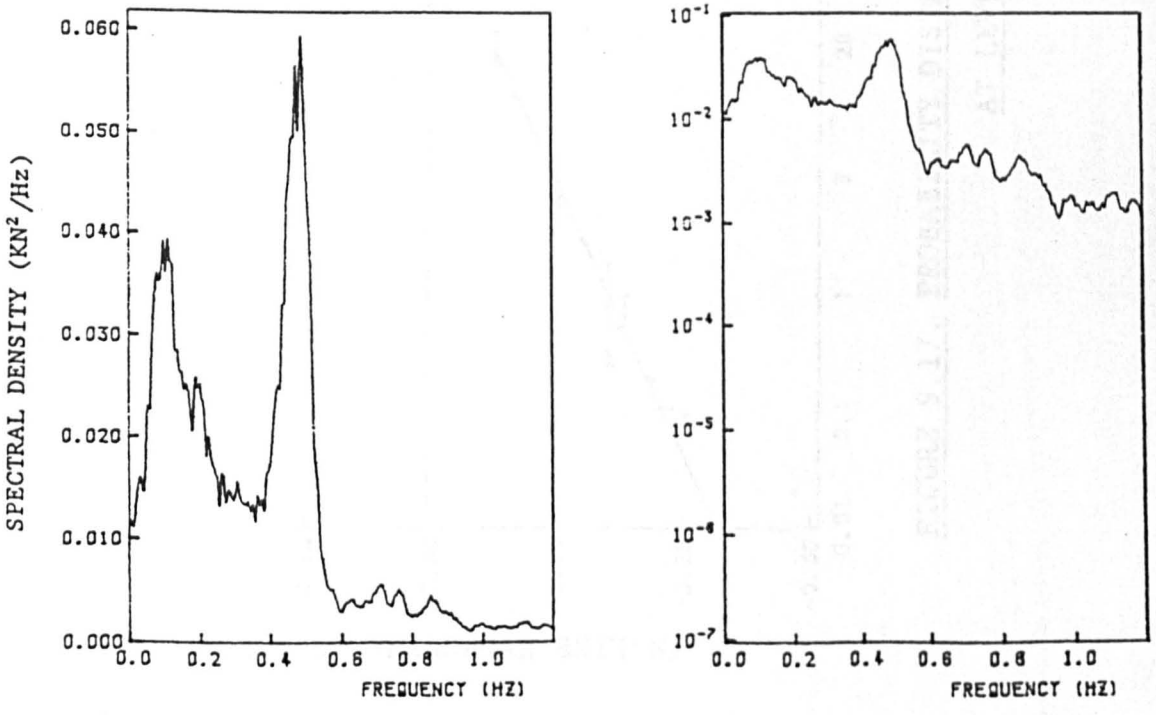

FIGURE 9.16. FREQUENCY SPECTRUM OF TRANSVERSE HYDRODYNAMIC FORCE AT LEVEL 3 FOR RUN 23

(TICKELL AND BURROWS, 1989)

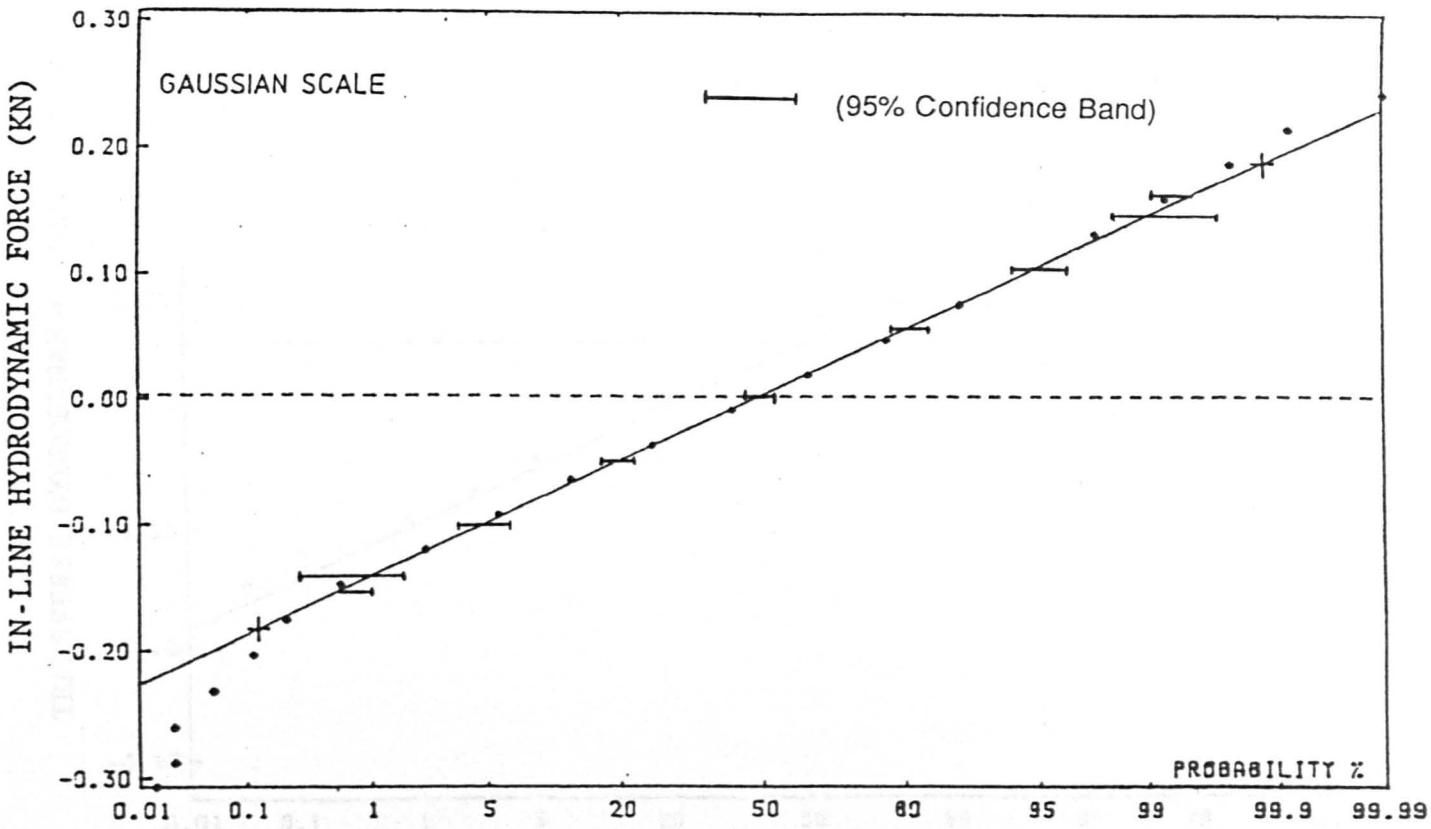

FIGURE 9.17. PROBABILITY DISTRIBUTION OF IN-LINE HYDRODYNAMIC FORCE AT LEVEL 3 FOR RUN 01 (Tickell and Burrows, 1989)

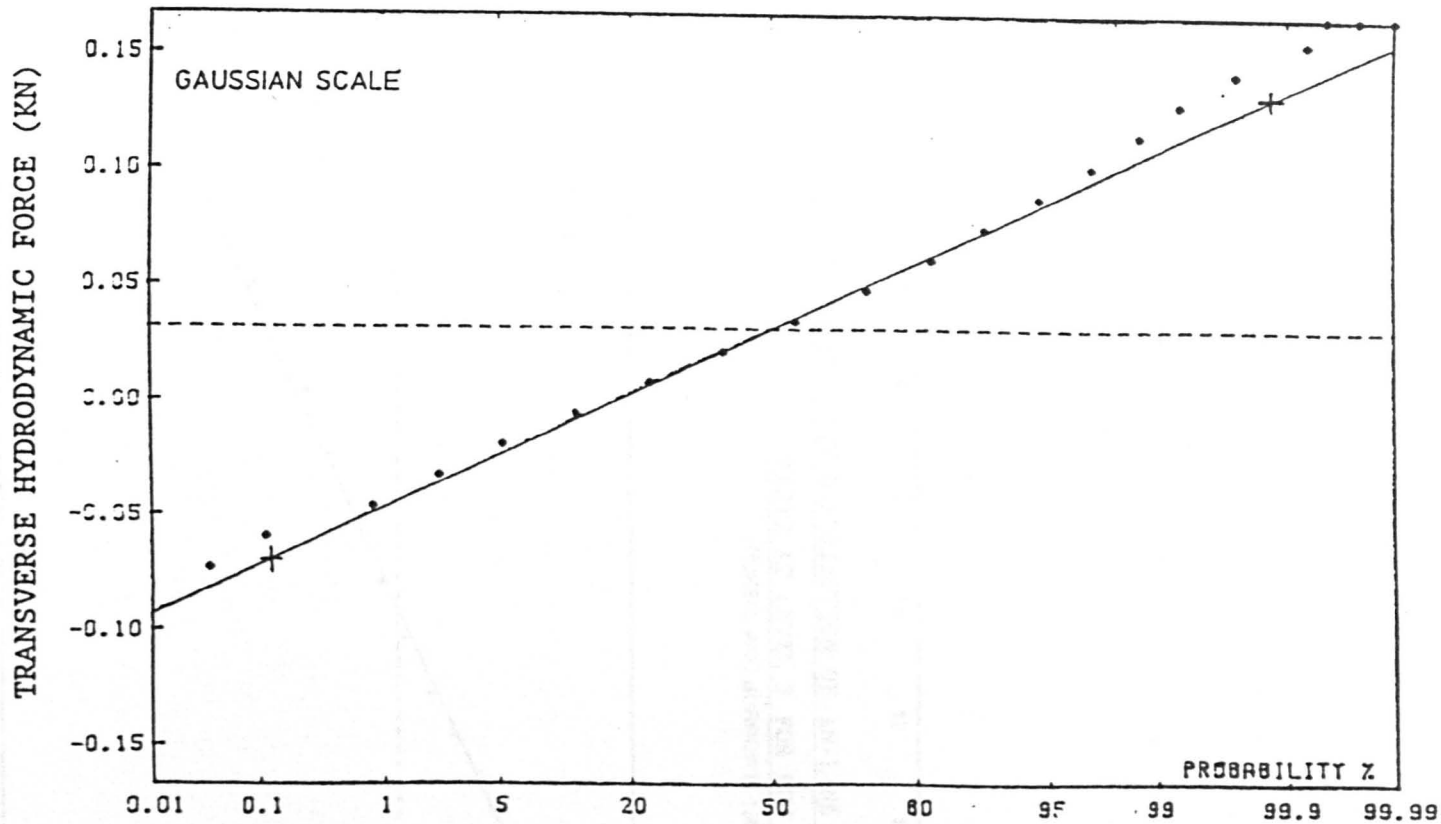

FIGURE 9.18. PROBABILITY DISTRIBUTION OF TRANSVERSE HYDRODYNAMIC FORCE AT LEVEL 3 FOR RUN 01 (Tickell and Burrows, 1989)

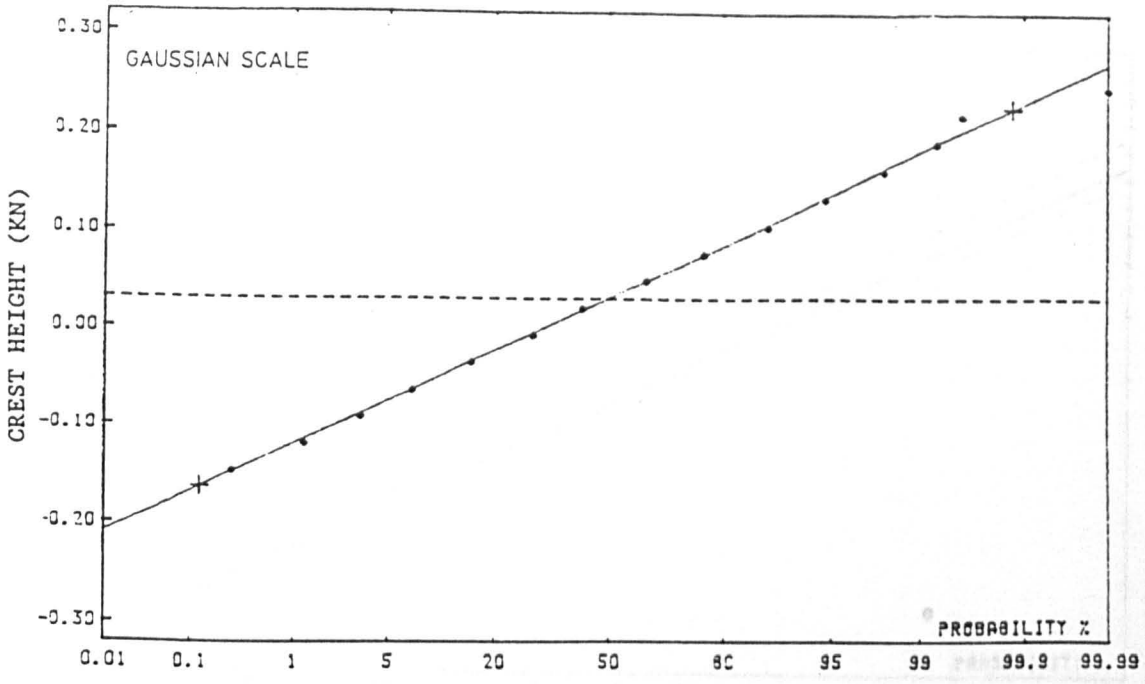

FIGURE 9.19. PROBABILITY DISTRIBUTION OF IN-LINE HYDRODYNAMIC FORCE CRESTS AT LEVEL 3 FOR RUN 01

(TICKELL AND BURROWS, 1989)

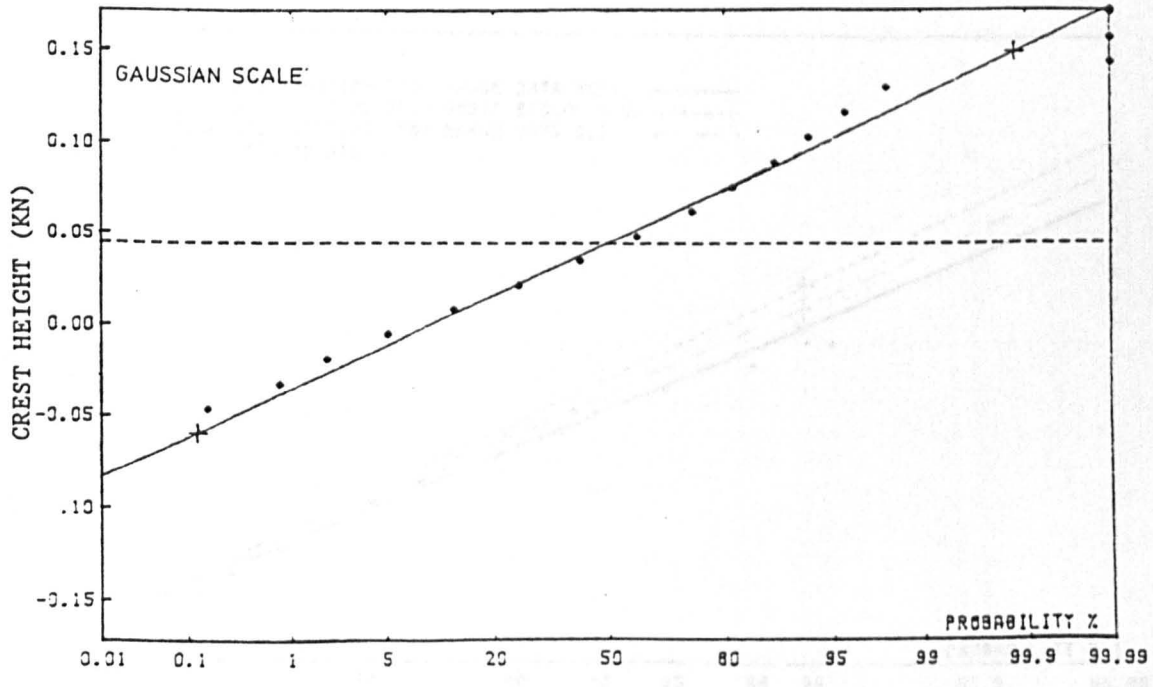

FIGURE 9.20. PROBABILITY DISTRIBUTION OF TRANSVERSE HYDRODYNAMIC FORCE CRESTS AT LEVEL 3 FOR RUN 01

(TICKELL AND BURROWS, 1989)

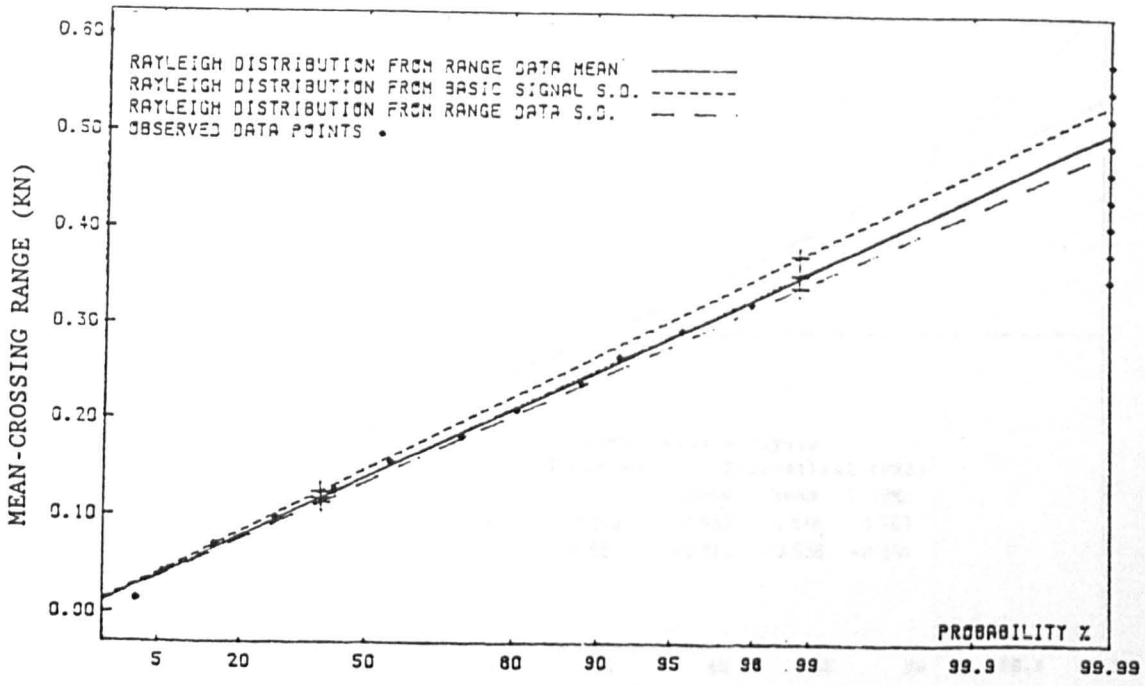

FIGURE 9.21. PROBABILITY DISTRIBUTION OF MEAN-CROSSING RANGES OF IN-LINE HYDRODYNAMIC FORCE AT LEVEL 3 FOR RUN 01

(TICKELL AND BURROWS, 1989)

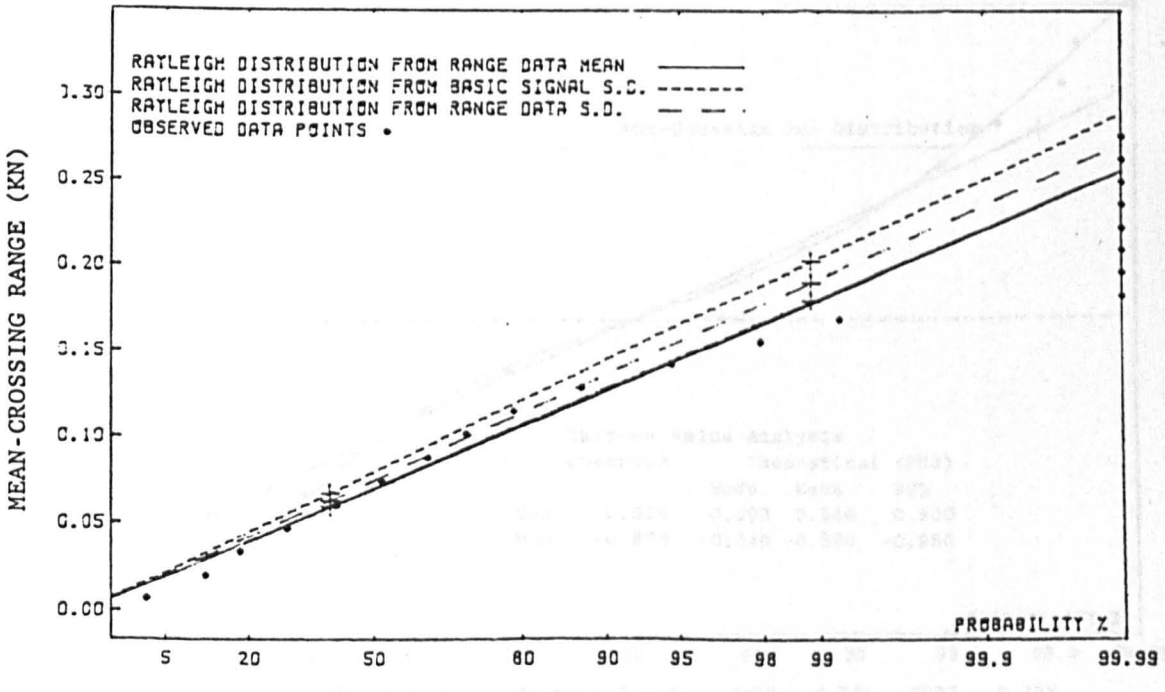

FIGURE 9.22. PROBABILITY DISTRIBUTION OF MEAN-CROSSING RANGES OF TRANSVERSE HYDRODYNAMIC FORCE AT LEVEL 3 FOR RUN 01

(TICKELL AND BURROWS, 1989)

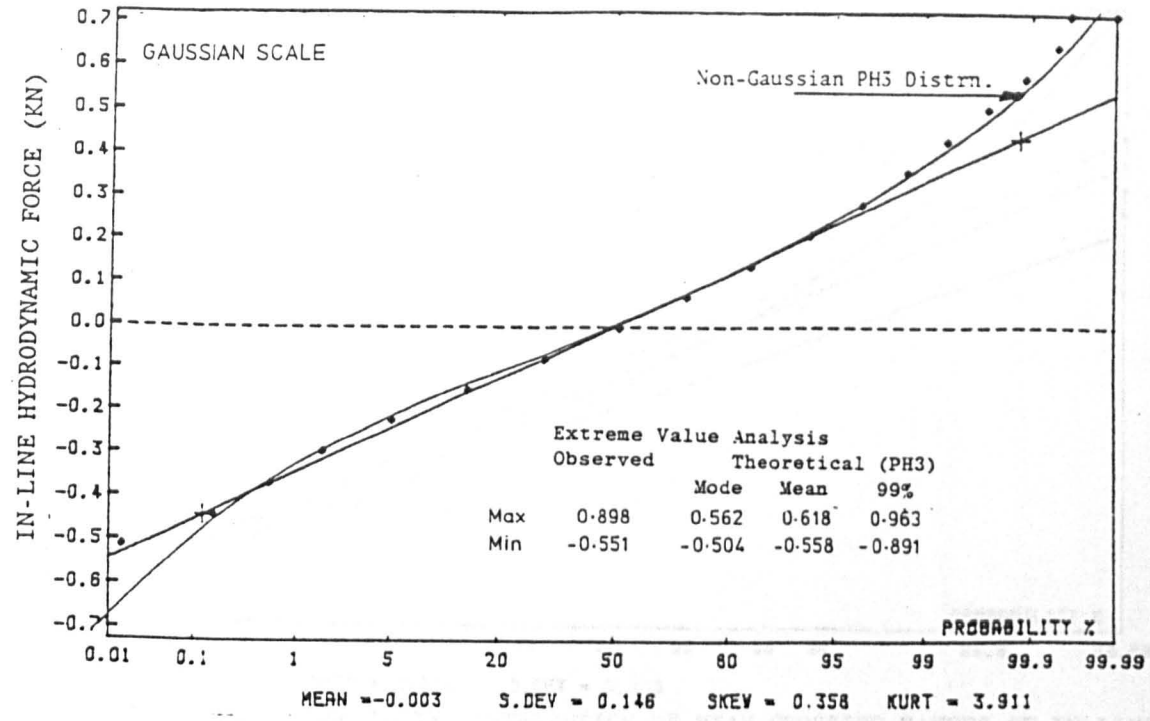

FIGURE 9.23. PROBABILITY DISTRIBUTION OF IN-LINE HYDRODYNAMIC FORCE AT LEVEL 3 FOR RUN 13

(TICKELL AND BURROWS, 1989)

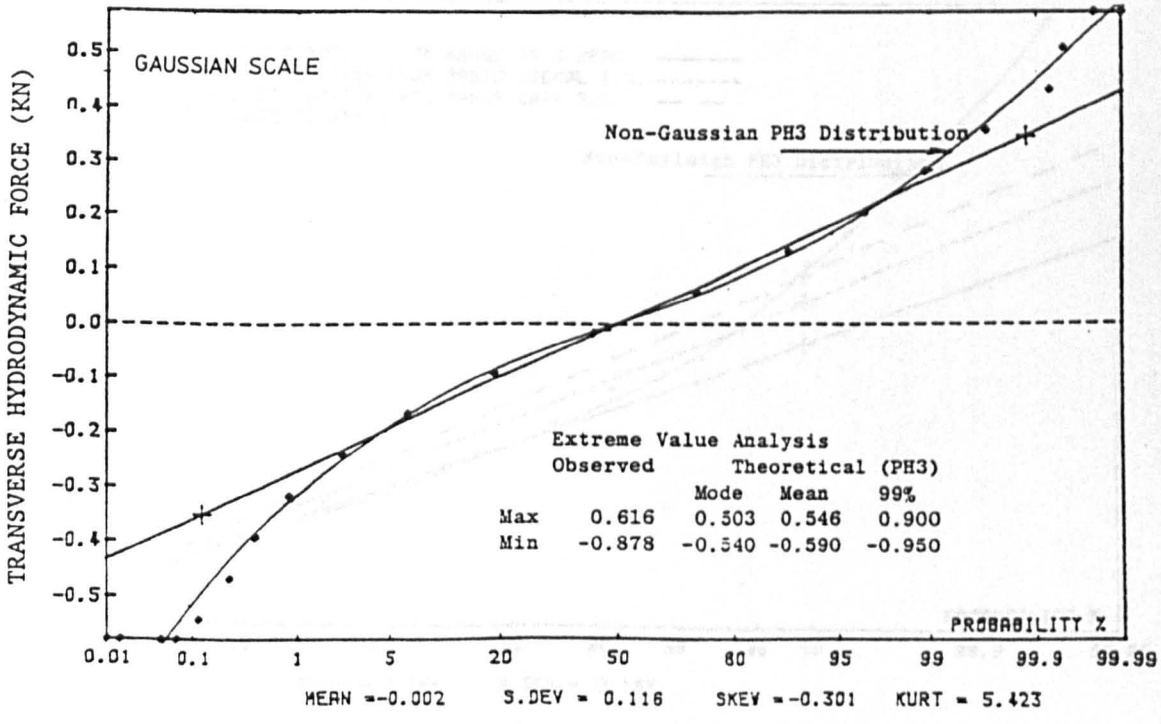

FIGURE 9.24. PROBABILITY DISTRIBUTION OF TRANSVERSE HYDRODYNAMIC FORCE AT LEVEL 3 FOR RUN 13

(TICKELL AND BURROWS, 1989)

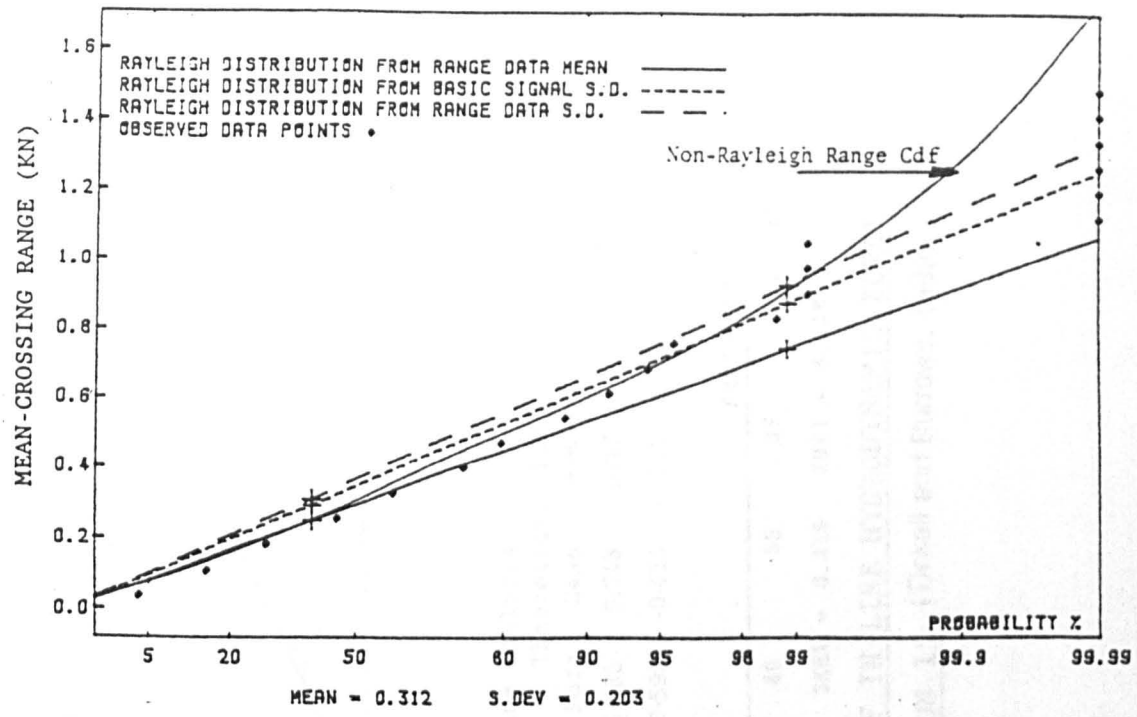

FIGURE 9.25. PROBABILITY DISTRIBUTION OF MEAN-CROSSING RANGES OF IN-LINE HYDRODYNAMIC FORCE AT LEVEL 3 FOR RUN 13

(TICKELL AND BURROWS, 1989)

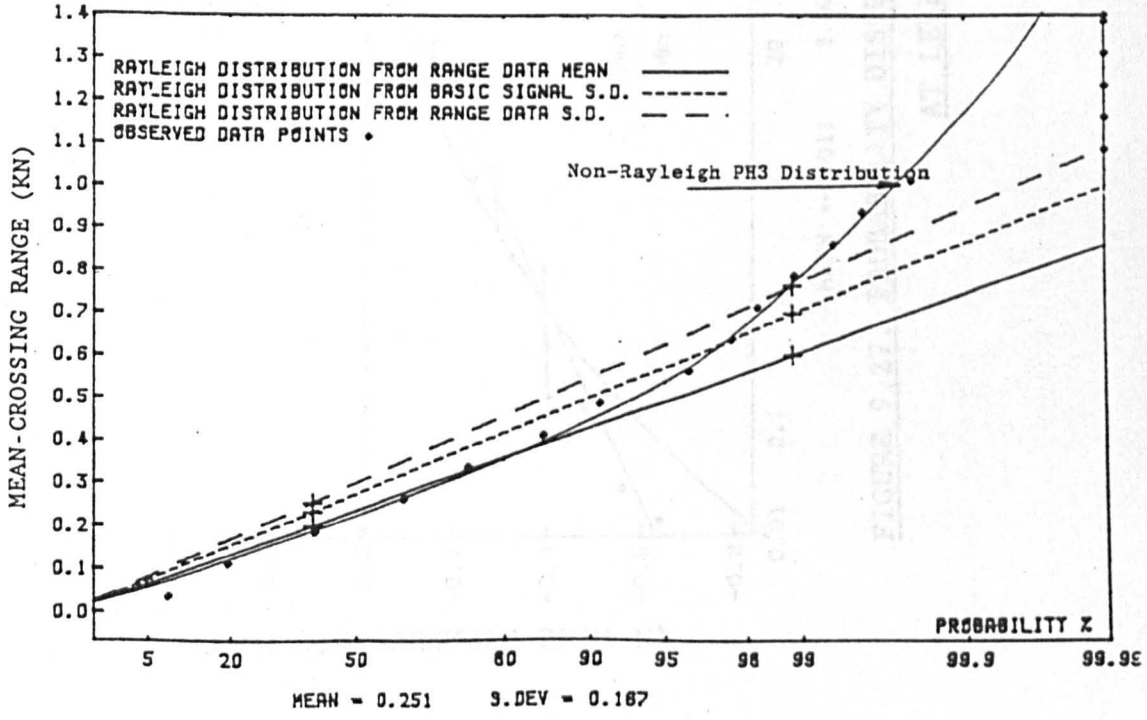

FIGURE 9.26. PROBABILITY DISTRIBUTION OF MEAN-CROSSING RANGES OF TRANSVERSE HYDRODYNAMIC FORCE AT LEVEL 3 FOR RUN 13

(TICKELL AND BURROWS, 1989)

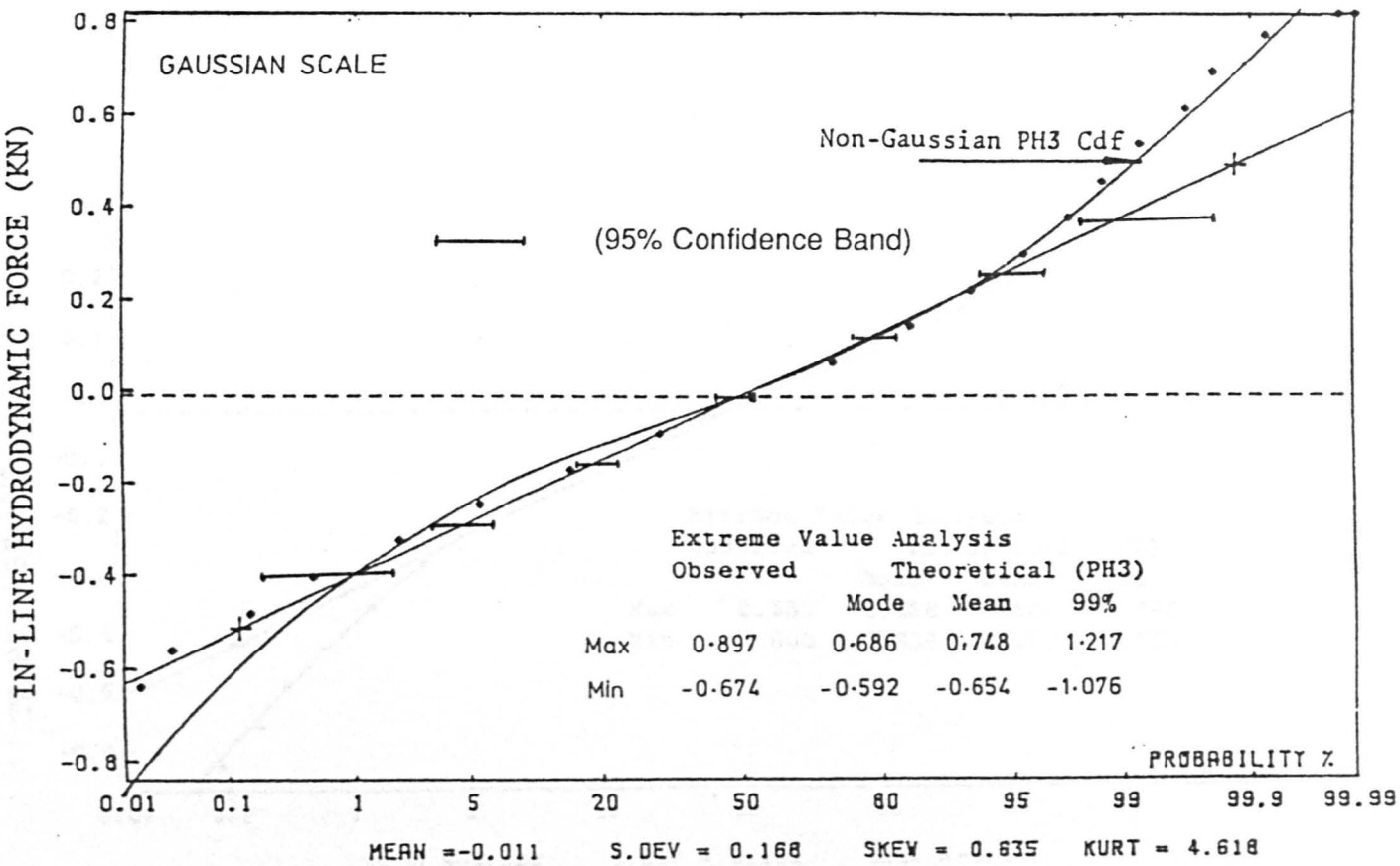

FIGURE 9.27. PROBABILITY DISTRIBUTION OF IN-LINE HYDRODYNAMIC FORCE AT LEVEL 3 FOR RUN 15 (Tickell and Burrows, 1989)

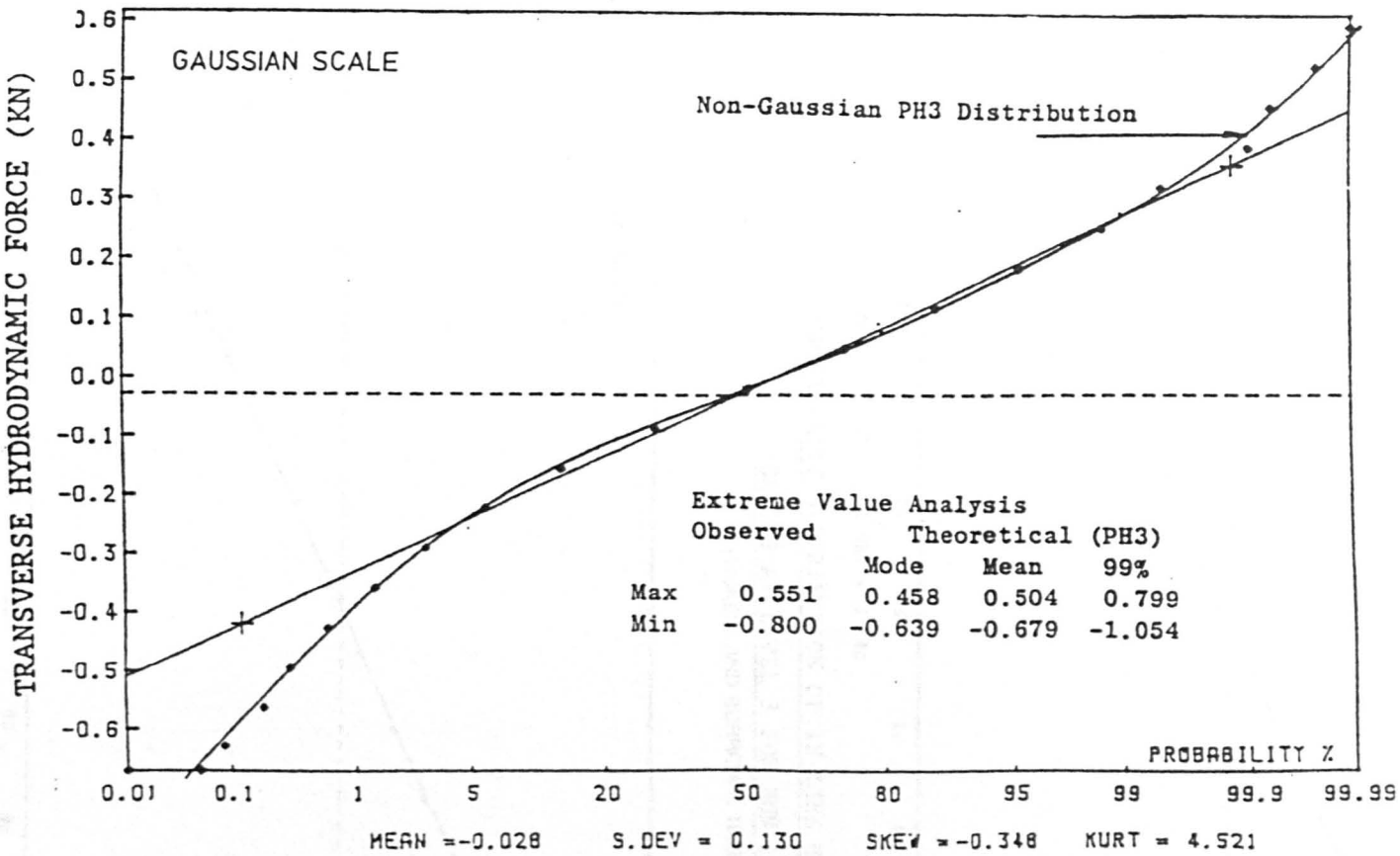

FIGURE 9.28. PROBABILITY DISTRIBUTION OF TRANSVERSE HYDRODYNAMIC FORCE AT LEVEL 3 FOR RUN 15 (Tickell and Burrows, 1989)

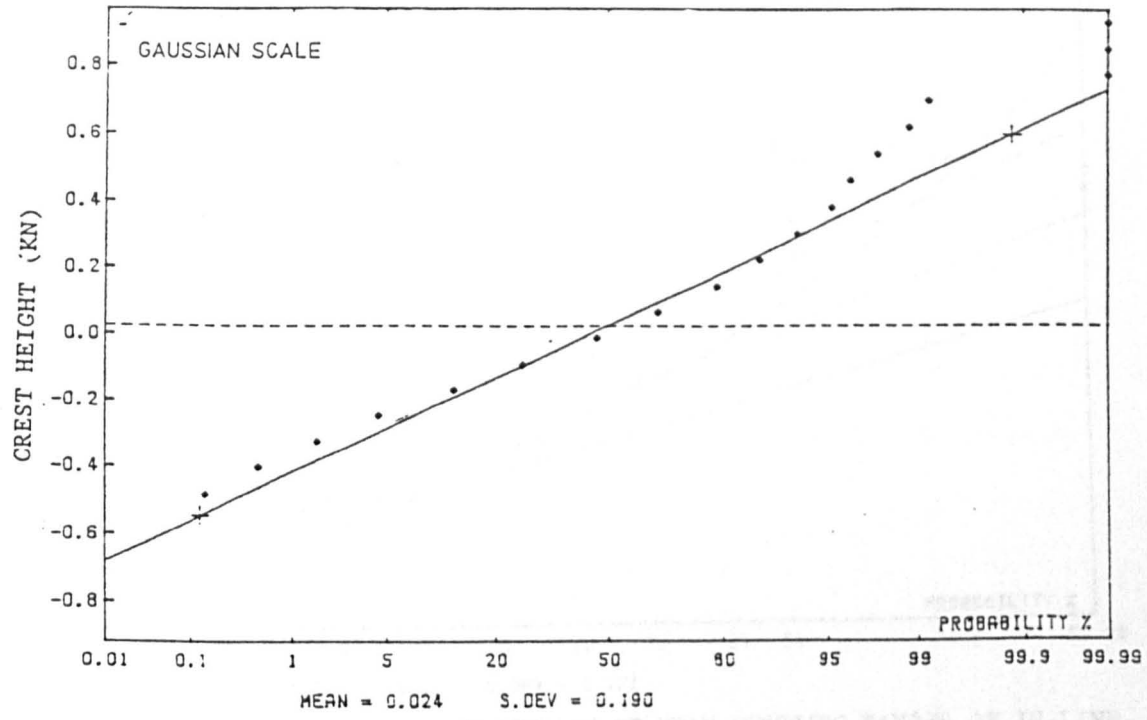

FIGURE 9.29. PROBABILITY DISTRIBUTION OF IN-LINE HYDRODYNAMIC FORCE CRESTS AT LEVEL 3 FOR RUN 15

(TICKELL AND BURROWS, 1989)

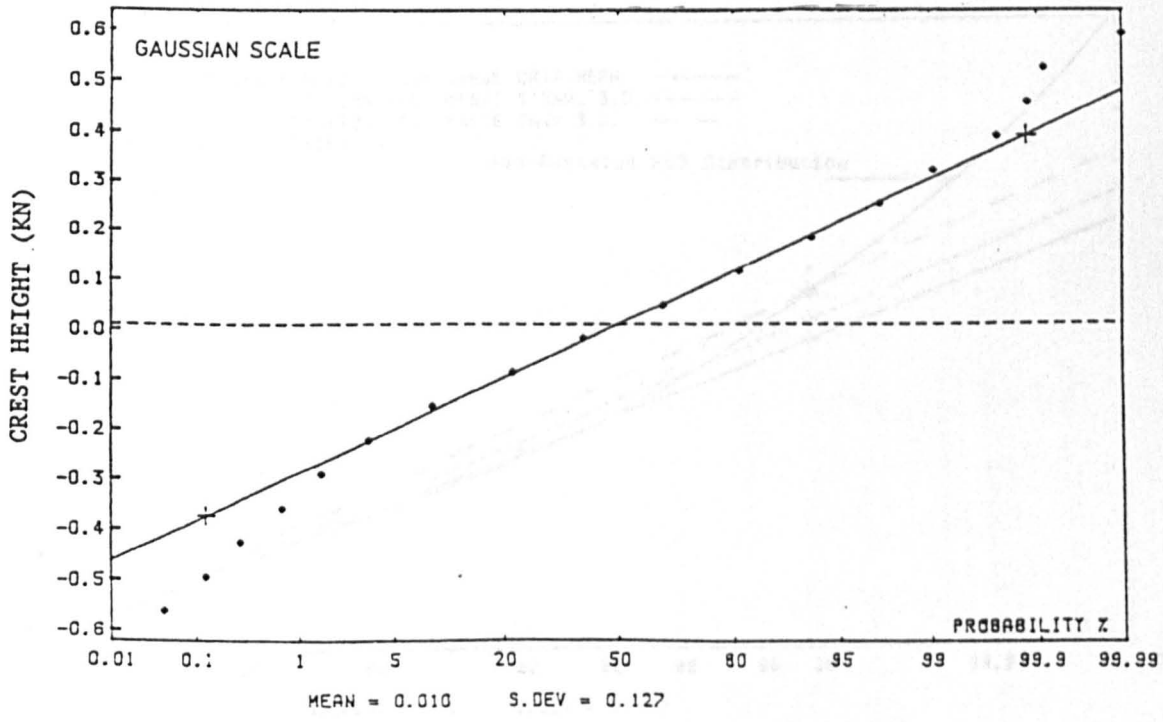

FIGURE 9.30. PROBABILITY DISTRIBUTION OF TRANSVERSE HYDRODYNAMIC FORCE CRESTS AT LEVEL 3 FOR RUN 15

(TICKELL AND BURROWS, 1989)

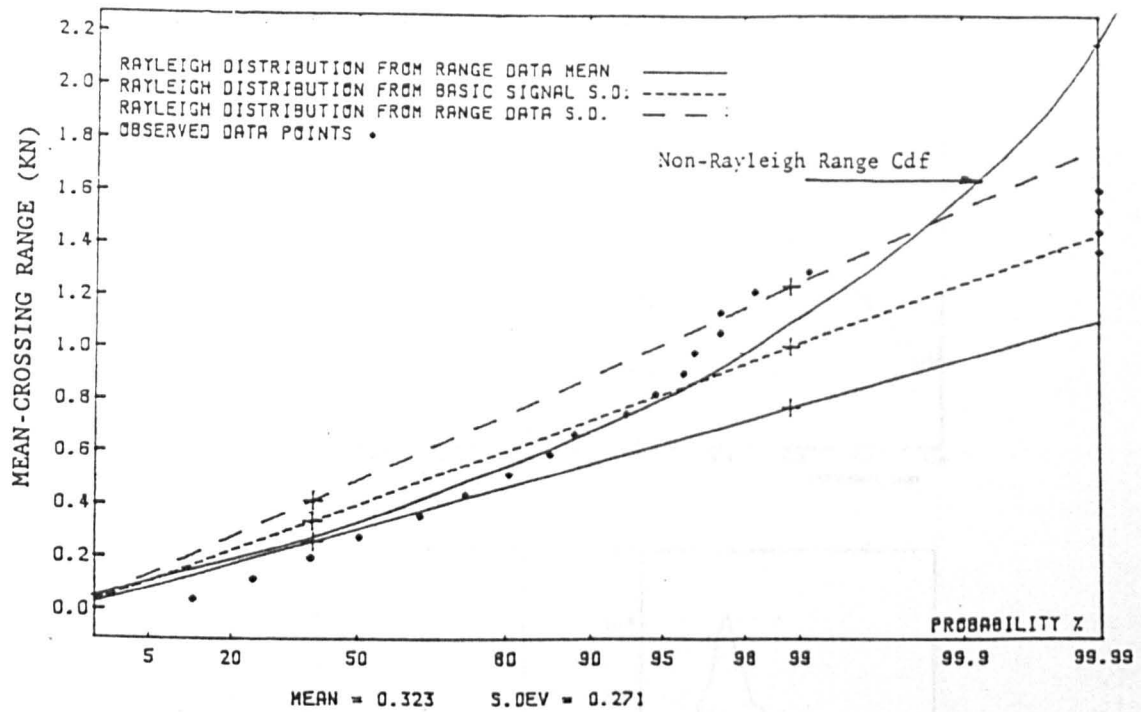

FIGURE 9.31. PROBABILITY DISTRIBUTION OF MEAN-CROSSING RANGES OF IN-LINE HYDRODYNAMIC FORCE AT LEVEL 3 FOR RUN 15

(TICKELL AND BURROWS, 1989)

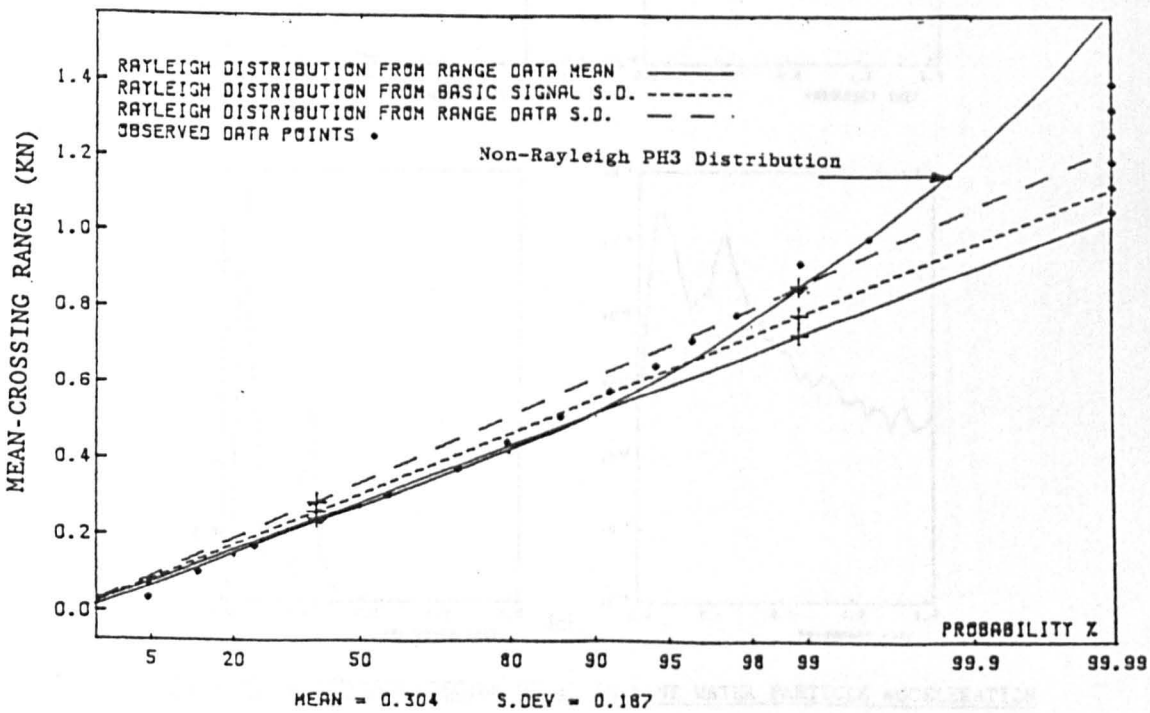

FIGURE 9.32. PROBABILITY DISTRIBUTION OF MEAN-CROSSING RANGES OF TRANSVERSE HYDRODYNAMIC FORCE AT LEVEL 3 RUN 15

(TICKELL AND BURROWS, 1989)

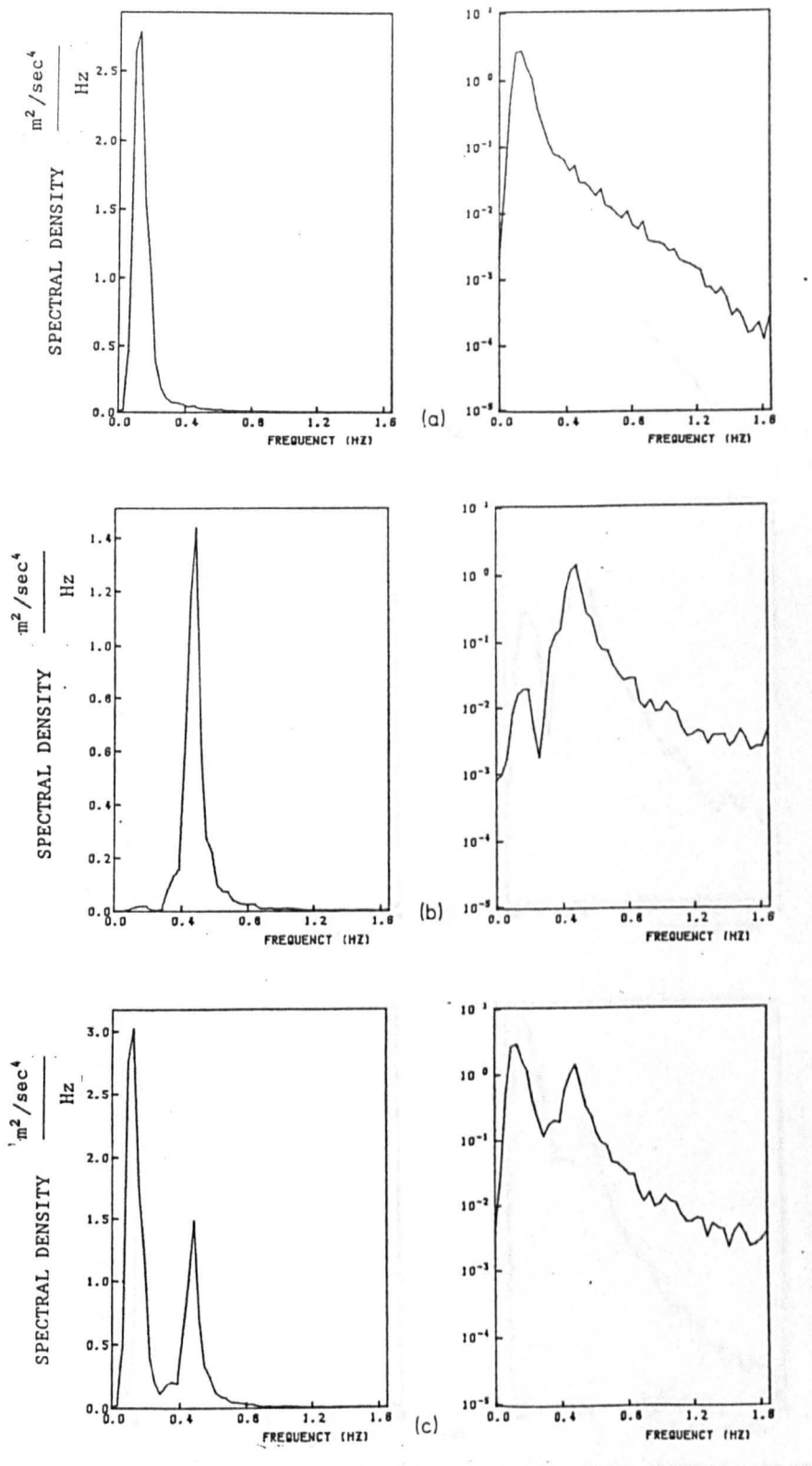

FIGURE 9.33. FREQUENCY SPECTRA OF a) IN-LINE WATER PARTICLE ACCELERATION b) CYLINDER ACCELERATION AND c) RELATIVE ACCELERATION AT LEVEL 3 FOR RUN 13

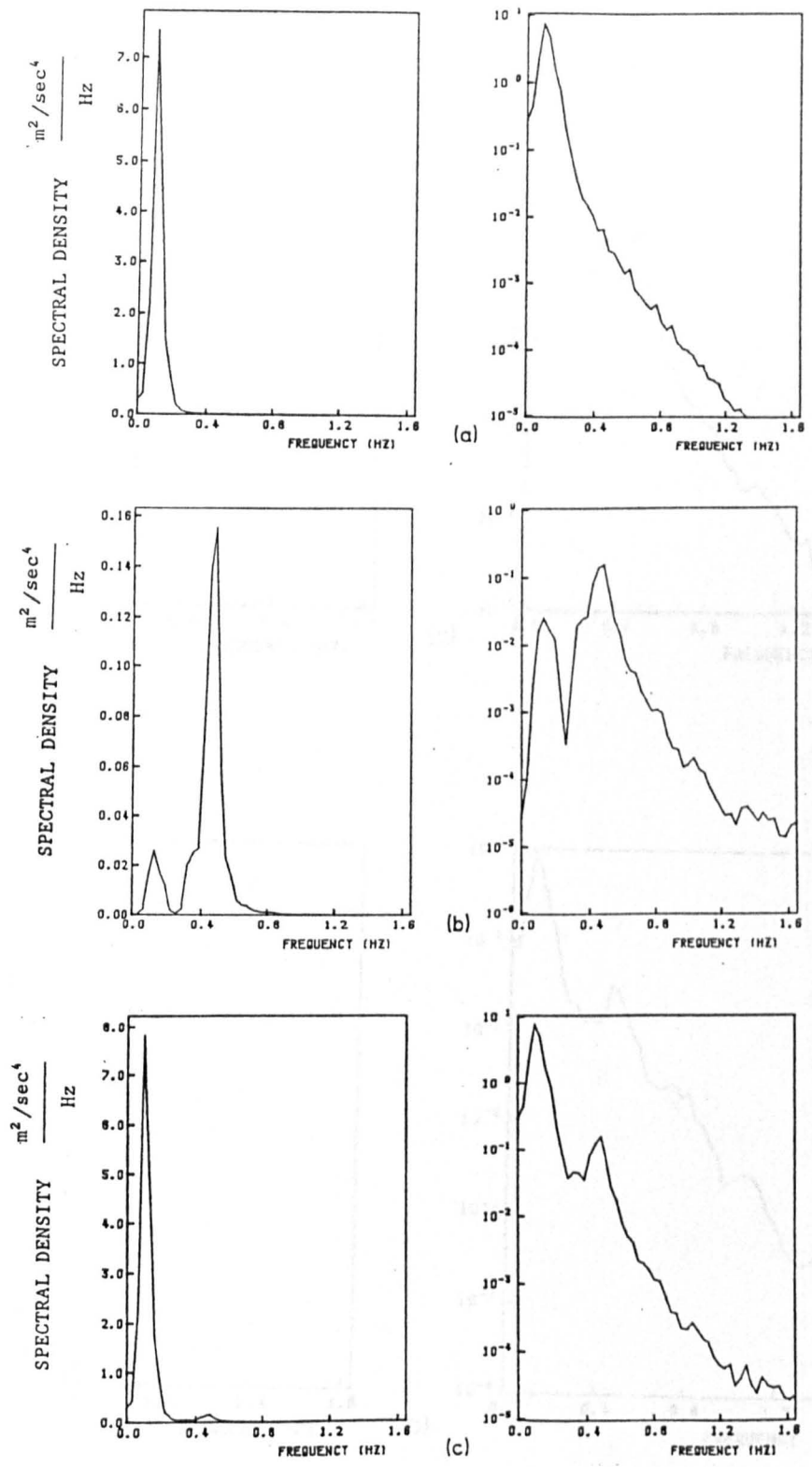

FIGURE 9.34. FREQUENCY SPECTRA OF a) IN-LINE WATER PARTICLE VELOCITY b) CYLINDER VELOCITY AND c) RELATIVE VELOCITY AT LEVEL 3 FOR RUN 13

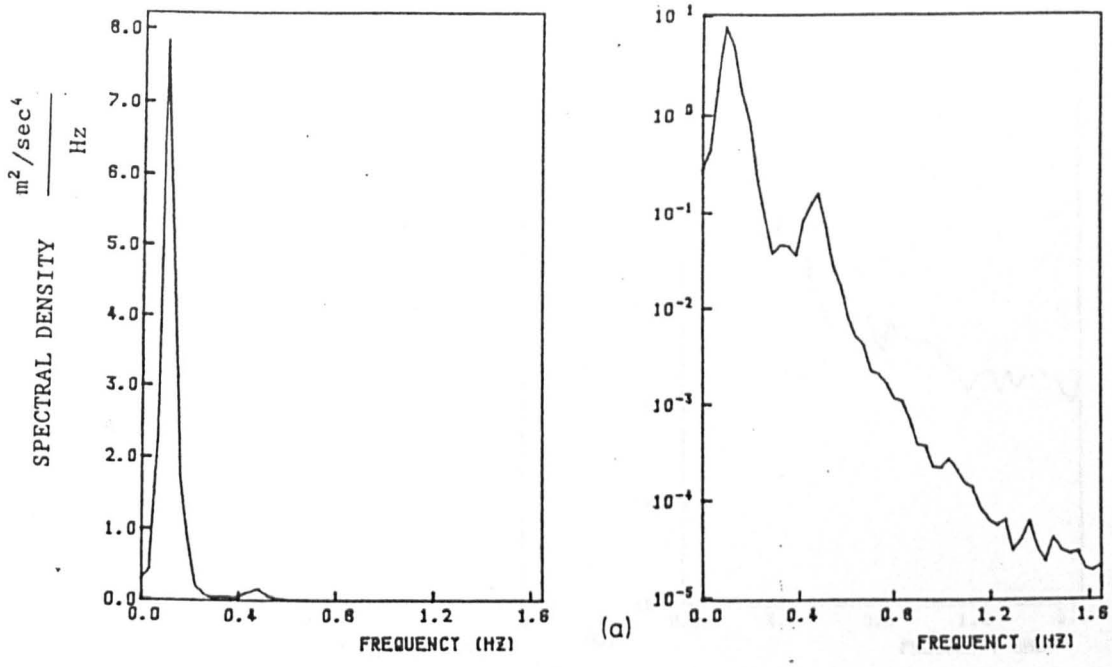

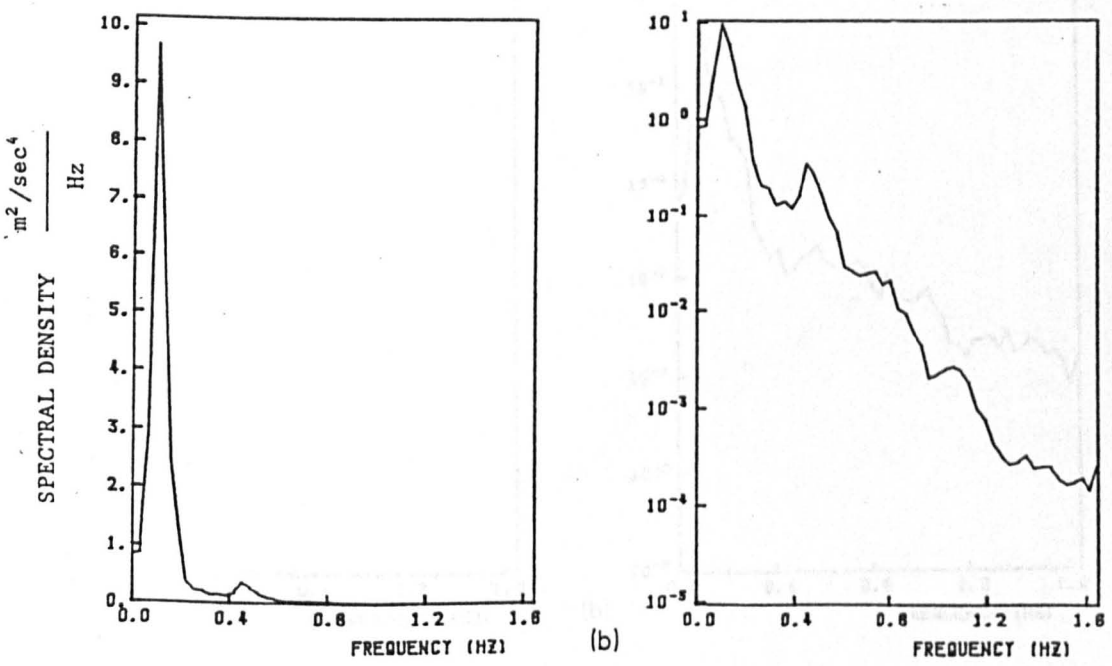

FIGURE 9.35. A COMPARISON OF THE FREQUENCY SPECTRA OF a)IN-LINE RELATIVE VELOCITY b) RELATIVE VELOCITY*|RELATIVE VELOCITY| AT LEVEL 3 FOR RUN 13

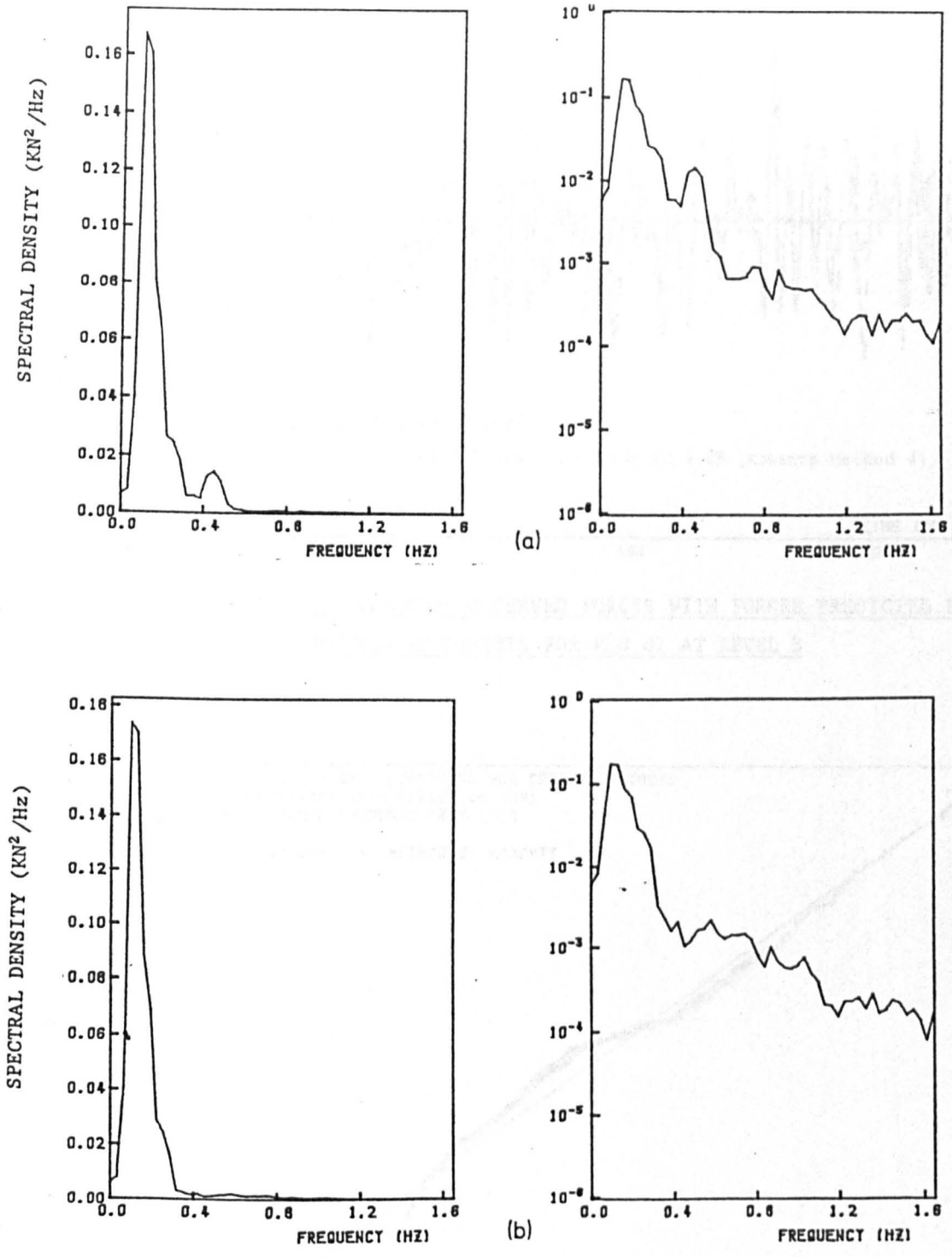

FIGURE 9.36. FREQUENCY SPECTRA OF IN-LINE HYDRODYNAMIC FORCE AND RELATIVE HYDRODYNAMIC FORCE AT LEVEL 3 FOR RUN 13

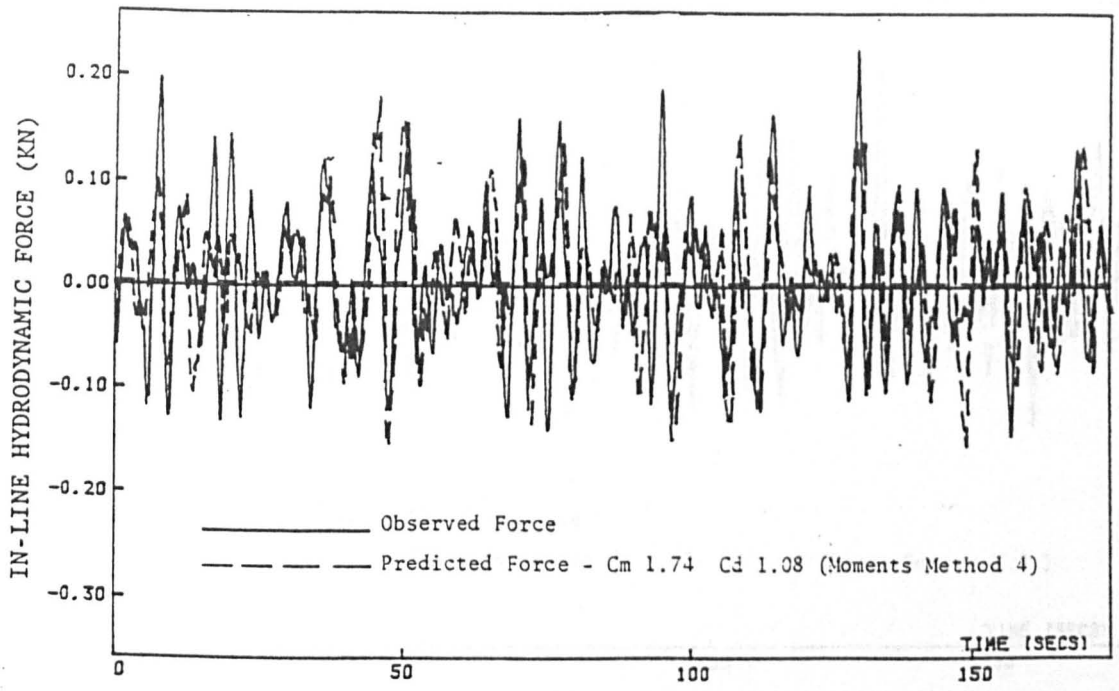

FIGURE 9.37. COMPARISON OF OBSERVED FORCES WITH FORCES PREDICTED FROM METHOD OF MOMENTS FOR RUN 01 AT LEVEL 3

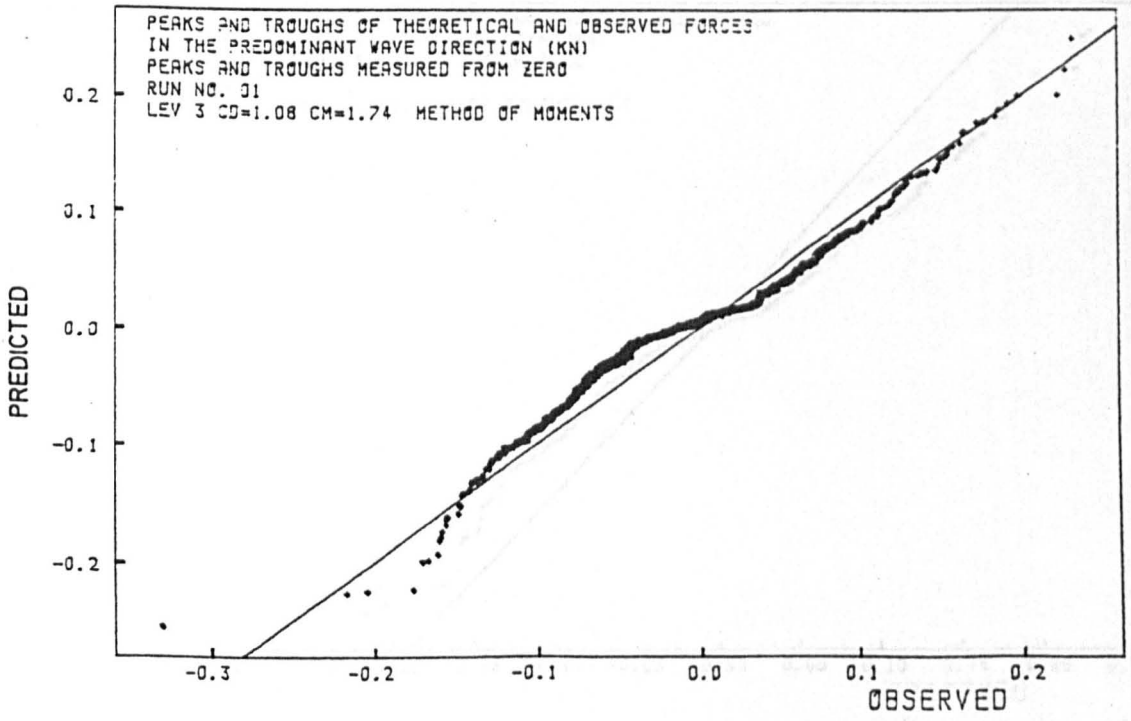

FIGURE 9.38. COMPARISON OF OBSERVED PEAK FORCES WITH PEAK FORCES PREDICTED FROM METHOD OF MOMENTS FOR RUN 01

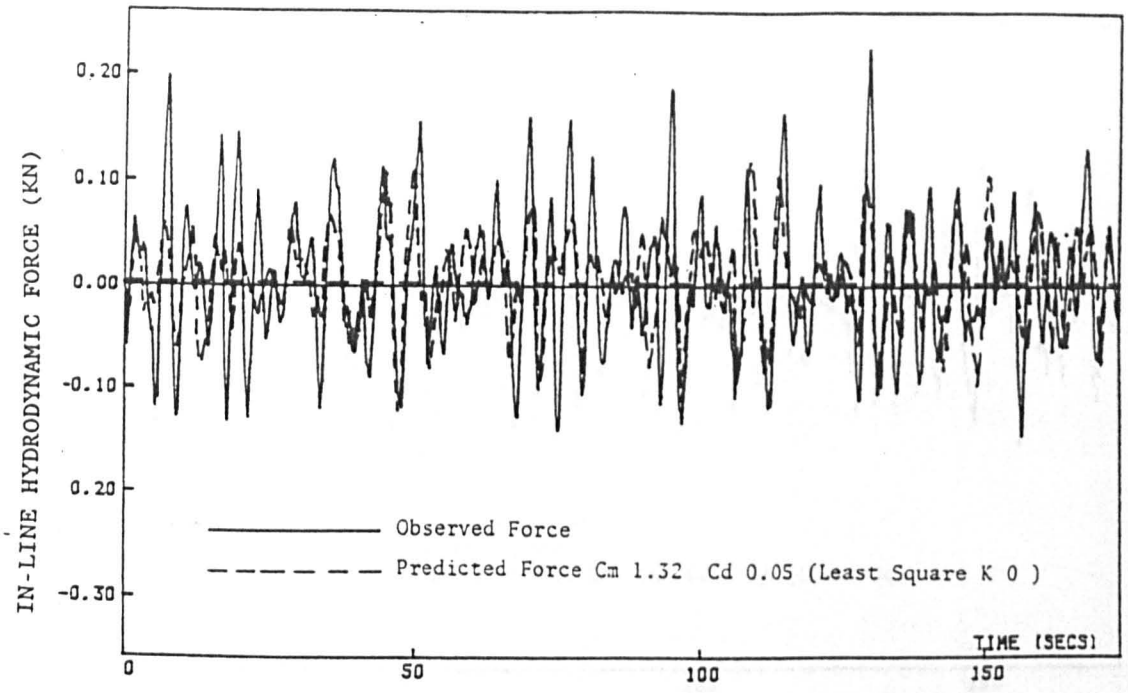

FIGURE 9.39. COMPARISON OF OBSERVED FORCES WITH FORCES PREDICTED FROM LEAST SQUARE ERROR METHOD (K=0) FOR RUN 01 AT LEVEL 3

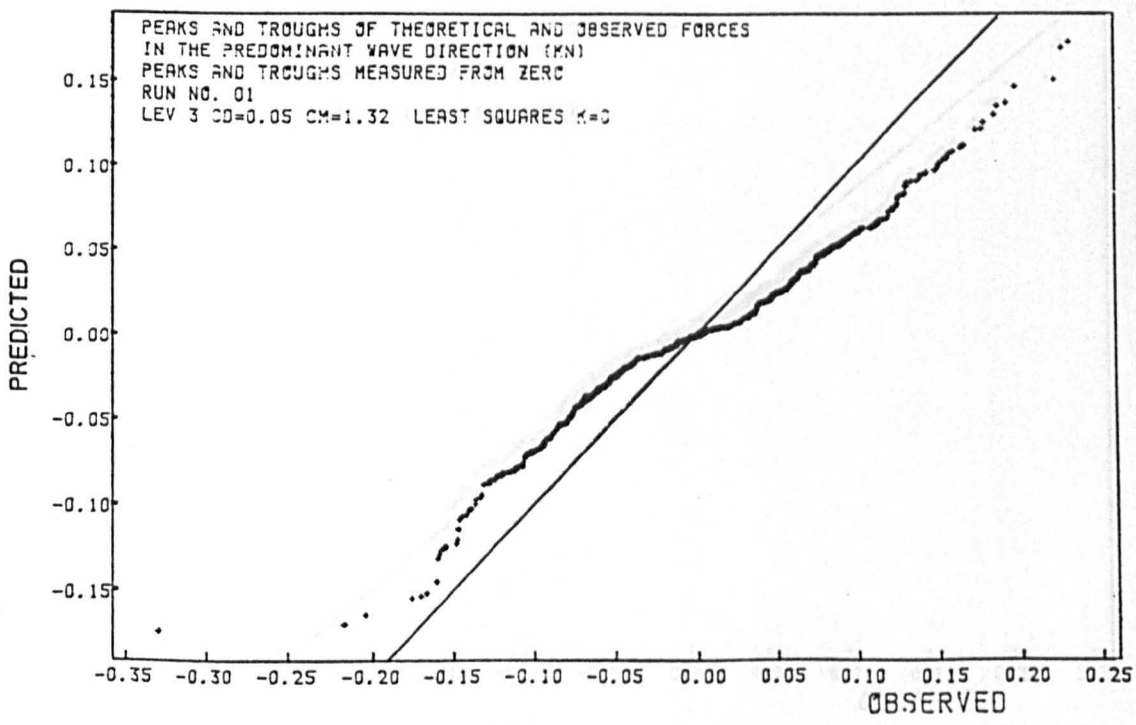

FIGURE 9.40. COMPARISON OF OBSERVED PEAK FORCES WITH PEAK FORCES PREDICTED FROM LEAST SQUARE ERROR METHOD (K=0) FOR RUN 01

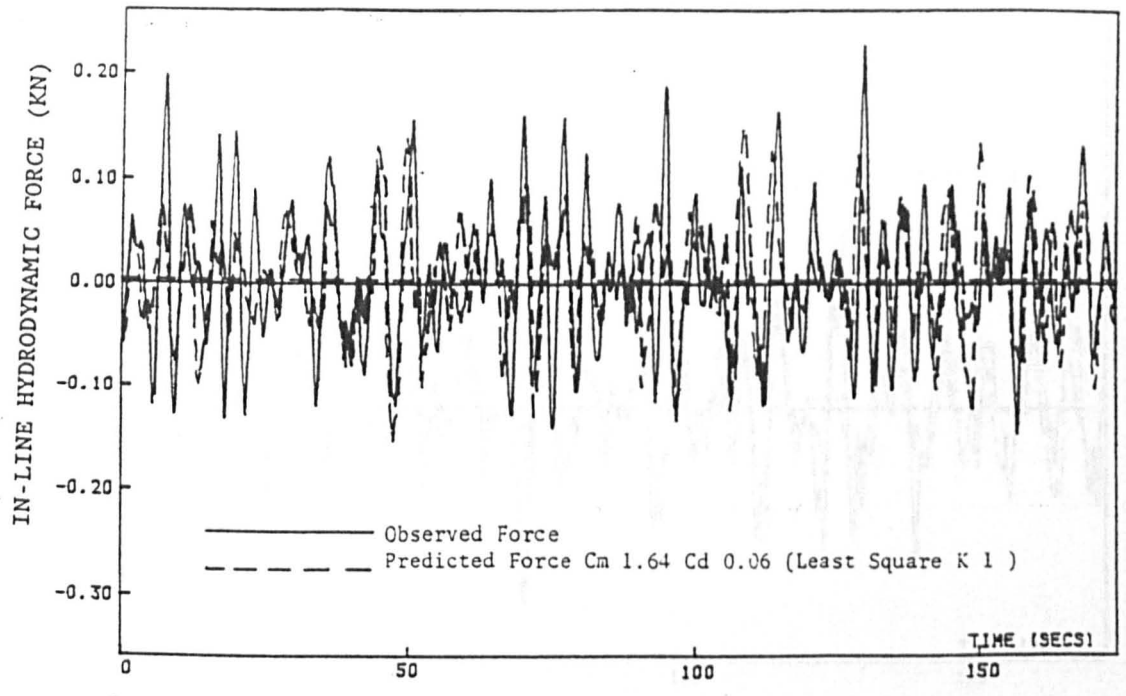

FIGURE 9.41. COMPARISON OF OBSERVED FORCES WITH FORCES PREDICTED FROM LEAST SQUARE ERROR METHOD (K=1) FOR RUN 01 AT LEVEL 3

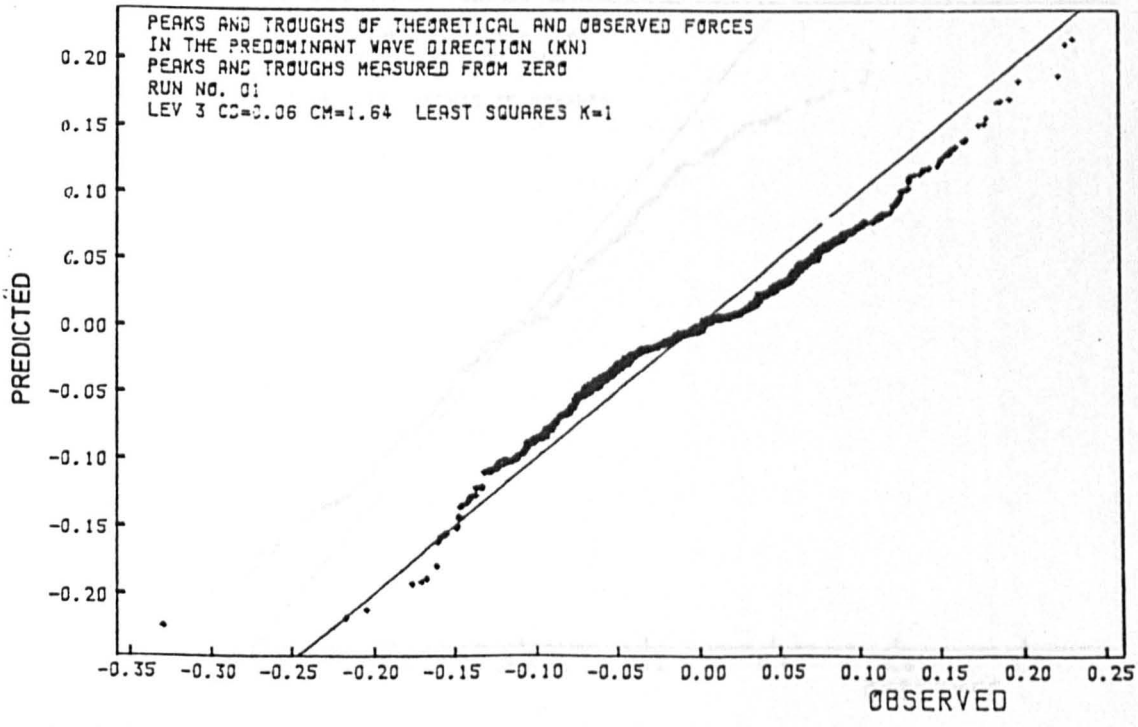

FIGURE 9.42. COMPARISON OF OBSERVED PEAK FORCES WITH PEAK FORCES PREDICTED FROM LEAST SQUARE ERROR METHOD (K=1) FOR RUN 01

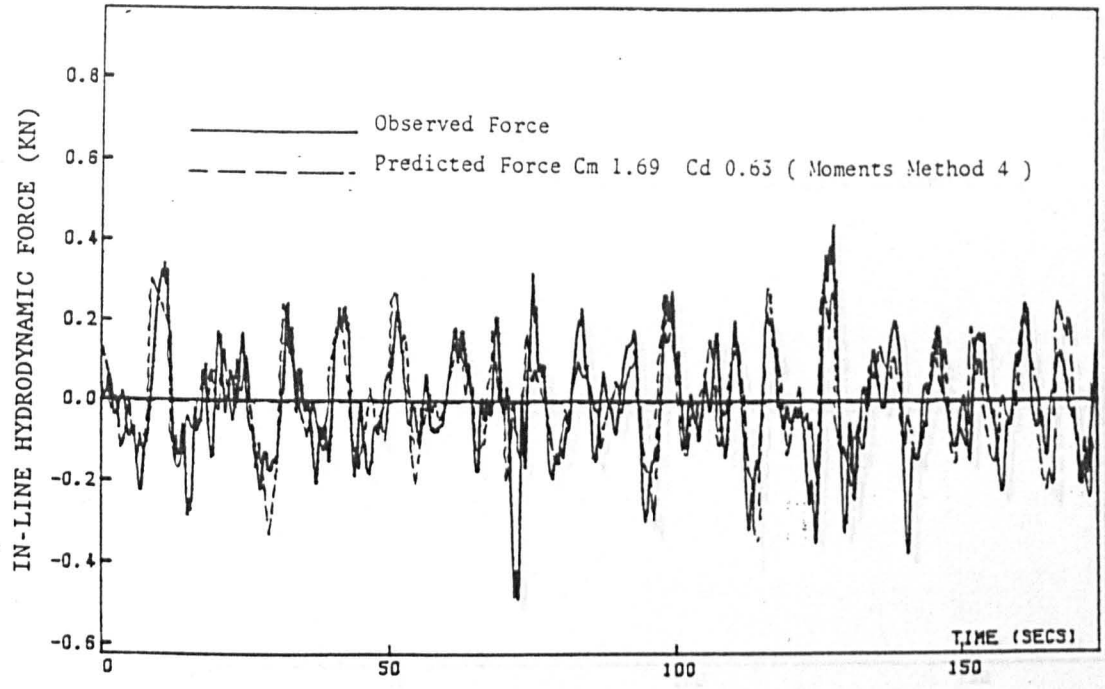

FIGURE 9.43. COMPARISON OF OBSERVED FORCES WITH FORCES PREDICTED FROM METHOD OF MOMENTS FOR RUN 13 AT LEVEL 3

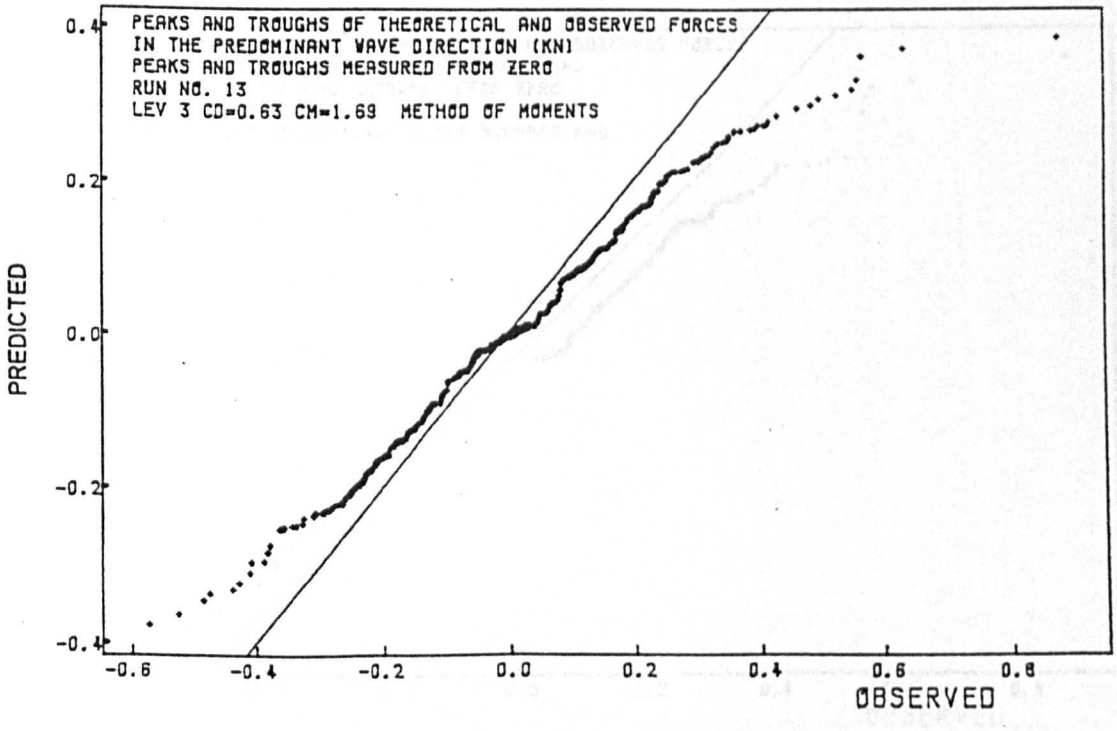

FIGURE 9.44. COMPARISON OF OBSERVED PEAK FORCES WITH PEAK FORCES PREDICTED FROM METHOD OF MOMENTS FOR RUN 13

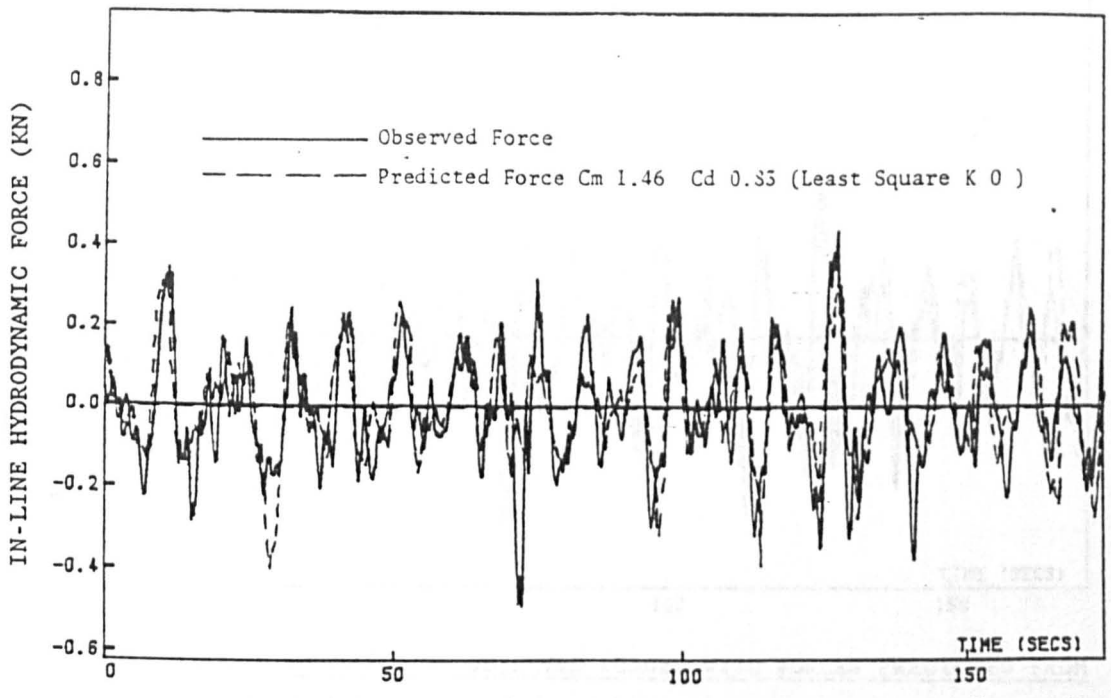

FIGURE 9.45. COMPARISON OF OBSERVED FORCES WITH FORCES PREDICTED FROM LEAST SQUARE ERROR METHOD (K=0) FOR RUN 13 AT LEVEL 3

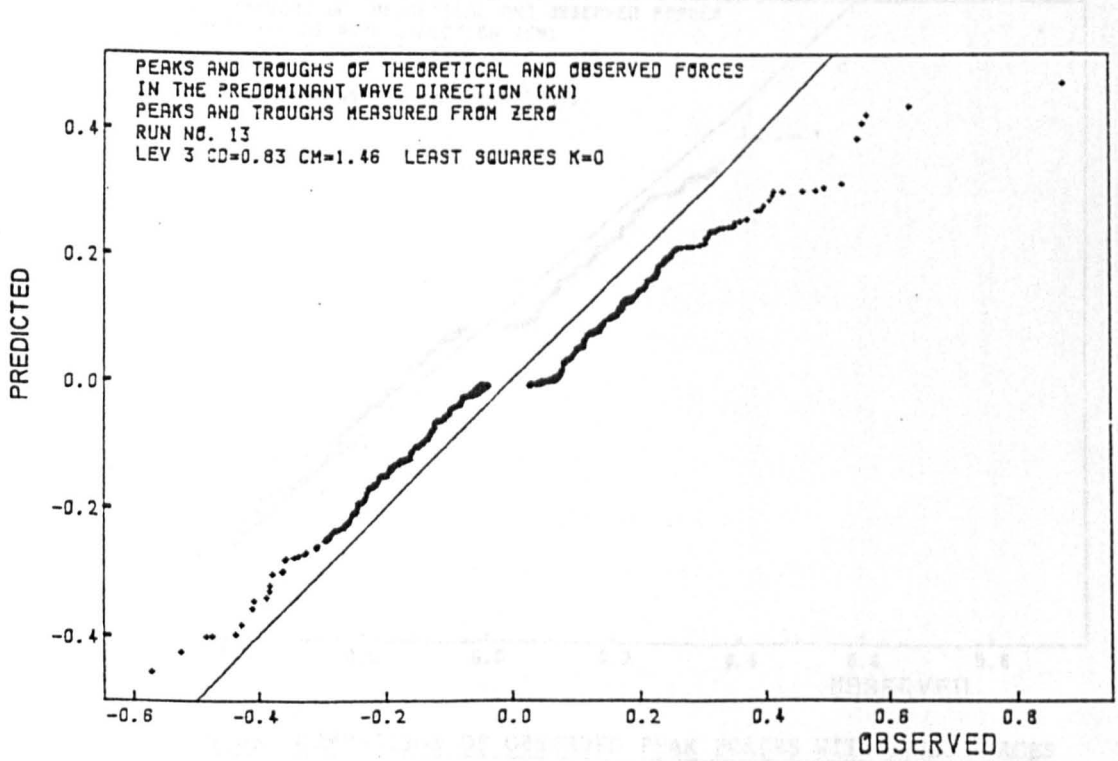

FIGURE 9.46. COMPARISON OF OBSERVED PEAK FORCES WITH PEAK FORCES PREDICTED FROM LEAST SQUARE ERROR METHOD (K=0) FOR RUN 13

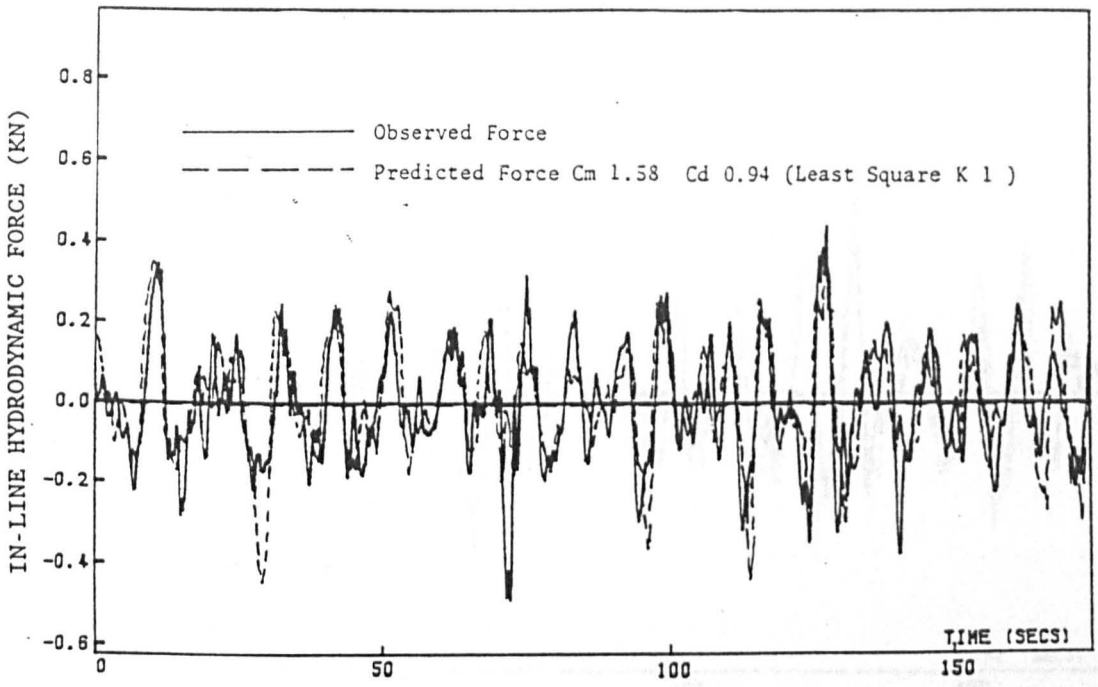

FIGURE 9.47. COMPARISON OF OBSERVED FORCES WITH FORCES PREDICTED FROM LEAST SQUARE ERROR METHOD (K=1) FOR RUN 13 AT LEVEL 3

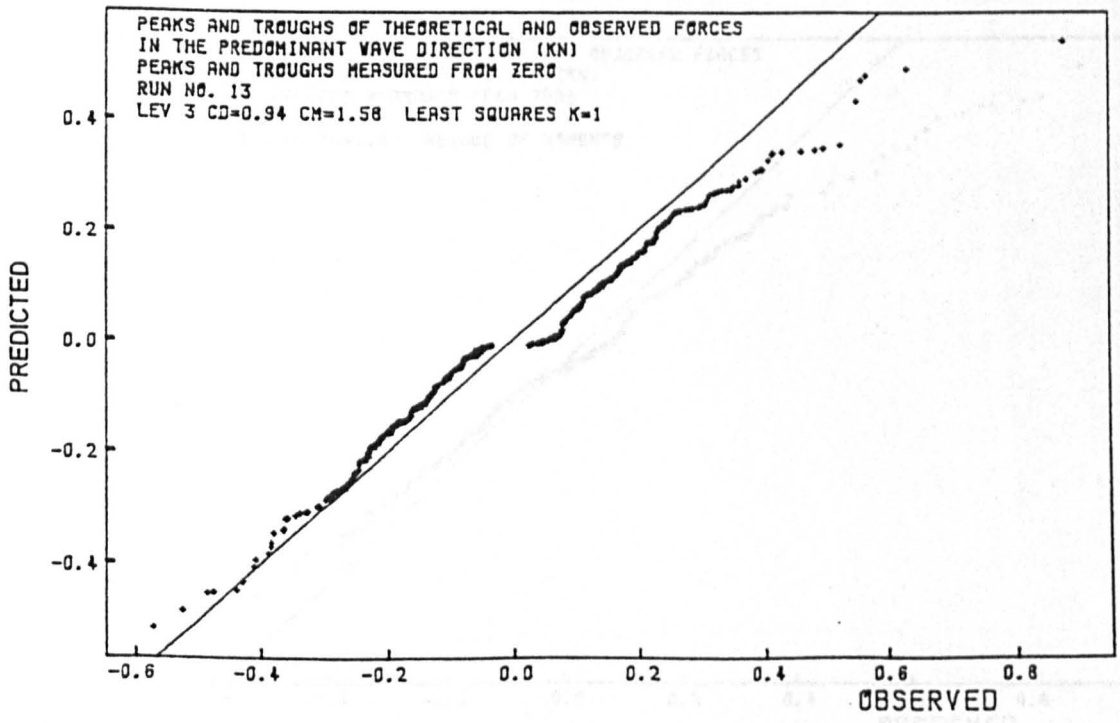

FIGURE 9.48. COMPARISON OF OBSERVED PEAK FORCES WITH PEAK FORCES PREDICTED FROM LEAST SQUARE ERROR METHOD (K=1) FOR RUN 13

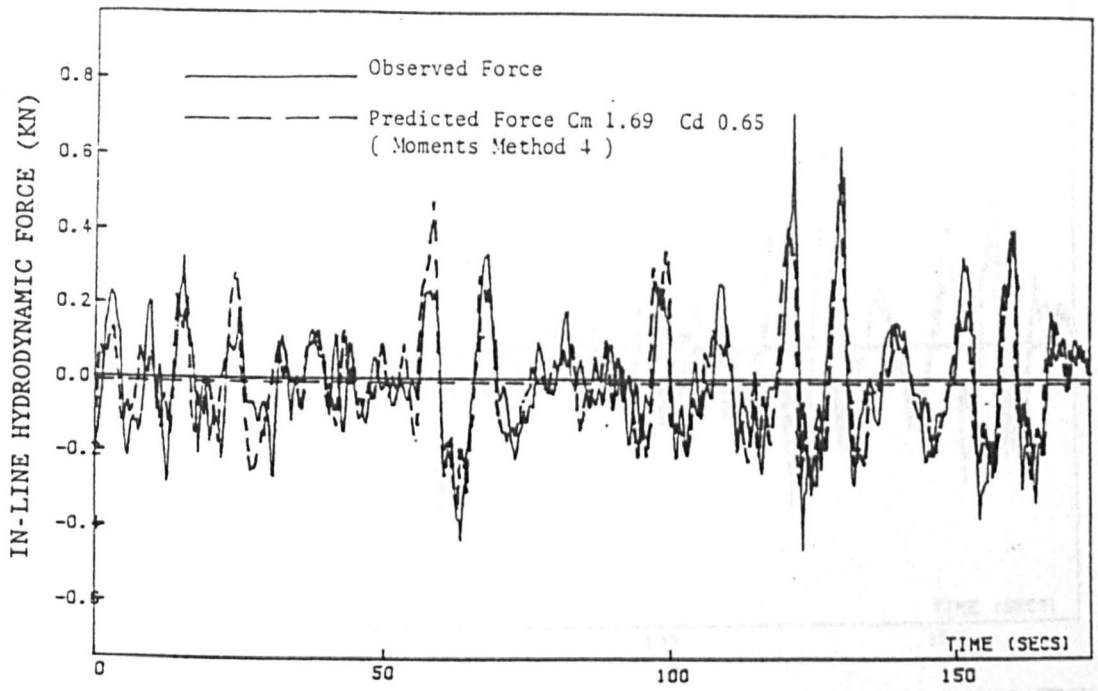

FIGURE 9.49. COMPARISON OF OBSERVED FORCES WITH FORCES PREDICTED FROM METHOD OF MOMENTS FOR RUN 15 AT LEVEL 3

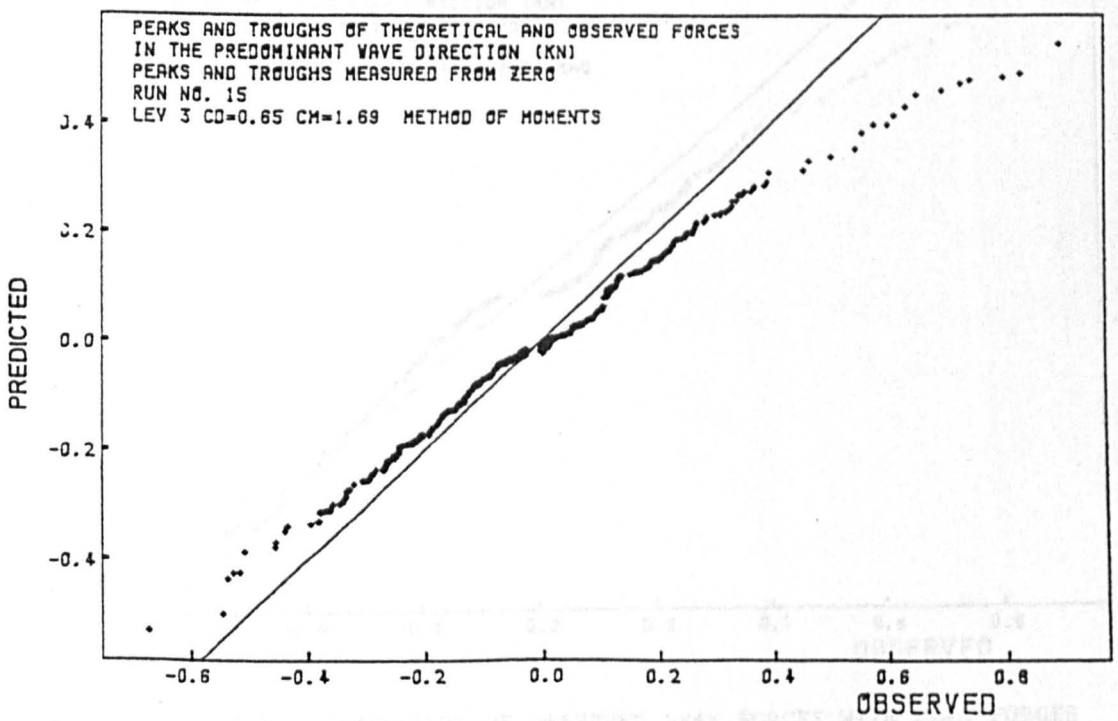

FIGURE 9.50. COMPARISON OF OBSERVED PEAK FORCES WITH PEAK FORCES PREDICTED FROM METHOD OF MOMENTS FOR RUN 15

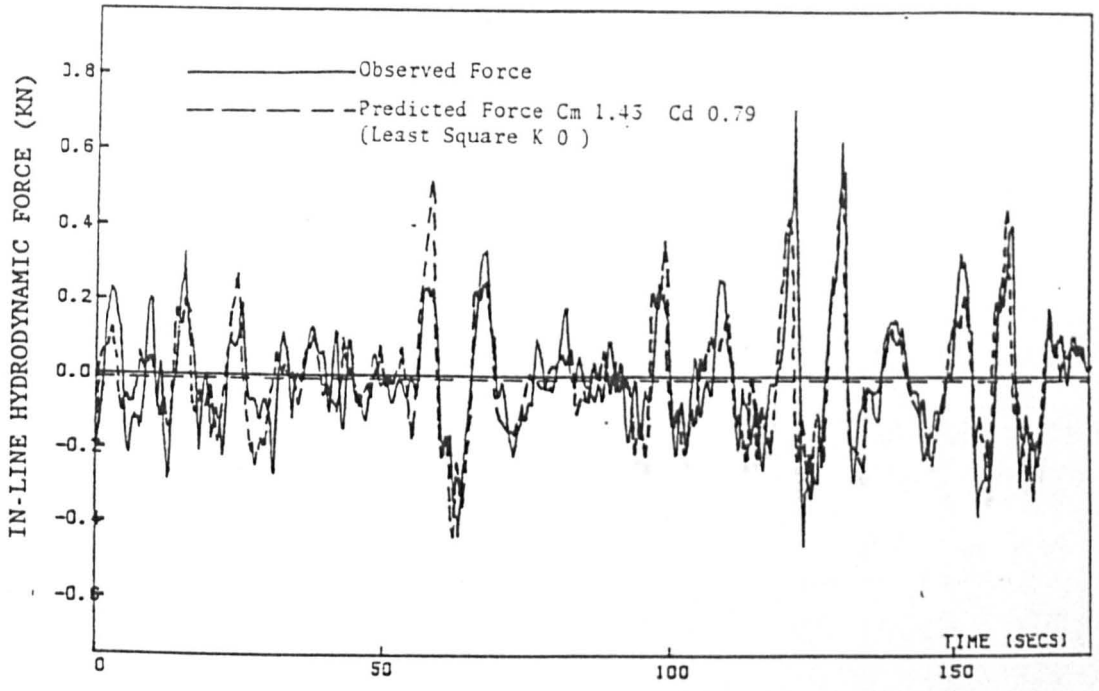

FIGURE 9.51. COMPARISON OF OBSERVED FORCES WITH FORCES PREDICTED FROM LEAST SQUARE ERROR METHOD (K=0) FOR RUN 15 AT LEVEL 3

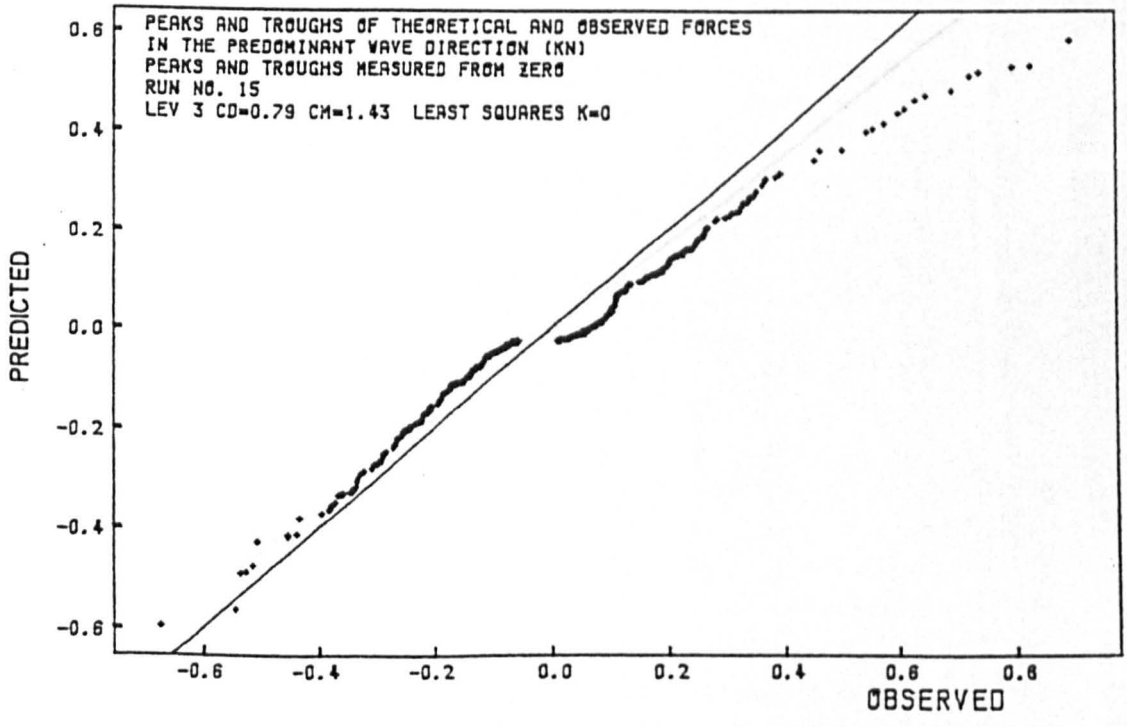

FIGURE 9.52. COMPARISON OF OBSERVED PEAK FORCES WITH PEAK FORCES PREDICTED FROM LEAST SQUARE ERROR METHOD (K=0) FOR RUN 15

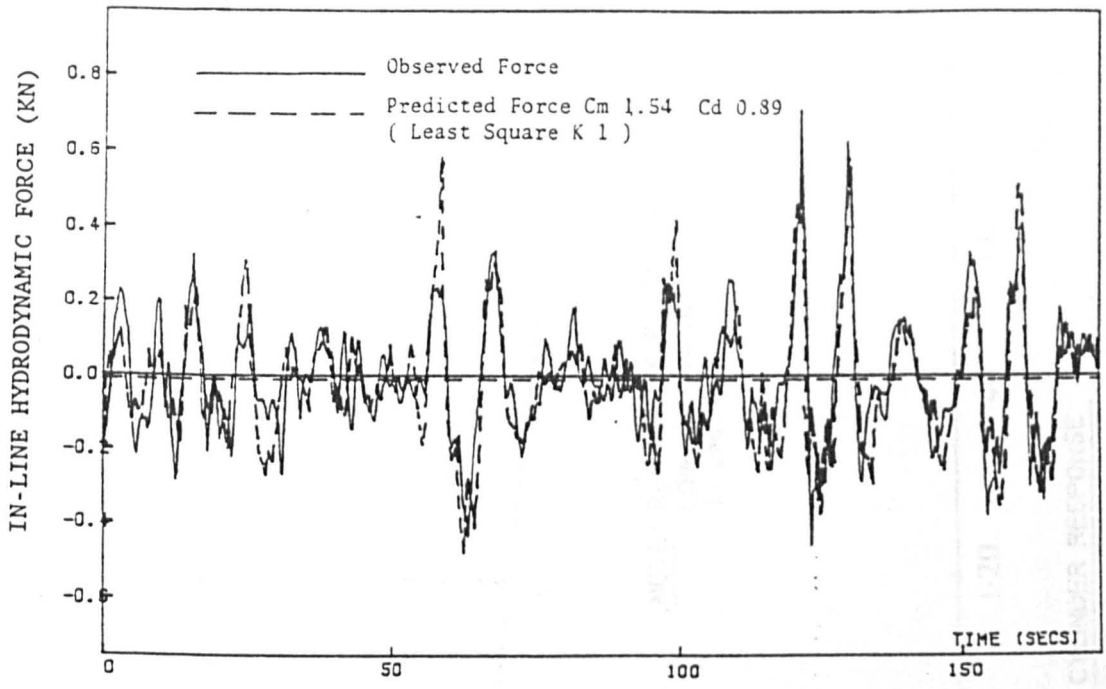

FIGURE 9.53. COMPARISON OF OBSERVED FORCES WITH FORCES PREDICTED FROM LEAST SQUARE ERROR METHOD (K=1) FOR RUN 15 AT LEVEL 3

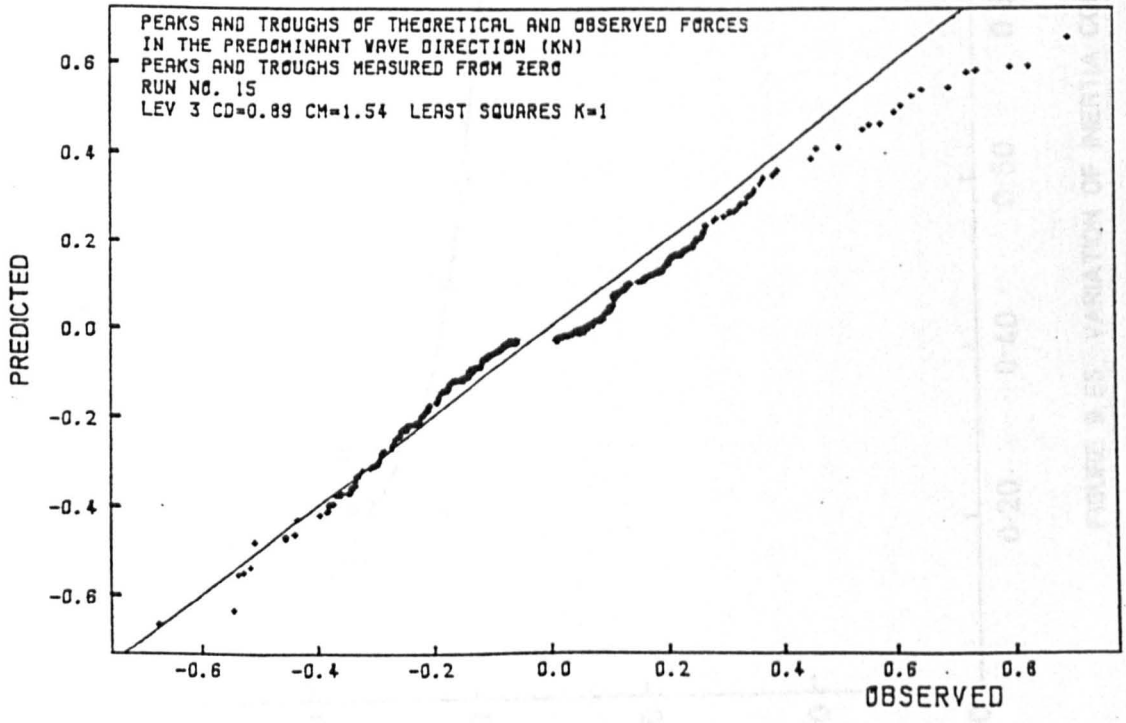

FIGURE 9.54. COMPARISON OF OBSERVED PEAK FORCES WITH PEAK FORCES PREDICTED FROM LEAST SQUARE ERROR METHOD (K=1) FOR RUN 15

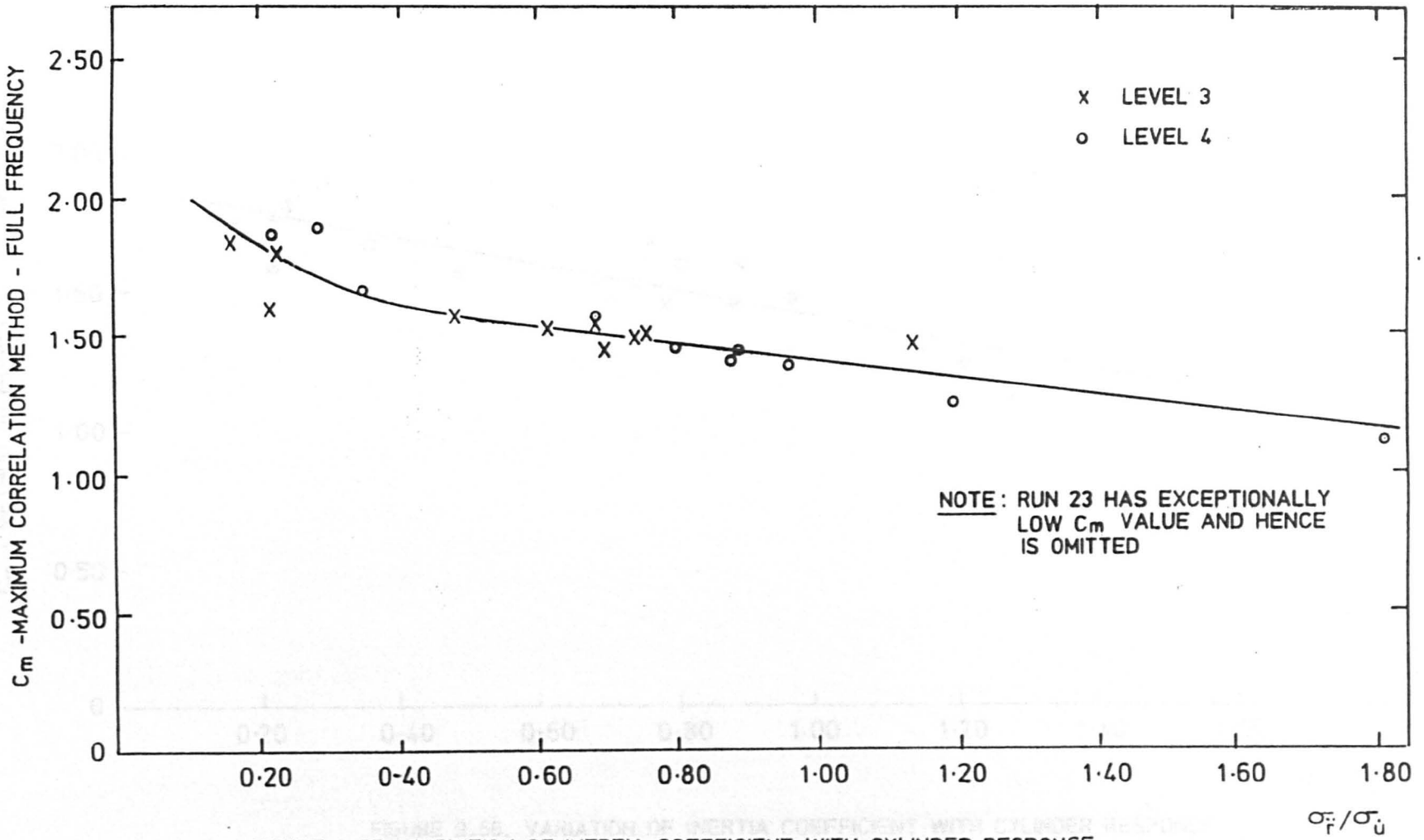

FIGURE 9.55. VARIATION OF INERTIA COEFFICIENT WITH CYLINDER RESPONSE

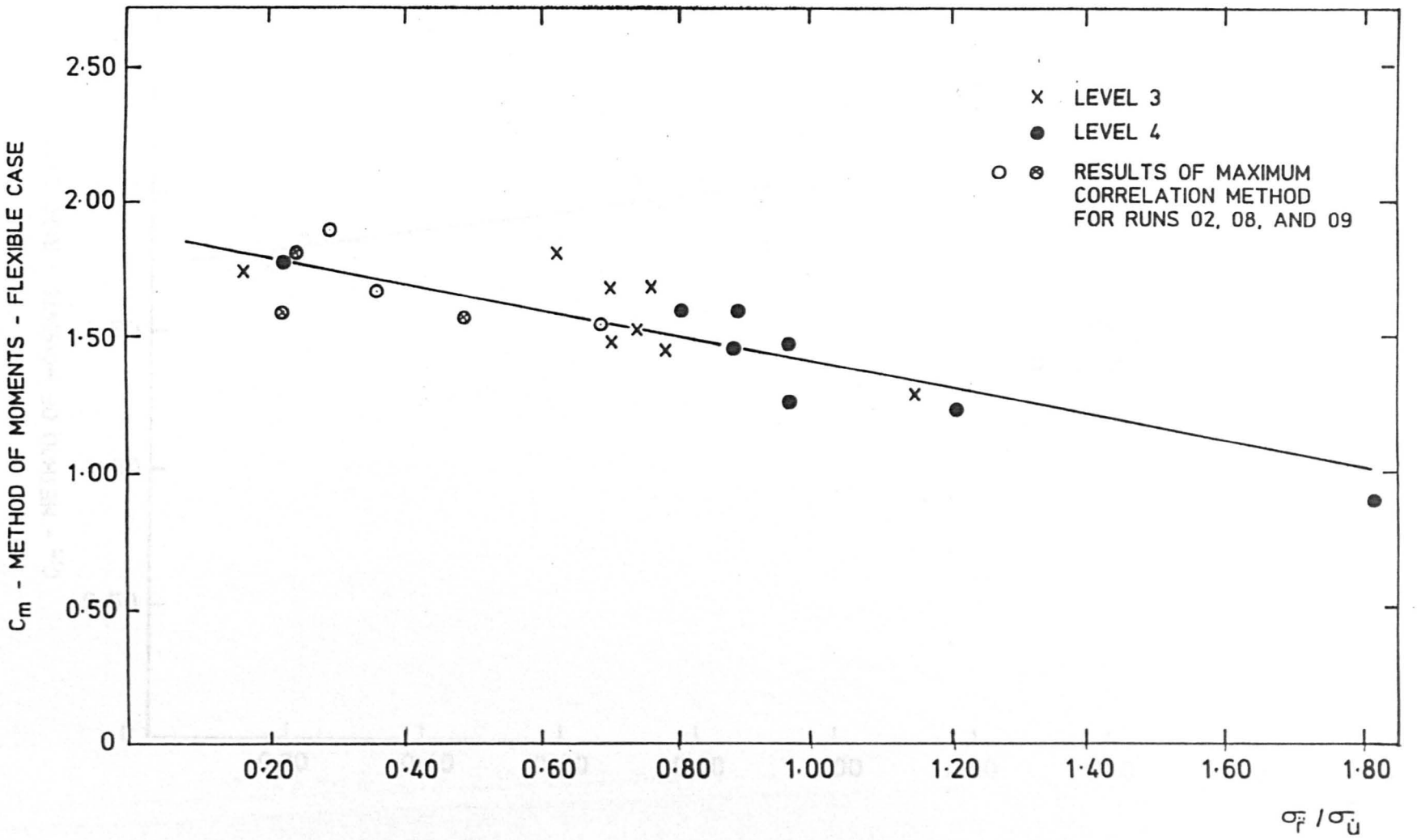

FIGURE 9.56. VARIATION OF INERTIA COEFFICIENT WITH CYLINDER RESPONSE

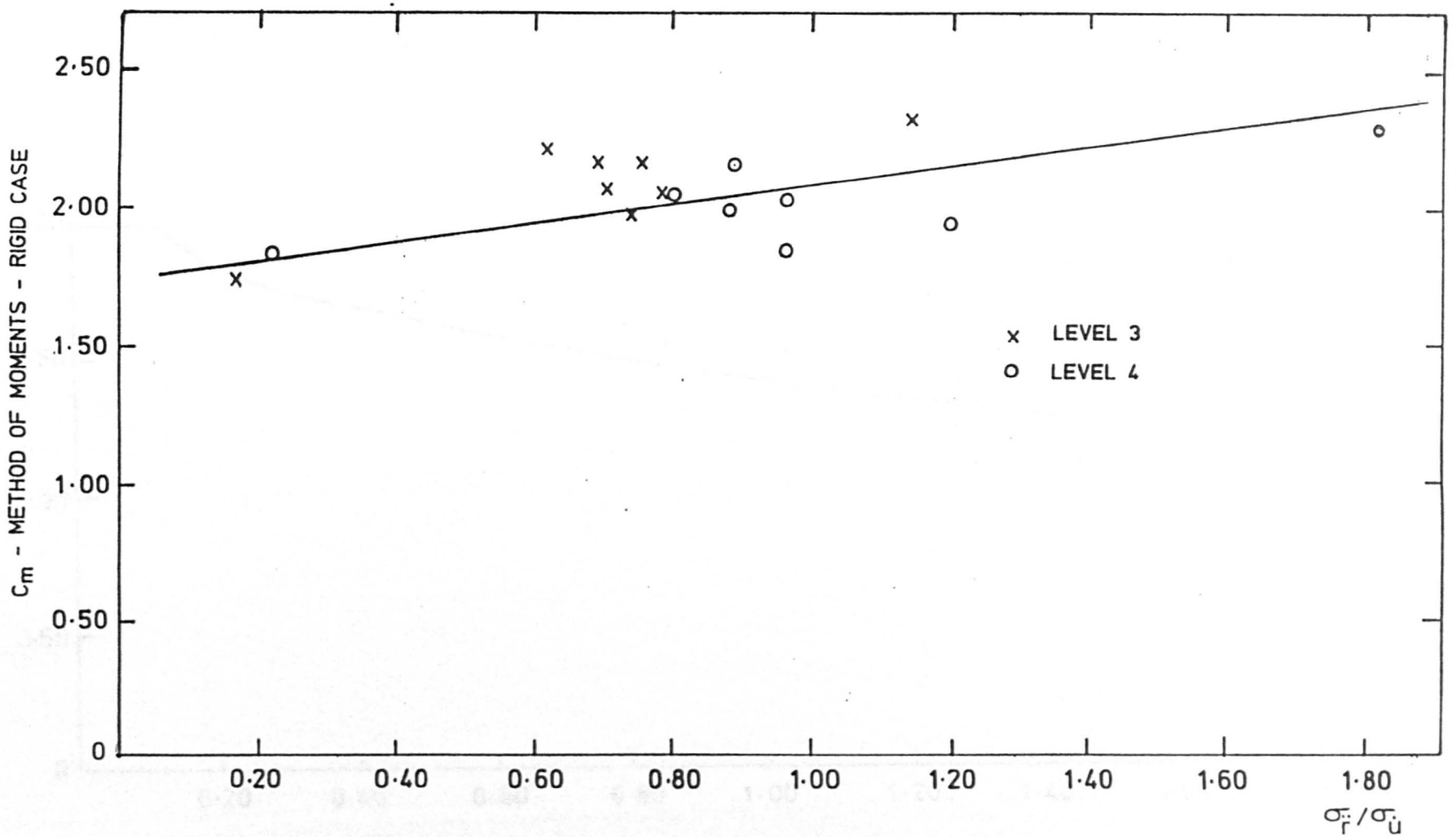

FIGURE 9.57. VARIATION OF INERTIA COEFFICIENT WITH CYLINDER RESPONSE

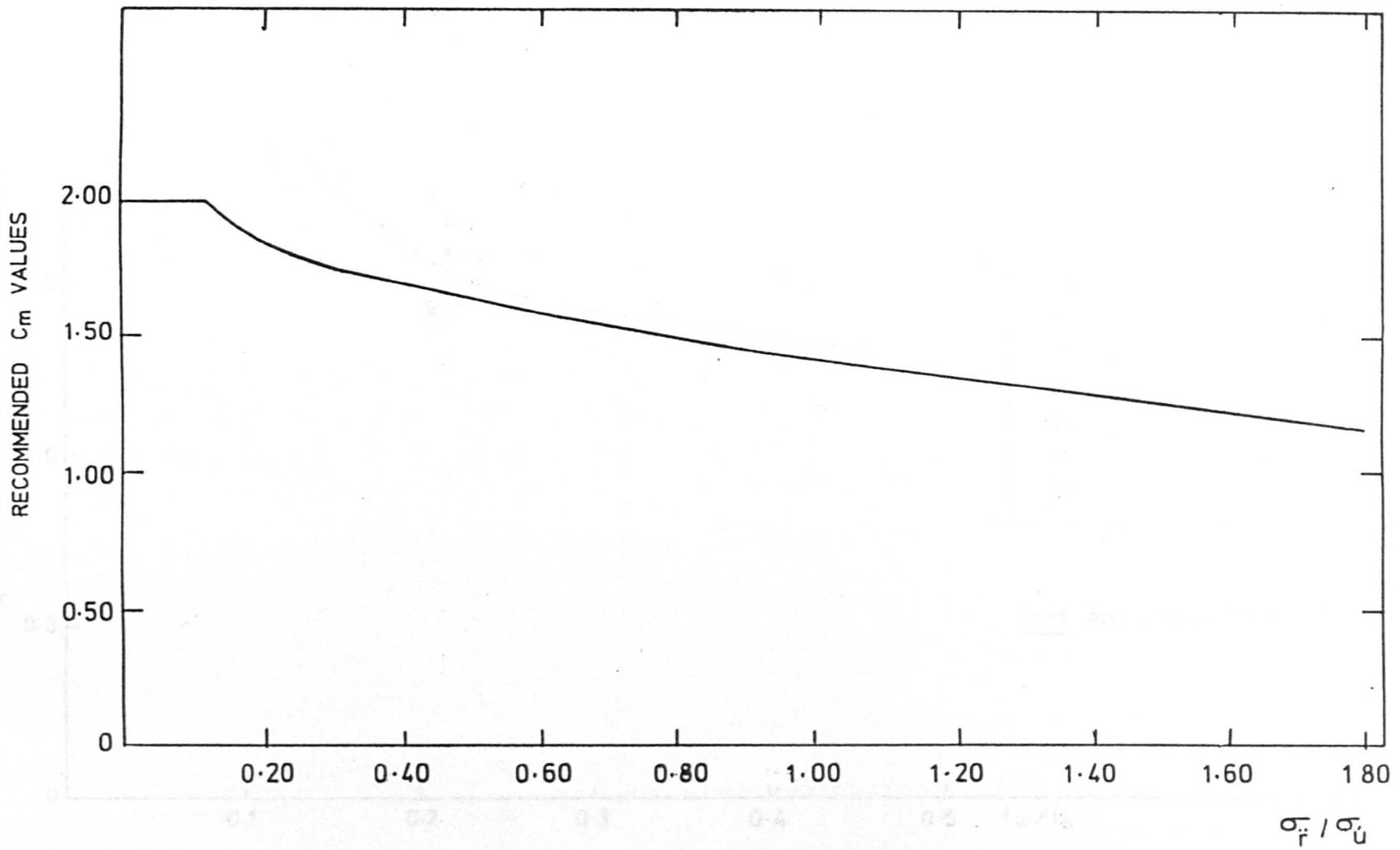

FIGURE 9.58. RECOMMENDED C_m VALUES AS A FUNCTION OF σ_r/σ_u

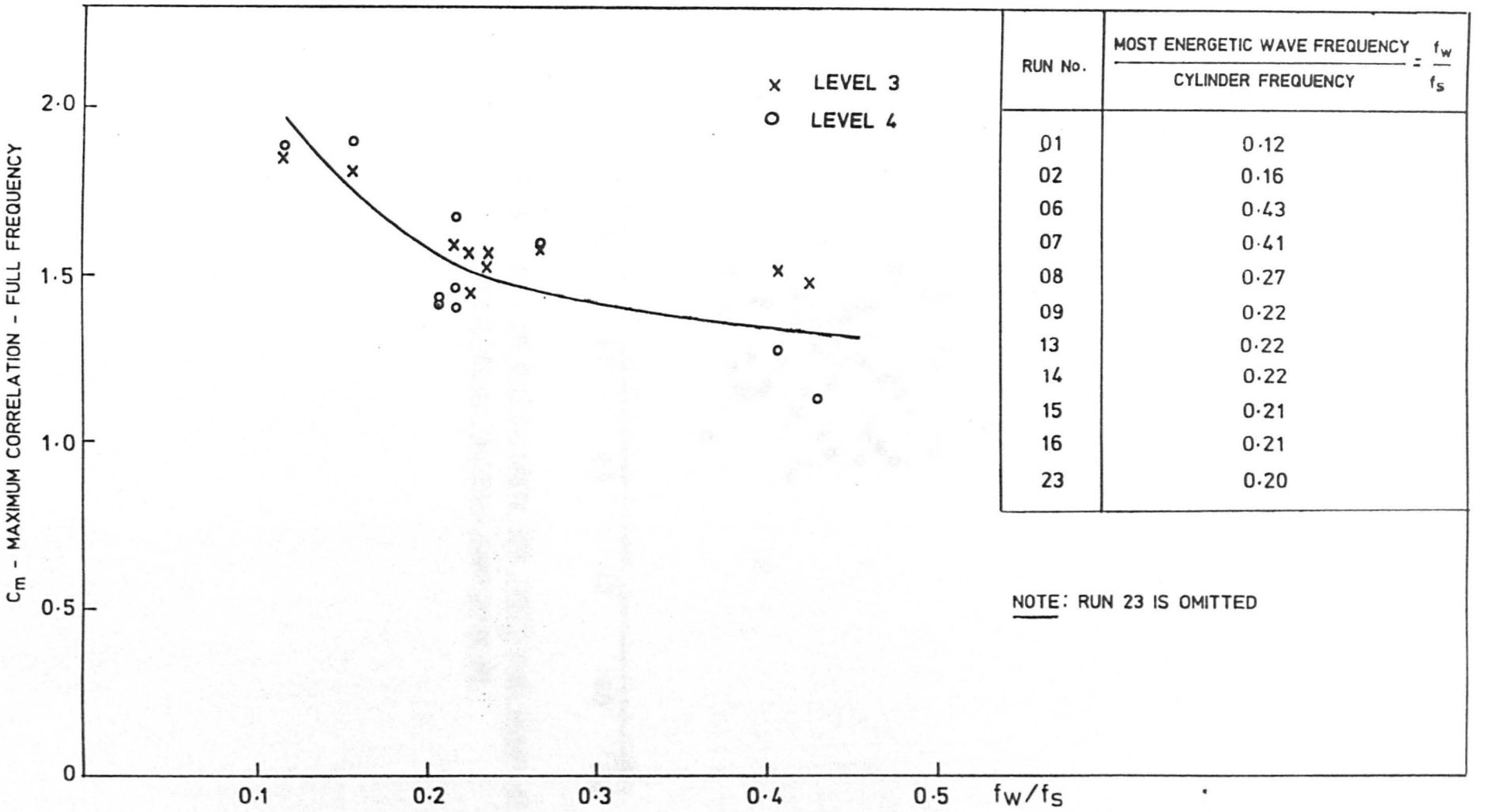

RUN No.	MOST ENERGETIC WAVE FREQUENCY / CYLINDER FREQUENCY = f_W/f_S
01	0·12
02	0·16
06	0·43
07	0·41
08	0·27
09	0·22
13	0·22
14	0·22
15	0·21
16	0·21
23	0·20

NOTE: RUN 23 IS OMITTED

FIGURE 9.59. VARIATION OF INERTIA COEFFICIENT WITH MOST ENERGETIC WAVE FREQUENCY / CYLINDER NATURAL FREQUENCY

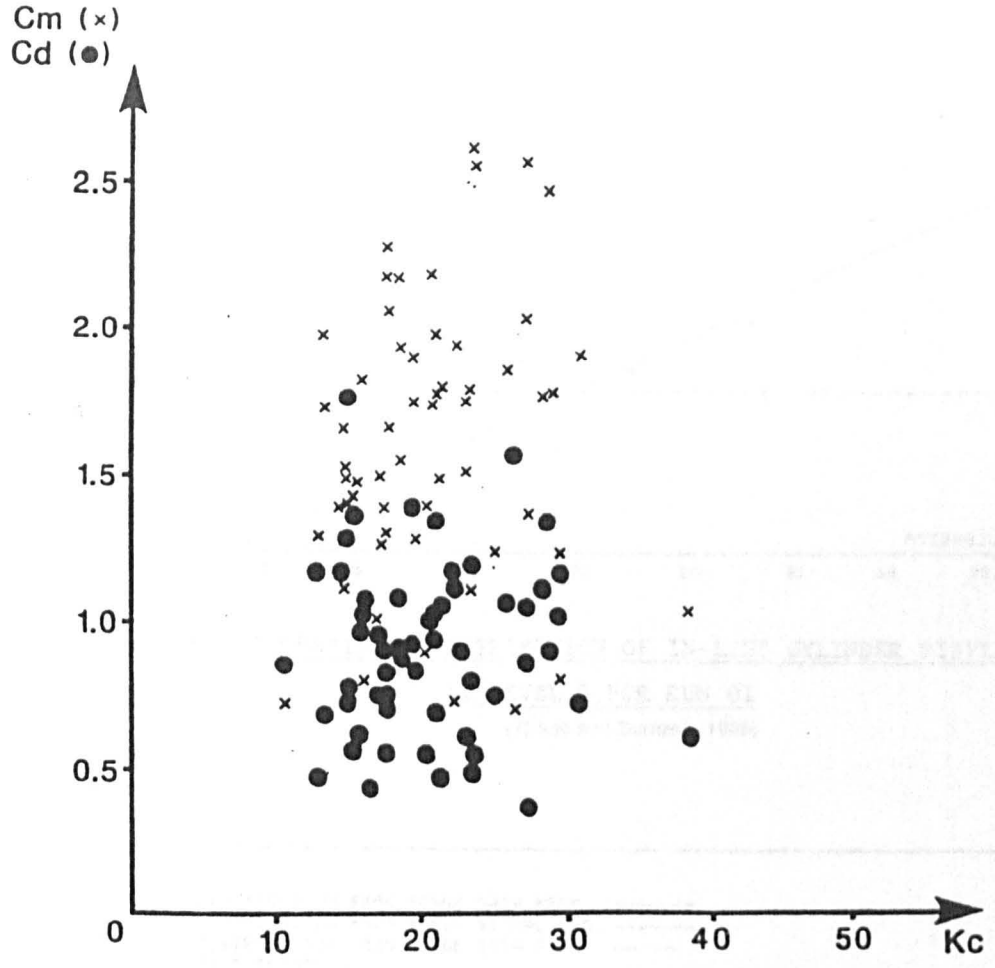

FIGURE 9.60. MORISON COEFFICIENTS FOR INDIVIDUAL WAVES AS A FUNCTION OF KEULEGAN-CARPENTER NO.

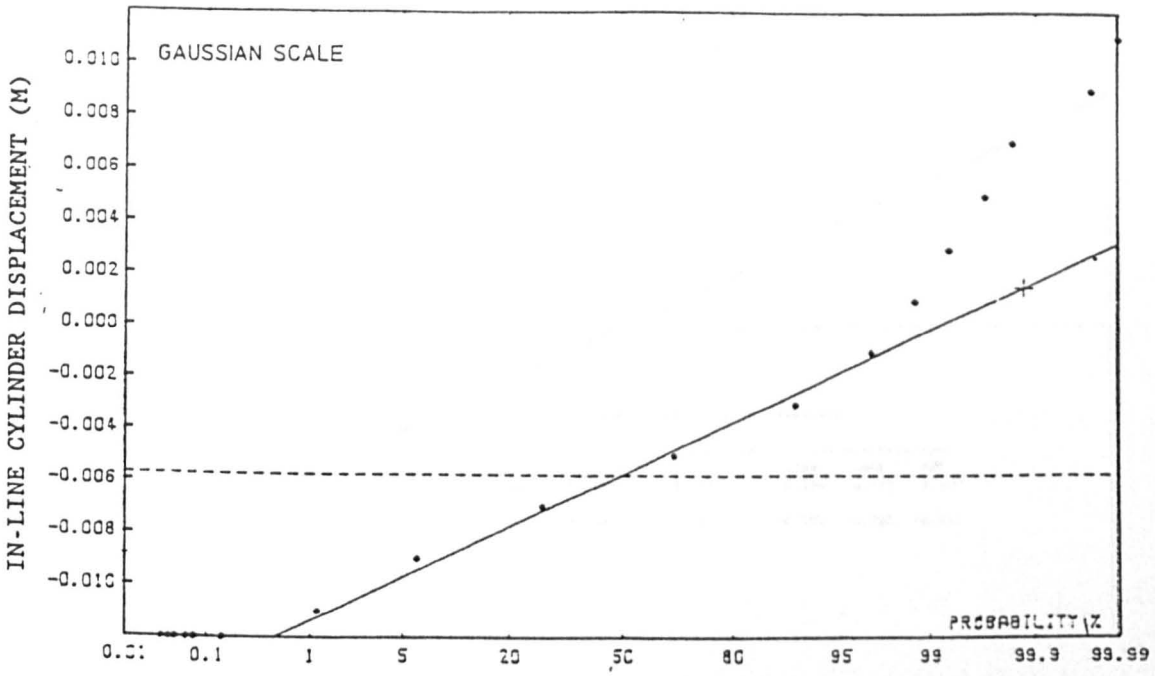

FIGURE 9.61. PROBABILITY DISTRIBUTION OF IN-LINE CYLINDER DISPLACEMENT AT LEVEL 3 FOR RUN 01

(Tickell and Burrows, 1989)

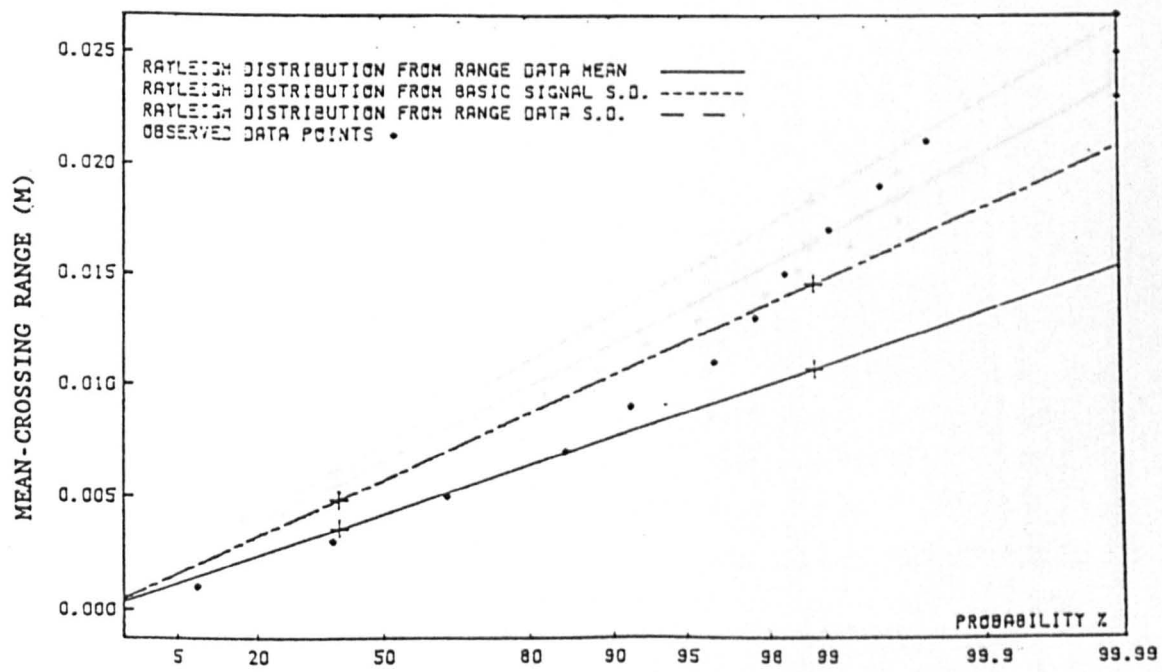

FIGURE 9.62. PROBABILITY DISTRIBUTION OF MEAN-CROSSING RANGES OF IN-LINE CYLINDER DISPLACEMENT AT LEVEL 3 FOR RUN 01

(Tickell and Burrows, 1989)

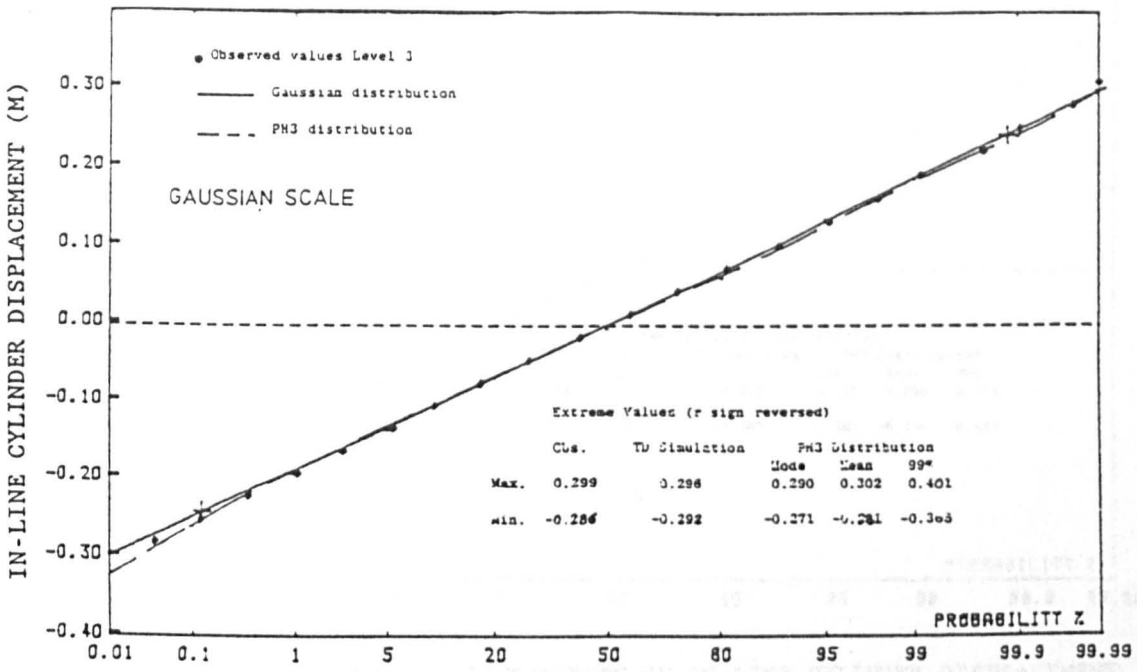

FIGURE 9.63. PROBABILITY DISTRIBUTION OF IN-LINE CYLINDER DISPLACEMENT AT LEVEL 3 FOR RUN 13

(Tickell and Burrows, 1989)

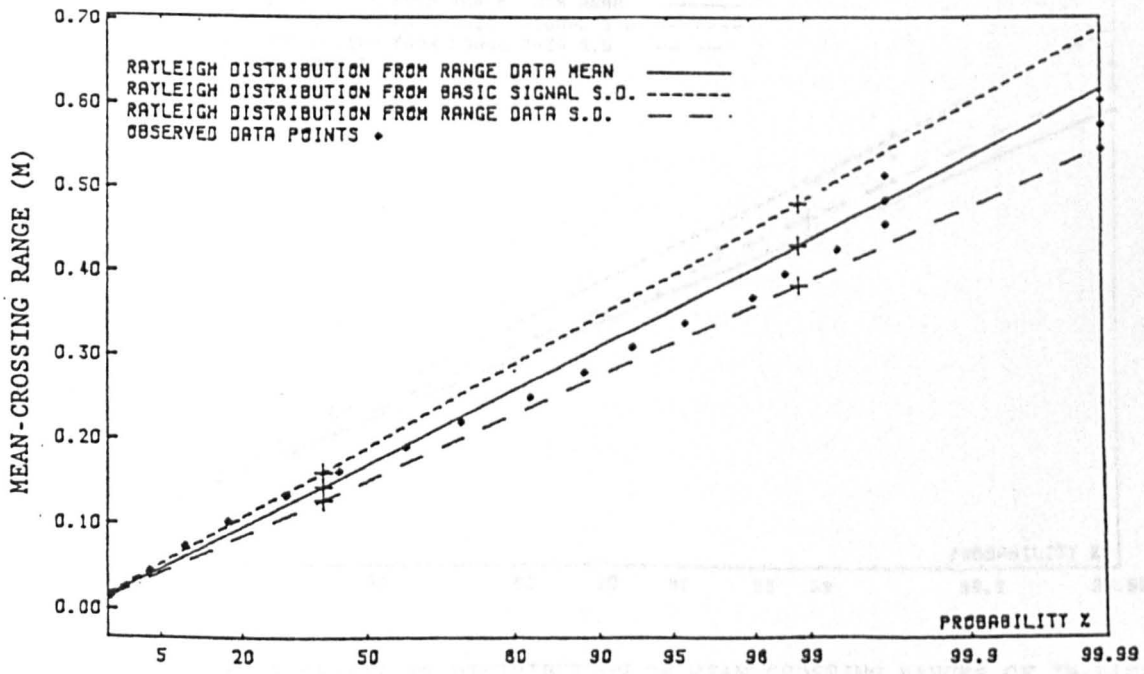

FIGURE 9.64. PROBABILITY DISTRIBUTION OF MEAN-CROSSING RANGES OF IN-LINE CYLINDER DISPLACEMENT AT LEVEL 3 FOR RUN 13

(Tickell and Burrows, 1989)

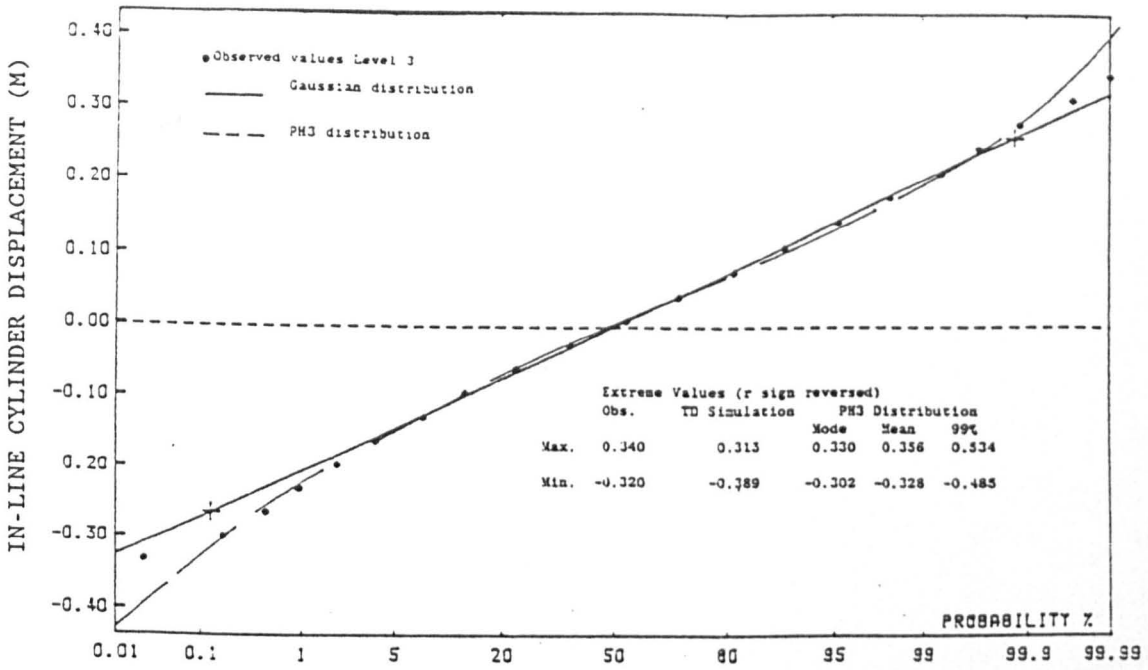

FIGURE 9.65. PROBABILITY DISTRIBUTION OF IN-LINE CYLINDER DISPLACEMENT AT LEVEL 3 FOR RUN 15

(Tickell and Burrows, 1989)

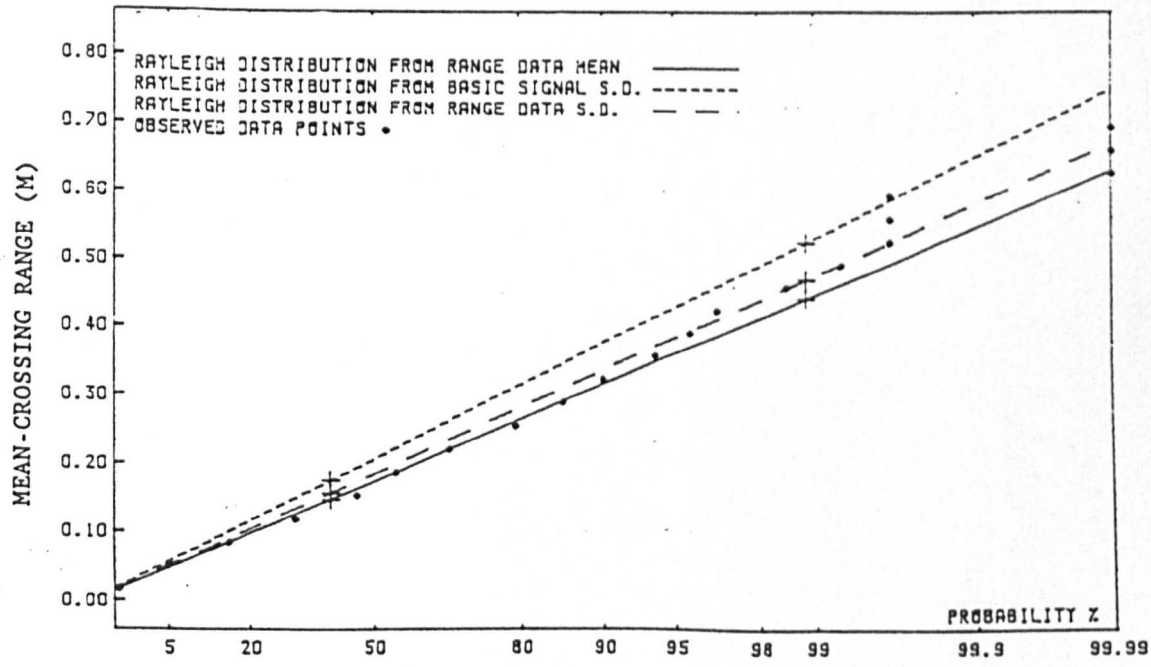

FIGURE 9.66. PROBABILITY DISTRIBUTION OF MEAN-CROSSING RANGES OF IN-LINE CYLINDER DISPLACEMENT AT LEVEL 3 FOR RUN 15

(Tickell and Burrows, 1989)

This page is left blank deliberately.

Chapter 10

Probabilistic Analysis of Fixed Jacket-Type Offshore Structures

10.1 INTRODUCTION

Deterministic and probabilistic methods were compared in Section 1.4. It was argued that in the deterministic method, the risks are associated with the environmental conditions. For example, the probability that the '50 year' design wave will be exceeded at least once during the service life of the structure can be calculated; however, this probability cannot be converted into the risk of failure for individual members. In fact, every member will have a different unknown probability of failure. In contrast, in probabilistic methods, the risks are associated with the responses themselves. For example, the probability that the '50 year' peak response will be exceeded at least once during the service life of the structure will be calculated. Therefore, members can be designed so that all responses will have equal risks of exceeding their design values during the service life of the structure. Alternatively, responses can be divided into two or three different groups with different acceptable risks of failure with regard to their importance in the overall safety of the structure. It can therefore be concluded that at least from a philosophical point of view, probabilistic methods are more satisfactory than deterministic ones.

In probabilistic methods the long-term distribution of response peaks is required. These long-term distributions are obtained by convoluting the short-term distribution of response peaks with the long-term distribution of sea states or wave conditions as discussed in detail in Chapter 5. Chapter 8 was devoted to the probability distribution of responses of fixed jacket type offshore structures, which were shown to be of Pierson-Holmes type. Furthermore, it was shown that if the response is considered to be narrow-banded and if it is assumed that

the response and its first derivative are statistically independent, then the pdf of the peaks can be readily obtained from the pdf of the response itself and that the resultant distribution (nb_2) is in reasonable agreement with the more accurate peak distributions obtained when these simplifying assumptions are not considered. Consequently, determination of the short-term distribution of response paves the way for the probabilistic analysis.

As was mentioned earlier, the pdf of response is of Pierson-Holmes type which has got thicker tails in comparison with an equivalent (same variance) Gaussian-distributed random variable. The assumption that the response is Gaussian distributed, as is done in the spectral analysis of offshore structures, leads to an underestimation of the response and its peaks at low levels of the probability of exceedence. The underestimation is increased with the increased importance of the non-linear drag component of the Morison-type wave loading.

The Pierson-Holmes distribution, is fully defined by its first four statistical moments. In the absence of current, the first and the third moments are zero and hence the distribution is fully defined by its second and fourth moments. These moments can be calculated in both time and amplitude domains. However, in order to obtain stable results in the time domain, long records of simulated response - typically in excess of 10,000 time steps (Burrows, 1982; Borgman, 1969b) are required, which is prohibitive in terms of computer run-time. Therefore, it is preferred to calculate these moments in the probability domain.

Finally, the discussion in this chapter is based on the assumption that

a) The structure is rigid, i.e. the fundamental natural frequency of the structure is well above the frequency range of the waves so that inertia forces due to dynamic effects are negligible. This is not a serious drawback since the great majority of jacket type offshore structures are in water depths less than 90m and hence do not respond dynamically to wave loading.

b) Current is negligible. The effect of current on the probability distribution of force and response is discussed by Tung et al (1976) (Section 8.1.1).

c) The intermittency of the elements in the splash zone is not considered (Tung, 1975).

10.2 DERIVATION OF THE SECOND AND THE FOURTH MOMENTS OF RESPONSE

The first step is the idealisation of the structure into a lumped system where member areas and volumes are concentrated into a discrete set of nodes. Following this procedure, the distributed wave loading on the structure can be modelled as a number of Morison-type nodal loads. Assuming that the jacket is stiff enough so that inertia forces due to its deflection under random wave loading is small, then the response (internal stress or deflection) can be considered as a linear function of the nodal loads. That is

$$y = \sum_{i=1}^{n} S_i F_i \qquad (10.1a)$$

where y is a typical response, F_i is the nodal load at node i and S_i is the contribution of a unit load at node i to the particular response under consideration (flexibility coefficient). Raising both sides of the above equation to the second and fourth power and taking expectations leads to

$$E[y^2] = \sum_{i=1}^{n} S_i^2 E[F_i^2] + 2\sum_{i=1}^{n-1} \sum_{j=i+1}^{n} S_i S_j E[F_i F_j] \tag{10.1b}$$

and

$$E[y^4] = \sum_{i=1}^{n} S_i^4 E[F_i^4] + 4\sum_{i=1}^{n} \sum_{\substack{j=1 \\ j \neq i}}^{n} S_i^3 S_j E[F_i^3 F_j] +$$

$$+ 6 \sum_{i=1}^{n-1} \sum_{j=i+1}^{n} S_i^2 S_j^2 E[F_i^2 F_j^2]$$

$$+ 12\sum_{i=1}^{n} \sum_{\substack{j=1 \\ j \neq i}}^{n-1} \sum_{\substack{k=j+1 \\ k \neq i}}^{n} S_i^2 S_j S_k E[F_i^2 F_j F_k]$$

$$+ 24\sum_{i=1}^{n-3} \sum_{j=i+1}^{n-2} \sum_{k=j+1}^{n-1} \sum_{l=k+1}^{n} S_i S_j S_k S_l E[F_i F_j F_k F_l] \tag{10.1c}$$

Therefore, determination of the second and fourth order moments of response leads to the calculation of all possible expectations of the form F_iF_j, $F_i^2F_j^2$, $F_i^3F_j$, $F_i^2F_jF_k$ and $F_iF_jF_kF_l$ between nodal loads. The required number of expectations for each of the above combinations as a function of the number of structural nodes are presented in Table 10.1 (Burrows, 1982). It is obvious that as the number of nodes increases, most of the computer run-time is spent to calculate expectations of the form $E[F_i^2F_jF_k]$ and $E[F_iF_jF_kF_l]$ because they are more complicated to calculate and because they are much greater in number. Therefore, it is of crucial importance to reduce the time needed to calculate each of these expectations.

Morison-type wave loading at node i is represented as

$$F_i = X_{2i-1}|X_{2i-1}| + X_{2i} \tag{10.2a}$$

where for a vertical pile

$$x_{2i-1} = (0.50\rho DC_d L)_i^{1/2}\, u_i \tag{10.2b}$$

and

$$x_{2i} = \left(\frac{\pi D^2}{4}\rho C_m L\right)_i \dot{u}_i \tag{10.2c}$$

All the variables in the above equations are defined as before and refer to the particular conditions at node i. Idealisation of the continuous load on nodes consisting of several members including inclined ones into the form of Equation (10.2a) has been discussed by Bound (1984). x_{2i-1} and x_{2i} are considered to be statistically independent Gaussian-distributed random variables. From Equation (10.2a), expectations of higher order moments of force required in the derivation of the second and fourth order statistical moments of response are

$$E[F_i^2] = \sum_{k=1}^{3} T_k \tag{10.3a}$$

$$E[F_i^4] = \sum_{k=4}^{6} T_k \tag{10.3b}$$

$$E[F_i^3 F_j] = \sum_{k=7}^{14} T_k \tag{10.3c}$$

$$E[F_i F_j] = \sum_{k=15}^{18} T_k \tag{10.3d}$$

$$E[F_i^2 F_j^2] = \sum_{k=19}^{27} T_k \tag{10.3e}$$

$$E[F_i^2 F_j F_k] = \sum_{k=28}^{39} T_k \tag{10.3f}$$

$$E[F_i F_j F_k F_l] = \sum_{k=40}^{55} T_k \tag{10.3g}$$

where

$$T_1 = E[x_{2i-1}^4]$$

$$T_2 = E[x_{2i}^2]$$

$$T_3 = E[x_{2i-1}|x_{2i-1}| * x_{2i}]$$

$$T_4 = E[x_{2i-1}^8]$$

$$T_5 = E[x_{2i}^4]$$

$$T_6 = E[x_{2i-1}^4 \; x_{2i}^2]$$

$$T_7 = E[x_{2i-1}^5|x_{2i-1}| * x_{2j-1}|x_{2j-1}|]$$

$$T_8 = E[x_{2i-1}^5|x_{2i-1}| * x_{2j}]$$

$$T_9 = E[x_{2i}^3 * x_{2j-1}|x_{2j-1}|]$$

$$T_{10} = E[x_{2i}^3 \; x_{2j}]$$

$$T_{11} = E[x_{2i-1}^4 \; x_{2i} * x_{2j-1}|x_{2j-1}|]$$

$$T_{12} = E[x_{2i-1}^4 \; x_{2i} \; x_{2j}]$$

$$T_{13} = E[x_{2i-1}|x_{2i-1}| * x_{2i}^2 * x_{2j-1}|x_{2j-1}|]$$

$$T_{14} = E[x_{2i-1}|x_{2i-1}| * x_{2i}^2 * x_{2j}]$$

$$T_{15} = E[x_{2i-1}|x_{2i-1}| * x_{2j-1}|x_{2j-1}|]$$

$$T_{16} = E[x_{2i-1}|x_{2i-1}| * x_{2j}]$$

$$T_{17} = E[x_{2i} \; x_{2j-1}|x_{2j-1}|]$$

$$T_{18} = E[x_{2i} \; x_{2j}]$$

$$T_{19} = E[x_{2i-1}^{4}\ x_{2j-1}^{4}]$$

$$T_{20} = E[x_{2i-1}^{4}\ x_{2j}^{2}]$$

$$T_{21} = E[x_{2i-1}^{4}\ x_{2j-1}|x_{2j-1}| * x_{2j}]$$

$$T_{22} = E[x_{2i}^{2}\ x_{2j-1}^{4}]$$

$$T_{23} = E[x_{2i}^{2}\ x_{2j}^{2}]$$

$$T_{24} = E[x_{2i}^{2}\ x_{2j-1}|x_{2j-1}| * x_{2j}]$$

$$T_{25} = E[x_{2i-1}|x_{2i-1}| * x_{2i}\ x_{2j-1}^{4}]$$

$$T_{26} = E[x_{2i-1}|x_{2i-1}| * x_{2i}\ x_{2j}^{2}]$$

$$T_{27} = E[x_{2i-1}|x_{2i-1}| * x_{2i} * x_{2j-1}|x_{2j-1}| * x_{2j}]$$

$$T_{28} = E[x_{2i-1}^{4} * x_{2j-1}|x_{2j-1}| * x_{2k-1}|x_{2k-1}|]$$

$$T_{29} = E[x_{2i-1}^{4} * x_{2j-1}|x_{2j-1}| * x_{2k}]$$

$$T_{30} = E[x_{2i-1}^{4}\ x_{2j} * x_{2k-1}|x_{2k-1}|]$$

$$T_{31} = E[x_{2i-1}^{4}\ x_{2j}\ x_{2k}]$$

$$T_{32} = E[x_{2i}^{2} * x_{2j-1}|x_{2j-1}| * x_{2k-1}|x_{2k-1}|]$$

$$T_{33} = E[x_{2i}^{2} * x_{2j-1}|x_{2j-1}| * x_{2k}]$$

$$T_{34} = E[x_{2i}^{2} * x_{2j} * x_{2k-1}|x_{2k-1}|]$$

$$T_{35} = E[x_{2i}^{2}\ x_{2j}\ x_{2k}]$$

$$T_{36} = 2E[x_{2i-1}|x_{2i-1}| * x_{2i} * x_{2j-1}|x_{2j-1}| * x_{2k-1}|x_{2k-1}|]$$

$$T_{37} = 2E[x_{2i-1}|x_{2i-1}| * x_{2i} * x_{2j-1}|x_{2j-1}| * x_{2k}]$$

$$T_{38} = 2E[x_{2i-1}|x_{2i-1}| * x_{2i}\ x_{2j} * x_{2k-1}|x_{2k-1}|]$$

$$T_{39} = 2E[x_{2i-1}|x_{2i-1}| * x_{2i}\ x_{2j}\ x_{2k}]$$

$$T_{40} = E[x_{2i-1}|x_{2i-1}| * x_{2j-1}|x_{2j-1}| * x_{2k-1}|x_{2k-1}| * x_{2l-1}|x_{2l-1}|]$$

$$T_{41} = E[x_{2i-1}|x_{2i-1}| * x_{2j-1}|x_{2j-1}| * x_{2k-1}|x_{2k-1}| * x_{2l}]$$

$$T_{42} = E[x_{2i-1}|x_{2i-1}| * x_{2j-1}|x_{2j-1}| * x_{2k} * x_{2l-1}|x_{2l-1}|]$$

$$T_{43} = E[x_{2i-1}|x_{2i-1}| * x_{2j-1}|x_{2j-1}| * x_{2k} * x_{2l}]$$

$$T_{44} = E[x_{2i-1}|x_{2i-1}| * x_{2j} * x_{2k-1}|x_{2k-1}| * x_{2l-1}|x_{2l-1}|]$$

$$T_{45} = E[x_{2i-1}|x_{2i-1}| * x_{2j} * x_{2k-1}|x_{2k-1}| * x_{2l}]$$

$$T_{46} = E[x_{2i-1}|x_{2i-1}| * x_{2j}\ x_{2k} * x_{2l-1}|x_{2l-1}|]$$

$$T_{47} = E[x_{2i-1}|x_{2i-1}| * x_{2j}\ x_{2k}\ x_{2l}]$$

$$T_{48} = E[x_{2i} * x_{2j-1}|x_{2j-1}| * x_{2k-1}|x_{2k-1}| * x_{2l-1}|x_{2l-1}|]$$

$$T_{49} = E[x_{2i} * x_{2j-1}|x_{2j-1}| * x_{2k-1}|x_{2k-1}| * x_{2l}]$$

$$T_{50} = E[x_{2i} * x_{2j-1}|x_{2j-1}| * x_{2k} * x_{2l-1}|x_{2l-1}|]$$

$$T_{51} = E[x_{2i} * x_{2j-1}|x_{2j-1}| * x_{2k}\ x_{2l}]$$

$$T_{52} = E[x_{2i}\ x_{2j} * x_{2k-1}|x_{2k-1}| * x_{2l-1}|x_{2l-1}|]$$

$$T_{53} = E[x_{2i}\ x_{2j} * x_{2k-1}|x_{2k-1}| * x_{2l}]$$

$$T_{54} = E[x_{2i}\ x_{2j}\ x_{2k} * x_{2l-1}|x_{2l-1}|]$$

$$T_{55} = E[x_{2i}\ x_{2j}\ x_{2k}\ x_{2l}] \qquad (10.4)$$

Examination of T_1 to T_{55} reveals that overall 23 different types of expectations as listed below need to be calculated.

$$E_1 = E[x_i^4]$$

$$E_2 = E[x_i^8]$$

$$E_3 = E[x_i x_j]$$

$$E_4 = E[x_i^2 x_j^2]$$

$$E_5 = E[x_i^3 x_j]$$

$$E_6 = E[x_i^4 x_j^2]$$

$$E_7 = E[x_i^4 x_j^4]$$

$$E_8 = E[x_i |x_i| * x_j]$$

$$E_9 = E[x_i^5 |x_i| * x_j]$$

$$E_{10} = E[x_i |x_i| * x_j^3]$$

$$E_{11} = E[x_i |x_i| * x_j |x_j|]$$

$$E_{12} = E[x_i^5 |x_i| * x_j |x_j|]$$

$$E_{13} = E[x_i^2 \; x_j \; x_k]$$

$$E_{14} = E[x_i^4 \; x_j \; x_k]$$

$$E_{15} = E[x_i |x_i| * x_j^2 \; x_k]$$

$$E_{16} = E[x_i |x_i| * x_j^4 \; x_k]$$

$$E_{17} = E[x_i |x_i| * x_j |x_j| * x_k^2]$$

$$E_{18} = E[x_i|x_i| * x_j|x_j| * x_k^4]$$

$$E_{19} = E[x_i\ x_j\ x_k\ x_l]$$

$$E_{20} = E[x_i|x_i| * x_j\ x_k\ x_l]$$

$$E_{21} = E[x_i|x_i| * x_j|x_j| * x_k\ x_l]$$

$$E_{22} = E[x_i|x_i| * x_j|x_j| * x_k|x_k| * x_l]$$

$$E_{23} = E[x_i|x_i| * x_j|x_j| * x_k|x_k| * x_l|x_l|] \qquad (10.5)$$

Calculation of E_1 to E_{23}

E_1 to E_{23} are expectations of functions of 2, 3 or 4 mean-zero Gaussian distributed random variables. Expectations E_1 to E_{21} have closed-form solutions (Burrows, 1983), but E_{22} and E_{23} must be calculated either by numerical integration in the four-dimensional Gaussian probability space or by introducing approximations. In general, the joint pdf of n Gaussian distributed random variables is (Miller, 1964)

$$p(x_1, x_2, \ldots, x_n) = \frac{1}{(2\pi)^{n/2}\sqrt{\mathrm{Det}([c])}} \exp\ -\frac{1}{2}\left\{(x - \bar{x})[c]^{-1}\ (x - \bar{x})^T\right\} \qquad (10.6)$$

where

$\{x\} = (x_1, \ldots, x_n)$ is the row vector of the random variables

$\{\bar{x}\} = (\bar{x}_1, \ldots, \bar{x}_n)$ is the row vector of the means

$\{x\}^T$ is the transpose of $\{x\}$, i.e. a column vector

$$c = \begin{vmatrix} c_{11}, & \ldots, & c_{1n} \\ c_{21}, & \ldots, & c_{2n} \\ . & & . \\ . & & . \\ c_{n1}, & \ldots, & c_{nn} \end{vmatrix}$$

c is the matrix of cross-covariances (Equation (B.49) between the random variables and turns out to be a symmetric positive definite matrix. Cross-covariances (or correlation coefficients) needed in the calculation of E_1 to E_{23} can be calculated in terms of cross-covariances of water particle kinematics at different nodes (Foster, 1967) (Equations 3.85 to 3.110). E_{22} can either be calculated in the four dimensional probability space or it can be broken down into the summation of three simpler expectations of the form (Burrows, 1983).

$$E_{24} = E[|x_i^3| * x_j|x_j| * x_k|x_k|] \tag{10.7}$$

Therefore, in order to calculate E_{22} and E_{23}, the following numerical integrations must be carried out

$$E_{24} = \int_{-\infty}^{+\infty}\int [|x_i|^3 * x_j|x_j| * x_k|x_k|]\ p(x_ix_jx_k)\ dx_idx_jdx_k \tag{10.8a}$$

$$E_{23} = \int_{-\infty}^{+\infty}\int\int [|x_i|x_i| * x_j|x_j| * x_k|x_k| * x_l|x_l|]\ p(x_ix_jx_kx_l)\ dx_idx_jdx_kdx_l \tag{10.8b}$$

Numerical integration over the three and four dimensional probability spaces for E_{24} and E_{23}, is performed by constant step integration using rectangular rule summations. For each cycle of integration, the relevant conditional probability distribution is Gaussian in form. Therefore, to centre the computations over the significant range of

this probability mass, the integration is performed over a range of ± 7 standard deviations of this conditional distribution about its conditional mean values, these moments being obtained from Equations (B.55) and (B.57) of Appendix B.

Burrows (1979) produced a computer model in which E_1 to E_{21} were calculated from their analytical solutions while E_{22} and E_{23} were obtained by numerical integration. The numerical integration demanded considerable computer run-time and therefore limited the application of the model to systems of 12 nodes within the 30 minute run-time available on the ICL 1906S computer at Liverpool University.

Approximations for E_{22} and E_{23}

In order to avoid the demanding integrations needed in the calculation of E_{22} and E_{23}, Burrows (1983) applied polynomial approximations to some of the $x|x|$ terms in E_{22} and E_{23} so that the resultant expectations can be calculated analytically in a manner similar to the remaining expectations. The polynomial approximations are obtained from the minimisation of the 'mean-square' error in a statistical sense and are given by Borgman (1969b). That is

$$x_i|x_i| = \sqrt{8/\pi}\ \sigma_i\ x_i \quad \text{(Linear approximation)} \tag{10.9a}$$

$$= \sqrt{2/\pi}\ \left(\sigma_i\ x_i + \frac{x_i^3}{3\sigma_i}\right) \quad \text{(Cubic approximation)} \tag{10.9b}$$

$$= \sqrt{2/\pi}\left(\frac{3}{4}\ \sigma_i\ x_i + \frac{x_i^3}{2\sigma_i} - \frac{x_i^5}{60\sigma_i^3}\right) \quad \text{(Quintic approximation)} \tag{10.9c}$$

where σ_i is the standard deviation of x_i.

These approximations are plotted in Figure 10.1. Examination of the figure shows that the linear approximation offers a reasonable solution only to about two standard deviations whilst the cubic to more than three and the quintic is good to about four standard deviations.

Burrows (1983) applied cubic approximation to $x_k|x_k|$ of E_{22}. E_{23} was calculated by applying linear approximation to $x_k|x_k|$ and cubic approximation to $x_l|x_l|$. As a result of these approximations, systems with 30 nodes can be analysed within the same time restriction as before. Comparison of approximate values of E_{22} and E_{23} with the 'exact' values obtained from numerical integration showed that these approximations are not always very good. However, it happens that the inaccuracies are large only for expectations with lower numerical values, reflecting a relatively low degree of mutual correlation, and hence the effect of these inaccuracies on the fourth moment of response are very small (less than 0.1% in the example given in Burrows (1983)). It can therefore be concluded that for engineering purposes, the computer model produced by Burrows is accurate and that the results of other forms of approximations introduced later can be compared with the results of Burrows' model to check their accuracy.

10.3 TWO DIFFERENT METHODS FOR REDUCING THE COMPUTER RUN-TIME

10.3.1 POLYNOMIAL APPROXIMATION METHOD

10.3.1.1 Theoretical Considerations

Analytical solutions to expectations which have more than two different x terms and at least one of the x terms is in the form of $x|x|$ are complicated and involve solving a set of two or three linear equations for calculating coefficients needed in the solution (Equation B.56 of Appendix B). Furthermore, functions such as Arcsin(ρ), for which

evaluation by computer is time consuming in comparison with simple algebraic operations (+, -, *), appear in the solutions. On the other hand, analytical solutions to expectations which have more than two x terms but with no $x|x|$, are relatively simple. This encourages the application of polynomial approximations to all expectations having terms of the $x|x|$ form. Bruce (1985) has suggested that $x|x|$ be approximated by

$$x_i|x_i| = a_1 x_i + a_3 x_i^3 \tag{10.10}$$

so that the second and the fourth moments of both sides are equal. Raising both sides of the above equation to the second and fourth powers, taking expectations and assuming for simplicity that $\sigma_i = 1$, the following two equations will be obtained.

$$a_1^2 + 15a_3^2 + 6a_1a_3 = 3.0 \tag{10.11a}$$

$$3a_1^4 + 60a_1^3a_3 + 630a_1^2a_3^2 + 3780a_1a_3^3 + 10395a_3^4 = 105 \tag{10.11b}$$

Solving the above set of two non-linear equations gives

$$\begin{cases} a_1 = 1.007907 \\ a_3 = 0.214243 \end{cases} \quad \text{(Compare with Equation (10.9b)} \tag{10.12}$$

For the general case when σ_i is not equal to unity, the approximation will be

$$x_i|x_i| \approx \sigma_i^2 (a_1 y_i + a_3 y_i^3) \tag{10.13}$$

where $y_i = x_i/\sigma_i$ has a standard deviation of unity.

The comparison of the above polynomial approximation with $x|x|$ in Figure 10.2 reveals that the approximation is good up to about four

standard deviations. Using this polynomial approximation, expectations having $x|x|$ terms (Equation 10.5) will be approximated by

$$E8/(\sigma_i^2\sigma_j) = a_1 E[y_iy_j] + a_3E[y_i^3y_j]$$

$$E9/(\sigma_i^6\sigma_j) = a_1 E[y_i^5y_j] + a_3E[y_i^7y_j]$$

$$E10/(\sigma_i^2\sigma_j^3) = a_1 E[y_iy_j^3] + a_3E[y_i^3y_j^3]$$

$$E11/(\sigma_i^2\sigma_j^2) = a_1^2 E[y_iy_j] + a_1a_3E[y_iy_j^3] + a_1a_3 E[y_i^3y_j] + a_3^2 E[y_i^3y_j^3]$$

$$E12/(\sigma_i^6\sigma_j^2) = a_1^2 E[y_i^5y_j] + a_1a_3E[y_i^5y_j^3] + a_1a_3 E[y_i^7y_j] + a_3^2 E[y_i^7y_j^3]$$

$$E15/(\sigma_i^2\sigma_j^2\sigma_k) = a_1 E[y_iy_j^2y_k] + a_3E[y_i^3y_j^2y_k]$$

$$E16/(\sigma_i^2\sigma_j^4\sigma_k) = a_1 E[y_iy_j^4y_k] + a_3E[y_i^3y_j^4y_k]$$

$$E17/(\sigma_i^2\sigma_j^2\sigma_k^2) = a_1 E[y_iy_jy_k^2] + a_1a_3E[y_iy_j^3y_k^2] + a_1a_3E[y_i^3y_jy_k^2] + a_3^2 E[y_i^3y_j^3y_k^2]$$

$$E18/(\sigma_i^2\sigma_j^2\sigma_k^4) = a_1^2 E[y_iy_jy_k^4] + a_1a_3E[y_iy_j^3y_k^4] + a_1a_3E[y_i^3y_jy_k^4] + a_3^2 E[y_i^3y_j^3y_k^4]$$

$$E20/(\sigma_i^2\sigma_j\sigma_k\sigma_l) = a_1 E[y_iy_jy_ky_l] + a_3E[y_i^3y_jy_ky_l]$$

$$E21/(\sigma_i^2\sigma_j^2\sigma_k\sigma_l) = a_1^2 E[y_iy_jy_ky_l] + a_1a_3E[y_iy_j^3y_ky_l] + a_1a_3E[y_i^3y_jy_ky_l] + a_3^2E[y_i^3y_j^3y_ky_l]$$

$$\begin{aligned} E22/(\sigma_i^2\sigma_j^2\sigma_k^2\sigma_l) = {} & a_1^3 E[y_iy_jy_ky_l] + a_1^2a_3E[y_iy_jy_k^3y_l] + a_1^2a_3E[y_iy_j^3y_ky_l] \\ & + a_1a_3^2E[y_iy_j^3y_k^3y_l] + a_1^2a_3E[y_i^3y_iy_ky_l] \\ & + a_1a_3^2E[y_i^3y_jy_k^3y_l] + a_1a_3^2E[y_i^3y_j^3y_ky_l] \\ & + a_3^3E[y_i^3y_j^3y_k^3y_l] \end{aligned}$$

$$E23/(\sigma_i^2\sigma_j^2\sigma_k^2\sigma_l^2) = a_1^4\,E[y_iy_jy_ky_l] + a_1^3a_3E[y_iy_jy_ky_l^3] + a_1^3a_3E[y_iy_jy_k^3y_l]$$
$$+ a_1^2a_3^2E[y_iy_jy_k^3y_l^3] + a_1^3a_3E[y_iy_j^3y_ky_l]$$
$$+ a_1^2a_3^2E[y_iy_jy_ky_l^3] + a_1^2a_3^2E[y_iy_j^3y_k^3y_l]$$
$$+ a_1a_3^3E[y_iy_j^3y_k^3y_l^3] + a_1^3a_3E[y_i^3y_jy_ky_l]$$
$$+ a_1^2a_3^2E[y_i^3y_jy_ky_l^3] + a_1^2a_3^2E[y_i^3y_jy_k^3y_l]$$
$$+ a_1a_3^3E[y_i^3y_jy_k^3y_l^3] + a_1^2a_3^2E[y_i^3y_j^3y_ky_l]$$
$$+ a_1a_3^3\,E[y_i^3y_j^3y_ky_l^3] + a_1a_3^3E[y_i^3y_j^3y_k^3y_l]$$
$$+ a_3^4E[y_i^3y_j^3y_k^3y_l^3] \qquad (10.14)$$

Substituting these approximations into T_1 to T_{55} (Equation (10.4)) whenever these approximations are necessary, approximate values for $E[F_iF_j]$, $E[F_i^3F_j]$, $E[F_i^2F_j^2]$, $E[F_i^2F_jF_k]$, $E[F_iF_jF_kF_l]$ can be calculated which are then used in the calculation of the second and the fourth moments of response (Equations (10.1b) and (10.1c)).

When polynomial approximations are introduced, all the resulting expectations in T_1 to T_{55} will be of the form $E[x_i^\alpha x_j^\beta x_k^\gamma x_l^\lambda]$ where α, β, γ and λ vary between 0 and 3. These expectations can be evaluated through Price's theorem (Price, 1958). According to the theorem for the case of $\sigma_i = \sigma_j = \sigma_k = \sigma_l = 1$, the following relationship holds true.

$$\frac{\partial E[x_i^\alpha x_j^\beta x_k^\gamma x_l^\lambda]}{\partial \rho_{ij}} = \alpha\ \beta\ E[x_i^{\alpha-1}x_j^{\beta-1}x_k^\gamma x_l^\lambda] \qquad (10.15)$$

Using this principle, higher order expectations can be calculated from lower order expectations, systematically. For example, $E[x_i^2x_j^2]$ is calculated in the following way.

$$\frac{\partial E[x_i^2 x_j^2]}{\partial \rho_{ij}} = 4E[x_i x_j] = 4\rho_{ij} \tag{10.16a}$$

Therefore,

$$E[x_i^2 x_j^2] = \int_0^{\rho ij} 4\rho_{ij} + c = 2\rho_{ij}^2 + c \tag{10.16b}$$

If $\rho_{ij} = 0$, then x_i and x_j are statistically independent and $E[x_i^2 x_j^2] = E[x_i^2] * E[x_j^2] = 1$. Hence, for $\rho_{ij} = 0$, the right hand side of Equation (10.16b) is equal to 1, which leads to $c = 1$. Consequently,

$$E[x_i^2 x_j^2] = 1 + 2\rho_{ij}^2 \tag{10.16c}$$

If σ_i and σ_j are different from unity, then

$$E[x_i^2 x_j^2] = (1 + 2\rho_{ij}^2)\, \sigma_i^2 \sigma_j^2 \tag{10.16d}$$

Bruce (1985) has evaluated these expectations. However, due to the importance of the expectations in this study, they have been calculated independently here. Furthermore, the resultant expressions have been checked by comparing their results with the results derived from numerical integration for a few data sets, as will be shown later. The complete list of expectations required in derivation of the second and fourth moments of response together with their solutions now follows.

$$E[y_i^2] = 1$$

$$E[y_i^4] = 3$$

$$E[y_i^8] = 105$$

$$E[y_i y_j] = \rho_{ij}$$

$$E[y_i^3 y_j] = 3\rho_{ij}$$

$$E[y_i^5 y_j] = 15\rho_{ij}$$

$$E[y_i^7 y_j] = 105\rho_{ij}$$

$$E[y_i^2 y_j^2] = 1 + 2\rho_{ij}^2$$

$$E[y_i^4 y_j^2] = 3 + 12\rho_{ij}^2$$

$$E[y_i^3 y_j^3] = 9\rho_{ij} + 6\rho_{ij}^3$$

$$E[y_i^5 y_j^3] = 45\rho_{ij} + 60\rho_{ij}^3$$

$$E[y_i^4 y_j^4] = 9 + 72\rho_{ij}^2 + 24\rho_{ij}^4$$

$$E[y_i^7 y_j^3] = 315\rho_{ij} + 630\rho_{ij}^3$$

$$E[y_i y_j y_k^2] = \rho_{ij} + 2\rho_{ik}\,\rho_{jk}$$

$$E[y_i^4 y_j y_k] = 3(\rho_{jk} + 4\rho_{ij}\,\rho_{ik})$$

$$E[y_i y_j^2 y_k^3] = 3[\rho_{ik}\,(1 + 2\rho_{jk}^2) + 2\rho_{ij}\rho_{jk}]$$

$$E[y_i^3 y_j^4 y_k] = 3[3\rho_{ik}\,(1 + 4\rho_{ij}^2) + 4\rho_{ij}\rho_{jk}\,(3 + \rho_{ij}^2)]$$

$$E[y_i^2 y_j^3 y_k^3] = 3\{6\rho_{ij}\rho_{ik}\,(1 + 2\rho_{jk}^2) + \rho_{jk}[(3 + 2\rho_{jk}^2) + 6(\rho_{ij}^2 + \rho_{ik}^2)]\}$$

$$E[y_i^3 y_j^3 y_k^4] = 9\{\rho_{ij}[(3 + 2\rho_{ij}^2) + 12(\rho_{ik}^2 + \rho_{jk}^2)] + 4\rho_{ik}\rho_{jk}[6\rho_{ij}(\rho_{ij} + \rho_{ik}\rho_{jk}) + 2(\rho_{ik}^2 + \rho_{jk}^2) + 3]\} \tag{10.17}$$

and

$$E[y_i y_j y_k y_l] = \rho_{ij}\rho_{kl} + \rho_{ik}\rho_{jl} + \rho_{il}\rho_{jk}$$

$$E[y_i y_j y_k y_l^3] = 3(\rho_{ij}\rho_{kl} + \rho_{ik}\rho_{jl} + \rho_{il}\rho_{jk}) + 6\rho_{il}\rho_{jl}\rho_{kl}$$

$$E[y_i y_j y_k^3 y_l^3] = 9(\rho_{ij}\rho_{kl} + \rho_{ik}\rho_{jl} + \rho_{il}\rho_{jk}) + 6\rho_{kl}[\rho_{ij}\rho_{kl}^2 + 3(\rho_{ik}\rho_{jk} + \rho_{il}\rho_{jl}) + 3\rho_{kl}(\rho_{ik}\rho_{jl} + \rho_{il}\rho_{jk})]$$

$$E[y_i y_j^3 y_k^3 y_l^3] = 18\{6(\rho_{ij}\rho_{kl} + \rho_{ik}\rho_{jl} + \rho_{il}\rho_{jk})(0.25 + \rho_{jk}\rho_{jl}\rho_{kl}) + (\rho_{ij}\rho_{kl}^3 + \rho_{ik}\rho_{jl}^3 + \rho_{il}\rho_{jk}^3) + 3[\rho_{ij}\rho_{jk}\rho_{jl} + \rho_{ik}\rho_{jk}\rho_{kl} + \rho_{il}\rho_{jl}\rho_{kl} + \rho_{ij}\rho_{kl}(\rho_{jk}^2 + \rho_{jl}^2) + \rho_{ik}\rho_{jl}(\rho_{jk}^2 + \rho_{kl}^2) + \rho_{il}\rho_{jk}(\rho_{jl}^2 + \rho_{kl}^2)]\}$$

$$E[y_i^3 y_j^3 y_k^3 y_l^3] = 81(\rho_{ij}\rho_{kl} + \rho_{ik}\rho_{jl} + \rho_{il}\rho_{jk}) + 54[\rho_{ij}\rho_{kl}(\rho_{ij}^2 + \rho_{kl}^2) + \rho_{ik}\rho_{jl}(\rho_{ik}^2 + \rho_{jl}^2) + \rho_{il}\rho_{jk}(\rho_{il}^2 + \rho_{jk}^2)] + 36(\rho_{ij}^3\rho_{kl}^3 + \rho_{ik}^3\rho_{jl}^3 + \rho_{il}^3\rho_{jk}^3) + 162[\rho_{ij}(\rho_{ik}\rho_{il} + \rho_{jk}\rho_{jl}) + \rho_{kl}(\rho_{ik}\rho_{jk} + \rho_{il}\rho_{jl}) + \rho_{ij}\rho_{kl}(\rho_{jk}^2 + \rho_{jl}^2 + \rho_{ik}^2 + \rho_{il}^2) + \rho_{il}\rho_{jk}(\rho_{ij}^2 + \rho_{ik}^2 + \rho_{jl}^2 + \rho_{kl}^2) + \rho_{ik}\rho_{jl}(\rho_{ij}^2 + \rho_{jk}^2 + \rho_{kl}^2 + \rho_{il}^2)] + 324[\rho_{ij}\rho_{jk}\rho_{jl}(\rho_{ik}^2 + \rho_{il}^2 + \rho_{kl}^2) + \rho_{ij}\rho_{ik}\rho_{il}(\rho_{jk}^2 + \rho_{jl}^2 + \rho_{kl}^2) + \rho_{ik}\rho_{jk}\rho_{kl}(\rho_{ij}^2 + \rho_{il}^2 + \rho_{jl}^2) + \rho_{il}\rho_{jl}\rho_{kl}(\rho_{ij}^2 + \rho_{ik}^2 + \rho_{jk}^2) + \rho_{il}^2\rho_{jk}^2(\rho_{ij}\rho_{kl} + \rho_{ik}\rho_{jl}) + \rho_{ik}^2\rho_{jl}^2(\rho_{ij}\rho_{kl} + \rho_{il}\rho_{jk}) + \rho_{ij}^2\rho_{kl}^2(\rho_{il}\rho_{jk} + \rho_{ik}\rho_{jl})] + 1296\rho_{ij}\rho_{ik}\rho_{il}\rho_{jk}\rho_{jl}\rho_{kl} \quad (10.18)$$

Validating Analytical Solutions to Expectations

Analytical solutions to expectations of Equations (10.17) and (10.18) can be checked in two different ways.

1. Checking the solutions for special conditions. For example, $E[y_i^5 y_j^3] = 45\rho_{ij} + 60\rho_{ij}^3$ can be checked for the following special conditions.

   a) If $y_i = y_j$, then $\rho_{ij} = 1$, and hence the analytical solution will reduce to $E[y_i^5 y_j^3] = E[y_i^8] = 45 + 60 = 105$

which is correct as $E[y_i^8] = 105$.

b) If y_i and y_j are statistically independent, then $\rho_{ij} = 0$ and the analytical solution will reduce to $E[y_i^5 y_j^3] = 0$ which is correct since for the condition of y_i and y_j being independent, we have $E[y_i^5 y_j^3] = E[y_i^5]E[y_j^3] = 0$

2. By comparing the results of the analytical solutions with the results of numerical integration for sample data sets. Five different data sets were used for the purpose of comparison. The data sets are composed of the matrices of cross-covariances between x_i, x_j, x_k and x_l (Table 10.2a). Furthermore, the matrix of correlation coefficients between the four Gaussian-distributed random variables are given in the same Table. These correlation coefficients are chosen randomly; however care has been taken to represent all different conditions. For example, data set number 5 refers to the condition that correlation coefficients between the random variables are high while data set number 3 refers to the condition that these correlations are low. In all cases the results (Table 10.2b) are the same up to four decimal places, giving confidence in both the analytical solutions and the programme developed for numerical integration. Only expectations involving more than two variables have been checked as other expectations are very simple and have been reported by many authors.

10.3.1.2 Developing and Checking the Computer Model

A computer model was produced that defines a Pierson-Moskowitz spectrum in terms of the significant wave height, H_s (Equation (3.120)). The upper and lower limits of the spectrum are taken to be $0.40\omega_p$ and $8.0\omega_p$

(same as Burrows' model) where ω_p refers to the frequency at the spectral peak, that is $G_{\eta\eta}(\omega_p)$ is the maximum of $G_{\eta\eta}(\omega)$. The spectrum is defined by its value at 32 equally spaced points starting from the lower limit (0.40 ω_p) and ending at the upper limit (8.0 ω_p) of the spectrum. For each discrete frequency the wave number is calculated (Section 6.2). The variances of water particle kinematics at different nodes and the cross-covariances and correlation coefficients between different pairs of kinematics at different nodes are calculated by numerical integration according to Equations (3.85) to (3.110). The flexibility coefficients are given as input to the programme and the second and the fourth moments of response are calculated from Equations (10.1b) and (10.1c). The T_k terms needed in calculating the expectations of different combinations of nodal forces are given by Equation (10.4). Those expectations having terms of the $x|x|$ form are approximated by those given in (10.14).

In order to make sure that the programme coding was right, the following checks were performed. Expectations used in calculating $E[F_i^3F_j]$, $E[F_iF_j]$ and $E[F_i^2F_j^2]$ were calculated for the matrix of cross-covariances given in Table 10.3a. The correlation coefficients (or cross-covariances) in Table 10.3a have been chosen randomly, i.e. they do not represent any specific arrangement of nodal points. In other words, the approach towards checking these expectations is purely mathematical. The results of the analytical solutions to the approximate expectations (expectations when polynomial approximations have been applied) are in reasonable agreement with the results of analytical solutions to the exact expectations. The maximum difference in this example is less than 7%. It is emphasised that the results of both exact and approximate expectations (i.e. expectations before and

after the application of polynomial approximations) have also been checked by numerical integration and are in agreement with the results of their corresponding closed-form solutions up to four decimal places.

Three different data sets were considered for checking expectations used in calculating $E[F_i^2F_jF_k]$ and $E[F_iF_jF_kF_l]$. The matrix of correlation coefficients and cross-covariances for these data sets are given in Tables 10.4a and 10.4b, respectively. Again, the correlation coefficients are chosen randomly and do not represent any specific arrangement of nodal points. The correlation coefficients between x_{2i-1} and x_{2i} in our model when applied to structures would be zero; however, in these examples, this point has not always been considered. This however, would not cause any particular problem as $\rho_{2i,2i-1} = 0$ is only a special value for the correlation coefficient which in general can vary between ± 1.

The comparison for expectations used in calculating $E[F_i^2F_jF_k]$ is done in Table 10.4c. Similar comparison for expectations used in calculating $E[F_iF_jF_kF_l]$ are presented in Table 10.4d. Again, the results are in good agreement with the maximum difference being less than 4%. As was the case in the previous example, both exact and approximate expectations have also been calculated by numerical integration and are in agreement with their corresponding analytical solutions up to four decimal places. For expectations of the form E_{22} and E_{23} analytical solutions do not exist and only the result of numerical integrations have been considered. The inverse of the matrix of cross-covariances for some particular combinations of cross-covariances did not exist and hence these expectations cannot be calculated for the associated data set.

However, all the expectations have at least been checked for one data set.

Finally, two different versions of the computer model based on the polynomial approximation method have been produced. In the first one polynomial approximation has been applied to the expectations in $E[F_iF_j]$, $E[F_i^3F_j]$, $E[F_i^2F_j^2]$, $E[F_i^2F_jF_k]$ and $E[F_iF_jF_kF_l]$. In the second version the polynomial approximation has been applied only to the expectations in $E[F_i^2F_jF_k]$ and $E[F_iF_jF_kF_l]$. This is more reasonable as the analytical solution to expectations in $E[F_iF_j]$, $E[F_i^2F_j^2]$, $E[F_i^3F_j]$ are relatively simple. Furthermore, as shown in Table 10.1, the number of expectations involving two nodal loads is by far smaller than the number of expectations involving three or four nodal loads for structures with a large number of nodes. In the remaining sections, only the second version has been applied to the test structures.

10.3.1.3 Testing the Model for a Few Sample Structures

In order to check how good the polynomial approximation method is, the resultant model was applied to a few sample structures and its results were compared with the results of Burrows' model, which is considered to be adequate for engineering purposes. Before the comparison is done, the following point must be considered.

For structures with a relatively small number of nodes (say less than 12), the number of expectations involving one or two nodal forces (i.e. $E[F_i^4]$, $E[F_i^3F_j]$, $E[F_i^2F_j^2]$) account for a large part of the fourth moment of response. However, as the number of nodes increases, the number of expectations involving three or four different nodal forces grows rapidly so that it is possible that the major part of the fourth moment

of the response is accounted for by these expectations. Now in our computer model, $E[F_i^4]$, $E[F_i^3F_j]$ and $E[F_i^2F_j^2]$ are calculated analytically and the number of nodes in our test structures are not high; therefore, the comparison of kurtosis from the polynomial approximation model against the exact value of kurtosis will not be a good indicator of the accuracy of the model. Instead, it is more reasonable to compare $\sum S_i^2S_jS_k \; E[F_i^2F_jF_k]$ and $\sum S_iS_jS_kS_l \; E[F_iF_jF_kF_l]$ from the polynomial approximation model against their corresponding exact values.

The response calculated for the test structures is base shear which is defined as the sum of all the nodal loads. That is $y = \sum F_i$. The test structures include a one-leg, a two-leg and a four-leg structure. The effect of member diameter, significant wave height and the distance between the legs on the accuracy of the model was investigated. C_d and C_m values were taken to be 0.70 and 2.00, respectively.

One-Leg Structure

The first structure to be considered was a riser of 2.5ft (0.7620m) diameter, in a water depth of 400ft (122m). Figure 10.3 shows that the level of inaccuracy increases with H_s; but it is always less than 3%. Significant wave heights up to 65ft (19.8m) have been considered in this study; however, it should be noted that values of H_s greater than 35ft (10.7m) are not realistic and therefore it can be concluded that inaccuracies are less than 1%. Another observation is that $\sum E[F_iF_jF_kF_l]$ is less accurate than $\sum E[F_i^2F_jF_k]$ as may be intuitively expected.

Two-Leg Structure

In a one-leg structure, there is no horizontal spacing between nodal forces. In order to investigate the effect of nodes with different horizontal coordinates on the performance of the model, two two-legged structures as shown in Figures 10.4 and 10.5 were investigated. Figure 10.4 shows that inaccuracies are less than 5% and that inaccuracies increase with increasing distance between the legs. Figure 10.5 is similar to Figure 10.4 except for the leg diameter which has reduced from 2.5ft (0.7620m) to 1.0ft (0.3048m). As a result, the inaccuracies have increased up to a maximum of 7.5%. When the diameter reduces, the drag term becomes more dominant and the force kurtosis increases. Therefore, it can be concluded that as the kurtosis increases, the level of inaccuracy increases, too. However, it should be considered that legs of 1.0ft diameter are not realistic. Furthermore, as far as the author is aware, the jacket dimensions are not more than 150ft (45.7m); therefore for more realistic conditions, the level of inaccuracy is limited to a maximum of 2%.

Four-Leg Structure

In the case of a two-legged structure, for an expectation of the form $E[F_iF_jF_kF_l]$, only two horizontal positions (coordinates) can be different for the four nodal loads. In order to investigate the accuracy of the model in cases when all the four horizontal positions (coordinates) can be different in $E[F_iF_jF_kF_l]$, two four-legged structures, as shown in Figures 10.6 and 10.7, were studied. Figure 10.6 shows that for a dimension of 300ft (91.4m) with a leg diameter of 2.5ft (0.7620m), the inaccuracies are limited to 4% up to a significant wave height of 40ft (12.2m). Figure 10.7 is similar to Figure 10.6 except that the leg diameter has reduced to 1.0ft (0.3048m). As a result, the inaccuracies

have increased to a maximum of 8%. Again, the structure with the larger diameter is more realistic and hence it can be concluded that the inaccuracies are less than 3% (up to an H_s of 35ft (10.7m)).

The results of the above investigations show that the polynomial approximation method is very satisfactory and that for realistic structures, inaccuracies are expected to be less than 3%. Obviously, there is need for further investigation of the model with regard to various responses of a real jacket structure. The computer time spent for calculating expectations of the form $E[F_i^2F_jF_k]$ and $E[F_iF_jF_kF_l]$ has reduced by about 28 times in comparison with Burrows' model (analytical solutions). Therefore, with reference to Table 10.1, it is expected that the number of nodes can be increased from 40 to about 85. That is a great achievement; however, the model is not yet adequate for analysis of complicated structures. A more drastic reduction in computer run-time is required so that the number of nodes can be increased to well above one hundred nodes.

10.3.2 FORCE-CORRELATION METHOD

10.3.2.1 Theoretical Considerations

Burrows' model and the polynomial approximation model have one point in common; both of them are based on the assumption that due to the non-Gaussian distribution of forces, expectations of functions of two, three or four forces cannot be calculated directly from parameters describing the inter-relationship between forces themselves. Instead, they have resorted to the Gaussian-distributed particle kinematics. Burrows' model has applied the analytical solution to the expectations of Gaussian-distributed random variables as far as possible; the other has introduced polynomial approximations at an earlier stage to ease

the computer run-time. In this section an intuitive attempt has been made to calculate the expectations of different combinations of forces using parameters describing the forces and the inter-relationship between the forces themselves.

The important parameters in describing an individual nodal load are its standard deviation and kurtosis. The most important parameter describing the relationship between loads at different nodes is the correlation coefficient between the two forces. These three parameters have been used in obtaining approximate solutions to expectations involving two, three or four nodal forces. These approximate solutions consist of two parts multiplied by each other. The first part is based on the assumption that forces are Gaussian distributed and calculates the expectation disregarding the fact that the kurtoses of forces are more than three (which is the kurtosis of a Gaussian random variable). The second part introduces functions of forces' kurtoses to compensate for this wrong assumption. The intuitive approximation for the general case of $E[F_iF_jF_kF_l]$ is

$$E[F_iF_jF_kF_l] = G * (\rho_{ij}\rho_{kl} + \rho_{ik}\rho_{jl} + \rho_{il}\rho_{jk}) * \sigma_{Fi}\,\sigma_{Fj}\,\sigma_{Fk}\,\sigma_{Fl} \tag{10.19a}$$

where

$$G = (1/3) * (\beta_i\beta_j\beta_k\beta_l)^{1/4} \tag{10.19b}$$

β_i refers to the kurtosis of F_i and ρ_{ij} refers to the correlation coefficient between F_i and F_j. Examination of the above equation shows that when the four nodal forces are Gaussian distributed, the equation is exact, i.e. G = 1 and Equation (10.19a) will reduce to

$$E[F_iF_jF_kF_l] = (\rho_{ij}\rho_{kl} + \rho_{ik}\rho_{jl} + \rho_{il}\rho_{jk}) * \sigma_{Fi}\sigma_{Fj}\sigma_{Fk}\sigma_{Fl} \tag{10.20}$$

which is the analytical solution to the expectation of the product of four Gaussian distributed random variables. Equation (10.19a) is exact for another specific condition, too. That is, when F_i, F_j, F_k and F_l are linearly related. When this is the case, $\beta_i = \beta_j = \beta_k = \beta_l = \beta$ and the following relationships hold true.

$$
\begin{aligned}
F_j &= \alpha_1 F_i \\
F_k &= \alpha_2 F_i \\
F_l &= \alpha_3 F_i \\
\sigma_{Fj} &= \alpha_1 \sigma_{Fi} \\
\sigma_{Fk} &= \alpha_2 \sigma_{Fi} \\
\sigma_{Fl} &= \alpha_3 \sigma_{Fi} \\
F_i F_j F_k F_l &= \alpha_1 \alpha_2 \alpha_3 F_i^4 \\
\sigma_{Fi}\sigma_{Fj}\sigma_{Fk}\sigma_{Fl} &= \alpha_1 \alpha_2 \alpha_3 \, \sigma_{Fi}^4
\end{aligned}
\tag{10.21}
$$

where α_1, α_2 and α_3 are constants. Therefore

$$
E[F_i F_j F_k F_l] = E[\alpha_1 \alpha_2 \alpha_3 F_i^4] = \alpha_1 \alpha_2 \alpha_3 \, E[F_i^4] = \alpha_1 \alpha_2 \alpha_3 \beta_i \sigma_{Fi}^4 = \beta \sigma_{Fi}\sigma_{Fj}\sigma_{Fk}\sigma_{Fl} \tag{10.22}
$$

When the nodal forces are linearly related, $\rho_{ij} = \rho_{ik} = \rho_{il} = \rho_{jk} = \rho_{jl} = \rho_{kl} = 1$ and considering that $\beta_i = \beta_j = \beta_k = \beta_l = \beta$, from Equation (10.19a), $E[F_i F_j F_k F_l]$ for this particular condition will be the same as that of Equation (10.22). That is

$$
E[F_i F_j F_k F_l] = \beta \sigma_{Fi}\sigma_{Fj}\sigma_{Fk}\sigma_{Fl} \tag{10.23}
$$

Therefore, for two particular conditions, the approximation introduced in (10.19a) will be exact, a) when forces are Gaussian distributed, b) when the correlation coefficients between the forces is ± 1. These two specific conditions relate to this study in the following way.

1. When H_s is small, the inertia component of Morison's force dominates and hence the forces are nearly Gaussian distributed. This means that for low values of H_s, the force correlation method (Equation (10.19a) is a good approximation.
2. On the other extreme, when H_s is very large, the associated wave lengths will be very large and therefore correlation coefficients between nodal forces which are not far apart will be close to one. Hence for very high values of H_s, the force correlation method is expected to be a good approximation, too.

Combining the above two comments, the following conclusion may be made. For low values of H_s, the force correlation method is good. As H_s increases, the departure from Gaussian distribution increases, too, but so does the correlation coefficients between nodal forces. It is expected that the second factor can partially compensate for the first one so that the inaccuracies may remain within acceptable limits. Another point to be considered is that it is the accuracy of $\sum E[F_iF_jF_kF_l]$ which is of importance not the accuracy of individual expectations. Expectations with high correlation coefficients between their constituent forces are expected to be much larger than those with low correlations and hence they are expected to contribute significantly to $\sum E[F_iF_jF_kF_l]$. On the other hand, these expectations are the more accurate ones; hence the level of accuracy for $\sum F_iF_jF_kF_l$ should be much better than the level of accuracy for some of the individual expectations,

which may suffer large inaccuracies. Finally, if the inaccuracies prove to be of a random nature (some underestimation, some overestimation) then they may cancel each other out so that $\sum E[F_iF_jF_kF_l]$ will have a better level of accuracy.

As previously stated, the force correlation approximation for the general case of $E[F_iF_jF_kF_l]$ is

$$E[F_iF_jF_kF_l] = (1/3) * (\beta_i\beta_j\beta_k\beta_l)^{1/4} * (\rho_{ij}\rho_{kl} + \rho_{ik}\rho_{jl} + \rho_{il}\rho_{jk}) * \sigma_{Fi}\sigma_{Fj}\sigma_{Fk}\sigma_{Fl} \quad (10.23a)$$

From the above equation, expectations of the other combinations of nodal forces will be

$$E[F_i^2F_jF_k] = (1/3) * (\beta_i^2\beta_j\beta_k)^{1/4} * (\rho_{jk} + \rho_{ij}\rho_{ik}) * \sigma_{Fi}^2\sigma_{Fj}\sigma_{Fk} \quad (10.23b)$$

$$E[F_i^2F_j^2] = (1/3) * (\beta_i\beta_j)^{1/2} * (1.0 + 2\rho_{ij}^2) * \sigma_{Fi}^2\sigma_{Fj}^2 \quad (10.23c)$$

$$E[F_i^3F_j] = (\beta_i^3\beta_j) * \rho_{ij} * \sigma_{Fi}^3\sigma_{Fj} \quad (10.23d)$$

10.3.2.2 Developing the Computer Model

The foundation of the force-correlation method is based on the argument that for low values of H_e, the approximation is good. As H_e increases, the departure from Gaussian distribution tends to cause an increase in the level of inaccuracies, but on the other hand, the increased correlation coefficients between nodal loads tend to bring the inaccuracies down. Therefore, it is expected that maximum inaccuracies should occur in the middle range of H_e where departure from Gaussian distribution is relatively high, but the correlation coefficients are not high enough to cause a significant improvement in the level of

inaccuracies. It was decided to test this theme before developing a full model based on the force-correlation method.

Figure 10.8 shows the results of such an investigation for a two-legged structure with 50ft (15.2m) distance between its two legs. The approximate values of $E[F_i^3 F_j]$ have been compared against their exact values for different combination of the 12 nodal loads. The following points can be noticed.

1. As H_s increases, the correlation coefficient between nodal loads increases, too.
2. At low levels of H_s, inaccuracies are very low. For example for H_s less than 10ft, the maximum inaccuracy occurs for $E[F_1^3 F_7]$ which is only 1.5%.
3. The maximum inaccuracy occurs in the range $20ft < H_s < 40ft$ where correlation coefficients are in the middle range (less than 0.70) but kurtoses are high.
4. For very high values of correlation coefficients, the inaccuracies are very low, although the kurtoses is high. For example, the maximum inaccuracy for $E[F_6 F_{12}]$ is 1%. Also consider the case of $E[F_1^3 F_7]$ for $H_s > 60ft$.
5. Comparison of inaccuracies for $E[F_1^3 F_{10}]$ and $E[F_1^3 F_7]$ shows that although $\rho_{1,7}$ is higher than $\rho_{1,10}$, the level of inaccuracy is higher for $E[F_1^3 F_7]$. This is believed to be due to the lower kurtosis of F_{10} in comparison with F_7 due to its higher depth of immersion. It will later be demonstrated that as the distance between the legs increases, the level of inaccuracies will increase, too. The great majority of offshore structures have

inclined legs so that the distance between the legs increase with depth of immersion. On the other hand, the forces become more inertia dominated and closer to Gaussian distribution. The increased distance between the legs has an adverse effect on the results of the force-correlation method; on the other hand, the reduced values of kurtoses tends to improve the results. The two effects are expected to cancel each other out. The conclusion is that it is the dimension of the structure at the water surface which serves as a measure of the inaccuracies rather than its dimension at mudline. The dimension at water surface is expected to be less than 150ft (≈45m).

The above observations do not contradict the foundation upon which the force correlation method is based. It was therefore decided to develop the model and test it for the same structures used in testing the polynomial approximation model. The correlation coefficient between nodal forces is determined by calculating $E[F_iF_j]$ analytically as was done in both Burrows' model and the polynomial approximation model.

10.3.2.3 Testing the Model for a Few Sample Structures

One-Leg Structure

Figure 10.9 shows that the level of inaccuracy increases with H_s and then decreases. The sum of the expectations involving four different nodal forces is the most inaccurate one but still the level of inaccuracy is below 3.6%. As expected, the model is less accurate than the polynomial approximation one with a level of inaccuracy below 1% (for $\sum S_iS_jS_kS_l\ E[F_iF_jF_kF_l]$) for the same structure (Figure 10.3).

Two-Leg Structure

Figure 10.10 shows the effect of increasing H_s on the inaccuracies for a two-legged structure with a spacing distance of 50ft between its two legs. Again, it is observed that inaccuracies increase with H_s and then decline. The sum of the expectations involving four different nodal loads is the least accurate one with a maximum inaccuracy of less than 3.5%.

The effect of horizontal spacing between the legs on $\sum S_i S_j S_k S_l E[F_i F_j F_k F_l]$ (the least accurate expectations) is investigated in Figure 10.11. It is observed that increasing distance between the legs has an adverse effect on the level of accuracy. However, the reasonable range for horizontal spacing between the legs is below 150ft and therefore, it can be concluded that the highest level of inaccuracy is less than 8%.

Figure 10.12 is similar to Figure 10.11 except for the leg diameter which has reduced from 2.5ft to 1.0ft. For a horizontal spacing of 100ft (30.5m), the inaccuracies have increased from 8% to 12% and for a spacing of 200ft (61m), the increase has been from 12% to 36%. As was previously stated, legs of 1.0ft diameter are not realistic and therefore it can be concluded that the inaccuracies for more realistic conditions are less than 8% (compare with 2% for polynomial approximation method).

Four-Leg Structure

Two four-legged structures as shown in Figures 10.13 and 10.14 were investigated. Figure 10.13 shows that for a dimension of 300ft (91.5m) and a leg diameter of 2.5ft, the inaccuracies are limited to 11%. Figure 10.14 is similar to Figure 10.13 except that the leg diameter

has reduced to 1.0ft. As a result, the inaccuracies have increased to a maximum of 25%. Again, the structure with the larger diameter is more realistic and hence it can be concluded that the inaccuracies are less than 11%.

The results of the above investigations show that the force-correlation method is satisfactory and that for realistic structures (reasonable dimensions, member diameters) the inaccuracies in kurtosis (fourth moment) are expected to be less than 11%. The computer time spent for calculating expectations of the form $E[F_i^2F_jF_k]$ and $E[F_iF_jF_kF_l]$ has reduced by about a thousand times in comparison with Burrows' model (analytical solutions) so that the number of nodes can be increased from 40 to about 200 nodes. Obviously, further investigation is required to validate the model with regard to various responses of a real jacket structure.

Summary and Conclusion

Two different models have been developed for reducing the computer run-time. The polynomial approximation model reduces the computer run-time by about 28 times in comparison with Burrows' model (analytical solutions) while the reduction for the force-correlation model is about 1000 times. As a result, the number of nodes can be increased from 40 (in Burrows' model) to 85 and 200, respectively (within the 30 minute run-time available on the ICL 1906S computer used by Burrows). For the test structures used in this study, the maximum level of inaccuracy in the kurtosis (fourth moment) was below 3% and 11% for the first and second models, respectively. In view of uncertainties in the input data to the model (such as environmental conditions, Morison's coefficients, etc.) these levels of inaccuracy are not significant. Furthermore, it

must be recognised that even the results of analytical model are only approximations to the observed values. It can therefore be concluded that for engineering purposes all three models are equally satisfactory. However, as previously mentioned, further investigation is required to validate the two approximate models with regard to various responses of a few typical jacket structures.

Ideally, the above models must be used at two different levels. In the first stage, a refined model of the structure with hundreds or even thousands of nodal loads will be used to calculate the variance of the response accurately. In the second stage, a coarser model of the structure (say, 200 nodes) will be used to estimate the fourth moments of the important responses. The second and the fourth moments of the response are then used to establish its probability distribution, which is required for calculating the extreme peak response.

Number of Nodes	$E(F_p^2)$ $E(F_p^4)$	$E(F_pF_q)$ $E(F_p^2F_q^2)$	$E(F_p^3F_q)$	$E(F_p^2F_qF_r)$	$E(F_pF_qF_rF_s)$
n	n	$\frac{n(n-1)}{2}$	n(n-1)	$\frac{n(n-1)(n-2)}{2}$	$\frac{n(n-1)(n-2)(n-3)}{4!}$
1	1	0	0	0	0
2	2	1	2	0	0
3	3	3	6	3	0
4	4	6	12	12	1
5	5	10	20	30	5
10	10	45	90	360	210
12	12	66	132	660	495
15	15	105	210	1,365	1,365
20	20	190	380	3,420	4,845
30	30	435	870	12,180	27,405
40	40	780	1,560	29,640	91,390
50	50	1,225	2,450	58,800	230,300
100	100	4,950	9,900	485,100	3,921,225

TABLE 10.1.
NUMBER OF EXPECTATIONS OF DIFFERENT COMBINATIONS OF
NODAL FORCES FOR A SYSTEM WITH n NODES
(BURROWS, 1982)

Data Set Number	Matrix of Correlation Coefficients of x_i, x_j, x_k, x_l				Matrix of cross-covariances of x_i, x_j, x_k, x_l			
1	0.1000E+01	0.0000E+00	0.2697E+00	0.0000E+00	0.1660E+05	0.0000E+00	0.76202+03	0.0000E+00
	0.0000E+00	0.1000E+01	0.0000E+00	0.6736E-01	0.0000E+00	0.7400E+09	0.0000E+00	0.1920E+07
	0.2697E+00	0.0000E+00	0.1000E+01	0.0000E+00	0.7620E+03	0.0000E+00	0.4810E+03	0.0000E+00
	0.0000E+00	0.6736E-01	0.0000E+00	0.1000E+01	0.0000E+00	0.1520E+07	0.0000E+00	0.6880E+06
2	0.1000E+01	0.2697E+00	0.2341E+00	0.2072E+00	0.1660E+05	0.7620E+03	0.4360E+03	0.2620E+03
	0.2697E+00	0.1000E+01	0.9683E+00	0.9060E+00	0.7620E+03	0.4810E+03	0.3070E+03	0.1950E+03
	0.2341E+00	0.9683E+00	0.1000E+01	0.9798E+00	0.4360E+03	0.3070E+03	0.2090E+03	0.1390E+03
	0.2072E+00	0.9060E+00	0.9798E+00	0.1000E+01	0.2620E+03	0.1950E+03	0.1390E+03	0.9630E+02
3	0.1000E+01	0.0000E+00	0.2697E+00	0.0000E+00	0.1660E+05	0.0000E+00	0.7620E+03	0.0000E+00
	0.0000E+00	0.1000E+01	0.0000E+00	0.3755E-01	0.0000E+00	0.7400E+09	0.0000E+00	0.2920E+06
	0.2697E+00	0.0000E+00	0.1000E+01	0.0000E+00	0.7620E+03	0.0000E+00	0.4810E+03	0.0000E+00
	0.0000E+00	0.3755E-01	0.0000E+00	0.1000E+01	0.0000E+00	0.2920E+06	0.0000E+00	0.8170E+05
4	0.1000E+01	0.0000E+00	0.2697E+00	0.2341E+00	0.1660E+05	0.0000E+00	0.7620E+03	0.4360E+03
	0.0000E+00	0.1000E+01	0.0000E+00	0.0000E+00	0.0000E+00	0.7400E+09	0.0000E+00	0.0000E+00
	0.2697E+00	0.0000E+00	0.1000E+01	0.9683E+00	0.7620E+03	0.0000E+00	0.4610E+03	0.3070E+03
	0.2341E+00	0.0000E+00	0.9683E+00	0.1000E+01	0.4360E+03	0.0000E+00	0.3070E+05	0.2090E+03
5	0.1000E+01	0.9683E+00	0.9060E+00	0.8348E+00	0.4810E+03	0.3070E+03	0.1950E+03	0.1310E+03
	0.9683E+00	0.1000E+01	0.9798E+00	0.9358E+00	0.3070E+03	0.2090E+03	0.1390E+03	0.9680E+02
	0.9060E+00	0.9798E+00	0.1000E+01	0.9869E+00	0.1950E+03	0.1390E+03	0.9630E+02	0.6930E+02
	0.8348E+00	0.9358E+00	0.9869E+00	0.1000E+01	0.1310E+03	0.9680E+02	0.6950E+02	0.5120E+02

TABLE 10.2a.
MATRIX OF CORRELATION COEFFICIENTS AND CROSS-COVARIANCES FOR DATA SETS
USED IN CHECKING THE EXPECTATIONS OF TABLE 10.2b

Expectations	First Set of Data		Second Set of Data		Third Set of Data		Fourth Set of Data		Fifth Set of Data	
	Analytical Solution	Numerical Value	Analytical Solution	Numerical Value	Analytical Solution	Numerical Value	Analytical Solution	Numerical Value	Analytical Solution	Numerical Value
$E[x_i x_j x_k^2]$	0.0000E00	-0.3110E-24	0.4270E+06	0.4270E+06	0.0000E00	0.000	0.0000E00	0.0000E00	0.8377E+05	0.8377E+05
$E[x_i^4 x_j x_k]$	0.0000E00	0.2522E-18	0.3200E+12	0.3200E+12	0.0000E00	0.000	0.0000E00	0.0000E00	0.4420E+09	0.4420E+09
$E[x_i x_j^2 x_k^3]$	0.8137E+15	0.8137E+15	0.6714E+09	0.6714E+09	0.8137E15	0.8137E+15	0.8137E15	0.8137E15	0.5904E+08	0.5904E+08
$E[x_i^3 x_j^4 x_k]$	0.6234E+26	0.6234E+26	0.8996E+14	0.8996E+14	0.6234E26	0.6234E26	0.6234E26	0.6234E26	0.4261E+12	0.4261E+12
$E[x_i^2 x_j^3 x_k^3]$	0.0000E+00	0.2516E-11	0.1040E+14	0.1040E14	0.0000E00	0.000	0.0000E00	0.0000E00	0.1258E+12	0.1258E+12
$E[x_i^3 x_j^3 x_k^4]$	0.0000E+00	-0.9052E-08	0.8255E+17	0.8255E17	0.0000E00	0.000	0.0000E00	0.0000E00	0.2314E+15	0.2314E+15
$E[x_i x_j x_k x_l]$	0.1158E+10	0.1158E+10	0.2714E+06	0.2714E+06	0.2225E+09	0.2225E+09	0.0000E00	-0.1955E-24	0.5836E+05	0.5836E+05
$E[x_i x_j x_k x_l^3]$	0.2391E+16	0.2391E+16	0.1210E+09	0.1210E+09	0.5454E14	0.5454E14	0.0000E00	0.5785E-22	0.1424E+08	0.1424E+08
$E[x_i x_j x_k^3 x_l^3]$	0.3450E+19	0.3450E+19	0.1779E+12	0.1779E+12	0.7869E17	0.7870E17	0.0000E00	-0.2290E-19	0.9663E+01	0.9663E+10
$E[x_i x_j^3 x_k^3 x_l^3]$	0.7681E+28	0.7681E+28	0.7491E+15	0.7491E+15	0.1749E27	0.1749E27	0.0000E00	0.4116E-09	0.1774E+14	0.1773E+14
$E[x_i^3 x_j^3 x_k^3 x_l^3]$	0.4011E+33	0.4011E+33	0.4310E+20	0.4308E+20	0.9131E+31	0.9131E31	0.0000E00	0.1332E-03	0.8261E+17	0.8257E17

TABLE 10.2b.
CHECKING ANALYTICAL SOLUTIONS TO EXPECTATIONS BY COMPARING
THE RESULTS WITH THE RESULTS OF NUMERICAL INTEGRATION

Matrix of Correlation Coefficients of X_{2i-1}, X_{2i}, X_{2j-1}, X_{2j}				Matrix of Cross-Covariances of X_{2i-1}, X_{2i}, X_{2j-1}, X_{2j}			
1.000	0.000	0.2692	0.000	$0.1664*10^{5}$	0.000	$0.7620*10^{3}$	0.000
0.000	1.000	0.000	$0.6747*10^{-1}$	0.000	$0.7398*10^{9}$	0.000	0.1522
0.2692	0.000	1.000	0.000	$0.7620*10^{3}$	0.000	$0.4815*10^{3}$	0.000
0.000	$0.6747*10^{-1}$	0.000	1.000	0.000	$0.1522*10^{7}$	0.000	$0.6876*10^{6}$

TABLE 10.3a.
MATRIX OF CORRELATION COEFFICIENTS AND CROSS-COVARIANCES
FOR DATA SETS USED IN CHECKING EXPECTATIONS OF TABLE 10.3b.

T Terms	Polynomial Approximation (1)	Analytical Solution & Numerical Integration (2)	Percentage Difference (3) = $\frac{(1)-(2)}{(2)} * 100$
T_7	0.3889E17	0.3882E17	0.18%
T_8	0.000	0.000	0.00%
T_9	0.000	0.000	0.00%
T_{10}	0.3377E16	0.3377E16	0.00%
T_{11}	0.000	0.000	0.00%
T_{12}	0.1264E16	0.1264E16	0.00%
T_{13}	0.4379E16	0.4103E16	6.73%
T_{14}	0.000	0.000	0.00%
T_{15}	0.5920E07	0.5559E07	6.49%
T_{16}	0.000	0.000	0.00%
T_{17}	0.000	0.000	0.00%
T_{18}	0.1522E07	0.1522E07	0.00%
T_{19}	0.9208E15	0.9208E15	0.00%
T_{20}	0.5712E15	0.5712E15	0.00%
T_{21}	0.000	0.000	0.00%
T_{22}	0.5146E15	0.5146E15	0.00%
T_{23}	0.5133E15	0.5133E15	0.00%
T_{24}	0.000	0.000	0.00%
T_{25}	0.000	0.000	0.00%
T_{26}	0.000	0.000	0.00%
T_{27}	0.9008E13	0.8439E13	6.74%

TABLE 10.3b.
CHECKING THE RESULTS OF POLYNOMIAL APPROXIMATION FOR EXPECTATIONS USED IN $E[F_i^3F_j]$, $E[F_iF_j]$, $E[F_i^2F_j^2]$

Data Set Number	Matrix of Correlation Coefficients between x_{2i-1}, x_{2i}, x_{2j-1}, x_{2j}, x_{2k-1}, x_{2k}, x_{2l-1}, x_{2l}							
1	0.1000E+01	0.2000E+00	0.3000E+00	0.4000E+00	0.5000E+00	0.6000E+00	0.70002+00	0.8000E+00
	0.2000E+00	0.1000E+01	0.3500E+00	0.4500E+00	0.5500E+00	0.6500E+00	0.7500E+00	0.8500E+00
	0.3000E+00	0.3500E+00	0.1000E+01	0.2800E+00	0.3800E+00	0.4800E+00	0.5800E+00	0.6800E+00
	0.4000E+00	0.4500E+00	0.2800E+00	0.1000E+01	0.3200E+00	0.4200E+00	0.5200E+00	0.6200E+00
	0.5000E+00	0.5500E+00	0.3800E+00	0.3200E+00	0.1000E+01	0.7200E+00	0.8200E+00	0.9200E+00
	0.6000E+00	0.6500E+00	0.4800E+00	0.4200E+00	0.7200E+00	0.1000E+01	0.2500E+00	0.3500E+00
	0.7000E+00	0.7500E+00	0.5800E+00	0.5200E+00	0.8200E+00	0.2500E+00	0.1000E+01	0.4500E+00
	0.8000E+00	0.8500E+00	0.6800E+00	0.6200E+00	0.9200E+00	0.3500E+00	0.4500E+00	0.1000E+01
2	0.1000E+01	0.2692E+00	0.2339E+00	0.2072E+00	0.1853E+00	0.1656E+00	0.1478E+00	0.1325E+00
	0.2692E+00	0.1000E+01	0.9683E+00	0.9059E+00	0.8375E+00	0.7674E+00	0.6991E+00	0.6377E+00
	0.2339E+00	0.9683E+00	0.1000E+01	0.9800E+00	0.9365E+00	0.8810E+00	0.8210E+00	0.7635E+00
	0.2072E+00	0.9059E+00	0.9800E+00	0.1000E+01	0.9866E+00	0.9537E+00	0.9099E+00	0.8636E+00
	0.1853E+00	0.8375E+00	0.9365E+00	0.9866E+00	0.1000E+01	0.9896E+00	0.9640E+00	0.9314E+00
	0.1656E+00	0.7674E+00	0.8810E+00	0.9537E+00	0.9896E+00	0.1000E+01	0.9921E+00	0.9736E+00
	0.1478E+00	0.6991E+00	0.8210E+00	0.9099E+00	0.9640E+00	0.9921E+00	0.1000E+01	0.9945E+00
	0.1325E+00	0.6377E+00	0.7635E+00	0.8636E+00	0.9314E+00	0.9736E+00	0.9945E+00	0.1000E+01
3	0.1000E+01	0.0000E+00	0.2339E+00	0.2072E+00	0.1853E+00	0.1656E+00	0.1478E+00	0.1325E+00
	0.0000E+00	0.1000E+01	0.0000E+00	0.0000E+00	0.0000E+00	0.0000E+00	0.0000E+00	0.0000E+00
	0.2339E+00	0.0000E+00	0.1000E+01	0.9800E+00	0.9365E+00	0.8810E+00	0.8210E+00	0.7635E+00
	0.2072E+00	0.0000E+00	0.9800E+00	0.1000E+01	0.9866E+00	0.9537E+00	0.9099E+00	0.8636E+00
	0.1853E+00	0.0000E+00	0.9365E+00	0.9866E+00	0.1000E+01	0.9896E+00	0.9640E+00	0.9314E+00
	0.1656E+00	0.0000E+00	0.8810E+00	0.9537E+00	0.9896E+00	0.1000E+01	0.9921E+00	0.9736E+00
	0.1478E+00	0.0000E+00	0.8210E+00	0.9099E+00	0.9640E+00	0.9921E+00	0.1000E+01	0.9945E+00
	0.1325E+00	0.0000E+00	0.7635E+00	0.8636E+00	0.9314E+00	0.9736E+00	0.9945E+00	0.1000E+01

TABLE 10.4a.
MATRIX OF CORRELATION COEFFICIENTS FOR CHECKING EXPECTATIONS
USED IN $E[F_i^2F_jF_k]$ (TABLE 10.4c) AND $E[F_iF_jF_kF_l]$ (TABLE 10.4d)

Data Set Number	Matrix of Cross-Covariances of x_{2i-1}, x_{2i}, x_{2j-1}, x_{2j}, x_{2k-1}, x_{2k}, x_{2l-1}, x_{2l}							
1	0.1660E+05	0.2287E+05	0.2204E+04	0.1186E+05	0.3678E+04	0.5028E+04	0.2606E+05	0.9021E+05
	0.2287E+05	0.7880E+06	0.1771E+05	0.9196E+05	0.2788E+05	0.3753E+05	0.1924E+06	0.6604E+06
	0.2204E+04	0.1771E+05	0.3250E+04	0.3675E+04	0.1237E+04	0.1780E+04	0.9555E+04	0.3393E+05
	0.1186E+05	0.9196E+05	0.3675E+04	0.5300E+05	0.4206E+04	0.6289E+04	0.3459E+05	0.1249E+06
	0.3678E+04	0.2788E+05	0.1237E+04	0.4206E+04	0.3260E+04	0.2674E+04	0.1353E+05	0.4597E+05
	0.5028E+04	0.3753E+05	0.1780E+04	0.6289E+04	0.2674E+04	0.4230E+04	0.4698E+04	0.1992E+05
	0.2606E+05	0.1924E+06	0.9555E+04	0.3459E+05	0.1353E+05	0.4698E+04	0.8350E+05	0.1138E+06
	0.9021E+05	0.6604E+06	0.3393E+05	0.1249E+06	0.4597E+05	0.1992E+05	0.1138E+06	0.7660E+06
2	0.1664E+05	0.7620E+03	0.4361E+03	0.2623E+03	0.1710E+03	0.1180E+03	0.8582E+02	0.6602E+02
	0.7620E+03	0.4815E+03	0.3071E+03	0.1951E+03	0.1315E+03	0.9303E+02	0.6905E+02	0.5405E+02
	0.4361E+03	0.3071E+03	0.2089E+03	0.1390E+03	0.9683E+02	0.7035E+02	0.5341E+02	0.4262E+02
	0.2623E+03	0.1951E+03	0.1390E+03	0.9631E+02	0.6927E+02	0.5171E+02	0.4019E+02	0.3274E+02
	0.1710E+03	0.1315E+03	0.9683E+02	0.6927E+02	0.5118E+02	0.3911E+02	0.3104E+02	0.2574E+02
	0.1180E+03	0.9303E+02	0.7035E+02	0.5171E+02	0.3911E+02	0.3052E+02	0.2467E+02	0.2078E+02
	0.8582E+02	0.6905E+02	0.5341E+02	0.4019E+02	0.3104E+02	0.2467E+02	0.2026E+02	0.1729E+02
	0.6602E+02	0.5405E+02	0.4262E+02	0.3274E+02	0.2574E+02	0.2078E+02	0.1729E+02	0.1492E+02
3	0.1664E+05	0.0000E+00	0.4361E+03	0.2623E+03	0.1710E+03	0.1180E+03	0.8582E+02	0.6602E+02
	0.0000E+00	0.7398E+09	0.0000E+00	0.0000E+00	0.0000E+00	0.0000E+00	0.0000E+00	0.0000E+00
	0.4361E+03	0.0000E+00	0.2089E+03	0.1390E+03	0.9683E+02	0.7035E+02	0.5341E+02	0.4262E+02
	0.2623E+03	0.0000E+00	0.1390E+03	0.9631E+02	0.6927E+02	0.5171E+02	0.4019E+02	0.3274E+02
	0.1710E+03	0.0000E+00	0.9683E+02	0.6927E+02	0.5118E+02	0.3911E+02	0.3104E+02	0.2574E+02
	0.1180E+03	0.0000E+00	0.7035E+02	0.5171E+02	0.3911E+02	0.3052E+02	0.2467E+02	0.2078E+02
	0.8582E+02	0.0000E+00	0.5341E+02	0.4019E+02	0.3104E+02	0.2467E+02	0.2026E+02	0.1729E+02
	0.6602E+02	0.0000E+00	0.4262E+02	0.3274E+02	0.2574E+02	0.2078E+02	0.1729E+02	0.1492E+02

TABLE 10.4b.
MATRIX OF CROSS-COVARIANCES FOR CHECKING EXPECTATIONS
USED IN $E[F_i^2F_jF_k]$ (TABLE 10.4c) AND $E[F_iF_jF_kF_l]$ (TABLE 10.4d)

Expectations	First Data Set			Second Data Set			Third Data Set		
	Polynomial Approximation	Analytical Solution and/or Numerical Integration	Percentage Difference	Polynomial Approximation	Analytical Solution and/or Numerical Integration	Percentage Difference	Polynomial Approximation	Analytical Solution and/or Numerical Integration	Percentage Difference
T_{28}	0.3046E17	0.3031E17	0.49%	0.3327E14	0.3351E14	-0.72%	0.3327E14	0.3351E14	-0.72%
T_{29}	0.3704E15	0.3649E15	1.51%	0.1762E13	0.1732E13	1.73%	0.1762E13	0.1732E13	1.73%
T_{30}	0.1328E16	0.1326E16	0.15%	0.8225E12	0.8040E12	2.30%	0.8225E12	0.8040E12	2.30%
T_{31}	0.1708E14	0.1708E14	0.00%	0.4913E11	0.4913E11	0.00%	0.4913E11	0.4913E11	0.00%
T_{32}	0.2077E14	0.2043E14	1.66%	0.5987E08	0.6232E08	-3.93%	0.2197E14	0.2178E14	0.87%
T_{33}	0.2697E12	0.2642E12	2.08%	0.2761E07	0.2830E07	-2.44%	0.1242E13	0.1207E13	2.90%
T_{34}	0.8692E12	0.8611E12	0.94%	0.1215E07	0.1233E07	-1.46%	0.6051E12	0.5876E12	2.98%
T_{35}	0.1186E12	0.1185E12	0.00%	0.6119E05	0.6119E05	0.00%	0.3825E11	0.3825E11	0.00%
T_{36}	-	-	-	-	-	-	0.000	0.000	0.00%
T_{37}	-	-	-	-	-	-	0.000	0.000	0.00%
T_{38}	-	-	-	-	-	-	0.000	0.000	0.00%
T_{39}	-	-	-	-	-	-	0.000	0.000	0.00%

TABLE 10.4c.
CHECKING THE RESULTS OF POLYNOMIAL APPROXIMATIONS FOR EXPECTATIONS USED IN $E[F_i^2 F_j F_k]$

Expectations	First Data Set			Second Data Set			Third Data Set		
	Polynomial Approximation	Analytical Solution and/or Numerical Integration	Percentage Difference	Polynomial Approximation	Analytical Solution and/or Numerical Integration	Percentage Difference	Polynomial Approximation	Analytical Solution and/or Numerical Integration	Percentage Difference
T_{40}	0.1998E18	0.2048E18	-2.44%	0.3486E11	0.3561E11	-2.11%	0.3486E11	0.3561E11	-2.11%
T_{41}	-	-	-	0.2673E10	0.2731E10	-2.12%	0.2673E10	0.2731E10	-2.12%
T_{42}	0.1549E16	0.1580E16	-1.96%	0.1440E10	0.1462E10	-1.50%	0.1440E10	0.1462E10	-1.50%
T_{43}	0.9271E13	0.9191E13	+0.87%	0.1218E09	0.1217E09	+0.08%	0.1218E09	0.1217E09	+0.08%
T_{44}	0.7385E16	0.7658E16	-3.56%	0.6658E09	0.6762E09	-1.54%	0.6658E09	0.6762E09	-1.54%
T_{45}	-	-	-	0.5491E08	0.5498E08	-0.13%	0.5491E08	0.5498E08	-0.13%
T_{46}	0.5561E14	0.5668E14	-1.89%	0.3026E08	0.2994E08	+1.07%	0.3026E08	0.2994E08	1.07%
T_{47}	0.3582E12	0.3613E12	-0.86%	0.2730E07	0.2659E07	+2.67%	0.2730E07	0.2659E07	2.67%
T_{48}	0.5802E16	0.5957E16	-2.60%	0.1197E09	0.1253E09	-4.47%	0.000	0.000	0.00%
T_{49}	-	-	-	0.9159E07	0.9578E07	-4.37%	0.000	0.000	0.00%
T_{50}	0.4455E14	0.4461E14	-0.13%	0.4977E07	0.5171E07	-3.75%	0.000	0.000	0.00%
T_{51}	-	-	-	0.4194E06	0.4281E06	-2.03%	0.000	0.000	0.00%
T_{52}	0.2105E15	0.2171E15	-3.04%	0.2381E07	0.2481E07	-4.03%	0.000	0.000	0.00%
T_{53}	-	-	-	0.1964E06	0.2015E06	-2.53%	0.000	0.000	0.00%
T_{54}	0.1541E13	0.1528E13	+0.85%	0.1096E06	0.1113E06	-1.53%	0.000	0.000	0.00%
T_{55}	0.1067E11	0.1067E11	0.00%	0.9893E04	0.9893E04	0.00%	0.000	0.000	0.00%

TABLE 10.4d.
CHECKING THE RESULTS OF POLYNOMIAL APPROXIMATIONS FOR EXPECTATIONS USED IN $E[F_iF_jF_kF_l]$

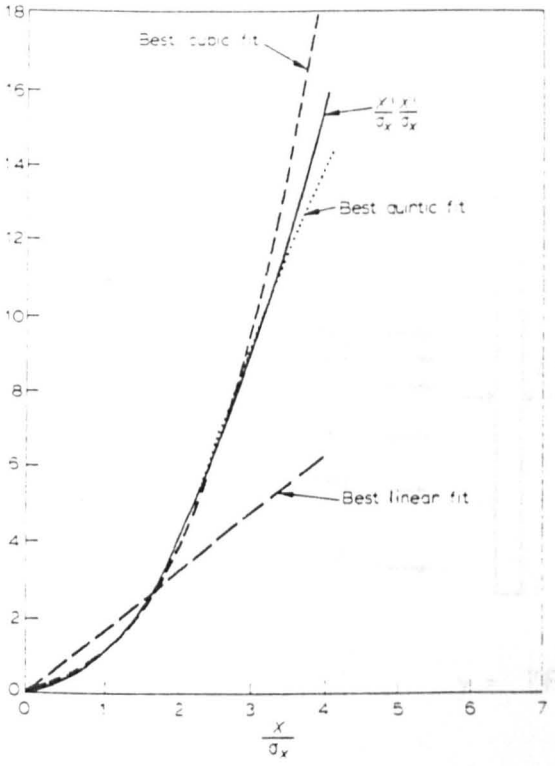

FIGURE 10.1. POLYNOMIAL APPROXIMATION TO X|X| FROM LEAST SQUARE ERROR FITTING (Burrows, 1983)

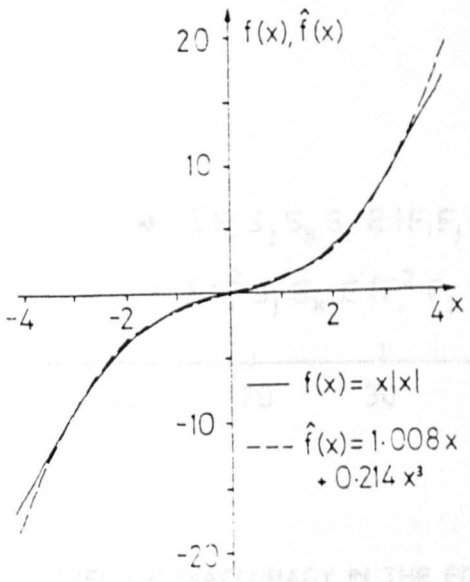

FIGURE 10.2. POLYNOMIAL APPROXIMATION TO X|X| FROM MOMENT FITTING (Bruce, 1985)

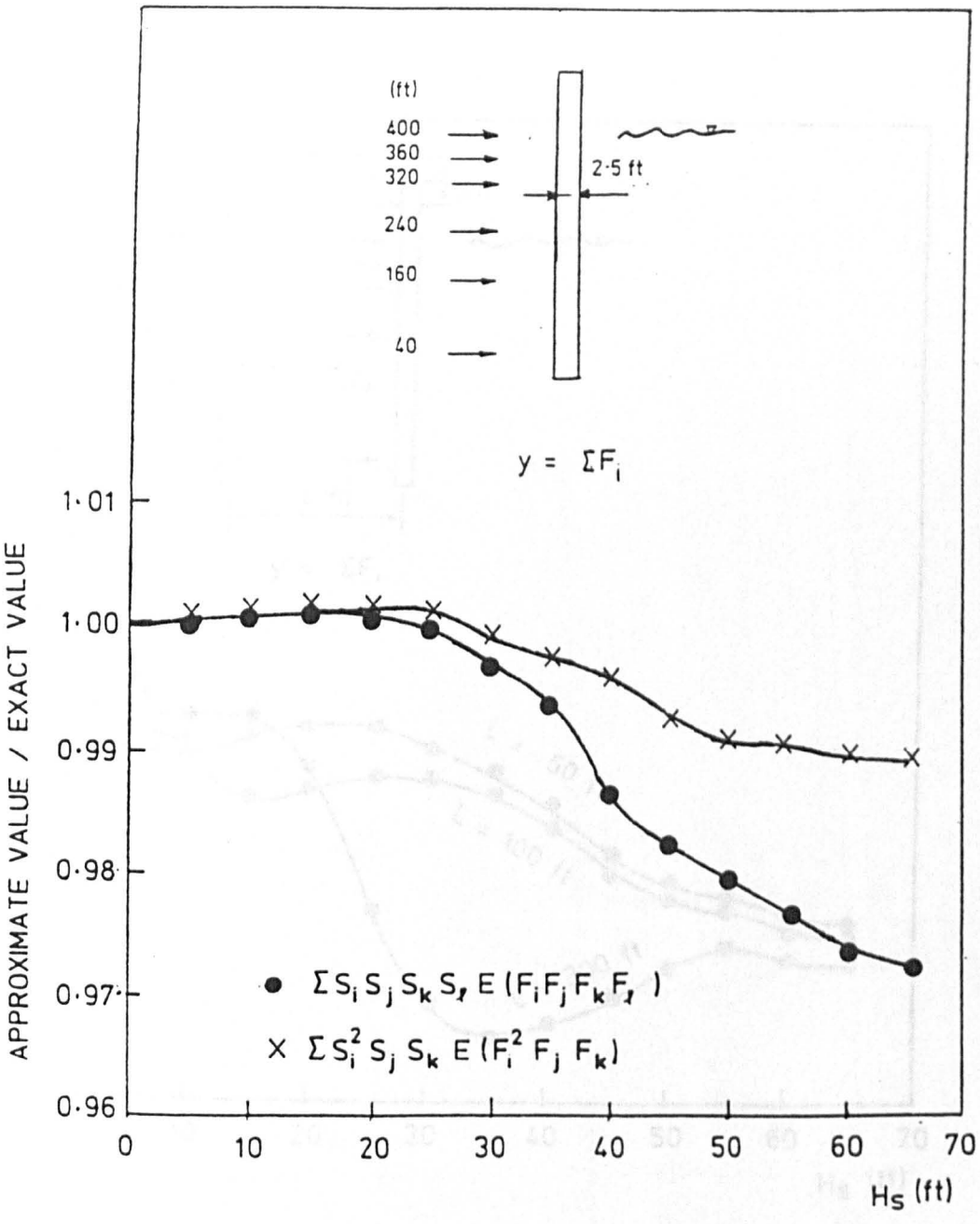

FIGURE 10.3. LEVEL OF INACCURACY IN THE POLYNOMIAL APPROXIMATION METHOD FOR SHEAR AT BASE

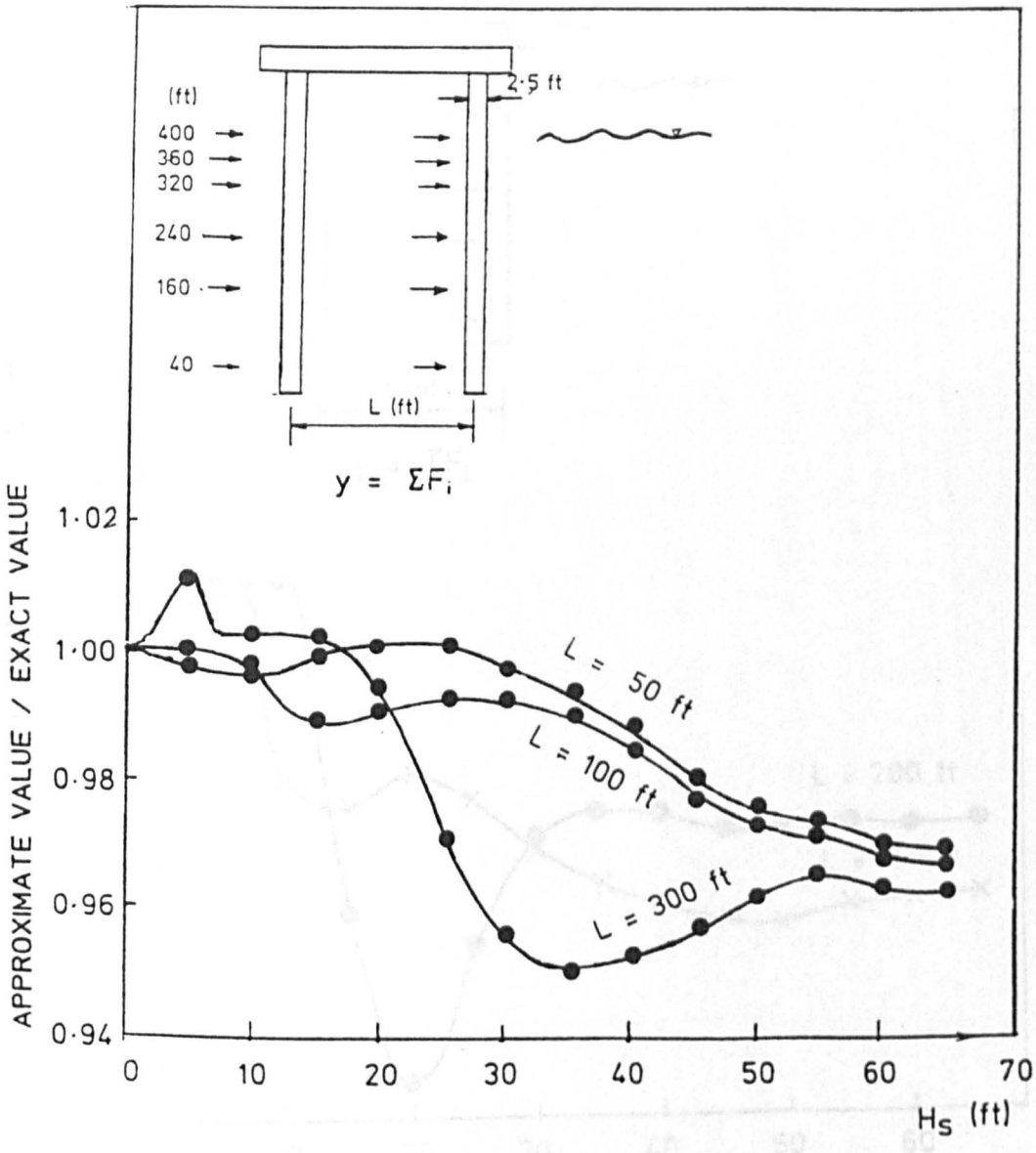

FIGURE 10.4. LEVEL OF INACCURACY IN $\Sigma S_i S_j S_k S_l E(F_i F_j F_k F_l)$ DERIVED FROM POLYNOMIAL APPROXIMATION METHOD FOR SHEAR AT BASE

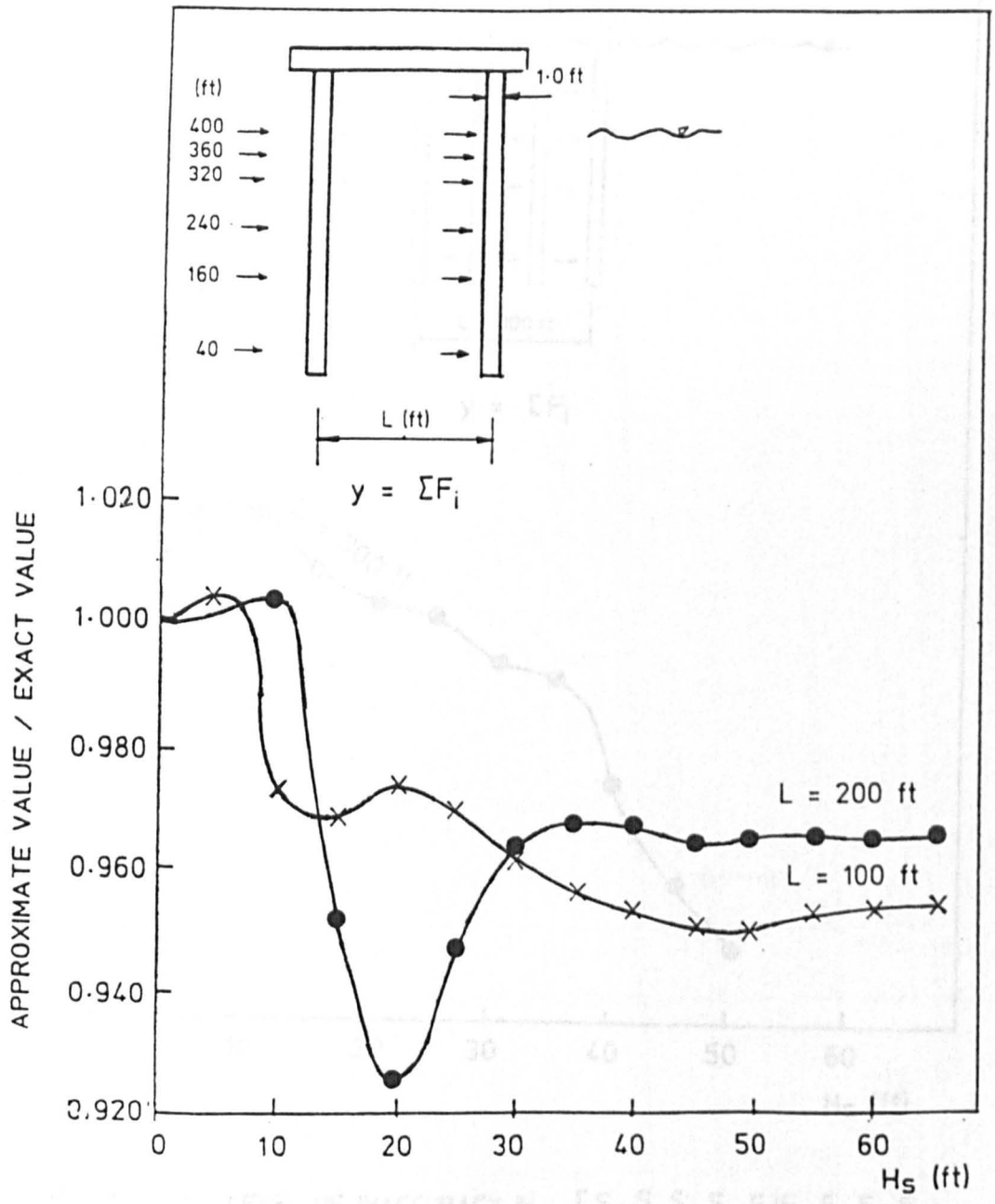

FIGURE 10.5. LEVEL OF INACCURACY IN $\Sigma S_i S_j S_k S_l E(F_i F_j F_k F_l)$ DERIVED FROM POLYNOMIAL APPROXIMATION METHOD FOR SHEAR AT BASE

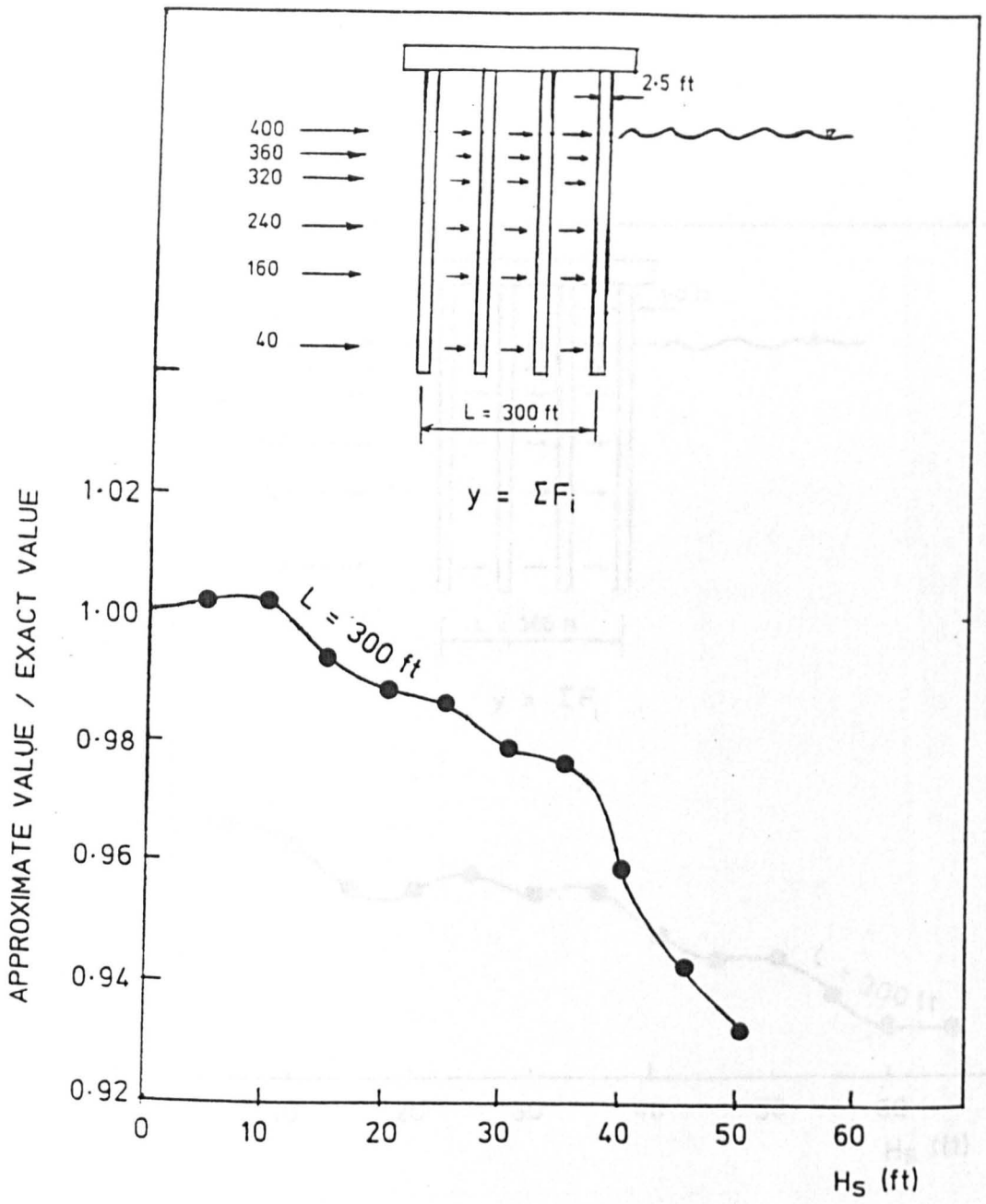

FIGURE 10.6. LEVEL OF INACCURACY IN $\Sigma S_i S_j S_k S_l E(F_i F_j F_k F_l)$ DERIVED FROM POLYNOMIAL APPROXIMATION METHOD FOR SHEAR AT BASE

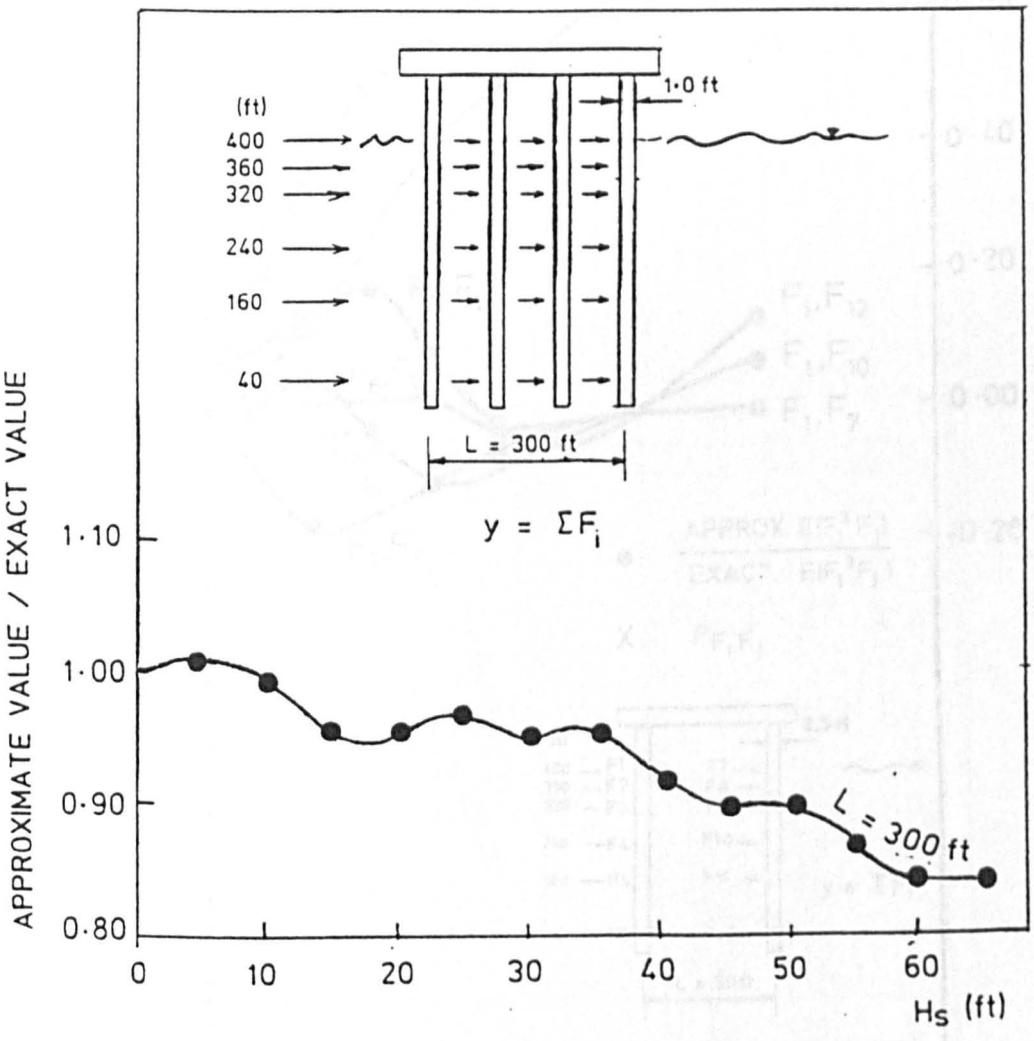

FIGURE 10.7 LEVEL OF INACCURACY IN $\Sigma S_i\ S_j\ S_k\ S_l\ E(F_i\ F_j\ F_k\ F_l)$ DERIVED FROM POLYNOMIAL APPROXIMATION METHOD FOR SHEAR AT BASE

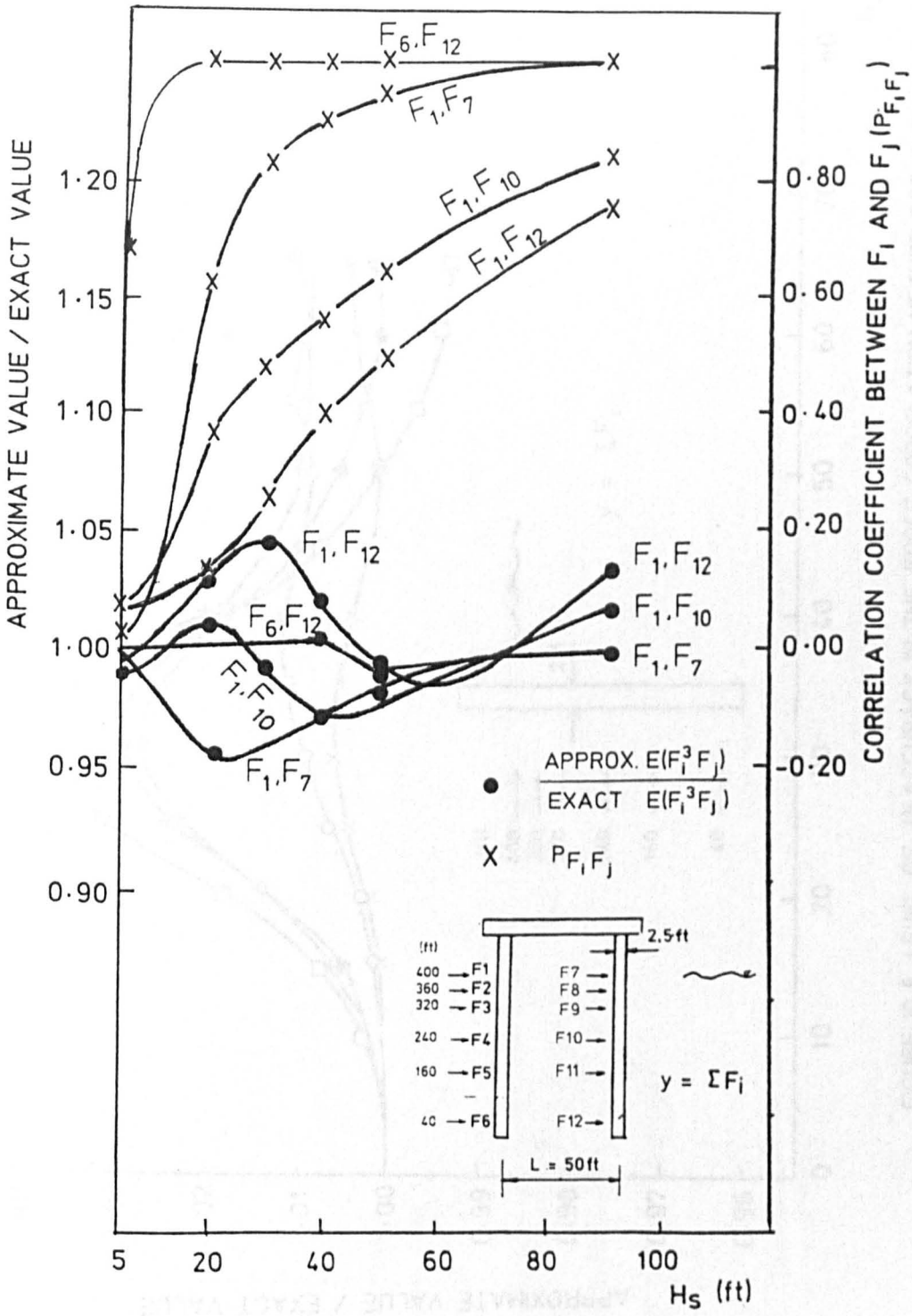

FIGURE 10.8 LEVEL OF INACCURACY IN $E(F_i^3 F_j)$ DERIVED FROM FORCE CORRELATION METHOD

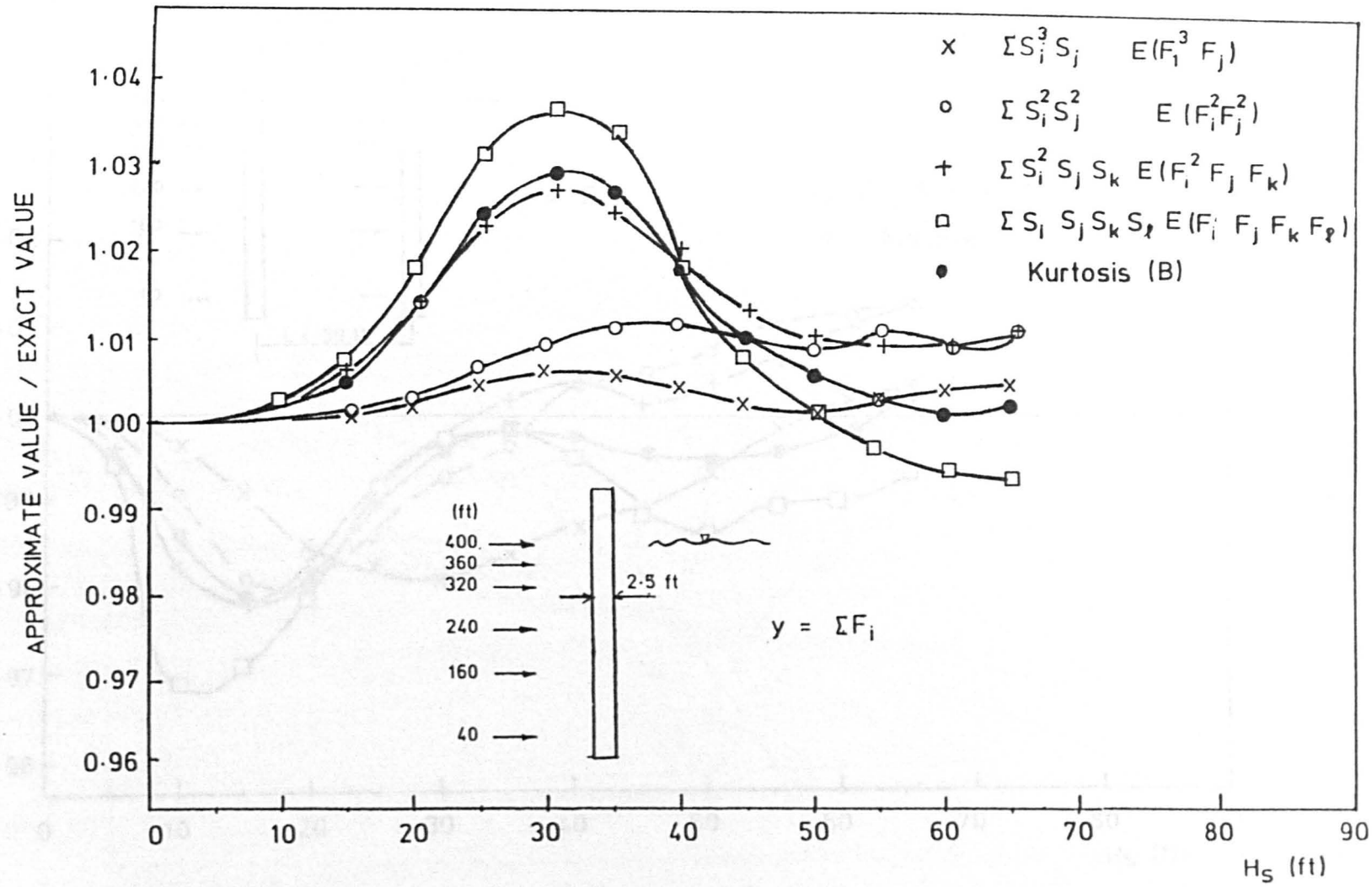

FIGURE 10.9. LEVEL OF INACCURACY IN THE FORCE CORRELATION METHOD FOR SHEAR AT BASE

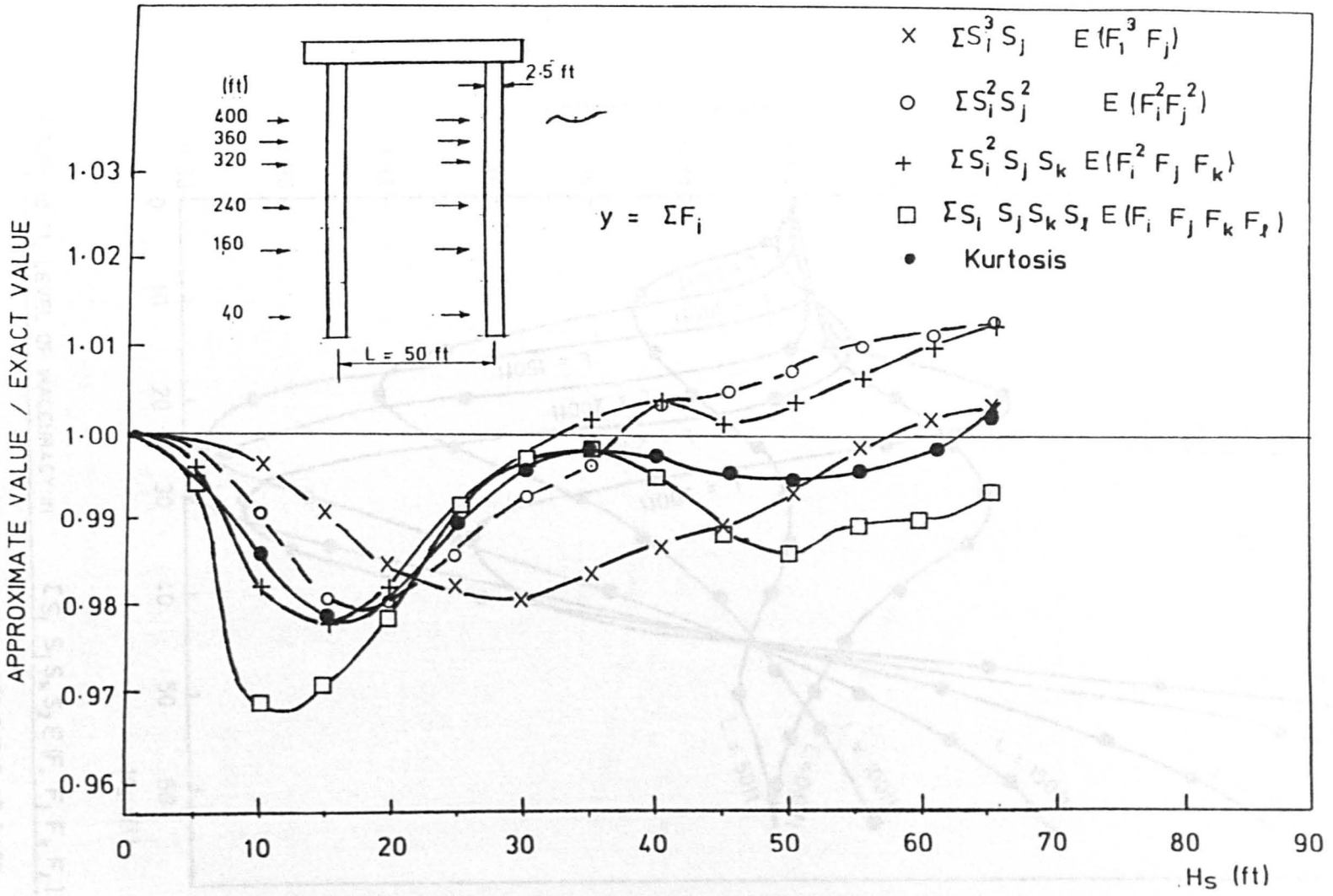

FIGURE 10.10 LEVEL OF INACCURACY IN THE FORCE CORRELATION METHOD FOR SHEAR AT BASE

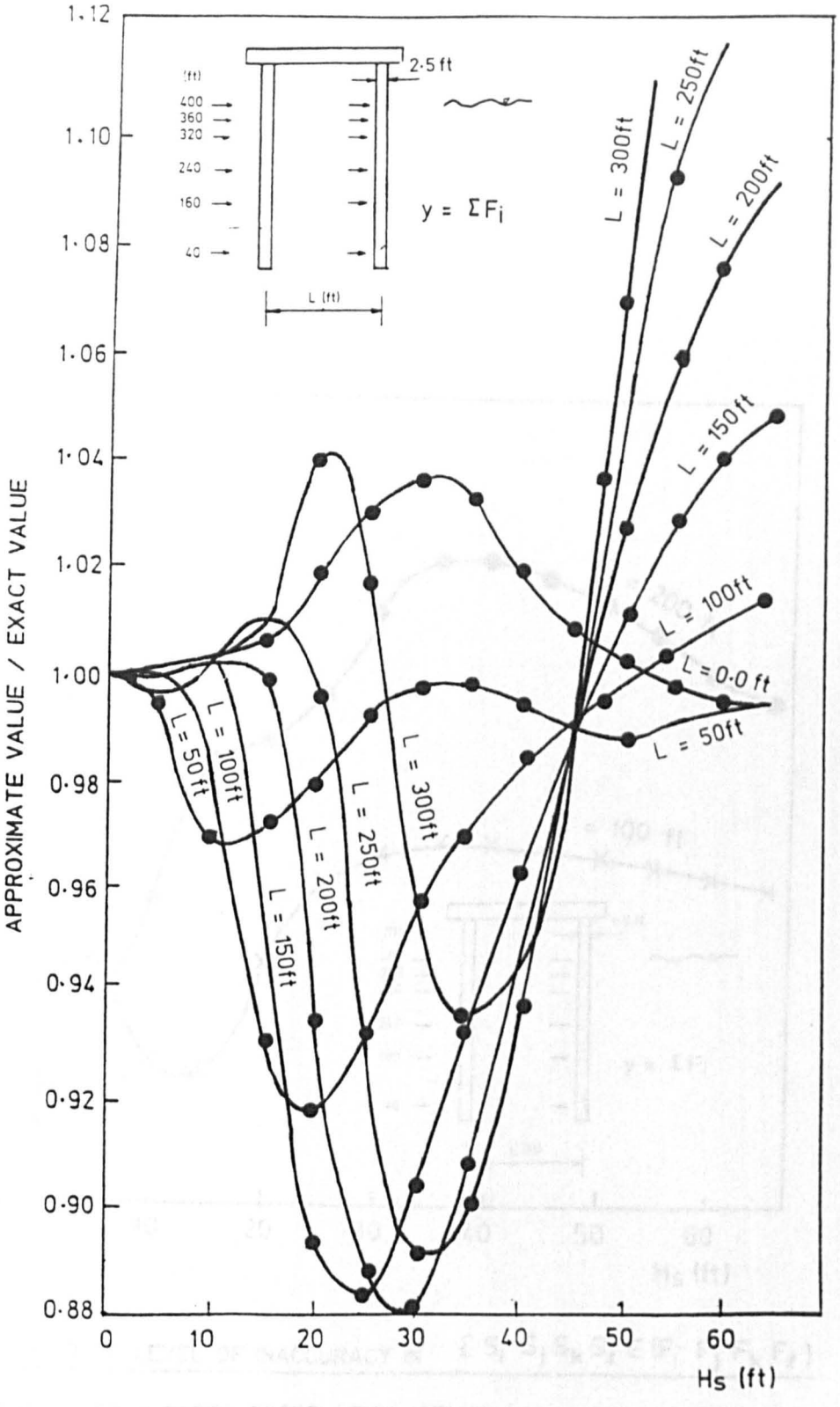

FIGURE 10.11. LEVEL OF INACCURACY IN $\Sigma S_i S_j S_k S_l E(F_i F_j F_k F_l)$

DERIVED FROM FORCE CORRELATION METHOD FOR SHEAR AT BASE

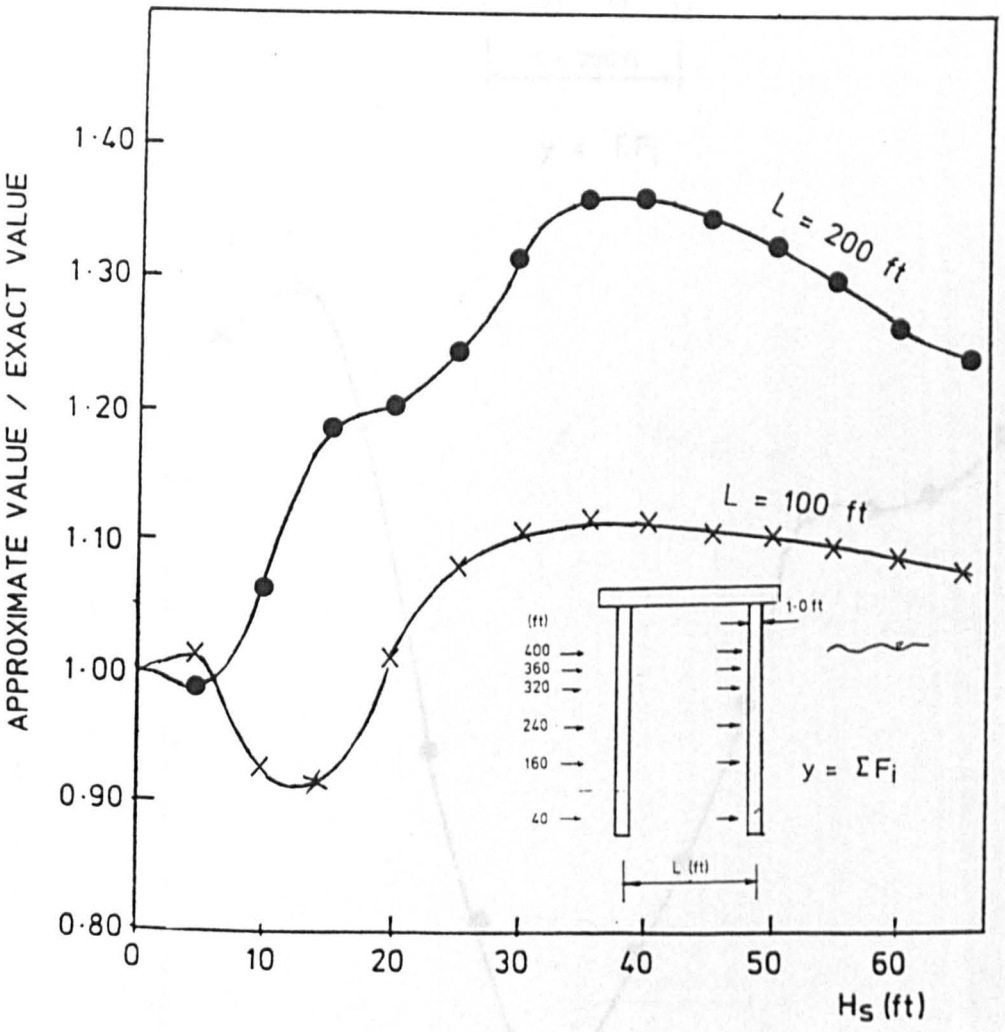

FIGURE 10. 12. LEVEL OF INACCURACY IN $\Sigma S_i S_j S_k S_l E(F_i F_j F_k F_l)$

DERIVED FROM FORCE CORRELATION METHOD FOR SHEAR AT BASE

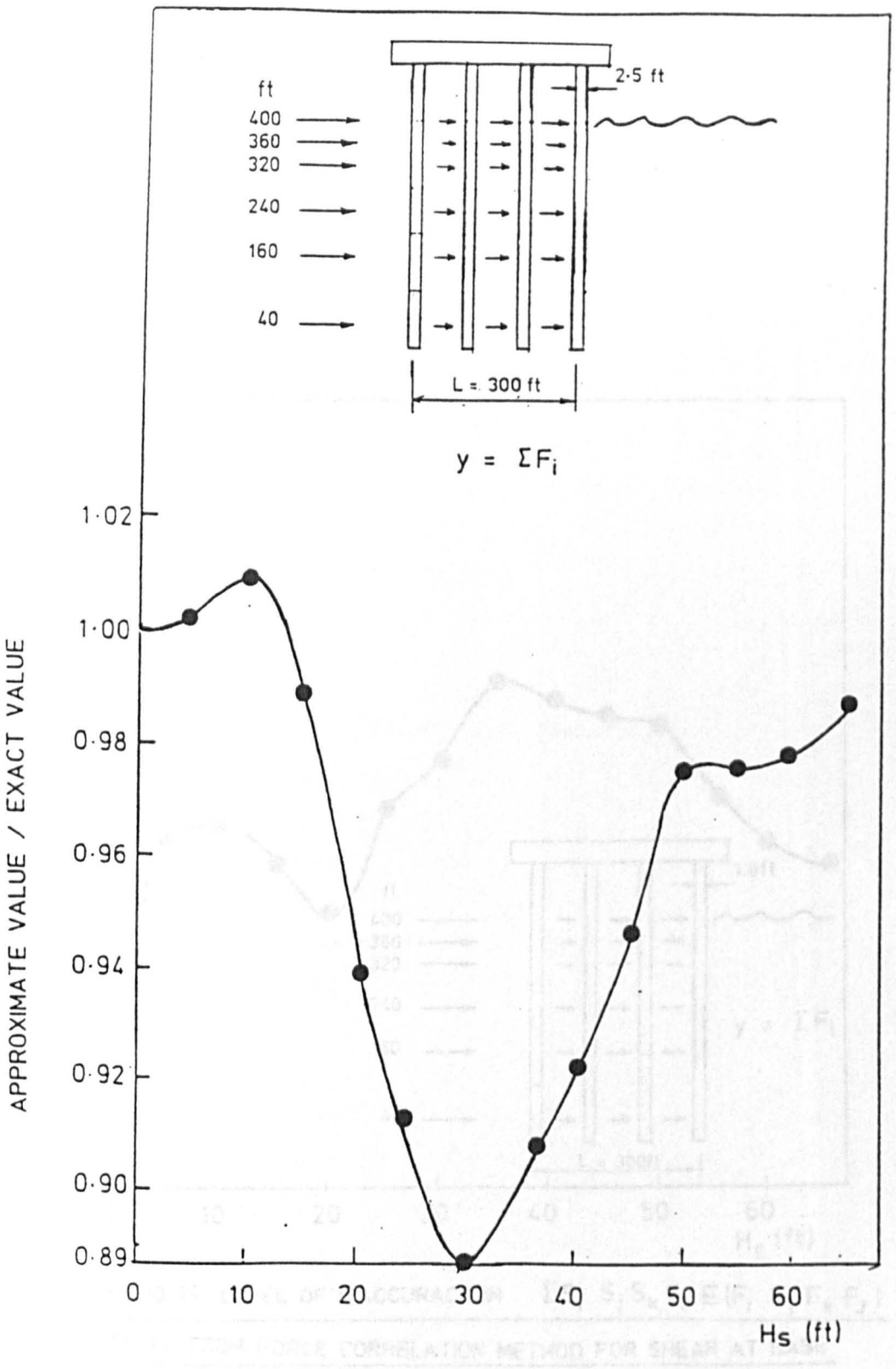

FIGURE 10.13 LEVEL OF INACCURACY IN $\Sigma S_i S_j S_k S_l E(F_i F_j F_k F_l)$

DERIVED FROM FORCE CORRELATION METHOD FOR SHEAR AT BASE

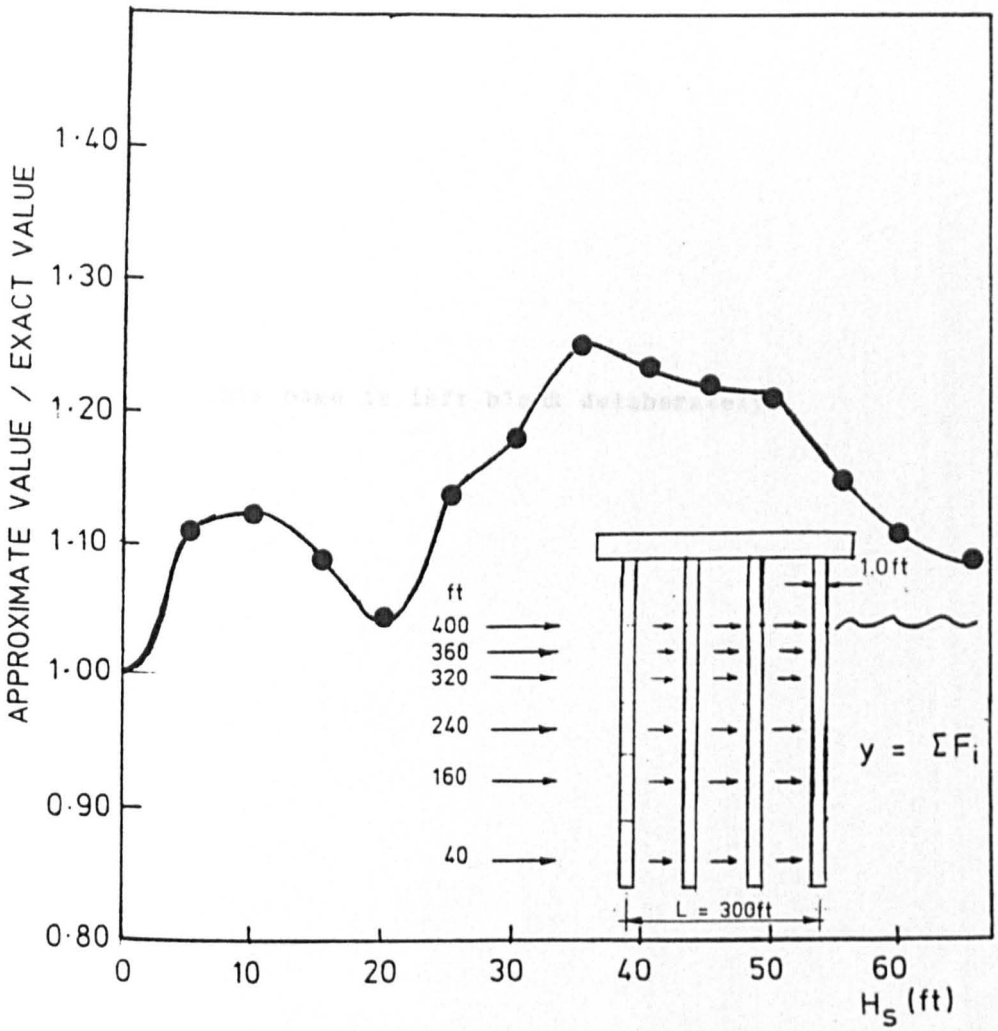

FIGURE 10.14. LEVEL OF INACCURACY IN $\Sigma S_i\ S_j S_k S_l\ E(F_i\ F_j F_k F_l)$ DERIVED FROM FORCE CORRELATION METHOD FOR SHEAR AT BASE

This page is left blank deliberately.

This page is left blank deliberately.

Chapter 11

Conclusions

Wave Loading on Flexible Cylinders

The objective of this study was to assess the suitability of the relative motion form of Morison's equation in describing random wave loading on flexible cylinders. The data base for this study was eleven 170-minute runs taken from an experimental programme on wave loading on and the response of a flexible (compliant) cylinder at Christchurch Bay, UK (1987). Furthermore, different methods of determining Morison's coefficients from the analysis of wave load data have been critically assessed. The following conclusions have been made.

1. The eleven data sets have been divided into two groups, low-intensity runs with a significant wave height of $H_s \approx 1.5$m and high-intensity runs with a significant wave height of $H_s \approx 3.75$m.

2. While close to Gaussian distribution, the surface elevation time series show departures consistent with finite amplitude effects.

3. The Rayleigh distribution based on significant wave height ($H_s = 4\sigma_\eta$) can lead to an overestimation of 7 to 14% for the upper 5% quantile of the wave heights at Christchurch Bay. The modified Rayleigh distribution (incorporating the factor 0.925) provides an improved fit.

4. Near the peak of the wave spectrum, the sea is almost long-crested with high powers of s in the full circle cosine-power spreading function ($12 < s < 24$). At twice the peak frequency, the sea is more short-crested with s in the range of 2 to 6.

5. Data for the cylinder collected in the lower sea-state corresponds to Keulegan-Carpenter numbers (K) in the range $8.5 < K < 12$ and Reynolds numbers (R_e) in the range $1.5*10^5 < R_e < 2.7*10^5$. The shear layers are expected to be turbulent under the effect of three-dimensional wave-induced flow. The reduced velocity is between $0.60 < u_r < 3.4$ so that synchronisation is not highly possible. In-line forces are inertia-dominated and hence C_d values are not reliable.

6. Data for the cylinder collected in the higher sea state corresponds to Keulegan-Carpenter numbers in the range $21 < K < 37$ so that in-line forces are in the drag-inertia regime. The Reynolds numbers lie in the range $3.6*10^5 < R_e < 5.7*10^5$; therefore the shear layers are turbulent. The reduced velocity ranges from 4.9 to 7.2; hence synchronisation is expected. This expectation was confirmed by the analysis of transverse forces.

7. Neglecting the relative motions between the fluid and the cylinder (rigid cylinder assumption) C_d and C_m were determined by the method of moments. It was shown that ignoring the directionality of the sea has a small effect on the values of C_d and C_m so that the assumption of uni-directionality for the waves in derivation of C_d and C_m is justified. Furthermore, it was shown that higher order moments such as $E[u^8]$ needed in the method of moments must be calculated based on the assumption that water particle kinematics are Gaussian distributed. The use of observed values of higher order moments leads to unstable

results. The rigid cylinder assumption leads to C_m values which are higher (1.8-2.2) than would normally be anticipated for these conditions based on R_e and K.

8. To derive drag and inertia coefficients from the relative motion form of Morison's equation, it was necessary to shift water particle kinematics from their point of measurement to the cylinder axis. It was shown that the effect of phase angle errors (introduced as a result of the shifting process) on the values of C_d and C_m determined from the method of moments is negligible.

9. From the evidence presented in Appendix A, it is believed that the cylinder displacement at about cylinder's natural frequency (after the sign of cylinder displacement was reversed) has the wrong sign. It was shown that the effect of this error on the C_d and C_m values determined from the method of moments is negligible.

10. A new relationship, which puts upper and lower limits on the correlation coefficient between two random processes when their frequency spectra are known, has been presented.

11. The Least Square Error Method has been critically assessed. It was proved that this method and Bearman's method lead to predicted forces with smaller variances than those of the observed forces. In particular, the two methods are not suitable for analysing long records of wave data, where the fit between the observed and predicted forces cannot be expected to be very good.

12. A new method, named Maximum Correlation method, has been introduced which has all the advantages of the Least Square Error Method but leads to predicted forces with variances equal to those of the observed forces.

13. It has been suggested that whatever method is used in derivation of Morison's coefficients, the results must be adjusted so that the variance of the observed and predicted forces are equal. It is expected that this exercise will eliminate some of the discrepancy between the reported results from different investigators.

14. Due to large phase angle errors in the high-frequency components of shifted water particle kinematics, it was decided to eliminate them in the time-domain analysis of the wave records. Removing the high-frequency components has the extra advantage that C_d and C_m values are not affected by the sign error in the high-frequency components of the cylinder displacement.

15. The C_d and C_m values from Maximum Correlation Method are higher than those of the Least Square Error Method. The average increase is about 10% for high-intensity runs and 35% for low-intensity runs (based on Level 3 and Level 4 results).

16. Time-domain Morison's coefficients have been obtained from the analysis of filtered data. It was therefore necessary to a adjust them to the full-frequency range. The adjustment was carried out by equating the variance of the observed and predicted forces

(full-frequency) so that C_m/C_d ratio would be the same as that obtained from the analysis of the filtered data.

17. The resultant C_d and C_m values from both method of moments and Maximum Correlation Method do not show a clear trend with basic hydrodynamic parameters. However, the C_m values decrease with increasing values of acceleration parameter (ratio between the standard deviations of the cylinder and water particle accelerations) when the cylinder's response is considered in the derivation of Morison's coefficients. When the response is ignored (rigid cylinder assumption), the C_m values show a tendency to increase with increasing values of acceleration parameter. The data base of this study does not allow a similar investigation to be carried out with regard to the variation of C_d with the velocity parameter (ratio between the standard deviations of the cylinder and water particle velocity).

18. The acceleration parameter ($\sigma_f/\sigma_{\dot{u}}$) is dependent on the ratio between the wave frequency content and the cylinder's natural frequency. Therefore, it is expected that C_m values should decline with f_w/f_s where f_w is the most energetic wave frequency and f_s is the cylinder's natural frequency. However, the cylinder's response is dependent on the entire wave frequency content and therefore, the correlation of C_m with f_w/f_s is not as good as its correlation with the acceleration parameter.

19. Based on the results of this study, the following values for Morison's coefficients are recommended. C_m is recommended to be read from Figure 9.58. For low-intensity runs, a C_d value of 1.0 and for high-intensity runs, C_d values in the range of 0.70 to 0.85 are recommended.

20. The extreme peaks of the predicted forces (from method of moments and Maximum Correlation Method) are lower than those of the observed forces by as much as 40%. However, applying the predicted forces to the cylinder the predicted and observed extreme peaks of the response are in reasonable agreement. One possible explanation for this phenomenon is that the extreme peak forces are not well correlated along the length of the cylinder and therefore, they do not lead to corresponding extreme responses.

21. There is a tendency for C_d values to reduce from Level 2 to Level 4, in agreement with previous Christchurch Bay studies. The reason behind this observation is not known.

22. It has been shown that the linearisation coefficient used in spectral techniques ($c = \sqrt{8/\pi}$) is not appropriate. The appropriate value for this coefficient is $c = \sqrt{3}$.

23. The overall conclusion of this study is that the relative motion form of Morison's equation with appropriate C_d and C_m values can adequately describe the response of an offshore structure exposed to random wave loading. Obviously further investigation is

required to establish the validity of this conclusion with regard to more complex structures.

Probabilistic Analysis of Offshore Structures

Risk analysis of offshore structures exposed to random wave loading calls for the establishment of the long-term peak distribution of critical responses. This, in turn, depends on the short-term distribution of the response itself, which is of the Pierson-Holmes (P/H) type.

The P/H distribution is fully defined by its first four statistical moments. In the absence of current, the first and third moments are zero, and hence the distribution is defined by its second and fourth statistical moments. These moments are functions of different combinations of nodal forces, which (according to Morison's equation) are functions of the (Gaussian-distributed) water particle kinematics at the nodes.

The existing model, developed by Burrows (1983), is based on the analytical solution to these expectations. However, due to excessive computer run-time, only a coarse model of the structure can be used in the analysis (say 40 nodes), which is not enough for the adequate description of the continuous wave loading on the structure. The objective of this study was to reduce the computer run-time by introducing appropriate approximations so that a more refined model of the structure (more nodes) can be used. Two different methods have been used for reducing the computer run-time, as explained below, and the following conclusions have been made.

1. In the first method, terms of the form $x|x|$ have been approximated by a cubic polynomial so that the second and fourth moments of $x|x|$ and the polynomial approximation are equal (Bruce, 1985). The resulting model is referred to as the polynomial approximation model.

2. In the second method, the expectations of different combinations of nodal forces are intuitively assumed to be functions of the kurtoses and standard deviations of individual nodal forces together with correlation coefficients between them. The resulting model is referred to as the force correlation model.

3. In both models, only the fourth moment is calculated according to the above approximations. The second moment is calculated analytically, as in Burrows' model.

4. In order to check how good the two approximate models are, they were applied to a few sample structures and the results were compared with the results of Burrows' model. The test structures used in this study include a one-leg, a two-leg and a four-leg structure. C_d and C_m were assumed to be 0.70 and 2.00, respectively. The response investigated was base shear, which was defined as the sum of all the nodal loads. The effect of member diameter, significant wave height and jacket dimensions (the distance between the legs) on the accuracy of the two models have been investigated.

5. For structures with a relatively small number of nodes (say less than 12), the number of expectations involving one or two nodal

forces (i.e. $E[F_i^4]$, $E[F_i^3F_j]$, $E[F_i^2F_j^2]$) account for a large part of the fourth moment of response. However, as the number of nodes increases, the number of expectations involving three or four different nodal forces grows rapidly so that it is possible that the major part of the fourth moment of the response is accounted for by these expectations. Now, the number of nodes in our test structures are not high; therefore, the comparison of the fourth moment (or kurtosis) from the two approximate models against its accurate value from Burrows' model is not a good indicator of the accuracy of the models. Instead, it is more reasonable to compare $\sum S_i^2S_jS_k\ E[F_i^2F_jF_k]$ and $\sum S_iS_jS_kS_l\ E[F_iF_jF_kF_l]$ from the two approximate models against their corresponding values from Burrows' model.

6. It was shown that $\sum S_iS_jS_kS_l\ E[F_iF_jF_kF_l]$ is the less accurate one of the above two summations for both models (as may be intuitively expected). Therefore, it was decided that $\sum S_iS_jS_kS_l\ E[F_iF_jF_kF_l]$ was the best indicator of the accuracy of the approximate models.

7. It was shown that as the member diameter decreases (kurtoses of individual nodal forces increase), the level of inaccuracy increases for both models.

8. It was shown that increasing distance between the legs (i.e. decreasing correlation coefficients between nodal forces) has an adverse effect on the level of accuracy of both models.

9. The great majority of offshore structures have inclined legs so that the distance between the legs increases with increasing depth of immersion. As a result, the correlation coefficients

between nodal forces on the lower parts of the legs decrease. This has an adverse effect on the level of the accuracy of the two approximate models. On the other hand, the kurtosis values for nodal forces on the lower parts of the legs are smaller than those for the nodal forces on the upper parts. This has a positive effect on the level of accuracy of the approximate models. It was, therefore, argued that it is the dimension of the structure at the water surface which serves as a measure of inaccuracy rather than its dimension at mudline. The dimension at water surface is ordinarily less than 150 ft (45m).

10. It was shown that for realistic structures (main member diameters > 2.5 ft, L < 150 ft) and realistic environmental conditions (H_s <35 ft), the maximum level of inaccuracy (in $\sum S_i S_j S_k S_l \; E[F_i F_j F_k F_l]$) is below 3% and 11% for the polynomial approximation and the force correlation models, respectively.

11. In view of the uncertainties in the data input to the models (such as environmental conditions, Morison's coefficients, etc.) these levels of inaccuracy are not significant. Furthermore, it must be recognised that even the results of analytical model are only approximations to the observed values. It can therefore be concluded that for engineering purposes all three models are equally satisfactory. However, as previously mentioned, further investigation is required to validate the two approximate models against typical real jacket structures.

12. The polynomial approximation model reduces the computer run-time by about 28 times in comparison with Burrows' model (analytical

solutions) while the reduction for the force-correlation model is about 1000 times.

13. As a result of the reduction in the computer run-time, the number of nodes can be increased from 40 (in Burrows' model) to 85 for the polynomial approximation model and to 200 for the force correlation model (within the 30 minute run-time available on the ICL 1906S computer used by Burrows).

14. Ideally, the above models must be used at two different levels. In the first stage, a refined model of the structure with hundreds or even thousands of nodal loads will be used to calculate the variance of the response accurately. In the second stage, a coarser model of the structure (say, 200 nodes) will be used to estimate the fourth moments of the important responses.

15. It is emphasised that the above models do not account for the presence of current or the intermittency of members in the splash zone. Furthermore, the structure must be rigid enough so that dynamic effects can be ignored.

REFERENCES

Battjes, J.A. (1970) "Long-Term Wave Height Distribution at Seven Stations Around the British Isles". National Institute of Oceanography, Godalming, Internal Report No A44.

Bearman, P.W., Chaplin, J.R., Graham, J.M.R., Kostense, J.K., Hall, P.F. and Klopman, G. (1985) "The Loading on a Cylinder in Post-Critical Flow Beneath Periodic and Random Waves". Proceedings of the 4th International Conference on the Behaviour of Offshore Structures. pp. 213-225.

Bearman, P.W. (1988) "Wave Loading Experiments on Circular Cylinders at Large Scale". Proceedings of the 5th International Conference on the Behaviour of Offshore Structures. pp. 471-487.

Bendat, J.S. (1964) "Probability Functions for Random Responses: Prediction of Peaks, Fatigue Damage and Catastrophic Failures". Los Angeles : Measurement Analysis Corporation.

Bendat, J.S. and Piersol, A.G. (1971) "Random Data: Analysis and Measurement Procedures". London: Wiley-Interscience.

Bishop, J.R. (1979) "Measurements of Wave Particle Motion at the Christchurch Bay Tower Using a Perforated Ball Instrument". National Maritime Institute Report No R55 (Also Department of Energy Report OT-R-7942).

Bishop, J.R. (1980) "A New Coefficient for Total Wave Force". National Maritime Institute Report No R77 (Also Department of Energy Report OT-R-8017).

Bishop, J.R., Tickell, R.G. and Gallagher, K.A. (1980) "The UK Christchurch Bay Project: a Review of Results". Proceedings of the 18th Offshore Technology Conference, Houston, Texas. Paper No OTC 3796, PP. 9-23.

Bishop, J.R. (1982) "Wave Force Investigations at the Second Christchurch Bay Tower". National Maritime Institute Report No R177.

Bishop, J.R. and Chalk, R.F. (1982) "Feasibility Study for Experiments with a Compliant Cylinder at the Christchurch Bay Tower". National Maritime Institute Report No R142.

Bishop, J.R. and Shipway, J.C. (1984) "Wave Force Coefficients from the Second Christchurch Bay Tower". National Maritime Institute Report No R178 (Also Department of Energy Report OT-O-82101 Part 1).

Bishop, J.R. (1988) "Compliant Cylinder Project (Christchurch Bay Tower): Final Report for Participants on British Maritime Technology Basic Analysis Work". British Maritime Technology (Commercial in Confidence).

Borgman, L.E. (1963) "Risk Criteria". ASCE, Journal of Waterways and Harbours Division, Volume 91, No WW3, pp. 65-90.

Borgman, L.E. (1967) "Random Hydrodynamic Forces on Objects". The Annals of Mathematical Statistics, Volume 38, pp. 37-51.

Borgman, L.E. (1969a) "Directional Spectra Models for Design Use". Proceedings of the 1st Offshore Technology Conference. Paper No OTC 1069, pp. 721-746.

Borgman, L.E. (1969b) "Ocean Wave Simulation for Engineering Design". ASCE, Journal of Waterways and Harbours Division, Volume 95, No WW4, pp. 557-583.

Borgman, L.E. (1972) "Statistical Models for Ocean Waves and Wave Forces". in Ven Te Chow (Ed) Advances in Hydroscience, London : Academic Press, Volume 8, pp. 139-181.

Borgman, L.E. (1977) "Directional Wave Spectra from Wave Sensors". in M.D. Earle and A. Malahoff (Ed) Ocean Wave Climate. New York: Plenum Press, pp. 269-300.

Bound, A.D. (1984) "The Idealisation of Wave Loading in the Probabilistic Analysis of Offshore Structures". Master of Science Thesis: University of Manchester.

Bruce, R.L. (1985) "Quasi-Static Response of Jacket Platforms Subject to Non-Linear Wave Loading". Proceedings of the 4th International Conference on the Behaviour of Offshore Structures, PP. 899-905.

Burrows, R. (1977) "Quasi-Static Response of Offshore Structures using Probabilistic Methods". Applied Mathematical Modelling, Volume 1, PP. 325-332.

Burrows, R. (1979) "Probabilistic Description of the Response of Offshore Structures to Random Wave Loading". in T.L. Shaw (Ed) Mechanics of Wave Induced Forces on Cylinders. London: Pitman Advanced Publishing Program, PP. 577-595.

Burrows, R. (1982) "Wave Loading on Offshore Structures: A Probabilistic Approach". Unpublished Doctoral Thesis, Civil Engineering Department, Liverpool University.

Burrows, R. (1983) "Expected Value Analysis for the Quasi-Static Response of Offshore Structures". Applied Mathematical Modelling, Volume 7, PP. 317-328.

Burrows, R. (1989) "Fundamentals of Ocean Wave (and Windspeed) Statistical Prediction Methods". CEEC COMET Seminar on Wave and Ice Forces on Offshore Structures, Dept. of Civil Engineering, University of Salford, U.K, PP. 1-25.

Cartwright, D.E. and Longuet-Higgins, M.S. (1956) "The Statistical Distribution of the Maxima of a Random Function". Proc. Roy. Soc. A, Vol. 237, PP. 212-232.

Chaplin, J.R. (1988a) "Loading on a Cylinder in Uniform Oscillatory Flow: Part 1 - Planar Oscillatory Flow". Applied Ocean Research, Volume 10, pp. 120-128.

Chaplin, J.R. (1988b) "Loading on a Cylinder in Uniform Oscillatory Flow: Part 2 - Elliptical Orbital Flow". Applied Ocean Research, Volume 10, pp. 199-206.

Dawson, T.H. (1983) "Offshore Structural Engineering". New Jersey: Prentice-Hall.

Dean, R.G. (1976) "Methodology for Evaluating Suitability of Wave and Wave Force Data for Determining Drag and Inertia Coefficients". 1st International Conference on the Behaviour of Offshore Structures, Trondheim, Volume 2, pp. 40-64.

Foster, E.T. (1967) "Statistical Prediction of Wave Induced Responses in Deep Ocean Tower Structures". University of California, Berkeley, Hydraulics Engineering Laboratory, Report HEL 9-14.

Haring, R.E. and Spencer, L.P. (1979) "The Ocean Test Structure Data Base". ASCE, Civil Engineering in the Oceans IV, Volume 2, pp. 669-683.

Hedges, T.S. (1987) "Combination of Waves and Currents: an introduction". Proceedings of the Institution of Civil Engineers, Volume 82, Part 1, pp. 567-585.

Heidman, J.C., Olsen, O.A., and Johannson, P.I. (1979) "Local Wave Force Coefficients (Ocean Test Structure)". ASCE, Civil Engineering in the Oceans IV, Volume 2, PP. 684-699.

Houmb, O.G. (1981) "Latest Developments in Wave Statistics" in P. Brunn (Ed) Port Engineering. Houston, Texas : Gulf Publishing Company, PP. 253-270.

Inglis, R.B., Pijfers, J.G.L. and Vugts, J.H. (1985) "A Unified Probabilistic Approach to Predicting the Response of Offshore Structures, Including the Extreme Response". Proceedings of the 4th International Conference on the Behaviour of Offshore Structures. PP. 95-109.

Kendall, M.G. and Stuart, A. (1969) "The Advanced Theory of Statistics" Vol. 1, London : Charles Griffin and Company Limited.

King, R., Prosser, M.J. and Verley, R.L.P. (1976) "The Suppression of Structural Vibrations Caused by Currents and Waves". 1st International Conference on the Behaviour of Offshore Structures, Trondheim, Norway, Vol. 1, PP. 263-284.

King, R. (1977) "A Review of Vortex Shedding Research and its Application". Ocean Engineering, Vol. 4, PP. 141-171.

Lin, Y.K. (1967) "Probability Theory of Structural Dynamics". New York: Krieger Publishing.

Longuet-Higgins, M.S. (1952) "On the Statistical Distribution of the Heights of Sea Waves". Journal of Marine Research, Volume II, pp. 245-266.

Longuet-Higgins, M.S. (1980) "On the distribution of Heights of Sea Waves: Some Effect of Non-Linearity and Finite Band Width". Journal of Geophysical Research, Volume 85, No C3, pp. 1519-1523.

Miller, K.S. (1964) "Multi-dimensional Gaussian Distributions". London: John Wiley & Sons.

Mitsuyasu, H. et al. (1975) "Observations of the Directional Spectrum of Ocean Waves using a Cloverleaf Buoy". Journal of Physical Oceanography, Volume 5, pp. 750-760.

Morison, J.R., O'Brien, M.P., Johnson, J.W. and Shaaf, S.A. (1950) "The Force Exerted by Surface Waves on Piles". ASME, Petroleum Transactions, Volume 189, pp. 149-154.

Newland, D.E. (1975) "An Introduction to Random Vibrations and Spectral Analysis". London: Longman.

Nolte, K.G. (1973) "Statistical Methods for Determining Extreme Sea States". Proceedings of the 2nd International Conference on Port and Ocean Engineering Under Arctic Conditions, University of Iceland, pp. 705-742.

Ochi, M.K. (1973) "On Prediction of Extreme Values". Journal of Ship Research, PP. 29-37.

Papoulis, A. (1965) "Probability, Random Variables and Stochastic Processes". London: McGraw-Hill Book Company.

Penzien, J. (1976) "Structural Dynamics of Fixed Offshore Structures". 1st International Conference on the Behaviour of Offshore Structures, Volume 1, Trondheim, Norway, PP. 581-592.

Pierson, W.J. (1955) "Wind Generated Gravity Waves". Advances in Geophysics, Volume 2, pp. 93-178.

Pierson, W.J. and Holmes, P. (1965) "Irregular Wave Forces on a Pile". ASCE, Journal of the Waterways and Harbors Division, Vol 91, No WW4, pp. 1-10.

Pierson, W.J. and Moskowitz, L.J. (1964) "A Proposed Spectral Form for Fully-Developed Wind Seas Based on the Similarity Theory of S.A. Kitaigorodskii". Journal of Geophysical Research, Volume 69, No. 24, PP. 5181-5190.

Price, R. (1958) "A Useful Theorem for Non-Linear Devices having Gaussian Inputs". IRE Transactions on Information Technology, Volume IT-4.

Price, W.G. and Bishop, R.E.D. (1974) "Probabilistic Theory of Ship Dynamics". London: Chapman and Hall.

Rajabi. F. (1979) "Hydroelastic Oscillations of Smooth and Rough Cylinders in Harmonic Flow". Ph.D. Thesis, Naval Postgraduate School, Monterey, California.

Sarpkaya, T. (1976a) "Vortex Shedding and Resistance in Harmonic Flow about Smooth and Rough Circular Cylinders at High Reynolds Numbers". Report No NPS-595L76021, Naval Postgraduate School, Monterey, California.

Sarpkaya, T. (1976b) "In-line and Transverse Forces on Smooth and Sand-roughened Cylinders in Oscillatory Flow at High Reynolds Numbers". Report No NPS-69SL 76062, Naval Postgraduate School, Monterey, California.

Sarpkaya, T. and Isaacson, M. (1981) "Mechanics of Wave Forces on Offshore Structures". London: Van Nostrand Reinhold.

Shipway, J.C. (1984) "An Investigation into Tidal Current, Current Induced Loadings and Zero Readings at Christchurch Bay Tower. National Maritime Institute Report No R181.

Streeter, V.L. and Wylie, E.B. (1979) "Fluid Mechanics". London: McGraw-Hill Book Company.

Starsmore, N. (1981) "Consistent Drag and Added-Mass Coefficients from Full-Scale Data". Proceedings of the 13th Offshore Technology Conference, Houston, Texas. Paper No OTC 3990, PP. 357-365.

Tickell, R.G., Burrows, R. and Holmes, P. (1976) "Long Term Wave Loading on Offshore Structures". Proceedings of the Institution of Civil Engineers, Volume 61, Part 2, PP. 145-162.

Tickell, R.G. (1977) "Continuous Random Wave Loading on Structural Members". The Structural Engineer, Volume 55, No 5, pp. 209-222.

Tickell, R.G. and Elwany, M.H.S. (1979) "A Probabilistic Description of Forces on a Member in a Short-Crested Random Sea". in T.L. Shaw, (Ed) Mechanics of Wave-Induced Forces on Cylinders, London: Pitman Advanced Publishing Program, PP. 561-576.

Tickell, R.G., Elwany, M.H.S. and Holmes, P. (1982) "Christchurch Bay Tower - Probabilistic Analysis of Data Recorded During September 1976". Department of Energy, Report No OT-R-8114.

Tickell, R.G. and Bishop, J.R. (1985) "Analysis of Waves and Wave Forces at the Christchurch Bay Tower". Proceedings of the 4th International Offshore Mechanics and Arctic Engineering Symposium, Vol. 1, PP. 142-150.

Tickell, R.G., Burrows, R. and Salih, B. (1987) "Advanced Probabilistic Properties of Wave Climates". in Society of Underwater Technology (Ed) Advances in Underwater Technology, Ocean Science and Offshore Engineering, London : Graham and Trotman, Volume 12, PP. 13-30.

Tickell, R.G. and Burrows, R. (1988) "Christchurch Bay Tower Compliant Cylinder Project: An Interim Report on the Analysis of Data". Unpublished Report, Civil Engineering Department, Liverpool University.

Tickell, R.G. and Burrows, R. (1989) "Christchurch Bay Tower Compliant Cylinder Project". Unpublished Report, Civil Engineering Department, Liverpool University.

Tung, C.C. (1975) "Statistical Properties of Wave Force". ASCE, Journal of Engineering Mechanics, PP. 1-11.

Tung, C.C. and Huang, N.E. (1976) "Interactions Between Waves and Currents and their Influence on Fluid Forces". 1st International Conference on the Behaviour of Offshore Structures, Trondheim, PP. 129-143.

Van Heteren, J., Keijser, H. and Schaap, B. (1988) "Comparison of Wave Directional Measuring Systems". Applied Ocean Research, Volume 10, No 3, pp. 129-143.

Wilson, J.F. (1984) "Dynamics of Offshore Structures". New York: John Wiley.

Appendix A

An Investigation into the Phase Relationship Between Hydrodynamic Forces and Cylinder Displacements

A.1 OBJECTIVE

It is the objective of this Appendix to investigate whether there is an ambiguity of some sort in the hydrodynamic forces and/or cylinder displacements supplied to the study.

A.2 BACKGROUND

Assuming that the compliant cylinder is a single degree of freedom system, one expects that the external hydrodynamic loadings and the cylinder displacements to be in phase for frequencies much smaller than the natural frequency of the cylinder (Bendat and Piersol, 1971). The natural frequency of the cylinder in its most flexible mode (F6 setting) is about 0.46Hz. Thus for frequencies less than 0.20Hz or periods greater than 5 seconds, the two time series must be more or less in phase. However, comparing the time series plots of the forces and displacements, it was noted that for large periods, they were out of phase (Figure A.1). This gave the impression that either the forces or the displacements had the wrong sign.

In order to remove the disguising effect of the higher frequencies, all the frequencies above 0.20Hz were filtered out. For all the runs, the correlation coefficients between the filtered forces and displacements at Level 3 in the x direction are given in Table A.1.

With the exception of Runs 08 and 09, all the coefficients are close to -1.0, confirming that the displacements and forces are out of phase. Figures A.2 and A.3 compare forces and displacements for frequencies between 0.05Hz and 0.15Hz in the x and y directions, respectively, and give a visual observation of the phenomenon. The results of Table A.1

and Figures A.2 and A.3 served as strong evidence for the suggestion that either forces or displacements had the incorrect sign.

TABLE A.1

CORRELATION COEFFICIENTS BETWEEN HYDRODYNAMIC FORCES AND CYLINDER DISPLACEMENTS AT LEVEL 3 IN THE X DIRECTION FOR FREQUENCIES LESS THAN 0.20Hz.

RUN Nº	CORRELATION COEFFICIENTS	DAMPED NATURAL FREQUENCY "Hz"
01	-0.76	1.69
02	-0.70	1.27
06	-0.93	0.46
07	-0.81	0.49
08	-0.14	0.73
09	-0.08	0.93
13	-0.98	0.46
14	-0.99	0.46
15	-0.99	0.47
16	-0.99	0.48
23	-0.98	0.49

In order to determine which signal had the incorrect sign, the following steps were taken. Mean forces and mean currents at Level 3 in both x and y direction, and the correlation coefficients between forces and shifted water particle kinematics in the x direction at Level 3 were calculated and are listed in Tables A.2 and A.3, respectively. The positive correlation between mean forces and currents in all cases indicate that the forces have the right sign. Furthermore, according to Morison's equation, the correlation coefficients between forces and

water particle kinematics must be positive. The results of Table A.3 shows that this is the case with the exception of correlation coefficients between forces and shifted velocities for Runs 01, 02 and 09. However, these runs are strongly inertia dominated and hence are very sensitive to small errors in water particle velocity due to shifting. The positive correlation between forces and water particle kinematics proves that forces cannot have the incorrect sign.

Also, it was noted that for Run no. 01 (the most rigid case), the correlation between end reaction forces and hydrodynamic forces (Table A.4) were close to +1.0, rather than -1.0 as expected. Thus, one can argue that it must be hydrodynamic forces, not the displacements, which have the wrong sign. However, the alternative explanation is that both the displacements and the end reaction forces have the incorrect sign. This seems more plausible because, if one assumes that the hydrodynamic forces have the wrong sign, then the currents and water particle kinematics must also have the incorrect sign.

TABLE A.2

MEAN FORCES AND CURRENTS AT LEVEL 3 IN BOTH X AND Y DIRECTIONS

RUN Nº	X DIRECTION		Y DIRECTION	
	mean force "KN"	mean current "m/sec"	mean force "KN"	mean current "m/sec"
01	0.0031	0.144	0.0313	0.439
02	0.0044	0.181	0.0345	0.478
06	0.0040	0.167	0.0393	0.475
07	0.0043	0.168	0.0366	0.466
08	0.0035	0.161	0.0346	0.456
09	0.0034	0.141	0.0302	0.455
13	-0.0034	-0.047	-0.0018	-0.020
14	-0.0054	-0.138	-0.0095	-0.068
15	-0.0174	-0.193	-0.0283	-0.229
16	-0.0177	-0.280	-0.0371	-0.350
23	0.0282	0.141	0.0931	0.557

TABLE A.3

CORRELATION COEFFICIENTS BETWEEN FORCES AND WATER PARTICLE KINEMATICS AT LEVEL 3 IN THE X DIRECTION

RUN Nº	CORRELATION COEFFICIENT BETWEEN FORCE AND SHIFTED	
	Water Particle velocity (m/sec)	Water Particle acceleration (m/sec**2)
01	-0.01	0.52
02	-0.05	0.54
06	0.14	0.50
07	0.14	0.57
08	0.02	0.61
09	-0.01	0.56
13	0.61	0.45
14	0.65	0.43
15	0.69	0.39
16	0.71	0.37
23	0.73	0.22

TABLE A.4

CORRELATION COEFFICIENTS BETWEEN END REACTION FORCES AND HYDRODYNAMIC FORCES FOR RUN NUMBER 01 (X DIRECTION)

Description	HYDRODYNAMIC FORCES			Top Shear Force	Bottom Shear Force
	Level 2	Level 3	Level 4		
Top shear Force	0.92	0.92	0.83	1.00	0.98
Bottom shear force	0.89	0.95	0.90	0.98	1.00

Based on the above arguments, it was decided that the cylinder displacements needed amendment and hence their signs were reversed. The amended data were used in determining force coefficients from the relative kinematics form of Morison's equation.

The question of the sign of the cylinder displacement was raised again when it was noted that for Run numbers 13 and 15, the hydrodynamic forces and cylinder accelerations (at Level 3 in both x and y directions) were positively correlated in the frequency range of 0.40-0.60Hz (Table A.5). This is contrary to what one expects from the analysis of the relative kinematics form of Morison's equation. The relative kinematics form of Morison's equation is

$$F = C_d \hat{k}_d (u-\dot{r})|u-\dot{r}| + C_m \hat{k}_i \dot{u} - C_a \hat{k}_i \ddot{r} \qquad (A.1)$$

since the natural frequency of the cylinder is well above the frequency content of water particle kinematics for all the runs, the frequency content of the hydrodynamic forces around the natural frequency is mostly due to cylinder acceleration (contribution from cylinder velocity is negligible as previously shown in the main text). Therefore,

$$F_{\text{around natural frequency}} \approx - C_a \hat{k}_i \ddot{r} \qquad (A.2)$$

According to the above relationship, the correlation coefficients between forces and cylinder accelerations must be highly negative at around the natural frequencies. However, these correlations for the amended data is positive, as mentioned before, indicating that for this frequency range the cylinder displacements did not need any amendment.

Table A.6, which lists the correlation coefficients between forces and cylinder displacements at around natural frequencies at Level 3 in the x direction, reveals that this is the case for all the runs. Note that cylinder displacements and accelerations are out of phase. Thus, negative correlations between forces and displacements indicate that forces and cylinder accelerations are positively correlated.

TABLE A.5

CORRELATION COEFFICIENTS BETWEEN FORCES AND CYLINDER ACCELERATIONS AT LEVEL 3 IN FREQUENCY RANGE OF 0.40-0.60Hz IN BOTH X AND Y DIRECTIONS (AMENDED DATA)

Run Nº	CORRELATION COEFFICIENT	
	Direction	
	X	Y
13	0.89	0.84
15	0.88	0.88

TABLE A.6

CORRELATION COEFFICIENTS BETWEEN FORCES AND CYLINDER DISPLACEMENTS AT AROUND THE NATURAL FREQUENCIES (LEVEL 3, X DIRECTION, AMENDED DATA)

RUN Nº	CORRELATION COEFFICIENT	FREQUENCY RANGE "Hz"	DAMPENED NATURAL FREQUENCY "Hz"
01	-0.99	1.60-1.80	1.69
02	-0.93	1.20-1.40	1.27
06	-0.96	0.40-0.60	0.46
07	-0.94	0.40-0.60	0.49
08	-0.96	0.60-0.80	0.73
09	-0.82	0.80-1.00	0.93
13	-0.92	0.40-0.60	0.46
14	-0.88	0.40-0.60	0.46
15	-0.89	0.40-0.60	0.47
16	-0.87	0.40-0.60	0.48
23	-0.83	0.40-0.60	0.49

This led to the intriguing suggestion that somehow the cylinder displacements had the wrong sign for low frequencies (0.00-0.20Hz) but the right sign for frequencies around the natural frequencies. Therefore, if there is a mistake in the displacements, it cannot be amended by a sign reversal.

In order to fully appreciate what has gone wrong, it was decided to review all the steps taken in measuring and calculating the hydrodynamic forces and cylinder accelerations and displacements.

A.3 HORIZONTAL CYLINDER ACCELERATIONS AND DISPLACEMENTS

Horizontal cylinder accelerations and displacements have been derived from measured accelerations (Bearman's comment on Tickell et al, 1988).

A.3.1 Acceleration Measurement

Accelerations were measured at three different levels, known as Levels 2, 3 and 4, in both x and y directions by duplicate accelerometers located in the force sleeve sections (Bishop et al, 1982).

A.3.2 Relationship Between Measured & Horizontal Cylinder Accelerations

As shown in Figure A.4, the measured acceleration (b) has two components: one due to horizontal cylinder acceleration ($\ddot{x}$), and the other is due to gravity (g). Thus at point (1),

$$b = \ddot{x}\cos(\theta) + g\cos(\pi/2 - \theta) \qquad (A.3a)$$

or

$$b = \ddot{x}\cos(\theta) + g\sin(\theta) \qquad (A.3b)$$

where θ, the local tilt of the cylinder, is the angle between the z axis and the tangent to the cylinder at point (1).

For small deflections of the cylinder, θ is a small angle. Therefore,

$$\cos(\theta) \approx 1.0 \qquad (A.4a)$$

and

$$\sin\theta \approx \theta \approx \tan\theta = (dx/dz) \qquad (A.4b)$$

Substituting Equations (A.4a) and (A.4b) into Equation (A.3b) leads to the following relationship between the measured and horizontal cylinder accelerations.

$$b = \ddot{x} + g*(dx/dz) \qquad (A.5)$$

A.3.3 Calculating Horizontal Cylinder Displacements and Accelerations

Since accelerations are measured at three different levels, displacements can, at best, be represented by three sinusoidal modal shapes (Figure A.5). Hence

$$x(z,t) = \sum_{n=1}^{3} a_n(t) * \sin(n\pi z/L) \tag{A.6}$$

where $a_n(t)$ (n = 1,2,3) are modal amplitudes, and L is the length of the cylinder.

The second derivative of x with respect to time, $\ddot{x}$, is the horizontal cylinder acceleration and is equal to

$$\ddot{x}(z,t) = \sum_{n=1}^{3} \ddot{a}_n(t) * \sin(n\pi z/L) \tag{A.7}$$

The local tilt is

$$\theta = (dx/dz) = \sum_{n=1}^{3} (n\pi/L) * a_n(t) * \cos(n\pi z/L) \tag{A.8}$$

Introducing Equations (A.7) and (A.8) into Equation (A.5) leads to

$$b(z,t) = \sum_{n=1}^{3} [\ddot{a}_n(t) * \sin(n\pi z/L) + g * (n\pi/L) * a_n(t) * \cos(n\pi z/L)] \tag{A.9}$$

Taking Fourier Transforms of both sides results in

$$B(z,\omega) = \sum_{n=1}^{3} \{-\omega^2 A_n(\omega) * \sin(n\pi z/L) + (n\pi g/L) * A_n(\omega) * \cos(n\pi z/L)\} \tag{A.10}$$

or,

$$B(z,\omega) = \sum_{n=1}^{3} [-\omega^2 * \sin(n\pi z/L) + (n\pi g/L) * \cos(n\pi z/L)] * A_n(\omega) \tag{A.11}$$

where $B(z,\omega)$ and $A_n(\omega)$ are the Fourier Transforms of the measured accelerations and modal amplitudes, respectively.

If Fourier Transforms of measured accelerations at Levels 2, 3 and 4 are denoted by $B_2(\omega)$, $B_3(\omega)$ and $B_4(\omega)$, respectively, then

$$B_2(\omega) = \sum_{n=1}^{3} [-\omega^2 * \sin(n\pi z_2/L) + (n\pi g/L) * \cos(n\pi z_2/L)] * A_n(\omega)$$

$$= \sum_{n=1}^{3} \alpha_{1,n} * A_n(\omega) \qquad \text{(A.12a)}$$

$$B_3(\omega) = \sum_{n=1}^{3} [-\omega^2 * \sin(n\pi z_3/L) + (n\pi g/L) * \cos(n\pi z_3/L)] * A_n(\omega)$$

$$= \sum_{n=1}^{3} \alpha_{2,n} * A_n(\omega) \qquad \text{(A.12b)}$$

$$B_4(\omega) = \sum_{n=1}^{3} [-\omega^2 * \sin(n\pi z_4/L) + (n\pi g/L) * \cos(n\pi z_4/L)] * A_n(\omega)$$

$$= \sum_{n=1}^{3} \alpha_{3,n} * A_n(\omega) \qquad \text{(A.12c)}$$

where $\alpha_{i,j} * A_j(\omega)$ $(i,j = 1,2,3)$ refers to the contribution of the jth modal shape to measured acceleration at Level (i+1), and is equal to

$$\alpha_{ij} * A_j(\omega) = -\omega^2 * \sin(j\pi z_{i+1}/L) * A_j(\omega) + (j\pi g/L) * \cos(j\pi z_{i+1}/L) * A_j(\omega) \qquad \text{(A.13)}$$

The first term of the above relationship is due to horizontal cylinder acceleration, and the second term is due to gravitational acceleration. An examination of this equation reveals that while the gravity term is independent of frequency, the cylinder acceleration term is a function of frequency squared. Thus, in a qualitative sense, for small

frequencies, the gravity term dominates, and for large frequencies, the cylinder acceleration term is dominant.

In matrix notation, Equations (A.12) are represented as

$$[\alpha]_{3*3} * [A]_{3*1} = [B]_{3*1} \tag{A.14}$$

The unknown quantities $[A]_{3*1}$ are calculated from the following relationship

$$[A]_{3*1} = [\alpha]_{3*3}^{-1} * [B]_{3*1} \tag{A.15}$$

solving the above equation leads to [A], i.e. the Fourier Transforms of the modal amplitudes. Taking the inverse Fourier Transforms of [A], one can calculate the modal amplitudes, [a(t)], and hence the cylinder displacements through Equation (A.6). $[\ddot{a}_n(t)]$ is similarly derived by taking the Inverse Fourier Transform of $-\omega^2[A]$. This paves the way for calculating horizontal cylinder accelerations from Equation (A.7).

The following points can be noticed from the examination of Equations (A.12) to (A.15).

1. If the measured accelerations have the incorrect sign, their Fourier Transforms and consequently the Fourier Transforms of the modal amplitudes will also have incorrect signs. This leads to wrong signs for modal amplitudes, which in turn reverses the sign of the cylinder displacements and accelerations.

2. In Bearman's (1988) comment on the interim report, the terms due to gravitational accelerations in Equations (A.12) and (A.13) have incorrect signs. If the sign of these terms in BMT's

calculations are wrong, then the contribution of the jth mode to measured acceleration at level (i+1) will be,

$$\acute{\alpha}_{i,j} * \acute{A}_j(\omega) = -\omega^2 * \sin(j\pi z_{i+1}/L) * \acute{A}_j(\omega) - (j\pi g/L) * \cos(j\pi z_{i+1}/L) * \acute{A}_j(\omega) \quad (A.16)$$

where $\acute{A}_j(\omega)$ (j = 1,2,3) refers to the Fourier Transforms of the modal amplitudes and are obtained from the following relationship,

$$[\acute{\alpha}]_{3*3} * [\acute{A}]_{3*1} = [B]_{3*1} \quad (A.17)$$

or,

$$[\acute{A}]_{3*1} = [\acute{\alpha}]_{3*3}^{-1} * [B]_{3*1} \quad (A.18)$$

The ratio between $\alpha_{i,j}(\omega)$ and $\acute{\alpha}_{i,j}(\omega)$, denoted by $e_{i,j}(\omega)$, is

$$e_{i,j}(\omega) = \frac{\alpha_{i,j}(\omega)}{\acute{\alpha}_{i,j}(\omega)} = \frac{-\omega^2 * \sin(j\pi z_{i+1}/L) + (j\pi g/L) * \cos(j\pi z_{i+1}/L)}{-\omega^2 * \sin(j\pi z_{i+1}/L) - (j\pi g/L) * \cos(j\pi z_{i+1}/L)} \quad (A.19)$$

Dividing both the numerator and denominator by $-4\pi^2\cos(j\pi z_{i+1}/L)$, leads to

$$e_{i,j}(f) = \frac{f^2 * \tan(j\pi z_{i+1}/L) - (jg/4\pi L)}{f^2 * \tan(j\pi z_{i+1}/L) + (jg/4\pi L)} \quad (A.20)$$

For frequencies smaller than a specific amount, $f^*_{i,j}$, the absolute value of the term containing g will be greater than that of the other term, i.e.,

$$f^2 * |\tan(j\pi z_{i+1}/L)| < jg/4\pi L \quad (A.21)$$

or,

$$f < (1/2) * \left(\frac{jg}{\pi L * |\tan(j\pi z_{i+1}/L)|} \right)^{(1/2)} = f^*_{i,j} \quad (A.22)$$

For $f<f^{\circ}_{i,j}$, $e_{i,j}$ is negative, indicating that $\alpha_{i,j}$ and $\acute{\alpha}_{i,j}$ are of opposite signs. The values of $f^{\circ}_{i,j}$ are given in Table A.7.

TABLE A.7

FOR FREQUENCIES LESS THAN $f^{\circ}_{i,j}$ "Hz", $e_{i,j}(f)$ IS NEGATIVE

Level	$f^{\circ}_{i,j}$ "Hz"		
	1st mode	2nd mode	3rd mode
2	0.132	0.471	0.438
3	0.114	0.551	0.361
4	0.224	0.179	0.658

For frequencies greater than the largest $f^{\circ}_{i,j}$ (0.658Hz), the $\acute{\alpha}$ terms will be different from α terms only in their magnitude, but their signs will be the same. For frequencies smaller than the smallest $f^{\circ}_{i,j}$ (0.114Hz), they will be different in both their magnitudes and signs while for frequencies between the two limits, they will all be different in magnitude, but only some of them will change sign.

If for frequencies less than 0.114Hz only the sign of $[\acute{\alpha}]$ terms were different from $[\alpha]$ ones, it could be concluded that the terms in $[\acute{\alpha}]^{-1}$ would be the negative of the terms in $[\alpha]^{-1}$, and hence the modal amplitudes and displacements would change sign, too. However, because of the change in the magnitude of these terms, one cannot conclude rigorously that the resulting displacements will have incorrect signs. Nevertheless, for cases when the first mode is dominant or for very

small frequencies, the resulting displacements will be of opposite sign.

The main conclusion from the above argument is that in a qualitative sense, the g term with wrong sign will cause displacements which are different from real ones in magnitude, for all frequencies, though more significantly for low ones, and in the direction for low frequencies.

This conclusion can explain the problems encountered in the examination of the displacement time series, i.e., it explains why, for low frequencies, the displacements appear to have incorrect signs while for higher frequencies (around cylinders natural frequencies) they seem to have correct signs. This view was further strengthened when it was noted that for a frequency range of 0.20-0.40Hz, the forces and displacements at Level 3 in the x direction were positively correlated as expected from theory unlike the frequency range of 0.00-0.20Hz (Table A.8).

TABLE A.8

CORRELATION COEFFICIENTS BETWEEN HYDRODYNAMIC FORCES AND CYLINDER DISPLACEMENTS AT LEVEL 3 IN THE X DIRECTION FOR FREQUENCY RANGE 0.20-0.40Hz

Run Nº	Correlation Coefficient	Damped Natural Frequency "Hz"
01	0.35	1.69
02	0.67	1.27
06	0.28	0.46
07	0.37	0.49
08	0.63	0.73
09	0.41	0.93
13	0.19	0.46
14	0.13	0.46
15	0.16	0.47
16	0.24	0.48
23	0.33	0.49

Further evidence for this view was obtained by comparing the standard deviations of the measured and horizontal cylinder accelerations for Runs 13 and 15 (Table A.9). Since the correlation coefficients between measured accelerations of Levels 2 and 4 for both x and y directions in frequency range of 0.40-0.60Hz are virtually one (0.998), the response in this frequency is dominated by the first mode. This implies that for Level 2 the measured accelerations must be greater than the horizontal cylinder accelerations (because the gravity components and cylinder accelerations are in the same direction) while for Level 4 the opposite must be true. The results of Table A.9 indicate that in the x direction, measured accelerations are greater than cylinder accelerations when they are expected to be smaller and vice versa. This

suggests that the sign of the g term is wrong. However, the results of the y direction indicate that the sign of the g term is right.

TABLE A.9

THE RATIO BETWEEN MEASURED AND HORIZONTAL CYLINDER ACCELERATIONS IN FREQUENCY RANGE 0.40-0.60Hz

Level	X Direction		Y Direction	
	Run No.			
	13	15	13	15
2	0.94	0.95	1.10	1.10
4	1.005	1.001	0.97	0.97

Extensive analysis thus far has shown that neither the assumption of the right sign for g nor the assumption of the wrong sign can explain the cylinder displacements obtained based on the intuitive shape of the cylinder.

A.4 FORCE MEASUREMENT

Forces are measured at three different levels by force measurement sleeves, 535mm long each. As shown diagrammatically in Figure A.6, each sleeve has three force measuring links, which are situated in the water filled space between the outer force sleeve and the inner structural column. The links are equally disposed around the circumference of the central tube.

The x and y components of the forces measured by the links are obtained from the known geometry of the system, thus

$$F_x = (FA)_x + (FB)_x + (FC)_x \quad \text{(A.23a)}$$

$$F_y = (FA)_y + (FB)_y + (FC)_y \quad \text{(A.23b)}$$

where FA, FB and FC refer to the forces measured by measurement links A, B and C, and $(FA)_x$, $(FA)_y$,..., etc., are their corresponding components on the x and y directions, respectively. When the links are under tension, they measure positive forces. Therefore, when they are reading positive values, the direction of forces exerted by them on the central tube are as shown in Figure A.6. Based on the geometry of the system, the components of these forces on the x and y directions must be of the signs listed in Table A.10. These signs were checked against the signs of the coefficients used in calculating F_x and F_y from FA, FB and FC by BMT (Bishop and Shipway, 1984), to ensure that F_x and F_y refer to the forces exerted by the links on the central tube rather than on the outer sleeve.

The movement of the force sleeve in either x or y directions can be represented by a single degree of freedom system as illustrated in Figure A.7. Consequently, the restoring forces, i.e., the forces exerted by the links on the outer sleeve are $-F_x$ and $-F_y$.

TABLE A.10

SIGNS OF THE COMPONENTS OF THE POSITIVE FORCES MEASURED BY THE THREE LINKS ON X AND Y DIRECTIONS

Direction	Measurement Link		
	A	B	C
x	+	+	-
y	-	+	+

If the motion of the outer sleeve is represented by r_e, and the inner tube is fixed (rigid cylinder), the equation of the equilibrium of the system is

$$F_h - kr_e - c\dot{r}_e - m\ddot{r}_e = 0 \qquad (A.24)$$

where F_h is the external hydrodynamic loading, and $-kr_e$, $-c\dot{r}_e$ and $-m\ddot{r}_e$ are the restoring, damping and inertia forces, respectively.

If the cylinder is flexible and the inner tube itself is moving, then the force measurement system is represented by a single degree of freedom system in which effective external loading is due to both hydrodynamic loading and foundation movement. If the movement of the inner tube with respect to a fixed reference system is represented by r, then the equation of the equilibrium of the force sleeve is

$$F_h - m\ddot{r} - kr_e - c\dot{r}_e - m\ddot{r}_e = 0 \qquad (A.25)$$

In the above equation, r_e is the displacement of the force sleeve with respect to the inner tube and $-m\ddot{r}$ is the effective external loading due to movement of the inner tube. The mass of the system, m, is equal to

$$m = m_s + \acute{k}m_w \qquad (A.26a)$$

in which m_s is the mass of the force sleeve and m_w is the mass of the water between the inner tube and the force sleeve. $\acute{k}$ is a factor allowing for the fact that only part of the inertia force of the internal water acts on the internal surface of the force ring. The rest acts on the central column. The factor $\acute{k}$ can be calculated (Bishop, 1982).

When the natural frequency of the force sleeve system is well above the frequency of excitation (both external hydrodynamic loading and the cylinder frequency), the system can be treated as a quasi-static one and the damping force, $-c\dot{r}_e$, and the inertia force, $-m\ddot{r}_e$, will be much smaller than the restoring force, $-kr_e$. Therefore, Equation (A.25) will reduce to

$$F_h - m\ddot{r} - kr_e = 0 \qquad \text{(A.26b)}$$

The components of $-kr_e$, the restoring force, in the x and y directions are $-F_x$ and $-F_y$, respectively, which are obtained from Equation (A.23). The above equation can be written as two separate equations for x and y directions, i.e.

$$(F_h)_x - m\ddot{r}_x - (kr_e)_x = 0 \qquad \text{(A.27a)}$$

$$(F_h)_y - m\ddot{r}_y - (kr_e)_y = 0 \qquad \text{(A.27b)}$$

or,

$$(F_h)_x = F_x + m\ddot{r}_x \qquad \text{(A.28a)}$$

$$(F_h)_y = F_y + m\ddot{r}_y \qquad \text{(A.28b)}$$

where $(F_h)_x$, F_x and $\ddot{r}_x$ are the components of the hydrodynamic force, measured force, and cylinder acceleration in the x direction. $(F_h)_y$, F_y and $\ddot{r}_y$ refer to similar terms in the y direction.

BMT's equations reported in their final report (Bishop, 1988) are as follows

$$(F_h)_x = -F_x + m\ddot{r}_x \qquad \text{(A.29a)}$$

$$(F_h)_y = -F_y + m\ddot{r}_y \qquad \text{(A.29b)}$$

However, in an earlier report (Bishop, 1982), they have reported equations of the form of Equations (A.28). Comparison of time series

plots of measured forces and hydrodynamic forces (Figure A.8) reported in BMT's final report reveals that the two forces are in phase at low frequencies. This implies that the sign of F_x cannot be wrong in BMT's calculations.

If the hydrodynamic force is represented by the relative kinematics form of Morison's equation, then

$$(F_h)_x = C_d\hat{k}_d(u-\dot{r}_x)|u-\dot{r}_x| + C_m\hat{k}_i\,\dot{u}_x - C_a\hat{k}_i\ddot{r}_x \qquad (A.30)$$

substituting the above equation into Equation (A.28a), the measured force will be

$$F_x = C_d\hat{k}_d|u-\dot{r}_x|(u-\dot{r}_x) + C_m\hat{k}_i\,\dot{u}_x - (C_a\hat{k}_i + m)\ddot{r}_x \qquad (A.31)$$

Comparison of Equations (A.30) and (A.31) indicates that the frequency spectrum of the measured force must be larger than that of the hydrodynamic force at frequencies near to the cylinder's natural frequency.

If the sign of the cylinder displacement is wrong or if $m\ddot{r}$ has got the wrong sign in BMT's equations, then, in effect, BMT has used the following equation for calculating hydrodynamic forces.

$$(F_h)_x = F_x - m\ddot{r}_x \qquad (A.32)$$

If this was the case, then from Equation (A.31), the calculated hydrodynamic force will be

$$(F_h)_x = C_d\hat{k}_d(u-\dot{r}_x)|u-\dot{r}_x| + C_m\hat{k}_i\,\dot{u}_x - (C_a\hat{k}_i + 2m)\ddot{r}_x \qquad (A.33)$$

According to the above equation, the frequency content of the hydrodynamic force must be greater than that of the measured force at

frequencies near to the cylinder's natural frequency. However, BMT's report shows that this is not the case (Figure A.9). This shows that BMT has used the right equations, i.e. Equations (A.28), in calculating hydrodynamic forces from measured forces. Furthermore, as mentioned earlier, the positive correlation between forces and shifted water particle kinematics indicate that forces have the right signs, at least at low frequencies.

A.5 SUMMARY AND CONCLUSION

Examination of force and displacement time series has shown that for low frequencies, they are out of phase against what is expected from the analysis of a single degree of freedom system. However, at around cylinder's natural frequency, the phase relationship agrees with the prediction of the relative kinematics form of Morison's equation. If the measured accelerations had the incorrect signs, the phase relationship between forces and displacements must have been wrong for all frequencies. Since this is not the case, the assumption of the wrong sign for measured accelerations cannot explain the problem. Furthermore, it was shown in Section A.4 that the hydrodynamic forces cannot have the incorrect signs. Consequently, the only possible explanation is that the gravity correction term, used in the calculation of the horizontal cylinder accelerations from measured accelerations, might have incorrect sign.

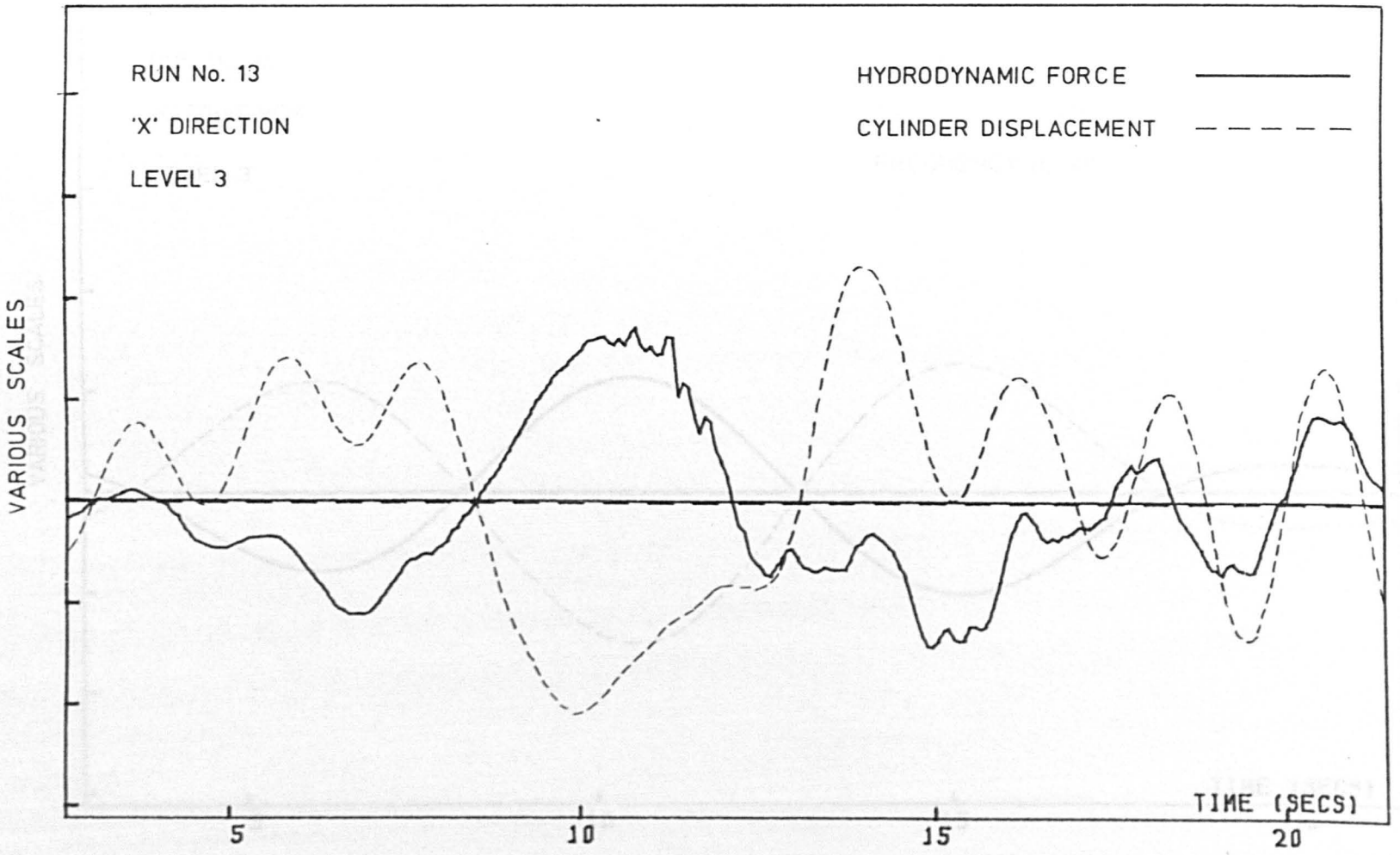

FIGURE A.1. TYPICAL TIME SERIES FOR HYDRODYNAMIC FORCE AND CYLINDER DISPLACEMENT

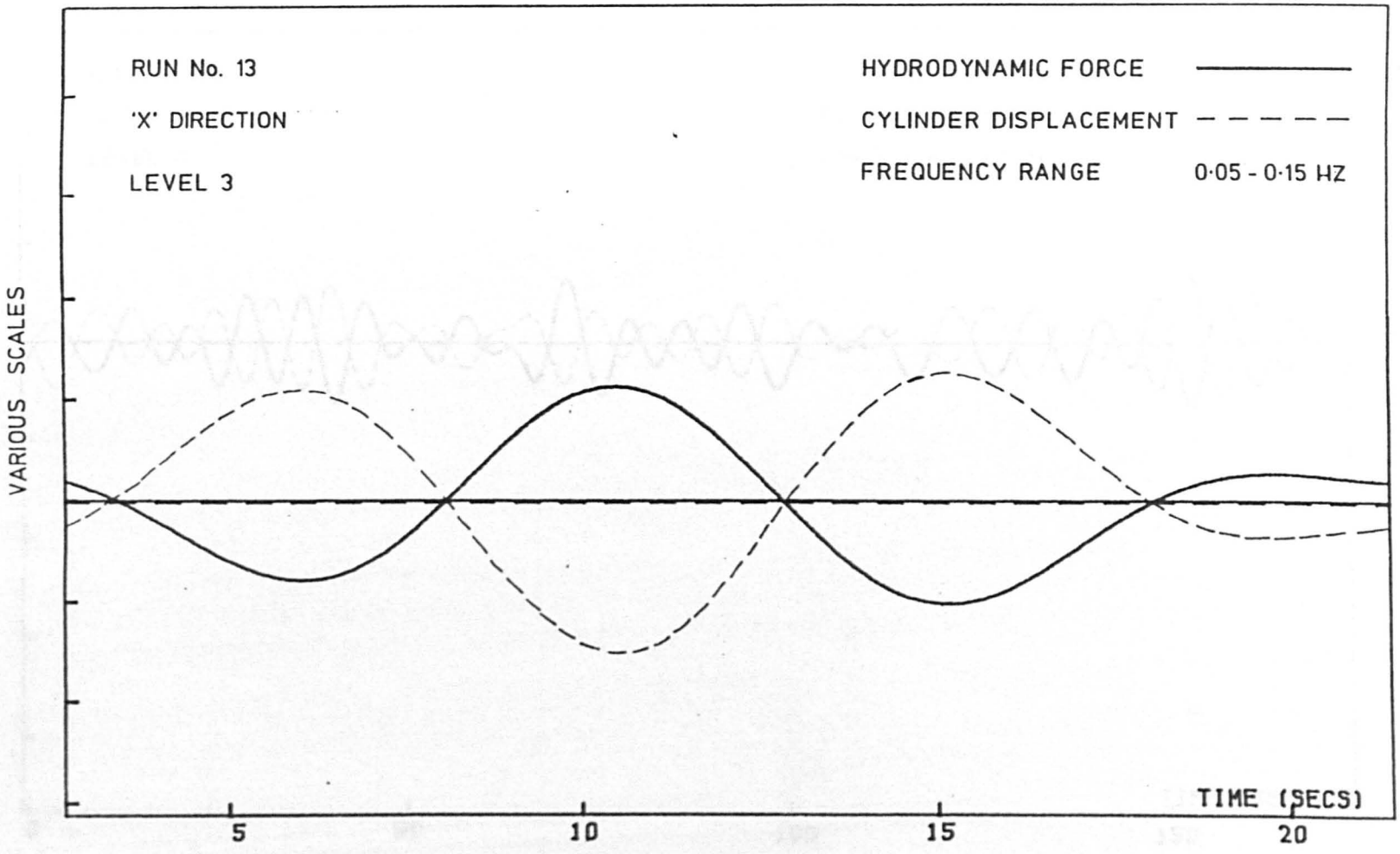

FIGURE A.2. PHASE RELATIONSHIP BETWEEN FORCE AND CYLINDER DISPLACEMENT AT LOW FREQUENCIES IN THE 'X' DIRECTION

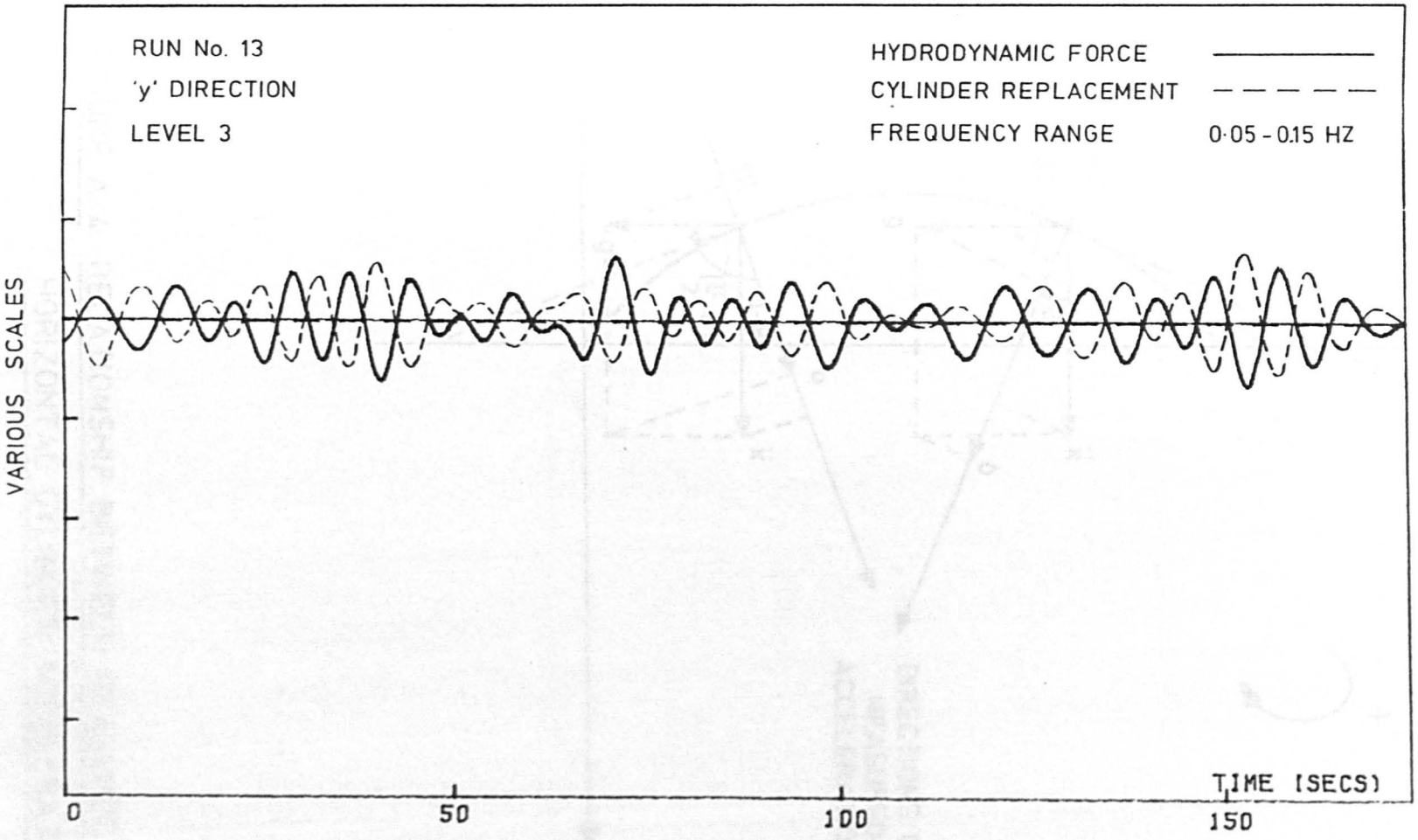

FIGURE A.3 PHASE RELATIONSHIP BETWEEN FORCE AND CYLINDER DISPLACEMENT AT LOW FREQUENCIES IN THE 'y' DIRECTION

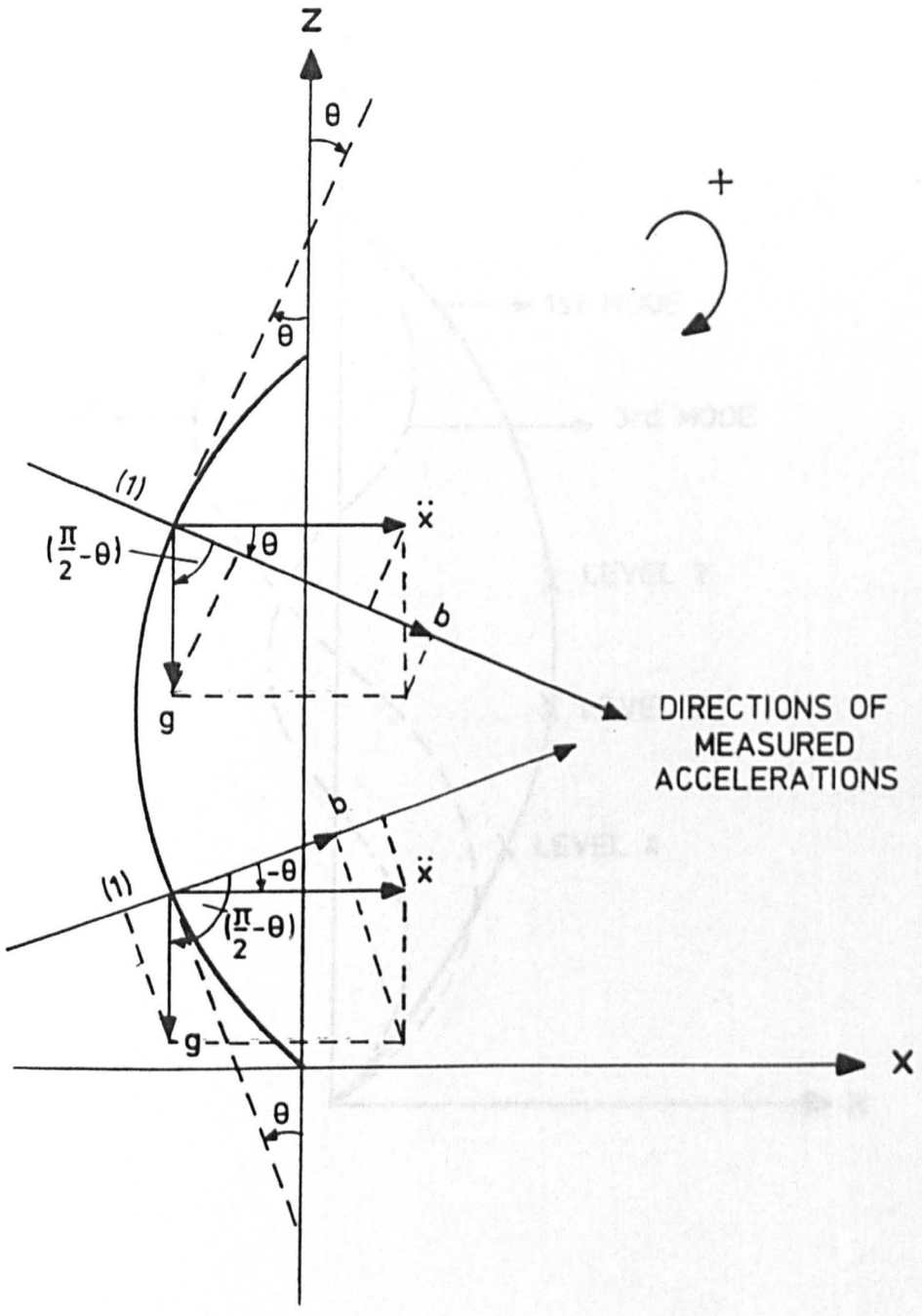

FIGURE A. 4. RELATIONSHIP BETWEEN MEASURED AND HORIZONTAL CYLINDER ACCELERATION

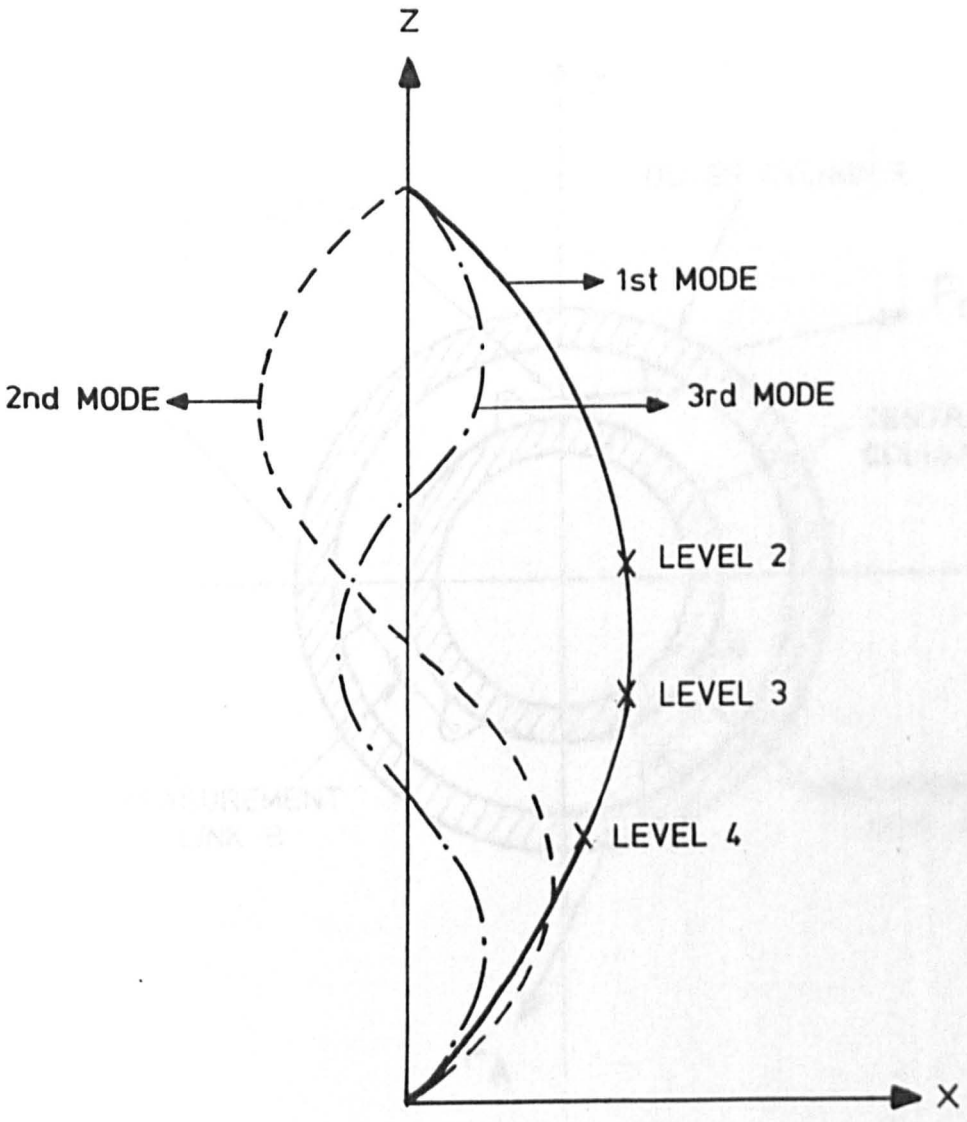

FIGURE A. 5. THE FIRST THREE SINUSOIDAL MODAL SHAPES OF THE CYLINDER

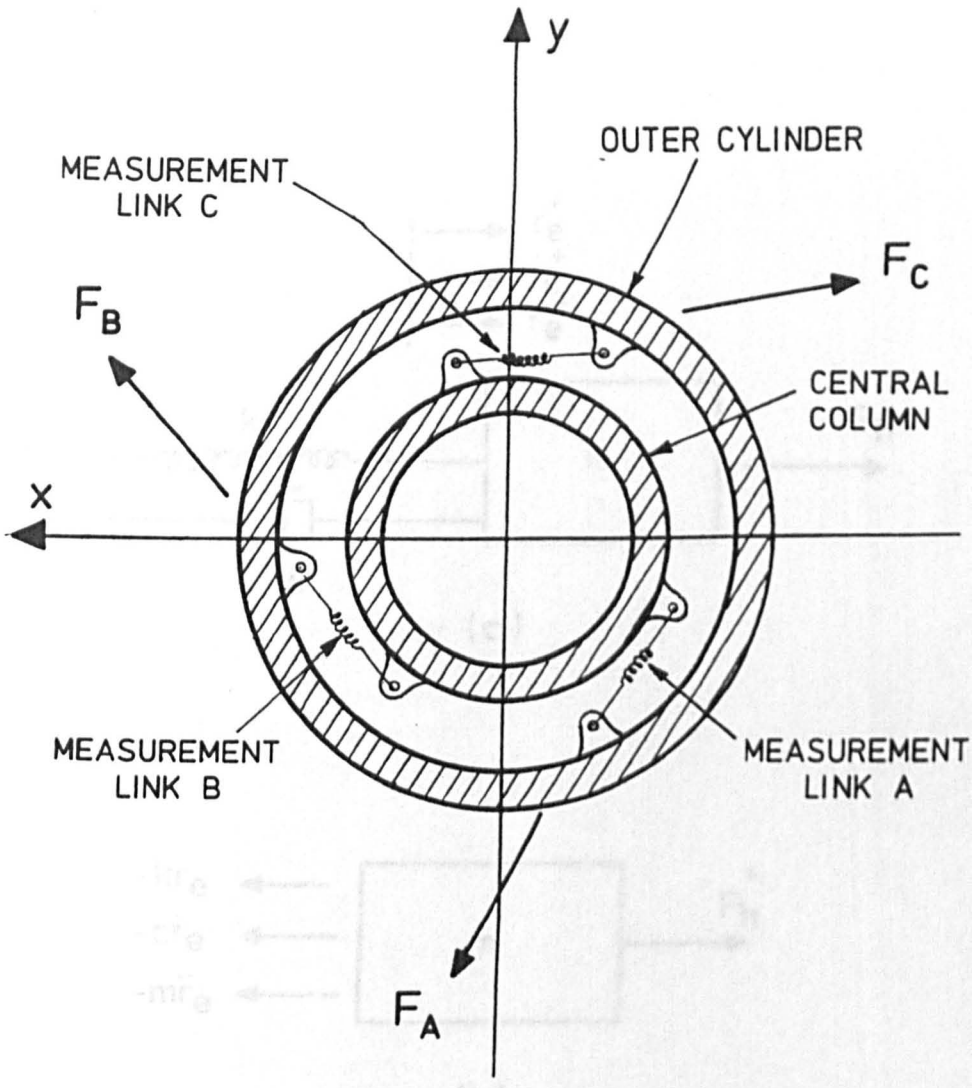

FIGURE A. 6. THE STRUCTURE OF FORCE SLEEVE

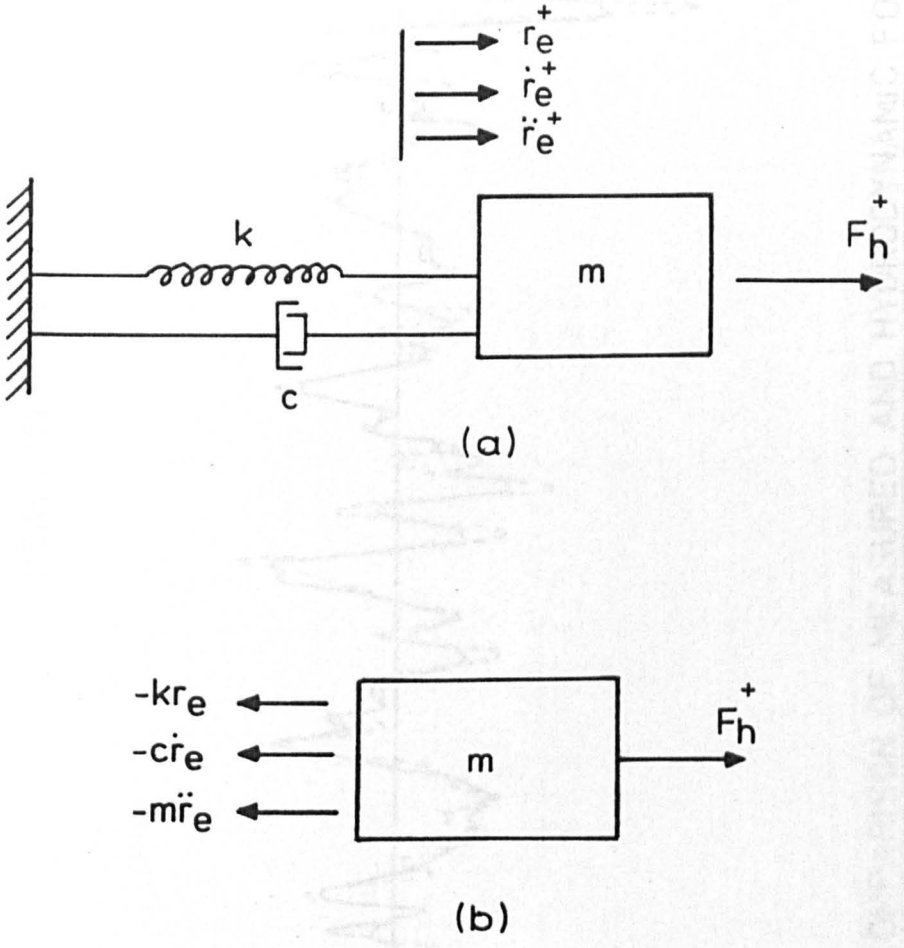

FIGURE A.7. A SINGLE DEGREE OF FREEDOM SYSTEM

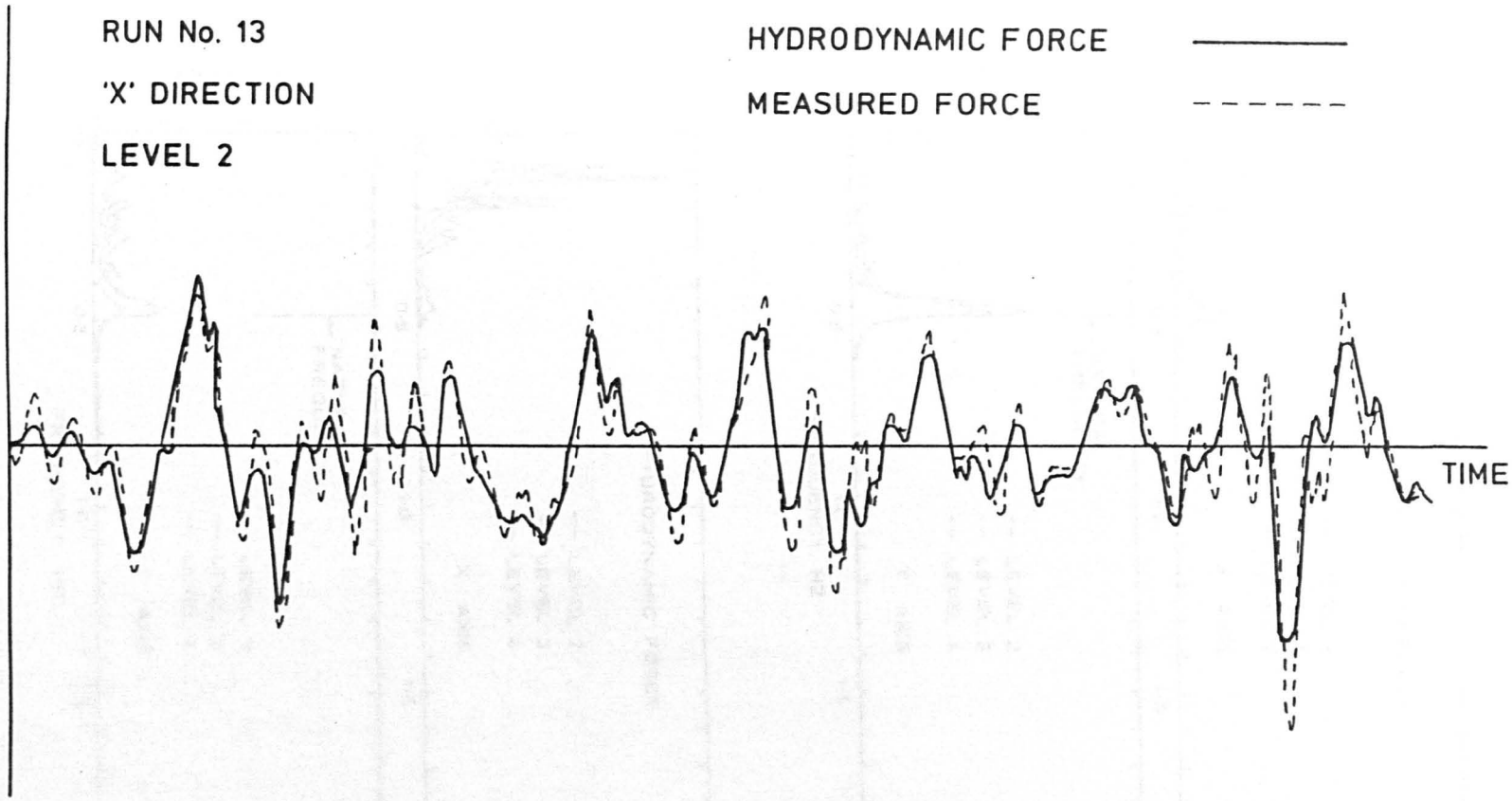

FIGURE A.8. COMPARISON OF MEASURED AND HYDRODYNAMIC FORCES IN THE TIME DOMAIN

(Bishop, 1988)

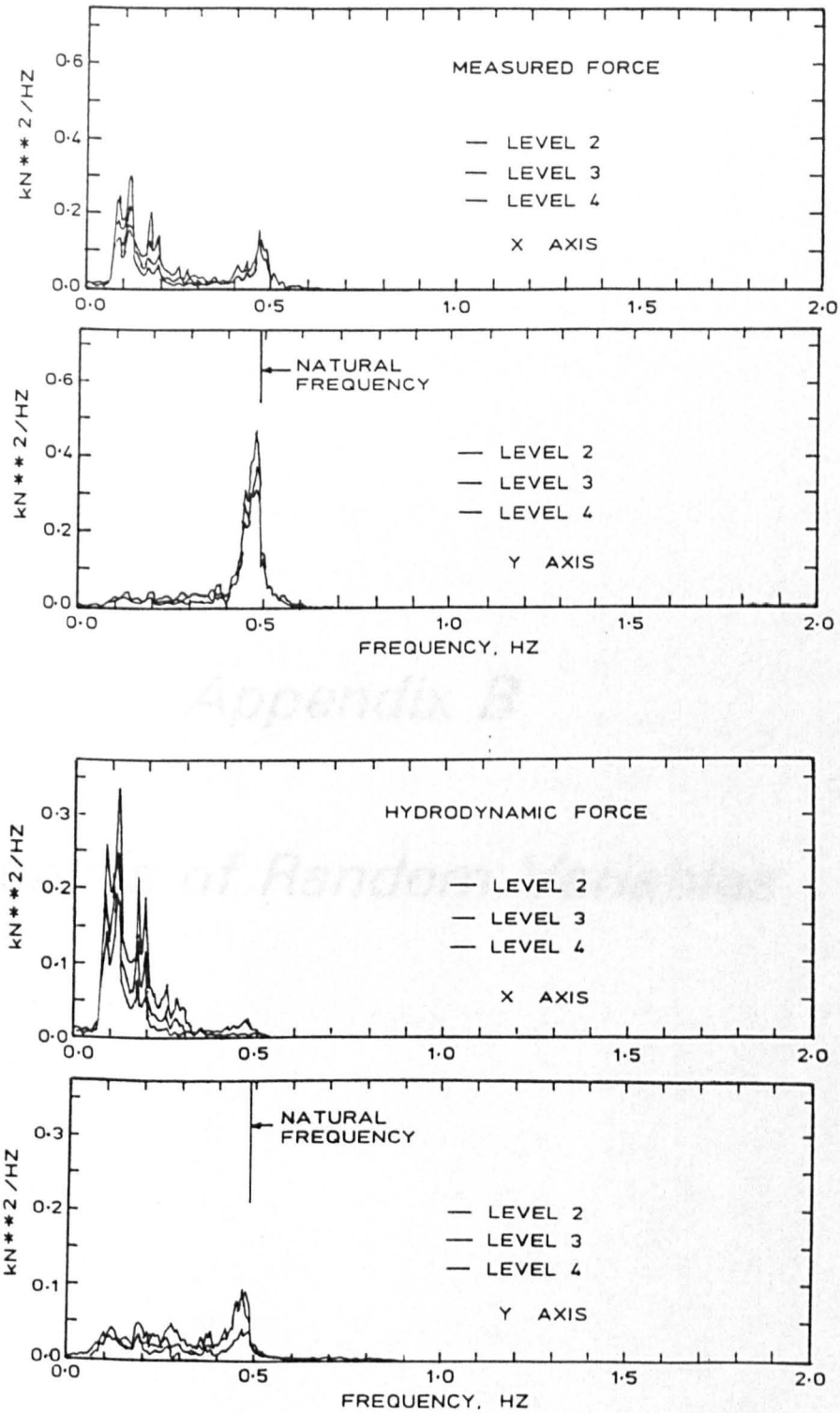

FIGURE A.9. COMPARISON OF FREQUENCY SPECTRA OF THE MEASURED & HYDRODYNAMIC FORCES (RUN No. 13)

(Bishop, 1988)

Appendix B

Analysis of Random Variables

INTRODUCTION

The purpose of this Appendix is to outline the essential concepts and statistical parameters used to describe continuous random phenomena. No attempt has been made to produce a comprehensive or rigorous account of all such concepts or parameters.

B.1 DETERMINISTIC AND RANDOM PHENOMENA

Any physical phenomenon can be broadly classified as being either deterministic or random.

Deterministic phenomena are those which can be predicted exactly in terms of known parameters of the problem.

Random phenomena must be described in terms of probability statements or statistical averages. In these cases, for time varying quantities, the value of the quantity of any point in time is unknown but it is possible to say that there is a certain probability that it will exceed a particular value.

B.2 DESCRIPTIVE PROPERTIES OF RANDOM VARIABLES

The properties of time varying random variables may be described in either the time, frequency or amplitude domains. The time and frequency domains are outlined below, a more detailed account being given by Bendat and Piersol (1971). Description in the amplitude domain concerns probability theory which is covered in Section B.3.

B.2.1 TIME DOMAIN

B.2.1.1 Basic statistical Parameters

Given the time history of a random variable x(t) as demonstrated in Figure (B.1), the following parameters are basic

the MEAN value

$$\bar{x} = \lim_{T\to\infty} \frac{1}{T} \int_{t=0}^{T} x(t)\, dt \tag{B.1}$$

the MEAN SQUARE value

$$\psi_x^2 = \lim_{T\to\infty} \frac{1}{T} \int_{t=0}^{T} x^2(t)\, dt \tag{B.2}$$

and the VARIANCE

$$\sigma_x^2 = \lim_{T\to\infty} \frac{1}{T} \int_{t=0}^{T} (x(t) - \bar{x})^2\, dt \tag{B.3}$$

where σ_x is the STANDARD DEVIATION

$$= (\psi_x^2 - \bar{x}^2)^{1/2}$$

These parameters are considered to be basic because they are sufficient to fully define most theoretical probability distributions used to describe continuous random variables, for example, the Gaussian distribution. However, this is not the case for all probability distributions and so it may be necessary to consider higher order parameters, as follows:

The n-th order (statistical) moment is defined as

$$M_n = \lim_{T\to\infty} \frac{1}{T} \int_{t=0}^{T} x^n(t)\, dt \tag{B.4}$$

with $M_1 = \bar{x}$ and $M_2 = \psi_x^2$

The n-th order central moment, or n-th order moment about the mean, is defined as

$$M_{cn} = \lim_{T \to \infty} \frac{1}{T} \int_{t=0}^{T} (x - \bar{x})^n \, dt \quad . \tag{B.5}$$

with $M_{c2} = \sigma_x^2$.

B.2.1.2 Auto-correlation Function

The general dependence of values of x(t) at one time to those at another time, τ units later, is described by the auto-correlation function

$$R_x(\tau) = \lim_{T \to \infty} \frac{1}{T} \int_{t=0}^{T} x(t) \, x(t + \tau) \, dt \tag{B.6}$$

which has the properties

$$R_x(-\tau) = R_x(\tau) \tag{B.7}$$

$$R_x(0) = \psi_x^2 \geq |R_x(\tau)| \tag{B.8}$$

B.2.1.3 Cross-correlation Function

The inter-relationship between two sets of random variables $x_1(t)$ and $x_2(t)$ can be described by the cross-correlation function

$$R_{x1x2}(\tau) = \lim_{T \to \infty} \frac{1}{T} \int_{t=0}^{T} x_1(t) \, x_2(t + \tau) \, dt \tag{B.9}$$

which has the properties

$$R_{x1x2}(-\tau) \neq R_{x1x2}(\tau)$$

$$= R_{x2x1}(\tau) \tag{B.10}$$

and if $R_{x1x2}(0) = 0$, then $x_1(t)$ and $x_2(t)$ are uncorrelated.

B.2.1.4 Auto-covariance Function, Cross-covariance Function and Correlation Coefficient

Auto-covariance and cross-covariance functions are similar to the corresponding correlation function but include an adjustment for the mean as follows:

$$C_x(\tau) = \lim_{T\to\infty} \frac{1}{T} \int_{t=0}^{T} [x(t) - \bar{x}]\,[x(t+\tau) - \bar{x}]\,dt \tag{B.11}$$

and

$$C_{x1x2}(\tau) = \lim_{T\to\infty} \frac{1}{T} \int_{t=0}^{T} [x_1(t) - \bar{x}_1]\,[x_2(t+\tau) - \bar{x}_2]\,dt \tag{B.12}$$

These expressions revert to $R_x(\tau)$ and $R_{x1x2}(\tau)$, respectively, when the random variables are mean zero ($\bar{x}_1 = \bar{x}_2 = 0$).

The correlation coefficient is defined as

$$r_{x1x2} = \frac{C_{x1x2}(0)}{\sigma_{x1}\,\sigma_{x2}} \tag{B.13}$$

B.2.1.5 Stationarity and Ergodicy

A random variable, x(t), is stationary if its statistical properties, described below, are independent of the time origin.

A stationary random variable is ergodic if its statistical properties calculated from one sample record, of the form of Figure B.1, are equal to those calculated from other samples of x(t) taken during the same time interval.

Random data representing stationary physical phenomena are generally ergodic and hence the properties of stationary random phenomena can be

estimated correctly from a single observed time history record, if the finite time interval, T, considered is sufficiently long.

B.2.2 FREQUENCY DOMAIN (SPECTRAL APPROACH)

B.2.2.1 Power Spectral Density Function

The power spectral density function (or autospectral density function) of a random variable, x(t), describes the distribution of the mean square value as a function of frequency.

The mean square value of the portion of x(t) within the frequency band between ω and $\omega + \Delta\omega$ is given by

$$\psi_x^2(\omega, \Delta\omega) = \lim_{T\to\infty} \frac{1}{T} \int_0^T x^2(t, \omega, \Delta\omega)\, dt \tag{B.14}$$

where ω is in radian measure.

As $\Delta\omega \to 0$ the power spectral density function may be defined as

$$G_{xx}(\omega) = \lim_{\Delta\omega\to 0} \frac{1}{\Delta\omega} \psi_x^2\ (\omega, \Delta\omega) \tag{B.15}$$

For a stationary random process, the spectral density function and the correlation function, Equation (B.6), are related by a Fourier transform

$$G_{xx}(\omega) = \frac{2}{\pi} \int_0^\infty R_x(\tau)\ e^{-i\omega\tau}\, d\tau$$

$$= \frac{2}{\pi} \int_0^\infty R_x(\tau) \cos \omega\tau\, d\tau \tag{B.16}$$

The mean square value of x(t) is obtained from the inverse relationship and setting $\tau = 0$

$$R_x(0) = \psi_x^2 = \int_0^\infty G_{xx}(\omega)\, d\omega \tag{B.17}$$

and is thus equal to the area under the spectral density function or 'spectrum'.

B.2.2.2 Spectral Moments

The n-th order moment of $G_{xx}(\omega)$ with respect to the origin, $\omega = 0$, is defined as

$$m_n = \int_0^\infty \omega^n\, G_{xx}\,(\omega)\, d\omega \tag{B.18}$$

and hence $m_0 = \psi_x^2 = R_x(0)$.

B.2.2.3 Spectral Bandwidth

The spectral bandwidth ϵ is used in connection with the probabilistic properties of the random variable, x(t), giving a measure of the number of 'extrema' or peaks of the process in relation to the number of crossings of the mean amplitude level, $\bar{x}$, and is defined as (see Section B.3.4.4)

$$\epsilon = [(m_0 m_4 - m_2^2)/m_0 m_4]^{1/2} \tag{B.19}$$

B.3 PROBABILITY THEORY

B.3.1 ONE RANDOM VARIABLE

Consider a continuous time-varying random variable, x(t), as sketched over a time interval from 0 to T in Figure B.2.

B.3.1.1 Probability Density Function (pdf.)

The pdf. $p(x)$, describes the probability that $x(t)$ will take a value within some defined range $(x, x + \Delta x)$ at any instant of time

$$\text{Prob}[x \leq x(t) \leq x + \Delta x] = \lim_{T \to \infty} \left(\frac{T_x}{T}\right)$$

and

$$p(x) = \lim_{\Delta x \to \infty} \frac{1}{\Delta x} \left[\lim_{T \to \infty} \left(\frac{T_x}{T}\right)\right] \tag{B.20}$$

This density function has the properties that

$$p(x) \geq 0$$

and

$$\int_{-\infty}^{\infty} p(x)\, dx = 1$$

B.3.1.2 Cumulative Probability Distribution Function (cdf.)

The cdf. describes the probability of $x(t)$ having a value less than or equal to a given value of x

$$P(x) = \text{Prob}[x(t) \leq x] = \int_{-\infty}^{x} p(\alpha)\, d\alpha \tag{B.21}$$

This distribution function has the properties that

$$0 \leq P(x) \leq 1$$

and

$$p(x) = \frac{dP(x)}{dx}$$

B.3.1.3 Statistical Moments

The n-th order moment of the pdf. about the origin is defined as

$$E\{x^n\} = \int_{-\infty}^{\infty} x^n \, p(x) \, dx \tag{B.22}$$

where E{ } is the expected value operator and represents the expected value, or expectance, of its argument.

With reference to the description of the time domain in Section B.2.1.

$$M_n = E\{x^n\} \tag{B.23}$$

and in particular, the mean value is

$$\bar{x} = M_1 = E\{x\} \tag{B.24}$$

and the mean square value

$$\psi_x^2 = R_x(0) = M_2 = E\{x^2\} \tag{B.25}$$

The n-th order moments of the pdf. about the mean are defined as

$$E\{(x - \bar{x})^n\} = \int_{-\infty}^{\infty} (x - \bar{x})^n \, p(x) \, dx \tag{B.26}$$

and again with reference to Section B.2.1.

$$M_{cn} = E\{(x - \bar{x})^n\} \tag{B.27}$$

and in particular

$$\sigma_x^2 = M_{c2} = E\{(x - \bar{x})^2\}$$

$$\gamma = \text{skewness} = M_{c3}/(M_{c2})^{3/2}$$

$$\beta = \text{kurtosis} = M_{c4}/(M_{c2})^2$$

By the linear nature of E{ } the central moments M_{cn} may be expressed in terms of the moments M_n by expanding the arguments as follows:

$$M_{c2} = E\{x^2 - 2x\bar{x} + \bar{x}^2\}$$

$$= E\{x^2\} - 2\bar{x}\, E\{x\} + \bar{x}^2$$

$$= E\{x^2\} - \bar{x}^2$$

$$M_{c2} = M_2 - M_1^2 = \sigma_x^2 \qquad \text{(B.28)}$$

as given in Equation (B.3).

Similarly

$$M_{c3} = M_3 - 3M_2M_1 + 2M_1^3 \qquad \text{(B.29)}$$

$$M_{c4} = M_4 - 4M_3M_1 + 6M_2M_1^2 - 3M_1^4 \qquad \text{(B.30)}$$

etc.

B.3.1.4 Expected Values of Functions of a Random Variable

Consider the arbitrary functions $g_1(x)$ and $g_2(x)$ and constants k_1 and k_2, then by the linearity of E{ } we may write

$$E\{k_1g_1(x) + k_2g_2(x)\} = k_1E\{g_1(x)\} + k_2E\{g_2(x)\} \qquad \text{(B.31)}$$

B.3.1.5 Properties of Gaussian (or normal) Random Variables

A random variable is Gaussian (or normally) distributed if its density function is of the form

$$p(x) = \frac{1}{\sqrt{2\pi}\,\sigma_x} \exp\left(-\frac{1}{2} * \frac{(x - \bar{x})^2}{\sigma_x^2}\right) \qquad \text{(B.32)}$$

as sketched in Figure (B.3a).

It is clear that p(x) is symmetrical with mean, mode and median values coincident (see Figure B.3) and is fully defined by the first two statistical moments, M_1 and M_2 with reference to Equations (B.24) and (B.28), as indicated in Section B.2.1.1.

If x(t) is mean zero the moments may be expressed as

$$M_n = E\{x^n\} = \begin{cases} 1.3 \quad \ldots \quad (n-1)\,\sigma_x^n & \text{for n even} \\ 0 & \text{for n odd} \end{cases} \qquad \text{(B.33)}$$

and the 'absolute' moments are

$$E\{|x|^n\} = \begin{cases} 1.3 \quad \ldots \quad (n-1)\,\sigma_x^n & \text{for } n = 2k \\ \sqrt{2/\pi}\; 2^k.k!\;\sigma_x^n & \text{for } n = 2k+1 \end{cases} \qquad k = \text{integer} \qquad \text{(B.34)}$$

B.3.1.6 Properties of a Random Variable Following the Rayleigh Distribution

The Rayleigh density function is given by

$$p(x) = \frac{x}{\alpha^2} \exp\left(-\frac{x^2}{2\alpha^2}\right) \qquad x \geq 0 \qquad \text{(B.35)}$$

and is sketched on Figure (B.3b). Its moments are

$$M_n = E\{x^n\} = \begin{cases} \sqrt{\pi/2}.1.3 \quad \ldots \quad n\alpha^n & \text{for n odd} \\ 2^k\; k!\alpha^{2k} & \text{for } n = 2k = \text{even} \end{cases} \qquad \text{(B.36)}$$

hence

$$M_1 = \bar{x} = \alpha\sqrt{\pi/2}$$

and

$$\sigma_x^2 = (2 - \pi/2)\,\alpha^2$$

Thus the Rayleigh distribution is an unsymmetrical one-parameter distribution, being fully defined by its first moment, M_1, through α.

B.3.2 MULTIPLE RANDOM VARIABLES

The concepts outlined in this Section are covered in more depth by Papoulis (1965).

B.3.2.1 Multi-variate cdf.

The cumulative distribution for n random variables $x_1(t)$, ..., $x_n(t)$ is defined as

$$P(x_1, \ldots, x_n) = \text{Prob}\{x_1(t) \leq x_1, \ldots, x_n(t) \leq x_n\} \quad \text{(B.37)}$$

This distribution is described as the n-th order multi-variate cdf. of random variables x_1 to x_n.

B.3.2.2 Multi-variate pdf.

The corresponding density function has the same interpretation as in the uni-variate case considered in the previous section and is obtained by differentiation.

$$p(x_1, \ldots, x_n) = \frac{\partial^n P(x_1, \ldots, x_n)}{\partial x_1, \ldots, \partial x_n} \quad \text{(B.38)}$$

and

$$P(x_1, \ldots, x_n) = \int_{-\infty}^{x_1}, \ldots, \int_{-\infty}^{x_n} p(x_1, \ldots, x_n)\, dx_1, \ldots, dx_n \quad \text{(B.39)}$$

with

$$P(\infty, \ldots, \infty) = 1 \quad \text{(B.40)}$$

B.3.2.3 Marginal pdf's

Variables can be integrated out of the multi-variate pdf. as follows

$$p(x_1, \ldots, x_{n-1}) = \int_{-\infty}^{\infty} p(x_1, \ldots, x_n)\, dx_n \tag{B.41}$$

Hence the uni-variate or marginal pdf. of a particular random variable can be obtained from the n-th order multi-variate pdf. for example

$$p(x_1) = \underbrace{\int_{-\infty}^{\infty} \cdots \int_{-\infty}^{\infty}}_{(n-1)\text{fold}} p(x_1, \ldots, x_n)\, dx_2, \ldots, dx_n \tag{B.42}$$

B.3.2.4 Conditional pdf.s

The conditional density function describes the probability of a sub-set of random variables each having a prescribed value when the values of the remaining set of variables are fixed. Hence

$$p(x_1, \ldots, x_k | x_{k+1}, \ldots, x_n) = \frac{p(x_1, \ldots, x_n)}{p(x_{k+1}, \ldots, x_n)} \tag{B.43}$$

is the conditional density of $x_1, \ldots, x_k$ assuming values for $x_{k+1}, \ldots, x_n$.

B.3.2.5 Expected Values of a Function of n-Random Variables

By analogy to the definition of the expected value operator in the uni-variate case, the expected value of function $g(x_1, \ldots, x_n)$ is

$$E\{g(x_1, \ldots, x_n)\} = \underbrace{\int_{-\infty}^{\infty} \cdots \int_{-\infty}^{\infty}}_{n\text{-fold}} g(x_1, \ldots, x_n)\, p(x_1, \ldots, x_n)\, dx_1, \ldots, dx_n \tag{B.44}$$

B.3.2.6 Conditional Expected Values

The conditional expected value of function $g(x_1, \ldots, x_k)$ given the values of $x_{k+1}, \ldots, x_n$ is obtained from the conditional pdf. as

$$E\{g(x_1, \ldots, x_k)|x_{k+1}, \ldots, x_n\} = \underbrace{\int_{-\infty}^{\infty} \int_{-\infty}^{\infty}}_{k\text{-fold}} g(x_1, \ldots, x_k) * p(x_1, \ldots, x_k|x_{k+1}, \ldots, x_n).dx_1, \ldots, dx_k \quad (B.45)$$

B.3.2.7 Independent Random Variables

Random variables $x_1, \ldots, x_n$ are said to be independent if the events $\{x_1(t) \leq x_1\}, \ldots, \{x_n(t) \leq x_n\}$ are independent for any values of $x_1, \ldots, x_n$. If this condition is satisfied.

$$P(x_1, \ldots, x_n) = P(x_1) \ldots P(x_n)$$
$$p(x_1, \ldots, x_n) = p(x_1) \ldots p(x_n) \quad (B.46)$$

and for arbitrary functions $g_i(x_i)$

$$E\{g_1(x_1), \ldots, g_n(x_n)\} = E\{g_1(x_1)\} \ldots E\{g_n(x_n)\} \quad (B.47)$$

It can be shown that Gaussian random variables are independent if they are uncorrelated (see Section B.2.1.3.)

B.3.2.8 Cross-correlation and Cross-covariance

The joint moment $E\{x_1x_2\}$ is the expected value of the product of x_1 and x_2 and, with reference to Section B.2.1.3.

$$E\{x_1x_2\} = R_{x1x2}(0) = R_{12} \quad (B.48)$$

where R_{12} will be defined as the cross-correlation between x_1 and x_2. Similarly, the joint moment $E\{(x_1 - \bar{x}_1)\ (x_2 - \bar{x}_2)\}$, with reference to Section B.2.1.4. is

$$E\{(x_1 - \bar{x}_1)\ (x_2 - \bar{x}_2)\} = C_{x1x2}\ (0) = C_{12} \qquad (B.49)$$

where C_{12} will be defined as the cross-covariance between x_1 and x_2 and $C_{12} = R_{12}$ when $\bar{x}_1 = \bar{x}_2 = 0$.

B.3.2.9 Transformations of Random Variables

Consider the two sets of random variables $y_1(t), \ldots, y_k(t)$ and $x_1(t), \ldots, x_n(t)$ for which the multi-variate density $p(x_1, \ldots, x_n)$ is known, together with the set of functions

$$y_i = g_i(x_1, \ldots, x_n) \qquad i = 1, k \qquad (B.50)$$

The problem to be solved is to determine the multi-variate density of the set $y_1, \ldots, y_k$.

Following the procedure from Papoulis (1965),

If $k > n$, the unknown density is singular and it is necessary to first compute the density of $y_1 - y_n$.

If $k < n$, auxiliary variables must be defined, for example

$y_{k+1} = x_{k+1}, \ldots, y_n = x_n$.

The multi-variate density of $y_1(t), \ldots, y_n(t)$ for a given set of values $y_1, \ldots, y_n$ is obtained by solving the system of simultaneous equations for the values of $x_1, \ldots, x_n$. If this system has a single real solution then

$$p(y_1, \ldots, y_n) = \frac{p(x_1, \ldots, x_n)}{|J(x_1, \ldots, x_n)|} \tag{B.51}$$

where J(.) is the Jacobian of the transformation matrix given by

$$J(x_1, \ldots, x_n) = \text{Det} \begin{bmatrix} \frac{\partial g_1}{\partial x_1}, & \ldots, & \frac{\partial g_1}{\partial x_n} \\ \vdots & & \vdots \\ \frac{\partial g_n}{\partial x_1}, & \ldots, & \frac{\partial g_n}{\partial x_n} \end{bmatrix}$$

Det represents the Determinant and the values of x_i on the right hand side of the equation are expressed as functions of y_i, the solutions of Equations (B.50).

If auxiliary variables are required, they may be removed by integration

$$p(y_1, \ldots, y_k) = \underbrace{\int_{-\infty}^{\infty}, ., \int_{-\infty}^{\infty}}_{(n-k)\text{fold}} p(y_1, \ldots, y_k)\, dy_{k+1}, \ldots, dy_n \tag{B.52}$$

B.3.3 MULTIPLE GAUSSIAN RANDOM VARIABLES

B.3.3.1 Multi-variate pdf.

$$p(x_1, \ldots, x_n) = \frac{1}{(2\pi)^{n/2}\sqrt{\text{Det}[c]}} \exp\left\{-\frac{1}{2}\{x\}\,[c]^{-1}\,\{x\}^T\right\} \tag{B.53}$$

where $\{x\} = (x_1, \ldots, x_n)$

$[c]$ = square matrix of cross-covariances, see Equation (B.49)

$$= \begin{vmatrix} c_{11}, & \ldots, & c_{1,n} \\ c_{n1}, & \ldots, & c_{nn} \end{vmatrix}$$

B.3.3.2 Conditional pdf.s and Moments

The conditional uni-variate pdf.s obtained from the multi-variate Gaussian pdf. are also Gaussian and are, therefore, defined by the corresponding conditional mean and variance. For example, the conditional pdf. of x_0 from the set of random variables $x_0, \ldots, x_n$ is

$$p(x_0|x_1, \ldots, x_n) = \frac{1}{\sqrt{2\pi}\,\sigma_c} \exp\left(-\frac{1}{2}\,\frac{(x_0 - \bar{x}_{oc})^2}{\sigma_{0c}^2}\right) \qquad (B.54)$$

It can be shown that the conditional mean $\bar{x}_{oc}$ is given by

$$\bar{x}_{0c} = E\{x_0|x_1, \ldots, x_n\} = a_1x_1 + \ldots + a_n\,x_n \qquad (B.55)$$

where a_i are obtained from the solution to

$$[R]\,\{a\} = \{R_0\} \qquad (B.56)$$

in which [R] is the matrix of cross-correlations R_{ij} of variables, x_1 to x_n (see Equation B.48)

$\{R_0\}$ is the vector $(R_{01}, R_{02}, \ldots, R_{0n})^T$

$\{a\}$ is the vector $(a_1, \ldots, a_n)^T$

The conditional variance or second central moment, σ_{0c}^2, is

$$\begin{aligned}\sigma_{0c}^2 &= E\{(x_0 - \bar{x}_{0c})^2|x_1, \ldots, x_n\} \\ &= R_{00} - (a_1\,R_{01} + \ldots + a_n\,R_{0n})\end{aligned} \qquad (B.57)$$

and conditional second moment is

$$E\{x_0^2|x_1, \ldots, x_n\} = \sigma_{0c}^2 + \bar{x}_{0c}^2 \qquad (B.58)$$

B.3.3.3 Price's Theorem and Joint Moments

Price's theorem (1958) states that for a set of Gaussian random variables $x_1, \ldots, x_n$ and arbitrary functions $g_1(x_1), \ldots, g_n(x_n)$

$$\left[\frac{\partial^k E\{\prod_{i=1}^{n} g_i(x_i)\}}{\prod_{m=1}^{N} (\partial C_{r_m s_m})^{k_m}}\right] = \left[(-)^{\frac{1}{2}\sum_{m=1}^{n} \gamma k_m}\right] \left[E\{\prod_{i=1}^{n} g_i^{\delta}(x_i)\}\right] \qquad (B.59)$$

where r_m, s_m; $m = 1, \ldots, N$, are integers lying between 1 and n inclusive and are not necessarily discinct;

$C_{r_m s_m}$ is the co-variance of x_{r_m} and x_{s_m} (see Equation (B.49));

k_m are positive integers with $k = \sum_{m=1}^{N} k_m$;

$\delta = \sum_{i=1}^{N} \epsilon_{im} k_m$ where ϵ_{im} is the number of time i appears in (r_m, s_m);

$g_i^{\delta}(x_i)$ denotes the δ-th derivative of $g_i(x)$, taken at x_i; and

$$\gamma = \begin{cases} 1 \text{ when } r_m = s_m \\ 0 \text{ when } r_m \neq s_m \end{cases}$$

This expression has been investigated in the bi-variate domain by Papoulis (1965) who states that for an arbitrary function $g(x_1 x_2)$ the theorem may be expressed as

$$\frac{\partial^n E\{g(x_1 x_2)\}}{\partial C_{12}^{\,n}} = E\{\frac{\partial^{2n} g(x_1 x_2)}{\partial x^n \, \partial y^n}\} \qquad (B.60)$$

Joint or bi-variate moments may be determined by a recursion formula developed from this equation. Consider joint moment $E\{x_1^k\ x_2^r\}$, from Equation (B.60)

$$\frac{\partial E\{x_1^k\ x_2^r\}}{\partial\ C_{12}} = kr\ E\{x_1^{k-1}\ x_2^{r-1}\} \tag{B.61}$$

If $C_{12} = 0$ then x_1 and x_2 are independent, and

$$E\{x_1^k\ x_2^r\} = E\{x^k\}\ E\{x^r\} \tag{B.62}$$

Therefore, integrating Equation (B.61) and using (B.62) we obtain the required formula

$$E\{x_1^k\ x_2^r\} = kr \int_0^{C_{12}} E\{x_1^{k-1}\ x_2^{r-1}\}\ d\ C_{12} + E\{x^k\}\ E\{x^r\} \tag{B.63}$$

B.3.4 PROBABILISTIC CHARACTERISTICS OF THRESHOLD CROSSINGS AND PEAK VALUES

The probability theory covered in the previous sections has been concerned with the characteristics of the basic continuous random variable, x(t) of Figure B.2, enabling solution to questions of the form; what will be the probability that x(t) exceeds a certain threshold level x? or, for what proportion of the time will the magnitude of x(t) exceed x?

In many problems involving continuous random variables additional probabilistic characteristics are required, namely:

1) Threshold crossings - description of the number of times that x(t) crosses a certain threshold x in a given period of time.

2) Peak distributions - description of the number of peaks (positive or negative peaks; maxima or minima; crests or troughs) in x(t) which exceed a certain threshold x in a given period of time.

The following sections outlining these concepts have been extracted from a more detailed account given by Lin (1967) and Bendat (1964).

B.3.4.1 Threshold Crossings

For a continuous random variable, x(t), Lin (1967) has shown that the expected rate of threshold crossing of the level x, E{N(x)}, is given by

$$E\{N(x)\} = \int_{-\infty}^{\infty} |\dot{x}|\, p(x, \dot{x})\, d\dot{x} \tag{B.64}$$

where $p(x, \dot{x})$ is the bi-variate pdf. of x(t) and its first time derivative $\dot{x}(t)$, itself a continuous random variable.

The rate of threshold crossing from below is required in some applications and since, for such crossings, the slope must be positive

$$E\{N^{+}(x)\} = \int_{0}^{\infty} \dot{x}\, p(x, \dot{x})\, d\dot{x}$$

$$= \frac{1}{2} E\{N(x)\} \text{ for stationary random variables} \tag{B.65}$$

B.3.4.2 Threshold Crossings for a Mean-Zero Gaussian Process

If x(t) is stationary and mean zero following a Gaussian distribution, its derivative $\dot{x}(t)$ will be statistically independent of x(t) and using Equation (B.53) the bi-variate pdf. may be expressed as

$$p(x, \dot{x}) = \frac{1}{2\pi\, \sigma_x\, \sigma_{\dot{x}}} \exp\{-\frac{1}{2}(\frac{x^2}{\sigma_x^2} + \frac{\dot{x}^2}{\sigma_{\dot{x}}^2})} \tag{B.66}$$

and

$$E\{N^+(x)\} = \frac{1}{2\pi}\frac{\sigma_{\dot{x}}}{\sigma_x} \exp\{-\frac{1}{2}\frac{x^2}{\sigma_x^2}\} \tag{B.67}$$

The expected rate of zero crossings from below is, therefore, given by

$$E\{N^+(0)\} = \frac{1}{2\pi}\frac{\sigma_{\dot{x}}}{\sigma_x} \tag{B.68}$$

This may be expressed in terms of the relevant spectral density functions since from the Equation (B.17), when $\bar{x} = 0$

$$\sigma_x^2 = R_x(0) = \int_0^\infty G_{xx}(\omega)\, d\omega = m_0 \tag{B.69}$$

and

$$\sigma_{\dot{x}}^2 = \int_0^\infty \omega^2\, G_{xx}(\omega)\, d\omega = m_2 \tag{B.70}$$

Hence

$$E\{N^+(0)\} = \frac{1}{2\pi}\,(m_2/m_0)^{1/2} \tag{B.71}$$

B.3.4.3 Peak Distributions

A positive peak on the time history of x(t) corresponds to the condition of zero slope, $\dot{x}(t) = 0$, and a negative value to the second derivative of x, $\ddot{x}(t)$. Using this criterion, Lin (1967) has shown that the number of positive peaks per unit time of magnitude greater than or equal to x is

$$E\{M(x)\} = -\int_x^\infty \int_{-\infty}^0 \ddot{x}\, p(x, 0, \ddot{x})\, d\ddot{x}\, dx \tag{B.73}$$

and the total number of positive peaks is, therefore

$$E\{M_T\} = -\int_{-\infty}^{\infty}\int_{-\infty}^{0} \ddot{x}\, p(x, 0, \ddot{x})\, d\ddot{x}\, dx \tag{B.74}$$

where $p(x, \dot{x}, \ddot{x})$ is the tri-variate pdf. of $x(t)$ and its first two time derivatives.

The ratio of $E\{M(x)\}$ to $E\{M_T\}$ gives the proportion of the total number of peaks that exceed the threshold level x. Using the heuristic assumption that this ratio may be related to the probability distribution of the peaks, the cdf. of the peaks of $x(t)$ is obtained as

$$P_p(x) = 1 - \frac{E\{M(x)\}}{E\{M_T\}} \tag{B.75}$$

and the corresponding pdf. is

$$P_p(x) = \frac{-1}{E\{M_T\}}\int_{-\infty}^{0} \ddot{x}\, p(x, 0, \ddot{x})\, d\ddot{x} \tag{B.76}$$

B.3.4.4 Peak Distributions for a Mean-Zero Gaussian Process

With the same requirements as those made in Section B.3.4.2. the tri-variate Gaussian pdf. can be expressed, using Equation (B.53), in terms of the variances of $x(t)$ and its first two derivatives, which may be expressed in terms of the spectral density functions using Equations (B.69) and (B.70) and

$$\sigma_{\ddot{x}}^2 = \int_0^{\infty} \omega^4\, G_{xx}(\omega)\, d\omega = m_4 \tag{B.77}$$

The expected total number of peaks per unit time is

$$E\{M_T\} = \frac{1}{2\pi}\frac{\sigma_{\dot{x}}}{\sigma_x} = \frac{1}{2\pi}(m_4/m_2)^{1/2}$$

and the ratio of the number of zero-crossings from below to the number of positive peaks is

$$\alpha = \frac{E\{N^+(0)\}}{E[M_T]} = \frac{\sigma_{\dot{x}}^2}{\sigma_x\,\sigma_{\dot{x}}} = \sqrt{\frac{m_2^2}{m_0\,m_4}} \qquad (B.78)$$

and the spectral bandwidth, defined in Equation (B.19), is

$$\epsilon = (1-\alpha^2)^{1/2} = [(m_0\,m_4 - m_2^2)/(m_0\,m_4)]^{1/2} \qquad (B.79)$$

Wideband Processes

If $\epsilon = 1$, $(\alpha = 0)$ the process is described as being wideband and there are many more positive peaks than zero-crossings.

Narrow-band Processes

If $\epsilon = 0$, $(\alpha = 1)$ the process is described as being narrow banded. Each threshold crossing with positive slope leads to a single positive peak and all positive peaks have positive magnitudes. Under these conditions the peak distribution may be simplified to

$$P_p(x) = 1 - \frac{E\{N^+(x)\}}{E\{N^+(0)\}} \qquad (B.80)$$

Furthermore, for the narrow band case, Lin (1967) has shown that this peak distribution is Rayleigh, as described in Section B.3.1.6., where

$$p_p(x) = \frac{x}{\sigma_x^2}\exp\left(-\frac{x^2}{2\sigma_x^2}\right) \qquad (B.81)$$

B.3.4.5 Approximate Peak Distributions for Non-Gaussian Narrow Band Processes

Equation (B.80) makes no restrictions on the distribution of the underlying narrow band process and can thus be employed when x(t) is non-Gaussian

$$P_p(x) = 1 - \frac{\int_{-\infty}^{\infty} |\dot{x}|\ p(x, \dot{x})\ d\dot{x}}{\int_{-\infty}^{\infty} |\dot{x}| p(0, \dot{x})\ d\dot{x}}$$

to give the narrow band 'type 1' cdf.

A further simplification can be made when x(t) is independent of $\dot{x}(t)$ since

$$p(x, \dot{x}) = p(x)\ p(\dot{x})$$

for which we have

$$E\{N^+(0)\} = p(0) \int_0^{\infty} |\dot{x}|\ p(\dot{x})\ d\dot{x} \tag{B.82}$$

and

$$P_p(x) = 1 - \frac{p(x)}{p(0)} \tag{B.83}$$

termed the 'type 2' narrow band cdf.

where p(0) is the pdf. of x(t) evaluated at x = 0

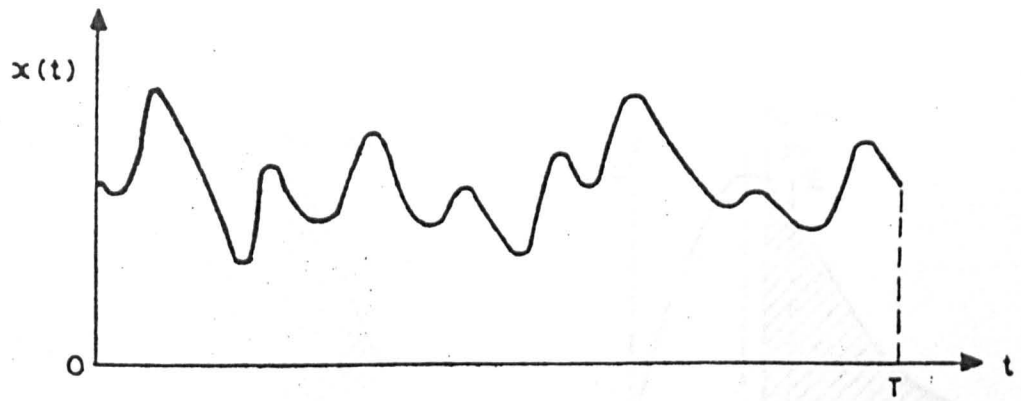

FIGURE B.1 - SAMPLE TIME HISTORY OF RANDOM VARIABLE x

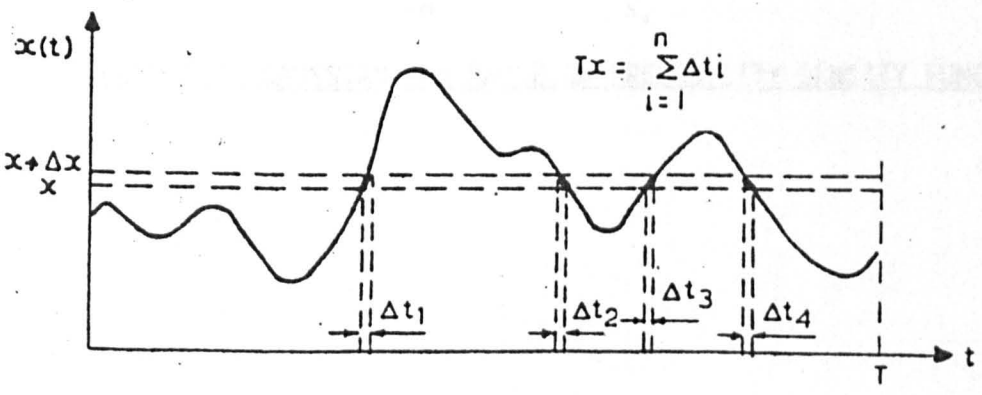

FIGURE B.2 - A CONTINUOUS TIME-VARYING RANDOM VARIABLE x

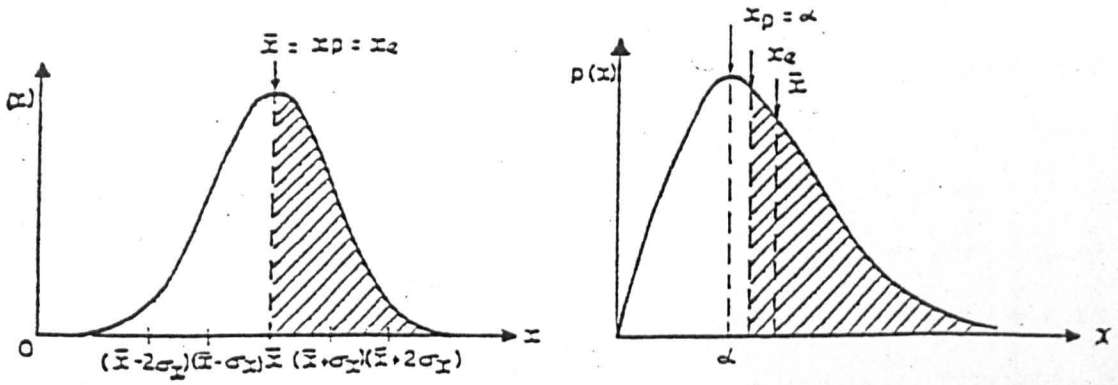

(A) GAUSSIAN pdf. (B) RAYLEIGH pdf.

Mean $\bar{x} = E\{x\}$

Mode x_p represents the peak of the pdf. given by $[dp(x)/dx] = 0$

Median x_e divides the area under the pdf. into two and is given by

$$P(x) = 0.5 = \int_{-\infty}^{x_e} p(x)\, dx = \int_{x_e}^{\infty} p(x)\, dx$$

FIGURE B.3 GAUSSIAN AND RAYLEIGH PROBABILITY DENSITY FUNCTIONS

Appendix C

Statistical Errors in Random Data Analysis

C.1 INTRODUCTION

Records of water particle kinematics, hydrodynamic forces, etc. used in this study are of finite duration (about 17 minutes). Various probability measures such as means, standard deviations, frequency spectra and probability distributions have been calculated from these finite-length records based on the assumption that each one is a sample function (realization) of a stationary and ergodic random process. However, it should be recognised that these statistics are subject to sampling variability, i.e. they vary from one realization to another one. Thus, they only serve as estimators for their corresponding parameters calculated from an ensemble of infinite realizations or a sample record of infinite length. It is, therefore, desirable to establish how close these estimated (from finite-length records) statistics are to their true values (calculated from an infinite length record) by studying their probabilistic properties.

The probabilistic properties of the statistics calculated from finite length records are very complex and the few statements which have been established (Bendat and Piersol, 1971) are somewhat restricted in application. In contrast, these statistics when calculated from statistically independent discrete observations (for example, from a large number of realizations at the same instant) are well established and will be presented in Section C.2. However, a large number of realizations are not practically available. Hence, the best approach is to establish a method to convert each sample record into an equivalent number of statistically independent random observations. An intuitive method is presented in Section C.3. Section C.4 is devoted to the study of the effect of sampling variability on various statistics used in this study, where it is shown that C_d and C_m values are not

significantly affected by sampling variability and hence are reliable. The sampling variability for probability distributions and frequency spectra will be discussed in Sections C.5 and C.6, respectively.

C.2 SAMPLING VARIABILITY OF STATISTICS

Variance of Statistics

The jth order absolute statistical moments of a random process, {x}, are defined as

$$M_j = E[x^j] = \int_{-\infty}^{\infty} = x^j p(x) dx \tag{C.1}$$

where p(x) is the probability density function of the process. The jth order moment may be estimated from a sample of N independent observations of the random process (all at the same instant) as follows

$$\hat{M}_j = \frac{1}{N} \sum_{i=1}^{N} x^j{}_i \tag{C.2}$$

This estimate is unbiased, i.e.,

$$E[\hat{M}_j] = M_j \tag{C.3}$$

Assuming that the observations are statistically independent, the variance of the estimate would simply be (Kendall et al, 1969)

$$var(\hat{M}_j) = \sigma^2(\hat{M}_j) = \frac{1}{N} (M_{2j} - M_j^2) \tag{C.4}$$

In a similar way, the jth order central moments of the random process, {x}, are defined as

$$m_j = E[(x - \bar{x})^j] = \int_{-\infty}^{+\infty} (x - \bar{x})^j \, p(x) \, dx$$

(C.5)

where $\bar{x}$ is the mean of the random process. The cental moments may be estimated from a sample of N independent observations of the random process in the following manner

$$\hat{m}_j = \frac{1}{N} \sum_{i=1}^{N} (x_i - \hat{M}_1)^j$$

(C.6)

and

$$E[\hat{m}_j] \approx m_j$$

(C.7)

The expressions for the variance of the central moments are more complex than those for the absolute moments because the mean itself is subject to sampling variability. An approximate expression is

$$var(\hat{m}_j) \approx \frac{1}{N} (m_{2j} - m_j^2 + j^2 m_2 m_{j-1}^2 - 2j m_{j-1} m_{j+1})$$

(C.8)

From Equations (C.4) and (C.8), the variance of the first four absolute and central moments are

$$\begin{aligned}
var(\hat{M}_1) &= (M_2 - M_1^2)/N = \sigma^2/N \\
var(\hat{M}_2) &= (M_4 - M_2^2)/N \\
var(\hat{M}_3) &= (M_6 - M_3^2)/N \\
var(\hat{M}_4) &= (M_8 - M_4^2)/N \\
var(\hat{m}_1) &= 0 \\
var(\hat{m}_2) &\approx (m_4 - m_2^2)/N = (\beta - 1)\sigma^4/N \\
var(\hat{m}_3) &\approx (m_6 - m_3^2 + 9m_2^3 - 6m_2 m_4)/N \\
var(\hat{m}_4) &\approx (m_8 - m_4^2 + 16 m_2 m_3^2 - 8 m_3 m_5)/N
\end{aligned}$$

(C.9)

The variance of the standard deviation and the coefficient of variation are (Kendall et al, 1969).

$$var\left(\hat{\sigma} = \sqrt{\hat{m}_2}\right) \approx (m_4 - m_2^2)/(4Nm_2) = (\beta - 1)\sigma^2/(4N)$$

$$var(\hat{V} = \hat{\sigma}/\hat{M}_1) \approx \frac{V^2}{N}\left[\frac{m_4 - m_2^2}{4m_2^2} + \frac{m_2}{M_1^2} - \frac{m_3}{m_2 M_1}\right]$$

(C.10)

For Gaussian-distributed populations, the following relationships hold true

$$\begin{aligned}
var(\hat{m}_2) &= 2\sigma^4/N \\
var(\hat{m}_3) &= 6\sigma^6/N \\
var(\hat{m}_4) &= 96\sigma^8/N \\
var(\hat{\sigma}) &= \sigma^2/2N \\
var(\hat{\lambda} = \hat{m}_3/\hat{m}_2^{3/2}) &= 6/N \\
var(\hat{\beta} = \hat{m}_4/\hat{m}_2^2) &= 24/N \\
var(\hat{v} = \hat{\sigma}/\hat{M}_1) &= \frac{v^2}{2N}\left[1 + 2\left(\frac{v}{100}\right)^2\right] \approx \frac{v^2}{2N}
\end{aligned}$$

(C.11)

The variance of the correlation coefficient between two random processes {x} and {y} is

$$var(\hat{\rho}) = \frac{\rho^2}{N}\left[\frac{m_{22}}{m_{11}^2} + \frac{1}{4}\left(\frac{m_{40}}{m_{20}^2} + \frac{m_{04}}{m_{02}^2} + \frac{2m_{22}}{m_{20}m_{02}}\right) - \left(\frac{m_{31}}{m_{11}m_{20}} + \frac{m_{13}}{m_{11}m_{02}}\right)\right]$$

(C.12)

where N is the number of pairs of observations and m_{rs} is defined as

$$m_{rs} = E[(x - \bar{x})^r (y - \bar{y})^s]$$

(C.13)

for the bivariate normal distribution the above equation reduces to

$$var[\hat{\rho}] = (1 - \rho^2)^2/N \qquad (C.14)$$

The above equation indicates that the variance of the correlation coefficient decreases as the correlation coefficient becomes higher.

It is noted that in the above equations, the variance of different statistics are functions of different population parameters, which are usually unknown. However, in a qualitative sense, if the sample size is large, the estimated values of these parameters from the sample, can be used instead of the parameters themselves. It should be obvious that larger samples are needed for estimating the variance of higher order statistics since their variance is dependent on the population moments of twice the order and these high-order moments are very unstable, i.e. they have large sampling variances.

Standard deviation of the sampling distribution of a statistic is referred to as the standard error of that statistic.

Probability distribution of statistics

According to central limit theorem, under very general conditions, the sum of N independent variables, distributed in whatever form, tends to normality as N tends to infinity. Now many of the ordinary statistics can be expressed as the sum of variates, e.g. all the moments, and many others may also be shown to tend to normality for large samples (Kendall et al, 1969). Therefore, in practice the following steps are taken to establish the probability distribution of the statistics:

a) Calculate the mean and the variance of the statistic's sampling distribution using the known values of the statistics from the sample rather than the unknown corresponding population parameter values.

b) Assume that the distribution is normal and hence determine probabilities from the normal integral with the aid of the sampling mean and the sampling variance.

Just how large N must be for the above procedure to be valid is not always easy to say. For some distributions, particularly that of the mean, quite a satisfactory approximation is given by low values of N, say N>30, for others N has to be much higher before the approximation begins to give satisfactory results, e.g. for correlation coefficient even values as high as 500 are not good enough in samples from a normal population. In fact, the form of the parent distribution as well as the statistic considered, influences the rapidity of approach of the sampling distribution to the normal form.

C.3 Equivalent Number of Independent Observations for a Sample Record of Length T

Tickell et al (1982) used the relationships in Section C.2 to calculate the variance of different statistics (moments) from sample records of N = 14538 data points. However, recognising that the data points could not be considered to be independent observations and since their time series had been subjected to low-pass filtering of 3Hz, they argued that the number of data points must be reduced to N = (3/12.76)*14536 = 3418 where 12.76Hz was the digitizing frequency (the author believes that, in the above calculation, the Nyquist frequency of 6.38Hz should have been used rather than the digitizing frequency of 12.76Hz). The above procedure is based on the assumption that the important frequency

range of the analysed signals covers all the frequencies from zero to 3Hz. However, the important frequency range for waves and wave forces are significantly less than 3Hz and hence the above procedure can be unconservative (lead to high estimates of N). The author suggests the following intuitive method for calculating the equivalent number of data points of a sample record based on the following arguments:

a) If the random process {x(t)} has a uniform spectral density between 0 and f_{nyq}, the approximate variance of its estimated mean is $\sigma_x^2/(2*f_{nyq}*T)$ where T is the length of the sample record and σ_x^2 is the variance of the random process (Bendat and Piersol, 1971).

b) If we consider $N = 2*f_{nyq}*T$ independent observations from a random variable {x}, according to Equation (C.9), the variance of the estimated mean is $\sigma_x^2/(2*f_{nyq}*T)$.

c) Comparing (a) and (b), it can be concluded that when the spectral density is uniform between 0 and f_{nyq}, the sample record can be considered to be composed of $N = 2*f_{nyq}*T$ independent data points.

d) when the frequency spectrum, G(f), is not uniform between 0 and f_{nyq}, the equivalent number of independent data points can intuitively be determined according to the following relationship.

$$N_{eq} = \frac{\int_0^{f_{nyq}} \sqrt{G(f)}\, df}{\int_0^{f_{nyq}} \sqrt{G(f_p)}\, df} * 2f_{nyq}\ T = 2T\int_0^{f_{nyq}} \sqrt{G(f)/G(f_p)}\, df \qquad (C.15)$$

where f_p is the frequency at which G(f) is maximum. Examination of the above relationship leads to the following conclusions:

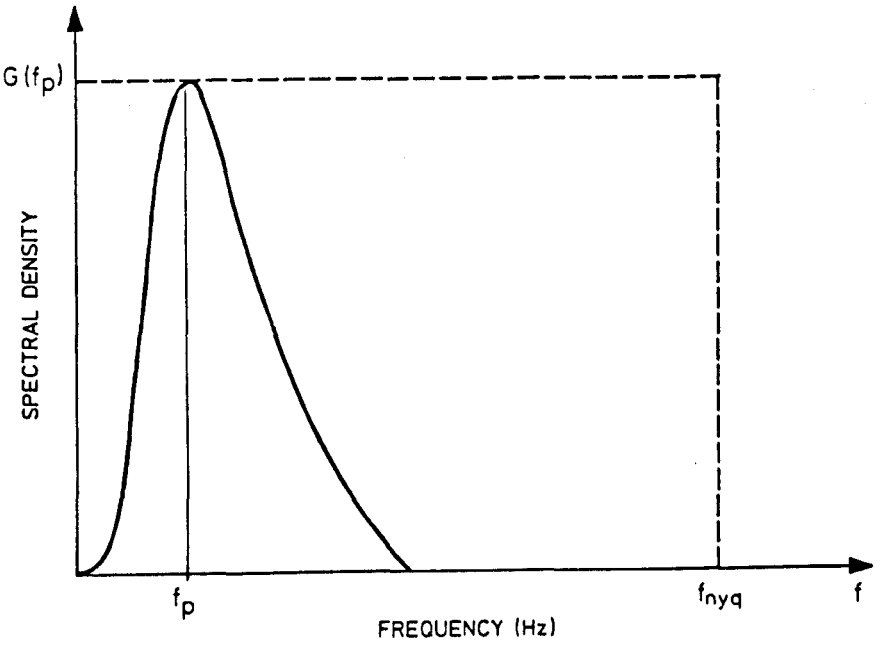

1) The equation takes account of the fact that the upper limit of the important frequency range can be less than the Nyquist frequency. This is because according to the above equation, the contribution of frequencies between the upper limit of the important frequency range and the Nyquist frequency to N_{eq} turns out to be small.

2) the relationship takes account of the shape of the frequency spectrum by giving smaller N_{eq} values for narrow-band spectra in comparison with broad-band spectra. Furthermore, when G(f) is uniform between 0 and f_{nyq}, then $N_{eq} = 2f_{nyq}T$, as expected.

3) the reason for the square root in the above relationship is that the frequency spectrum is proportional to the square of its components' amplitudes.

The above equation is intuitive and there is room for further improvement. For example, it does not account for the position of the peak frequency (of the frequency spectrum) with respect to the Nyquist frequency; that is in its present form, if the frequency spectrum is shifted along the frequency axis as long as its upper limit is below the Nyquist frequency, there will be no change in N_{eq}. It is possible to account for this effect by including an appropriate function of the spectral bandwidth (this is because shifting a given spectrum along the positive frequency axis leads to a reduction in spectral bandwidth). However, further investigation of this topic is beyond the scope of this work.

C.4 EFFECT of SAMPLING VARIABILITY ON DIFFERENT STATISTICS USED IN THIS STUDY

In Section C.3 an intuitive method for determining the equivalent No. of independent data points of a finite-length sample record (N_{eq}) was discussed. Following that method, the equivalent numbers of independent data points for water surface elevation for typical low-intensity and high-intensity runs (Runs 01 and 15) were determined to be 840 and 500, respectively. In view of the similarity between water surface elevation and water particle kinematics' spectra and also because of the approximate nature of the method used in determining N_{eq}, it is assumed that N_{eq} for water particle kinematics are equal to those of the corresponding water surface elevations. A similar study for in-line forces (at Level 3) yields N_{eq} values of 840 and 550, respectively.

Based on these values of N_{eq}, standard errors and confidence bands for various statistics used in this study have been calculated. The results for in-line water particle velocities and in-line forces are presented

in Sections C.4.1 and C.4.2, respectively. In addition, when relevant, comments have been made on the effect of sampling variability of these statistics on C_d and C_m values.

It should be noted that in the following calculations, the parent distributions (i.e. the distribution of an infinite-length record) are assumed to be of the Gaussian form so that the much simpler equations (Equation C.11) can be used in determination of the standard errors. This assumption is justifiable because of the approximate nature of these calculations and also because the deviations of in-line water particle kinematics and hydrodynamic forces from Gaussian distribution are not excessive.

C.4.1 IN-LINE WATER PARTICLE KINEMATICS (X DIRECTION, LEVEL 3)

High-Intensity Runs

The estimated mean and standard deviation of water particle velocity for Run 15 are $\hat{M}_1$ = -0.193 m/sec and $\hat{\sigma}_u$ = 0.823 m/sec. From Equation (C.9), the standard error of the mean is $\sigma(\hat{M}_1) = 0.823/(500)^{1/2} = 0.037$, leading to the following normalised standard error for the sample mean, $\epsilon_r = |\sigma(\hat{M}_1)/\hat{M}_1| = 0.19$. Assuming that the sample mean is Gaussian distributed, the 95% confidence band for $\hat{M}_1$ is, $-0.265 < \hat{M}_1 < -0.120$.

it is observed that the normalised standard error of the mean is large. This may give the impression that the effect of sampling variability of the mean (current) on Morison's coefficients could be significant. However, it should be noted that it is the value of $|\gamma| = |\bar{u}|/\sigma_u = 0.193/0.823 = 0.23$ which is important and since this number is small, even relatively large variations in its value will have a small effect on the resulting C_d and C_m values.

From Equation (C.11), the standard error of the standard deviation is $\sigma(\hat{\sigma}_u) = 0.823/(2*500)^{1/2} = 0.026$ and the corresponding normalised standard error is $\epsilon_r = 0.026/0.823 = 0.032$. The normalised standard error is small and hence the effect of the sampling variability of the standard deviation on Morison's coefficients would be small, too.

From Equation C.11, the standard errors of the skewness and kurtosis for a typical high-intensity run are

$$\sigma(\hat{\lambda}) = (6/500)^{1/2} = 0.109$$

$$\sigma(\hat{\beta}) = (24/500)^{1/2} = 0.219$$

and therefore, the corresponding 95% confidence bands are

$$\hat{\lambda} - 0.21 < \lambda < \hat{\lambda} + 0.21$$

$$\hat{\beta} - 0.43 < \beta < \hat{\beta} + 0.43$$

Low-Intensity Runs

The estimated mean and standard deviation of water particle velocity for Run 01 are $\hat{M}_1 = 0.144$ m/sec and $\hat{\sigma}_u = 0.293$ m/sec. Calculations similar to those for Run 15 leads to the following results: $\sigma(\hat{M}_1) = 0.005$ m/sec; $\epsilon_r = 0.035$ and the 95% confidence band for $\hat{M}_1$ is, $0.134 < \hat{M}_1 < 0.154$. In this case, ϵ_r is small and hence the effect of sampling variability of the mean on Morison's coefficients would be small.

The standard error and the normalised standard error for the standard deviation are calculated to be: $\sigma(\hat{\sigma}_u) = 0.007$ and $\epsilon_r = 0.024$. The normalised standard error is small and hence Morison's coefficients are insensitive to the sampling variability of the standard deviation.

The standard errors of the skewness and kurtosis for a typical low-intensity run are (Equation C.11)

$$\sigma(\hat{\lambda}) = (6/840)^{1/2} = 0.084$$

$$\sigma(\hat{\beta}) = (24/840)^{1/2} = 0.169$$

and therefore, the corresponding 95% confidence bands are

$$\hat{\lambda} - 0.16 < \lambda < \hat{\lambda} + 0.16$$

$$\hat{\beta} - 0.33 < \beta < \hat{\beta} + 0.33$$

C.4.2 IN-LINE HYDRODYNAMIC FORCES (X DIRECTION, LEVEL 3)

High-Intensity Runs

The standard deviation of the in-line hydrodynamic force for Run 15 is 0.168 KN. The standard error and the normalised standard errors are calculated to be $\sigma(\hat{\sigma}_f) = 0.005$ KN and $\epsilon_r = 0.030$. As observed, ϵ_r is small and hence C_d and C_m are not affected by the sampling variability of the standard deviation of the force.

The standard error of the skewness and kurtosis for a typical high-intensity run are

$$\sigma(\hat{\lambda}) = 0.104$$

$$\sigma(\hat{\beta}) = 0.209$$

and the corresponding 95% confidence bands are

$$\hat{\lambda} - 0.20 < \lambda < \hat{\lambda} + 0.20$$

$$\hat{\beta} - 0.41 < \beta < \hat{\beta} + 0.41$$

According to Equations (9.15a) and (9.15b), Morrison's coefficients, when determined from the method of moments, are dependent on the value of $(\beta - 3)$. For Run 15, the estimated value of kurtosis is 4.62, which

corresponds to $(\beta - 3) = 1.62$. C_d is dependent on $(\beta-3)^{1/4}$, whose value for the estimated value of β is 1.13 . The lower and upper limits of the 95% confidence band for β lead to values of 1.05 and 1.19 for $(\beta-3)^{1/4}$. This is equivalent to a few percent variation in the value of C_d, which is not significant. On the other hand C_m is dependent on $(1 - 0.34(\beta-3)^{1/2})^{1/2}$, which is equal to 0.75 for the given value of β. Its value for the lower and upper limits of the confidence band are 0.79 and 0.72, respectively . Again, the variation is not significant and hence C_m values can be considered to be stable.

In the time-domain methods, Morison's coefficients are proportional to the correlation coefficients between hydrodynamic forces and water particle kinematics (Equations 9.72b and 9.73b). Therefore, the effect of the sampling variability of the correlation coefficients on C_d and C_m values must be assessed. In the case of high-intensity runs, the correlation coefficients are in the order of 0.70. From Equation (C.14), the corresponding standard error is $\sigma(\hat{\rho}) = (1-0.70^2)/(500)^{1/2} = 0.023$, when N_{eq} is assumed to be 500. This leads to a normalised standard error of $\epsilon_r = 0.023/0.70 = 0.033$ and the corresponding 95% confidence band will be $0.655 < \rho < 0.745$. Since the normalised standard error is small, It can be concluded that for high-intensity runs, both C_d and C_m values are only slightly affected by the sampling variability of the correlation coefficients and hence are reliable.

Low-Intensity Runs

The standard deviation of the in-line hydrodynamic force for Run 01 is 0.0621 KN. The standard error and the normalised standard errors are calculated to be $\sigma(\hat{\sigma}_f) = 0.00152$ KN and $\epsilon_r = 0.024$, which are very small.

Therefore, the effect of the sampling variability of the standard deviation of the force on the C_d and C_m values is negligible.

The standard error of the skewness and kurtosis for a typical high-intensity run are

$$\sigma(\hat{\lambda}) = 0.084$$

$$\sigma(\hat{\beta}) = 0.169$$

and the corresponding 95% confidence bands are

$$\hat{\lambda} - 0.16 < \lambda < \hat{\lambda} + 0.16$$

$$\hat{\beta} - 0.33 < \beta < \hat{\beta} + 0.33$$

The estimated value of kurtosis for Run 01 is 3.30. The lower and upper limits of the 95% confidence band for β lead to values of 0.0 and 0.89 for $(\beta-3)^{1/4}$. Therefore, the resultant variation in C_d values is large and hence it can be concluded that for the low-intensity runs, C_d values are unstable and unreliable. On the other hand, the lower and upper limits of the 95% confidence band for β lead to values of 1 and 0.85 for $(1 - 0.34(\beta-3)^{1/2})^{1/2}$. Since the variation is not very large, it can be concluded that for the low-intensity runs, C_m values are stable and hence reliable.

In the case of low-intensity runs, the correlation coefficients between hydrodynamic forces and water particle accelerations are high (o.70 or higher). On the other hand, the correlation coefficients between forces and water particle velocities are low (say, 0.20). Again, N_{eq} is conservatively assumed to be 500. As was shown for the case of high-intensity runs, $\rho = 0.70$ leads to reliable C_m values. However, when $\rho = 0.20$, the standard error of the correlation coefficient is $\sigma(\hat{\rho}) =$

$(1-0.20^2)/(500)^{1/2} = 0.043$, leading to a normalised standard error of $\epsilon_r = 0.043/0.20 = 0.21$. The corresponding 95% confidence band will be $0.116 < \rho < 0.284$. As observed, ϵ_r is large and hence for the case of (inertia-dominated) low-intensity runs, C_d values are significantly affected by the sampling variability of the correlation coefficients and hence are unreliable.

C.5 CONFIDENCE INTERVALS FOR CUMULATIVE DISTRIBUTION FUNCTIONS

The cumulative distribution of the sampled data may be compared with the theoretical distribution which has been fitted in some way to the data. In deciding whether to accept the theoretical model ($P_T(x)$), confidence limits are established in the following way (Tickell et al, 1982).

The probability of exceeding a level x_a is

$$Q = \int_{x_a}^{\infty} p_T(x)dx = 1 - P_T(x_a) \qquad (C.16)$$

If we consider a sample of N independent observations from a population with probability distribution $P_T(x)$, on average NQ values in the sample would be found to exceed x_a. However, because of sampling variability, the number of observations exceeding x_a can vary between 0 to N. In terms of the binomial distribution, the probability of observing M values above x_a in a sample of N independent observations when the rate of success for each trial is Q is given by:

$$prob(M) = \binom{N}{M} Q^M (1-Q)^{N-M} \qquad M = o, \ldots, N$$

(C.17)

where $\binom{N}{M}$ is the binomial coefficient defined as

$$\binom{N}{M} = \frac{N!}{(M!)(N-M)!} \qquad (where\ N!\ is\ factorial\ N)$$

(C.18)

Now, if a confidence limit of γ is desired, calculate J such that

$$\gamma = prob(M = NQ) + \Sigma_{I=1}^{J} [prob(NQ - I) + prob(NQ + I)]$$

(C.19)

The above relationship states that the probability of observing K values above x_a, when K is any integer number in the range NQ±J inclusive, is γ. Now if there is (NQ - J) values above x_a in a sample of N observations, the probability of any random observation from the sample (x_i), be less than or equal to x_a is

$$P_u = prob_s(x_i \leq x_a) = 1 - \frac{NQ-J}{N} = (1-Q) + \frac{J}{N} = P + \frac{J}{N}$$
$$= prob_T(x_i \leq x_a) + \frac{J}{N}$$

(C.20)

Similarly, if there are (NQ + J) values above x_a in a sample of N observations, the probability of any independent observation from the sample (x_i) be less than or equal to x_a is

$$p_l = prob_s\ (x_i \le x_a) = 1 - \frac{NQ+J}{N} = 1 - Q - \frac{J}{N} = P - \frac{J}{N}$$
$$= prob_T(x_i \le x_a) - \frac{J}{N}$$

(C.21)

In summary, the probability of having K values above x_a when K is in the range NQ ± J and the population from which the sample of N observations is chosen has a probability distribution of $P_T(x)$, is γ (Equation C.19). On the other hand, from Equations (C.20) and (C.21), the calculated probability from the sample would be in the range P ± J/N. Therefore, the probability of the calculated distribution being out of the range of P ± J/N is (1 - γ). Hence, if the calculated probability deviates from the theoretical probability by more than ± J/N, the hypothesis that P_T is the theoretical distribution is rejected at a level of significance of 1-γ.

It should be noted that in evaluating (C.19) the two components in the summation are not evaluated beyond the limit (NQ - I) = 1 or (NQ + I) = N.

Finally, having computed P_l and P_u about Q, the hypothesis that $P_T(x)$ describes the sample data is rejected at a level of significance of 1-γ if the cdf of the observed data at x_a, $P(x_a)$, lies outside the P_l to P_u range for any x_a within the range of X. Table C.1 (Tickell et al, 1982) gives some typical values for the confidence band as a function of γ and N. These figures have been used in establishing confidence intervals for some of the probability distributions in Chapters 4 and 9.

C.6 CONFIDENCE INTERVALS FOR SPECTRAL ESTIMATES

Spectral estimates obtained from the analysis of records of length T from one random process are subject to sampling variability and hence are different from one record to another. The distribution of each spectral estimate is approximately equal to a chi-square distribution, x_n^2, with two degrees of freedom (Bendat and Piersol, 1971). This means that the standard deviation of the spectral estimate is equal to its mean and hence the accuracy is poor. It is important to recognise that increasing the record length does not lead to an improved accuracy in the spectral estimates. It only increases the number of spectral components between 0 and the Nyquist frequency. In other words, the spectral bandwidth (1/T = the distance between two successive spectral components) decreases.

In practice, the random error of a spectral estimate is reduced by smoothing the calculated spectrum in two different ways. The first way is to smooth over an ensemble of estimates. This can be done by computing individual estimates from q independent sample records and averaging the q spectral estimates at each frequency. The second way is to smooth over frequency. This can be done by averaging together the results for r adjacent spectral components obtained from a single record. Of course the two methods can be combined so that the resultant smoothed spectral estimates are chi-distributed with n=rq degrees of freedom. It should be noted that the latter procedure leads to an increase in effective bandwidth, that is, $\Delta f' = r\Delta f = r/T$.

Once the distribution of the spectral estimates are known, their confidence intervals can be determined by referring to appropriate tables. The $(1 - \alpha)$ confidence interval is given by

$$\frac{n\hat{G}(f)}{\chi^2_{n:\alpha/2}} \leq G(f) \leq \frac{n\hat{G}(f)}{\chi^2_{n:1-\alpha/2}}$$

(C.22)

where $\hat{G}(f)$ and $G(f)$ refer to sample and ensemble frequency spectra, respectively. In this study six segments of each record have been Fast-Fourier transformed (q=6) with five point frequency smoothing (r=5). Thus spectra have 60 degrees of freedom (Tickell and Burrows, 1989) and the 95% confidence intervals are

$$\frac{60}{83.30}\hat{G}(f) \leq G(f) \leq \frac{60}{40.48}\hat{G}(f)$$

o r

$$0.72\ \hat{G}(f) \leq G(f) \leq 1.48\ \hat{G}(f).$$

(C.23)

The above relationship has been used to establish 95% confidence bands for typical frequency spectra in Chapters 4 and 9.

γ=0.9	P_T 0.5	P_T 0.8	P_T 0.9	P_T 0.95	P_T 0.99	P_T 0.995	P_T 0.999	P_T 0.9995
N	P_ℓ P_u	P_ℓ P_u	P_ℓ P_u	P_ℓ P_u	P_ℓ P_u	P_ℓ P_u	P_ℓ P_u	P_ℓ P_u
250	0.448 0.552	0.760 0.840	0.868 0.932	0.928 0.976	0.976 1.0	-	-	-
500	0.463 0.537	0.770 0.830	0.878 0.922	0.934 0.966	0.982 0.998	0.988 1.0	-	-
1000	0.474 0.526	0.779 0.821	0.884 0.916	0.939 0.961	0.985 0.995	0.991 0.999	-	-
5000	0.4883 0.5117	0.7907 0.8093	0.8930 0.9070	0.9449 0.9551	0.9876 0.9924	0.9934 0.9966	0.9982 0.9998	0.9988 1.0
10000	0.4917 0.5082	0.7934 0.8066	0.8950 0.9049	0.9464 0.9536	0.9884 0.9916	0.9938 0.9962	0.9985 0.9995	0.9991 0.9999
15000	0.4933 0.5067	0.7946 0.8054	0.8960 0.9040	0.9471 0.9529	0.9887 0.9913	0.9941 0.9959	0.9986 0.9994	0.9993 0.9998
γ=0.95	P_T 0.5	P_T 0.8	P_T 0.9	P_T 0.95	P_T 0.99	P_T 0.995	P_T 0.999	P_T 0.9995
N	P_ℓ P_u	P_ℓ P_u	P_ℓ P_u	P_ℓ P_u	P_ℓ P_u	P_ℓ P_u	P_ℓ P_u	P_ℓ P_u
250	0.440 0.560	0.752 0.848	0.864 0.936	0.924 0.980	-	-	-	-
500	0.456 0.544	0.764 0.836	0.874 0.926	0.930 0.970	0.982 0.998	-	-	-
1000	0.469 0.531	0.775 0.825	0.881 0.919	0.937 0.963	0.984 0.996	0.991 0.999	-	-
5000	0.4861 0.5139	0.7889 0.8111	0.8917 0.9083	0.9440 0.9560	0.9872 0.9928	0.993 0.997	0.9982 0.9998	-
10000	0.4902 0.5098	0.7922 0.8078	0.8941 0.9059	0.9457 0.9543	0.9881 0.9919	0.9936 0.9964	0.9984 0.9996	0.9991 0.9999
15000	0.4912 0.5080	0.7936 0.8064	0.8952 0.9048	0.9465 0.9535	0.9884 0.9916	0.9939 0.9961	0.9985 0.9995	0.9992 0.9999

TABLE C.1
DISTRIBUTION-FREE CONFIDENCE LIMITS FOR CUMULATIVE DISTRIBUTIONS

(Tickell et al, 1982)